Insights into temperature controls on rockfall occurrence and cliff erosion

IGNACIO EDUARDO IBARRA-COFRE

Insights into temperature controls on rockfall occurrence and cliff erosion

Ignacio Eduardo Ibarra Cofré

Thesis submitted in partial fulfilment of the requirements for the University of Durham for the degree of Doctor of Philosophy

Department of Geography
Durham University

2023

This page is intentionally left blank

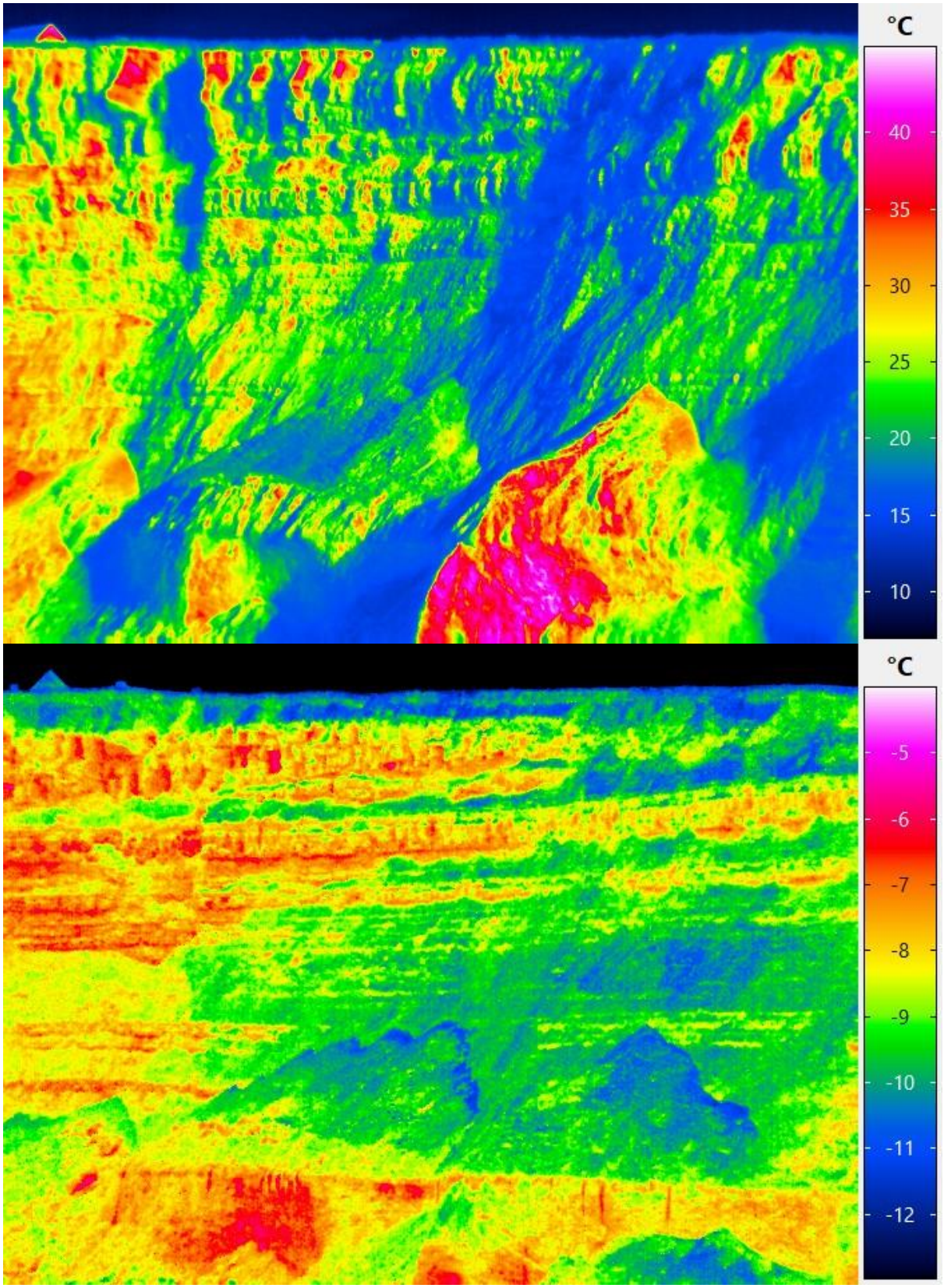

Cover images: Thermal imagery of the East Cliff of Whitby, UK, captured during high-resolution Infrared Thermography monitoring of the cliff face. The upper image shows the time in which the maximum surface temperatures were detected (14th of July 2023 at 14:00 h). The lower image shows the time in which the minimum surface temperatures were observed (13rd of February 2023 at 08:00 h).

This page is intentionally left blank

Declaration

I confirm that no part of the material presented in this thesis has previously been submitted for a degree in this or any other university. In all cases the words of others, where relevant, have been fully acknowledged.

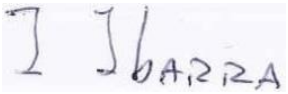

Ignacio Ibarra

Durham University

March 2023

This page is intentionally left blank

Abstract

A variety of environmental triggers have been associated with the occurrence of rockfalls however their role and relative significance remains poorly constrained. This is in part due to the lack of concurrent data on rockfall occurrence and cliff face conditions at temporal resolutions that mirror the variability of environmental conditions, and over durations for large enough numbers of rockfall events to be captured. The aim of this thesis is to fill this data gap, and then to specifically focus on the role of temperature in triggering rockfall that this data illuminates. To achieve this, a long-term multiannual 3D rockfall dataset and contemporaneous Infrared Thermography (IRT) monitoring of cliff surface temperatures has been generated. The approaches used in this thesis are undertaken at East Cliff, Whitby, which is a coastal cliff located in North Yorkshire, UK. The monitored section is ~ 200 m wide and ~65 m high, with a total cliff face area of ~9,592 m². A method for the automated quantification of rockfall volumes is used to explore data collected between 2017–2019 and 2021, with the resulting inventory including >8,300 rockfalls from 2017–2019 and >4,100 rockfalls in 2021, totalling > 12,400 number of rockfalls.

The analysis of the inventory demonstrates that during dry conditions, increases in rockfall frequency are coincident with diurnal surface temperature fluctuations, notably at sunrise, noon and sunset in all seasons, leading to a marked diurnal pattern of rockfall. Statistically significant relationships are observed to link cliff temperature and rockfall, highlighting the response of rock slopes to absolute temperatures and changes in temperature. This research also shows that inclement weather constitutes the dominant control over the annual production of rockfalls but also quantifies the period when temperature controls are dominant. Temperature-controlled rockfall activity is shown to have an important erosional role, particularly in periods of iterative erosion dominated by small size rockfalls. As such, this thesis provides for the first high-resolution evidence of temperature controls on rockfall activity, cliff erosion and landform development.

Acknowledgments

I would like to say thank you very much indeed, for everything, to Prof. Nick Rosser and Prof. Matt Brain, who have been the supervisors of this thesis. In fact, this investigation would not be possible at all without both, as they have been de designers and developers of the COBRA project, from which the resources to buy all the expensive equipment and so, the possibility to collect the original datasets presented here come from. Importantly, thanks for the key scientific insights, curiosity, unvaluable support and willingness to guide this work. I would also like to say thanks for everything I learnt with both, for instance, for the understanding gained related to the nature of a PhD research and many other aspects, such as on how to think and conduct an original investigation, how to best show and analyse the results, and much more, which in turns, made of myself a better professional. Apart from the professional aspect, I will always remember and miss the funny moments and laughs that we had, indeed, countless of times. The last aspect, for some people perhaps an important aspect of life, helped me a lot to move through the hardest moments of this investigation (very frequent and long lasting), which for sure had a positive effect to reach the end of this research marathon. Equally importantly, I would like to thanks for their solidarity, key human values sometimes missing in this times. Also, thanks for their patience with my spoken and written English! as I am aware that I gave lots of headaches to both! As the words can be blown by the wind, I reiterate here my gratitude to both, a gratitude that I will bring for sure with myself to the next life.

I would like to say thanks to the internal and external examiners of this thesis, Profesor Daniel Donoghue (Durham University) and Dr. Brian Collins of the US Geological Survey for their time and interest in reading this thesis, for the interesting discussions during the viva, and for helpful comments and corrections that greatly improved the thesis.

Lots of thanks to Sam and Dave, for all the support during fieldwork activities, for the key help and patience in the testing, installation and maintenance of the used equipment, and perhaps most important, for all the funny and long conversations we had while driving to Whitby, the countless radio songs we enjoyed listening planet rock, and for the countless fish and chips we had. Thanks a lot to Kathy Wood, Neil, Chris, Michael and Merv for all the support and always enjoyable conversations in the corridors of the Department of Geography.

Thanks to all friends I have had the pleasure to find in this process, for the support, funny moments and lots of pints we had in Durham pubs, specially Rodrigo & Ale, Gopi, Felipe, Burag, Shobhit, Ikenna, Marisa, Sophie, Ian, Harry, Belén, Ritwika, Miklos, Christina and Ayushman.

Thanks to the Ustinov Football boys 2018-2019, of which I had the pleasure to be one of the Capitans during one season. Thanks to the friends of all life, to those supporting from the distance, specially Mr. Ayala, Covos, Gastón, Nacho Pérez, Rafa. Tomás and Isa.

Special thanks to Dad, Mom, Caco, Andresito, Amanda and Yayita. For their always constant and background support along this process. Special thanks to Dad and Mom, as without your support and efforts I wouldn't have the opportunity to get an undergraduate education, thus, I wouldn't be reaching this qualification. Thanks for listening specially in the hardest moments. Lots of thanks to Daniela & Nacho Loyola, tío Polo, tía Margarita, tío Miguel, tía Ceci and Prof. Carmen Paz for their sincere support too.

Finally, my deepest thanks to the love of my life, Katherine, for your deep understanding, constant support, and patience. For the many efforts made. For your comprehension in the many hours that we lost. For your deep solidarity and constant company through this process, which gives spring colors, life, and deep happiness to every hour of my life. Thanks for your support during countless pandemic nights when the noisy ventilators of my computers took place due doe to the heavy data processing! And so, thanks for being a source of constant motivation and vital energy in this process as well as in many others too…

Dedication

Again, with love to:

Katherine & Maite

Contents

List of Figures

Chapter 1 - Introduction

Chapter 2 – Methodological development for 4D quantification of rockfall activity

Chapter 3 – Geomorphic behaviour of the 4D rockfall activity and cliff erosion

Chapter 4 – Evaluating cliff surface temperatures using high-frequency Infrared Thermography

Chapter 5 – The characteristics of cliff surface temperatures changes through time

Chapter 6 – Exploring controls on rockfall

List of Tables

Chapter 5 – The characteristics of cliff surface temperatures through time

Chapter 6 – Exploring controls on rockfall

Chapter 1 – Introduction

1.1 Rationale for research - overview

Rockfalls occur in steep rock-slope settings; they are a key agent of landform change and sediment production, and are a significant hazard (Guzzetti et al., 1999; Dussauge-Peisser et al., 2002; Chau et al., 2003; Fell et al., 2008; Matsuoka, 2019; de Vilder et al., 2019). Rock slope susceptibility to failure is a function of its intrinsic properties, such as the cohesional strength of intact rock bridges (Jennings, 1970; Hoek and Bray, 1981), the form and strength of discontinuities (Einstein et al., 1983; Goodman and Shi, 1985), and its morphometric setting (e.g., Matsuoka and Sakai, 1999; Sass, 2005; Martel, 2006; Messenzehl et al., 2017). Rockfalls can occur rapidly in response to triggering mechanisms that create abrupt changes in stress conditions, such as those resulting from heavy rainfall (e.g., Veveakis., 2007; Delonca et al., 2014; D'Amato et al., 2016; Leyva et al., 2022; Birien and Gauthier, 2023) and/or strong earthquake ground shaking (Keefer et al., 1987; Iverson, 2000; Marzorati et al., 2002; Stoffel et al., 2019; Zhen et al., 2022). In addition, rock-slope susceptibility to failure can develop over annual to decadal and multi-centennial timescales in response to mechanisms that induce an incremental yet cumulative reduction in the cohesional strength of rock bridges via subcritical cracking (Gunzburger et al., 2005; Collins and Stock, 2016; Eppes and Keanini, 2017), microseismicity (e.g., Rodrıguez et al., 1999; Yagoda-Biran et al., 2010; Brain et al., 2014; Arosio et al., 2018; Feng et al 2021), tidal and wave energy inputs (e.g., Rosser et al., 2007; Lim et al., 2011; Norman et al., 2013; Vann Jones et al., 2015; Williams 2017), and salt weathering (Grossi et al., 2011; Lawrence., 2013). Cumulatively, these processes can result in failure of a rock slope (manifest as rockfalls) when rock-mass strength has been incrementally reduced to values lower than those of the in-situ stresses (Finlayson and Statham, 1980; Julian and Anthony, 1996; Gunzburger et al., 2005).

Many of the processes that drive progressive weakening of rock-mass strength are linked to climate and weather; for example, freeze-thaw of interstitial water and along discontinuities (e.g., Williams, 1995; Murton et al., 2006; Matsuoka, 2008), and ambient temperature variations causing thermal-stress cycling (e.g., Collins et al., 2018), can result in subcritical cracking and, ultimately, macro-scale rock fracture. Whilst the role of high-magnitude, low-frequency storm events on increased rock-slope erosion has been documented (e.g., Williams 2017, Benjamin 2018), the role and relative significance of temperature in driving shallow rock slope failures is currently poorly constrained. Establishing the link, if any, between temperature and rockfall occurrence is a key research goal because all areas of UK, for example, are projected to show an

increased likelihood of (i) warmer, wetter winters; (ii) hotter, drier summers; and (iii) an increase in the frequency and magnitude of extreme events, notably heavy precipitation (UKCP18, 2021). Indeed, by 2070, under the lower and higher emissions scenario (10% and 90% probability levels, respectively), average temperatures in the UK are expected to increase by in 1.3 - 5.1°C in the summer and 0.6 - 3.8 °C in winter (UKCP18, 2021). There is therefore a pressing need to obtain representative rockfall inventories to understand and model the erosional response of cliffs to rapidly changing environmental forces due to inclement weather conditions and/or temperatures (Trenhaile, 2011) and, in turn, constrain whether rockfall activity is temperature controlled.

An acceleration in the rate of cliff recession via rockfalls is anticipated under projected climate change (Gilham et al., 2019), though there is currently limited empirical/mechanistic insight and/or conceptual grounding. A conceptual figure of the potential effect of climate change on rockfall occurrence and resultant cliff erosion by season is proposed in Figure 1.1, which is used here to show that the overall pattern and volume of eroded material may differ in a scenario of increased likelihood of (i) warmer, wetter winters, and (ii) hotter, drier summers. Figure 1.1 shows a schematic view of the magnitude and frequency of rockfalls during a one-year monitoring period under current climate conditions (blue data series). In this example, large rockfalls typically occur in winter, spring, and autumn due to inclement weather, producing stepped increments in the cumulative curve of monitored rockfall volumes (Williams, 2017). Here, three events of large magnitude punctuate three main periods of background erosion, which are represented by lower gradients in the cumulative erosion curve. However, under projected climatic conditions, an increase in the frequency and magnitude of extreme events (including winter storms and summer heat waves) may cause an increase in magnitude and frequency of total rockfall volume loss, particularly during winter but also in the summer months due to heat waves (Gruber et al., 2004; Saas et al., 2012; Moore and Mclnnes, 2020); the latter may be manifest as a higher rate of cumulative erosion, punctuated by more frequent large rockfall events (red data series). Using a representative and appropriate rockfall dataset, these curves could be empirically defined, including as-yet unconstrained feedbacks, providing greater insight into the erosive efficacy of different driving mechanisms.

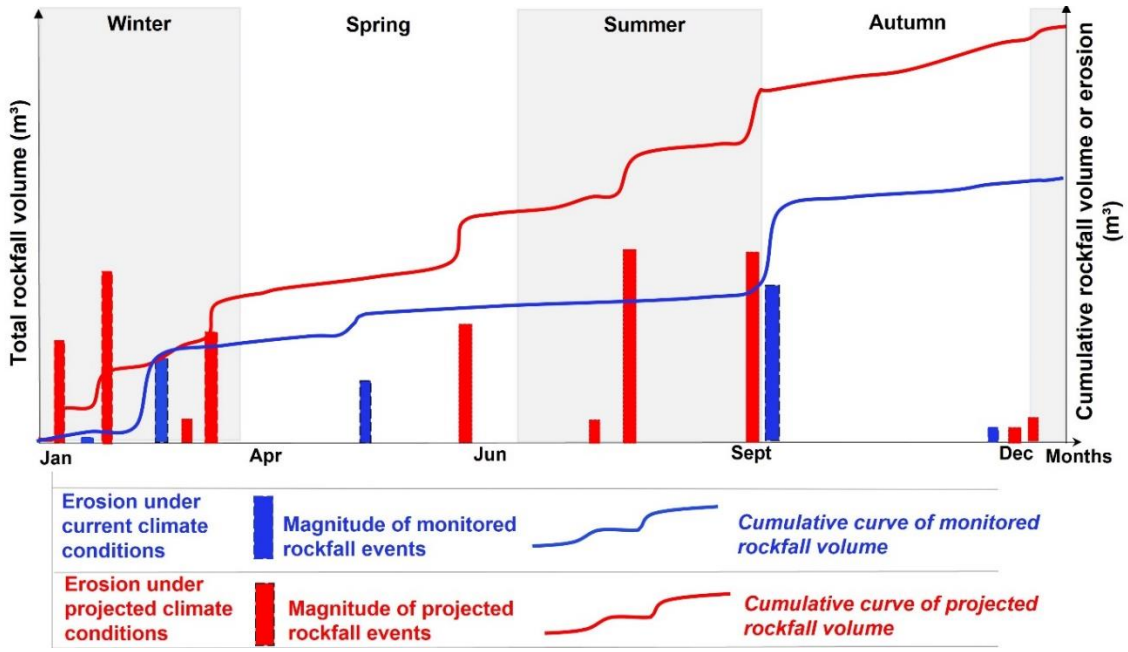

Figure 1. 1: *Conceptual figure of the expected effect of climate change on rockfall activity and cliff erosion.*

Current discrepancies in the scales and frequencies of monitoring data that describe temperature effects on rock-slopes (e.g., Sass and Oberlechner, 2012; D'Amato et al., 2016; Williams, 2017; Birien and Gauthier, 2022) limit our understanding of temperature controls on rockfall activity and longer-term erosion ($\geq 10^0$ years of observations). Critically, the limited frequency of monitoring makes associations with triggers, beyond seasonal variability, difficult to assess (e.g., Sass and Oberlechner, 2012; D'Amato et al., 2016; Van Veen et al., 2017; Dietze et al., 2020; Birien and Gauthier, 2022). Quantifying the rockfall activity using long-term and high-frequency monitoring can be of crucial importance to constrain thermal controls on rockfall occurrence and cliff erosion, to improve the accuracy of modelling projections, and to support the resilience of coastal communities and engineering structures in a changing climate (Mclnnes and Moore, 2011; Moore and Mclnnes, 2020). However, we lack an appropriate methodological approach to obtain concurrent data on rockfall occurrence and cliff-face temperature conditions. Recently, high-frequency (hourly to diurnal) monitoring of rockfalls has been undertaken (Williams, 2017). In conjunction with research that addresses the nature, rate, scale and causes of microcracking (e.g., Eppes et al., 2010; 2015; 2016), there are indications of a thermal effect on rock cracking, but this has to date only been assessed using proxies such as air temperature and/or isolated measurements of rock-surface temperature using, for example, thermocouples. This limit understanding of the full range and distribution of surface temperature conditions and thermal variability across, for example, a whole cliff face. In addition, such approaches rarely consider a period of time of sufficient duration to capture a large number of rockfalls in a range of environmental conditions sufficient to determine process-response relationships. The aim of this

research is therefore to improve understanding of temperature controls on rockfall occurrence and cliff erosion. To achieve this aim, this research uses both long-term (≥ 1 year) terrestrial laser scanner (TLS) and Infrared Thermography (IRT) monitoring, at high-frequency (1 h).

The following sections provide an overview of the current state of knowledge regarding temperature influences on rock expansion and contraction (Section 1.1.1), microcrack growth (Section 1.1.2), physical controls on rock surface temperatures (Section 1.1.3), and the challenges associated with monitoring rockfall activity and surface temperatures using long-term continuous monitoring (Section 1.1.4), providing further rationale for this thesis.

1.1.1 Thermal influences on rock expansion and contraction

Records of 'spontaneous' rockfall and displacements along discontinuities that did not correspond with any commonly studied trigger event (e.g., seismic loading, precipitation, wave and tides, and wind) have been reported in, for example, France (Gunzburger et al., 2005), Slovakia (Vlcko et al., 2009), Switzerland (Gischig et al., 2011a, b), Japan (Mufundirwa et al., 2011), Brazil (Do Amaral Vargas et al., 2012), UK (Williams, 2017), and USA (Collins et al., 2018). The timing and pattern of such ostensibly enigmatic failures and displacements along discontinuities may result from solar-heating effects, which can generate outward expansion and contraction of rock via conduction in accordance with Fourier's law, driving mechanical changes as a function of thermal expansion (Gunzburger et al., 2005; Collins and Stock, 2016). For example, using high-precision total-station surveying to assess rock deformation and through correlation with monitored air temperature at Rochers de Valabres gneiss slope (France's Southern Alps), Gunzburger et al., (2005) noted that the largest slope surface displacements occurred at around 18:00 h, after slow cooling before sunset, and with a delay of approximately 3 hours with respect to the highest temperature (23°C) recorded in the mid-afternoon. Importantly, displacements tended to occur during periods when rates of temperature change were highest.

Similarly, Vlcko et al., (2009) examined slope deformation in a castle in Slovakia, using crack-gauge monitoring and explored further with 2D slope stability models. Crack monitoring data highlighted key trends in fracture behaviour that occurred in response to ambient temperature. Crack closure was observed to occur in winter months, characterised by temperatures between 0 and -10°C. In contrast, crack widening was observed during the summer months, particularly at times of maximum observed temperature (~30°C).

Seasonal and diurnal temperature variations that are sufficient to trigger cyclic and cumulative opening of cracks were noted by Collins and Stock (2016), using data from 3.5 years of fracture monitoring of a granitic exfoliation sheet in California (USA). Outward deformation at the mid-zone of the exfoliation sheet averaged 8 mm d^{-1}, with a maximum of 13 mm d^{-1}. Notably, maximum outward deformations took place during the afternoon (~13:00 to 16:00 h) when temperatures were highest. Conversely, maximum inward deflection of the sheet occurred during the mid-morning when temperatures were still low (~07:00 to 09:00 h). Overall, the exfoliation sheet deformed synchronously with light intensity and temperature, suggesting that some rock-slope failures might be more likely to occur in hot summer months, when exfoliation sheeting joints achieve their maximum aperture. Significantly, the maximum range of diurnal dislocation did not correlate with the warmest time of the year, but rather with the highest daily temperature range.

Using observations of seasonally variable discontinuity deformation rates at Randa, southern Switzerland, Gischig et al., (2011a) modelled thermo-elastic deformations using a simplified 2D slope geometry. The results showed that, by simulating 10 years of sinusoidal cycles of temperatures between -15 and 15 °C, shear displacement along joints can have both a reversible component controlled by discontinuity compliance, and an irreversible component that promotes failure. However, Gischig et al., (2011a) noted that the efficacy of thermomechanical controls was defined by rock-slope kinematics. For instance, for a toppling failure, the normal stress on joints reduced as the rock cools and contracted during winter, which promoted failure. Conversely, in summer, the rock warmed and expanded and so normal stress along joints increased, preventing failure. The opposite seasonal effect occurred for planar sliding: the shear stress on joints increased in summer as rock-mass expanded, hence, failure was observed to occur more readily during summer. By contrast, in winter, as the rock contracted, the shear stress along the sliding surface declined, inhibiting planar failure.

Overall, to date, a growing body of research has provided evidence that the effects of temperature control rock expansion and contraction. In turn, this demonstrates that, regardless of the geologic and morphoclimatic setting, cyclical thermal stresses can have an effect on discontinuity displacements and, ultimately, slope failures (e.g., Gischig et al., 2011b; Mufundirwa et al., 2011; Bakun-Mazor et al., 2013; Greif et al., 2017; Collins et al., 2018; Marmoni et al., 2020; Fiorucci et al., 2020). However, there is a lack of reliable evidence on if and how thermally-induced rock expansion and contraction may be reflected in the occurrence of smaller-scale rockfall events that may be dominated by loss of cohesion and rock-bridge fracture (de Vilder et al., 2017) in response to, and during, a range of cliff-face and ambient environmental conditions.

1.1.2 Thermal influences on microcrack growth

The initial stage of physical weathering of rocks is the development of incipient microcracks (i.e., fractures having lengths less than 0.1 mm; Anders et al., 2014), which are critical in permitting all other types of subsequent weathering mechanisms to occur (Eppes et al., 2010). It has been demonstrated that cracks propagate subcritically (i.e., steadily, slowly and in a dispersed manner, such that macroscale fracture does not result) and at stresses much lower than critical stresses such as the crack damage threshold (Anderson, 2005). Significantly, the environmental regime in terms of temperature and moisture strongly control the velocity of subcritical cracking, which preferentially exploits microstructural predispositions, particularly grain boundaries, petrological structures, pore spaces and microscopic flaws (Anderson, 2005; Eppes and Keanini, 2017).

All cracks, either subcritically or critically, develop due to stresses that arise at fracture tips, where molecular bonds must be broken for fractures to grow and coalesce (Eppes and Keanini, 2017). Once a critical stress intensity factor is exceeded, various physical and chemical mechanisms act at crack tips to develop cracks (Anderson, 2005). All of them include stressed microfractures that grow due to chemical reactions between pore water and the fractured solids (Atkinson, 1984; Brantut et al., 2013). It has been proposed that these chemical reactions are efficient at crack tips where crystal lattice bonds are stretched and weakened, permitting the chemical reactions to take place there. As a result, environmental conditions such as temperature and water availability can influence chemical reactions, controlling the cracking growth rates (Eppes and Keanini, 2017; Voigtländer et al., 2018).

Analysis of subcritical cracking activity using acoustic emissions combined with strain, moisture and temperature monitoring has been used to examine the consequences of solar-induced thermal stress on an isolated granitic boulder, for 4 and 11 months of surveying by Warren et al., (2013) and Eppes et al., (2016), respectively. Seasonally, the timing of cracking activity clustered in summer and winter. Both studies observed two main clusters of activity occurring during midday and sunset (around 13:00 and 18:30 h, respectively). Overall, 82% of all cracking events took place in two ±3 hours periods with respect to the diurnal temperature cycles, with a third cluster occurring around midnight. Also, most events occurred after storms or other weather events, suggesting that moisture plays a key role as a catalyst for microcracking. The strain data showed that when the boulder was cooled and warmed, the maximum primary strain on the surface fell and rose, respectively, revealing cyclic elastic expansion and contraction. This pattern was also observed by Vlcko et al., (2009) and Collins and Stock (2016). Overall, these data suggested that cyclical diurnal to seasonal variations in thermal stresses are sufficient to create

slow, subcritical crack development, and also to efficiently lower the stress threshold for microcracking by other weathering processes, which in turn can increase mechanical weathering, weakening the rock (Eppes et al., 2016).

Regarding solar-induced thermal stress acting on desert pavement rocks, a statistically significant portion of sub-vertical to vertical cracks on surface clasts analysed at California, New Mexico, Arizona, Mojave, Strzelecki and Gobi deserts, are aligned in an approximately north-south orientation (azimuth from 2 to 33°), referred to as meridional cracks: fractures with orientations not readily attributable to rock shape or fabric (McFadden et al., 2005; Eppes et a., 2010). It has been hypothesized that these meridional fractures result from tensile stresses that arise within the rock mass due to strong radial gradients created by the directional diurnal cooling and heating of the rock surface (McFadden et al., 2005). Furthermore, tensile stresses are often reported to be efficient for creating a rock fracture (McFadden et al., 2005). However, rock size, surface age and latitude have been shown to have a significant role in controlling rock cracking driven by diurnal temperature changes (Eppes et al., 2010). Importantly, it has been suggested that very cold temperatures and strong diurnal rates of temperature change may promote crack growth during winter, given the greater potential for intense and rapid heating during sunrise (Eppes et al., 2010).

The influence of solar-induced thermal stress on mechanical breakdown of clasts has also been found in humid-temperate climates, such as in North Carolina and Pennsylvania (Aldred et al., 2015). However, crack densities were reported to be higher on north-facing surfaces of clasts and in humid forested areas, further suggesting that together with temperature, moisture availability also has an influence on crack development (Aldred et al., 2015). Martian directional cracks on surface boulders have been observed using Mars Exploration Rover images (Eppes et al., 2015). Cracks showed orientations similar to those found in mid-latitude deserts, which demonstrate that both critical and subcritical fracture growth direction is strongly linked to the direction of the solar-induced applied stress (Eppes et al., 2015). Therefore, as thermal (and moisture) influences on crack growth play key roles in the physical weathering and weakening of the rock, it is therefore possible that the cyclical thermal influences on cracking are also key mechanism that can result in rockfall activity. However, to date, it is unknown if and how the above processes may result in differences in the rate and magnitude of rockfall and, ultimately, cliff erosion. To address this, both long-term and high-frequency rockfall inventories and cliff temperature data are required to constrain the controls on rockfall activity.

1.1.3 Controls on rock surface temperature

This section provides a summary of the physical controls on rock surface temperatures, providing a theoretical background to inform the methodological approach to measuring and understanding the cliff surface temperatures using IRT Monitoring (Chapters 4 and 5). Rock-surface temperatures are primarily controlled by radiation from the sun, with the surface heat balance controlling the amount of radiation affecting both surface and internal temperatures of the rock mass over different time scales (Lockwood, 2017). The heat balance is schematically presented in Figure 1.2, and can be described using the following form (Gunzburger et al., 2010; Lockwood, 2017):

$$q_{cond}\,(R_n) \;=\; (1-\alpha)\big(q_{(sw)beam} + q_{(sw)ind}\big) - q_{(lw)out} - q_{conv} + q_{(lw)in} \qquad \text{[Eq. 1.1]}$$

Where q_{cond} is the heat flux (W m^2) transmitted towards the depth of the cliff face by conduction (or net radiation reaching the cliff surface, R_n); $q_{(sw)beam}$ and $q_{(sw)ind}$ are the direct and indirect shortwave solar radiation reaching the cliff face, respectively; the term $q_{(sw)ind}$ includes both the diffuse radiation (i.e., received from the sun after its direction has been changed by atmospheric scattering) and the radiation reflected by adjacent surfaces, such us the wave-cut platform and sea surface (Figure 1.2) located on the foreshore at the study site in this thesis - East Cliff, Whitby, UK (section 1.4). $q_{(lw)out}$ represents the longwave (infrared) radiation lost by the heated rock face, but that is captured by the thermal camera. It is important to note here that the atmosphere represents a reflector itself, generating a scattered, extraneous path radiance that can be also captured by a thermal sensor (Lillesand et al., 2015), as shown in Figure 1.2. However, it is acknowledge that for a thermal camera located close to the earth' surface, such is in this research (mean distance ~ 427 m between the thermal camera and the cliff face, See Chapter 4), the path radiance will commonly be negligible or small, essentially because the atmospheric path distance from the sensor to the surface is too short for scattering to take place (Lillesand et al., 2015); q_{conv} is the convective heat flux associated with air movements near the cliff face; $q_{(lw)in}$ is the incoming longwave radiation from the atmosphere; and α is the fraction of the shortwave radiation received (direct and indirect) that is reflected by the cliff surface, which is known as albedo. The albedo has been recognised as a major factor that influences surface temperatures (Kelly and Zumberge, 1961; Peel, 1974; Kerr et al., 1984), as it controls the fraction of the incoming solar radiation that can be absorbed by the cliff face. This absorbed radiation is then available to heat the surface of the cliff (Lockwood, 2017), which can be captured by a thermal camera and then transformed into temperature values using the Stefan-Bolzmann's Law, which forms the basis for radiative heat

loss estimates, and constitutes the theoretical basis for Infrared Thermography (Rees, 2001; Frodella et al., 2017). This law follows the form:

$$q_{(lw)out} = \varepsilon_{rock}\sigma T_{surf}^{4} \quad \text{[Eq. 1.2]}$$

where the longwave radiation term ($q_{(lw)out}$) includes the gray-type radiation emitted by the heated cliff face (also known as total radiant exitance from the surface of the material, expressed in W m^{2}); σ is the Stephan Boltzmann constant (5.6697 x 10^{-8} $Wm^{-2}K^{-4}$); T_{surf} is the absolute temperature (expressed in K) of the cliff face; and ε_{rock} is the emissivity of the rock, which can be defined as a factor that describes the efficiency of the rock in radiating energy compared to a black body. The emissivity can have values between 0 and 1 and has an inverse relationship with reflectance of the rock since the lower the reflectance, the higher its emissivity and vice-versa (Frodella et al., 2017). Overall, the Stefan-Bolzmann's Law states that the electromagnetic energy emission (radian power) per area of unit of the rock depends on the fourth power of the absolute temperature and on its value of emissivity (FLIR, 2018).

In addition to the Stefan-Bolzmann's Law (Eq. 1.2), a key concept for Infrared Thermography applications is the brightness temperature (T_b), as it has been commonly used in remote sensing and ground-based thermal infrared investigations (Babaeian & Tuller, 2023). As such, the brightness temperature is the temperature of a blackbody ($\varepsilon = 1$) (Khan et al., 2021), and it is usually defined as the temperature at which a black body in thermal balance with its surrounding would emit the sensed measured temperature (Babaeian & Tuller, 2023). This can be calculated using the inversion of the Plank' law, as follows (Babaeian & Tuller, 2023):

$$T_b = \frac{C_2}{\lambda \, ln\left(\frac{C_1}{E_r(\lambda,T)\lambda^5+1}\right)} \quad \text{[Eq. 1.3]}$$

Where E_r represents the spectral radiance (W m^{-2} μm^{-1}) at wavelength λ (μm) and temperature T (K) with $c_1 = 3.7417 \times 10^{8}$ $W \mu m^{4} m^{-2}$ and $c_2 = 1.4388 \times 10^{4}$ $\mu m\, K$. It is important to note that the Eq. 1.3 is inverted to solve for the surface temperate (T) of the surface of interest. A comprehensive review of the theoretical principles of IRT is provided by Frodella et al. (2017) and FLIR (2018).

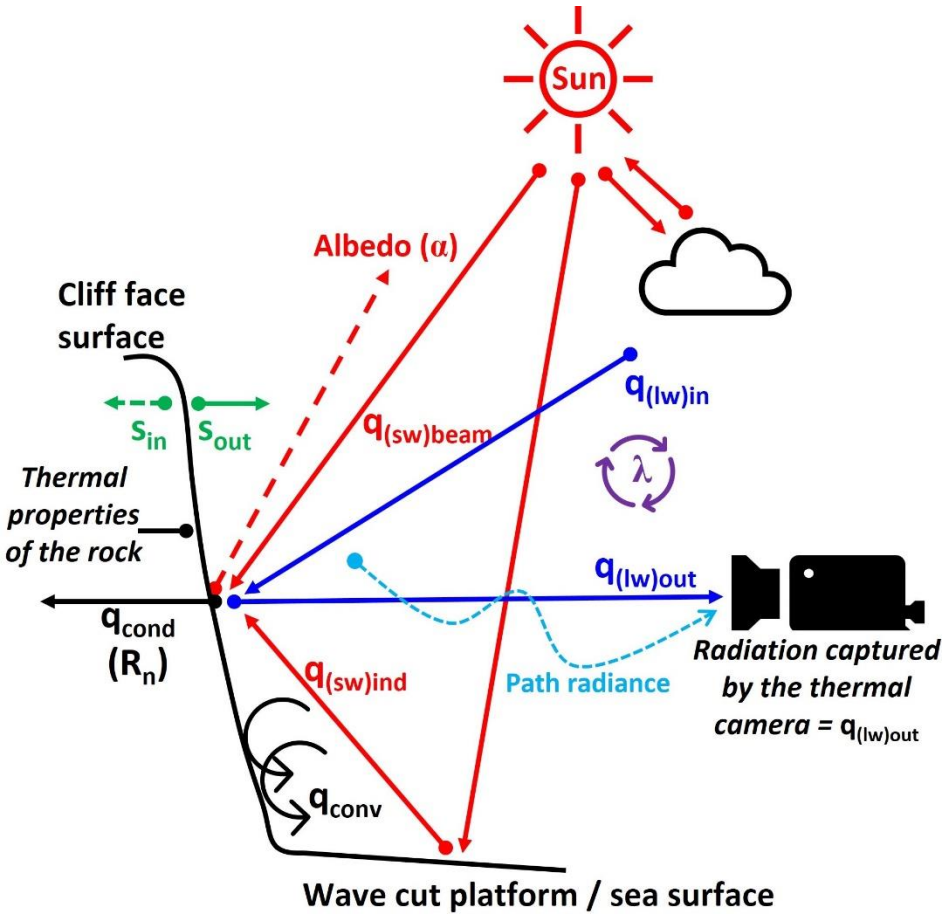

Figure 1. 2: *Conceptual scheme of the radiative and non-radiative energy fluxes affecting the heat balance at the cliff face. Here, $q_{(sw)beam}$ and $q_{(sw)ind}$ are the direct and indirect shortwave solar radiation reaching the surface of the cliff face, respectively (red arrows). $q_{(lw)in}$ and $q_{(lw)out}$ shows the incoming and outcoming longwave radiation, respectively (blue continuous arrows). q_{cond} (black arrow) is the heat flux transmitted towards the depth of the cliff face by conduction (or the net radiation reaching the cliff, R_n). q_{conv} is the convective heat flux associated with air movements (semi-circular black arrows). α is the albedo of the cliff face (dashed red arrow). s_{in} and s_{out} are the incoming and outgoing sensible heat, respectively (green arrows). λ is the latent heat of vaporization (circular purple arrows). The path radiance represents the scattering effects produced by the atmosphere, which generate extraneous radiance that is also captured by the thermal camera (Figure modified from Figure 1 in Gunzburger et al., 2011, p. 1578).*

Overall, Eq. 1.1 shows that the net radiation (R_n) at the cliff surface is the difference between the total incoming and outgoing radiation. Therefore, the net radiation indicates whether net surface heating (positive) or cooling (negative) is occurring across the cliff face at different time scales. For example, the net radiation will usually be negative at night, indicating cooling thermal conditions (negative heat flux), but throughout the day it may be positive or negative depending on the energy balance between the incoming and the outgoing radiation (Lockwood,

2017). The energy balance is also influenced by the time of the year, as the cliff face receives different amounts of radiation during different seasons, as controlled by the orbital position of the Earth around the sun (Jenkins and Smith, 1990). Furthermore, cloud cover at night restricts the long-wave radiation loss ($q_{(lw)out}$), thus producing small net radiative losses and temperature decreases. When the sky is clear of clouds during the night, long-wave radiative loss is large, so the net radiative loss is also large, causing a large nocturnal temperature decrease (Lockwood, 2017).

Importantly, the full energy balance affecting the cliff includes not only radiative fluxes as described in Eq. 1.1., but also fluxes of energy in the form of sensible heat (which may be both incoming and outgoing the cliff), and latent heat (e.g., energy included in evaporated vapour of water near the cliff). Overall, the energy available for the sensible and latent heat fluxes depends on the net radiation (R_n), which can be described in the following form (Lockwood, 2017):

$$(R_n) = \lambda E + s_{in} + s_{out} \qquad \text{[Eq. 1.4]}$$

Where λ is the latent heat of vaporization; E is the rate of evaporation; s_{in} represents the sensible heat flux into the cliff; and s_{out} indicates the sensible heat going towards the atmosphere. Figure 1.2 shows a conceptual scheme of the radiative and non-radiative fluxes affecting the cliff face.

The direct shortwave radiation term ($q_{(sw)beam}$) reaching the cliff surface depends on three additional factors (Gunzburger et al., 2011):

1. The solar irradiance reaching the outer surface of the atmosphere, which is known as the solar constant (q = 1,370 W m^{-2});
2. The latitude, solar altitude and azimuth angles, which determine the local position of the sun in the sky above the horizon as well as the level of exposure of the surface being heated, hence controlling the direction and amount of direct shortwave radiation entering to the heat balance;
3. atmospheric attenuation caused by gases, such as aerosols and cloud particles, which depends on the thickness of the atmospheric section crossed by the sunbeams and on the optical density of the atmosphere. These factors are important in steep coastal-cliff settings that display complex surface morphology and varying aspect over a range of spatial scales (e.g., >200 m length), as is also common in steep mountainous environments.

In addition to the effects of these primary controls, there is a range of other factors that can control the absolute temperatures and temperature regimes at the cliff surface (Gómez-Heraz et al., 2006). For instance, properties of the rock mass such as the specific heat capacity, thermal conductivity and moisture content have been indicated as influences on surface and internal temperature of the rocks (McGreevy, 1985; Jenkins and Smith, 1990; McGreevy et al., 2000), while the effect of rapid and local wind variations has also been noted as these can induce sudden (2°C min^{-1}) temperature fluctuations on rocks located in continental and coastal settings of USA (Death Valley and Mountain View, respectively) (Molaro and McKay, 2010). Furthermore, it has been noted that besides large-scale climate changes, local geographical conditions can have a key role in the surface energy balance, which may result in amplification or dampening of the radiative fluxes (Westermann et al., 2009). For example, it has been observed that in the high-artic, the longwave radiation emitted by seawater can increase the surface temperature of coastal cliffs by 1.5°C during winter when compared with near-coastal cliffs (Schmidt et al., 2021). Overall, these factors inform the design and implementation of an IRT approach to monitor rock slopes, as they contribute to the surface variability of temperatures over different timescales.

The specific heat capacity of the rock controls the quantity of heat needed to raise the temperature of a single unit of mass by one degree (J kg^{-1} K^{-1}). As such, given similar heating conditions, rocks with relatively low specific heat capacity will undergo more rapid temperate change and so, can experience higher surface temperatures when heated than rocks with high specific heat capacity. Also, the thermal conductivity of the rock controls the rate of heat flow through a material (W m^{-1} k^{-1}). As a result, it has been suggested that if the thermal conductivity is high, then the heat will be conducted easily from the cliff surface to greater depths within rock mass, causing lower surface temperatures. Conversely, if the thermal conductivity is low, then the conductive heat loss may be decreased and so, allowing the accumulation of heat across the rock surface, thus increasing the likelihood of capturing high surface temperatures. Consequently, the capacity for a rock to attain high surface temperatures is inversely related to its albedo, specific heat capacity and thermal conductivity (McGreevy, 1985). Moreover, in crystalline rocks (such as granite), the colour of minerals (a surrogate of their albedo) appears to be the main direct control on the maximum temperatures attained by individual minerals, while crystal size is shown to be a major control on surface temperature differences between minerals. As a result, rocks with large differences in grain size might be expected to experience magnified near-surface stresses due to differences in the magnitude and rate of thermal expansion of individual grains (Gómez-Heraz et al., 2006).

Overall, the factors described in this section influence the IRT monitoring field design, as the calibration of each thermal imagery acquired from a fixed monitoring position (as in this research) is a critical step to acquire meaningful surface temperatures and capture the full range of thermal variability across differing lithologies. As such, an appropriate IRT monitoring strategy and data correction protocol, which consider the site-specific characteristics, is presented in Chapter 4.

1.1.4 High-frequency monitoring of rockfall activity and cliff surface temperatures

The duration of rockfall monitoring relative to the return period of all potential rockfall events of varying magnitude and frequency determines the likelihood of capturing changes that are representative of how rock slopes evolves over longer time scales (Williams et al., 2018). Combined with the duration of observation, high-frequency monitoring between surveys is important to examine the evolution of rockfalls through time, as this can provide detailed insight into the nature of the rates of activity, failure propagation, and precursory activity (e.g., Williams, 2017; Williams et al., 2018). However, the ability to capture surface changes that are representative of how cliff faces evolve across annual and multi-annual times scales has been hindered due to challenges affecting either the duration or the frequency of monitoring. This, in turn, constrains our understanding of the long-term evolution of rockfalls at high temporal resolution and importantly, the possibility to establish links with rapidly changing environmental controls at hourly resolution, such as temperatures or precipitation. These challenges are commonly generated by the combination of three main factors:

1. Challenges related to the field capacity to install remote-sensing equipment to monitor rock faces continuously and importantly, from a fixed and stable location. These challenges have been commonly reflected in low frequencies of data collection (e.g., monthly or weekly surveys, such us in Rosser et al., 2007 and Barlow et al., 2012), so that the intervals of data acquisition have been longer than the intervals needed to assess, for instance, temperature triggers on rockfalls and more widely, any geomorphic changes on hillslopes of sudden occurrence (such as the product of sudden energetic storms, among many other geomorphic processes);

2. The limited duration of near-continuous high-frequency monitoring, with the longest being conducted by Williams et al., (2018), which involved ten months of near-continuous monitoring at a data acquisition frequency of one hour. Similarly, Kromer et

al. (2017) carried out a six-week monitoring campaign using 30-minute data collection intervals (Kromer et al., 2017). However, existing limitations to permanent equipment installation, protection and constant power supply, as well as software stability, data acquisition and processing limit the extent to which a sufficiently large number of rockfalls can be captured in an appropriate range of environmental driving conditions;

3. Limitations related to the replicability of published methods that have been specially designed for large point cloud processing in order to estimate rockfall volumes (e.g., Williams et al., 2018), or the availability of an integrated geo-informatic workflow that can efficiently automatize the processing of big dataset of point clouds or meshes. These limitations have hindered the generation of 4D rockfall inventories that encompass the fundamental requirements of long-term monitoring and high frequency detection of rockfalls (e.g., hourly data and annual or multi-annual near constant observations).

The same challenges described above can be observed more widely in Infrared Thermography (IRT) monitoring of rock slopes, affecting the duration and the frequency of surface-temperature data that describes thermal activity across cliff surfaces. As a result, studies addressing patterns of rock-slope temperature using thermal cameras have been limited to short monitoring periods involving only small numbers of days of monitoring, an incomplete range of the diurnal thermal cycle (e.g. just between 07:00 to 17:00 h, and thus, during sunlight), low frequency monitoring programs (e.g. using monthly surveys) or capturing data across small (~5.0 m^2) areas of a cliff face (e.g. Fiorucci et al., 2018; Pappalardo and Mineo, 2017; Pappalardo et al., 2016; Wu et al., 2005). Therefore, a gap in the literature exists in the understanding of if and how thermal cycles correlate with remote-sensed rockfall activity using both, high temporal resolution of data acquisition and long-term constant monitoring. As such, the development of a parallel monitoring program of laser scanning and infrared thermography capable to provide a unique dataset is required to be able to link both, rockfall occurrence and surface temperatures. This is because while the laser scanner monitoring can produce high-resolution point clouds in 3D (allowing the estimation of the surface change between sequential point clouds, and so, the detection of rockfalls), the infrared thermography monitoring can provide high-resolution temperature imagery of the cliff surface before, during and after the occurrence of rockfalls. Thus, the contemporaneous acquisition and combination of high-resolution (here, ~10 cm) and high-frequency (here, 1 h) data represent a unique opportunity to fill the gaps addressed in this study.

1.2 Research aim, questions, and objectives

The aim of this research is to use high-frequency laser scanning and infrared thermography monitoring to improve understanding of temperature controls on rockfall activity and cliff erosion.

To achieve this aim, the following research questions will be addressed:

RQ1. How do rockfall magnitude, frequency and timing vary over hourly, diurnal, and seasonal timescales?

RQ2. How do surface cliff temperatures vary over hourly, diurnal, and seasonal timescales?

RQ3. To what extent does cliff-surface temperature variability trigger rockfall?

RQ4. What is the relative erosive contribution of rockfall activity resulting from (a) inclement weather conditions versus (b) temperature effects?

To address the above research questions, this thesis will meet the following objectives:

O1. To develop a method of processing large time series (>10^4) sequential terrestrial laser scans, to consistently monitor rockfall due to the combined importance of analysing a large number of scans over large time periods (Chapter 2).

O2. To generate a multi-annual 4D rockfall inventory (2017 – 2019), to quantify the timing, magnitude, and frequency of rockfall (Chapter 3).

O3. To develop an approach to continuously monitor cliff surface temperatures using Infrared Thermography (IRT) (Chapter 4).

O4. To use constant IRT monitoring to investigate the variability of surface cliff temperatures at 1 h resolution through 2021 (Chapter 5).

O5. To combine the rockfall inventories and contemporaneous IRT data to constrain temperature controls on rockfall occurrence (Chapter 6).

1.3 Thesis structure

This thesis comprises seven chapters. Their relation to the research questions and objectives are presented in Figure 1.3.

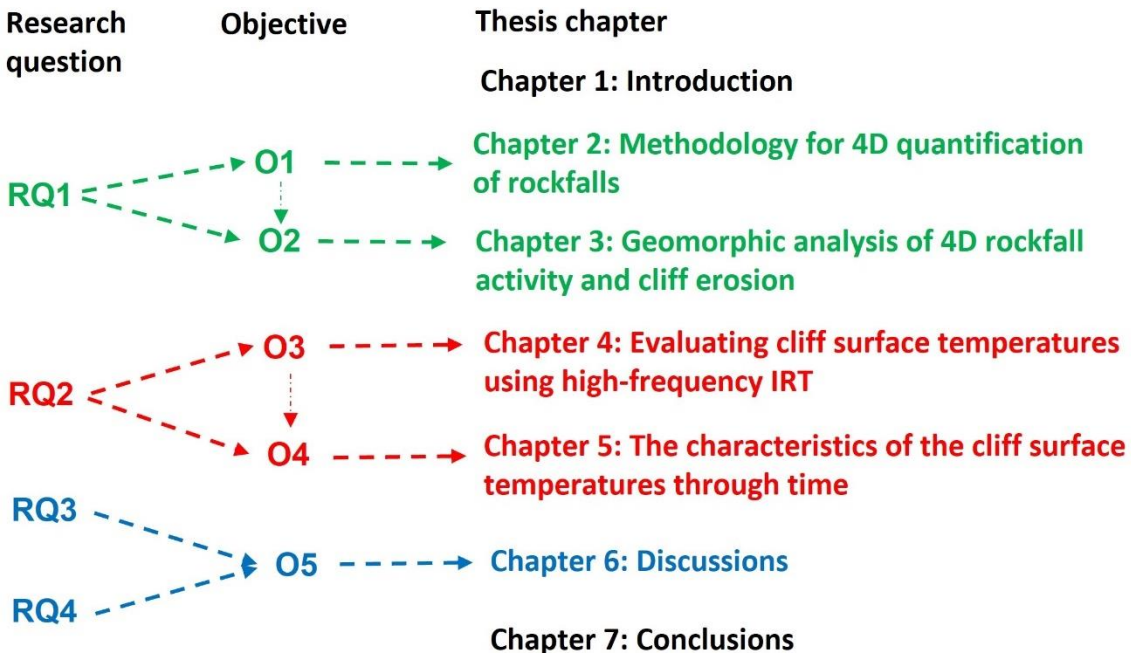

Figure 1. 3: *Schematic overview of the thesis structure with respect to the research questions and objectives.*

Chapter 2 presents the methods for the detection and quantification of 4D rockfall activity, which comprises the description of a constant terrestrial laser scanner (TLS) monitoring system and development of a novel computational routine capable of automatically handle big point-cloud datasets. The workflow presented in Chapter 2 includes the development of quality-control steps, such us the detection of partials scans, use of high-density scan filters, registration between sequential point clouds, the application of the 3D change detection using the Multiscale Model to Model Cloud Comparison (M3C2) algorithm (Lague et al., 2013), the development of new geo-informatic workflows for the estimation of the rockfall volume, and volumetric error. This workflow is applied to generate, for the first time, high-frequency and multi-annual 4D rockfall inventories over a three-year duration.

Chapter 3 is based on the Objective 2 of this thesis (O2, see Section 1.2 and Figure 1.3) and represents the first of three chapters of results. It builds on *Chapter 2* by using a multi-annual 4D rockfall inventory (2017 – 2019) to quantify and examine the magnitude, frequency and timing of hourly rockfall activity. The analysis presented in this chapter explores and compares the magnitude-frequency distribution of rockfalls between years and seasons. It also explores how

small, medium and large rockfalls evolve and integrate into a multi-annual erosional signature, providing the first findings of cliff evolution over different time-scales, characterising periods of rapid and high erosion as well as periods of steady landform evolution.

Chapter 4 is based on the Objective 3 of this thesis (O3, see Section 1.2 and Figure 1.3). As such, it presents an approach to continuously monitor cliff surface temperatures using high-resolution and high-frequency infrared thermography (IRT) during one year of hourly monitoring (2021). To automatically handle big thermal datasets, the method presented in this chapter includes the development of a novel monitoring set-up in the field for thermal imagery acquisition, filtering and calibration. From this, an initial evaluation of the surface temperatures is presented, as a verification of the quality of the data collected and the degree to which this thermal dataset reflects the nature of the cliff surface under inspection.

Chapter 5 is based on the Objective 4 of this thesis (O4, see Section 1.2 and Figure 1.3). As such, this chapter builds upon *Chapter 4* as it uses the constant IRT monitoring dataset to investigate how surface cliff temperatures vary over hourly, diurnal, and seasonal timescales at 1 h resolution through 2021. As such, this chapter begins with the characterization of the surface temperatures, with emphasis on the range of temperature fluctuations observed throughout the seasons. This is followed by an analysis of diurnal temperature fluctuations to examine the magnitude and timing of the heating and cooling phases and how these vary by season, providing insight into potential thermal rockfall triggering. This chapter ends by exploring how the cliff aspect controls the timing, magnitude and spatial distribution of the diurnal heating and cooling phases of different sections of the cliff face.

Chapter 6 draws on the combination of the 4D rockfall inventory and contemporaneous IRT data to quantify the controls on rockfall occurrence in 2021 (Objective 5 of this thesis, O5, see Section 1.2 and Figure 1.3). As such, this chapter present evidence for temperature controls on seasonal rockfall activity. This is followed by an investigation of the thermal characteristics of the cliff face when rockfalls do and do not occur. Finally, this chapter investigates the role and relative significance of temperature-induced rockfall occurrence across the subaerial section of the cliff face, and the implications of the findings are discussed in the context of climate change. It is important to note here that the results from the rockfall inventory of the period 2017-2019 (Chapter 3) are used independently from the results of the rockfall inventory 2021 (Chapter 6).

Chapter 7 summarises the major findings of this thesis in relation to the research questions outlined above. Here, the key, novel findings are identified, alongside recommendations for future research.

1.4 Study site

1.4.1 Geomorphology and region of research

The approaches used in this thesis build on research previously undertaken at East Cliff, Whitby (the cliff is ~200 m across and ~65 m high), North Yorkshire, UK (Figure 1.4a). At East Cliff, and the coastal cliffs of the North Yorkshire more generally, few statistically significant relationships (R^2 = 0.2 - 0.5) have been reported between microseismic ground motions as a proxy for marine conditions (notably waves and tides) and rockfall occurrence (Vann Jones et al., 2015). Similarly, Brain et al. (2014) concluded that for the cliffs located at North Yorkshire, Staithes (~14 Km from Whitby) there is improbable to be sufficient opportunity for microseismic ground motions to generate considerable rock weakening, especially when considered in the context of other mechanisms (e.g., rainfall). Furthermore, at the base of the East Cliff, a 4 m-high rock armour revetment was installed in 2000 to limit the effects of marine erosion at the cliff toe (Figure 1.4b), thus, attenuating the energy of the waves. In addition, there is limited, if any, evidence of wave-notch development and upward failure propagation in the evolution of these coastal cliffs; thus, wave action at the base of the cliff face has a limited control on rockfall activity (Rosser et al., 2007; Vann Jones et al., 2015; Williams, 2017). The relationships between the duration of the inundation across the cliff toe, marine energy transfer to the cliffs, and resultant erosion is more complex than indicated by tidal inundation models alone across these coastal cliffs (Vann Jones et al., 2015). Hence, despite its coastal context, the rock slopes of East Cliff behave in a manner representative of non-marine rock slopes. As such, the findings of thesis have implications for understanding rock slope behaviour more generally.

The monitored section is ~ 200 m wide and 65 m tall, with a total cliff face area of ~9,592 m^2. The cliff is formed by sub-horizontal bedded strata, with upper beds stained orange from downslope wash from glacial till of variable depth. The upper section of the cliff is composed of widely jointed orange-stained surfaces of protruding bedded sandstones, as well as darker indented interbedded sandstones and siltstones. The lower section comprises gray coloured and relatively harder shales (Barron et al., 2012; Williams, 2017). Overall, the surface texture and morphology of the cliff face strongly reflects the geology (Rosser et al., 2005), with the relatively hard sandstones protruding from the cliff, forming well defined over hanging beds (the geology is further described in section 1.4.2). On the seaward side of the cliff there is narrow sandy beach (~20 m mean width, perpendicular to the cliff), which is bounded on the seaward side by a low-angle (< 2°), near-planar wave cut platform extending ~300 m seaward. This platform is exposed at low tides but can be submerged to a depth of ~6 m during high tides.

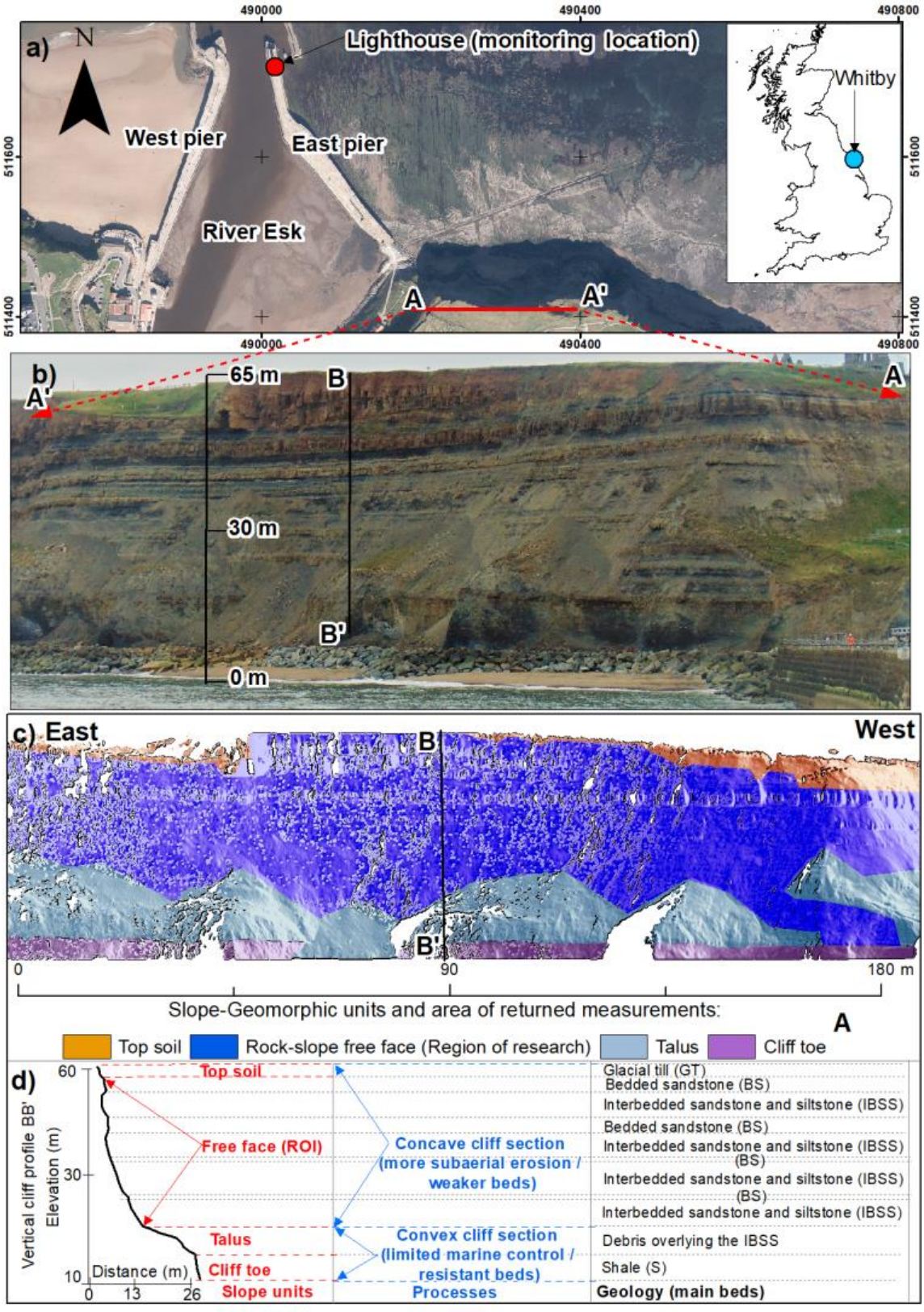
a)
N
Lighthouse (monitoring location)
West pier
East pier
River Esk
Whitby
A
A'
490000
490400
490800
511600
511400
b)
65 m
30 m
0 m
B
B'
A
A'
c) East
West
0
90
180 m
Slope-Geomorphic units and area of returned measurements:
A
Top soil
Rock-slope free face (Region of research)
Talus
Cliff toe
d)
Vertical cliff profile BB'
Elevation (m)
60
30
10
Distance (m)
0
13
26
Top soil
Free face (ROI)
Talus
Cliff toe
Slope units
Concave cliff section (more subaerial erosion / weaker beds)
Convex cliff section (limited marine control / resistant beds)
Processes
Glacial till (GT)
Bedded sandstone (BS)
Interbedded sandstone and siltstone (IBSS)
Bedded sandstone (BS)
Interbedded sandstone and siltstone (IBSS)
(BS)
Interbedded sandstone and siltstone (IBSS)
(BS)
Interbedded sandstone and siltstone (IBSS)
Debris overlying the IBSS
Shale (S)
Geology (main beds)

Figure 1. 4: *Overleaf. Location of the study site and cliff face geomorphology.* ***a)*** *Location of the East Cliff of Whitby (section AA') and monitoring set up in the field. The laser scanner and the thermal camera were installed within the East Pier Lighthouse (red circle). Aerial imagery courtesy of Channel Coastal Observatory (CCO), UK.* ***b)*** *Frontal view of the East Cliff of Whitby 2019 (photograph © Ignacio Ibarra). BB' is the vertical cliff profile shown in figure d.* ***c)*** *Geomorphological units of the cliff face, where the region of research (ROI) of this thesis correspond to the free face of the cliff (blue), which encompasses an area of ~5,459 m². BB' is the vertical cliff profile shown in figure d.* ***d)*** *Representative vertical cliff profile across the central section of the cliff (BB'), where the relationship between the geomorphic units of the cliff face, dominant processes and main lithologies are presented.*

Using the hillslope unit model proposed by Dalrymple et al. (1969), it can be seen that the monitored cliff face comprises a total of four slope units (Figure 1.4c). From the top to the base of the East Cliff, the first unit is located across the upper section of the cliff face and comprises the crest and topsoil unit of the cliff, formed by glacial till. Here, the main mass movement processes are dominated by soil failures. However, in the monitored section of the East Cliff, the area of the topsoil unit is ~800 m^2 (equating to ~ 8% of the total cliff face area of ~ 9,592 m^2) and so it is not the dominant mechanism of erosion in these settings.

The second slope unit of the East Cliff of Whitby is the free/fall face, which correspond to the near-vertical cliff section formed by protruding bedded sandstones as well as indented surfaces of interbedded sandstones and siltstones. Across the free face of the study site, the mass movement processes are discontinuity-controlled rockfalls (Rosser et al., 2013). As such, typical rockfalls involve small-scale joint-defined wedges and rockfalls released via rock bridge breakage, which can be inferred from the exposed fresh fracture surfaces visible after failure (de Vilder et al., 2017; Williams et al., 2018). At East Cliff, rockfalls have been measured up to 200.4 m^3, but the volume loss has been commonly dominated by smaller-volume rockfalls (0.001 – 0.01 m^3), with median volumes of rockfalls approaching 0.015 m^3 (Rosser et al., 2013; Williams et al., 2018). In the monitored section of East Cliff, the area of the free/fall face unit is ~5,459 m^2, which is ~57.3% of the total area of the cliff face, thus, representing the largest slope unit (Figure 1.4.c).

The third slope unit of the monitored cliff is the talus, formed by small fragments of rockfalls released from the free face. The area of the talus is ~ 2,345 m^2 (equating 24.4% of the cliff) and is composed by both relatively stable surfaces that have been colonised by vegetation, and unstable surfaces formed by superficial deposits actively subject to slope wash and downslope transport (Figure 1.4c).

The fourth unit of the East Cliff is the cliff toe, which is the near vertical rock section of the cliff that can in part, be inundated during high tides and significant wave heights (Figure 1.4c). The exposed surface of the cliff toe (i.e., not covered by the talus) is primarily composed by shales (capped by a thin layer of siderite sandstones) and comprises an area of ~ 950 m^2 (equating ~10% of the total cliff area).

Figure 1.4d shows a representative vertical cliff profile across the central section of the East Cliff. It can be seen that the topography of the cliff face is dominated by two types of cliff profiles: a) the upper section, that comprises the free/fall face, shows a distinctive concave cliff profile, which indicates greater subaerial erosion across weaker sub-horizontal layers of bedded sandstones and interbedded sandstones and siltstones; and b) the lower section, that comprises relatively resistant siderite sandstones and shales, shows a notable convex cliff profile, thus supporting the existence of limited marine controls across the base of the cliff. Even before the installation of the rock armour in 2000, Agar (1960) observed that the upper section of the East Cliff Whitby underwent more efficient subaerial erosion compared to the wave action at the toe of the cliff.

The region of research (ROI) of this thesis is the free face section of East Cliff, where rockfalls seem to be generated by subaerial processes. More specifically, this section has been selected for investigation due to:

1. The dominance of subaerial processes reflected in a distinctive concave cliff profile, where cliff recession has been dominated via constant rockfall activity. Here, it is important to investigate how rockfall magnitude, frequency and timing vary over diurnal, diurnal and seasonal timescales (RQ1); and
2. The need for research into temperature controls on rockfall occurrence (RQ2 and RQ), which requires the isolation of the ROI, in which rockfalls may occur due to surface temperature variability affecting the subaerial exposure of the rock outcrop. As a result, the topsoil, the deposits forming talus, and the cliff toe have been removed from all analyses.

Figure 1.5 shows an oblique 3D view of the study site, where the cliff aspect as well as the sunrise and sunset direction are highlighted to indicate the nature and direction of solar insolation relative to the cliff face during the diurnal thermal cycle. This is needed to understand key outcomes of the Chapters 4 and 5, which are then discussed in Chapter 6.

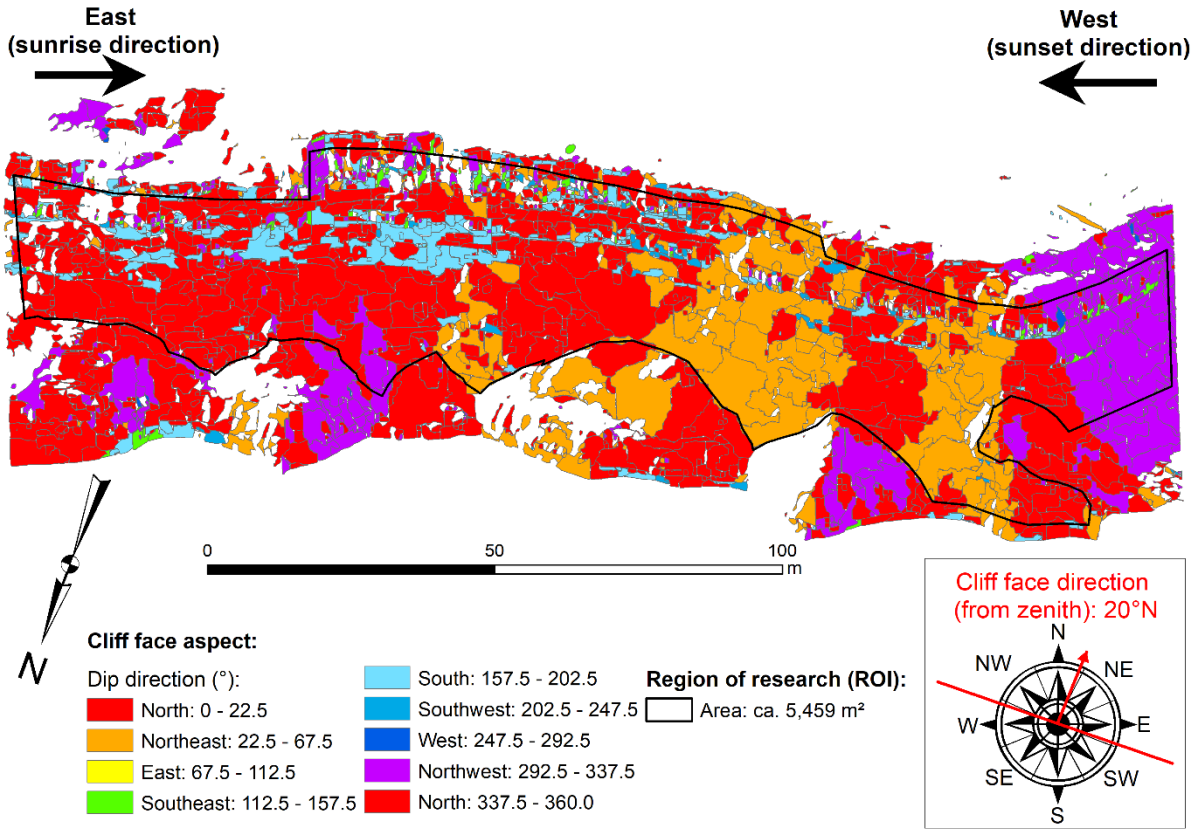

Figure 1. 5: *Oblique 3D view of the East Cliff of Whitby relative to the sunrise and sunset direction. Arrows show the approximate direction of the sunrays when striking the cliff face during sunrise and sunset. The aspect of the cliff face was derived from a 3D point cloud collected the 1st of December 2021 and calculated using the Cloud Compare plug-in 'Facets' (Dewez et al., 2016). The region of research (ROI) of this thesis is highlighted using a black polyline (free face of the cliff, which is the area of rockfall occurrence across the subaerial section of the cliff).*

1.4.2 Geology

The near-horizontally bedded strata forming East Cliff is formed of Early to Middle Jurassic sedimentary rocks (Rosser et al., 2005). The cliff toe comprises gray, fissile shales of the Whytby Mudstone Formation, commonly known as the Upper Lieas Group of sediments (Cox et al., 1999), which represents Early Jurassic marine sedimentation (Figure 1.6). The shales of the Whitby Mudstone Formation are overlain unconformably by the shallow marine Dogger Formation, which comprises yellow-brown siderite sandstone and phosphatic pebbles, outcroppiong ~13 m up the cliff face (Powell et al. , 2010; Barron et al., 2012). Structurally, the East Cliff is bounded to the west by the Whitby Fault, which is a normal fault with a north-south trend and downthow of ~12 m to the west (Rawson and Wright, 2000).

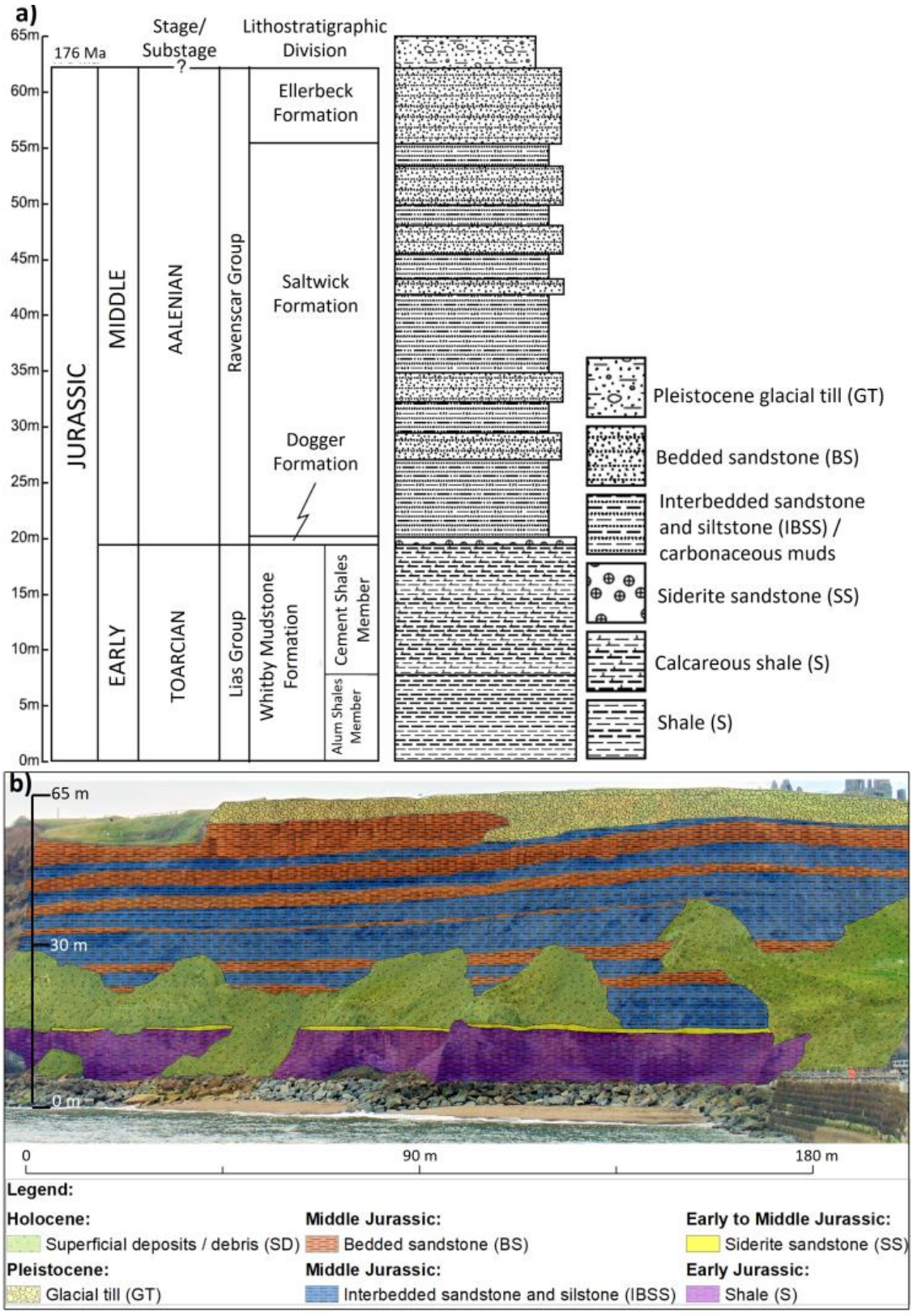

Figure 1. 6: *Geology of the study site.* ***a)*** *Stratigraphy and schematic lithic log of the Early to Middle Jurassic sequence at the East Cliff of Whitby (Figure modified from Figure 3 in Rosser et al., 2005, p. 365).* ***b)*** *Frontal view of the East Cliff of Whitby, where the principal beds that outcrop were identified and then mapped using a high resolution oblique photograph taken in March 2019.*

Overlying the Dogger Formation, at elevations of ~14 – 45 m from the cliff toe, is the non-marine fine-grained Saltwick Formation, which comprises fine-grained Middle Jurasic sandstones that are interbedded with carbonaceous clays and silstone. Within the Saltwick Formation, layers of bedded sandstone protrude beyond the weaker interbedded sandstone and siltsone between them (Barron et al., 2012). Across the upper section of the cliff, at ~45 – 60 m, there is the Ellerbeck Formation, which is formed by a band of widely jointed Middle Jurasic marine sandstones (Figure 1.6). This Formation is capped by the Pleistocene glacial till derived from Late Denvensian ice (Rawson and Wright, 2000).

Rosser et al., (2005) noted that the rockfall geometry strongly reflects the lithology and structure of the cliff. To exemplify this, the mudstones, shales and siltstone that form the lower half of the cliff face are fissile laminated rocks. It has been observed that these layer of laminated rocks release small rockfalls in which the width is approximately equal to the height, reflecting the dense joint network from which these rockfalls are originated (William, 2007). Joint width commonly increases with increasing elevation up the cliff face. For example, towards the upper section of the cliff, more widely jointed bedded sandstones of the Ellerbeck Formation tend to generate more elongated rockfalls, reflecting the relatively shallow bed depths and wider joint spacing (Rosser et al., 2005). As such, it has been noted that the rockfall height tends to be more variable than width, suggesting that the bed thickness (i.e., the height of each bed) tend to limit the permissible dimensions of released rock mass (William, 2007). Overall, the clustering of rockfalls appears to follow the near-horizontal bedding in the cliff face. As such, the size of the rockfalls is controlled by the geology of the East Cliff, as rockfall geometry often corresponds well with the depth of the beds (Rosser et al., 2005).

1.4.3 Climate and weather

According to the Köppen-Geiger climate classification scheme, the study site is dominated by a marine climate (Cfb), which is characterized by frequent precipitation and humidity through the year due to the oceanic influence of the North Sea (Peel et al., 2007). Based on longer-term records collected at Whitby by the UK Met Office (1962 – 2021), the mean monthly rainfall (presented as annual averages), ranges between ~30 and 74 mm, with an overall increase in both rainfall and temperature, which is indicative of increased storminess and climate extremes in the study site (Figure 1.7a). The winter months (December – February) are characteristically colder and marginally wetter than summer months (June – August), with mean monthly air temperatures of ~4.3°C experienced in January and February. As noted by Rosser et

al., (2007), minimum air temperatures are moderated by the marine climate; the mean daily minimum in winter at Whitby is -2.2°C. The highest mean monthly air temperatures are observed in July and August (~15°C), with a mean maximum temperature of ~19°C. November and December are the wettest months (mean monthly precipitation of ~62 mm), while February to April represent the driest months (~40 mm). The mean monthly precipitation recorded during the summer (51.6 mm) is marginally lower than in winter (52.4 mm) (Figure 1.7b).

The climate of the North Sea coast is dominated by distinct seasonal variations in wind speed and direction, much of which is controlled by pressure anomalies that arise from the North Atlantic Oscillation (NAO; Woolf et al., 2002). Mean monthly wind speeds tend to be highest in January, February and October (~13.5 km/h). The lowest mean wind speeds occur in May, June and July, fluctuating between ~8.5 and 10 km/h. Based on data recorded by a weather station installed at the top of the East Cliff in 2015, winds were onshore for 43% of the time, with a median speed of ~3 km/h and a maximum recorded speed of ~115 km/h during a significant storm that occurred in December 2015 (Williams, 2017). Mean monthly relative humidity is high (generally >80%), excluding August and September (Figure 1.7.c), reflecting the marine control over the moisture available in this setting. Between 1962 and 2021, the mean monthly days with air frost was highest in winter, ranging between ~6 and 8 days per month. Air frost is absent between June and September (Figure 1.7d).

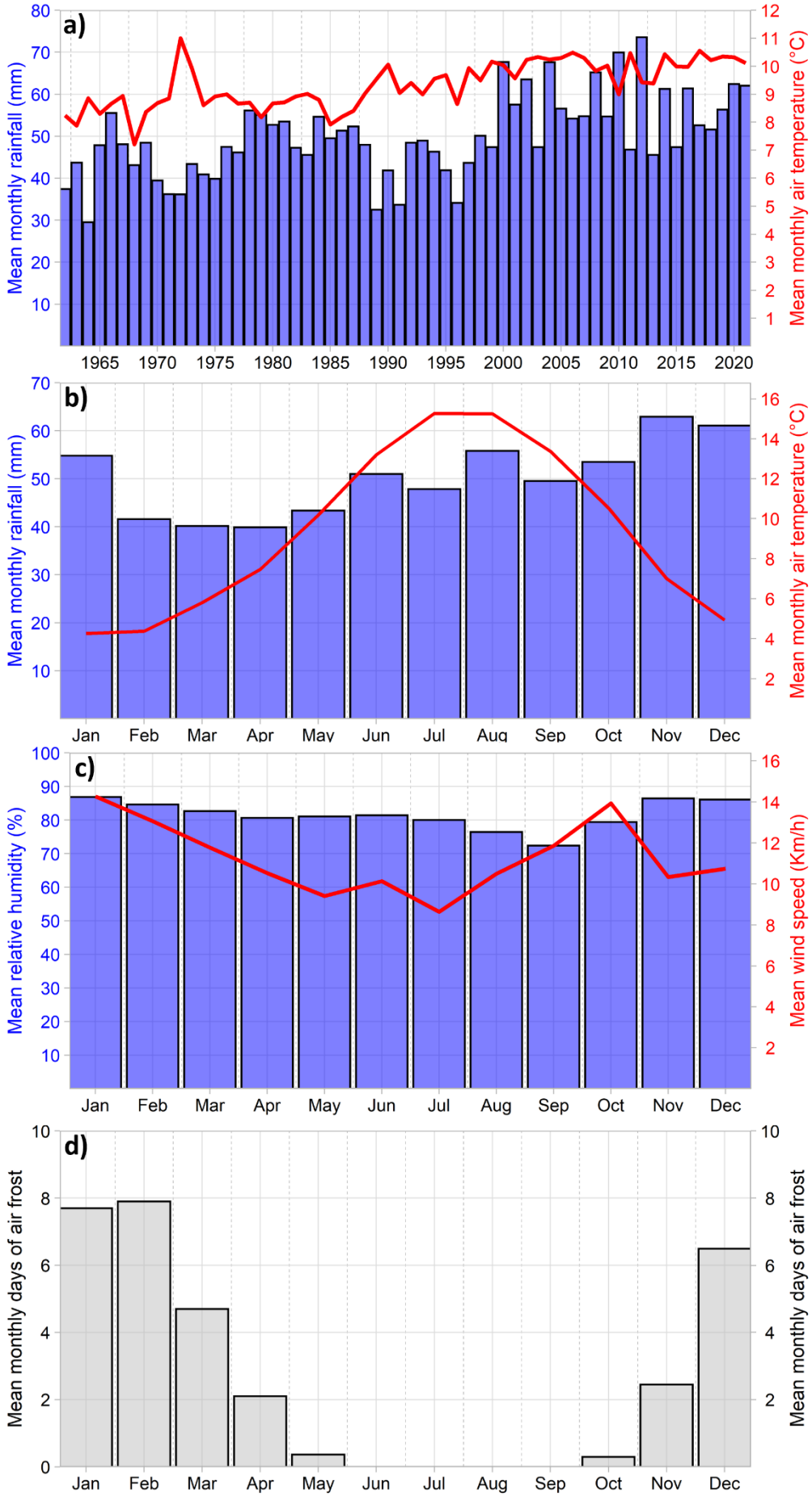
a)
Mean monthly rainfall (mm)
Mean monthly air temperature (°C)
1965 1970 1975 1980 1985 1990 1995 2000 2005 2010 2015 2020
b)
Mean monthly rainfall (mm)
Mean monthly air temperature (°C)
Jan Feb Mar Apr May Jun Jul Aug Sep Oct Nov Dec
c)
Mean relative humidity (%)
Mean wind speed (Km/h)
Jan Feb Mar Apr May Jun Jul Aug Sep Oct Nov Dec
d)
Mean monthly days of air frost
Mean monthly days of air frost
Jan Feb Mar Apr May Jun Jul Aug Sep Oct Nov Dec

Figure 1. 7: *Overleaf. Long-term weather data for Whitby. a) Mean monthly rainfall and temperature, presented as annual averages from 1962 - 2021. b) Mean monthly rainfall and temperature, presented as monthly averages from 1962 - 2021. c) Mean monthly relative humidity and wind speed, presented as monthly averages, recorded between 2017 – 2020. d) Mean monthly days presenting air frost over the period 1962 - 2021. Source: The data presented in figures a), b) and d) was recorded by the Whitby meteorological station published by the Met Office, available from metoffice.gov.uk. The data presented in figure d) was recorded by a privately-owned weather station located at Whitby.*

1.4.4 Tidal regime and wave climate

The coast of the North Yorkshire is macro-tidal, experiencing two daily tides that cycle between spring and neap levels over a range of ~6 m during spring tides (Ordnance Datum) (Figure 1.8a). In this setting, the toe of the cliffs are often submerged during high spring tides, in some places up to a depth of 3 m (Rosser et al., 2013). Wave climate data was recorded from the Channel Coastal Observatory (CCO) wave buoy between 2017 – 2021. The wave climate is dominated by mixed swell wave and wind conditions, which can be inferred from their statistical properties, including significant wave height (Benjamin, 2018). Significant wave height represents the mean height of the highest third of waves, from trough to crest (Figure 1.8b). Maximum significant wave heights of ~16 m were recorded at a buoy 1.5 Km offshore in January 2017 and October 2020, with a mean significant wave of ~1 m.

When high tides coincide with high swells and significant wave heights, the vertical reach of the tide can exceed 4.3 m above the cliff toe (Rosser et al., 2013). Although a rock armour was constructed in 2000 to prevent the marine erosion as noted in Section 1.4.1, from the empirical rockfall monitoring and statistical approaches, at East Cliff, few statistically significant relationships have been reported between tides, waves and rockfall occurrence of >1.0 m^3 (Williams, 2017). Williams (2017) proposed that the lack of significant correlations may be related to the spatial topographic offset between the toe of the cliff and near-vertical rock face of the upper cliff section, as demonstrated by the vertical cliff profile that characterizes the study site (see Figure 1.4d, Section 1.4.1). As such, this further supports the need to consider patterns and causes of rockfall across the subaerial section of the free/fall face using a multi-annual, high-resolution 4D rockfall inventory, capable of capturing rockfalls of all magnitudes in different surface thermal conditions.

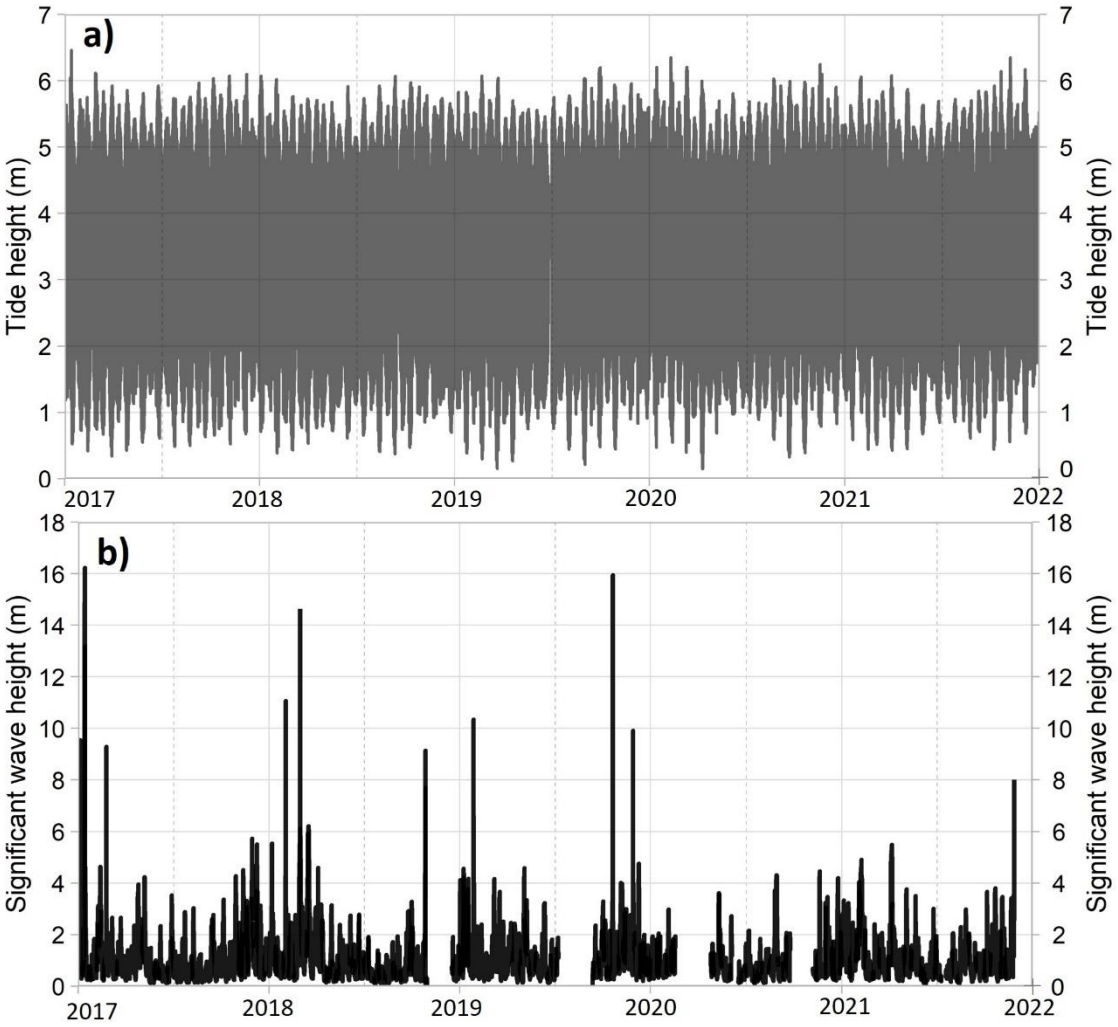

Figure 1. 8: *Tide regime and wave climate data for Whitby (2017 – 2021). a) Tide height from Whitby tide gauge data located in the Whitby Harbour. b) Significant wave height data measured at a wave buoy ~1.5 km offshore from Whitby. Tide and wave data courtesy of Channel Coastal Observatory, UK (www.channelcoast.org).*

1.4.5 Rates of rockfall activity and erosion

Monitoring at East Cliff of Whitby builds upon a substantial body of research into the nature and timing of cliff erosion across the North Yorkshire coastline (e.g., Rosser et al., 2005; 2007; Miller, 2007; Lim et al., 2010; Barlow et al., 2012; Rosser et al., 2013; Brain et al., 2014; Vann Jones et al., 2015; Williams et al., 2018 and 2019; Benjamin et al., 2020, among others). Using field observations across the shore platform and historical Ordnance Survey maps (1982 edition), the first estimation of the erosion rates of East Cliff were conducted by Agar (1960), who observed that the upper section of the cliff was exposed to more efficient subaerial erosion

compared to the marine action at the cliff base, with an overall erosion rate of 0.19 m a^{-1} (Table 1.1).

More recently, using DEMs of difference (DoDs), which estimate the pixel-by-pixel change derived from monthly terrestrial LiDAR surveys, Rosser et al. (2005) observed a total number of 810 rockfalls between September 2003 and December 2004. The mean retreat of the whole Cliff face during this period was 19.7 m, with a mean retreat rate of 0.18 m a^{-1} for the whole cliff (Table 1.1). At the study site, using DoDs from multi-sensor datasets of historical aerial photography and airborne LiDAR, Miller (2007) observed a total eroded volume of 59,326 m^3 between March 1994 and May 2006. This research highlighted an important contrast between erosion rates on the upper section of the East Cliff (the topsoil and free/fall face) and the lower parts of the cliff (talus and cliff toe), at 0.50 m a^{-1} and 0.15 m a^{-1} respectively, with 0.22 m a^{-1} for the whole cliff face. The largest and near-continuous terrestrial laser scanner monitoring of the East Cliff of Whitby was undertaken by Williams et al. (2018), where the rockfall occurrence was monitored for ten months, between March and December 2015. In this research, more than 180,000 rockfalls were detected, and the total eroded volume, including failures across the topsoil, talus and cliff toe, was 110.87 ± 52 m^3 at 1 h frequency, equating an annual cliff retreat of 0.013 m a^{-1} (Table 1.1).

Table 1. 1: *Erosional history of the East Cliff of Whitby, reported from previous research.*

Reference	Period of observation	Monitoring interval	Area of analysis (m^2)	Method	Largest cliff failure event (m^3)	Total eroded volume (m^3)	Annual erosion rate (m a^{-1})
Williams et al., (2018)	Mar. – Dec. 2015	Hourly	8,561	LiDAR, M3C2	7.3	110.87	0.013
Miller (2007)	1994–2006	Annual	14,000	LiDAR, DoDs	Not reported	59,326	0.22
Rosser et al., (2005)	2003-2004	Monthly	>10,000	LiDAR, DoDs	200	24,400	0.18
Agar (1960)	1960 - 1982	-	Not reported	Field survey / OS maps	Not measured	Not measured	0.19

1.5 Summary

An overview of the rationale for research has been presented in this Chapter (Section 1.1). Here, gaps identified in the literature indicate discrepancies in the scales and frequencies of monitoring data that are used to investigate temperature effects on rock-slope stability, limiting our understanding or temperature controls on rockfall activity and the relative erosive role of these into a long-term erosional signature ($\geq 10^0$ years of observations). Critically, these discrepancies make associations with rapidly changing environmental triggers, beyond seasonal variability, difficult to assess. As a result, the role and relative significance of temperature in driving rockfalls is currently poorly constrained. Investigating temporal links, if any, between surface temperatures and rockfall occurrence is a key research goal, specially under the context of a global climate change. The aim of this research is therefore to use high-frequency laser scanning and infrared thermography monitoring to improve understanding of temperature controls on rockfall activity and cliff erosion. To achieve this aim, a series of research questions and objectives were outlined (Section 1.2). These questions and subsequent objectives define the structure of this thesis (Section 1.3). The justification of the region of research of this thesis, and its key systems controls (geomorphology, geology, and climate) were presented in Section 1.4. The following chapter presents a methodological development to allow the automated quantification of 4D rockfall activity and cliff erosion (Research objective 1).

Chapter 2 – Methodological development for 4D quantification of rockfall activity

2.1 Introduction

In *Chapter 1*, the first thesis objective (O1) has been defined, which is the development of a method for 4D quantification of rockfalls, to then examine temporal patterns of rockfall activity using high-resolution and high-frequency terrestrial laser scanning. This objective has been formulated to be able to examine (1) how the erosional work done by small, medium and large-scale episodic rockfall events accumulate into a long-term rate of erosion, (2) to unravel the behaviour of spontaneous rockfalls that did not apparently correspond with any particular trigger event, and (3) to explore at a new level of frequency the seasonal and diurnal patterns of rockfall activity. Therefore, this chapter outlines a novel methodological workflow critically needed to detect and quantify volumes of slope failures that are ultimately used in order to compile a 4D rockfall inventory and develop subsequent geomorphic analysis (*Chapter 3*). This method is used to detect rockfalls along the region of research of the East Cliff of Whitby (*Chapter 1*).

This method builds upon previous research undertaken with terrestrial laser scanning for automatic monitoring, by developing a unique set of geomatic data filters and workflows for point cloud registration and change detection. Here the focus is on optimizing the speed of data processing and providing flexibility for future geoscience applications as well as an easy to manipulate code for future use. The data processing workflow described in this chapter is a computational routine, defined by a sequence of codes that are called upon and applied repeatedly through *Cloud Compare*, triggered on a rolling basis using the *Command Prompt of Windows*. The routine is made up of three principal stages of automatization, which are referred here as *Main scripts*, alongside with a set of *Satellite scripts* for completing more minor methodological tasks, which combined allow to obtain a complete automatized process for rockfall detection. The stages for automatization are summarized in Figure 2.1, and they form the core structure of the methods applied to this dataset and hence, defining the organization of the sections of this chapter. The focus of this chapter is to provide a detailed description of the method for point cloud processing, and as such, the sources and descriptions of other types of key datasets including infrared thermography and weather data, are explored in the corresponding results chapters (*Chapters 4, 5* and *6*).

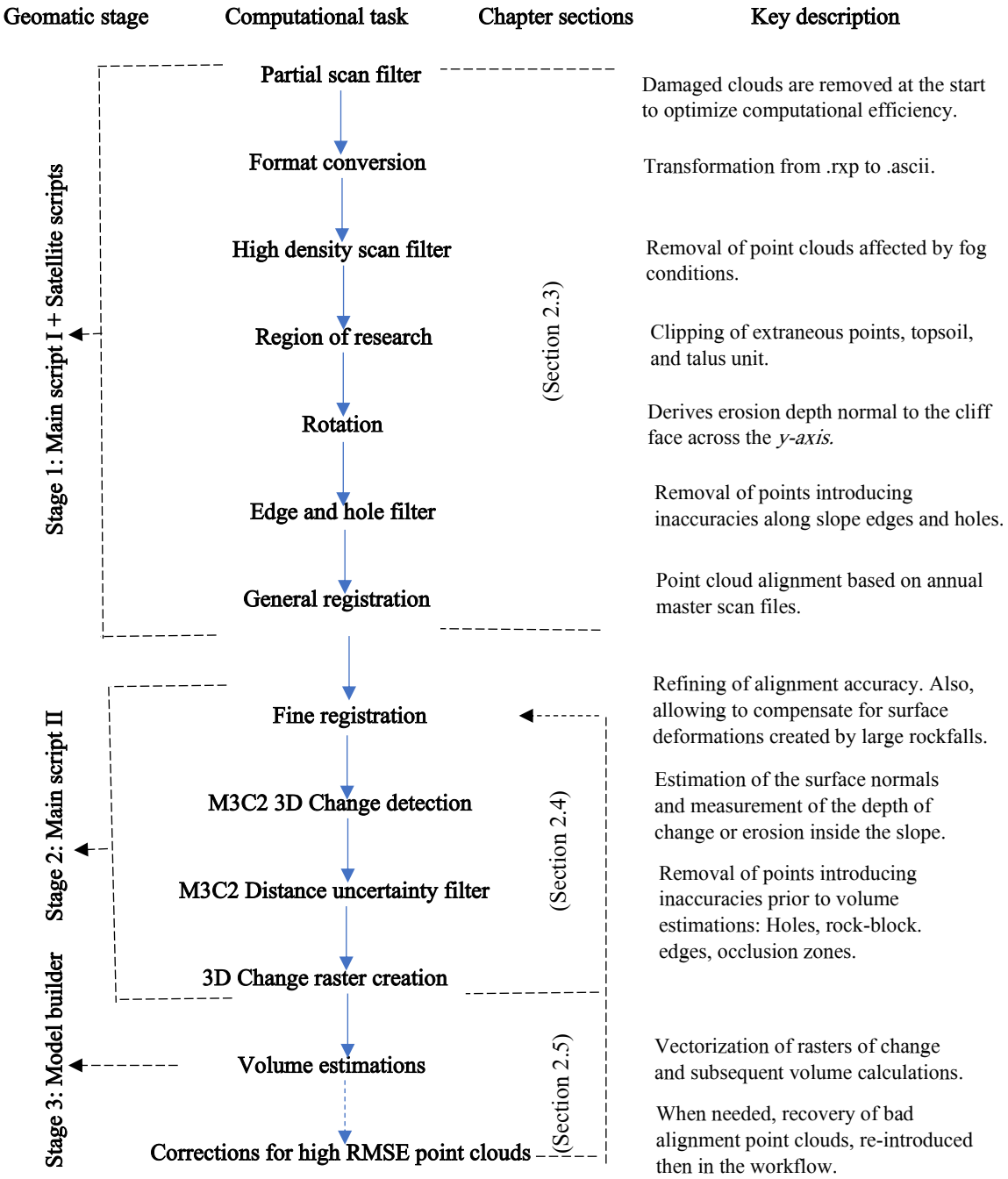

Figure 2. 1: *Workflow of the computational routine applied to quantify rockfall activity.*

This chapter begins with a description of the terrestrial laser scanner used (TLS), alongside with the field deployment, monitoring system, and data collection (Section 2.2). This is then followed by the *Stage I* of automatization, where the *Main script I* is used to undertake data format conversions, undertake a set of geomatic filtering steps and a general point cloud registration (Section 2.3). Then, *Stage II* of the workflow is presented, where 3D cloud-to-cloud change detection is undertaken using the M3C2 algorithm (Lague et al., 2013), followed by the execution of a 3D distance uncertainty filter to minimize the inclusion of errors in the measurements of the depth of change, and finally the resulting surface change is rasterized for

individual slope failures (Section 2.4). The change detection routine has been then coupled with a geomatic algorithm to estimate rockfall volumes, volumetric errors, and key morphometric properties of the failures, which has been implemented using a *Model Builder* in *ArcMap*. Also, a method for correction and recovery of point clouds with high root mean square errors (RMSE) is presented (Section 2.5). Finally, the method for the correction of highly misaligned point clouds is described (Section 2.6). Due to the application of different types of geomatic filters within the data processing workflow, a summary of the data retention in the workflow is presented towards the end of this chapter (Section 2.7).

2.2 Description of a constant TLS monitoring system

2.2.1 Instrument description

The terrestrial laser scanner (TLS) used was a remotely controlled Rigel VZ-1000, which is a time-of-flight measurement system that provided a high speed and contactless data acquisition using a narrow infrared laser beam (NIR; λ = 1,064 nm) and a fast scanning mechanism. Under good atmospheric conditions, the scanner operates up to a very long range (2.5 to 1,400 m) with high distance accuracy (8 mm), high precision ranging (5 mm) and provides a maximum effective measurement rate of 122,000 points s^{-1}, meaning that for instance, it is possible to acquire 1×10^6 points from a rock-slope at ~ 100 m range in 20 minutes. Importantly, the Riegl VZ-1000 is a compact and lightweight surveying instrument that also provides a wide field of view (Table 2.1), making it suitable for a wide range of field deployments, such as this. The instrument has an estimated angular resolution of 0.0005° and a beam divergence of 0.3 mrad, corresponding to an increase in the beam diameter of approximately 0.03 m per 100 m of distance when the laser beam width strikes any given scene orthogonally. The XYZ position, surface reflectance and deviation of each point within a point cloud are the main outputs of the instrument (Riegl, 2007). Whilst the scanner collects 'full waveform' data, this was not utilised in this research, but was archived.

Table 2. 1: *Key technical data of the terrestrial laser scanner Riegl VZ-1000.*

Max. scan rate (points s^{-1})	Max. range (m)	Min. Range (m)	Distance accuracy (mm)	Precision (mm)	Field of view (Hor./Vert.)	Weight (Kg)
122,000	1,400	2.5	8	5	360°/300°	9.8

Source: Riegl 2017, Technical manual.

2.2.2 Field deployment and monitoring setup

The laser scanner has been installed inside the former lantern room at the top of the East Pier lighthouse and has been near-continuously collecting data since March 2015, after the initial installation of the monitoring system in December 2014. The system has been custom designed and developed between Durham University and 3D Laser Mapping Ltd (now GeoSlam Ltd). The scanner was mounted on a horizontal steel base plate installed inside a custom-built aluminium frame, fixed to a custom-built hardwood doorframe, facing towards the cliff face. On the hardwood doorframe, a small pane of laser permissible glass was installed, allowing the laser beam to pass through with minimal interference or data loss, whilst also protecting the scanner from the weather. Also, the aluminium frame was secured with a removable panel at the back. Next to the scanner, a controls system that included a miniature computer alongside with power switches, which were used to control the scanner and collect the data, was installed and secured inside another custom-built metal housing (Figure 2.2). The system was linked to a broad band internet connection via a long-range directional Wi-Fi connection across the harbour to Whitby Yacht Club.

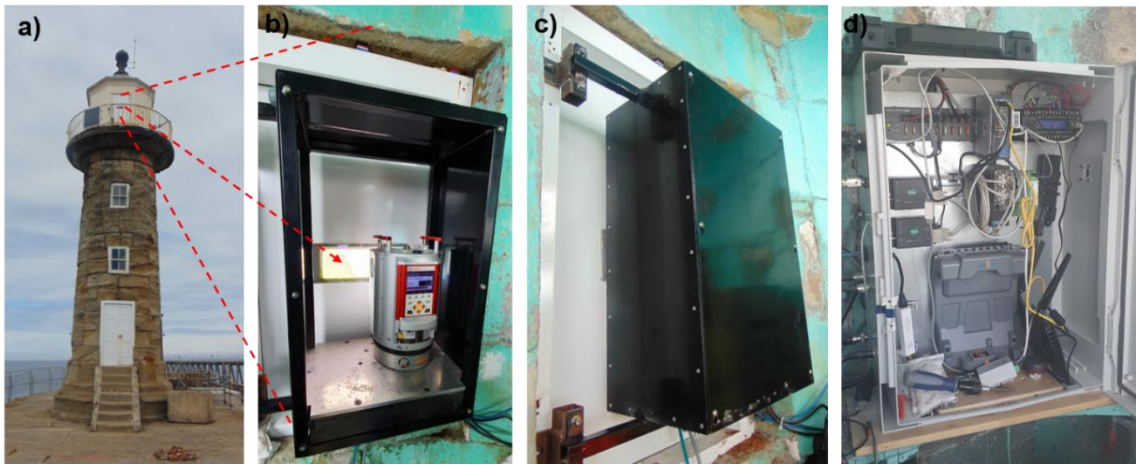

Figure 2. 2: *Riegl VZ-1000 field deployment to monitor rockfall activity: a) Image of the East Pier Lighthouse facing towards the cliff face and the lantern room at the top of the lighthouse where the scanner was installed is highlighted with red dashed lines; b) The scanner was mounted inside an aluminium frame, where a glass panel suited to allowing the laser beam to pass through with minimal interference (Red arrow); c) The aluminium frame was coupled with a secure removable panel at the back; d) Computational system that runs the software SiteMonitor (GeoSlam Ltd.), which was used to collect the scans and remotely send the data to the Whitby Yacht Club.*

The laser scanner, a webcam (that is used to monitor via streaming the site conditions), and the controls system running the scanner were continuously powered by a dedicated mains power supply from Whitby harbour, which was essential to minimising the risk of interruptions

in the data collection and the need of site-visits during the monitoring period. The scanner monitoring schedule and the possibility to switch the scanner on and off was controlled using the software package *SiteMonitor,* provided by *GeoSlam Ltd.* The *SiteMonitor* software was managed using a miniature fanless computer system called *fit-PC* (Provided by *CompuLab* Ltd.), forming the core of the controls system used to remotely run the scanner, collect, correct and send the data. Then, the data acquired from the scanner was transferred to a Network-Attached Storage (NAS) device. Finally, the NAS device, which is a file-level computer data storage system, stored and copied the data to Durham University servers (Figure 2.3).

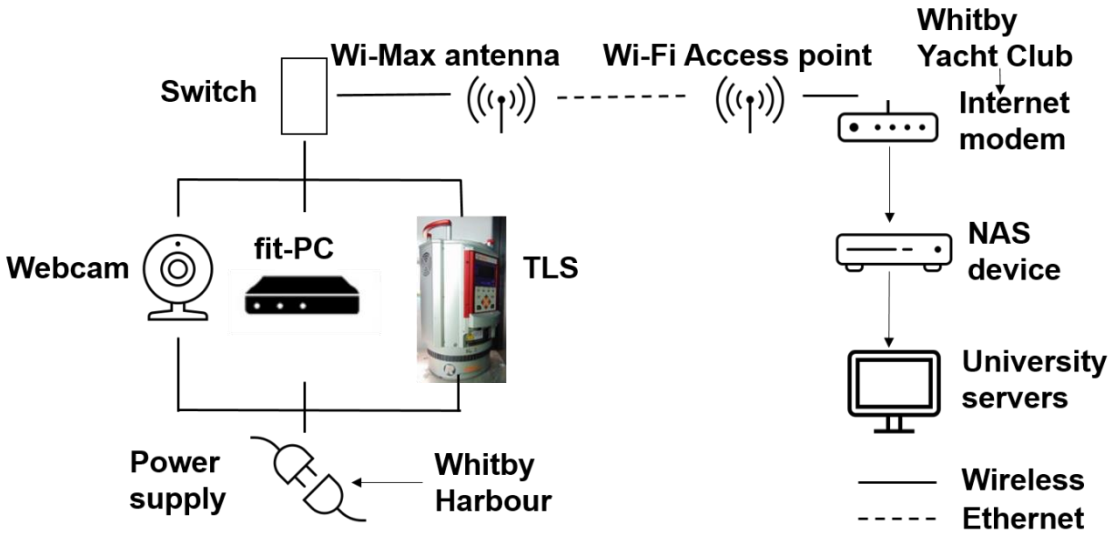

Figure 2. 3*: Conceptual diagram of the monitoring setup that was used for surveying the rockfall activity. The mains power supply for the TLS, fit-PC device and webcam was provided from the Whitby harbour. The fit-PC device runs SiteMonitor (GeoSlam Ltd.) which was the software used to control the TLS and save the scan data to a NAS device for upload through the Whitby Yacht Club broadband, which was then copied to the Durham University servers. Figure modified from Williams (2017).*

During this stage, drift in the data was compensated by using six-fixed retroreflective control targets of 0.25 m^2 mounted on the periphery of the cliff face, which provided precise relative position from scanner. These targets were used to periodically check data aligned and to correct for long-term drift. They also enabled the software to automatically undertake atmospheric corrections related to changes in range associated with fluctuations in temperature, humidity and pressure, and feed into a precise point-cloud registration conducted every 3 hours which runs an affine rigid-body rotation matrix to compensate for apparent yaw and tilt in the scanner position. It is important to note here that this process of initial correction is needed to compensate for small shifts in the location of the laser scanner and also because of potential drifts between subsequent scans that are generated by variable atmospheric conditions as mentioned above, but also because

of any relative changes in the position of the scanner and the lighthouse as a result of tidal loading of the coast (see Section 2.3.6). To date, atmospheric range corrections using a set of pre-existing stable targets installed on the slope are standard methodological practices during automated laser scanning landslide monitoring (e.g., Kromer et al., 2017a) and rock-slope surveys (e.g., Williams et al., 2018). As such, atmospheric corrections are necessary as the atmospheric conditions may have an impact on the precision, total number and signal-to-noise ratio of the returned measurements of the laser beam (Williams, 2017), compromising the strength of the signal or laser velocity but not necessarily the accuracy (Abellán et al., 2014). For example, for the range of the targets such as in the East Cliff (~ 342 to 533 m, see Section 2.2.3), it is considered that the atmospheric conditions do not pose a significant effect upon the precision of the range estimates and accuracy (Boehler et al., 2003; Williams, 2017). However, as in the monitoring campaign of 2015 (Williams, 2017), to compensate for this effect, the application of range corrections factors was automatically conducted using the six-fixed retroreflective control targets of 0.25 m^2, but also due to the installation of the laser scanner behind the white-painted wooden door installed at the lighthouse front, which minimize direct insolation of the scanner.

2.2.3 Data acquisition

Over 20,000 individual hourly scans were captured between the monitored period of 4th January 2017 and 31st December 2019, totalling 36 months of near continuous TLS survey (Table 2.2), making this perhaps one of the highest resolution and longest duration rock-slope monitoring campaigns accomplished to date. All scans were collected at 1 h frequency interval using an automatic scan schedule, compromising point clouds of ~ 2.6 million points before the application of the geomatic mask defining the region of research. Whilst the scan area was constant, the point number varied based on atmospheric conditions and the tides which influenced the degree of data captured over the intertidal zone in the survey scene. In this survey, the minimum obtained point spacing was ~ 0.05 m at the closest section of the cliff face to the scanner (342 m) while the maximum point spacing was ~ 0.15 m at the farthest zone of the cliff (533 m), averaging ~ 0.08 – 0.1 m across most of the zones of the cliff face.

As discussed by Abellán et al. (2014), the point spacing is commonly interpreted as the spatial resolution of a TLS dataset, which depends on the distance between the cliff face and the location of the TLS, and the user-defined angular spacing between adjacent scan lines. As such, the point spacing determines the level of detail that can be detected from the scenes, and so the area of each cell during the rasterization of the point clouds. Importantly, during TLS surveys, the spatial resolution also depends on the spot/footprint dimension, which is a measurement of the

laser beam width (Jaboyedoff et al., 2012). The spot dimension increases with the distance because of the beam divergence (0.3 mrad for the used TLS). Therefore, the scanner footprint may be greater than the point spacing especially at long distances (Shan & Toth, 2008). It is suggested that the ideal point spacing for any given scene should be 0.86 (86%) times the beam width (Lichti & Jamtsho, 2006), otherwise, fine details of the scene may become blurred if the point spacing is below this threshold (Jaboyedoff et al., 2012). In the study site, it was estimated that the beam width was ~0.10 – 0.16 m when it reached the surface of the cliff face. Therefore, the point spacing acquired in this survey meet the point spacing to beam width ratio of 0.86 and as a result, the acquired dataset provides a suitable spatial resolution for rock slope monitoring and characterization of the rockall activity.

Table 2. 2: *Total number of collected scans by year.*

	2017	**2018**	**2019**	**Total**
Collected scans	7,248	5,412	7,438	20,098

As part of the TLS survey protocols suggested by Abellán et al. (2014), and also due to the long-term and constant monitoring nature of this research, a 1 h frequency interval of data acquisition has been chosen in order to consider the durability of the scanner system for this specific monitoring environment. A combination of the scanning duration and scanning interval defines the amount of time that the scanner is remotely power off, being critically needed to ensure that the instrument does not fail as a result of burning out due to continuous operation. Therefore, based on Williams (2017), a balance was needed between the frequency of data collection to examine long term behaviours of the rockfall activity and periods where the instrument was inactive. Although using 1 h monitoring frequency was critical for the durability of the instrument, this monitoring frequency also enabled the detection and description of weekly and diurnal temporal patterns of rockfall occurrence alongside the possibility to examine potential relationships between the rockfall activity and rapidly changing environmental conditions with a temporal length scale of 1 h, such as storms or diurnal temperature fluctuations.

The cumulative number of collected scans, plotted as time-series, and the principal and minor gaps in the time series are shown in Figure 2.4. Gaps occurred due to technical faults in the scanner or software-derived failures affecting the scan schedule. The first main gap was during the 2017, occurring in spring (Z1) compromising a loss of 18 days of continuous data between the 17th of April and the 4th of May. In winter 2018 a second gap zone of 9 days length (Z2) took place, while the largest gap of the whole inventory occurred in autumn, compromising 51 days between 9th October and 18th November (Z3). In the transition between 2018 and 2019 occurred

another main gap of 26 days duration (Z4), while the last main gap zone of the monitored period occurred in autumn 2019, involving 17 days of continuous lack of data (Z5). Minor gaps involved between one hour intervals and a maximum of four days without data. As such, between 2017 – 2019, the total percentage of hourly missing at the time of data acquisition scans was 23.5% of an ideal dataset (i.e., a year without missing data of 8760 hourly scans collected per year). Overall, despite the occurrence of gaps in the data acquisition (Figure 2.4), the cumulative number of collected scans shows a near-constant and consistent acquisition rate at 1 h interval, providing a suitable dataset size to quantify and assess the temporal behaviour of the rockfall activity and rates of cliff erosion.

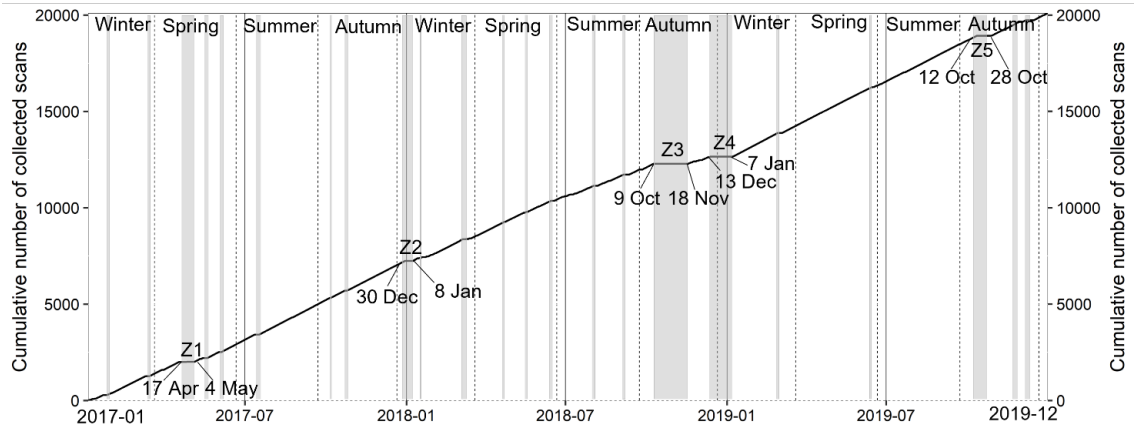

Figure 2. 4: *Cumulative number of scans acquired between 4th January 2017 and 31st December 2019, plotted as time-series. The gradient of the trend line indicates the acquisition rate at 1 h of data collection interval. Z1 to Z5 show the major gap zones (higher than nine days without continuous data). Minor gaps (between one hour intervals and up to four days) are shown with non-numbered thinner gray bars. Vertical continuous lines show boundaries between the monitored years while vertical dashed lines show boundaries between astronomical seasons.*

2.3 Optimized point cloud workflow: Stage I

This section describes the first stage of automation, where a total of 20,098 initially acquired scans were used as input dataset. This stage begins with the description of the partial scan and high density scan filters, which were applied at the beginning of the workflow to remove anomalous point clouds and so, reducing computational time for subsequent data processing. Then, after the scans were transformed from the native to a standard ASCII format, the area of interest on the cliff was extracted, followed by the rotation of the dataset, which was needed to obtain a frontal view of the cliff (where across cliff, and up cliff are aligned to x and y, and cliff normal is z). An edge and hole filter was then applied to remove points with the potential of

introducing uncertainty in the surface change estimates. This stage ended with the application of a general registration, where point clouds were aligned using an annual master scan which again compensates for any long term drift in the data. This drift was typically generated in this research due to for example, technical maintenance of the equipment that shifted the exact spatial location of the scanner. As a result of this stage, filtered and registered point clouds were obtained, which were then used as input dataset for the second stage of automatization (Section 2.4). While the partial scan, high density scan filters and format transformation were undertaken using *Satellite scripts,* the other procedures describe in this section were implemented inside the *Main script I.*

2.3.1 Partial scans filter

Partial scans are point clouds where an absence of points over specific or most of the area of the cliff face are observed, generating incomplete scenes of the study site. They were created by inclement conditions during the data acquisition such as adverse weather (e.g., fog or rainfall) which can totally or partially obscure the cliff from the scanner and hence the quality of the point clouds. In this survey, the partial scans were characterized by a marked drop in the total number of points, generally falling below ~ 2,200,000 points, which is ~ 96% of the point population of a complete scan of 2,300,000 to 2,400,000 points. This fall in the number of points created areas with either a total absence of points, or a greater loss of data at increasing distance, primarily on either concave slope surfaces, between beds, bellow hanging rock bridges, on the talus, the cliff toe, or at times a general uniformly random loss of points over the 90% of the scene (Figure 2.5).

As Figure 2.5 demonstrates, the partial scans truncated different geological and geomorphic features, constraining the possibility to undertake a spatially homogenous and consistent pairwise surface change detection between scans. Hence, the partial scans were removed at the beginning of the workflow to optimize the computational efficiency. Similar to Kromer et al., (2017a), this stage represented a necessary quality-control step consisting of the rejection of scans if they did not contain a specified minimum number of points. In this study, it was noted that the size of each scan file depended on the total number of points forming a point cloud, so that partial scans were smaller than an average normal scan *.RXP* file format at the time of data collection. For example, in this survey, an average normal scan, formed by ~ 2,300,000 to 2,400,000 points (or higher) had a size of ~ 37 Mb, while an average partial scan, composed by ~ 1,250,000 points had a size of ~ 26 Mb. Consequently, per each year of monitoring, histograms of scan frequencies by scan size were used to examine the distributions of the weight of the scans and then, using the breaks of the histograms, identify potential thresholds from which the region of the partial scans started to occur (Figure 2.6).

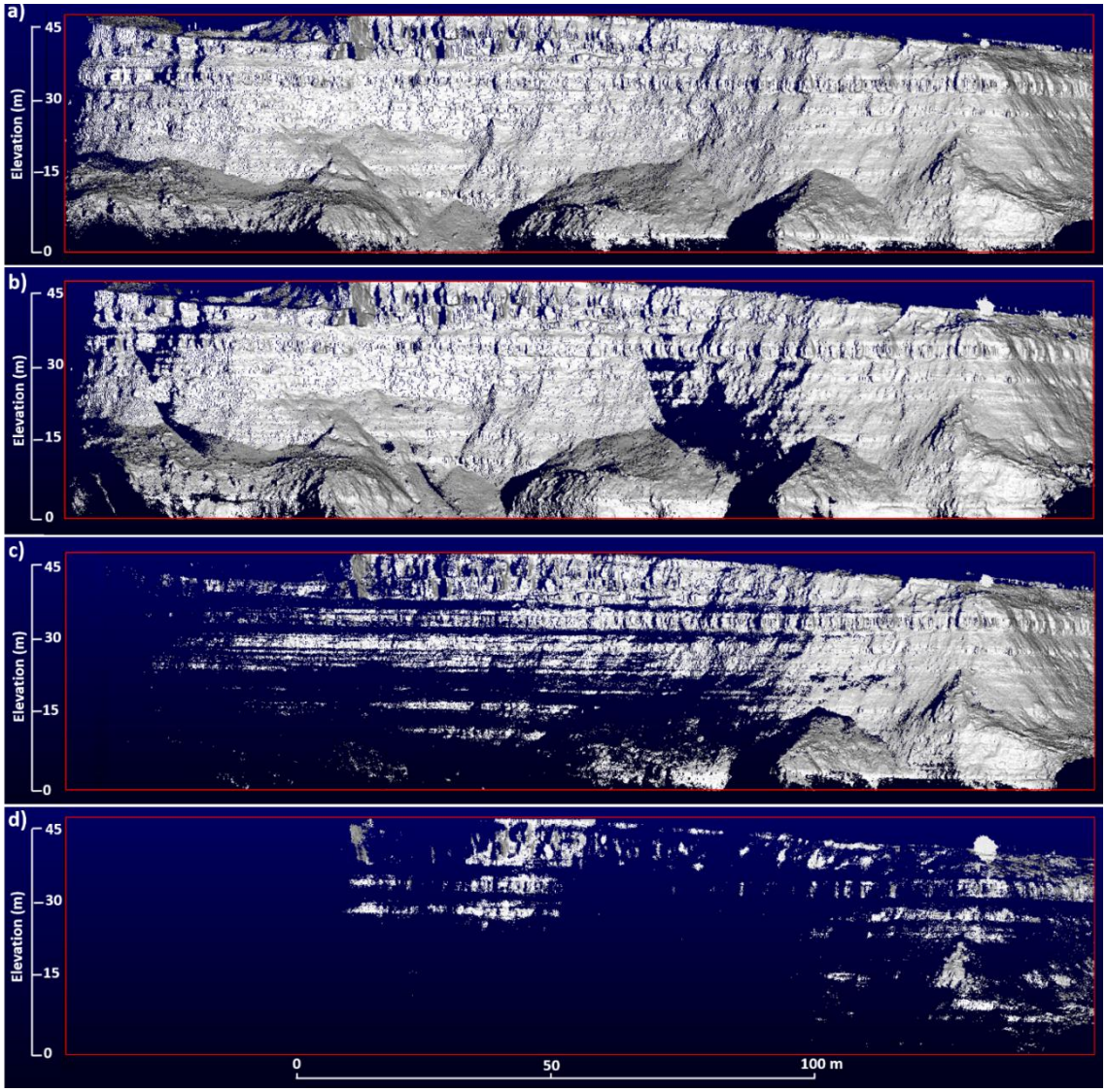

Figure 2. 5: *Example of partial scans captured in January 2017. a) Frontal view of a typical normal scan of 34.5 MB size (Point cloud of ~ > 2,400,000 points). b) Partial scan of ~ 33.8 MB size (~ 2,200,000 points), where the areas with absence of points are observed on concave slope zones either towards the left and central-right regions of the cliff face. c) Partial scan of ~ 32.1 MB size (~ 1,600,000 points), where the regions with absence of points are observed on the principal beds, talus, and cliff toe. d) Partial scan of ~ 18 MB size (~ 140,000 points), with a significant general absence of points over the cliff face. The red box indicates the principal boundaries of the study site. All scans are shown using hillshade effects.*

Figure 2.6 illustrates that scan frequencies ranged in size from ~ 1.0 to a maximum of 111 Mb, with a mean size that fluctuated between ~ 36 and 38 Mb and a mode that ranged between ~ 37 and 39 Mb. Furthermore, the examination of the histograms showed that the thresholds from which the region where partial scans started to occur was below the ~ 34 to 36 Mb, depending on the year of data acquisition. Per each month of the monitored years, based on the features showed in Figure 2.5, a visual inspection of the point clouds across the boundaries of the partial scan

region was undertaken to confirm that the thresholds were accurately identified, although it is important to note here that due to the size and complexity of the dataset, some partials scans entered to the workflow, but these were then visually inspected and deleted after the application of the stage presented in Section 2.6. A satellite script was used to automatically filter partial scans below the thresholds of 34, 35 and 36 Mb for the annual dataset of the 2017, 2018 and 2019, respectively. Although the size of the scans was normally distributed, for this dataset, the application of a standard statistical criteria such as the 95% confidence level at two standard deviation (2σ) ranged between ~ 48 and 57 Mb, and hence, it was not possible to use this criteria to identify potential thresholds since it did not show correspondence with the true or empirical observed thresholds.

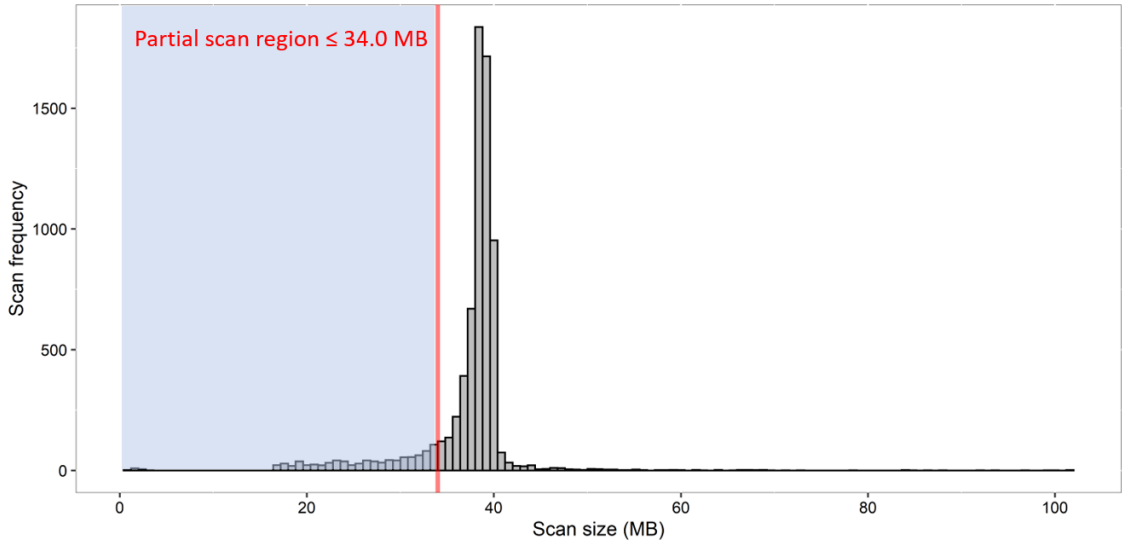

Figure 2. 6: *Example of identification of partial scans using an annual histogram of scan frequencies by scan size (Mb). For the 2017 dataset, the partial scans were found below ~ 34 Mb (Red vertical line), compromising a total of 1,027 scans for this year (~ 14 % of the annual dataset). Scans below this threshold (Blue area) were automatically filtered at the beginning of the workflow to optimize the efficiency in terms of the time of computational processing.*

As a result of the partial scan filtering, 2,907 out of 20,098 scans were removed, equating a reduction of 14.5% in the dataset, leaving 17,191 scans for further geomatic processing (Table 2.3). Importantly, because of the large size of the collected scans, to gain computational speed in terms of the time of data processing, the partial scans were automatically filtered at the beginning of the workflow, before the file format conversion stage, which involved the transformation from the original manufactured laser scanner type of data file (*.RXP*) to a standard ASCII text file format (*.TXT*) needed for further data processing and automatization. Using a i7-9750H CPU equipped with 2.60 GHz, 16GB RAM and six cores, for each average normal scan file of ~ 37

Mb size, the format conversion stage took ~ 38 s, while for each average partial scan file size of ~ 26 Mb this process took 18 s, which was approximately half of the time of the conversion of a complete scan. Consequently, as over 2,907 scans skipped the file conversion process, it is estimated that, at this stage, ~ 15 h of continuous computational processing time was gained. However, this estimation is underestimated when considering that the partial scans did not enter to the next stages of the workflow, such us point cloud registration, normal calculations, and M3C2 distance calculations (Figure 2.1 in Section 2.3.1).

Table 2. 3: *Filtered partial scans per year of monitoring.*

Year	Collected scans	Filtered scans	Scan loss (%)	Available scans
2017	7,248	1,027	14.2	6,221
2018	5,412	1,114	20.6	4,298
2019	7,438	766	10.3	6,672
Total	20,098	2,907	14.5	17,191

2.3.2 High density scans filter

Anomalously high density scans are point clouds containing artefact points, spatially scattered within the field of view of the laser scanner. These were found to have an average density of ~ 1.1 points per 100 m^3 in front and at the back of the cliff face, and hence generating occluded scenes of the study site. Like the partial scans, these data were created by adverse weather conditions, promoting high atmospheric moisture, resulting in the scattering of the measurements taken by the infrared laser beam. The high density scans were characterized by an increase in the total number of points, generally ranging between ~ 2,500,000 and 6,000,000 points at the time of data collection. This rise in the number of points generated a dense, radially arranged or fan-shaped dispersion of points from the TLS position (Figure 2.7a). As a result, they prevented the implementation of key process of the workflow such as the registration between scans and the calculation of the point cloud normal. Failure to remove these scans terminated in failure or crashing of the computations. Therefore, high density scans were automatically detected after the file format conversion stage and removed before the definition of the region of research and subsequent stages of automatization of the workflow. It is important to note that the high density scan filter removes scan files rather than filtering particular points inside these scans (Figure 2.1 in Section 2.1).

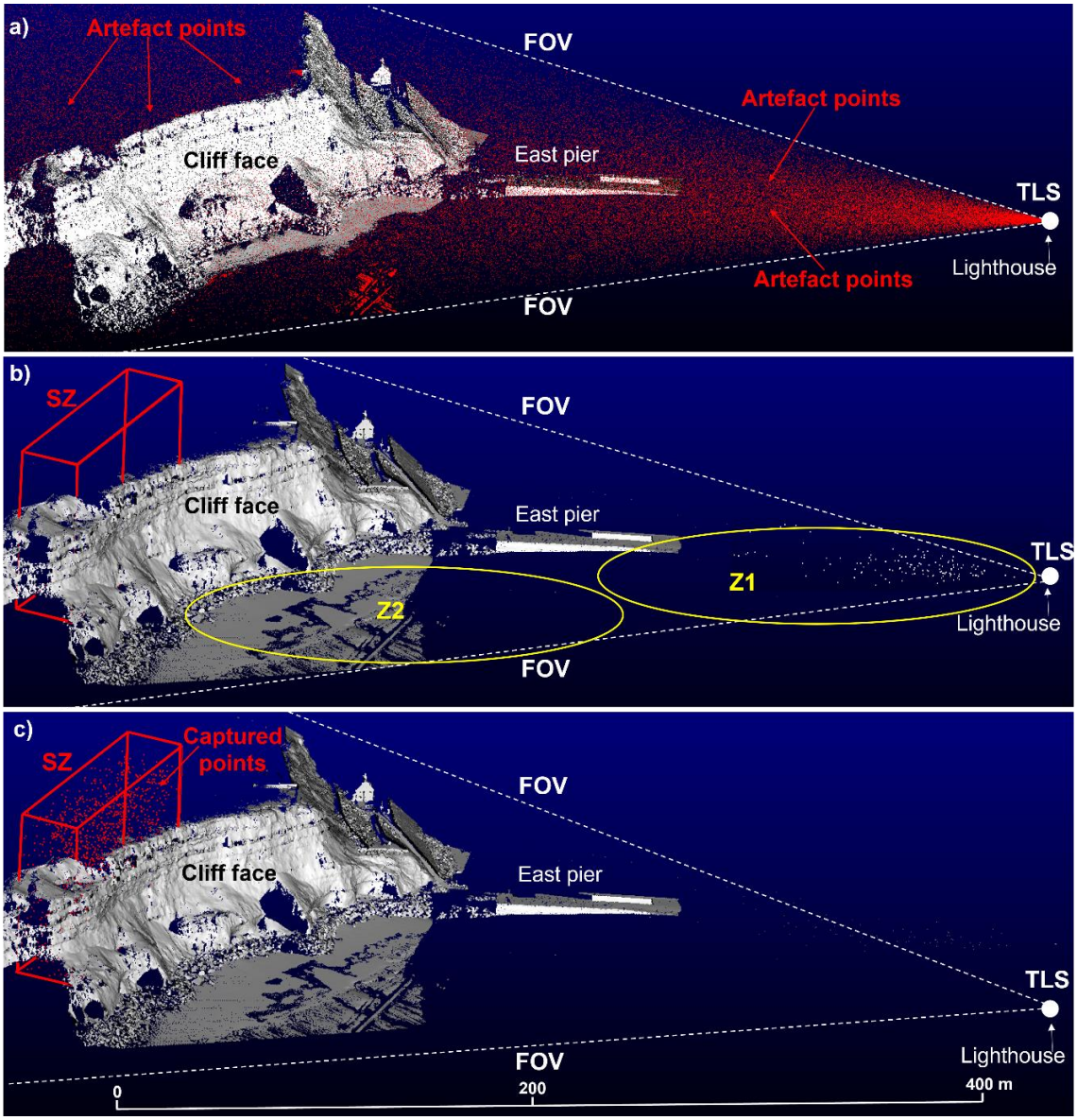

Figure 2. *7: 3D view* showing *the method for detection of the high density scans. a) Typical high density scan made by anomalous or artefact points spatially scattered in front and at the back of the cliff face (Highlighted in Red) with a radially arranged dispersion of points from the TLS position. b) Method for detection of* dense scans, *where the searching zone (ZS) to detect and count the artefact points was a 3D box of ~ 270 m³, fixedly located at the back of the cliff face (Highlighted in red). This figure also shows a typical normal scan with the presence of points in front of the TLS (Z1) and/or across the shore platform (Z2), generating a high density scan that is not associated with artefact points. c)* Method *for detection of dense scans, where over 1,500 artefact points (red) were captured inside the searching zone box. Yellow ellipses highlight the zones where point can be normally found either nearby the TLS (Z1) or on the shore platform (Z2). Figures b) and c) are based on a hillshade effect.*

High density scans are believed to arise as a result of weather conditions (for example, fog may reflect the laser immediately as the beam leaves the lighthouse), light conditions (for example, sun light is known to contain some wavelengths that overlap with that of the scanner

which can generate false returns) and reflections (for example, from the sea surface, or from the lighthouse window and scanner aperture glass, which may occur under certain coincidences of geometry and lighting). Each of the effects results in a characteristic pattern of erroneous points, composing scan files that must be identified and then removed. However, when such erroneous point are present in a scan, it is also more likely that the quality of the point cloud on the cliff face will be reduced, and so these scan files are identified and then removed from the time series. As such, similar to Kromer et al., (2017a), this stage represented a second quality-control step of the dataset but in this study, by removing unwanted scans inducing crashing of the computations during registration and change detection.

By examining the location and density of points forming normal scans under normal conditions of data acquisition, it was observed that apart from the cliff face, there are two preferential zones where erroneous points may be detected, without generating occlusion of the study site due to artefact points. The first zone was immediately in front of the location of the laser scanner, where a fan-shaped distribution of points between the lighthouse and up to half of the east pier was usually observed (Z1), while the second zone was detected when the scanner captured the shore platform, especially during low tides (Z2). However, the unique distinctive geomorphic zone where normal scans did not show points, with exemption of the normal detection of man-made structures and occasional birds, was immediately behind the cliff face, seemingly inside the cliff, where high density scans always showed a dense scattering of anomalous points. Consequently, a searching zone (SZ) for the automatic detection and trapping of anomalous or artefact points, indicative of the existence of high density scans was fixedly located at the back of the cliff face (Figure 2.7b).

The searching zone was a 3D box of up to ~ 270 m^3 that was implemented in a satellite script to automatically trap and count the number of points falling inside the box (Figure 2.7c). If point clouds containing artefact points were detected, then an automatic copy of this scan file was generated and moved to a folder to store high density scans. Conversely, using a logging file to monitor the process of automatization, if there were no points falling inside the 3D box, which was indicative of a normal scan, then no further copies of the point cloud were created but a logging file was generated with a specific statement indicating that "*no points fall inside the input box*". Finally, a visual inspection of the high density scan file copies was undertaken to confirm that these scans were accurately detected and filtered. Also, although high density scans were characterized by a large file size, which fluctuated between ~ 78 and 178 Mb, it was observed that there can be normal scans of similar size (e.g., 100 Mb) that did not show the occurrence of artefact points. Instead, their size was due to the acquisition of points on both the shore platform (Z2) and in front of the lighthouse (Z1). Thus, the identification of thresholds based on histograms

of scans frequencies by scan size as was used for the detection of partial scans (Section 2.3.1) was not a suitable method to solve this combined geomorphic and geomatic influence on point cloud quality.

As a result of the high density scan filtering, a total of 359 out of 17,191 input scans were removed, equating a total loss of the 2% of the initial available scans after the application of the partial scan filtering. The remaining 16,832 scans were considered good quality data, and thus available for the next stages of data processing (Table 2.4). Importantly, in terms of the optimization of the overall computational workflow, the advantages of the application of this filtering method were twofold. First, this filtering offered a low computationally demand as the application of this filter took an average time of ~ 10s per scan to be completed. Hence, as this method was applied to over 17,000 input scans on four parallel computers, the total computational processing time was ~ 12h per computer. Second, there was no need to visually inspect scans that were collected during inclement weather conditions. Consequently, this method relies on a computationally efficient and an entirely remote sensing approach.

Table 2. 4: *Filtered high density scans per year of monitoring.*

Year	Filtered during partial scan stage	Input scans for stage 2.3.2	Filtered high density scans	Scan loss (%)	Available scans
2017	1,027	6,221	0	0	6,221
2018	1,114	4,298	242	5.6	4,056
2019	766	6,672	117	1.8	6,555
Total	2,907	17,191	359	2.0	16,832

Note: Input scans are the scans available after the application of the partial scan filtering (Section 2.3.1).

2.3.3 Region of research

The geomorphological criteria to define the region of research, which is the free/fall face of Whitby East Cliff, defined as the vertical rock-slope zone where the mechanisms to produce rockfalls occur, driving the evolution of the near-vertical cliff face, have been described in *Chapter 1* (Section 1.4.1). To clip the point cloud zones forming the area of research, a cuboidal bounding box of ~ 200 m length, 47 m height and 76 m depth was initially used to mask the principal boundaries of the study site, permitting the removal of extraneous points such us anthropogenic buildings at the top of the cliff face, detected parts of the east pier, the shore platform and birds. Then, 3D geomorphological mapping of the free face unit of the cliff was undertaken to mask the region of interest, clipping the geomorphic units that were not under

examination, such as the topsoil, debris forming the talus, and the cliff toe where a high point spacing as well as reduced range precision was observed (Figure 2.8). Indeed, similar to this stage, in rock-slope studies assessing either pre-failure deformation patterns and magnitude-frequency relationships of rockfalls using laser scanner data, the exclusion of slope zones reducing range precision and potentially affecting the quality of the registration were also undertaken by Kromer et al., (2015a) and (van Veen et al., 2017).

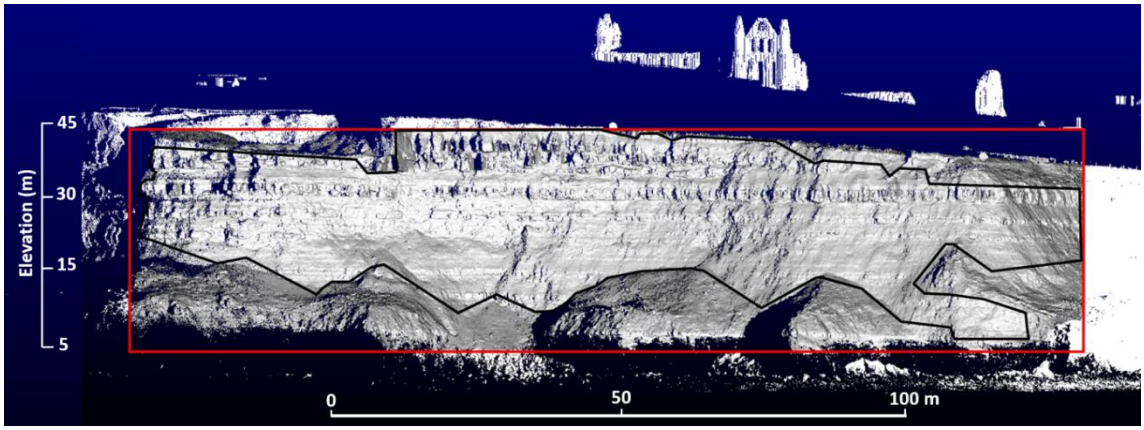

Figure 2. 8*: Definition of the slope region of research. For each point cloud, a cuboidal bounding box (Highlighted in red), defined by four coordinates was used to automatically clip the principal boundaries of the study site (Shown as hillshade), allowing the removal of extraneous points such as man-made structures at the top of the cliff face. Then, a 3D geomorphological mapping of the rock-slope free face unit where discontinuity controlled rockfalls occur, forming the region of research, was used to apply a geomatic mask (black) to clip the topsoil, talus and the cliff toe.*

The 3D mapping yielded a total of 66 coordinates that were then used in *Main script I* to apply a mask using the *crop2D* command in Cloud Compare. Finally, this method was automatically and iteratively applied to each scan, yielding a total area of research of ~ 5,459 m^2 per point cloud. Importantly, the process of extraction of the area of research typically reduced a raw point clouds from 2,300,000 points (i.e., total points of an initially acquired normal scan) to ~ 800,000 points (34 %). As a result, the fall in the number of points reduced the file size of the point clouds and the number of calculations needed for each, which was critical to increase the speed of the subsequent data processing (Figure 2.8).

2.3.4 Rotation

Because of that the subtraction of sequential scans derives erosion depth perpendicular to the cliff face (Rosser et al., 2005, 2013), point clouds need to be rotated to align the most planar surface possible through the $x - z$ plane, which ensures that the depth of each point cloud is

measured across a new arbitrary axis (here, the *y axis*) normal to the dominant strike of the cliff face, rather than across the original line of sight of a given global coordinate system used by the scanner (Williams, 2017). Therefore, the rotation of the point clouds was a fundamental procedure for determining the degree to which the erosion, quantified using methods such as the DEM of Difference (DoD) or M3C2 distance change detection, characterizes the true surface deformation of the slopes (Rosser et al., 2007). Furthermore, the rotation was important for enabling the solution of normal direction ambiguities, where the *y* component of each normal vector should always be directed out of the surface of the cliff face (Williams et al., 2018), as well as for the rasterization of the point clouds. This also allowed frontal views of the slope to be analysed in a GIS environment, permitting the delineation and calculation of the area, volume and morphometry of the failures. It also enabled the data processing to take early advantage of the speed of 2 / 2.5D data processing as opposed to more cumbersome 3D routines.

In raw point cloud datasets obtained during this TLS survey, the *y-axis* was oriented along the cliff face, while the depth, which is the distance between the lighthouse and the cliff face, was oriented across the *x-axis.* Also, the elevation was represented by the vertical *z-axis.* Consequently, to obtain measurements of the erosion depth perpendicular to the cliff face running across the *y-axis*, a fixed counterclockwise rotation of 90° around the *z-axis* was undertaken around the central point of the cliff face until it became approximately planar along the *x-z* plane using the fixed front view of the console of Cloud Compare (Figure 2.8). As shown by Dunn and Parberry (2002) and Teza et al., (2007), the rotation uses a standard affine transformation matrix formed by a rotation (3x3 matrix) and a translation (a 3D vector), which is typically written as a 4x4 matrix where the rotation *R* corresponds to the upper part of the three first columns, while the translation vector corresponds to the upper part of the fourth column (i.e., the column [0;0;0;1]). Hence, the applied rotation is given by Dunn and Parberry (2002):

$$R = R_x(\phi)R_y(\theta)R_z(\psi) \qquad \text{[Eq. 2.1]}$$

$$\begin{bmatrix} cos\psi & -sin\psi & 0 & 0 \\ sin\psi & cos\psi & 0 & 0 \\ 0 & 0 & 1 & 0 \\ 0 & 0 & 0 & 1 \end{bmatrix} \qquad \text{[Eq. 2.2]}$$

This rotation was implemented inside the *main script I* using the command *apply_trans* of Cloud Compare by automatically loading a *.txt* file containing the input matrix values resulting from a counterclockwise rotation of 90°, which was applied to the first point cloud of the dataset. Finally, this procedure allowed the automatic rotation of each point cloud of the inventory.

2.3.5 Edge and hole filter

Once the region of research was clipped (Section 2.3.3) and the rotation was undertaken (Section 2.3.4), an edge and hole filter was applied to remove points with high positional uncertainties, enhancing the accuracy of the point clouds used during the change detection stage (Section 2.4.3). The edge and hole filter has been described as a morphological filter as it removes points along edges, defined as sharp topographic breaks in the gradient of the rock-slope surface, as well as points detected inside holes, defined as features that surround zones of occlusion in the slope system, which commonly occur at edges because of high surface gradients (Williams et al., 2018). In addition, points forming surfaces with very low densities were also filtered as, such as those around edges and holes, which have the potential to generate unrealistic high values of change since these points are less probable to be measured in similar physical locations between successive point clouds, producing unreliable change detection along these slope zones (Williams, 2017). As a result, this filter aimed to remove points on slope features that cannot be consistently measured.

The detection of structural and geomorphic features that cannot be consistently measured are created by scanning a morphometrically complex and highly inclined surface from a single fixed location (Lato et al., 2010; Abellán et al., 2014). Indeed, scanning from a fixed location has an impact on the similarity of the distribution of points between consecutive scans due to occlusion, generating holes around zones invisibles to the scanner. Also, at sharp morphological edges, range measurements may be averaged from multiple beam returns recorded from separate discontinuity surfaces that are intersected in only one laser footprint, creating positional uncertainties (Williams et al., 2018). Furthermore, as the scanner never measures exactly the same point twice (Hodge et al., 2009), it has been observed that the location of the sharp edges and the perimeter of any holes will shift between consecutive scans, despite no displacements of the scanner (Williams et al., 2018). The scan lines in most scanners result in a non-uniform data distribution, with observed heterogeneity often on an orientation and scale comparable to the slope surface structure, leading to aliasing, which is the tendency to omit or include edges between scans when the scan-line spacing exceeds the scale of the outcropping discontinuities (Lichti and Jamtsho, 2006). Also, it has been noted that the impact of these combined effects is amplified if the scanner view is oblique to the examined scene, like in the study site (Williams et al., 2018).

Therefore, a Statistical Outlier Removal (SOR) filter was applied to remove, as first instance, points along edges, holes, low density areas and points representing birds. Indeed, for the monitoring of landslides using TLS data, the SOR algorithm has been already used for filtering areas with low density points and sparse outilers, where it has been noted that by removing these

points, errors in estimating surface normals, in registration of point clouds and change detection were minimised (Lichti et al., 2005; Kromer et al., 2017a). The SOR is a method available in Point Cloud Library (PCL) and implemented in Cloud Compare that, assuming a normal distribution of the data, removed outlying points by performing a statistical analysis on each point's neighbourhood and then filtering those points which do not meet a certain criteria. Measuring the 3D Euclidean distance between two points (d_i) with *xyz* coordinates, the SOR computed first the mean distance, $d_{\bar{x}}$, of each point to its neighbours (i.e., considering n nearest total neighbour's points as first parameter). Then, all points whose mean distances were outside the maximum distance threshold (d_{max}), which was defined by the mean distance plus a multiple of the standard deviation (i.e., using a standard deviation multiplier, k, as second parameter), can be considered as outliers and removed from the dataset. Hence, for each point cloud forming the inventory, the SOR filter was computed as follows:

$$d_i = \sqrt{(X_{p1} - X_{p2})^2 + (Y_{p1} - Y_{p2})^2 + (Z_{p1} - Z_{p2})^2}$$

$$d_{\bar{x}} = \frac{\sum_{i=1}^{n} d_i}{n} \quad \text{[Eq. 2.4]}$$

$$\sigma = \frac{\sum_{i=1}^{n} (d_i - d_{\bar{x}})^2}{n} \quad \text{[Eq. 2.5]}$$

$$d_{max} = d_{\bar{x}} + k \times \sigma \quad \text{[Eq. 2.6]}$$

The standard statistical criteria of the 95% confidence level at two standard deviations was used as the multiplier ($k = 2$), ensuring that artefact points forming holes and edges were not introduced into the point clouds by removing too many points. This criteria was also selected as an inflection in the cumulative number points indicative of holes and edges was observed at around 2σ (Williams et al., 2018), thresholding an alternative edge and hole filter at 95% confidence interval in the same study site under similar conditions of data acquisition and overall point spacing. Then, a trial-and-error approach was used to define a suitable number of neighbour's points (n) needed to calculate the mean distance per point based on the geometry of the cliff under examination. By examining the spatial distribution of points of a normal point cloud including edges and holes it was observed that smaller neighbour's points ($n \leq 5$ points) sample too few points from each point cloud, yielding to many zones with artefact points (Figure 2.9a). Conversely, larger neighbour's points ($n \geq 50$ points) sample many points, causing over filtering of the data, especially around the borders of low density areas where the average normal

point spacing is ~ 0.1 m (Figure 2.9b). Hence, the number of neighbour's points, n, used to compute the distance to neighbours for each point was therefore specified as 25 points. This ensured a balance in the sampled points, minimising the inclusion of points along most of the edges, holes and zones of low point density (Figure 2.9c), while ensuring that the minimum recommended number of points for an edge and hole filter that was applied in the same study site ($n = 4$), following Williams et al., (2018), will always be exceeded.

The implementation of the edge and hole filter removed points whose maximum distances, around their closest neighbours, ranged from a minimum of 0.08 m for the case of outliers surrounded by zones dominated by a low and relatively homogeneous point spacing (0.05 to 0.07 m). The maximum of 0.6 m was for the case of isolated outliers falling inside the centre of the largest holes, while average thresholded values fluctuated between 0.2 to 0.4 m around sharp edges, holes, occluded slope zones or surfaces with low point densities (Figure 2.10). Also, for an average sized point cloud, this metric filtered ~ 20,000 out of a total of ~ 830,000 (2.4%). Finally, the filter was implemented inside the *main script I* using the command *SOR* in Cloud Compare, allowing the automatic removal of points representing positional uncertainties for each point cloud of the inventory. Also, a second stage for filtering of artefact points along edges and holes was undertaken after the change detection, using the M3C2 distance uncertainty filter (described in Section 2.4.4).

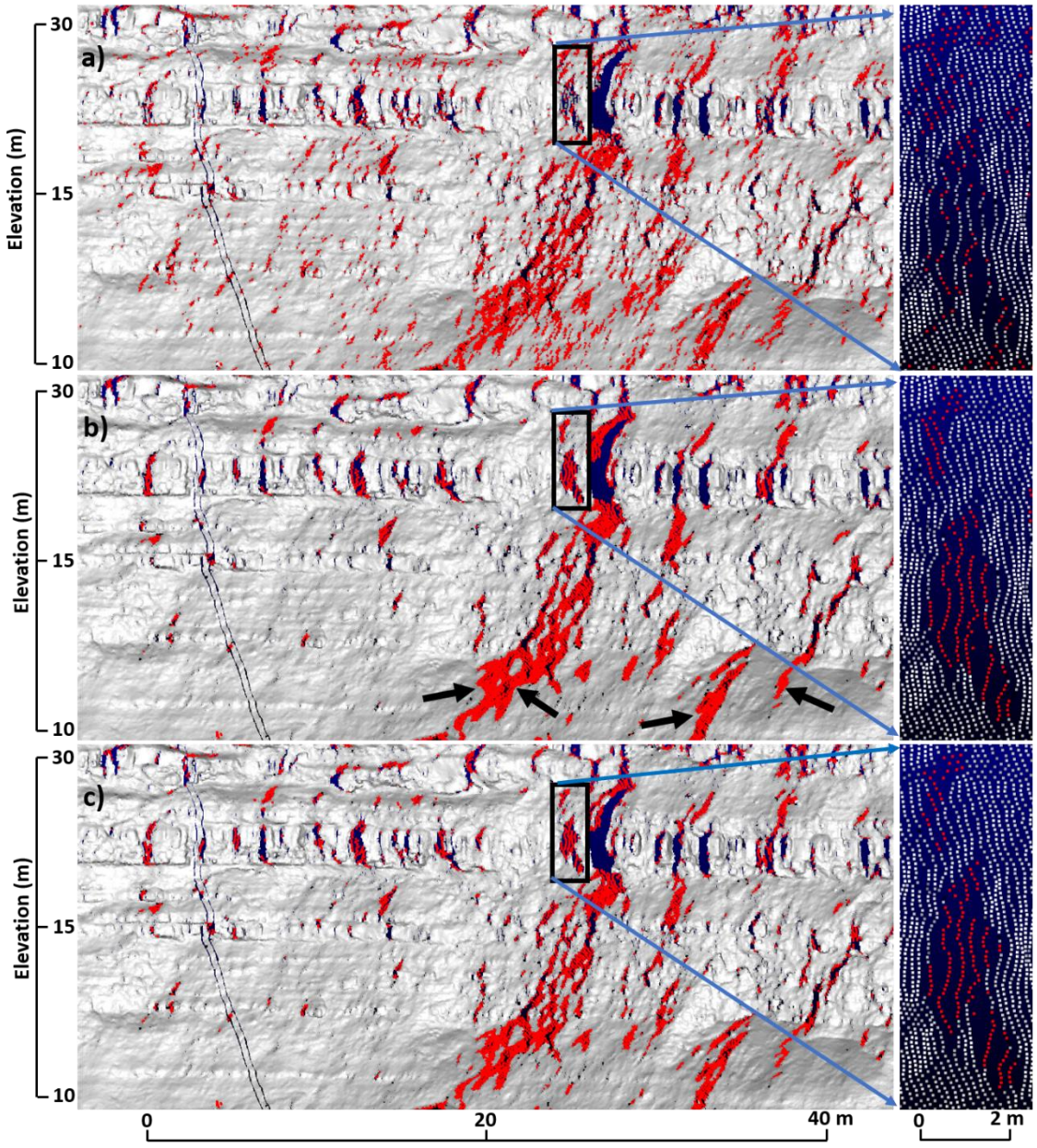

Figure 2. 9*: Application of the edge and hole filter along a central section of the study site, with filtered points coloured in red (frontal view), which are surrounded by a grey hillshade effect. a) Outcome of the filter using a total of 5 neighbour's points (n = 5), where artefact points inside holes were still observed. b) Outcome of the filter using a total of 50 neighbour's points (n = 50), where an over filtering of the points was observed along the perimeter of areas of low density points towards the bottom of the cliff face (Highlighted by black arrows). c) Outcome of the filter using a total of 25 neighbour's points (n = 25), minimising the presence of artefact points along most of the edges, holes and zones of low point density. To the right, each figure is coupled with a detailed view showing a typical hole with the removed points in red.*

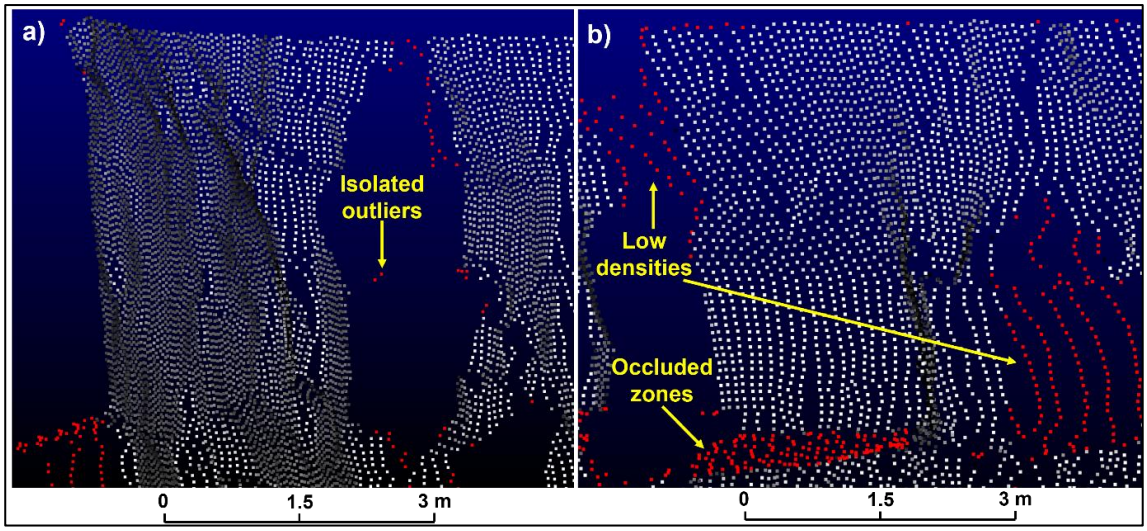

Figure 2. 10: *Oblique view of the edge and hole filter, with filtered points coloured in red. a) Filtering of isolated outliers falling inside a large hole (d_{max} = 0.6 m). b) Filtering of points on occluded slope surfaces and/or along surfaces with low point density (d_{max} = 0.2 to 0.4 m). Red points are surrounded by a grey hillshade effect.*

2.3.6 General registration

Scan registration or alignment refers to the process that combines or joins the spatial position of two contiguous or overlapping point clouds and that locates the scans in a reference coordinate system, and at large scale applies projections to a grid system (Abellán et al., 2014). Importantly, this process is needed to compensate for small shifts in the location of the laser scanner and also because of potential drifts between subsequent scans that are created by variable atmospheric conditions during data collection, or in the case of Whitby any relative changes in the position of the scanner and the cliff as a result of tidal loading of the coast. Furthermore, for point clouds acquired from a single fixed location, such as in this research, it has been noted that repeated laser scanning, without moving of the instrument, produced misaligned point clouds over different scan epochs (Kromer et al., 2017a), reassuring the need of registration of the acquired dataset. Also, it has been noted that small shifts in scanner inclination have the potential to propagate to several centimetres over distances of several hundred metres (Williams et al., 2018). In rock-slope monitoring applications, registration permits the accurate measurement of engineering parameters such as dip and dip direction (e.g., Sturzenegger and Stead, 2009a, 2009b) as well as the precise quantification of the erosion derived from pairwise change detection analysis between contiguous scans (e.g., Rosser et al., 2005, 2007; 2013).

As discussed by Abellán et al. (2014), registration of scans can be carried out using feature based registration methods that are based on the curvature and planarity of surfaces (e.g., Rabbani et al., 2007; Bae and Lichti, 2008; Brenner et al., 2008); target-based registration algorithms that rely on the precise DGPS survey of field control targets (e.g., Teza et al., 2007; Olsen et al., 2009); and point-to-point (and point-to-surface) methods that use Iterative Closest Point (ICP) registration, which is based on the progressive minimization of the distance between corresponding points in two overlapping scans (e.g., Besl and McKay, 1992; Yang and Medioni, 1992). Overall, these methods depend on the presence of corresponding elements and surface structures between successive scans for a precise registration (Abellán et al., 2014).

In this research, a least squares Iterative Closest Point registration algorithm (ICP) was automatically undertaken using the *ICP* command in Cloud Compare. This method searched for the closest point (p_i) in a reference scan (known as model, fixed or master scan), for each corresponding point of the contiguous scan (q_i), and then estimated the combination of a rigid Euclidean transformation that combined a 3D rotation and translation (α) that best minimize the distance (d) between both point clouds. Then, this method was applied iteratively until a user-defined convergence distance or Root Mean Square Error (RMSE) was achieved, which is commonly the mean square distance (ε) between the two closest points (Mitra et al., 2004). Hence, for this dataset, the point-to-point distance was computed as follows:

$$\varepsilon(\alpha) = \sum_{i=1}^{N} d^2(\alpha(q_i), p_i) \qquad \text{[Eq. 2.7]}$$

Importantly, this algorithm relies on two principal assumptions: first, consecutive scans are approximately although not perfectly registered, and so require some spatial adjustment; and second, both scans represent the same object or at least the same shape, permitting the overlap between successive point clouds. For this dataset, both assumptions were achieved as all the scans were collected from a single fixed location, providing the same distance-to-object, scale and shape of the cliff face, and extent. Also, after data collection, an automatic initial point-cloud registration conducted every 3 hours and an affine rigid-body rotation matrix to compensate for yaw and tilt in the scanner position based upon the scanned control target positions was undertaken (Section 2.2.2). Hence, prior to this stage of registration, point clouds were approximately aligned using these stable control points. Although over the periphery of the cliff face, six-fixed control targets provided with coordinates from total station surveying were available, the translation of the point cloud coordinates into a local datum is a usual methodological procedure to reduce the data volume (Abellán et al., 2014). As such, point clouds with preserved *xyz* coordinates in a local

project coordinate system were used during registration to reduce the data volume by removing the need for full multi-digit coordinates for each point (Williams, 2017). As a result, the scans weights were approximately halved due to the shortening of the multi-digit coordinates (Williams, 2017), which was critical to gain speed during the data processing.

To date, there is no established methodological protocol for selecting the ideal reference or master scan for registration. Therefore, this master scan can be the first collected scan of the whole inventory, the first scan of each scan pair, a regular sampled point cloud, or an average point cloud made from a sample of previously acquired scans (Williams et al., 2018). In this study, as first stage of overall registration or initial alignment, a general registration of the dataset was undertaken starting, as master scan, with the first acquired scan of the entire inventory. Nevertheless, due to maintenance of the instrument and the monitoring set-up, small shifts (> 1 cm) in the exact location of the laser scanner were produced, generating displacements of up to 23 m between the spatial position of the scans collected immediately before and after maintenance. As a result, a total of six master scans were needed to accomplish the change detection between 2017 and 2019 (Table 2.5).

In terms of the key parameters that were used to run this stage of the *main script I*, as suggested by (Benjamin et al., 2020), to improve the quality of the registration between surveys, a maximum permissible 3D registration error of 0.10 m was used. Also, in order to apply a spatially complete registration by using all the points forming each scan, no sub-sampling of the point clouds was undertaken. As such, the registration was run using a 100% overlap between the actual surface of each spatially adjusted point cloud and the corresponding master scan as in theory each scan covered an identical scene extent. In fact, during monitoring and characterization of rockslides using terrestrial laser scanning at Åknes in western Norway, it was suggested that a minimum overlap of approximately 20% between different point clouds is needed to ensue good spatial matching between scans(Oppikofer et al., 2009). Therefore, the applied overlap ensured that the minimum recommended overall will always be exceeded. Importantly, a 100% overall criteria was also applied as this ensured that, after the occurrence of big cliff collapses, the stable or non-eroded surfaces of the cliff face were used for alignment, as suggested by Teza et al., (2007), Oppikofer et al., (2009) and Kromer et al., (2015a).

As a result, this process was automatically run for 16,832 filtered scans, yielding an average root mean square error of 0.07 m, while the standard deviation remained constant at 0.01 m. Values of mean convergence distance were notably smaller for those scans belonging to months that were closer in time to each master scan (e.g., RMSE = 0.03 m) with a tendency to rise towards the scans belonging to months that were collected farthest with respect to their

corresponding master scans, approaching the maximum permissible 3D error of 0.1 m (Table 2.5). However, as the cliff is characterized by frequent rockfall / erosion which can include large rockfalls (e.g., ≥ 10 m^3) that change the overall surface of the cliff and so, constraining the possibility to use annual-scale master scan files, a fine registration between each subsequent scan pair was undertaken before the M3C2 change detection stage, which produced a notable decrease in the global registration errors for most of the individual scans (described in Section 2.4.2).

Table 2. 5: Root Mean Square Error (RMSE) of general registration between periods of master scans.

Master scan	Date & time	Mean RMSE value (m)	S. Deviation RMSE (m)	Minimum RMSE (m)	Maximum RMSE (m)
1	2017-Jan-04 06:00	0.07	0.01	0.05	0.09
2	2017-Jul-01 09:00	0.07	0.01	0.07	0.1
3	2018-Jan-08 10:00	0.07	0.02	0.03	0.1
4	2018-Jun-07 14:00	0.07	0.01	0.04	0.1
5	2019-Jan-07 13:00	0.05	0.01	0.04	0.06
6	2019-Mar-19 14:00	0.06	0.01	0.04	0.1

Note: RMSE values represent the general registration error between periods of master scans (e.g., 0.07 m of average convergence distance for the dataset collected between the Master scan 1 and 2).

2.4 Optimized point cloud workflow: Stage II

This section describes the stage II of the computational routine applied to quantify rockfall activity and obtain a 4D rockfall inventory. This stage includes the description of the workflow for automatization, the automatic fine registration between sequential scan pairs, the estimation of the depth of the erosion on the cliff face using the M3C2 3D distance change detection algorithm, and the application of the M3C2 distance uncertainty filter using 3D maps of distance uncertainty levels. This stage was undertaken using the *Main script II,* where each filtered point cloud with a general registration based on annual-master scan files was used as the input dataset (Section 2.3, previously processed using the *Main script I*). As a result of this stage, M3C2 point clouds with measurements of the erosion depth and equivalent rasters of surface change were obtained, which were then used as input data to run stage III of the automatization, where a minimum Level of Detection (LoD) was applied to then quantify rockfall volumes (Section 2.5).

2.4.1 Map of automation

To allow a fully automatized and computationally efficient routine for data processing, pairwise change detection between subsequent scans in time was undertaken based loosely on a concept best visualised as the *Pac-Man* game (Namco Ltda.), where the *Pac-Man* must "eat" all the "dots" inside an enclosed labyrinth following specific "paths". In this research, each scan pair resembles the concept of the "dots" that instead of being "eaten" must "enter" the workflow at the same time. This was achieved using an initial parallel folder structure resembling two parallel "paths" with two processing workflows, or *Pac-Mans*, with one exclusively "eating" master scans while the second exclusively "eating" their corresponding sequential scans (Figure 2.11). To implement this concept, the algorithm started with the command *start*, which allowed access to each corresponding scan pair that were initially stored inside two parallel folders containing the same number of total scans. The first folder stored every input master or model scan (e.g., any given scan collected at 03:00 h), while the second folder stored every input sequential scan in the time (e.g., any given correspondent scan acquired at 04:00 h). Then, inside both folders, a *STACK* or *LIFO* (Last In, First Out) computational structure was used, which are abstract data types that functions as a sequential collection of elements (here, each scan file, sequentially collected in time), with two principal operations or commands: *Push*, which adds a scan file to the collection, in this study each scan was added from the top of the STACK; and *Pop*, which is the inverse operation of *Push*, and so removed the most recently added scan file, in this study the scan that was stored at the bottom of the STACK. Importantly, the *Push-Pop* operation occurs only at one end of the STACK structure, here, pushing (i.e., Last In) and then removing (i.e., First Out) those scans sequentially located towards the base of the STACK. Also, the scan pairs that were stored towards the bottom of the STACK corresponded to the scan files that were collected later in time by the scanner (e.g. a master scan collected at 03:00 h, defining the first scan pair entering to the routine), while the next scan pair that was processed, and so entering to the workflow, were those scan files collected first in time by the instrument (e.g., a master scan collected at 02:00 h, defining the second scan pair entering to the routine, and so on) (Figure 2.11).

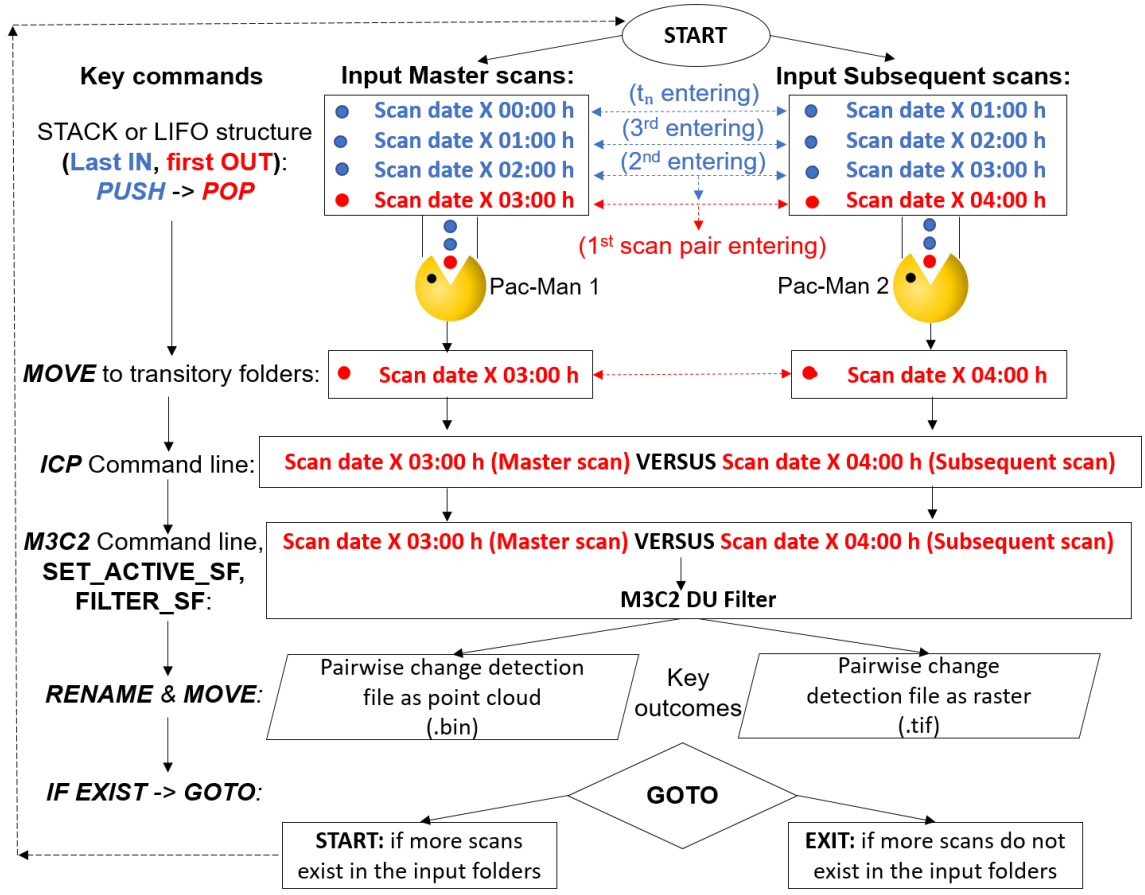

***Figure 2. 11**: Map of automatization implemented inside the Main Script 2 (Stage II of the computational routine applied to quantify rockfall activity).*

After the execution of the command *Pop* (that removed the scan pairs at the base of both input folders), a *Move* command was executed in order to relocate the two corresponding scans to be processed into transitory folders, which was needed to avoid ambiguities in the workflow prior to the registration of each scan pair. Then, both scans were passed into the *ICP* command line, and after direct registration, they passed onto the *M3C2* command line. After the 3D distances were computed, the M3C2 3D Distance Uncertainty filter was run using the command *Set_Active_SF* (which defined the specific Scalar Field of the M3C2 distance file containing the point clouds with a 3D map of distance uncertainty levels), followed by the execution of the command *Filter_SF* (that filtered points with high positional uncertainties). As a result of this workflow, a pairwise change detection point cloud was obtained (.bin), which was then exported as a raster file containing filtered values of slope surface change (.tif). Finally, towards the end of the workflow, a conditional *Goto* command was implemented. If more scan files exist in both initial parallel input folders, each step of the workflow was automatically iterated by going to the *start* command located at the beginning of the routine. Thus, the next available pair of scans located at the bottom of the STACK entered into the workflow (second scan pair entering to the

routine). Conversely, if both initial folders were empty (which was an indication that all scans were successfully processed), the routine went to its *exit*, located at the end of the script (Figure 2.11).

As a result of the implementation of this computational routine, a total of 15,776 scan pairs were automatically processed to build the 4D rockfall inventory between January 2017 and December 2019. Significantly, the average time of automatization for each scan pair entering into the workflow was ~ 1 minute and 30 seconds, yielding a total data processing time of ~ 16.4 continuous days. Thus, considering the large size of the dataset, this algorithm supplied a rapid and computationally efficient method for the geomatic and geomorphic processing of point clouds. Importantly, as long as the scans have been sequentially collected in time, this routine offers a flexible method for pairwise registration, subsequent change detection and post-processing filtering of surface change as any given frequency interval of data collection can be used, that is, sub-hourly, hourly, daily, weekly or monthly scan pairs, allowing multiple timescales for 4D geomorphic analysis.

2.4.2 Fine registration between each scan pair

Using a set of annual-scale master scans, the general registration stage was designed to initially align the scans since the exact position of the scanner may have changed, due to for example maintenance (Section 2.3.6). Such as in this research, general registration has been used to obtain a good initial spatial fit, to get the two point clouds close enough such that a subsequent fine registration algorithm converges more quickly (Kromer et al., 2017a). In fact, although with some methodological variations, the application of initial or general registration steps followed by stages of fine registration have been undertaken in order to ensure a good spatial fit between point clouds that were collected in complex rock-slope settings, such as in Whitby (e.g., Kromer et al., 2015a, 2017a; Bonneau and Hutchinson, 2019). Therefore, in this research, after the initial alignment, a fine registration was undertaken by directly aligning each scan pair before conducting the change detection. For methodological consistency within and between monitoring intervals, the fine registration was run using the point-to-point Iterative Closest Points registration algorithm (ICP), keeping the same parameters used during the computation of the general registration, such as the maximum permissible 3D registration error and 100% overlap (Section 2.3.6).

In this study, a fine registration stage using the corresponding previous scan was undertaken for three reasons. First, the geomorphic processes acting on the cliff result in frequent

erosion, including near-continuous spalling of rock that may also deform the overall slope surface, overprinted by occasional larger cliff collapse events that may suddenly alter the wider cliff face topography (e.g., Rosser et al., 2005; Williams et al., 2018). These processes constrain the ability to obtain precise alignment from an annual master scan as the surface reference, may through time will become more and more geometrical different to the original scan. These limitations may be considerable considering the duration of this monitoring campaign, since the topography of the first collected point cloud may severely change after one, two or three years of cumulative erosion. For instance, like in this study, Schürch et al., (2011) registered scans using the previous scans, instead of the first of the surveying campaign, in order to obtain more precise change detection between surveys. This process has proven to be advantageous since it makes sure that the topography of a potentially suddenly altered rock-mass can be spatially adjusted to the previous point cloud, rather than one collected months or years earlier (Schürch et al., 2011). As shown in Section 2.3.6, a fine registration using the previous point cloud at 100% overlap also ensured that, after the occurrence of rockfalls, a high percentage of stable rock-slope zones relative to the eroded parts of the cliff were used for alignment, as recommended by Kromer et al., (2015a); Teza et al., (2007; Oppikofer et al., (2008, 2009). Second, considering the length of this monitoring campaign and the size of the processed dataset, direct and automatic registration between each scan pair was performed to avoid the need for visual and / or manual identification of change. Indeed, in order to maintain the accuracy of the alignment, the need to change the master scan for a newer and therefore more geometrically similar point cloud after the occurrence of big cliff collapses has been suggested as a potentially beneficial methodological practice (Williams, 2017). Third, the accuracy of the registration is one of the main sources of error during change detection (Teza et al., 2007; Williams et al., 2018). As such, a fine registration stage was undertaken to decrease the RMSE of alignment, improving the quality of the alignment between surveys, and hence the ability to detect rockfalls of smaller sizes.

As a result of the fine registration stage, this process was automated for the 15,776 used scan pairs, yielding a mean value of RMSE of 0.03 m for most of the scans. When compared this value with the mean value of convergence distance obtained after the general registration stage (RMSE = 0.07 m), a decrease of 0.04 m is obtained, representing ~ 57% of improvement in the overall accuracy of the alignment. Significantly, the reported tendency of a rise in the mean RMSE values during initial alignment (Section 2.3.6), which is characterized by higher values found in scans belonging to months that were collected over greater intervals as compared to the master scans was no longer observed, since the direct registration provided more stable RMSE point cloud convergences of around 0.03 $\pm$ 0.005 m, regardless of the date of data acquisition. Minimum RMSE values, representing scan pairs with the best convergence distance for this

dataset, remained constant at 0.02 m during the whole monitored period, while the standard deviation values varied from 0.004 to 0.009 m. Conversely, point clouds with maximum convergence distances fluctuated between 0.04 and up to 0.06 m (Table 2.6). Furthermore, using the 95% confidence level criteria, point clouds with high values of spatial separation between subsequent scans (RMSE ≥ 0.045 m) were identified, corrected and then, if successfully matched, re-entered the workflow using an additional method for correction of alignment, which is presented in Section 2.5. Finally, assuming that the mean registration error of 0.03 m is representative, isotropic and spatially uniform across the dataset, it was then used as a key parameter to estimate the level of achievable change detection, allowing the generation of 3D maps of distance uncertainty for subsequent filtering of points that show high 3D distance uncertainty levels.

Table 2. 6: *Root Mean Square Error (RMSE) of fine registration between periods of master scans.*

Master scan	Date & time	Mean RMSE value (m)	S. Deviation RMSE (m)	Minimum RMSE (m)	Maximum RMSE (m)
1	2017-Jan-04 06:00	0.03	0.008	0.02	0.06
2	2017-Jul-01 09:00	0.03	0.007	0.02	0,06
3	2018-Jan-08 10:00	0.03	0.007	0.02	0.06
4	2018-Jun-07 14:00	0.03	0.009	0.02	0.06
5	2019-Jan-07 13:00	0.03	0.004	0.02	0.04
6	2019-Mar-19 14:00	0.03	0.009	0.02	0.05

Note: RMSE values represent the fine registration error between periods of master scans (e.g., 0.03 m of average convergence distance for the dataset collected between the Master scan 1 and 2).

2.4.3 M3C2 3D change detection

A number of methods have been developed to compute surface change in the context of geomorphic applications. The most common method is known as DEM of difference (DoD), which is based on differencing two DEMs, where two point clouds or meshes are gridded to generate DEMs either directly if the large scale surface is near horizontal or after rotation (e.g., Rosser et al., 2005, 2007; Schürch et al., 2011; Barlow et al., 2017). Although widely used to quantify erosion, however, DoD cannot operate properly in truly 3D environments, deriving 1D measurements of surface change and even if the surface approximates 2D at large scale, gridding point cloud data is a difficult task for highly textured slope surfaces (Lague et al., 2013). The second technique is the simplest and quickest 3D comparison between point clouds, which is known as Direct Cloud-to-Cloud comparison (C2C), or Hausdorrf distance, where the surface change is directly estimated from the distance between point neighbours in successive point

clouds, eliminating the need for gridding or meshing, nor calculating point cloud surface normals (Girardeau-Montaut et al., 2005; Williams, 2017). Commonly, C2C techniques suffers of three major drawbacks as the measured distance is sensitive to the cloud roughness, outliers, point spacing and no spatially variable confidence interval of the distance accuracies are calculated (Lague et al., 2013). The C2C distance also contains no directional information, and so can range from cliff normal to cliff parallel, which is problematic when deriving volumetric change. The third method is the most common approach in inspection software, known as Cloud-to-Mesh or Cloud-to-Model distance (C2M), where surface change is estimated by measuring the distance between a point cloud and a meshing 3D or triangulated surface (e.g., Abellán et al., 2009, 2010; Olsen et al., 2010). Although C2M works well on flat slope surfaces, generating a surface mesh is complex for point clouds representing significant slope roughness at all scales (Olsen et al., 2015), defined by significant topographic or discontinuity variability such as in the study site. In addition, similar to the DoD method, interpolation over areas with missing data introduces uncertainties that are difficult to quantity, and mesh construction also smooths out slope details that may be important in order to assess local roughness properties (Lague et al., 2013).

In this workflow, the Multiscale Model to Model Cloud Comparison (M3C2) algorithm was used to automatically detect and measure the depth of the surface change or erosion between two scans. This algorithm has been developed by Lague et al. (2013), which is a function freely available in Cloud Compare. To date, this method has been widely used in several geoscience applications such as the monitoring and quantification of the erosion in bedrock gorges (Beer et al., 2017; Cook, 2017), landslide analysis (Stumpf et al., 2015), lava lake monitoring (Smets et al., 2017), and for the estimation of the depth of cliff erosion and subsequent quantification of rockfall volumes (Bonneau and Hutchinson, 2019; Sala et al., 2019; Zahs et al., 2019; Benjamin et al., 2020; DiFrancesco et al., 2020). Therefore, this method was chosen due to a number of reasons: first, due to its ability to estimate 3D surface change from point cloud datasets and to handle 3D differences in complex geomorphic settings, such in the examined study site (e.g., near-vertical rock-slopes and rough slope planes); second, due to its capability to compute point cloud surface normals, critically needed to accurately estimate the magnitude and direction of the surface change (Williams et al., 2018); third, due to the possibility to minimize uncertainty related to point cloud roughness and to generate 3D maps of distance uncertainty levels (constructed from spatially variable confidence intervals) (Lague et al., 2013; Benjamin, 2018), which in this research were used to filter point clouds introducing change detection inaccuracies; fourth, it provides a simpler and more robust alternative to DEM differencing, C2C and C2M techniques as it operates in 3D, being robust to variations in point density and noise across the point cloud, returning a signed measured of surface change (Lague et al., 2013); and fifth, due to its proven capability to accurately estimate change detection along near-vertical cliff faces using point

clouds that were collected from laser scanner surveying, such as in this research (e.g., Bonneau and Hutchinson, 2019; Sala et al., 2019; Zahs et al., 2019; Benjamin et al., 2020; DiFrancesco et al., 2020).

The M3C2 algorithm uses a set of calculation "core" points for which one distance and confidence interval is estimated, which are also used to speed up the computations. For each point cloud, the M3C2 is implemented in two stages: first, a normal vector is calculated for each core point *i* in the cloud by fitting a normal plane through a neighborhood zone within a radius *D*/2 from the core point, where *D* is the normal scale and is related to the local roughness of the cloud. As such, the normal scale is the diameter of the spherical neighborhood extracted around each core point to compute a local normal. Also, each normal vector is oriented positively towards the closest of a set of user-defined orientation points, defining the direction in which the surface points (e.g., typically towards the scanning position). The standard deviation of the distance of the neighbours NN_i to a best fit plane is registered and used as a measure of the point cloud roughness $\sigma_i(D)$ at the scale *D* in the vicinity of *i*. Second, once the surface normal is computed, it is used to generate a cylinder of radius *d*/2 that runs through the core points, where *d* is the projection scale of the cylinder (Figure 2.12).

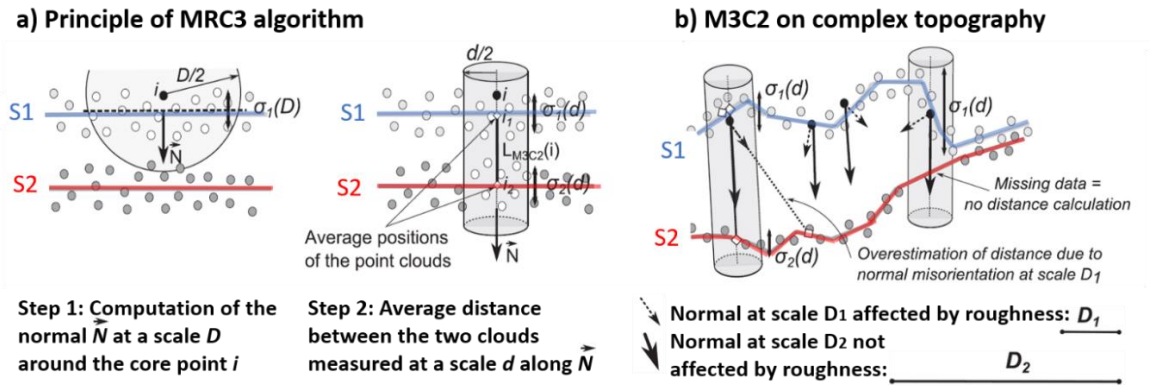

Figure 2. 12: *Description of the Multi Model to Model Cloud Comparison (M3C2) method. The method uses two key user-defined parameters: D (normal diameter) and d (projection scale). In the first step (a), the surface normal at each point in the reference cloud (S1) is calculated by using all points falling in a neighbourhood of radius D/2 (In this example, the normal is calculated from the reference cloud, S1). Then, the average distance between the two clouds (S1 and S2) is estimated as the mean distance between all points falling in a neighbourhood of the size d/2 (Cylinder radius). On complex topography (b), surface normals can be calculated at a scale too small with respect to the surface roughness (D_1), resulting in strong variations in the normals orientations. The using of a larger scale (D_2) results in more uniform normal orientations. Figure modified from Figure 3 in Lague et al. (2013, p. 14).*

Furthermore, the projection scale controls the size of the neighbourhood that is enclosed within the cylinder for each point cloud. In addition, a maximum depth of the cylinder is imposed to speed up the computations. Once the size of the cylinder has been defined, the average local distance between the two point clouds is defined as the mean distance between the centres of each neighbourhood point, across the normal vector, yielding a distribution of the 3D distances along the normal direction (Figure 2.12).

In 2015, a previous monitoring campaign of ten months of near-continuous surveying at East Cliff Whitby was undertaken to quantify patterns of rockfall erosion. In this monitoring campaign, the key user-defined parameters to run an adaptation of the M3C2 algorithm were tested and defined by (Williams et al., 2018, 2019). By fluctuating the size of neighbourhood radius for each core point between 0.1 and 2.5 m, Williams et al (2018) demonstrated that the mean search radius that generated the most planar surface, which is ideally suited to normal estimation (Lague et al., 2013), was identified and defined as 1.1 m prior to change detection. For volumetric estimation of rockfalls, this radius has proven to provide surface normals at a scale that is small enough to capture medium-to-large scale changes in surface orientation, such as the cliff aspect, but large enough to avoid variations of the resulting normals because of small scale changes in slope roughness, such as along of sharp overhanging rock-blocks, that are common slope features at the study site (Williams et al., 2018, 2019; Benjamin et al., 2020). On this basis, a normal diameter, D, of 2.2 m was selected as a compromise. Also, each normal vector was oriented positively towards the scanning position by pointing them towards the negative *y-axis*, which ensured that the resultant surface normals and subsequent measurements of the surface change pointed out of the cliff face.

The projection scale, d, defines the degree of spatial averaging in surface change calculations, where the smaller the projection scale, the finer the spatial detail of change that can be calculated, while larger scales may generate artefacts, smearing and average out many of the largest changes detected (Kromer et al., 2015b; Benjamin et al., 2020; DiFrancesco et al., 2020). For the point spacing and slope roughness conditions of the study site, Williams et al., (2018) demonstrated that by varying the radius of the projection scale ($d/2$) from 0.15 to 1.5 m, as the radius increases, the rockfall scar detected expands by averaging change across a wider slope area, which also tends to generate false forward movements within rockfall scars. As such, an optimum balance where enough points are included to yield accurate change measurements but not enough to include false change was found at a projection scale radius of 0.25 m. On this basis, a projection scale diameter, d, of 0.5 m was selected to run the M3C2 algorithm.

Also, as discussed by Kromer, et al., (2015b) and DiFrancesco et al., (2020), where the effects of the variations of the M3C2 projection scale were tested to accurately generate rockfall inventories, the smallest possible projection scales, equal to or slightly larger than the point spacing, were recommended. As such, the applied projection scale of 0.5 m (cylinder radius = 0.25) yielded a searching area of ~ 0.19 m^2, which was in fact slightly larger than the maximum point spacing of 0.15 m. As a result, the application of this recommendation ensured that a minimum of one to two points within the searching cylinder will always be captured to estimate the surface change, reducing the likelihood of censoring of lower magnitude rockfall events (DiFrancesco et al., 2020).

To speed up the computations, a maximum cylinder depth of 10 m was selected to undertake distance measurements. However, the occurrence of a single large rockfall event with a theoretical depth of surface change higher than 10 m at the study site, would have required an extended cylinder depth. If so, as a compromise, it would be necessary to make a modification of this parameter and then re-run the algorithm for all subsequent scan pairs. In this workflow, to obtain distances and confidence interval levels for each point defining the region of research, all the points forming each point cloud were used as core points, meaning that no sub-sampling was undertaken. Finally, the mean fine registration error of 0.03 m was also used to compute 3D distances and so, to be considered in the computation of 3D maps of distance uncertainty levels. Such as in this study, the incorporation of the registration error in the M3C2 distance estimation has also been undertaken for laser scanning characterization of cliff systems, currently representing a common practice for the detection of slope failures (Bonneau and Hutchinson, 2019; Benjamin et al., 2020).

2.4.4 M3C2 Distance uncertainty filter

The application of the M3C2 algorithm for surface change detection included the explicit calculation of 3D maps of Distance Uncertainty levels (DU), which were generated based on the computation of a Spatially Variable Confidence Interval (SVCI) associated with each point and combining common sources of uncertainties such as the registration error, surface roughness and point cloud density. The SVCI is defined at a prescribed 95% confidence interval and is used to estimate the distance measurement accuracy for each point forming the dataset, being an indicator of the surface noise (Lague et al., 2013). Also, the SVCI can be also used to assess the statistical significance of any measured change at 95% confidence (Barnhart and Crosby, 2013; Earlie et al., 2013; Stumpf et al., 2015). As the confidence interval boundary corresponds to the minimum detectable surface change, it is also referred to as the Level of Detection at 95%, $LoD_{95\%}$, enabling

an approximation of the minimum detectable change (Zahs et al., 2019). In this research, 3D maps of distance uncertainty levels were used, as first instance, to automatically identify and remove points generating high M3C2 distance uncertainties due to potential surface noise, minimising the likelihood of introducing false surface changes in point cloud zones that cannot be consistently measured, such as occluded slope planes, points adjacent to edges and inside holes. Hence, this filter was applied to complement the initial edge and hole filter (Section 2.3.5), representing here a post-processing filter as it was applied after the measurement of the 3D surface change.

Since the spatial variations of the positioning and the alignment errors cannot be measured easily (Lague et al., 2013), the SVCI is computed based on the 95% confidence interval of the registration error, *reg*, and the local surface roughness measured for each point, $\sigma_1(d)$ and $\sigma_2(d)$, calculated along the surface normal. The mean fine registration error is therefore assumed spatially uniform and isotropic over the cliff face (here, *reg* = 0.03 m). $\sigma_1(d)$ and $\sigma_2(d)$ are measured on both point clouds (S1 and S2) of projection diameter d (here, d = 0.5 m), and size n_1 and n_2 which are used to determine the mean positions of i_1 *and* i_2 (Figure 2.12, Section 2.4.3). Also, $\sigma_1(d)$ and $\sigma_2(d)$ depend on the actual surface roughness, the scanner related noise and the correct orientation of the surface normal. To measure the 95% confidence interval, the SVCI uses a parametric estimate assuming a Gaussian distribution of the dataset. The two distributions of distances along the normal direction of estimated mean (i_1, i_2) and size (n_1, n_2) are assumed to be independent Gaussian distributions with two possibly different variances measured by $\sigma_1(d)^2$, $\sigma_2(d)^2$ (Lague et al., 2013). Therefore, for each point forming the dataset, 3D maps of distance uncertainty (DU) levels were computed as follows:

$$LoD_{95\%}(DU) = \pm 1.96\left(\sqrt{\frac{\sigma_1(d)^2}{n_1} + \frac{\sigma_2(d)^2}{n_2}} + reg\right) \quad \text{[Eq. 2.8]}$$

3D maps of distance uncertainty levels were obtained for each resultant M3C2 point cloud forming the whole inventory, however, due to the large size of the dataset, the extraction of samples representing up to 10% of the monthly dataset were used to examine histograms of DU levels and identify the region from which high DU values begins. Three main criteria were used to select key sampled months extracted from each year of monitoring: First, months representing seasonal contrast were selected to assess potential variations in the DU levels associated with winter and summer, respectively. As such, January and August were chosen for each year under analysis. Second, months representing dataset collected closest, around the mid-range, and farthest with the respect to the changes in the master scan files were chosen (Table 2.5, Section 2.3.6), in order to assess potential drifts in DU levels associated to data that was initially registered

using different reference scans. As such, January, August and December were chosen. Third, for each month, 3.3% of the dataset was extracted for the first, middle and last days of the months, totalling up to 10% of the monthly dataset. A summary of the outcomes is presented in the Table 2.7, where it was observed that DU values were normally distributed, and that the mean value of DU remained constant at 0.087 m (~ 0.9 m) as well as did the standard deviation (0.01 m). The points with minimum DU values were found at 0.07 m, while maximum values fluctuated between 1.0 and 1.4 m.

Table 2. 7: *Summary of sampled values of 3D maps of Distance Uncertainty (DU) levels.*

Year	Sum of monthly samples per year	Mean DU value (m)	S. Deviation DU (m)	Minimum DU (m)	Maximum DU (m)	High DU at 95% CI (m)
2017	180	0.087	0.01	0.07	1.4	0.1
2018	180	0.087	0.01	0.07	1.0	0.1
2019	180	0.087	0.01	0.07	1.4	0.1
Total	540	0.087	0.01	0.07	1.4	0.1

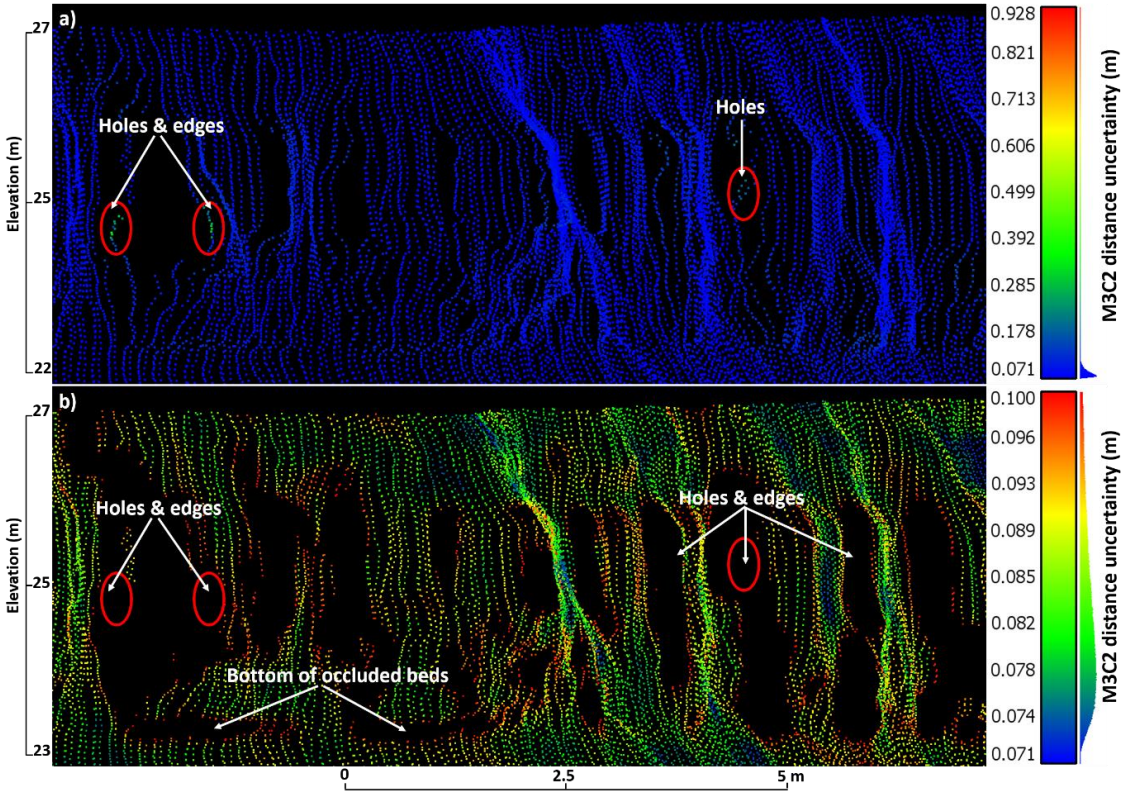

Figure 2. 13: *Example of a zoomed section of 3D maps of distance uncertainty levels. a) Non-filtered 3D map of distance uncertainty levels, where points with high values of positional uncertainty (In this example, DU ~ ≥ 0.2 m) were commonly located inside holes and edges (Highlighted as red ellipses), inducing unreliable rockfalls after change detection. b) Filtered 3D map of distance uncertainty levels, where points with high uncertainty values inducing false rockfalls were removed of the point cloud (Highlighted as red ellipses). The location of this section along the whole cliff face is shown as a red rectangle in Figure 2.15.*

Furthermore, no variation in DU levels were found for the dataset belonging to the different sampled months as the mean, standard deviation, minimum and maximum DU values remained relatively constant regardless of the season and moment of data collection. Then, using the 95% confidence interval criteria on the resultant 3D maps (2σ), points with high DU levels were identified (DU $\geq$ 0.1 m). An example of non-filtered versus filtered 3D map of uncertainty levels is shown in Figure 2.13.

Minimum and mean values of DU across the cliff face spatially corresponded to relatively flat and non-occluded cliff areas (Figures 2.13a and 2.15a). Conversely, high DU levels were typically located towards point cloud areas that cannot be consistently measured due to higher slope roughness and occlusion, such as across sharp rock-block edges, strings of points located inside and/or at the border of holes, or highly occluded slope zones like the upper and bottom sections of topographically abrupt hanging beds (Figure 2.13b). Significantly, when M3C2 distances were rasterized without the removal of points showing high DU levels, a high range of surface change was observed, having the potential to introduce false surface change estimates. To exemplify this, using a minimum LoD of -0.1 m depth, Figure 2.15b shows a typical raster of surface change without filtering DU values, where change estimates ranged from -1.18 to 1.83 m, introducing a total of 25 potentially unreliable rockfalls that were the direct result of the rasterization of points with high DU levels. Also, across the sampled inventory, it was observed a consistent pattern of repetition of occurrence of rockfalls along slope zones corresponding with high DU points, which have the potential to overestimate mass lost from the cliff face.

Using the normally distributed DU histograms of the sampled dataset, regions with points containing high DU levels were automatically identified and filtered at a $DU_{95\%\,CI} \geq 0.1$ m (Figure 2.14). After filtering, DU values ranged between 0.07 and up to 0.09 m (Figure 2.15c), while a significant fall in the equivalent M3C2 raster of surface change values was observed, in the example dataset, fluctuating between -0.01 and 0.11 m (Figure 2.15d). Consequently, using a minimum LoD of -0.1 m depth, no rockfalls were included in slope zones containing high DU levels. As a result of the implementation of the M3C2 3D Distance Uncertainty filter into the workflow, previous to the rasterization stage, a total of 15,776 scan pairs were automatically filtered to minimize the inclusion of false change estimates around areas with high surface noise. Depending on the 3D convergence distance after registration and level of surface roughness, this filter removed between the 5% and up to the 12% of the points falling in the region of high DU levels.

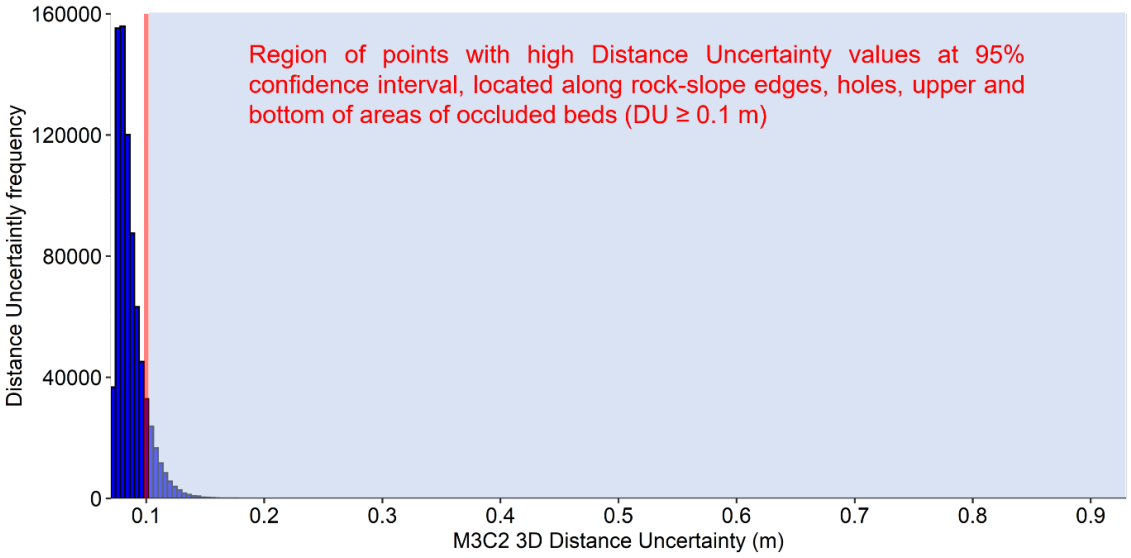

***Figure 2. 14**: Example of a typical normally distributed histogram of M3C2 3D Distance Uncertainty levels. For each point of the dataset, these levels were calculated using the Eq. 2.8. Applying the 95% Confidence Interval criteria on each DU map, points with high levels of distance uncertainty were automatically identified and filtered. The red vertical line indicates the threshold distance used for filtering (DU ≥ 0.1 m), and the gray shaded zone of the histogram represents the region of points with high positional uncertainties, having the potential to generate unrealistic values of surface change. These points were typically located along the rock-slope edges, holes, upper and bottom areas of occluded beds.*

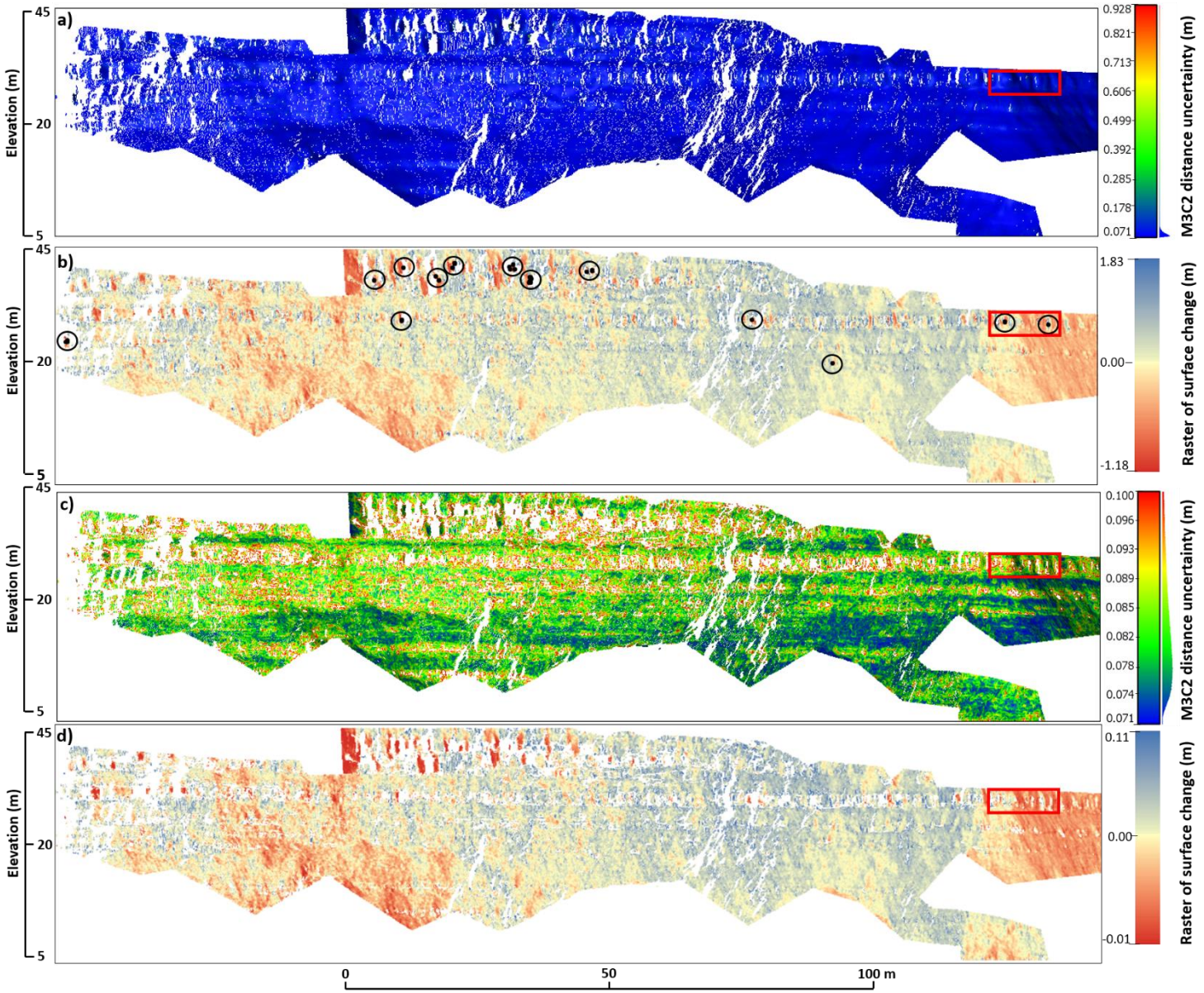
a)
b)
c)
d)
Elevation (m)
45
20
5
0.928
0.821
0.713
0.606
0.499
0.392
0.285
0.178
0.071
M3C2 distance uncertainty (m)
1.83
0.00
-1.18
Raster of surface change (m)
0.100
0.096
0.093
0.089
0.085
0.082
0.078
0.074
0.071
0.11
-0.01
0
50
100 m

Figure 2. 15: *Overleaf. General view of 3D maps of distance uncertainty levels and associated rasters of surface change.* ***a)*** *Non-filtered 3D map of distance uncertainty levels, where uncertainly values ranged between 0.07 and 0.9 m depth.* ***b)*** *Raster of surface change without distance uncertainty filter. Without filtering, high range of surface change values were observed, in this example ranging from -1.18 m to 1.83 m, introducing a total of 25 potentially unreliable rockfalls (minimum LoD ≥ -0.1 m) that were typically located either around sharp rock-block edges, holes, the upper and bottom areas of occluded beds (The location of the potentially unreliable rockfalls are highlighted with black dots, surrounded by circles).* ***c)*** *Filtered 3D map of distance uncertainty levels, where uncertainly values fluctuated between 0.07 and up to 0.09 m depth.* ***d)*** *Raster of surface change with distance uncertainty filer. By applying the uncertainty filter, points with high values of positional inaccuracy were automatically filtered (DU ≥ 0.1 m), yielding a significant decrease in the surface change values, now ranging between -0.01 and 0.11 m. Using a minimum LoD of -0.1 m, no unreliable rockfalls were observed along edges, holes or occluded beds. This figure represents an example of a common M3C2 derived point cloud, representing the slope surface change between 00 and 01 h of 17 January 2018. To the right side of the figure, the red rectangle shows the position of the zoomed cliff section shown in Figure 2.13.*

2.5 Optimized point cloud workflow: Stage III

This section presents the last stage of the workflow to obtain a 4D quantification of rockfalls, where a total of 15,776 M3C2 filtered rasters of surface change were used as input dataset (Section 2.4.4). This stage begins with the definition of the minimum Level of Detection (LoD), which was critically needed to determine the minimum depth of erosion to be quantified, followed by the estimation of the rockfall volumes and associated volumetric errors. Then, a method for the correction of point clouds showing high registration errors was undertaken, which if successfully corrected, were re-inserted into the workflow from Section 2.4.1. Volumes and volumetric errors were automatically calculated using a *Model Builder* implemented in *ArcMap*, while the correction stage for registration was implemented using a *Satellite Script.*

2.5.1 Level of Detection (LoD)

The minimum Level of Detection (LoD) is the smallest detectable surface movement, and so, for this research, the smallest depth of cliff normal erosion to be measured. The application of the LoD involves masking or removing regions of surface change that exceed a threshold at the defined LoD, which may be estimated either across the whole point cloud (e.g., Rosser et al., 2005; Abellán et al., 2009; Benjamin et al., 2020) or locally (e.g., Wheaton et al., 2010; Lague et al., 2013). In this research, the LoD was used to remove areas of slope deposition defined by

positive surface change, to minimize the likelihood of capturing surface noise or erroneous pixels in the resulting rockfall inventory, to determine and delineate the smallest depth of erosion or rockfall volume to be quantified, and so to obtain consistency in the estimation of erosion across the cliff face (e.g., Benjamin et al., 2020).

Based on probabilistic thresholding using a user defined confidence interval, the LoD can be typically determined as 1.96 times the standard deviation of the surface change estimates, representing the 95% confidence interval of the dataset (Abellán et al., 2009). Also, by assuming that no physical change occurred, there is a normal distribution of errors across the dataset, and that the error in successive dataset remain similarly distributed, the minimum LoD is commonly estimated from the root sum square of errors associated with each DEMs or point cloud as follows:

$$LoD_{min} = \pm 1.96\left(\sqrt{{\sigma_1}^2 + {\sigma_2}^2}\right) \quad \text{[Eq. 2.9]}$$

Where σ_1 and σ_2 are the standard deviation of surface change error for the reference and subsequent point cloud, respectively, and 1.96 represents the 95% confidence interval at 2σ (Williams, 2012). Hence, for this workflow, the maximum standard deviation of the fine registration error across the entire dataset was used to initially estimate the LoD (Table 2.6 in Section 2.4.2), which produced a standard deviation of ~ 0.01m and a theoretical LoD threshold of ~ 0.02 m.

Nevertheless, in order to consider the depths of the slope region likely affected by M3C2 Distance Uncertainty levels, where it was demonstrated that for this dataset, spatial variability of uncertainty from multiple parameters exist until ~ 0.09 m (Section 2.4.4), the minimum LoD used in this research was therefore 0.10 m depth. In fact, in the field of laser scanning monitoring for rock-slope change detection, the using of the distance uncertainly levels (Eq. 2.8) to estimate and threshold the minimum detectable change have been also applied by Kromer et al., (2017a) and Zahs et al., (2019). Therefore, although a low LoD of 0.02 m could have been used from a standard criteria (Eq. 2.9), a conservative approach of LoD was applied (here, 0.10 m) to exceed the likelihood of capturing erroneous pixels directly rasterized from points that are within the range of distance uncertainty values (Figure 2.16). Indeed, using terrestrial laser scanner data, conservative limits of detection using the maximum confidence error, such in this study, has been applied by Kromer et al., (2017b). This has been proven to be an advantageous practice as the estimated surface changes exceeding the LoD threshold may represent an erosional dynamic that actually occurred with high probability (Zahs et al., 2019).

Also, as the purpose of this research is to obtain a 4D rockfall inventory in which the analysis of the relative magnitude-frequency distribution between events is important, a single LoD threshold was used as it ensures consistency in the minimum detectable rockfall volume across the whole region of research, after Williams et al., (2018). Importantly, as noted by Williams et al., (2018), the application of a single LoD becomes computationally efficient when dealing with a large number of scan pairs, such as in this study.

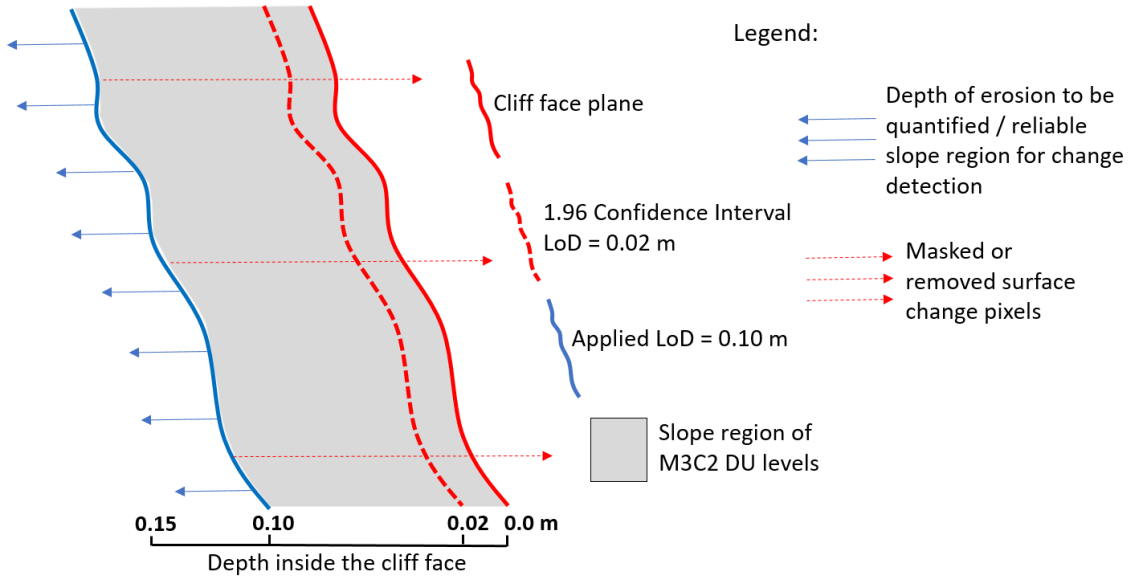

Figure 2. 16: *Conceptual definition of the applied minimum Level of Detection (LoD = 0.10 m). The depth of erosion that was quantified (> 0.10 m) was of a greater magnitude than the magnitudes falling inside the slope region potentially affected by M3C2 Distance Uncertainty levels, where spatial variability of uncertainty from multiple parameters exist until 0.09 m distance (e.g., registration error, high slope roughness, occluded slope zones). As such, for each M3C2 raster of surface change, the applied LoD masked or removed the region of change between 0.0 and 0.10 m of depth for the reasons explained above (Gray slope zone and/or masked region of pixels, indicated by red arrows).*

Following Williams (2017), point clouds were rasterized at 0.15 m interval as this approaches the maximum point spacing across the cliff face, defining the spatial resolution of the dataset. Then, using a minimum LoD of 0.10 m, the minimum recorded rockfall volume, V_{min}, was estimated as follows:

$$V_{min} = LoD \times A_C \qquad \text{[Eq. 2.10]}$$

Where LoD is 0.10 m, and A_C is the area of a single pixel (0.15 m pixel size). Therefore, the application of the Eq. 2.10 yielded a minimum pixel area of 0.0225 m^2 and a minimum detectable rockfall volume of ~ 0.002 m^3. Finally, the resulting LoD was used to threshold 2.5D rasters of

3D change estimates data, created by linear interpolation of change values across the $x - y$ plane. It is important to note here that a higher value of rasterization (i.e., larger than 0.15 m) would have produced a coarser pixel size and thus, increasing the actual magnitude of erosion for the same minimum LoD value. As such, keeping the rasterization at 0.15 m and LoD at 0.10 m, for the reasons explained above, provides sufficient resolution to characterize the minimum detectable rockall volume and so, cliff erosion (~ 0.002 m^3).

2.5.2 Volume estimation and volumetric error

Once the LoD was defined, using the distance uncertainty filtered M3C2 change detection rasters, the rockfall volume, V_{RF}, was estimated applying the equation implemented by Williams et al., (2018) as follows:

$$V_{RF} = \sum_{i=1}^{N} d_i \times A_c \qquad \text{[Eq. 2.11]}$$

Where N is the number of pixels that were detected as surface erosion, d_i is the depth of change or erosion in the slope in cell i, and A_C is the pixel area. The geomatic workflow developed to automatize the computation and compilation of rockfall volumes is summarized in Figure 2.17.

The core of the computational routine started with the application of an iteration that allowed access to and then the insertion of each individual raster into the overall workflow. Once a change detection raster was thresholded according to the LoD (pixels depth ≤ -0.1 m), a binary erosional mask was created to differentiate between those pixels that represented reliable erosion (field value = 1) and those that indicated positive surface change or geomorphic deposition, as well as pixels that were in the range of distance uncertainty levels (field value = 0). Using a raster math, pixels that exclusively represent rockfalls were extracted by multiplying the values of the erosional mask and a file containing the original surface change values, yielding only slope failures. Then, vectorization was undertaken to delineate the perimeter of failures and to extract key 2d (cliff parallel) morphometric properties, such as the area and perimeter of each polygon. Once the area and depth were recorded, merge and dissolve geoprocessing techniques were applied to unite polygons representing the same rockfall event, followed by summary statistics. Neighbour pixels that represent negative surface change (i.e., erosion) were detected and then united using minimum LoD threshold (0.1 m) so that, any pixel depths ≤ -0.1 m and the adjacent spatial neighbours (when present) were then united using the merge technique. After merging the pixels, the dissolve technique was applied in order to delineate the boundaries of the pixels involving negative surface change that were previously thresholded. Then, summary statistics was used to count and sum the values of the depths of change of the pixels delineated by the dissolve.

Then, the rockfall volumes were computed using the Eq. (2.11). Finally, once rockfalls were exported as polygons, the iterator was automatically applied again to access and insert the next available change image, looping through the overall workflow, allowing to obtain a fully automatized method for volume estimations (Figure 2.17). A summary table of the key variables derived at this stage is shown in the inventory description section (Table 3.2, Chapter 3, Section 3.2).

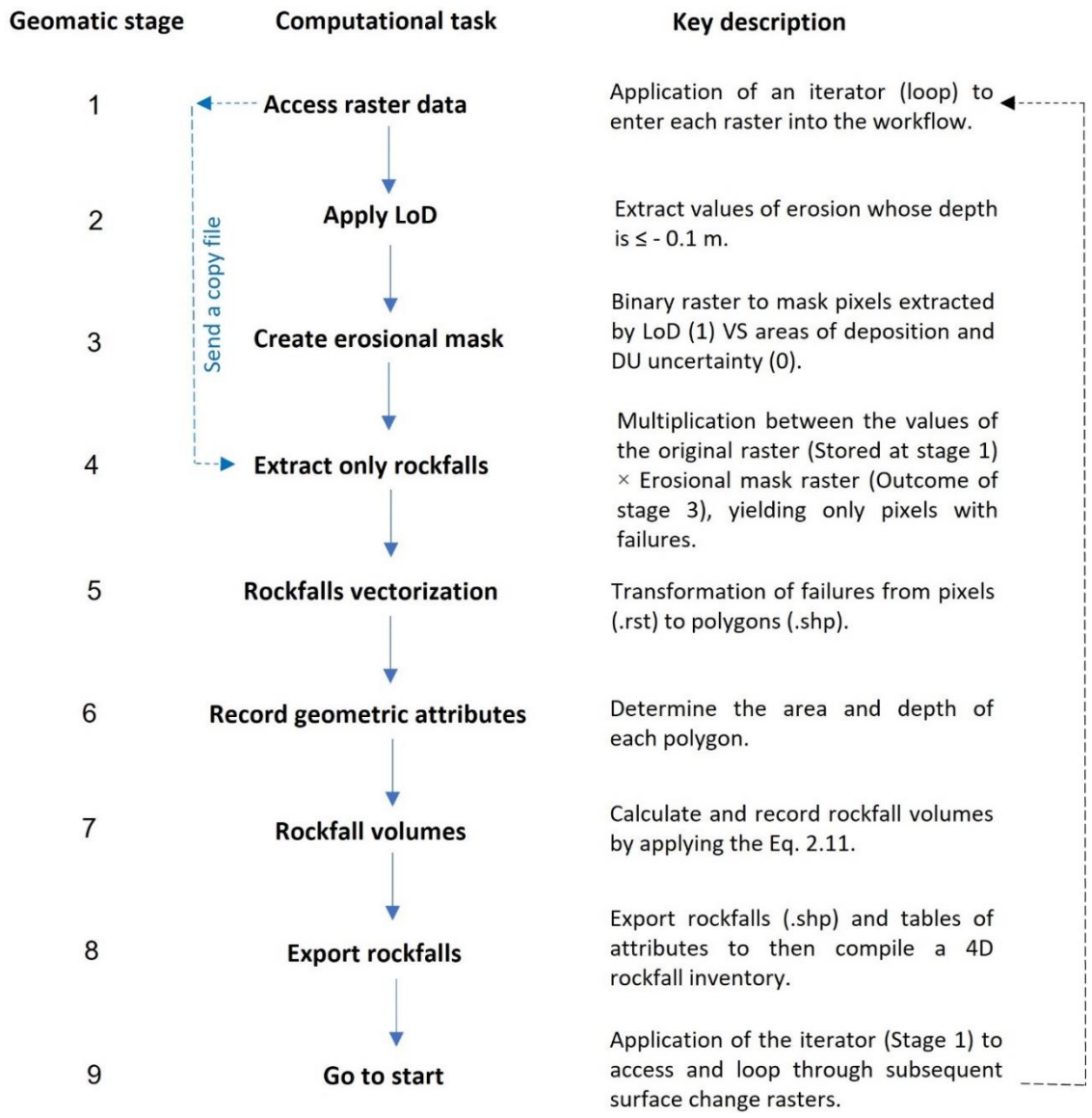

Figure 2. 17: **Synthesis of the computational routine developed to quantify and compile a 4D Rockfall volumes. This method was implemented into a Model Builder of the software ArcMap.**

Basic assumptions about how uncertainty in aerial extent propagates into volumetric uncertainty were needed, which is of crucial significance when considering the relatively low spatial resolution of the raster (0.15 m) relative to the accuracy of the change in depth within

pixels acquired by laser scanning (Williams, 2017). Indeed, for near-vertical rock slope monitoring studies using fixed laser scanning surveying, volumetric error calculations have been recently added as attributes to rockfall inventories (e.g., Williams et al., 2018; Benjamin et al., 2020). Therefore, in order to estimate the error that was present in the volume estimates of this dataset, the volumetric error associated to each rockfall, V_{error}, was estimated based on the equation suggested by Williams et al., (2018) as follows:

$$V_{error} = \sum_{i=1}^{N_b} 0.5 d_i \times \frac{2}{\sqrt{12}} A_c \qquad \text{[Eq. 2.12]}$$

Where the number of border pixels around the periphery of the rockfall is N_b. Importantly, equation (2.12) indicates that the number of border pixels relative to the total number of pixels within the area of failure was crucial in estimating the net volumetric error, where a higher ratio of border pixels to the total number of pixels resulted in a greater proportional area of volumetric error (Williams et al., 2018). Also, in this research, it was assumed that the likelihood that border pixels are completely covered by the true rockfall area was small and that in border pixels the depth of surface change was lowest, comprising up to 50% the depth of the failure area cells ($0.5 d_i$).

Due to the large size of the dataset processed and demanding computational stages, such as the vectorization and volume calculation, this workflow was undertaken with the full time-series cut into individual months, each of which required a data processing time of ~ 18 hours. However, to speed up the computation, this routine was implemented using parallel processing functions in four computers, each equipped with six to eight cores, 16GB RAM, yielding a total data processing time of ~ 162 hours per computer.

2.6 Correction of high RMSE registered point clouds

The accuracy of the registration is one of the principal sources of error when measuring surface change between two point clouds (Teza et al., 2007; Lague et al., 2013). Consequently, to avoid false change estimates, point clouds showing high RMSE values, which were indicative of a high convergence distance or spatial misalignment between two point clouds, were identified and corrected at the end of the workflow. As such, it is important to note here that this stage is an entirely separated part of the registration algorithm (the latter is only used here to discriminate the high RMSE values after fine registration), however, as the presented workflow is entirely flexible, it is possible to undertake this stage immediately after the fine registration (Section

2.4.2). However, in this research, this stage is presented in this section of the workflow following the sequence of methodological developments (i.e., after having obtained the shapefiles with volumes estimations and associate errors). By identifying the 95% confidence interval of fine registration errors over the whole dataset, it was observed that high spatial separation between scans begins to occur when the RMSE is ~ ≥ 0.04 m. As such, a method was developed to improve the quality of the alignment for those scan pairs in which the fine registration RMSE ranges between ~ 0.04 and 0.06 m. As discussed by Abellan et al. (2009), the exact position of each point cloud has the potential to drift due to inclement weather conditions (rain, fog) and also due to small shifts in the scanner inclination (Williams et al., 2018), among other factors (see Section 2.3.6). This condition may propagate the spatial offset between point clouds, from a few centimetres to meters, affecting one of the key assumptions of the ICP registration algorithm: that consecutive scans are approximately aligned, which constrains the degree of success of the algorithm.

The method for the correction of high RMSE values between scan pairs compromised three principal stages. The first stage aimed to reduce the initial convergence distance between two clouds (e.g., 0.06 m of misalignment), by merging a monthly master point cloud (i.e., the first scan collected of a given month) and the first point cloud of a given scan pair (e.g., a cloud collected at 17:00 h). If the monthly master scan was located in between the spatial position of a given scan pair (i.e., approximately equidistant, located at 0.03 m within a total separation distance of 0.06 m), by merging the two point clouds, the initial convergence distance was decreased by ~ 0.03 m, allowing to obtain a new "closer" united "reference" point cloud to facilitate the subsequent alignment. Then, a subsampling of the new reference cloud was needed to reduce the number of points, to reduce the computational load. For this dataset, using i7 computers with 16GB RAM and six to eight cores, it was observed that if the ICP registration is performed without subsampling, then the performance of the CPU and the memory limit were exceeded, crashing the process. As such, the new closer reference point cloud was subsampled at 0.15 m since it approaches the maximum point spacing of the dataset, providing a spatially uniform point cloud structure as well as a less dense and smaller dataset. Figure 2.18 shows a conceptual model of this correction method.

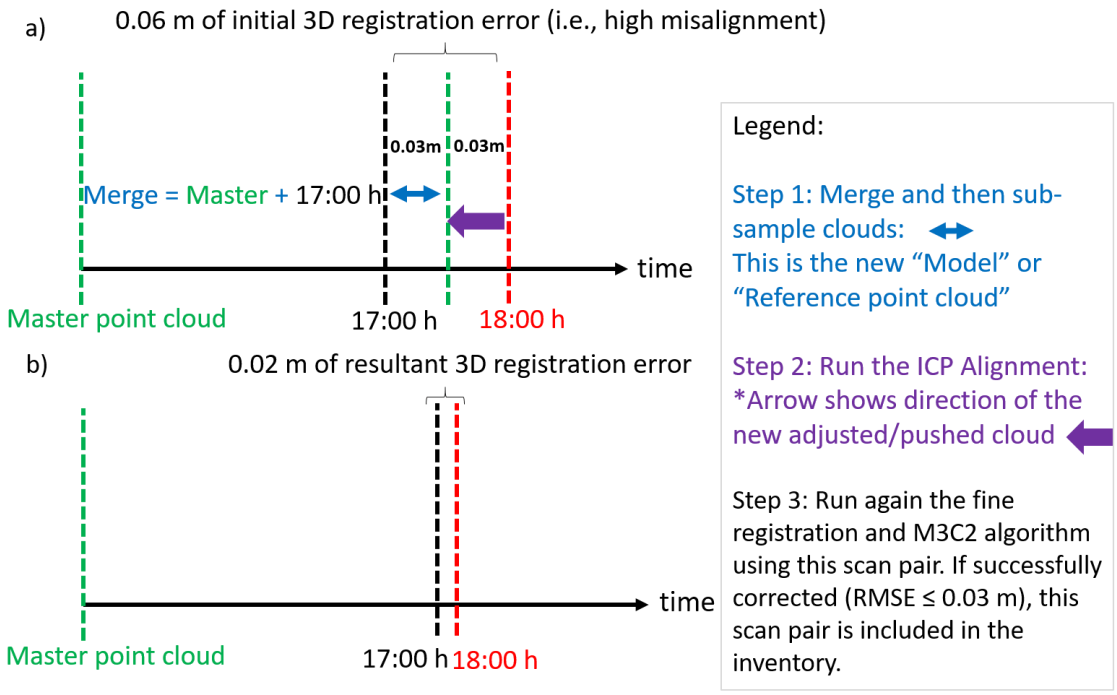

Figure 2. 18: *Conceptual model of the correction method for highly misaligned point clouds.* ***a)*** *Initial highly misaligned point clouds, with a 3D registration error of 0.06 (i.e. for this dataset, it was the maximum 3D convergence distance obtained after the fine registration stage).* ***b)*** *Successfully corrected point clouds, with a 3D registration error of 0.02 m (i.e., for this dataset, it was the lowest 3D convergence distance obtained after the fine registration).*

Once this merging and subsampling were accomplished, the second stage involved the registration between the new reference cloud and the second point cloud of the scan pair (e.g., a cloud collected at 18:00 h), spatially adjusting the second cloud towards the position of the new reference cloud. For methodological consistency within and between monitoring intervals, the registration was run using the same parameters as used in the general and fine registration stages (Sections 2.3.6 and 2.4.2). The third stage involved the re-insertion of the recently registered second cloud along a shorten distance into the Stage II of the general workflow (Section 2.4), where a fine registration followed by the M3C2 change detection stage were performed again between the original first cloud of a given scan pair (e.g., 17:00 h) and the corrected version of the second cloud forming the scan pair (e.g., 18:00 h). Finally, if the resultant fine registration RMSE value is ≤ 0.03 m, meaning that the overall accuracy of the alignment was improved, then the associated M3C2 surface change raster was included in the inventory, otherwise it was removed from the dataset. An example of a successfully corrected scan pair acquired in August 2019 is shown in Figure 2.19.

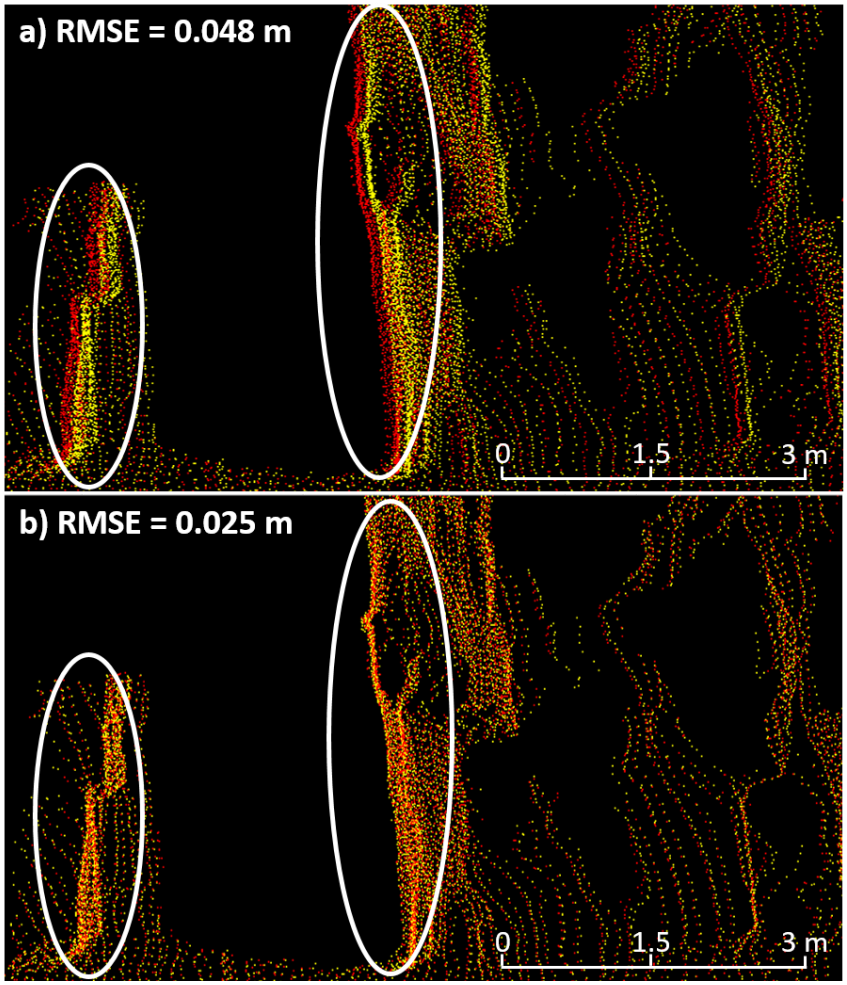

Figure 2. 19*: Example of the application of the correction method for highly misaligned point clouds. a) Initial highly misaligned point clouds, with a 3D registration error of 0.048 m. b) Successfully corrected point clouds, with a 3D registration error of 0.025 m. In both images, the reference point cloud (Collected at 17:00 h) is shown in red, while the adjusted point cloud is shown in yellow (Collected at 18:00). Also, vertical ellipses are used to highlight the 3D* ***mean*** *convergence distance of the point clouds before and after the application of the method. This represents an actual example of the dataset, collected the 1st of August 2019 at 17:00 and 18:00 h.*

The correction stage for high RMSE scan pairs was automated using a *Satellite script* and applied on a monthly basis for easier checking of the results. For the monitored period, this process was undertaken for 2,366 highly misaligned scans out of a total of 15,776 initial scan pairs, representing the 14.9 % of the whole dataset. Of the input misaligned dataset, 1,331 scan pairs were successfully corrected (56.2%). Conversely, a total of 1,035 scan pairs were unsuccessfully corrected (43.8%), decreasing the total available M3C2 change estimates from 15,776 to 14,741 that were finally used to build the rockfall inventory (Table 2.8). In terms of the computational efficiency of the developed method, the data processing time per scan pair was ~ 18 seconds, yielding a total additional processing time of ~ 12 hours.

Table 2. 8: Summary of the outcomes of the correction stage for high RMSE registered point clouds.

Year	Scan pairs for M3C2	High RMSE scan pairs	Recovered scan pairs	Scan pairs loss	% of recovered scan pairs	Total used M3C2 files
2017	5,885	493	160	333	32.5	5,552
2018	3,611	304	110	194	36.2	3,417
2019	6,280	1,569	1,061	508	67.6	5,772
Total	15,776	2,366	1,331	1,035	56.2	14,741

The main drawback of the developed scheme for correction was that it relied on the relative position between the monthly master scan (i.e., the first scan of any given month, captured by the laser scanner) and the two scans forming a given scan pair, which ultimately explained the relatively high percentage of unsuccessfully corrections (43.8%). As such, the method was highly sensitive to two unfavourable scenarios: the first occurred when the monthly master scan was located around the same position, or at the back of, the first cloud of the scan pair; the second scenario occurred when the monthly master scan was located around, or at the back of, the second cloud forming the scan pair. In both cases, the relative position of the scans constrained the capability to reduce the initial convergence distance between the dataset as the spatial separation remained the same (Figure 2.20). However, to date, this approach does represent perhaps the first attempt to compensate for highly misaligned scan pairs and hence to compensate for what would otherwise be a significant data loss.

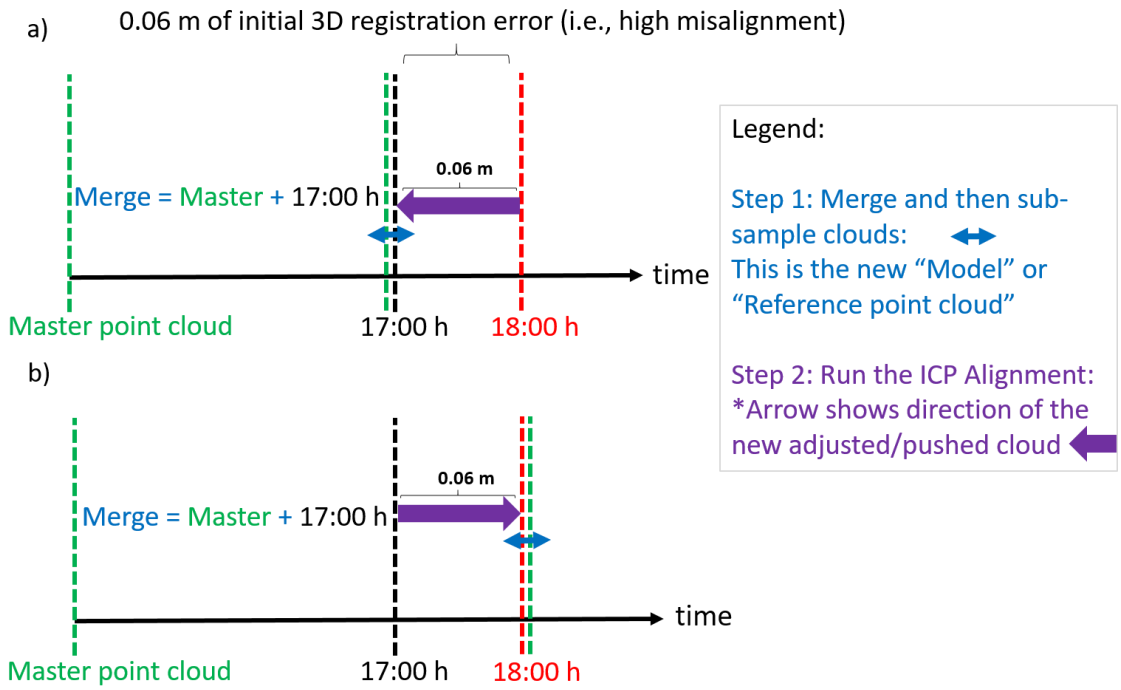

Figure 2. 20: *Conceptual model demonstrating the sensitivity of the method to the relative position between the monthly master scan, and the scan pairs to be corrected.* ***a)*** *In the first case, the monthly master scan was located at the same position or at the back of the scan collected at 17:00 h, and so the mean convergence distance between both scans was not reduced.* ***b)*** *In the second case, the monthly master scan was located at the same position or at the back of the scan collected at 18:00 h, constraining the capability to reduce the initial converge distance.*

2.7 Data retention summary

Figure 2.21 shows a summary of the data retention during the application of the workflow. Between 2017 and 2019, a total of 20,098 point clouds were collected by the scanner, equating 100% of the initial dataset. The first stage of data retention occurred during the application of the partial scan filter (Section 2.3.1), where over 2,900 scans were filtered, equating ~ 14.5% of data loss, and so, representing the stage where the highest data loss was observed. Then, a total of 359 scans were retained after the application of the high density scan filter (Section 2.3.2), causing ~ 1.8% of data loss, and yielding a total of 16,832 scans available for the stage II of the workflow (Section 2.4). Of the 16,832 scans, a total of 15,776 scans pairs where available for change detection as the application of the filtering stages generated time-isolation of single or more scans, producing missed scan intervals, inducing ~ 5.2% of data loss. The effect of time-isolation is further explored in Section 3.2 of Chapter 3 (Inventory description). Finally, of the 15,776 M3C2 processed scan pairs, a total of 1,035 scan pairs were not recovered during the application of the method to correct highly misaligned scan pairs, causing a further ~ 5.2% of data

loss (Section 2.6). In summary, in this chapter, four quality-control steps were applied, yielding a total of 14.741 M3C2 scan pairs that were used to build the rockfall inventory, equating ~ 73.3% of the initial dataset.

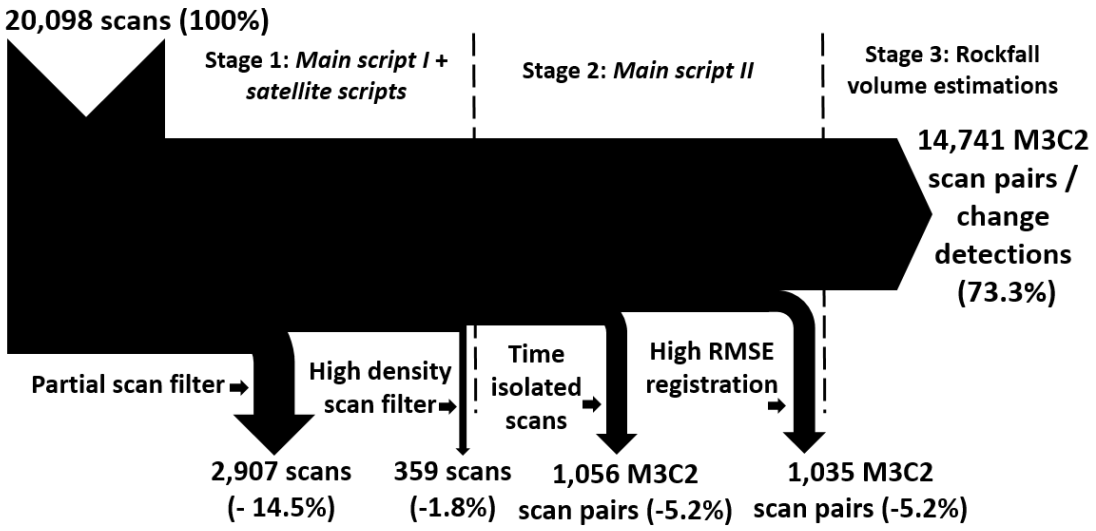

Figure 2. 21: Data retention pipe. Overall, a total of four stages of data retention occurred during the application of the computational routine for rockfall quantification, where a total of 14,741 scan pairs were used to estimate rockfall volumes and build a 4D inventory of failures.

For the whole monitored period, Figure 2.22 shows the time-series of the cumulative number of initially collected scans before the application of the filters and the cumulative number of used scans, after filtering. To examine the possible emergence of temporal bias created by the retention of data due to filtering, this figure was also coupled with the trend line showing the cumulative difference between the scans before and after the application of the filters. Importantly, the trend lines representing the collected and used scans show a constant and similar gradient, demonstrating that continuous periods with data predominates in the rockfall inventory. Principal plateaus of both trend lines occurred due to the occurrence of main gaps in the data collection (Z1 to Z5), which have been described in Section 2.2.3 (Data acquisition). Also, it is demonstrated that separation or gap between both cumulative trend lines occurred due to the application of the filtering stages, causing the higher changes in the differences between collected and used scans, ending in over 20,000 and around 15,000 scans for the collected and used scans, respectively.

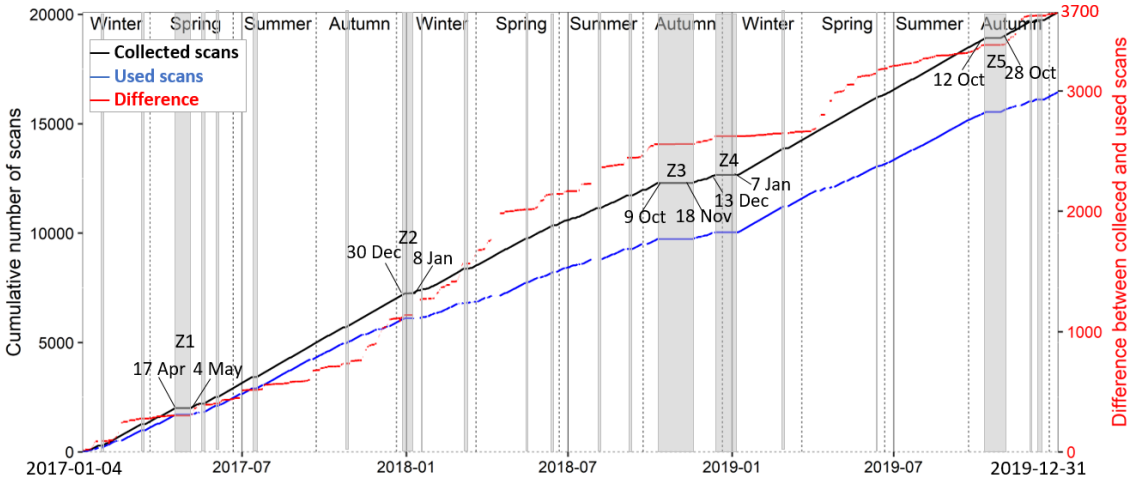

Figure 2. 22: *Cumulative number of scans before and after the application of the workflow, plotted as time-series. Collected scans at the beginning of the workflow are shown as black lines. The scans used to build the rockfall inventory after filtering are shown as blue lines. The cumulative difference between the collected and used scans is shown as red lines. Such as in Figure 2.4 of the section data acquisition (2.2.3), Z1 to Z5 indicate the major gap zones of data collection (higher than nine days without continuous data). Minor gaps (between sub-daily hour intervals and up to 4 days) are shown with non-numbered thinner gray bars. Vertical continuous lines show boundaries between the monitored years while vertical dashed lines show boundaries between astronomical seasons.*

In 2017, the highest cumulative changes in data retention occurred, as it may be expected, in mid-winter (84 scans), and in autumn (60 scans), due to inclement weather conditions promoting the generation of either partial scans, high density point clouds or time-isolation of scan sequences. When the total number of hours of a year (8,760 h) is divided by the total number of scan pairs at 1 change detection (5,552 scans), it resulted in an annual average of ~ 1.5 hour per scan, being an overall indicator of the average used scanning interval for this year (meaning that in theory, a perfect year, where no data collection gaps nor data retention occurred, this indicator should be 1 h). As described in Section 2.2.3 (Data acquisition), the 2018 was the year with the higher gaps in data collection due to technical faults in the scanner or software-derived failures affecting the scan schedule. Also, due to harsh weather, the highest cumulative changes in data retention of the whole inventory occurred in this year, particularly in winter (129 scans), spring (220 scans) and summer (127 scans). As a result, despite the predominance of continuous periods with data, the lowest annual average of used scanning interval is observed in 2018 as a total of 3,417 scan pairs were used, yielding an average of ~ 2.5 hours per scan. In 2019, the highest cumulative changes in data retention occurred in spring (116 scans) and autumn (80 scans). During this year, a total of 5,772 scan pairs were used, yielding the same annual average of used scanning interval than 2017 (~ 1.5 hours per scan). Significantly, during the whole monitored period, most of the cumulative changes in data retention fluctuated, in average,

between one and five scans, generating small step-wise cumulative retentions of data, which is the dominant trend in most of the seasons belonging to each year of monitoring (Figure 2.22).

As a consequence, seasonal variability was detected in the highest cumulative changes in data retention, with no repeated temporal patterns occurring, systematically, in particular seasons. To exemplify, while winter 2017 and 2018 showed higher data retention trends, this pattern was not observed for winter 2019, where a small step-wise trend predominates. Similarly, while summer 2017 and 2019 showed small step-wise trends of data retention, summer 2018 showed a higher data retention trend. Again, while spring 2017 showed small step-wise retentions, in spring 2018 and 2019 took place higher data retentions trends. Similar patterns of variations were detected for subsequent autumn time periods. In addition, the fact that periods with small step-wise retentions of data were the dominant trend and that longer periods with continuous used scans predominates in the dataset, especially during the 2017 and 2019, suggest that no significant temporal bias of data were generated due to geomatic filtering. Indeed, the fact that data retention occurred in different seasons, including winters, springs and summers, demonstrate the inherent complexities and challenges associate with long term monitoring campaigns, where data gaps due to technical or software failures may be expected, as well as the application of quality-control stages to remove low quality point clouds are essentially needed steps. A such, these dataset provides a suitable inventory to assess long-term high resolution rock slope dynamics.

2.8 Summary

To accomplish the first objective of this thesis (O1), this chapter has outlined a new methodological workflow for 4D detection and quantification of rockfall activity. As such, a novel computational routine was developed which has been capable to automatically process over 20,000 initial scans, minimising the need of manual manipulation and the sources of error in the dataset. Here, a new set of filtering methods were applied to computationally optimize the overall workflow, such as the partial scan and high-density scan filters, allowing a rapid and fully automatic detection and removal of anomalous point clouds collected during harsh weather conditions. After the application of standard techniques for TLS data manipulation, such as the definition of the region of research, rotation, edge and hole filters using a statistical outlier removal algorithm, a general registration was undertaken to obtain a good initial spatial fit of the dataset and a quicker convergence during the fine registration stage. Also, the direct fine registration stage between scan pairs permitted to compensate for either large topographic deformations after the occurrence of big cliff collapses or cumulative slope deformation created

by long term accumulation of erosion, without the need to manually change master scan files of annual or monthly scale. Significantly, an automated process was developed based loosely on the concepts of the *Pac-Man* game (Namco Ltda.), permitting a fully automated and computationally rapid fine registration, change detection and post-processing distance uncertainty filtering, with an average data processing time of 1 minute and 30 seconds per scan pair. From the very beginning of the workflow where partial scan filtering was undertaken, until the end of the method, where a 4D inventory of rockall events was automatically compiled, the total data processing time for three years of surveying collected at 1 h interval represented six months of time, or two months per year of data, demonstrating the speed the method and its efficiency in handling a large volume of data.

In the context of big data applications for engineering geomorphology purposes, in which the volume, variety, complexity of the data as well as the speed of data processing are key concepts, this computational routine offers a new tool to examine quasi continuous and long-term patterns of geomorphic activity, never seen before. Also, as long as the dataset represents point clouds or meshes, this method can also be adjusted and applied to geomorphic analysis in which the dataset has been collected from the zenith or oblique views, such us in airborne LiDAR or UAV-based surveys. For instance, the routine for volume estimation can be performed regardless of the orientation of the dataset, as long as the depth of surface change is consistent with a given set of axis. Also, it can be rapidly adjusted to examine depositional processes, such as rates of deposition along the talus, creep dynamic, among others. If adjusted, this method may also offer a new tool for the fields of rockfall hazard monitoring, modelling and near-real time emergency inventory of failure events after earthquakes or rainfall storms. In this research, the resulting rockfall inventory is used to generate a multi-annual 4D rockfall inventory and analyse the timing, magnitude and frequency of rockfalls (Thesis Objective 2 - O2). As such, an analysis of the timing and how the erosional work done by small, medium and large-scale episodic events accumulates in a long-term erosive signature is presented in the following chapter.

Chapter 3- Geomorphic behaviour of the 4D rockfall activity and cliff erosion

3.1 Introduction

In *Chapter 2*, a new methodology has been developed to automatically process an extensive monitoring dataset of 3D point clouds (3 years of rock-slope scans collected at 1 hour interval), which has been collected using a permanently installed laser scanner (Thesis Objective 1 – O1), permitting to obtain the longest rockfall inventory so far generated at annual scale, hourly resolution and capturing very small rockfalls (~0.002 m^3). In this Chapter, the resulting multi-annual 4D rockall inventory is used to examine the timing and nature of hourly rockfall activity and rates of cliff erosion (Thesis Objective 2 – O2). As such, an analysis of how the erosive work done by small, medium size, as well as large rockall events accumulates into a long-term erosional signature is presented.

To analyse the dataset, the negative power law scaling of modelled magnitude-frequency distributions and 4D time-series of rockfall activity are principal and axiomatic metrics in this chapter. In this study, magnitude-frequency distributions have been chosen as they provide numerical indicators of the level of erosional activity acting on the examined landform, as well as they reflect the relative size distribution and erosional efficiency of different rockfalls. Also, this metric has been selected as it has been used in a wide range of research undertaking erosive analysis over rock-slopes, allowing full comparability of the outcomes. Time-series have been selected as they allow the examination of changes in rockfall volumes, rates of erosion, and rockfall yield over the time, permitting the analysis of unique patterns emerging from the inventory.

This chapter begins with a description of the rockfall inventory (Section 3.2), followed by an analysis of the magnitude-frequency distributions at annual-scales (Section 3.3). Then, 4D time-series analysis of the rockall activity and cliff erosion, coupled with finer-resolution magnitude-frequency distributions are analysed between Sections 3.4 and 3.6, where the changes in the rockfall yield are examined as non-cumulative and cumulative time-series. These are then followed by Sections 3.7 where the analysis is undertaken at the seasonal scale. Finally, Section 3.8 shows a summary of key findings and some implications on long-term high-resolution rock-slope dynamics.

3.2 Inventory description

Pairwise change detection between point clouds, collected at 1h interval, were used to compile the rockfall inventory. Table 3.1 shows a key summary of the processed dataset. Between 2017 and 2019, a total of 20,098 scans were collected. Of these, a total of 3,266 scans (17%) were filtered during either the partial scan filtering or the high-density scan filtering stage (Section 2.3, Chapter 2), thus a total of 16,832 scans were available for further data processing. However, from the available scans for data processing, a total of 15,776 scan pairs (93%) were available to undertake the M3C2 3D change detection stage. The drop in the number of available scan pairs is because, after the application of the filtering stages, time-isolation of single or more scans was produced between immediate subsequent hours, generating missed scan intervals, constraining the possibility of applying direct 1 h pairwise change detection consistently. As a result, change detection over intervals of time with missed scans was not undertaken and so, was not included in the analysis (Figure 3.1).

Table 3. 1: *Summary of the data processed, filtered and total number of scan pairs (rasters of change detection) used to build the rockfall inventory.*

Year	Collected scans	Filtered scans	Available scans	Scan pairs for M3C2	High RMSE scan pairs	Recovered scan-pairs	Total used scan pairs
2017	7,248	1,027	6,221	5,885	493	160	5,552
2018	5,412	1,356	4,056	3,611	304	110	3,417
2019	7,438	883	6,555	6,280	1,569	1,061	5,772
Total	20,098	3,266	16,832	15,776	2,366	1,331	14,741

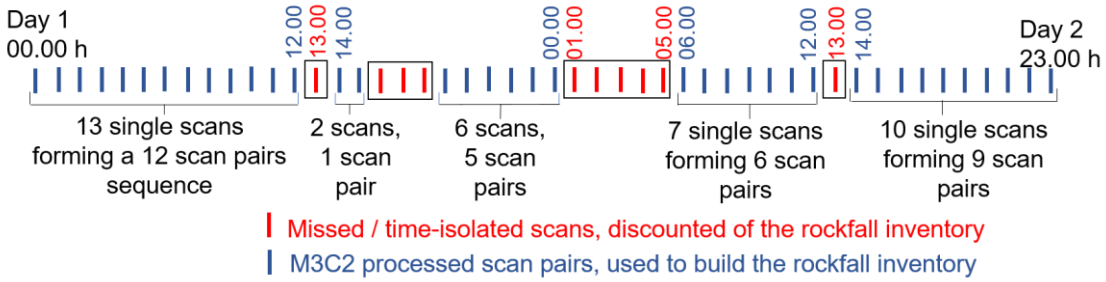

Figure 3. 1: *Conceptual model of the missed scans after either geomatic filtering or due to high RMSE registration values. Scan pair sequences available for the M3C2 change detection stage are formed by a minimum of two immediately continuous single scans (blue) forming at least 1 scan pair of 1 h interval. Time intervals missing scans were excluded from the calculation (red).*

Of the 15,776 scan pairs used in the M3C2 change detection, a total of 2,366 scan pairs (15%) showed high RMSE values indicating an offset in alignment (RMSE ≥ 0.04m), of which 1,331 (56%) were recovered using the correction method (Section 2.6, Chapter 2). As a result, a total of 14,741 scan pairs (93% of the initial M3C2 processed scan pairs) were used to build the rockfall inventory (Table 3.1). Importantly, this number of scan pairs is used to derive the rasters for change detection that were automatically processed to estimate the rockfall volumes.

Figure 3.2 shows the cumulative number of used scan pairs as a time-series and the gaps in the dataset. Rockfalls were monitored continuously between the 4th of January of 2017 and 31st December of 2019 (a total of 36 months), however there are a total of 35 gaps that were created because of either due to a lack of scans due to failures in the equipment or after geomatic filtering, which involved the partial scans filter, high-density scan filter or due to high RMSE registration values associated with poor data quality for the reasons explained previously.

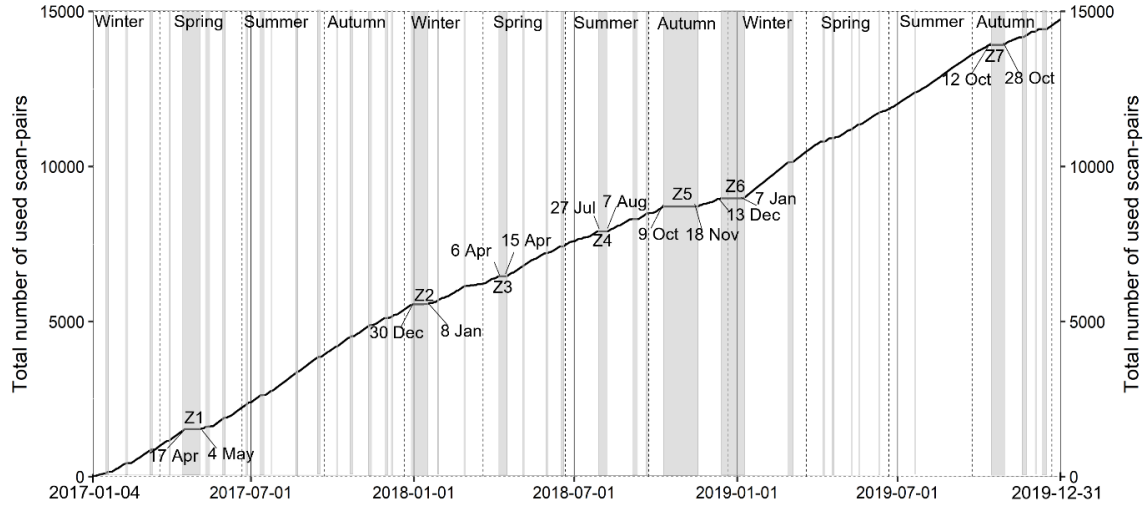

Figure 3. 2: *Cumulative number of the used scan pairs (rasters of change detection) plotted as time-series. Vertical gray bars show the gaps of the scan pairs used to build the rockfall inventory. Z1 to Z7 indicate the major gap zones (higher than nine days without continuous data). Minor gaps (between sub-daily hour intervals and up to 4 days) are shown with non-numbered thinner gray bars. Vertical continuous lines show boundaries between the monitored years while vertical dashed lines show boundaries between astronomical seasons.*

One principal data gap is observed during the year 2017, in spring (Z1) compromising 18 days of continuous data loss between the 17th of April and the 4th of May. The largest number of gaps occurred during the 2018, starting in winter with 9 days without data (between the 30th of December and 8th of January, generating the gap zone two or Z2), followed by a gap in spring between the 6th and the 15th of April (Z3), then between the 27th of July and 7th of august (Z4), in

addition to a gap in autumn compromising 51 days (the largest of the inventory) between 9th October and 18th November (Z5), and finally a gap between the 13th December 2018 and the 7th of January 2019 (Z6). A gap of 17 days is identified in 2019, between the 12th and 28th of October. Minor gaps are also observed during the whole monitored period, most of them ranging between single missing scans to a maximum period of four days without data. Overall, between 2017 and 2019, principal gaps (Z1 to Z7) compromising a total of 143 days, equivalent to a 13% data loss for the whole monitored period. When adding in minor gaps, this number rises to a total of 234 days without data, representing ~ 21.4% of data loss between January 2017 and December 2019 (Figure 3.2).

Continuous periods with scan-pair data are observed throughout the whole monitoring period. For example, for the year 2017, the majority of these periods ranged from a minimum of 8 to 25 days, while the longest interval occurred in summer, between 17th of July and 15th September, compromising a total of 61 days. In 2018, most of the intervals with continuous scan data fluctuated between two and 15 days, however, the longest interval is observed in spring, immediately after the third principal gap zone (Z3), between 15th of April and 14th of June, involving again a total of 61 days. Longer periods with continuous data are observed during the year 2019, most of these fluctuating between 12 and 52 days, with the longest of the whole inventory occurring towards summer and autumn, between 22nd of July and 12th of October (before Z7), compromising a total of 83 days. As a result, despite the occurrence of data gaps, the gradient of the line of the cumulative number of scan pairs shows that continuous periods of data predominate, providing a suitable dataset to assess the geomorphic behaviour of the rockfall activity and rates of cliff erosion (Figure 3.2).

Despite that those periods with continuous scans predominates in the dataset as demonstrated above (Figure 3.2), change detection over intervals of time with missed scans was not undertaken. An important implication of this is that the periods of missed scans induced a probable reduction in the total number of observed rockfalls and so, an underestimation of the total eroded volume across the cliff face for the period 2017 - 2019. In Chapter 6, it is demonstrated that ~59% of total eroded volume across the cliff in 2021 was produced between change detections greater than 1 hour, which includes change estimates between periods of missed scans (i.e., non-hourly change detections, see Table 6.2, Chapter 6). Therefore, although this underestimation of the total erosion is not significant for the interpretation of the results of this Chapter, as the objective here is to investigate how small, medium, and large rockfalls accumulates (at 1 hour resolution) into a long-term erosional signature (which is a signature that cannot be seen in periods of uncertainty of the timing of rockfalls due to data gaps, as it not

possible to precisely differentiate the timing of occurrence of rockfall due to spatial and temporal occlusion), this could be significant in cases in which the total eroded volume is necessary, such as in Chapter 6 of this thesis, where a more precise estimation of the total eroded volume was needed in order to assess the relative erosive contribution of rockfalls resulting from inclement weather conditions (including data gaps) versus temperature controls on rockfalls. The later case needs to be assessed at a higher resolution of data collection and processing (such as here, 1 hour), as this temporal resolution can mirror the nature of the environmental variability, such us temperature or rainfall (research question four of this thesis, RQ4, see Section 1.2, Chapter 1).

For each rockfall event, the parameters detailed in the table 3.2 were extracted, including properties related to date and time, critical for developing time-series analysis of the geomorphic rates of activity, as well as the erosive and morphometric properties, such us the volume, volumetric error, area on the cliff face, and the depth of failure. These properties form the basis of the rockfall inventory, and therefore the core of the geomorphological analysis presented in this chapter.

Table 3. 2: Summary of the rockfall properties compiled for each failure event.

Rockfall date and time			Rockfall properties					
ID	Date	Date & time	Volum.	Area	Depth	Perimeter	B. Pixels*	Vol. Error
(-)	yyyy-mm-dd	yyyy-mm-dd hh:mm:ss	m^3	m^2	m	m	(-)	m^3

Note: B. Pixels* is the number of boundary pixels used to calculate the perimeter of failure and volumetric errors.

3.3 Magnitude-frequency distribution of rockfall activity

Over 8,300 rockfalls were captured across a cliff surface of ~5,459 m² at the East Cliff of Whitby between 2017 and 2019. A total of 3,079 rockfalls were observed during 2017, representing the monitored year with the highest number of rockfalls. By contrast, the 2018 showed the lowest rockfall yield totalling 2,408 failures (22% less than 2017), while a total of 2,880 rockfalls were observed in 2019 (16% more than 2018). The average and median rockfall volume remained constant for each year, with values of 0.02 ± 0.008 m^3 and 0.003 ± 0.002 m^3, respectively. The largest single rockfall event of the inventory occurred in February 2019 (22 ± 4 m^3), followed in magnitude by a cliff collapse of 18 ± 4 m^3 in July 2017 and another of 12 ± 3 m^3 during September 2018. These three rockfalls alone totalled 52 ± 11 m^3 of volume loss, comprising c.a. 29% of the total eroded volume, indicating that their geomorphic contribution to

the overall cliff erosion is almost one third of the total eroded rock-mass observed between 2017 and 2019 (Table 3.3).

Variability can be seen for the total eroded volume, measured as the cumulative sum of the individual rockfall volumes for each year, where the highest annual volumetric loss occurred in 2017 with 73 ± 30 m^3 (41% of the total eroded volume loss of the monitored period) while in 2018 and 2019 it was detected a relatively similar volume loss of 54 ± 21 m^3 (30.3%) and 51 ± 20 m^3 (28.7%), respectively. Overall, the total eroded volume from 2017 to 2019, was 178 ± 71 m^3 (Table 3.3).

The total eroded volume measurements equate to annual cliff-face retreat of 0.013, 0.009 and 0.009 m for 2017, 2018 and 2019 respectively, totalling 0.03 m during the whole monitored period. Significantly, during 2017, a total of 33% of days of this year were rainy, which resulted in 60% of annual rockfall numbers. Similarly, in 2018, a total of 47% of days of the year were rainy, which contributed 56% of rockfall numbers. This trend is again observed in 2019, where a total of 53% of days of the year were rainy, which resulted on 61% of the annual rockfall numbers. As a result, between 2017 and 2019, a total of 38.5% were rainy days, which led to 59% of rockfalls occurred on a day when precipitation was also occurring, suggesting a significant influence of rainfall on rockfall occurrence, or at least some degree of precipitation control on the timing of these failures (Table 3.3). However, it is important to note here that other controls cannot be ruled out, such as thermal triggering or surface moisture. These other potential controls are quantified and discussed in Chapter 6, Section 6.5.1.

Table 3. 3*: Summary of the rockfall activity and cliff erosion for the East Cliff of Whitby, 2017 to 2019.*

	Monitored years			
Erosive metric	**2017**	**2018**	**2019**	**Total**
Detected number of rockfalls	3,079	2,408	2,880	8,367
Minimum rockall volume (m^3)	0.002	0.002	0.002	0.002
Average rockfall volume (m^3)	0.02	0.02	0.02	0.02
Median rockfall volume (m^3)	0.003	0.003	0.003	0.003
Largest rockfall (m^3)	18 ± 4	12 ± 3	22 ± 4	52 ± 11
Total eroded volume (m^3)	73 ± 30	54 ± 21	51 ± 20	178 ± 71
Cliff face annual retreat (m)	0.013	0.01	0.01	0.033
Rainy-days-rockfall (%)	60	56	61	59
Dry-days-rockfall (%)	40	44	39	41

Note: monitored cliff face area was 5,459 m^2. The metric, rainy-days rockfall (%) indicates the percentage of the annual total number of rockfalls that were detected when daily rain was also occurring.

It is well stablished that modelling magnitude-frequency is a method by which the erosive imprint of geomorphological processes over a given landform may be quantified, being a critical indicator of the relative size distribution of geomorphic events (here, rockfalls) as well as to assess the overall level of geomorphic activity or rate of erosion (Wolman and Miller, 1960; Stark and Guzzetti, 2009; Barlow et al., 2012). In this research, therefore, magnitude-frequency relationships are reported using four complementary metrics in order to allow a full characterization of the geomorphic behaviour of rockfall activity at different time-scales, making the analysis comparable with published literature and allowing the deficiencies of each individual power law modelling approach to be overcome. These metrics are: 1) rockfall frequency density, 2) normalised rockfall frequency, 3) rockfall frequency, and 4) cumulative rockfall magnitude-frequency. Magnitude-frequency distributions exhibit a negative power law scaling that can be modelled using (Brunetti et al., 2009):

$$f(V_R) = sV_R{}^{-\beta} \quad \text{[Eq. 3.1]}$$

Where $f(V_R)$ is the frequency density, V_R represents the volumetric rockfall magnitude, s is the intercept, and β is the exponent of the power law scaling. As such, β represents the relative frequency of rockfall magnitudes, analogous to the ratio of small to large rockfall events. To calculate the negative power law scaling (Eq. 3.1), rockfall volumes were divided into logarithmically spaced bins and the number of events were counted in each bin. Frequency densities were then calculated for rockfalls of differing magnitude using the formula given by Malamud et al., (2004):

$$f(V_R) = \frac{\delta N_R}{\delta V_R} \quad \text{[Eq. 3.2]}$$

Where $f(V_R)$ is the frequency density of a rockfall magnitude V_R, δN_R is the number of rockfalls with estimated volumes that fall in the range of δV_R, and $\delta V_R$is the bin width, measured in m^3. By plotting the magnitude-frequency distribution on a plot of log-volumes against log-frequency, Eq. 3.2 represents the straight-line form of Eq. 3.1 as follows (Williams, 2017):

$$\log f(V_R) = \log s - \beta \log V_R \quad \text{[Eq. 3.3]}$$

The normalised rockfall frequency $f(V_R)$ for each bin was calculated using the formula given by Williams, (2017):

$$f(V_R) = \frac{\delta N_R}{\max \delta N_R} \quad \text{[Eq. 3.4]}$$

Where $\max \delta N_R$ is the maximum rockfall frequency computed across all bins. The third metric is the actual frequency of events that fall in each bin, and so, here the frequency of each bin is no longer normalised. Hence, the actual rockfall frequency was calculated as follows (Williams, 2017):

$$f(V_R) = \delta N_R \quad \text{[Eq. 3.5]}$$

For all metrics of magnitude-frequency, the estimation of the parameters s and β were modelled applying a least-square regression (LSR) on the logarithmically transformed data (Goldstein et al., 2004). LSR may be inaccurate along the tails of the power law due to the log-log transformation (Barlow et al., 2012), nevertheless, LSR is used in this research due to two principal reasons: first, it has been demonstrated that LSR produces identical models to the alternative maximum likelihood estimator (MLE) method (Goldstein et al., 2004); second, LSR has been applied in a wide body of research undertaking magnitude-frequency analysis on rock-slopes, hence, ensuring full comparability with other findings (e.g., Rosser et al., 2005; Barlow et al., 2012; Williams et al., 2019; Benjamin et al., 2020). As demonstrated by Barlow et al., (2012), the exponent β characterizes the relative size distribution of rockfalls, and as such, higher exponents (expressed as a steeper slope of the power law in a log-log plot) indicate a higher proportion of smaller rockfalls relative to larger events, while lower exponents manifest the imprint of a higher proportion of larger rockfalls in the overall erosional flux (reflected as a gentler slope in a log-log plot).

Figure 3.3a shows the frequency density calculated for the whole monitored period, using all the rockfalls of the 4D inventory between 2017 and 2019 (8,367 failures), which is overlaid upon annual-scale frequency densities using all the rockfalls captured in each year (Table 3.3). The rate of geomorphic activity for the whole monitored period was characterized by the predominance of a negative power law where the overall size distribution of rockfalls is reflected by an exponent of -1.85 and an intercept of 23.9 m^3, a value which approximates the magnitude of the maximum rockfall occurring during the monitoring period (22 ± 4 m^3). While the slope of the modelled relationship reflects the overall proportional contribution of the smaller to larger rockfalls, the position of the line on the plot reflects annual differences in the net rate of cliff activity, and hence material loss. Interestingly, similar rates of geomorphic activity are detected for 2017 and 2019 as the distributions have a similar exponent (-1.75 and -1.77, respectively), and the position of the power law are almost identical, which corresponds well with the total number of rockfalls detected for both year. This primarily represents the years with higher production rates of rockfalls, as well as with the occurrence of the two largest volume rockfall (Table 3.3). The rate of geomorphic activity was marginally lower during the 2018, being the year with the

lowest rockfall production rate, as well as a lower maximum rockfall volume (Table 3.3). However, in 2018 the exponent was the highest (β = -1.83), suggesting a greater contribution of relatively smaller magnitude rockfalls, which tended towards the exponent for the whole monitored period (β = -1.85).

Figure 3.3a shows three distinctive erosional patterns in the magnitude frequency data. First, a 'roll-up' distribution of higher rockfall densities of very low magnitude, which is punctuated by an upper erosive threshold involving very small rockfalls $\leq$ 0.005 m^3 and > ~ 1 × 10^5 m^{-3} frequency density. The roll-up of rockfall activity is interpreted to represent small spalling rockfalls that do not adhere to a negative power law and may more closely reflect the disaggregated of a heavily weathered and unstable surface. This roll-up distribution begins around the upper erosive threshold, which was identified as the first observed frequency density deviation above the upper zone of the power law (~ 1 × 10^5 m^{-3}), however, it is more evident over the 1 × 10^6 m^{-3} of frequency density. Second, a region involving small (0.005 – 0.01 m^3), medium (0.01 – 0.1 m^3) towards larger rockfall volumes (up to 1.0 m^3) that adheres well to a negative power law is observed for all years, which is located between ~ 1 × 10^0 and 1 × 10^5 m^{-3} frequency density, where a concentration of observed rockfalls have a higher frequency density than the LSR model. Third, a 'heavy-tail' distribution of relatively high rockfall densities is detected but, in this case involving larger rockfalls $\geq$ 6.5 m^3, and below ~ 1 × 10^0 m^{-3} frequency density exceeding the power law modelled values. This heavy-tail distribution of rockfall activity begins around the lower erosional threshold, which was defined as the first observed frequency density deviation above the tail of the modelled power law (bellow ~ 1 × 10^0 m^{-3} of frequency density).

Importantly, the detection of a marked roll-up and a heavy tailed distribution for very small and the large rockfall magnitudes, respectively, may in part be explained by the unique insight provided by very high frequency 4D change detection, which here is undertaken for the first time over a multi-annual observation period of three years. Such resolution and duration of observation reduces the likelihood of underrepresentation of certain sizes of rockfall due to the effects of superimposition and coalescence commonplace where monitoring intervals are long, and so enhances the likelihood of capturing the smallest failures. This is combined here with an extended monitoring duration to minimise the censoring of the largest rockfalls based on temporally limited observation, and hence provides perhaps one of the most robust representations of rockfall magnitude and frequency.

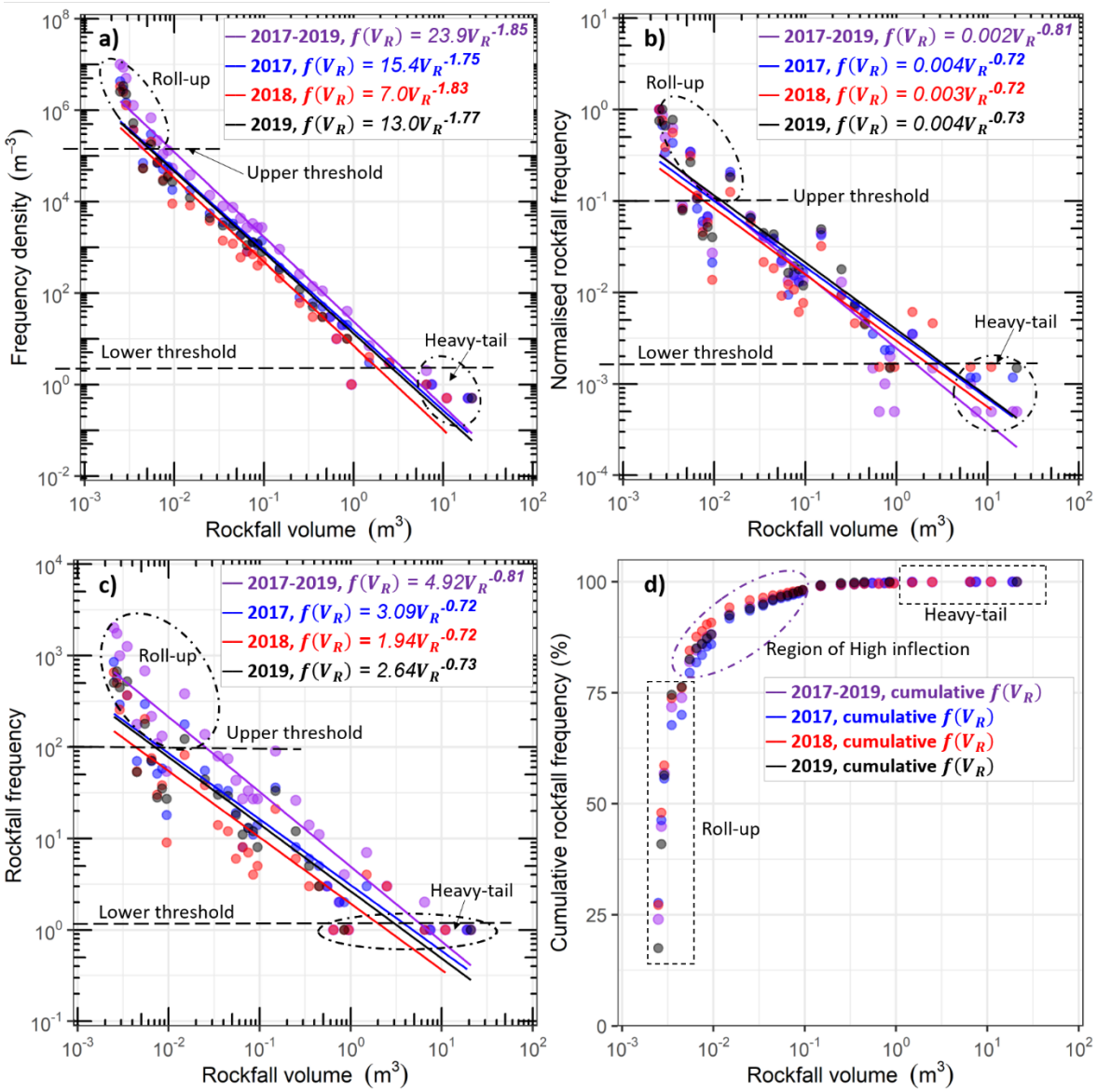

Figure 3. 3: *Magnitude-frequency modelling of the cliff erosion.* ***a)*** *Negative power law scaling using the frequency density in each volumetric bin (Eq. 3.2). The roll-up and heavy tail patterns are shown using dashed ellipses and the corresponding upper and lower thresholds are shown using horizontal dashed lines. Best-fit relations of the power low for the whole monitored period was r^2 = 0.96, while for 2017, 2018 and 2019 r^2 = 0.97, 0.95 and 0.95, respectively.* ***b)*** *Negative power law scaling using the normalised rockfall frequency (Eq. 3.4). Best-fit relations for the whole monitored period was r^2 = 0.88, while for 2017, 2018 and 2019 r^2 = 0.87, 0.81 and 0.81 respectively. Roll-up and heavy tail distributions are shown using ellipses.* ***c)*** *Negative power law scaling using the actual rockfall frequency (Eq. 3.5). Best-fit relations for the whole monitored period was r^2 = 0.79, while for 2017, 2018 and 2019 r^2 = 0.71, 0.73 and 0.73, respectively. Roll-up and heavy tail zones are shown using ellipses.* ***d)*** *Cumulative frequency - magnitude. Zones of inflection in the relationships are shown using ellipses. Roll-up and heavy tail distributions of figures a) to c) are shown as dashed rectangles.*

Figure 3.3b shows the normalised rockfall frequency of rockfall volumes, with normalised frequencies per year, which ranged from 1×10^{0} for the maximum frequencies of very small rockfall, to ~ 1×10^{-3} and 10^{-4} for the lowest frequencies representing the largest rockfall. For this dataset, while the normalisation of rockfall frequencies yielded a greater distinction between the magnitude-frequency relationship for each year across most volumes, where there was a greater deviation in observations from the fitted power law model, normalising also had the effect of reducing and homogenizing the differences between the annual-scale exponent of the negative power law (β = -0.72 to -0.73). This generated low scaling coefficients as compared to those for the rockfall volume frequency densities. Nevertheless, the relative position of the annual-scale power law models (reflecting the relative net flux of rockfall material in each year) is preserved, and as such, the level of geomorphic activity was marginally lower for the 2018, whilst 2017 and 2019 remain similar.

Figure 3.3b also highlights both regions with roll-up and heavy tail distributions. For normalised frequencies associated with the size of small rockfalls, the upper erosive threshold is found above the ~ 1×10^{-1}, where again, a dense and vertically shaped clustering of frequencies is detected. On the other hand, the lower erosional threshold, punctuating the beginning of the heavy tail distribution associated to large rockfalls is found at ~ 1×10^{-3}, however, in this region of failures, the normalisation of frequencies enhanced the differences in volumetric magnitude while keeping the normalised frequency constant, and so, generating horizontal distributions of frequencies across the *y-axis* below the lower threshold.

To exemplify this point, for the years 2018 and 2019, normalised volume frequencies associated with the largest rockfalls were found at ~ 1×10^{-3}, however they are distributed across a range of rockfall volumes from ~ 1×10^{0} to 1×10^{2} m^3. Similar results are found for normalised frequencies in 2017, in addition to those representing the whole monitoring period. For small to moderate towards large sized rockfalls (here, between ~ 0.045 and up to 1.0 m^3), normalisation of the frequencies enhanced the differences between each year, generating differences in the scaling coefficient. Overall, using normalised rockfall frequencies, the roll-up and heavy tail distributions of rockfall activity are retained, again showing these to be important features of the magnitude-frequency data. However, one key difference with the frequency density (Figure 3.3a), is that the range in volume size of low to medium to large rockfalls is showing a greater degree of deviation from the modelled power law (Figure 3.3b).

Figure 3.3c represents the actual rockfall frequency (non-normalised), where the frequencies per year and for the whole period of observation ranged from 1×10^{3} to 1×10^{4}, for

the highest frequencies representing the smallest rockfalls, to ~ 1×10^0 for the largest rockfall, again demonstrating the low frequency of the largest failures. Again, as in the normalised frequencies (Figure 3.3b), the using of actual rockfall frequencies showed a greater degree of deviation of the magnitude-frequencies relationships plotted, while homogenising and reducing the disparities between annual power law exponents. As such, the negative power law exponents remained very close to those derived from the normalised frequencies (β = -0.72 to -0.73), demonstrating a certain degree of consistency in using these magnitude-frequency metrics. The roll-up and heavy tail distributions are again retained, reinforcing the emergence of these unique patterns using 1 h change detection over a multi-annual measurement period. As a result, the normalised rockfall frequency and actual rockfall frequency showed the same overall features of the magnitude-frequency data. The main key difference when compared with Figures 3.3a and 3.3b is the position of the upper (~ 1×10^2) and lower (~ 1×10^0) threshold punctuating the beginning of the roll-up and heavy tail distributions of rockfall activity, respectively.

The cumulative frequency-magnitude data demonstrate that a substantial majority of detected rockfalls were below ~ 1×10^{-2} m^3 (very small rockfall sizes) representing ~ 88.1% of the total number of failures. Notably, about 75% of the total number of rockfalls fall within the roll-up distribution of failures showed by the frequency density, normalized and actual rockfall frequencies graphs. Over the limit of the ~ 75% of rockfall frequency, it is detected the beginning of a marked deviation in the cumulative curves. This zone of deviation terminates around 1×10^{-1} m^3 (here, the limit between small towards medium rockfall sizes), representing ~ 98% of the total number of detected rockfalls, which adhered a typical negative power law in the non-cumulative magnitude-frequency plots of figures 3.3a-c. Significantly, the end of the region of deviation punctuate the beginning of a marked plateau in the total number of rockfall events (above 1×10^{-1} m^3), representing the size of medium towards the largest rockfalls. Bellow 1×10^0 m^3, the total number of rockfalls is ~ 99.8%. This limit punctuates the beginning of the heavy tail distribution of failures, were it is demonstrated that they are the less common of the 4D inventory. Importantly, the cumulative curves are similar, smooth and consistent for the three years under analysis, demonstrating a similar behaviour of the erosive work over the time (Figure 3.3d).

To examine the erosive contribution of different rockall sizes and the relative effectiveness of the possible processes controlling the magnitude and frequencies of the events measured between 2017 and 2019, the rockfall activity has been segmented by rockfall magnitude, ranging from very small rockfalls (0.001 – 0.01 m^3), small-medium rockfalls (0.01 – 0.1 m^3), medium-large rockfalls (0.1 – 1.0 m^3), to the large rockfalls (≥ 1.0 m^3). Then, the non-

cumulative frequency density and associated negative power law (Figure 3.4a), as well as the cumulative magnitude-frequency (Figure 3.4b) has been estimated and fitted for each category of rockfall size, providing insight into the erosional role or distribution of different magnitudes over the overall cliff erosion.

Figure 3.4a shows that the size of very small rockfalls (0.001 – 0.01 m^3) are characterized by a positive deviation above the negative power law straight line (β = -3.71), being nearly two times higher than the commonly reported exponents found in a wide range of research characterizing the erosion of rock-slopes along the North Yorkshire, where exponents range from -1.0 to -2.0 (Table 3.4). This is, perhaps not surprising given the exclusively very small size of the rockfalls and that the highest densities are clustered between ~ 1×10^6 and 1×10^7 m^{-3} of frequency density, forming the region of marked roll-up activity for the whole dataset and so, controlling the upper tail and inclination of the modelled power law. The range of small to medium rockfalls (0.01 – 0.1 m^3) are characterized by a gentler slope, which is well reflected by a lower exponent (β = -1.46), ranging between ~ 1×10^3 and 1×10^5 m^{-3} of frequency density, adhering well to the overall negative power law that characterizes the entire observation period (β = -1.85). Medium to large rockfalls (0.1 – 1.0 m^3) adhere well to the overall power law of the whole monitored period, however a steeper power law gradient is detected (β = -2.32), which is explained by a higher clustering of failures between ~ 1×10^2 and 1×10^3 m^{-3} of frequency density controlling the upper tail of this fitted power low. The range of large rockfalls (≥ 1.0 m^3) show the lowest negative power law gradient (β = -0.59), which is, perhaps, not unexpected due the exclusive high size of the failures and that the lowest densities are clustered around ~ 1×10^0 and 1×10^{-1} m^{-3} of frequency density, forming the region of heavy tailed rockfall activity, which ultimately control the bottom of the tail of the locally fitted power law.

Overall, the locally fitted power low by rockfall magnitude provides new insights into our understanding of the magnitude-frequency relationships, as these demonstrate that the exponents of the relationships (β) can be two times higher in the roll-up region of smallest rockfalls (0.001 – 0.01 m3), but two or three times lower in the heavy-tail region of largest rockfalls (≥ 1.0 m3) when compared with commonly reported values (β = -1.0 to -2.0, see Table 3.4) captured form monthly monitoring and importantly, using a single power law that represents all rockfalls. As such, these results provides new levels of variability in cliff erosion that can be obtained from locally-fitted power laws, but that can only be observed using high-resolution and long-term (i.e., multi-annual) rockfall monitoring. This is particularly important if the detection and analysis of the smallest and largest rockfalls is important, such as in this study (see for example Chapter 6).

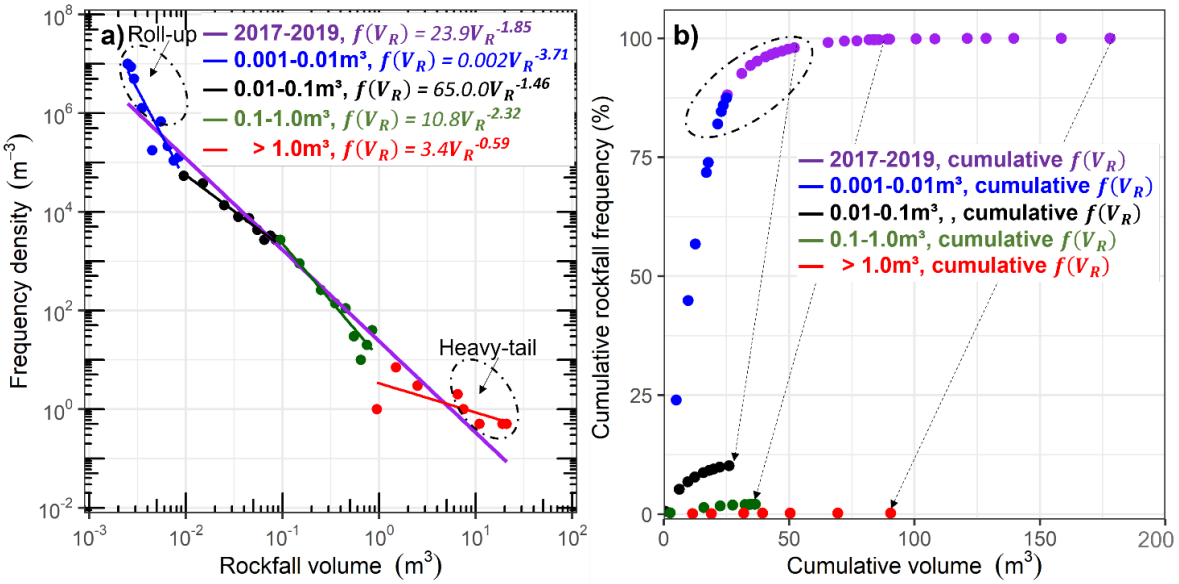

Figure 3. 4*: Magnitude-frequency distribution for the whole monitored period (2017-2019) segmented by rockfall magnitude and its geomorphic contribution to the overall cliff erosion.* ***a)*** *Negative power law scaling using the frequency density (Eq. 3.2), calculated for five principal categories of rockfall magnitude, from very small spalling of rock-masses (0.001-0.01 m³) to large rockfall events (≥ 1 m³). Roll-up distributions are highlighted using dashed ellipses.* ***b)*** *Cumulative magnitude-frequency distribution for each principal categories of rockfall magnitude, where the dashed ellipse shows the region of inflection between overall cumulative rockfall frequency (purple) and the estimated best-fit trend line. Also, dashed arrows indicate the cumulative contribution of the different rockfall sizes over the overall cumulative frequency. For comparative analysis, the general negative power low scaling representing the whole monitored period from 2017 to 2019 is overlapped in figure a) using purple trendlines (This general negative power law is also shown in Figures 3.3a using purple trend lines).*

Figure 3.4b demonstrate that very small rockfalls (0.001 – 0.01 m^3) supplied the highest erosional contribution in terms of the occurrence, reaching over ~ 88.1% of the total number of detected rockfall between 2017 and 2019, nevertheless, this group supplied ~ 25.1 m^3 of the total volume observed (~ 14.1% of the total eroded volume detected during the whole monitored period of 178 m^3), and so, supplying the lowest volumetric contribution to the overall cliff erosion. Whilst it is possible that errors in data processing may have generated a proportion of false surface change estimates (i.e., included here as very small rockfalls), it is considered here that the inclusion of false change estimates is minimal due to the application of a set of quality control steps and filtering (such as the partial scan filer, edge and hole filter, and M3C2 Distance Uncertainty filter, among others, see Chapter 2), so that the majority of the reported numbers of very small rockfalls represent actual failures. Importantly, regardless of the potential inclusion of some false change estimates, the highest frequency of very small rockfalls indicates a degree of background erosion

and steady baseline of activity during the monitored period. In terms of the possible processes controlling the magnitude and frequency of this size of rockfalls, these results may suggest the relative effectiveness of failures controlled by small fragmentation of rock-masses, such as iterative physical weathering as a response to a complex combination of long term forcing due to, for instance, temperature fluctuation inducing rock-mass expansion and contraction, cumulative microfracture nucleation, cumulative seismic loading due to tides and waves, and/or rainfall activity acting on highly fractured rock-block sets. These processes are quantified and discussed in more detail in Chapter 6, Section 6.5.1.

Table 3. 4: *Magnitude-frequency β values obtained from previous studies undertaken TLS monitoring across the North Yorkshire cliffs.*

Cliff location	β	Date	Survey interval	Reference
	-	m/yy	Days	-
Whitby	1.85	01/2017 – 12/19	1 h	This research
Whitby	1.75	01/17 – 12/17	1 h	This research
Whitby	1.83	01/18 – 12/18	1 h	This research
Whitby	1.77	01/19 – 12/19	1 h	This research
Whitby[1]	3.71	01/2017 – 12/19	1 h	This research
Whitby[2]	1.46	01/2017 – 12/19	1 h	This research
Whitby[3]	2.32	01/2017 – 12/19	1 h	This research
Whitby[4]	0.59	01/2017 – 12/19	1 h	This research
Boulby-Staithes	1.12 – 2.37	09/02 – 05/05	~30	Rosser *et al.* (2013)
Boulby-Staithes	1.80	10/03 – 04/05	~30	Lim *et al.* (2010)
Boulby-Staithes	1.12 – 2.12	09/03 – 03/05	~30	Barlow *et al.* (2012)
Boulby	2.17	07/08 – 06/10	~30	(Norman, 2012)
Boulby	0.82	05/12 – 06/14	~30	(Whadcoat, 2017)
Cowbar	0.71	05/12 – 06/14	~30	Whadcoat (2017)
Cowbar	0.82	05/12 – 06/14	~30	Whadcoat (2017)
Staithes	0.86	05/12 – 06/14	~30	Whadcoat (2017)
Whitby	2.27	03/15 – 12/15	1 h	Williams *et al.* (2018)
Whitby	1.78	03/15 – 12/15	30	Williams *et al.* (2018)
N. Yorkshire	1.54 – 1.69	08/14 – 03/17	294 - 356	Benjamin *et al.* (2020)

Note: Table modified from Table 3.04 in Benjamin (2018, p. 46). Whitby [1-4] indicates β values calculated here for rockfalls of differing volumetric magnitude, from very small (0.001 – 0.01 m^3), small-medium (0.01 – 0.1m^3), medium-large (0.1 – 1.0m^3), to large size (≥ 1.0 m^3), respectively.

Conversely, the erosive contribution of large rockfall events (≥ 1.0 m^3) was the highest as they supplied ~ 90.5 m^3 of the total volume loss, equating ~ 50.8% of the total volume

measured. Notably, this volume loss was supplied primarily via a total of 17 large rockfalls, representing ~ 0.2% of the detected rockfall numbers. For this range of the rockfall sizes, where heavy tail features above the power laws has been demonstrated, these magnitude-frequency data demonstrate a lowest geomorphic episodicity or less common recurrence, however the highest volumetric contribution to the cliff erosion. In terms of the likely processes controlling the magnitude and frequency of this size of rockfalls, these results may indicate the relative effectiveness of rockfalls controlled by, perhaps, shorter term forcing or geomorphic episodicity if temporal discontinuity is inherent in the forcing process (Crozier, 2006). For example, sudden and energetic weather such as from big storms (e.g., same day rainfall or precedent storms), or from seismic loading associated to extreme tides and waves, both forcing conditions exceeding some form of threshold. In the absence of evident episodic energetic forcing, these rockfalls may be induced by, for instance, iterative destabilization and/or rock weakening where the magnitude of the forcing does not correlate with the magnitude of the rockfall that occurs. The discussion about some of these mechanisms is presented in Chapter 6, Section 6.5.1.

Figure 3.4b also shows that the size of low to medium rockfalls (0.01 – 0.1 m^3) supplied ~ 10% of the total number of rockfall. However, this rockfall size yielded a total of ~ 26.1 m^3 of cumulative volume loss, equating ~ 14.6% of the total volume observed, which is of similar magnitude when compare with the volumetric erosional contribution of very small rockfalls (0.001 - 0.01 m^3). On the other hand, medium to large rockfall sizes (0.1 – 1.0 m^3) represents ~ 2% of the total number of rockfalls. Nevertheless, this size of rockfalls produced 36.5 m^3 of material, equating to ~ 20.5% of the total volume observed. The inference of the possible processes controlling the magnitude and frequency of both rockfall sizes may be complex as they represent the mid-range magnitudes that likely span processes of small scale spalling of the rock-mass to more discrete and isolated rockfall events, where a good adherence to the overall negative power law of the entire monitored period (β = -1.85) has been demonstrated. As such, while the size of small rockfalls may reflect disaggregation of the cliff surface in response to weathering, the detection of larger medium to large volumes may reflect either rock-mass fragmentation that occurs proximal to previous or developing rockfall scars, or new isolated events which develop in response to the cumulative effects of episodic forcing. In the next section of results (Section 3.4), time-series analysis of the 4D rockfall activity are used to examine the temporal change, at different time-scales, of the rockfall activity and how these accumulates into a long-term rate of geomorphological evolution.

3.4 Evolution of rockfall volumes and cliff erosion

To explore changes through time, 4D time-series of the rockfall activity has been divided into 5-day intervals from the hourly monitoring time series. Rosser et al., (2007) demonstrated over monthly intervals that larger detachments tended to be preceded by periods of increasing numbers and volumes of precursory rockfalls, and appeared also to be followed by periods of relative quiescence with fewer and smaller rockfalls. Here it is explored the timing and nature of periods of greater rockfall through the monitoring period, as shown in Figure 3.6a. This figure highlights the principal erosive episodes of the rockfall occurrence, defined by periods of abrupt changes in the volume of rockfall due to the detection of single large-scale rockfalls, or contemporaneous clusters of smaller rockfall that in sum add up to a large volume (Episodes 1 to 23). In addition, temporal coincidence between episodes of rockfall occurring either on a day when rainfall or after up to two days of preceding rainfall with respect to a significant rockfall event being detected within each five-day interval are also shown. These points of coincidence are shown as vertical blue bars and numbered according to their timing through within the erosive episode, from (1) to (23). Hence, blue bars suggest rockfall activity that may have been driven by precipitation, involving rainy-day rockfalls volumes (Table 3.3).

A conceptual model of the erosional work done by large-scale rockfall events, defining erosive episodes, and how they accumulate over the time, is presented in Figure 3.5. Based on this conceptual model, a period of gradual erosion (as opposed to the periods of abrupt change in the volume of rockfalls, generating sudden erosional jumps) is defined by a steady increase in the cumulative curve of erosion, so that during stages of gradual erosion, the occurrence of iterative small rockfalls dominates the erosion of the cliff face, and so, the evolution of the cliff in time.

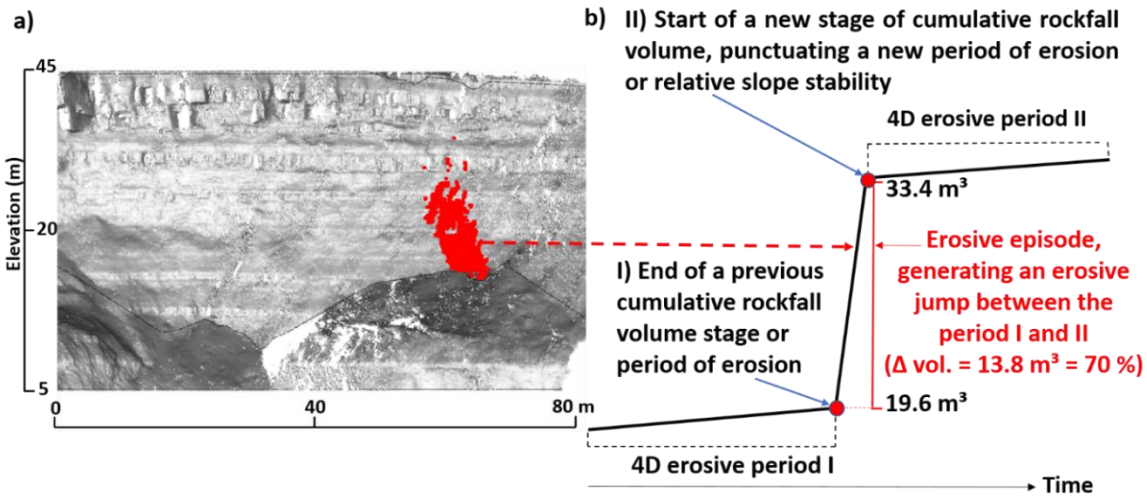

Figure 3. 5*: Conceptual model of the erosional work done by a large-scale and episodic rockfall event, defining an Erosive Episode (EP).* ***a)*** *Frontal view of a single rockfall event of 7.7 ± 1.2 m³, composing an erosive episode that occurred the 10th of June 2017, detected between 08:00 and 09:00 h (Episode 2).* ***b)*** *Conceptual model, showing how this erosive episode accumulates over a 4D geomorphic time-series, generating an erosive jump or abrupt change in the erosion between the periods I and II that represent gradual erosion. This figure also shows how an erosive episode is typically composed by a principal rockfall event of highest magnitude, in this case of 7.7 ± 1.2 m³, alongside with rockfalls of lower magnitude that occurred either in the same hourly interval, day and/or within an interval of five-days, totalling 13.8 ± 3 m³ of volume.*

The first abrupt erosive period occurred in winter 2017 and involved a total rockfall volume of 10.5 m^3, equating to 12.7 m^3 of cumulative rockfall volume and it was associated with rainfall conditions of 7.1 mm of one-day antecedent precipitation (Episode 1), punctuating the end of the first period of gradual erosion (I). A second period of abrupt erosion is observed in spring resulting in 13.8 m^3 of rockfall during a period with 6.2 mm of rain (Episode 2). This episode increases the cumulative rockfall volume to 33.4 m^3, hence yielding an erosive jump with respect to the end of the previous cumulative rockfall volume stage (Δ_{Vol} = 70%). Between the episodes (1) and (2), it is observed a period of relative stability of about 124 days length or four months (II), characterized by only a low rate of rockfall, dominated by small (0.001-0.01 m^3) events, where the average total rockfall volume was 0.3 m^3 (Figure 3.6a).

The sharpest erosional rise occurred in summer 2017 driven by a large rockfall of 22.9 m^3 (Episode 3) likely induced by a two-day storm event (14.6 mm), equating 59.5 m^3 of the cumulative rockfall volume and so, representing an abrupt erosive jump when compared with the termination of the previous cumulative rockfall volume stage (Δ_{Vol} = 62%). Between the episodes (2) and (3) it is detected a second but shorter period of gradual slope evolution of 24 days duration

(III), where the average total rockfall volume was 0.6 m^3 and the average cumulative volume was 35 m^3 (Figure 3.6a).

After episode 3, which was the last abrupt erosive episode of 2017, it is detected a longer period of gradual erosion (IV), comprising 254 days length (8 months and 11 days) from the beginning of summer 2017 to the beginning of spring 2018 (Episodes 10 and 11). This period of gradual erosion is characterized by the occurrence of six erosive episodes that ranged from 0.6 to 2.7 m^3 of total rockfall volume (4) to (9), creating small step-wise cumulative rockfall volume trend. Furthermore, in this period the average total rockfall volume was 0.4 m^3. The erosive episodes (10) and (11) punctuated a new abrupt erosive jump driven by rockfalls of volume of 6 and 11 m^3, respectively, equating 94.6 m^3 of cumulative rockfall volume (Δ_{Vol} = 21%). Also, both episodes corresponded with 3.4 and of 29.7 mm of rainfall (Figure 3.6a).

A new period of gradual erosion is detected after the episode (11) in spring 2018, comprising 139 days length (4 months and 17 days), two minor magnitude episodes (12) and (13) coincident with rainfall, and an average total rockfall volume of 0.5 m^3 (V - VI). This gradual erosive period terminates with an erosive jump generated by the erosive episode (14) that occurred in the end of summer 2018, driven by 13.5 m^3 of total rockfall volume, equating 123.4 m^3 of cumulative rockfall volume (Δ_{Vol} = 13%). After the episode (14), another period of gradual erosion begins (VII), compromising 134 days length (~ 4 months) from autumn of 2018 and about half of the winter 2019, and including three rainy-days rockfall episodes from (15) to (17) of smaller volumetric magnitude (Figure 3.6a).

The last abrupt erosive rise of the monitored period occurred in winter 2019 (Episode 18), reaching a total rockfall volume of 22.8 m^3 and likely related to a one-day precedent rainfall of 12.7 mm. This episode equates 152.4 m^3 of cumulative rockfall volume, yielding the last detected erosive jump (Δ_{Vol} = 18%). Also, this event shows similarities with the erosional episode (3) as both are the largest detected erosive jumps of the time-series, approaching 23 m^3 of total rockfall volume and both coincident with antecedent storms. The episode (18) punctuates, again, the beginning of a longer and gradual erosive period (VIII), compromising 254 days length (8 months and 22 days) or half of winter, spring, summer, and one-third of autumn, including two minor magnitude episodes (19 and 20) and terminating in the erosive episode (21). This period of relative slope stability is driven by an average total rockfall volume of 0.3 m^3 (Figure 3.6a).

Towards the end of the time-series in autumn 2019, it is observed the incidence of smaller-magnitude but shorter occurrence erosional episodes of about 3, 2.6 and 2 m^3 of total

rockfall volume and separated by about 20 days between them (Episodes 21, 22 and 23, respectively). As a result, between the episodes (21) and (23) the cumulative rockfall volume trend tends to show a higher gradient when compared with the previously described gradual erosive periods, suggesting a new type of acceleration in the erosion rates (period IX), driving a maximum cumulative rockfall volume of 178.2 ± 71 m^3 at the end of the time-series (Figure 3.6a).

To assess whether large rockfalls (≥ 1.0 m^3) tended to be clustered in time, the mean time of occurrence between largest events (i.e., the actual intervals between large failures) was compared with the mean time if they were uniformly distributed through the whole monitored period. The results indicated that the mean time for uniformly distributed rockfalls is ~ 84 days between events, however the actual mean interval of occurrence was ~ 56 days, yielding a difference of ~ 28 days (almost one month) between both metrics. These results suggest that the largest rockfalls tend to not be clustered in time and that high variability of mean intervals was detected, ranging from 1 to 4 days (e.g., between the largest rockfalls contributing to the erosive episodes 10 and 11) up to 128 days (e.g., between largest failures of episodes 4 and 10).

During the monitored period, the maximum volume rockfall event per 5-day period showed significant fluctuations in volume, ranging from 0.002 m^3, the minimum detected volume (due to the occurrence of only one small rockfall toward the end of November 2019) and up to ~ 22 ± 4 m^3, the largest detected rockfall within the inventory (Erosive episode 18, occurring in February 2019). Here it was considered the degree to which single large rockfalls are isolated, or are accompanied by other rockfalls that occur in the same period, here defined by the 5-day windows. As such, the erosive contribution of large-magnitude rockfall events (here defined as those rockfalls > 1.0 m^3) fluctuated between the 46 and 95% of the total rockfall volume observed within each erosive episode (Figure 3.6b). For example, the two largest volumetric rockfalls in the time-series showed a maximum failure volume of ~ 18 ± 4 and 22 ± 4 m^3 and they supplied 79 and 95%, respectively of the total rockfall volume in erosive episodes (2) and (18). Other rockfalls that also had relatively large volumes (~ 6 ±2 and 12 ± 3 m^3) supplied between the 52 and 88% of the total eroded volume in each of erosive episodes (1), (2), (11) and (14). Rockfalls of volumes between ~ 1 and 3 m^3 showed significant contributions to the 5-day erosion total, ranging from 46 to 88% of the rockfall volume (e.g., erosional episodes 4, 10, 12, 13 and 15). Therefore, it is demonstrated that the larger rockfalls supplied a consistent proportion of the total volume loss in 5-day periods, and so, pre-failure and post-failure are likely to scale in size with the volume of the largest event, as observed by Rosser et al. (2007) using monthly datasets.

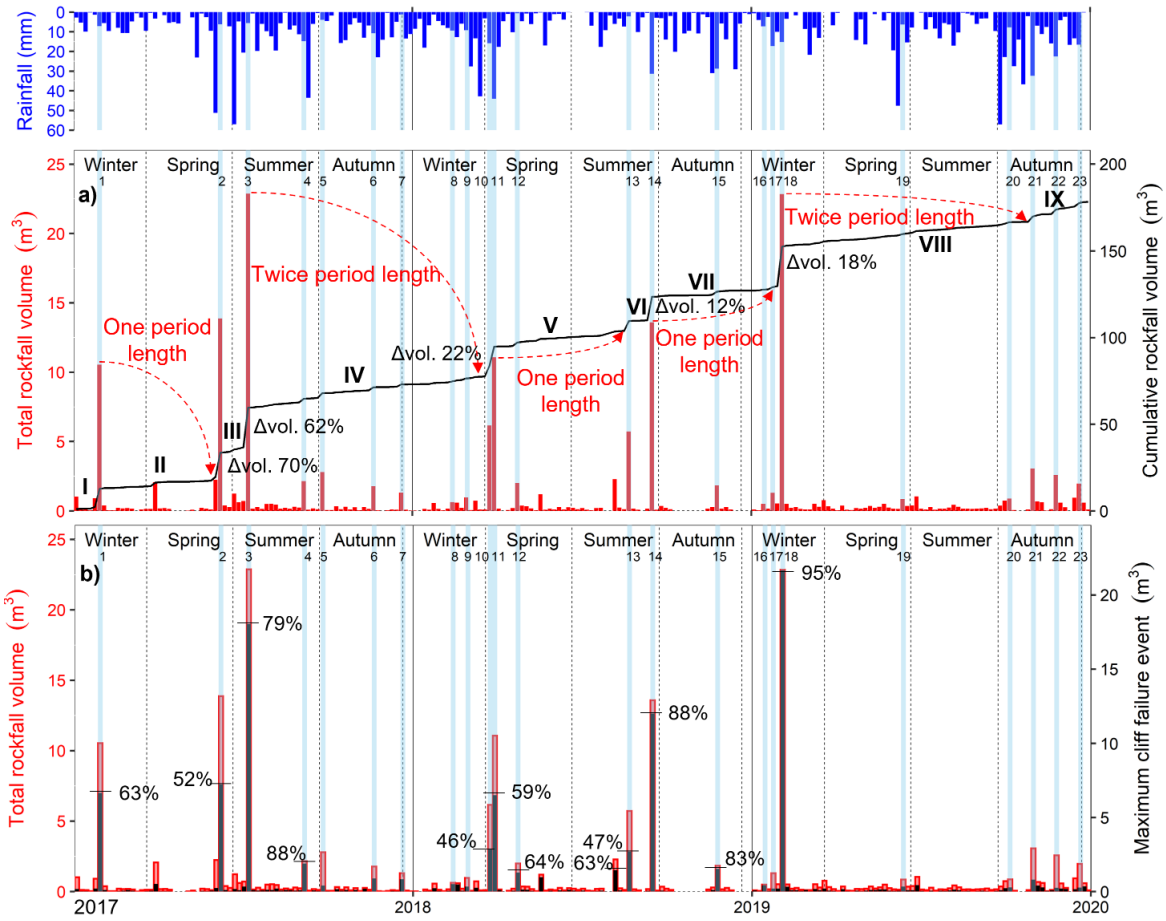

Figure 3. 6*: Time-series of the 4D Rockfall activity binned using five-day windows:* ***a)*** *Evolution of the total and cumulative rockfall volume (m^3) coupled with the total rainfall at the top. Red-dashed arcs show the length of the Gradual Erosion (GE) periods following the main Erosive Episodes (EP), starting from the top of the total rockfall volume and ending before the beginning of the next main erosive episode (red arrow). Delta symbols show the change (%) between the end of the previous cumulative rockfall volume stage (red arrow) and the new cumulative rockfall volume reached after each erosive jump. This percentage was calculated as the difference in the volumetric value of the erosive episode with respect to the total cumulated rockfall volume value observed before the occurrence of the erosive jump (100%).* ***b)*** *Erosive contribution (%) of the maximum single rockfall event (black bars) in relation the total rockfall-eroded volume observed in the same five-day window (100% is the top of the non-filled red bars). As such, the percentage on the bars indicates the erosive contribution of large "single" rockfall events (here defined as those rockfalls > 1.0 m³) with respect to the "total" volume observed within a five-days. The erosional episodes that matched with rainfall are shown as vertical blue bars and numbered according to occurrence from 1 to 23. Periods of gradual erosion are shown from I to IX.*

Overall, in terms of the recurrence of the principal erosive episodes, it is observed that the two highest erosive episodes of the time-series (Episodes 3 and 18), both reaching about 23 m^3 of total rockfall volume, are followed by the longest periods of subsequent relative slope stability of 254 and 264 days (periods IV and VIII, respectively). When these quiescence periods

of time of relative slope stability (IV and VIII) are then compared with the periods of time that follow the erosive episodes of immediately lower volumetric magnitude (Episodes 1, 11 and 14), that range between 10.5 and 13.5 m^3 of total rockfall volume, it is observed that they are followed by shorter periods of relative slope stability (periods II, V and VII) ranging from 124 to 139 days length (i.e., about half of the period of time that follows the biggest magnitude rockfall episodes). Therefore, this relationship suggests that the quiescence periods that follow the largest-magnitude erosive episodes (i.e., periods IV and VIII) are about two times longer than the period of time that follows the lower-magnitude erosive episodes (i.e., periods II, V and VII).

Significantly, this temporal recurrence pattern may hold geomorphic and slope-hazard implications in terms of the evolution of the erosion and overall rock-slope stability as an apparent rockfall magnitude-post relaxation time relationship is detected. However, for this dataset and stage of analysis, it is important to note that large rockfalls may occur at opposite sides of the cliff face, and so, these results do not imply that these rockfalls are mechanical or spatially linked (Figure 3.8). As such, the temporal signal detected suggests that after large magnitude events, a return to a steady baseline of gradual erosion or rockfall activity occurs (Periods I to IX), whose length of duration tend to scale, at certain times, with the magnitude of the preceding erosive episode.

Given the apparent temporal rockall magnitude-relaxation time relationship detected using high resolution 4D time-series (Figure 3.6a), to provide insight into the likely recurrence or geomorphic episodicity of the large rockfall events generating erosive jumps between periods of relative slope stability, the mean recurrence interval (or return period) has been estimated using the *Generalized Extreme Value* (GEV) distribution (*Maximum Likelihood Estimation*), implemented using the package *extReme* in *R*. Indeed, extreme value statistics is used principally to quantify the stochastic behaviour of processes showing unusually large (or small) magnitudes (Gilleland, 2021). As such, the quantities provided by GEV distributions are of particular interest providing mean return periods of extreme natural hazards such as storms or earthquakes (Gilleland and Katz, 2016). In this study, the maximum rockfall magnitude detected within each month of the 36-month monitoring period has been used to estimate the mean recurrence interval. The computed GEV is given by Gilleland and Katz (2016):

$$G(z) = exp\left[-\left\{1+\xi\left(\frac{\mathcal{Z}-\mu}{\sigma}\right)\right\}^{-1/\xi}\right] \quad \text{[Eq. 3.6]}$$

Where ξ represents the shape parameter of the GEV distribution, $\mathcal{Z}$ is the rockfall volume, μ represents the location parameter of the distribution, and σ is the scale parameter, controlling the

spread of the distribution. The variable expected to be exceeded on average once every $1/p$ periods, where $1 - p$ is the specific probability associated with the quantile. Letting $y_p = -1/\ln(1 - p)$, then the associated return level z_p is given by Gilleland and Katz (2016):

$$z_p \begin{cases} \mu + \frac{\sigma}{\xi}\left[y_p^{\xi} - 1\right], & if\ \xi \neq 0 \\ \mu + \sigma\ ln y_p\ , & if\ \xi = 0 \end{cases} \qquad \text{[Eq. 3.7]}$$

To estimate the temporal probability of the maximum rockfall magnitudes, the Poisson model has been adopted since it has been widely used to investigate temporal occurrence of landslides (Guzzetti et al., 2005; Coe et al., 2000; Crovelli, 2000; Jaiswal and van Westen, 2009). A comprehensive summary of key assumptions of the Poisson model is provided by Guzzetti et al., (2005). Based on the Poisson model, the exceedance probability or the probability of experiencing one or more rockfalls of a given maximum magnitude during time t is given by Crovelli (2000):

$$P[N(t)] = 1 - exp(-t/\mu) \qquad \text{[Eq. 3.8]}$$

Where $N(t)$ is the number of landslides (here, a rockfall of a given monthly maximum magnitude), that occur during a given period of time t of interest based on the statistics of past landslide events (as such, here, t is the total period of rockfall monitoring of 36 months), and μ represents the estimated man recurrence interval, computed using the GEV distribution.

Figure 3.7 indicates that events of magnitude ≥ 0.03 m^3 (equivalent to a 0.3 m cube) which fall within the size of small to medium rockfall, have a mean recurrence interval of 1 month, while events of ~ 1.0 m^3 have a recurrence interval of 1 – 4 months, both type of magnitudes showing 100% of probability to be equalled or exceeded within the estimated return interval, which suggests good correspondence with the empirical observations derived from 4D time-series. The maximum detected rockfall event of the whole time series of ~ 22 m^3 (forming the erosive episode 18) has a recurrence interval of ~ 20 to 21 months (almost two years) with a ~ 80% of exceedance probability. It is important to note that this is somewhat smaller than rockfall volumes previously observed at this site, by 2 to 3 orders of magnitude (see, for example: Rosser et al., 2005). The recurrence interval of the cliff collapse of 18 m^3, driving the second higher erosive jump (episode 3) is estimated to be ~ 18 months with a ~ 85% exceedance probability. Interestingly, these results suggest consistency with the empirically observed 4D time-series, as both principal rockfall events occurred within ~ 19 months of separation between them. Large rockfalls of lower and similar magnitude such as ~ 6 and 7 m^3 (erosive episodes 1 and 11) show

a recurrence interval of 9 and 10 months (almost one year), respectively, while the probability that these events are detected again or exceeded following such interval of time is ~ 97 to 98%, which again, indicates a good level of agreement with the time-series with rockfall of comparable magnitude detected once in 2017 and 2018. As a result, based upon a multiannual and high hourly resolution rockfall database, the estimated recurrence intervals of episodic and large rockfall events suggests that the bigger the magnitude of the failure, the larger the period between events of comparable magnitude will be, suggesting that the period of apparent post-failure quiescence tend to scale, in average over the long term in duration with the preceding rockfall volume.

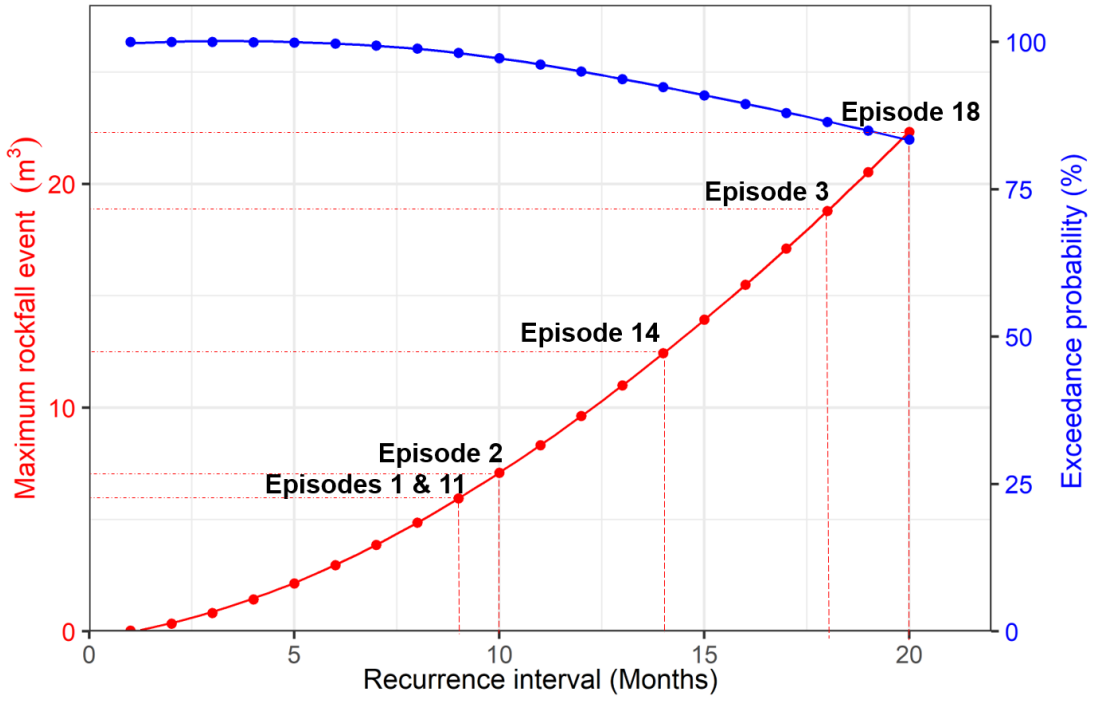

Figure 3. 7*: Mean recurrence interval and exceedance probability for the maximum rockfall event forming key erosive episodes. Recurrence intervals have been estimated extracting the maximum volumetric event of each month of the monitored period and then calculating the Generalized Extreme Value (GEV) distribution, using the Maximum Likelihood Estimation (MLE) for the parameter estimation of the computed GEV. Exceedance probabilities have been derived from the recurrence intervals adopting the Poisson model. Dashed red lines separated by arrows indicate rockfall magnitudes in which the recurrence interval is nearly half the interval that follows events of double magnitude (e.g., between the maximum rockfall events forming the erosive episode 14 and 18).*

Within each year, the spatial distribution of the rockfall events across the monitored cliff, grouped by month, is shown in Figure 3.8. The largest-single rockfall magnitude events that occurred within each 5-day interval forming the principal erosive episode are shown and numbered according to their occurrence (1-23). Rockfalls occurred along the whole cliff face, however, small, and medium magnitude events tend to cluster along the rock-block bridges, the

bottom of over-hanging beds or between master sets of bedding. The spatial extent of the large magnitude rockfalls is characterized by crossing multiple sets of beds, varying in their morphology, although elongated shapes following the vertical-axis are common. Also, spatial-precursory contiguity of monthly scale is detected (e.g., events 4 and 7 of 2017; 10, 11b, and 14 of 2018; or events 21 and 22 of 2019). The spatial distribution of events also shows that for a given year, large rockfalls contributing to erosive jumps as time-series may occurred either at opposite sides of the cliff face or with ~ 20 - 45 m of separation between them, and hence, the temporal signatures detected do not imply that these rockfalls are mechanical or spatially linked. Also, annual rockfall overlaps indicates concentrated zones of erosion and slope instability as well as annual-scale spatial contiguity (Figure 3.8d).

In summary, using a long-term 4D rockfall inventory based on 1h change detection measurements, it is demonstrated that the development of erosion over the cliff face is driven by the cumulative occurrence of intense erosive episodes that are composed of large-magnitude rockfall events – comprising small numbers of larger rockfall-, generating abrupt increases in volume lost interspersed by periods of more gradual erosion, ranging from 12 and up to 70% in the increases of volume loss. In this dataset, a total of 23 erosive episodes have been identified, and most were coincident with precipitation. These events punctuate what is otherwise a period of gradual erosion indicative of relative slope stability (Periods I to IX), where the erosional work tends to be dominated by iterative low magnitude rockfalls. As a result, this dataset provides new insights about the nature of the erosive evolution of structurally controlled rock-slopes, demonstrating how the erosional work done by small, medium and large-scale episodic rockfall events accumulates into a long-term erosional signature. In the next section, the geomorphological analysis of the evolution of the cliff from the point of view of the equivalent retreat rate is presented, alongside with magnitude-frequency distributions modelled for each erosive episode (EP) and period of gradual erosion (GE).

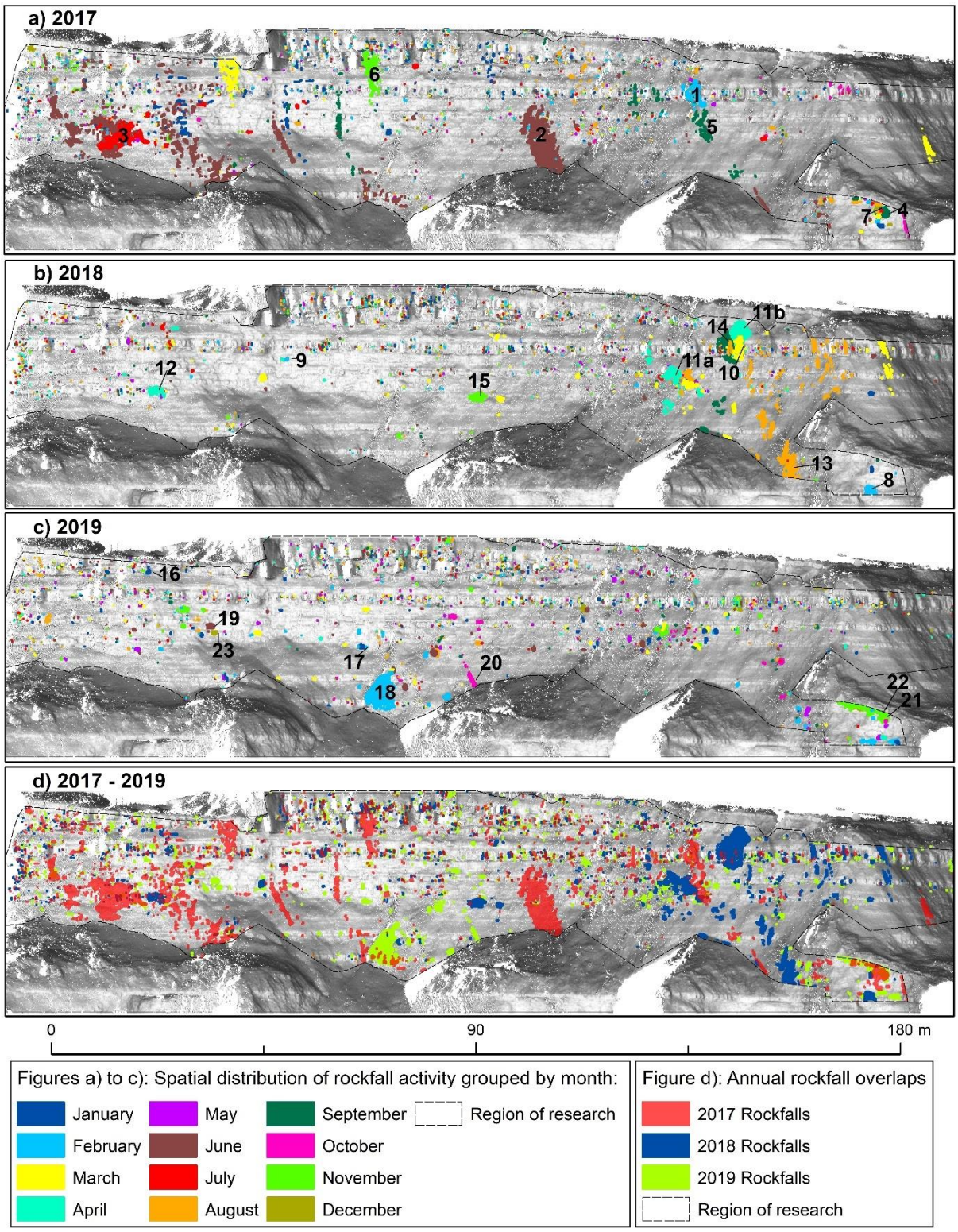

Figure 3. 8*: Geomorphic distribution of the 4D rockfall activity across the region of research. (a) January to December 2017. (b) January to December 2018. (c) January to December 2019. (d) Annual spatial overlaps of rockfalls from 2017 to 2019. The main episodes of the geomorphic evolution that corresponded with same-day rain events or up to two days of antecedent rain are numbered according to occurrence of the episode from 1 to 23. These episodes are the same as those shown in the Figure 3.6 of time-series of rockfall activity and cliff erosion behaviour.*

3.5 Evolution of the cliff retreat rate

Monitoring the rates of erosion of the East Cliff of Whitby builds upon a large body of research quantifying the erosion across the North Yorkshire cliffs, however the majority of these studies used monthly TLS surveys through years, or 1 h change detection involving up to 10 months of monitoring (e.g., Rosser et al., 2005; 2007; Lim et al., 2010; 2011; Barlow et al., 2012; Rosser et al., 2013; Vann Jones et al., 2015, Williams et al., 2018). Therefore, to get insight into the evolution of the retreat rates from a multi-annual and near-constant 1 h change detection dataset, it is considered here the variability in the magnitude and frequency of retreat rate through time. The results are presented using 4D time-series of the cliff-face annual retreat rate, which were calculated over five-day periods (pentads) of total volume loss (mm y^{-1}), permitting more straightforward examination of the emergent patterns of erosion from this dataset. Furthermore, it was calculated the net cumulative retreat (mm) from cumulative volume loss detected across the monitored area (~ 5,500 m^2). The average retreat rate throughout the three-year monitoring period, expressed in mm y^{-1}, was also quantified. The principal periods of gradual erosion (GE) were isolated from those characterized by higher rates (Erosive episodes; EP 1 to 23) and the average rate for these periods of quiescence were also quantified (Figure 3.9).

The average retreat rate between January 2017 and December 2020 was 11 mm y^{-1}, suggesting a relatively high but similar rate of volume loss of the examined cliff face to other observed rates (e.g., Lim et al., 2005, 2010; Rosser et al., 2013). Hence, for this dataset and analysis, this value represents a key synthetic geomorphic metric of the overall evolution throughout the subaerial section of the cliff as it is a result of both the large-magnitude and abrupt erosive episodes (EP: 1-23) and the subsequent periods of gradual cumulative cliff erosion (GE: I to IX). By examining the retreat rate calculated within pentads, it is observed high variability in the shorter-term erosion rate, which varied between ~ 0 mm y^{-1} during periods of minimum volume loss to maximum rates of ~ 305 mm y^{-1}, which were driven, for example, by two peaks of rock-mass loss of ~ 23.0 ± 5 m^3 that occurred in summer 2017 and in winter 2019 (Erosive episodes 3 and 18, respectively). In 2017 and 2018, an additional four episodes of high retreat rate were also detected throughout winter, spring and summer (~ 140 – 185 mm y^{-1}), while in 2019 the higher retreat rates were detected in winter and autumn. Also, the retreat rates during these periods of higher erosional activity generated marked differences compared to the long-term cumulative retreat curve. Overall, the minimum value of the cumulative retreat curve was 0.2 mm, reaching a total retreat of ~ 33 mm by the end of December 2019 (Figure 3.9).

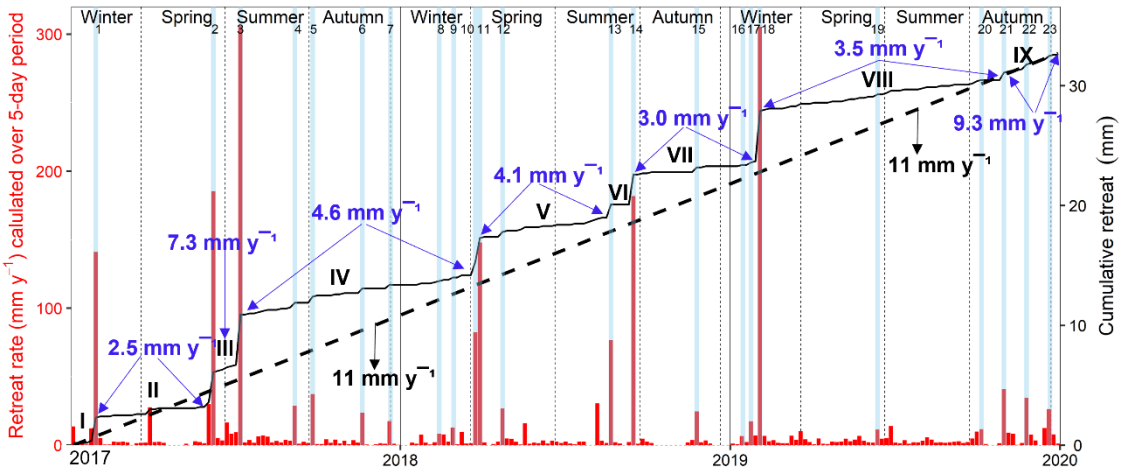

Figure 3. 9: *Evolution of the annual retreat rate (mm y^{-1}) calculated over five-day periods, and cumulative retreat (mm) between January 2017 and December 2019. The black dashed line shows the average retreat rate between these two dates (11 mm y^{-1}). The blue arrows indicate the average rate calculated for periods of gradual erosion (GE), where the average values are showed in blue. Periods of gradual erosion (GE) are shown from I to IX. From the top to the bottom, the main episodes of the geomorphic evolution, that corresponded with same-day rainfall or up to two days of precedent rainfall are shown as vertical blue bars and numbered according to occurrence of the erosive episode from 1 to 23. Approximate boundaries between astronomical seasons are shown using dashed vertical lines.*

It is observed prolonged periods of gradual cliff erosion (II, IV, V-VI, VII and VIII), showing near-constant rates of volume loss between 2.5 and 4.6 mm y^{-1}; these rates were quasi-constant over continuous periods lasting between 124 and 264 days. These periods of gradual cliff retreat resulted from the dominance of incremental, ongoing and iterative low volume failures. As expected, these periods were about two to four times lower when compare with the average retreat rate between 2017 and 2019 (11 mm y^{-1}), evidencing a general reduction in the dynamic of the erosion between large rockfall events (Figure 3.9).

Similarities can be seen between the erosive episodes (1) to (2) and (14) to (17) as both gradual erosional periods show a constant rate of erosion (2.5 – 3.0 mm y^{-1}) over a similar length of time of 124 and 134 days or four months (periods II and VII, respectively). Other periods of relative quiescence show similar rates of change. For instance, between the erosive episodes (3) and (10), the average rate was 4.6 mm y^{-1} over a length of time of 254 days (Period IV, lasting eight months and 11 days). In this period (IV), although the length of time was longer when compared, for example with the gradual erosive period II, the resultant average rate was slightly higher due to the erosive contribution of higher volumetric events (Erosive episodes 4 to 9). Similarly, in the period IV, the average rate was 4.1 mm y^{-1} lasting 139 days.

By contrast, shorter periods of gradual cliff evolution were also identified (periods III and IX). These showed elevated rates of erosion that ranged between 7.3 and 9.3 mm y^{-1}, and thus, approaching the average rate of erosion that characterizes the whole monitored period (11 mm y^{-1}). For example, between the erosive episodes (2) and (3), punctuating, respectively, the beginning and termination of the gradual erosional period III, the average rate was 7.3 mm y^{-1} lasting 25 days. Towards the end of the time-series, between the erosive episodes (21) and (23), defining the length of the relative stability period IX, the average rate was 9.3 mm y^{-1} over 65 days. Therefore, these measurements suggest that there were shorter periods of gradual erosion controlled by elevated cliff erosion, occurring either between two sequential large rockfall events (e.g., between episodes 2 and 3) or between events of medium to large volumetric magnitude, as between the erosive episodes (21) to (23) (Figure 3.9).

Figure 3.10a shows the frequency density and associated negative power law modelled for each of the principal erosive episodes (EP), which are shown as a cliff retreat time-series in Figure 3.9. As such, the exponents of the power law are used here to characterize the periods where an in increase in the erosion rate was detected (EP). As it may be expected, the erosive episodes show lower exponents compared to the whole monitored period (β = -1.85, which is a reflect of average retreat rate of 11 mm y^{-1} between 2017 and 2019), fluctuating between β = -1.18 to -1.68 and averaging -1.48. Also, the values of the EP exponents are all of a similar magnitude. Hence, these exponents suggest that larger magnitude rockfall events drive the erosional jumps as reflected by the higher retreat rates shown in Figure 3.9.

Figure 3.10a also shows that, using the 5-day binned data, a change in the upper erosive threshold, defining the beginning of the region of roll-up activity for the size of small magnitude events, is detected during erosive episodes. As such, the upper threshold of magnitude-frequencies for EP's is observed here around ~ 1×10^4 m^{-3} of frequency density, instead of ~ 1×10^5 m^{-3} which is characteristic of the upper erosional threshold of the whole monitored period (Figure 3.3a, Section 3.3). On the other hand, the lower erosive threshold, defining the beginning of the heavy-tail activity for larger rockfall remained constant at ~ 1×10^0 m^{-3} frequency density. Again, medium-size events falling between the roll-up and the beginning of the heavy tail showed a good fit with the modelled power laws.

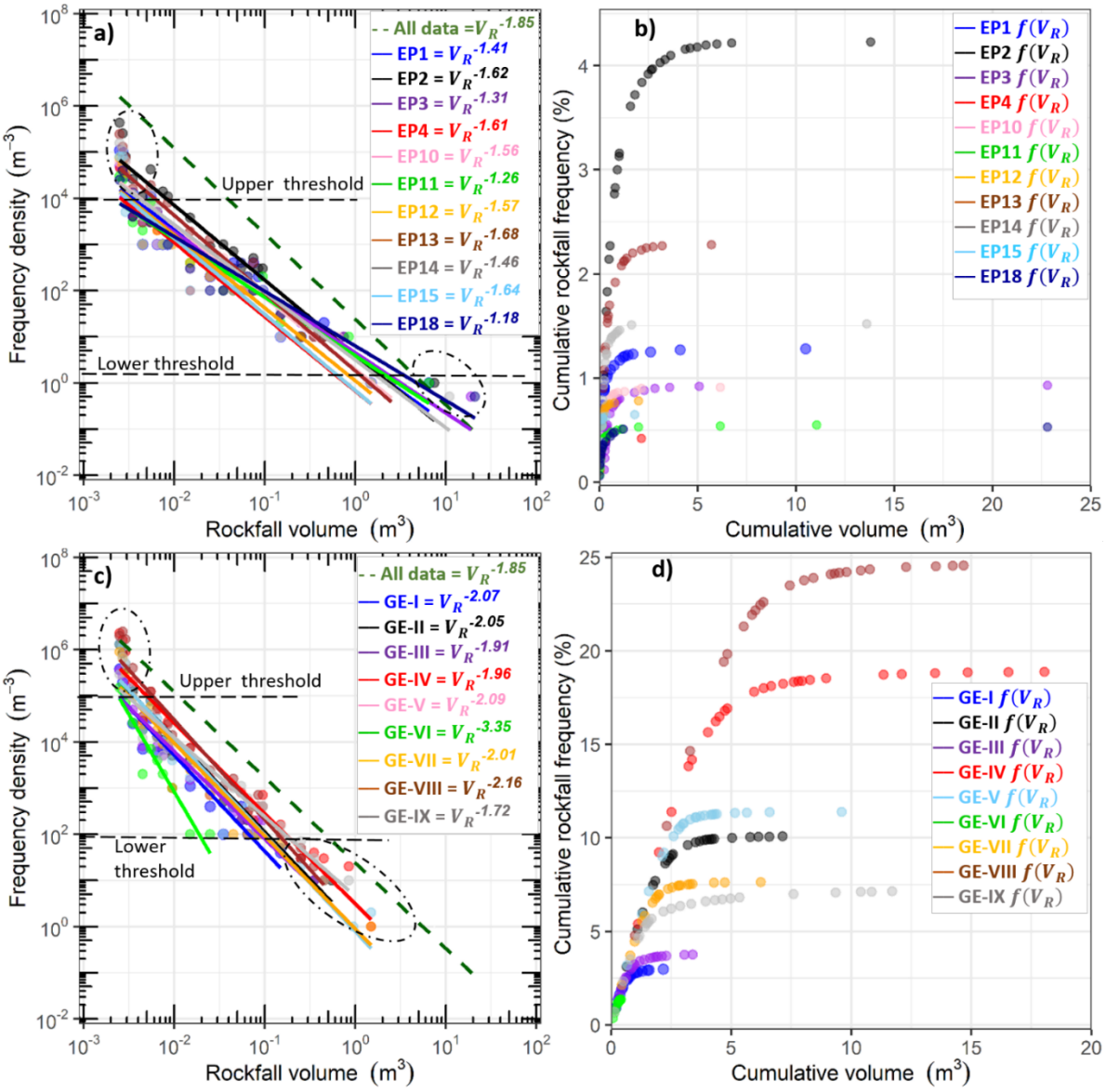

Figure 3. 10: *Magnitude-frequency distributions modelled for the principal Erosive Episodes (EP) and periods of Gradual Erosion (GE).* ***a)*** *Negative power law scaling using the frequency density, calculated for Erosive Episodes (EP) whose maximum rockall event is higher than 1.0 m^3.* ***b)*** *Cumulative magnitude-frequency distribution for each corresponding Erosive Episodes (EP), where the percentages of cumulative rockfall frequency were calculated with respect to the total number of rockfalls (8,367 failures) detected between 2017 and 2019.* ***c)*** *Negative power law scaling using the frequency density, calculated for periods of Gradual Erosion (GE) from I to IX (Time-series of Figure 3.9).* ***d)*** *Cumulative magnitude-frequency distribution of each GE, where the percentages of cumulative rockfall frequency were calculated with respect to the total number of rockfalls (8,367 failures). For comparative analysis, the general negative power low scaling representing all the dataset from 2017 to 2019 is overlapped in figures a) and c) using dashed dark-green trendlines.*

During periods of higher retreat rates, the cumulative rockfall frequencies fluctuated between 0.4% (EP4) and up to 4.2% (EP2) of the total number of rockfalls, averaging ~ 1.3% and totalling ~ 13% of the total rockfall numbers detected between 2017 and 2019. However, high variability is observed between the cumulative magnitude frequency data characterizing each erosive episode. For example, while the EP3 and EP18 showed lower frequencies (~ 0.9 and 0.5% of the total rockfall numbers, respectively), they are characterized by the highest volumetric flux loss of ~ 22.9 m^3, equating to the highest short-term retreat rates of ~ 305 mm y^{-1} (Figure 3.9) and thus, one of the lowest negative power laws during the entire period of monitoring (β = -1.31 and -1.18, respectively). Conversely, during EP2 and EP13 a higher cumulative rockfall yield is observed (~ 4.2% and 2.3% of the total number of rockfalls, respectively) alongside a lower volumetric flux loss, which is also reflected by one of the highest negative power laws (β = -1.62 and -1.68, respectively), but lower retreat rates of ~ 185 mm y^{-1} (EP2) and ~ 76.5 mm y^{-1} (EP13), respectively. Therefore, the cumulative magnitude-frequencies demonstrate here the relative rockfall size distribution and variability levels that dominates during erosive episodes inducing abrupt temporal changes in the erosion (Figure 3.10b).

Figure 3.10c illustrates the frequency density and associated negative power law modelled for the principal periods of background or gradual erosion (GE), which are shown as cliff retreat time-series in Figure 3.9 (Periods I – IX). The negative power low exponents describing periods of relative slope stability and low cliff retreat rates ranged between β = -1.72 and -3.35, with an average of β = -2.14. As such, these exponents reflects periods in which a general decrease in the rate of erosion is detected. As it may be expected, due to the dominance of iterative small magnitude rockfalls, the majority of these exponents are higher than the exponent characterizing the magnitude-frequency data of the whole observation period (β = -1.85), as well as being higher than the exponents reflecting the rate of erosion measured for abrupt erosive episodes (EP), and hence, numerically describing some form of steady background erosion in the retreat rates for the relative quiescence periods I to IX.

Figure 3.10c also shows that roll-up distribution is again detected at this level (5-day bins) of temporal resolution. For small magnitudes, the upper erosional threshold is found at ~ 1×10^5 m^{-3} of frequency density, which is the same threshold level detected for the entire monitored period (Figure 3.3a, Section 3.3). Interestingly, a heavy tail is detected for larger magnitudes occurring within periods of gradual erosion (between ~ 1×10^{-1} and around ~ 1×10^0 m^3), however, a change in the lower erosional threshold is observed below ~ 1×10^2 m^{-3} frequency density, which may be explained by occurrence of lower magnitude events controlling the tail of

the modelled power law (for the whole dataset, this threshold begins bellow ~ 1×10^{0} m^{-3}, Figure 3.3a in Section 3.3).

Figure 3.10d shows the cumulative magnitude-frequency distributions for each period of gradual erosion. During periods of relative quiescence, the cumulative rockfall frequencies fluctuated between 1.4% (GE-VI) and up to 24.5% (GE-VIII) of the total number of rockfalls, averaging ~ 9.7% and totalling ~ 87% of the total rockfall numbers detected during the whole monitored period (8,367 rockfalls). Furthermore, this metric demonstrates that during periods of background erosion, the plateau in the maximum cumulative rockfall frequencies differ as a function of the duration of the period of relative quiescence. To exemplify, GE-IV and GE-VIII reached a plateau in their cumulative frequencies over the ~ 18 and 24% of the total number of rockfalls, however they were associated with the largest periods of relative slope stability of 254 and 264 days, respectively (Figure 3.9). Conversely, steady periods with the shortest duration, such as GE-III and GE-VI generated the lowest cumulative total number of rockfall (~ 3.7 and 1.4%, respectively). As such, the rockfall yield and the cumulative volumetric flux loss of periods of gradual evolution tended to scale with the duration of such geomorphic period of erosion.

In summary, it is demonstrated that longer periods of quiescence after large rockfall events (periods II, IV, V, VI, VII and VIII), were characterized by steady background erosion, numerically reflected by lower average rates of material loss (~ 2.5 – 4.6 mm y^{-1}) as well as by higher magnitude-frequency scaling coefficients (β = -1.96 to -3.35) due to the dominance of iterative small magnitude rockfalls during these periods. Also, shorter periods of relative slope stability occurring between large rockfalls (periods III and IX) showed an increase in the average rate of erosion with a higher rate of material loss (~ 7.3 – 9.3 mm y^{-1}) and the lower power law scaling coefficients (β = -1.72 and -1.91) which approach the overall character of the whole time-series (~ 11 mm y^{-1}, β = -1.85). However, regardless of the duration and erosive mode, these metrics numerically reflect a return to a steady baseline behaviour of the erosion after the occurrence of large rockfalls. Conversely, erosive episodes driven by sudden erosive jumps, inducing the highest retreat rates measured in 5-days (~ 76.5 – 305 mm y^{-1}), are characterized by lower negative power law scaling coefficients (β = -1.18 to 1.68) as they reflect the dominance of smaller numbers and larger individual rockfalls. At this temporal resolution, roll-up features are again detected for the smallest failures size and a heavy tail for the largest, suggesting a higher number of both the smallest and largest rockfalls than would not be predicted by a simple power law alone, and importantly that differs from behaviour that has been observed by other researcher elsewhere (Table 3.4). In the next section, a geomorphic assessment is undertaken based on the analysis of temporal changes in the actual rockfall yield and mean rockall volumes.

3.6 Evolution of the rockfall frequencies and mean rockfall volumes

The investigation of the rockfall activity using binned frequencies of failure events, representing different sections of the North Yorkshire coast, has been proven to be a consistent metric, where systematic variations in the rockfall yield and erosion rate have been demonstrated across contiguous sections of the coastline (Benjamin et al., 2020). In this research, the assessment of the rockfall activity using binned frequencies, measured as the total number of rockfall events detected into each 5-day interval, is used here to examine changes in the rockfall frequency over the time-series. 5-day intervals have been selected as for this large dataset, this allowed an easier examination of the emergent patterns when compared to for example, shorter windows of time (e.g., 1 day). Also, the mean rockfall volume, measured as the total rockfall volume divided by the total number of rockfall events occurring in each interval (m^3 per interval), represents an erosive metric used here to examine the mean volume yield per interval of time (Figure 3.11).

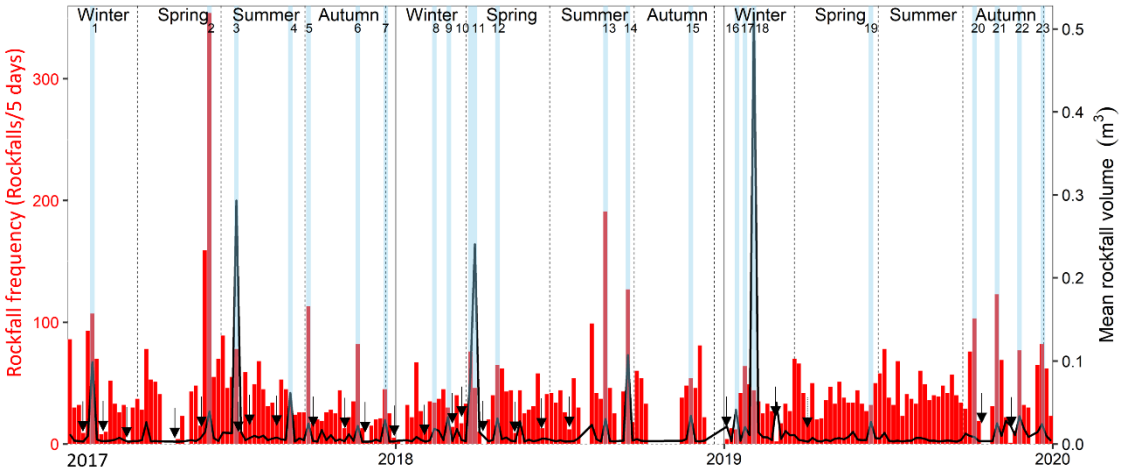

Figure 3. 11*: Time-series of the 4D evolution of the rockfall frequency and mean rockfall volume (m^3 per rockfalls). Periods with low rockfall activity are indicted with black arrows (Below 22 rockfalls per 5-day window). Boundaries between astronomical seasons are shown using dashed vertical lines. From the top to the bottom, the main episodes of erosion, defined by abrupt changes in the erosion, that corresponded with same-day rainfall or up to two days of precedent rainfall are shown as vertical blue bars and numbered according to occurrence of the erosive episode from 1 to 23.*

During the monitored period, rockfall frequencies were highly variable, ranging from a minimum of one single event captured in 5-day windows, which demonstrates the occurrence of periods characterized by marked cliff stability (~ 0 mm y^{-1} of annual retreat rate, see Figure 3.9), up to 354 events occurring in spring 2017 (driving ~ 185 mm y^{-1} of annual retreat rate, see Figure 3.9), reassuring the existence of periods of high cliff instability and rapid erosive evolution.

Across the whole time series and given the LoD of 0.10 m, the average of the rockfall occurrence was 43 events and the mode was 33 events, and for each year, peaks of activity were detected in spring for the 2017 (354 events), summer of 2018 (191 events) or autumn of 2019 (123 events).

The distribution of the rockfall frequencies across the time-series indicates that there were intervals of time with a notable increase in the production of rockfalls. In fact, most of the significant changes in rockfall activity, defined here as intervals in which the number of events exceeded double the average number of events occurring across the whole monitored period (> 86 events per interval, where an interval is a 5-day period), occurred within the principal erosive episodes including: (1), (2), (3), (5), (6), (7), (13), (14), (20), (21), (22) and (23) (see Figure 3.11). Significantly, these patterns of increased activity occurred in periods within different seasons, and interestingly not just in winter or autumn, which are commonly at least anecdotally associated with more erosive conditions. To exemplify, in winter 2017, the peak rockfall frequency reached 107 rockfalls in January, coincident with the first erosive episode (1) of the time-series of ~ 10.5 m^3. Then, in spring 2017 the highest peak of the rockfall frequency of the whole monitored period was detected, reaching 354 failures in June, driving the rainy-related episode (2) with a total rockfall volume of ~ 13.9 m^2, and a mean volume of ~ 0.04 m^3. In autumn of the same year, the peak rockfall activity reached 113 failures towards the end of August (Episode 5), alongside with a low mean rockfall volume (0.01 m^3). In summer 2018, it was found the second higher rockfall frequency of the whole time-series, reaching 191 failures in August (Episode 13) while the mean rockfall volume was low (0.03 m^3). In 2019, the annual peak rockfall yield was detected in autumn (October), reaching 123 failures and a low mean rockfall volume of 0.02 m^3 was observed (Episode 21).

Conversely, there were intervals of time where a reduced rate of erosion is observed, due to notable decreases in rockfall activity. Significantly, the majority of periods with significant drops in the rockfall yield, defined here as 5-day periods in which the number of events drops 50% below the average rockfall occurrence of the whole time series (> 22 events per interval), occurred not only in the warmer seasons of spring and summer, but also were common in winter and autumn. Also, periods with notably reductions in the erosion commonly occurred before and after the occurrence of periods with higher rockfall activity, which is distinctive pattern that can be seen during most of the seasons of the monitored period. For instance, in winter 2017, a drop in rockfall activity was observed 10-15 days before and after the main winter peak (> 10 rockfalls). In spring, periods with a critically low rockfall activity were also observed (> 4 rockfalls). In summer, the 5-day windows after the erosive episode (3) showed the lowest rockfall frequency of the summer (10 rockfalls), while in autumn 2017, the interval with the lowest annual

rockfall activity was observed towards the end of November, with only two detected rockfalls. Moreover, in winter 2018, minimum rockfall activity occurred in the first week of January (2 rockfalls), while in summer, the lowest rockfall activity was observed in mid-July, where 12 rockfalls were detected. The lowest rockfall yield of the whole time series occurred in November 2019 (one single failure detected within five days). As a result, 26 out of a total of 196 intervals (~ 13%) were associated with critical reductions of the erosion rate, representing periods with apparent higher slope stability. These are shown with black arrows in Figure 3.11.

The overlap between rockfall frequencies and mean rockfall volumes per 5-day periods indicates that the annual peaks of mean rockfall volumes did not match with annual peaks of rockfall activity. For example, in 2017, the peak rockfall frequency and the peak mean rockfall volume differed in time since the peak rockfall frequency showed 354 rockfalls alongside with a low mean rockfall volume (0.04 m^3 per event), defining the erosive episode (2). Instead, the peak mean volume of the 2017 was the second higher of the whole time-series, reaching 0.3 m^3 (July) in the erosive episode (3). Similarly, in 2018, the peak of the mean rockfall volume was detected in winter (Episode 11) with 0.24 m^3 of mean volume loss, while the peak rockfall frequency occurred in summer (Episode 13). The highest mean rockfall volume of the whole time-series occurred in winter 2019, reaching a peak of 0.52 m^3, while the rockfall frequency reached 44 rockfalls (Episode 18) and the annual peak of rockfall activity occurred during the episode (23). Nevertheless, although less frequent, temporal coincidences between both metrics were detected at the seasonal scale, for instance, during the erosive episodes (1), (2) and (22). As a result, the highest annual values of mean rockfall volumes occurring in intervals where the overall rockfall activity was lower suggests the occurrence of periods in which the erosion tended to be dominated by larger rockfalls, as demonstrated by the magnitude-frequency data.

In summary, the analysis of the rockfall frequencies suggests the existence of five distinctive patterns that combined define erosion by rockfall of the rock face: First, there were periods with increased erosion due to higher rockfall activity, mostly coincident with the main erosive episodes that generated erosive jumps; Second, there were intervals with increased rockfall yield, sometimes driving apparent annual peaks, that were importantly not only restricted to winter and autumn; Third, there were periods with remarkably reduced rockfall yield (> 22 events per 5-day window), indicating a relative degree of slope stability, although these periods were the less frequent over the monitored period (~ 13% of occurrence); Fourth, the reduction in erosion tended to be observed in seasons associated with harsh environmental conditions, such as in autumn and winter, which could suggest the cliff face reaches a condition of exhaustion of available / suitably unstable material to generate rockfall in this period. Fifth, the reduction in erosion, occurred before and after the occurrence of intervals with higher rockfall frequency,

indicating that there was a steady background rates of uniformly but spatially randomly distributed smaller rockfall events, reinforcing the emergent pattern observed in Section 3.4, where an apparent post-relaxation time of ongoing or gradual erosion was detected.

3.7 Annual and seasonal comparison of the rockfall activity and the cliff erosion

Monitoring rockfall activity may be subject to multiple superimposed influences, including the effect of the seasons (Paluš et al., 2004), where it has been suggested that seasonal and diurnal patterns of rockfall yield may closely reflect climatic controls, depending on the slope aspect and the physical characteristics of the cliff face (Luckman, 1976). For the East Cliff of Whitby, Rosser et al., (2007) demonstrated over monthly intervals of change detections a limited seasonal control upon the occurrence of rockfalls, with events $\geq$ 1.0 m^3 (here, named as large rockfalls) occurring in all months of the year. Therefore, to fully explore emergent patterns from the obtained 4D rockfall inventory, a seasonal assessment of the dynamic of the erosion using, for the first time, a unique multi-annual dataset at 1 h change detection measurements is undertaken in this section.

4D comparative time-series of the annual and seasonal behaviour of the total and cumulative rockfall volume using 5-day intervals, coupled with the average retreat rate for the 2017, 2018 and 2019 are shown in Figure 3.12a. In addition, the analysis is complemented with a seasonal summary of the total number of rockfall events and total seasonal volume loss (Table 3.5). Such us in previous time-series, during the monitored period, astronomical seasons punctuated by the solar radiation received between equinoxes and solstices are used, ranging between 21st December to 19th March for winter, 20th March to 20th June for spring, 21st June to 21st September for summer, and 22nd September to 20th December for autumn.

The year showing the highest erosive activity was 2017 as it showed the steepest average rate of material loss (13.4 mm y^{-1}), which was in response of a total cumulative rockfall volume of 73 $\pm$ 30 m^3 driven by the occurrence of three principal abrupt erosive jumps that ranged between ~ 10.5 and 22.9 m^3 of total rockfall volume (Episodes 1, 2 and 3), followed by three periods of steady erosion, and an average total rockfall volume of ~1.0 m^3. By contrast, the erosive work done by the erosion was lower during 2019, equivalent to a lower average rate of material loss (9.4 mm y^{-1}), driven by a total cumulative rockfall volume of ~ 51.2 $\pm$ 20 m^3 and the occurrence of only one principal abrupt rise in the erosion of ~ 22.8 m^3 taking place in winter (Episode 18), alongside an average rockfall volume of ~ 0.7 m^3 during this period. When compared with 2019, 2018 showed a similar total cumulative rockfall volume of ~ 54 $\pm$ 21 m^3,

however, the average rate of erosion was steeper (10.3 mm y^{-1}), suggesting higher geomorphic activity as time-series, which was ultimately driven by three main erosive jumps that ranged between ~ 6.1 and 13.6 m^3 (Episodes 10, 11 and 14), three subsequent periods of gradual erosion and an average total rockfall volume of ~ 0.9 m^3 (Figure 3.12a). As a result, using near constant 1 h change detection across three years of monitoring, it is shown that the rates of material loss were characterized, as it may be expected, by variability at the annual scale, however, it is demonstrated that the recurrence and magnitude of the erosive jumps and the length of subsequent periods of relative slope stability were key processes controlling the steepness of the erosive behaviour at annual basis.

Using the total and cumulative rockfall volumes, comparative time-series of the annual retreat rate (mm y^{-1}) and net cumulative retreat (mm) were calculated for each season over five-day periods (pentads) of total volume loss (mm y^{1}). The average retreat rate throughout seasons, expressed in mm y^{-1}, was also quantified (Figure 3.12b). Here, the average rate of erosion calculated per season included the volume of the large rockall events composing the erosive episodes (1) to (23) occurring in particular seasons. Therefore, in this section, the average retreat rates were used to compare the overall rates of material loss at seasonal scale. During 2017, the annual retreat rate fluctuated between ~ 0 and 305 mm y^{-1} for pentads, averaging 13.4 mm y^{-1} of cliff retreat when considering the period of time between the start and the end of the time series (general trend line, Figure 3.12a), while the net cumulative frontal retreat ended in 13.4 mm. By contrast, during 2018 it was observed lower range of retreat rates, ranging from ~ 0 and 182 mm y^{-1}, however the average retreat rate was 10.3 mm y^{-1} (general trend, Figure 3.12a), while the cumulative retreat ended in 9.9 mm by the end of the time-series. 2019 showed the same range of fluctuations in the retreat rate than 2017 (~ 0 and 305 mm y^{-1}) but lower average retreat rate if compared with 2017 and 2018 (9.4 mm y^{-1}), nevertheless the net cumulative retreat was about 9.4 mm, which was of similar magnitude than the cumulative retreat observed by the end of 2018 (Figure 3.12b).

Erosion was, as it may be expected, the highest during winter 2017 and 2019, where steep average rates of material loss were detected (12.6 and 27.3 mm y^{-1}, respectively), equating ~ 14.0 and 30.2 m^3 of total volume loss by the end of the season, respectively (see Table 3.5). Although winter 2018 showed a lower average rate of erosion as it approaches the gradient of a typical period of gradual erosion (3.6 mm y^{-1}), two sharp erosive jumps were observed just 10 days after winter 2018. Slower average rates of material loss were observed in spring 2017, 2018 and 2019 (3.9 to 16.4 mm y^{-1}), equating between ~ 5.5 m^3 and up to 23 m^3 of total volume loss (Table 3.5). Notably, faster average rates of material loss were detected in summer 2017 and 2018 (17.0 and

22.1 mm y^{-1}, respectively), equating a total volumetric loss of ~ 24 and 31 m^3 (Table 3.5), and so, exceeding the average annual rates of activity (10.3 and 13.4 mm y^{-1}). Then, lower average rates of material loss were detected in autumn 2017, 2018 and 2019 (2.5 to 7.7 mm y^{-1}), approaching those observed for periods of relative slope stability (Section 3.5).

As a result, the comparative analysis of the rates of erosion at seasonal scale reveals two distinct erosive behaviours: First, highest average rates of material loss occurring in winter and at the same time in spring and summer, especially during 2017 and 2018, where autumn represents a transitional season with intermediate levels of rates of erosion; Second, a 'typical' year was observed in 2019, since the highest average rates of material loss were detected exclusively in winter (27.3 mm y^{-1}), followed by notably lower rates of material loss during spring and summer (3.2 to 3.9 mm y^{-1}), and then higher activity towards autumn as a transitional season to winter (7.7 mm y^{-1}). The marked difference between years however raises questions about what an average and normal erosive behaviour is, based upon these data.

The comparative 4D time-series of the rockfall frequencies, indicative of the seasonal yield from rockfall events, tended to be highly variable, without distinctive temporal or systematic clustering on the production of rockfalls or peaks of rockfall frequencies concentrated, repetitively, in specific seasons. For instance, the peaks of rockfall frequency were observed in spring and summer for 2017 and 2018 (354 and 191 rockfalls, respectively), while for 2019 the highest production of rockfalls occurred in autumn, with 123 registered failures (Figure 3.12c). By examining cumulative rockfall frequencies, it was observed that seasonal repetition of plateaus of the rockfall activity, indicative of seasons with steady production of rockfalls, were rarely observed, and when this does happen, they were associated to weekly-scale data gaps (Section 3.2) rather than due to a decrease in the actual production of rockfalls (e.g., in October 2018) (Figure 3.12d). However, although the time-series of rockfall frequencies and cumulative frequencies do not show distinctive patterns across seasonal scales, by examining the seasonal summary of the total number of rockfall events and total seasonal volume loss (Table 3.5), it is noted that the warmer seasons of spring and summer, supplied the higher total number of rockfalls. Over 2,400 rockfalls occurred in spring, reaching a maximum in summer, where over 2,500 rockfalls were captured during the whole monitored period. By contrast, colder seasons show a lower and relatively similar number of total rockfalls, where over 1,600 failures occurred in both autumn and winter. This is perhaps surprising given the perception that erosion is higher during seasons where the environmental conditions are more aggressive, such as winter.

Overall, the comparative analysis of the 4D time-series of the annual and seasonal behaviour of the total and cumulative rockfall volumes suggest that the abrupt erosive jumps of

high volumetric magnitude were not only occurring, as it may be expected, in the coldest and rainiest season of winter (e.g., 2017 and 2019) or immediately after winter (e.g., 2018), but also were frequent in the warmest season of summer, particularly after summer rainfall events (e.g., 2017 and 2018). While the erosive jumps were also present in spring, autumn was the only season with a total absence of abrupt erosion events during the period monitored. Furthermore, average rates of erosion tended to be steeper during winter and, remarkably in spring and summer, but more gradual in autumn, which may suggest a variable degree of seasonal controls on the occurrence of large rockfalls. Indeed, the total seasonal volume loss reveals that summer was the season driving the highest cliff erosion, reaching ~ 59.5 m^3 of volume loss. Winter and spring supplied the second higher volumetric contributions as a total seasonal volume loss of ~ 48.2 and 48.5 m^3 was observed, respectively. By contrast, autumn was the season driving the lowest cliff erosion, supplying a total seasonal volume loss of 22 m^3 (Table 3.5).

On the other hand, the seasonal summary of the total number of rockfalls and total seasonal volume loss (Table 3.5) indicates that spring and summer were key in the overall production of rockfalls, especially for very small (0.001 – 0.01 m^3) and small-medium magnitudes (0.01 – 0.1 m^3). Significantly, this also suggests the role that other environmental and geological processes, such as the temperatures or nucleation of microfractures may play in the failure development (see Chapter 6, Section 6.3 of Discussions). As a result, a marked signature of higher erosion rates occurring in winters, springs and summers was detected, depending on the year of observation. Consequently, using multi-annual and 1 hour change detections, no clear seasonal control upon the occurrence of rockfalls was observed, which agree with the observations made by Rosser et al., (2007). The results presented in this section rise new questions about what an expected seasonal erosive behaviour is, especially in the context of global climate change, and highlight the importance of the quantification of the total volume loss using non-hourly change detections, calculated across gaps of laser scanner data generated by inclement weather (see Chapter 6, Section 6.5 of Discussions).

Table 3. 5*: Seasonal comparison of the number of rockfall events and volumetric loss for each monitored year.*

Season	Events 2017	Vol. (m^3) 2017	Events 2018	Vol. (m^3) 2018	Events 2019	Vol. (m^3) 2019	Total events	Total Vol. (m^3)
Winter	650	14	414	4	594	30.2	1,658	48.2
Spring	1,059	20	688	23	745	5.5	2,492	48.5
Summer	810	31	870	24	853	4.5	2,533	59.5
Autumn	560	8	436	3	688	11	1,684	22

Total	3,079	73	2,408	54	2,880	51	8,367	178.2

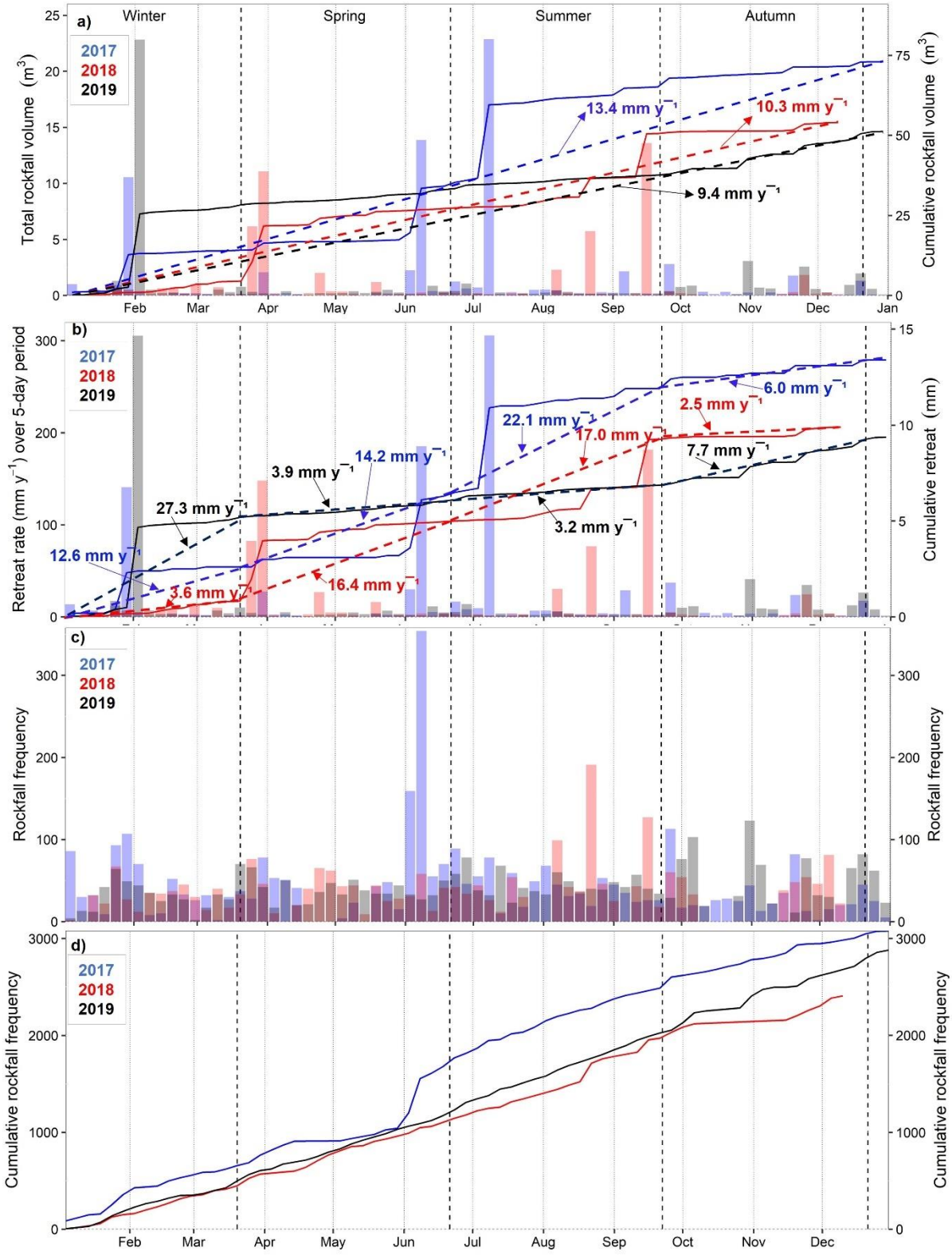

Figure 3. 12: *Overleaf. Annual and seasonal comparison of the hourly rockfall activity and cliff erosion.* ***(a)*** *Comparison of the total and cumulative rockfall volume (m^3). Blue, red and black dashed lines show the average retreat rate for the 2017, 2018 and 2019, respectively.* ***(b)*** *Comparison of the annual retreat rates (mm y^{-1}) calculated over five-day period, and cumulative retreat (mm). Blue, red and black dashed lines show the average retreat calculated for each season for the 2017, 2018 and 2019, respectively.* ***(c)*** *Comparison of the rockfall frequencies for each year.* ***(d)*** *Annual comparison of the cumulative rockfall frequency. As in Figures 3.6, 3.9 and 3.11, all the time-series data have been binned using 5-day intervals. For each year, the boundaries between months are shown using continuous gray vertical lines. Boundaries between astronomical seasons are shown using dashed vertical lines.*

3.8 Summary

Using a unique, extensive high resolution 4D dataset based on 1 h change detection measurements of 3D rock-slope monitoring, in this chapter it has been explored the nature and timing of rockfall activity and rates of cliff erosion during three years of monitoring, and so, at a multi-annual and hourly length of observation never examined before (Thesis Objective 2 – O2). As such, based on a total of 14,741 fully automatic 3D change detection measurements and 0.10 m of Level of Detection, over 8,300 rockfalls were detected across the subaerial section of the East Cliff of Whitby, equating a total volume loss of ~ 178 ± 71 m^3 and ~ 0.03 m of overall cliff retreat over a 3-year time period. The resulting 4D rockfall inventory was used to demonstrate that:

1) In this setting, the erosive behaviour, in terms of how the cliff face has been evolved in time, has been controlled by an assemblage of large rockall events (≥ 1.0 m^3), driving erosive jumps or abrupt changes in the volume loss (here, defined as erosive episodes) between periods of gradual erosion or steady baseline of activity. A total of 23 erosive episodes were detected, six of them punctuating the beginning and end of a total of nine marked principal periods of gradual erosion (Periods I – IX), representing distinct periods of time of relative quiescence in the erosional dynamic, where the erosion tended to be dominated by background and iterative small rockfalls (0.001-0.01 m^3).

2) Using one hour frequency change detections, periods of post-failure quiescence tend to scale in duration with the preceding volumetric rockfall magnitude. To exemplify,

the two highest magnitude rockfall events, of ~ 22 ± 4 and 18 ± 4 m^3 (erosive episodes 18 and 3, respectively), were followed by the longest periods of gradual erosion of 254 and 264 days (stability periods IV and VIII, respectively). When these periods were then compared with the ones that followed large rockfall events of lower magnitude of ~ 7 ± 2 and 12 ± 3 and m^3 (erosive episodes 1 and 14, respectively), it was detected that they were followed by shorter periods of quiescence of 124 and 139 days (periods VII and II, respectively), which is about 50% of the quiescence periods that followed the erosive episodes 18 and 3. Indeed, using the maximum likelihood estimation, the estimated return period for the erosional episodes 3 and 18 was nearly two years with ~ 80% exceedance probability, while for the erosional episodes 1 and 14 is about one year with ~ 95% probability.

3) From the point of view of landform development and landscape sensitivity, this apparent signature of rockfall magnitude-temporal scaling of quiescence suggest that a failure magnitude and post-relaxation time associated with the preceding geomorphic event may exist in some instances. This erosional signature may be the result of long-term accumulation of rock damage inducing final failure (Rosser et al., 2007), so that, after the occurrence of erosional episodes of large magnitude, the cliff face may reach a condition of exhaustion of the available / suitably prone-to-fail unstable material to generate rockfalls.

4) While the modelled magnitude-frequency distributions for the whole monitored period showed a negative power law scaling parameter of β = -1.85, the erosive episodes were characterized by a lower scaling exponent fluctuating between β = -1.18 and -1.68 (averaging β = -1.48), demonstrating a higher erosive contribution controlled by higher magnitude rockall events. Conversely, the rate of erosional activity that characterizes the principal periods of gradual or steady erosion were characterized by higher scaling exponents, ranging from β = -1.72 to -3.35 (averaging β = -2.14), indicating that the overall level of activity has been mainly supplied by iterative small rockfalls.

5) While the scaling exponents associated with the erosive episodes numerically describe the relative size distributions that operated during erosive jumps in time, these group of scaling parameters (β = -1.18 to -1.68) may also reflect the effectiveness of the work done by short term forcing and/or some form of geomorphic episodicity if temporal discontinuity is inherent in the forcing process, such as sudden and energetic weather, efficiently acting on wider joint shear surfaces.

6) The scaling exponents associated with periods of gradual erosion (β = -1.72 to -3.35) represent key numerical indicators of relative size distribution of events that operates during periods of steady baseline activity or background erosion dominated by small rockfalls. However, these exponents also describe the relative effectiveness of rockfalls controlled by processes inducing small fragmentation of rock-masses, such us, iterative destabilization and/or rock weakening due to progressive physical weathering, efficiently acting on low spacing beds or highly prone-to-fail fractured rock-blocks.

7) From a direct or empirical monitoring approach, it has been shown that the erosional contribution of iterative small rockfall size (0.001 – 0.01 m^3) supplied the ~ 88% of the total number of rockfall numbers, however, this event size supplied only the ca 14.1 % of the total volume observed. Using magnitude-frequency distributions, these size of rockfalls were characterized by marked roll-up distribution, where the upper erosional threshold, punctuating the beginning of a roll-up deviation above the modelled power laws, was found over ~ 1×10^5 m^{-3} of frequency density.

8) Conversely, erosive episodes in which the maximum rockfall event was $\geq$ 1.0 m^3, supplied 50.8% of the total volume observed via a total of 17 individual events, equating 0.2% of the total number of rockfall numbers. Marked heavy-tail distribution has also been detected for this size of rockfalls, where the erosional threshold of occurrence was found bellow 1×10^0 m^{-3} of frequency density. Small to medium to large range rockfalls (0.01 to 1.0 m^3) tended to adhere well to the modelled power laws, together supplying ~ 35.1% of the total volume observed via 10.2% of the total number of rockfalls.

9) For discontinuity controlled rock-slope settings, the finding 7) and 8) may hold some implications regarding the relative importance of magnitude and frequency of geomorphic events, where it has been suggested that a large portion of the erosive contribution over some landforms is supplied by relatively frequent events of moderate magnitude, and that it cannot be assumed that large size, less common events are the most significant (Wolman and Miller, 1959). However, the need of more examples was stated by these authors. As such, using a suitable, unique long 4D dataset of events, this chapter provided an example to demonstrate that via 17 large rockfalls it was supplied around half (50.8%) of the total volume loss, while the medium magnitude size of rockfalls supplied around one third (~ 35.1%) of the total

volume loss. Therefore, in this setting and during the examined monitored period, it is demonstrated that although medium size rockfalls in fact contributed to a large proportion of the work done by the erosion, the highest (volumetric) effectiveness was supplied by large rockfall sizes of lowest frequency of occurrence.

10) Notably, the seasonal analysis of the rockall activity suggests that large rockfall events driving erosive jumps of higher volumetric magnitude are not only prone to occur, as it could be expected, in the coldest and rainiest seasons of winter (e.g., 2017 and 2019) or just after winter (e.g., 2018), but they are also likely to occur in the warmest season of summer, particularly after summer storms (such as in 2017 and 2018). As such, given the context of global climate change, where extreme storms may be more frequent, these results may not only hold crucial implications in terms of potential increases in the rates of cliff erosion during winters and summers, but also in terms of the future surface hazard and risk mitigation on coastal rock-slopes.

The results shown in this chapter demonstrate that hourly-resolution fixed laser scanning monitoring coupled with a suitable computational routine of automatization to process historical archives of 3D point clouds provides a robust tool to examine the rockfall activity and the accumulated patterns of erosion over multi annual-scales of analysis. As such, this research has not only upscaled previous works undertaken rock-slope monitoring over the North Yorkshire coast, but also by providing the longest, hourly resolution erosive analysis of rockfall activity examined, to date. In the next chapters of results (*Chapters 4 and 5*), an analysis of the cliff surface temperatures is undertaken using a unique thermal imagery dataset collected from a one-year of constant infrared thermography monitoring. This thermal dataset is then used in *Chapter 6* to improve understanding into temperature controls on rockfall activity and cliff erosion.

Chapter 4 – Evaluating cliff surface temperature using high-frequency infrared thermography

4.1 Introduction

In chapter 3, a multi-annual and high-resolution rockfall dataset was used to examine the timing and nature of rockfall that drive cliff erosion (Thesis Objective 2 – O2). In this chapter, and as a means to try to better understand the controls on rockfall, a high-frequency Infrared Thermography (IRT) monitoring approach is developed and analysed (Thesis Objective 3 – O3). The monitoring is intended to describe the timing and nature of the rock face thermal dynamics at East Cliff in Whitby between 1st January and 31st December 2021. Thermal imagery was collected, archived and analysed at 1 h frequency using a bespoke automatic data acquisition system. This interval allows near-continuous monitoring and capture of both absolute temperatures and rates of change in temperature across nearly 2,830 m^2 of coastal rockface, and is collected in parallel to a 3D laser scan data that are combined in *Chapter 6*. This chapter represents the first observations of temperatures over the surface of a rock-slope system with both long-duration (1 year) and high-frequency (1 hour) monitoring. The dataset is needed to progress understanding of rock slope failure, including: (1) The ability to capture the absolute temperatures through by hour, day, month and season; (2) To accurately quantify and assess the rates of change in temperature; (3) To provide data to underpin modelling of the thermomechanical behaviour of cliff faces; and (4) To understand links between temperature and rockfall.

To accomplish Objective 3 of this thesis (O3), this chapter presents the method for the collection of continuous thermal imagery at East Cliff in Whitby. The present chapter includes the description of the thermographic system used for monitoring (Section 4.2.1), its field deployment and monitoring set-up (Section 4.2.2), rates of data acquisition (4.2.3), and how the dataset was handled (Section 4.2.4). Then, the methodology to undertake temperature corrections is presented considering the site-specific conditions (Section 4.2.5). Then, an initial analysis of the surface temperature is presented, as a verification of the quality of the data collected and the degree to which this dataset reflects the nature of the cliff surface under inspection (Section 4.3). This chapter ends with a summary of the developed approach and main findings (Section 4.4).

4.2 Constant IRT monitoring of the cliff face

4.2.1 Instrument description

The instrument employed was a remotely controlled full-frame thermal camera (VarioCAM HDx head 675), which is an optical measurement system that operates in the Long-Wave Infrared spectral range (LWIR) of 7.5 to 14 μm, which is specifically designed for precise and contactless measurement of surface temperatures (Figure 4.1a). The camera was equipped with an uncooled microbolometer FPA detector (Focal Plane Array) with a resolution of 640 × 480 IR pixels and pixel pitch of 17 μm (see Table 4.1 for further technical specifications). The lens of the thermal camera collects the IR radiation in the field of view emitted by the measured object and reproduces this radiation on the microbolometer detector array, from which the electrical signal of the detector array is processed. The electronics comprises all functions required for the thermal camera calibration and operation, such as actuation of the microbolometer array, A/D conversion, offset and gain correction and pixel correction (InraTec GmbH, 2017). Also, the back of the thermal camera was equipped with connections for power and ethernet, making the instrument suitable for continuous thermography.

The camera was equipped with a 60 mm prime (fixed length) lens, F/1.0, providing a minimum focus distance of 1.5 m, field of view (FOV) of 10.4 × 7.8° and an instantaneous field of view (IFOV) of 0.28 mrad (milliradians), which defined, respectively, the horizontal and vertical size of the thermal scenes and the subsequent image resolution. These characteristics, alongside with an average distance between the location of the instrument and the cliff face (~ 430 m) provided an average IR spatial resolution of ~ 10 cm/pixel across a rock-slope section of ~ 64 m width (along cost) and 48 m in height at ± 2°C accuracy. Critically this area falls within that monitored by the fixed laser scanner and is commensurate in terms of average spatial resolution of the scanner (~ 10 cm), permitting the later combination of these datasets.

Table 4. 1: *Key technical data of the thermography system VarioCAM HDx head.*

IR spectral range	Measurement range (thermal)	Measurement accuracy	Operation range	Maximum image frequency	Field of view (Hor./Vert.)	Thermal sensitivity
7.5 to 14.0 μm	-40 to 600°C	± 2.0°C	-25 to 55°C	60 Hz	10.4° × 7.8°	40 mK

Source: InfraTec GmbH, 2017.

4.2.2 Field deployment and monitoring setup

The thermal camera was installed together with the laser scanner inside the former lantern room at the top of the eastern lighthouse of Whitby Harbour (Section 2.2.2, Chapter 2), and has been continuously collecting data since 1st of January 2021, after initial installation in December 2020. Both instruments were collocated, to allow a parallel monitoring of rockfall and surface thermal character, permitting the later combination of the rockfall inventories and contemporaneous IRT data in order to get insight into temperature controls on rockfall occurrence (Thesis Objective – O5). This set up also removed the need for additional power and network access provision (Section 2.2.2, Chapter 2), and the optical centre of both instruments is approximately identical (offsets are minimal at < 20 cm) aiding their spatial and temporal overlay.

The system for monitoring was custom designed at Durham University. The thermal camera was mounted in a metal framework above the laser scanner, with both instruments facing the cliff face (Figure 4.1b). As the thermal camera needs a suitable thermal window to allow IR radiation to pass with minimal interference, a mount cut to ~ 31° to allow the camera to point directly at the cliff face was installed (Figures 4.1b and 4.1f). Next to the thermal camera, a controls PC running IRBIS 3.1 Professional (InfraTec GmbH Ltd) was used to remotely control the camera, monitor its performance and to archive the data (Figure 4.1c).

The glass in the thermal window was made of Germanium as it offers the highest IR transmission across the 3 – 14 μm spectral range, and is commonly used as the front optic in thermal imaging cameras working in across 7.5 to 14 μm, such here (Knight Optical Ltd., 2015). The window had an anti-reflective coating to optimize the performance (Figure 4.1d). The camera was bolted in position and was sealed to the window glass with an "o" ring gasket to provide protection from external and inclement weather (Figure 4.1e).

The monitoring equipment is continuously mains powered meaning there were no power interruptions. The data acquired by the thermal camera was transferred to the PC, from which the rate of data acquisition and the quality of the thermal scenes was monitored in real time. A Wi-Fi access point and modem installed at the Whitby Yacht Club, was used to transfer data to cloud storage, from which it was downloaded to Durham University servers (Figure 4.2).

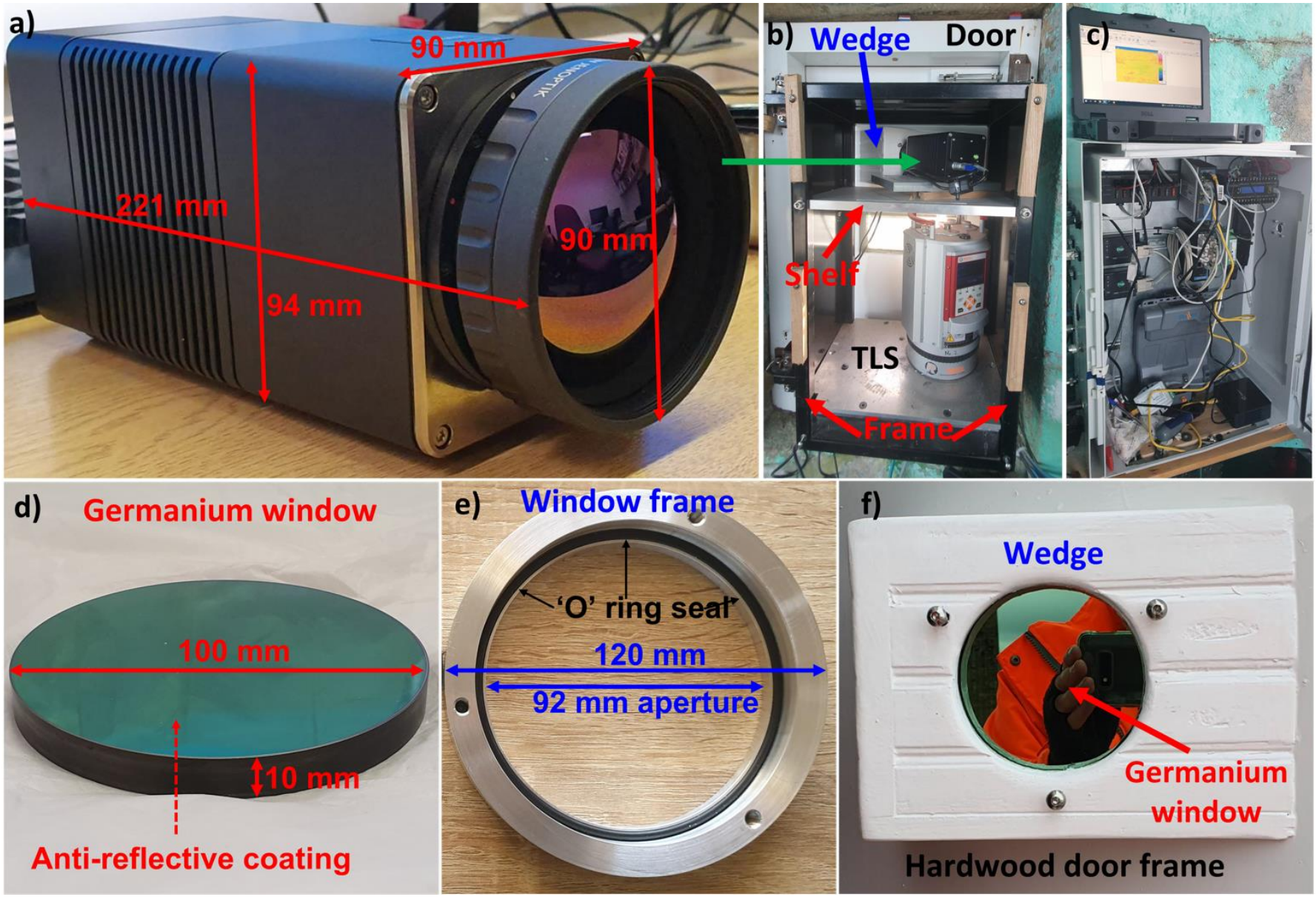
a)
90 mm
221 mm
94 mm
90 mm
b)
Wedge
Door
Shelf
TLS
Frame
c)
d)
Germanium window
100 mm
10 mm
Anti-reflective coating
e)
Window frame
'O' ring seal
120 mm
92 mm aperture
f)
Wedge
Germanium window
Hardwood door frame

Figure 4. 1: *Overleaf. Thermal camera field deployment to monitor the thermal activity across the cliff face. a) Thermal camera model VarioCAM HDx head 675, where red arrows indicate the key dimensions of the instrument. b) The thermal camera (indicated by a green arrow) was mounted over a horizontal aluminium shelf (red arrow) which was placed over the position of the laser scanner, both instruments being installed and protected inside a black aluminium frame. This image also shows the wooden wedge installed on the hardwood door frame in front of lens of the thermal camera (blue arrow). c) Computational systems that runs the software IRBIS 3.1 Professional (InfraTec GmbH Ltd), which was used to remotely control the thermal camera. d) Germanium thermal window dimensions and its anti-reflective coating, allowing the IR radiation to pass through with minimal interference. e) Custom-built aluminium frame, where the thermal window was mounted and secured. f) Frontal view of the wooden wedge with the thermal window installed.*

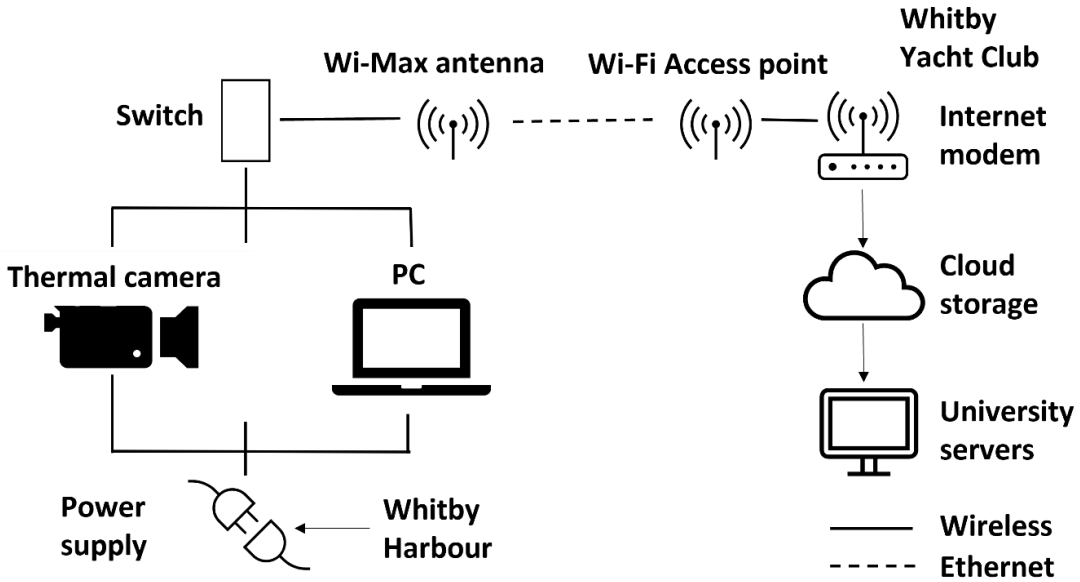

Figure 4. 2: *Conceptual diagram of the automatic monitoring setup that was used for surveying the surface temperatures of the cliff face.*

4.2.3 Data acquisition

Over 8,000 individual thermal images were collected at hourly intervals for the 12 months between 1st January and 31st December 2021 (Table 4.2). As such, this dataset is perhaps one of the longest and highest frequency monitoring campaigns accomplished to date. Each thermal scene compromises a grayscale matrix of temperature values (640 columns × 480 rows) (see: Section 4.2.1).

Table 4. 2 *:Total number of collected thermal images by season.*

	Winter	Spring	Summer	Autumn	Total
Collected images	2,119	1,896	2,153	1,928	8,096

A 1h interval of acquisition was chosen due to a number of reasons: to allow a parallel monitoring program between the laser scan data and the thermal imagery, where both instruments were set to collect data at the same time and frequency through 2021; a smaller interval was avoided to minimise the chances of either or both instruments failing due to near-constant use; and, to provide accurate measurements of absolute temperatures and rates of change with respect to the known scale of diurnal fluctuations in temperature at the site. A longer interval would reduce the likelihood of capturing extremes, for example.

The cumulative number of collected thermal images plotted as time-series, and the gaps of data in the series are shown in Figure 4.3. Gaps occurred due to errors with the PC controlling the thermal camera, or as a result of software failure. The first principal gap was in the winter (labelled in Figure 4.3 as Z1) over a period of 5-days between 19th and 25th March. In spring a second gap of 5-days occurred (Z2). The longest gap occurred in autumn over 8-days between 6th and 14th October (Z3). More minor gaps involved single to multiple hours up to a maximum of 2 days of data loss. As a result, 664 out of a total of 8,760 possible thermal images were not acquired, equating to 7.6% when considered at hourly intervals. Despite the occurrence of gaps, the number of thermal images provides a near-constant acquisition rate averaging 64.9 minutes between images during the monitored period, totalling 8,096 scenes during the year.

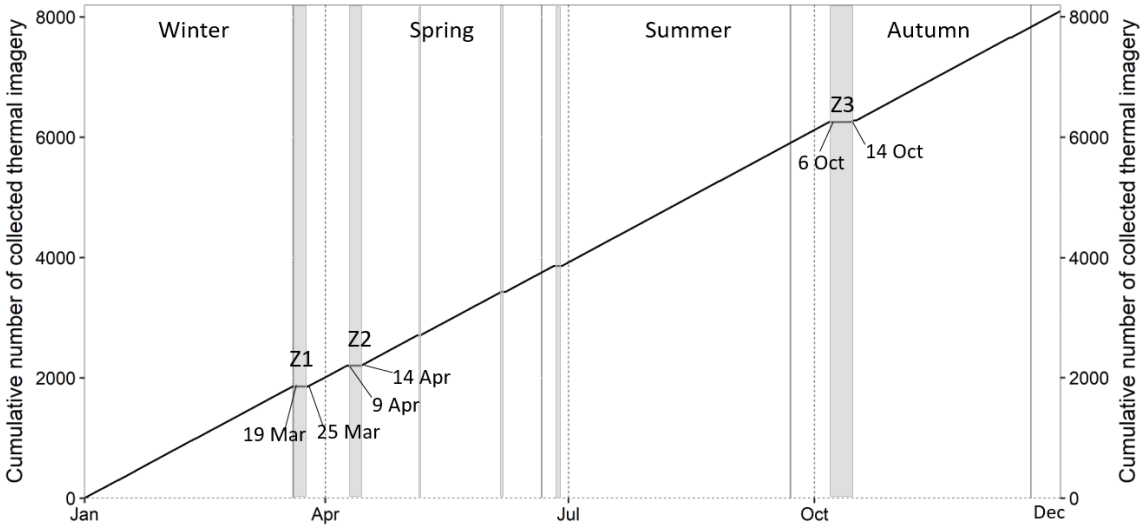

Figure 4. 3*: Cumulative number of thermal images acquired between 1st January and 31st December 2021, plotted as time-series. The gradient of the trend line indicates the acquisition rate at 1 h of data collection interval. Z1 to Z3 show the major gap zones (higher than eight days without continuous data). Minor gaps (between sub-daily hour intervals and up to two days) are shown with non-numbered thinner gray bars.*

4.2.4 Data filtering

The atmosphere has a variable effect on the intensity and spectral composition of the energy collected by the thermal camera, as the principal attenuation factor usually considered when processing thermal imagery (Lillesand et al., 2015). The absorption of infrared by water vapour is significant in the 8 - 14 μm spectral region, where air humidity and rainfall can affect the overall quality of thermal images (Chiodini et al., 2007; Spampinato et al., 2011). As such, fog and rain appear as essentially opaque to thermal radiation (Lillesand et al., 2015). Consequently, in this study, the thermal imagery collected during many period of adverse weather were considered unsuitable, and so were identified and removed as the cliff face surface temperatures were unreliable (Figure 4.4).

As Figure 4.4a demonstrates, good quality thermal images were typically characterized by both a clean, sharply focused scenes of the cliff face, where different geological and topographic features can be identified. Additionally, good quality imagery had an average file size in the native file format (*.IRB*) of ~ 328 Kb or higher. Conversely, very poor-quality thermal images with complete occlusion of the cliff face and homogeneous temperatures, has file sizes of ~ 310 Kb (Figure 4.4b), and poor quality imagery affected by fog or rainfall were blurred with a file size of ~ 313 Kb (Figure 4.4c, d). Consequently, similar to the partial scan filter (Chapter Methodology, see Section 2.3.1), the distribution of the thermal image file size was used to threshold and remove poor-quality data (Figure 4.5).

Figure 4.5 illustrates that the thermal image file size exhibit a bimodal distribution, with the major and the minor mode at ~ 110 and 335 Kb, respectively, and the file sizes ranging from ~ 109 to ~ 417 Kb, averaging ~ 328 Kb. The breaks in the distribution identified where poor quality data occurred was <320 Kb. However, after automatic selection, visual inspection and manual removal was needed to minimise good quality data loss.

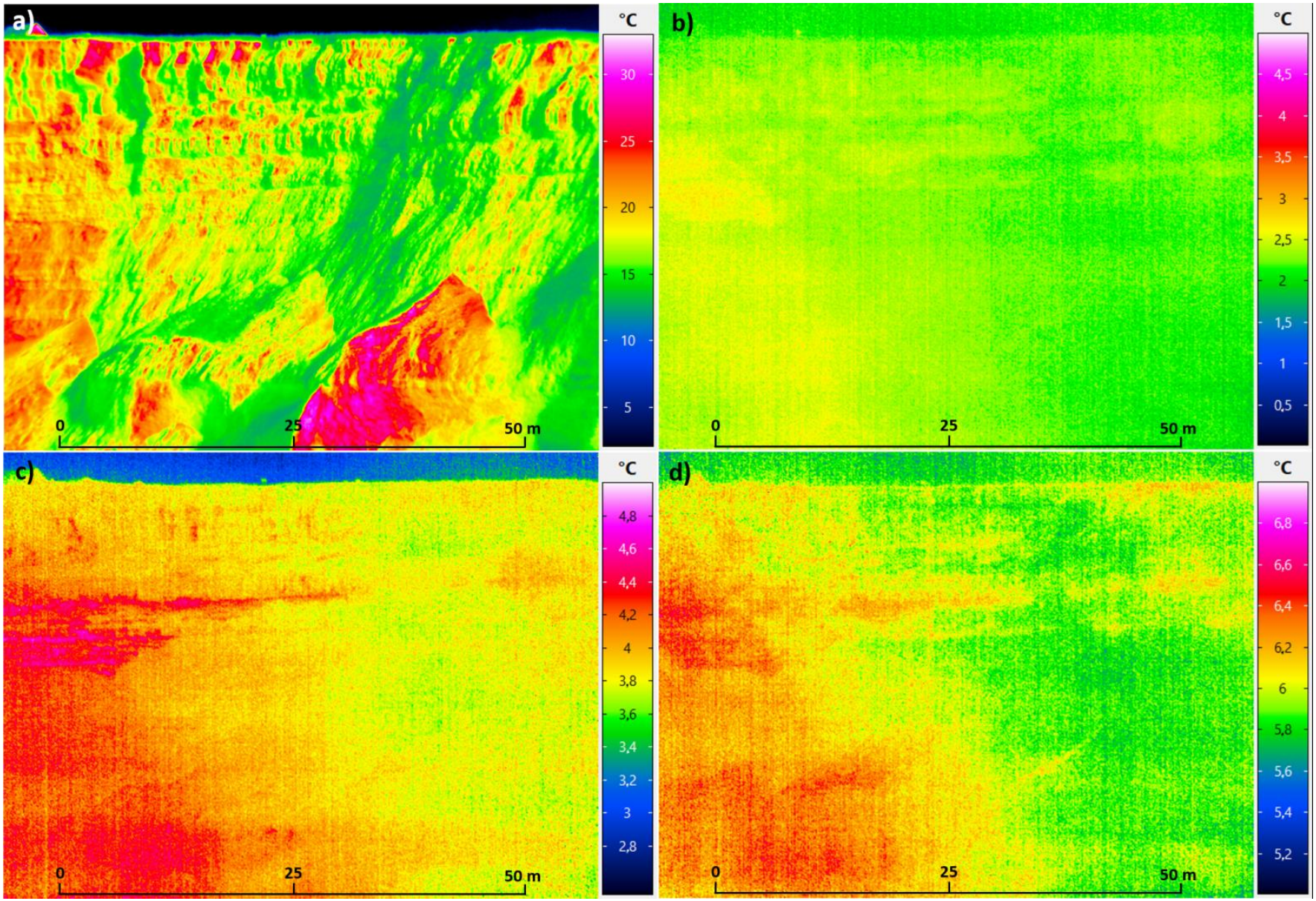
a)
°C
30
25
20
15
10
5
0
25
50 m
b)
°C
4,5
4
3,5
3
2,5
2
1,5
1
0,5
0
25
50 m
c)
°C
4,8
4,6
4,4
4,2
4
3,8
3,6
3,4
3,2
3
2,8
0
25
50 m
d)
°C
6,8
6,6
6,4
6,2
6
5,8
5,6
5,4
5,2
0
25
50 m

Figure 4. 4: *Overleaf. Example of a non-filtered versus filtered thermal images.* ***a)*** *Example of a good quality thermal scene as no fog or rain is observed between the instrument and the cliff face.* ***b)*** *A typical poor quality filtered scene of the lowest size (310 Kb), where the rain obstructs the detection of the cliff face.* ***c)*** *Example a filtered scene of 313 Kb.* ***d)*** *Example a poor-quality filtered scene of high size (391 Kb). Note that colour scale are different in each scene.*

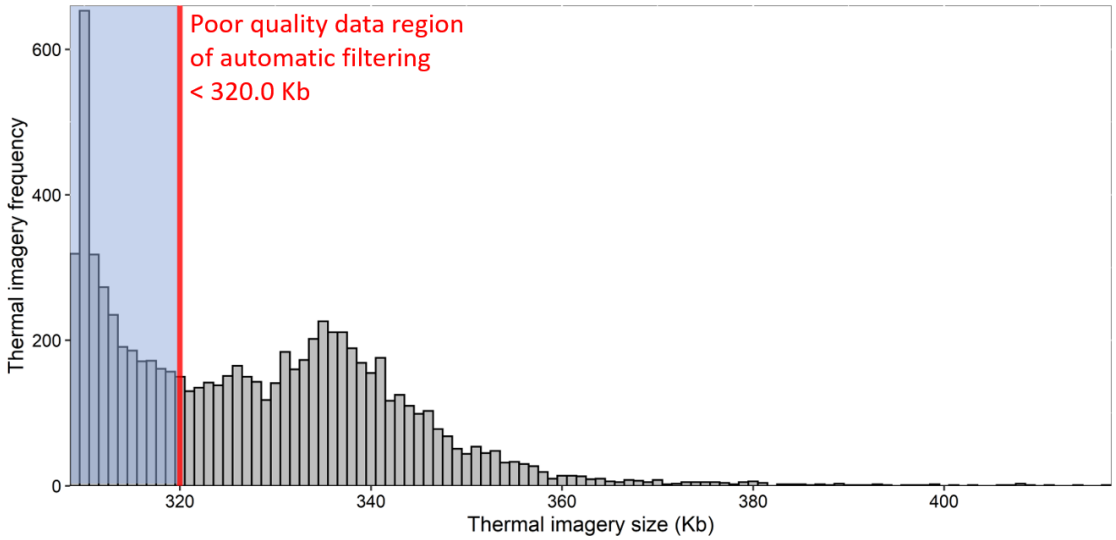

Figure 4. 5: *Identification of poor-quality thermal imagery using an annual histogram of thermal data frequencies by size (Kb). The region where thermal scenes were frequently affected by fog or rain was below ~ 320 Kb (Red vertical line). Thermal scenes below this threshold (Blue area) were automatically filtered. Scenes over this threshold were visually inspected and filtered if needed. This histogram was generated using all the images collected during the monitored period.*

As a result of this filter, 3,819 of 8,096 collected images were removed, equating to 47.2% of the dataset, leaving 4,277 images usable for further data processing and analysis. Of the total number of filtered images (3,819), more were filtered during winter and autumn (1,244 and 1,023, respectively) as compared to 562 and 990 images removed during spring and summer (see: Table 4.3). These differences reflect a higher proportion of data loss during adverse weather conditions. Importantly, because of the large number of the thermal scenes captured, it was more efficient to remove poor quality images at the beginning of the workflow, resulting in a significant reduction in the number of images that required further processing such as radiometric corrections (Section 4.2.5).

Table 4. 3*: Total number of filtered thermal images by season.*

	Winter	Spring	Summer	Autumn	Total filtered	Total usable images
Filtered images	1,244	562	990	1,023	3,819	4,277

Figure 4.6 shows the cumulative number of images before the application of the filter and the cumulative number of usable images after filtering. As with the laser scanner dataset (Chapter 2, see Section 2.7), to examine the possible emergence of temporal bias generated by this filtering, figure 4.6 also shows the cumulative difference between the raw imagery collected and that suitable for processing. After filtering, four principal data gaps were identified, of which only the first was associated with filtering due to adverse weather over six days (Z1). Z2, Z3 and Z4 were associated with gaps due to acquisition (see Section 4.2.3). Minor gaps, which involved either one hour intervals up to a maximum of 2 days of data loss were generated in all seasons, however, more minor gaps were detected in winter, then summer, and finally autumn.

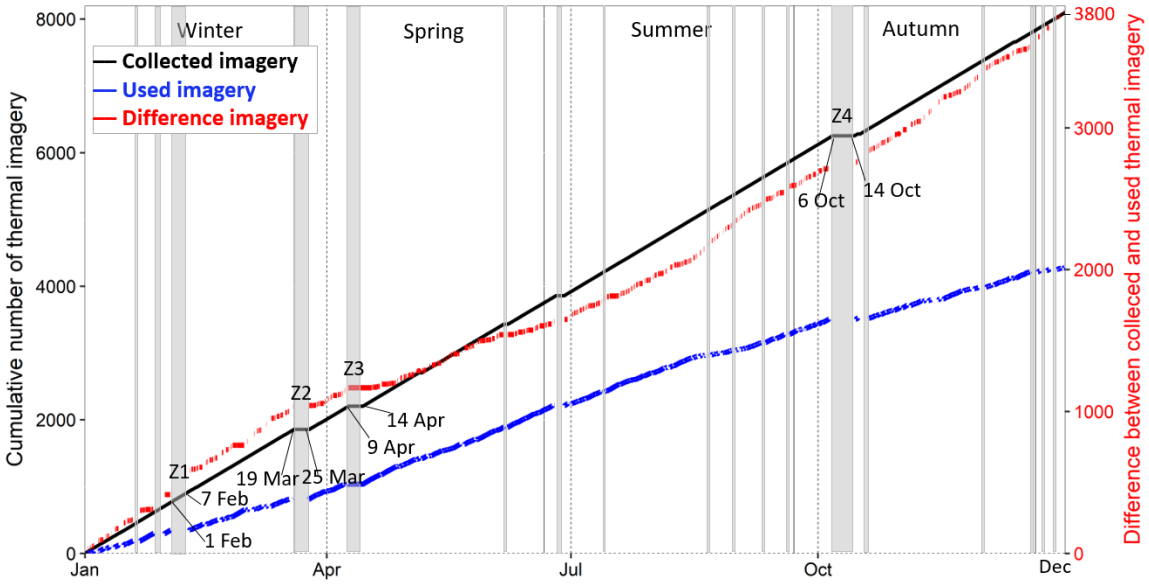

Figure 4. 6: *Cumulative number of thermal images before and after the application of the filtering. Thermal images collected at the stage of data acquisition are shown using a black line (Collected imagery, also shown in Figure 4.3 in Section 4.2.3). The number of used thermal images after filtering is shown as a blue line (Used imagery). The cumulative difference between the collected and used thermal images is shown as red line (Difference imagery). Such as in Figure 4.3 of the section data acquisition (Section 4.2.3), Z1 to Z4 indicate the major gap zones (up to nine days without continuous data). Minor gaps (between sub-daily hour intervals and up to 2 days) are shown with non-numbered thinner gray bars. Vertical continuous lines show approximate boundaries between astronomical seasons.*

Figure 4.7 shows the seasonal distribution of the total number images during the diurnal cycle. In winter, spring and summer, a consistent pattern of higher data loss was detected between midnight to sunrise, reaching a peak rate of data loss at either the end of sunrise (e.g., > 60 thermal images at 09:00 h in winter) or one hour after sunrise (e.g., >55 images at 08:00 h in summer). Throughout the year, lower data loss was observed around midday (between 12:00 and 14:00 h), however, the lowest loss of data at this time was during the warmest seasons, with only 10 and

up to 20 thermal scenes filtered out. After midday, an increase in the rate of data loss is again observed during and after sunset removing up to 50 thermal images (e.g., in winter and summer). As a result, whilst a systematic pattern of data loss was detected from sunset to mid-night towards sunrise, most probably associated with time-of-day-dependent weather (e.g., sea fret / mist), a significant number of images were retained for all hours of the day.

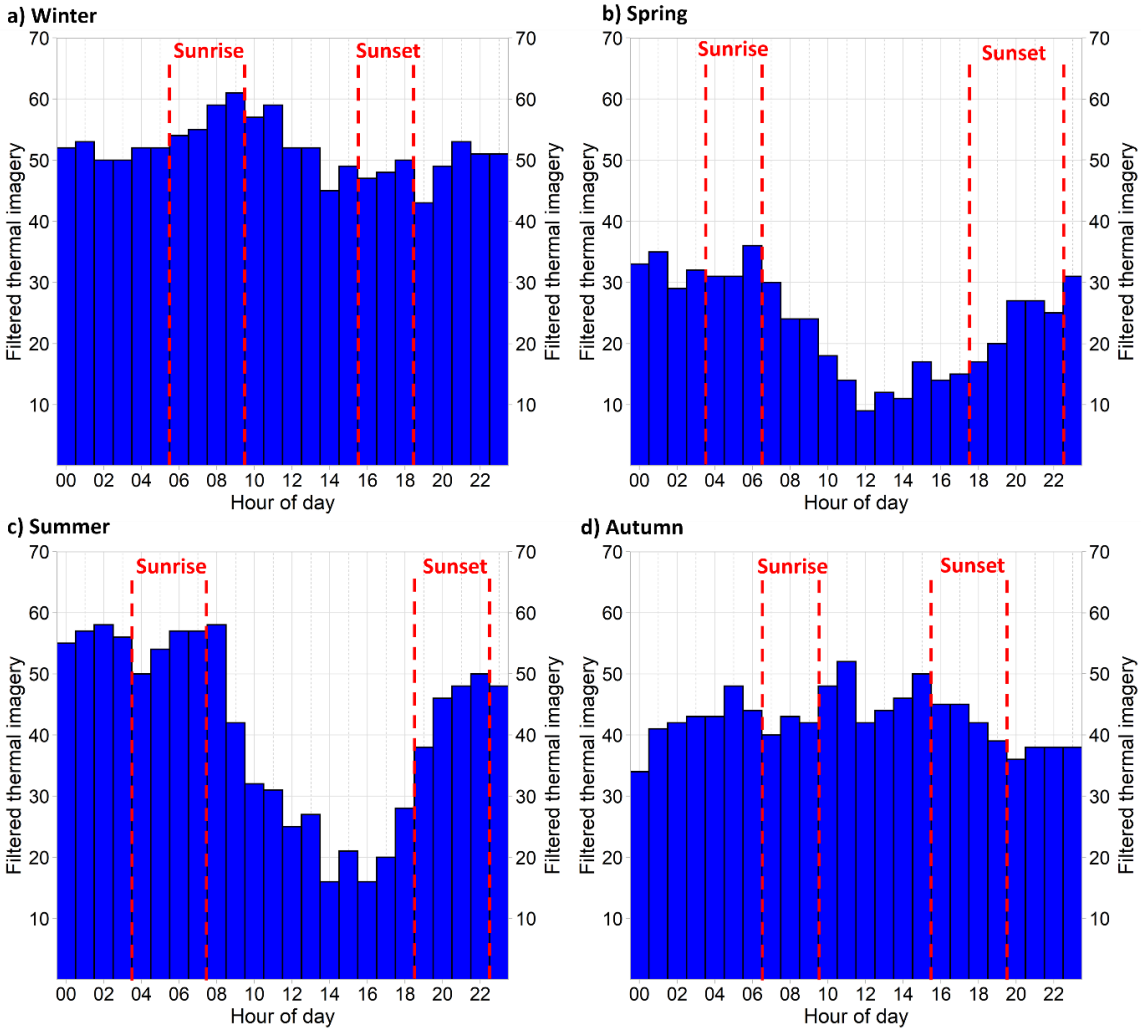

Figure 4. 7: *Seasonal histograms of the total number of filtered thermal images by hour. Vertical dashed lines show the approximate boundaries between the sunrise and sunset times, which were obtained from astronomical tables for the latitude and longitude of Whitby.*

Figure 4.7 also shows a varying pattern of data loss between warmer and cooler seasons: the histograms of winter and autumn display a low variation in data filtering through time, while abrupt changes by hour were detected in spring and summer. In winter, the maximum hourly data loss varied between ~ 60 images at sunrise to a minimum of ~ 45 around midday, yielding a diurnal range in data loss of ~ 25 images per hour. Conversely, in summer data loss fluctuated more significantly, from a total of 58 thermal images after sunrise (09:00h) to a minimum of 15

images around midday (14:00h), resulting in a diurnal range of data loss of ~ 43 images. The overall pattern of hourly data loss was therefore relatively constant in winter and autumn, compared with spring and summer.

The systematic patterns in data loss from sunset to midnight to sunrise can be explained by the coastal setting of the study site which can experience high levels of water vapor, particularly due to advective fog generated by warm inland air intersecting cool moist air from the North Sea. Known locally as Haar, this phenomenon is most common in spring and summer, particularly between April and September, when air temperatures begin to warm up, but the sea surface remains relatively cold. As such, these conditions promote the differential patterns of data loss between seasons. In addition to Haar, the occurrence of winter and autumn rainstorms also contributes to generate relatively constant data volumes as the occurrence of rain exhibits a more random pattern, generating in sum lower differences in data loss through the day.

4.2.5 Data correction

Surface temperatures acquired from thermal cameras are subject to errors as a result from five principal factors: (1) An unknown or incorrect characterisation of the emissivity of the target, where emissivity (which varies between 0 and 1) is defined as the ratio between the radiant energy emitted by the surface of the measured target and that emitted by a perfect blackbody at a given temperature. Hence, emissivity describes the spectral quantity and efficiency of the target in radiating energy compared to a black body (Ball and Pinkerton, 2006); (2) Atmospheric attenuation due to scattering as a result of airborne particulate and absorption by gases; (3) Integrated averaging of radiance over increasing pixel areas caused by an increased distance between the taget and the thermal camera within a single scene; (4) Viewing the target at oblique angles (>40°); and (5) Instrument error caused by system noise and systematic offsets in the thermographic system (Ball and Pinkerton, 2006). In particular, factors such as the relative humidity and the distance to target generate transmission losses in the optical channel between the target and the thermal camera or when measuring through windows permeable to infrared radiation (InfraTec GmbH, 2018). Therefore, to correct for these artifacts, and to obtain absolute surface temperatures, calibration of the surface temperatures is needed (Guerin et al., 2019).

Figure 4.8 shows a conceptual model of the thermographic calibration protocol used in this IRT survey, were several parameters were measured or monitored, including the mean distance bewteen the cliff face and the thermal camera, transmission and reflection of the thermal

window, as well as key environmental parameters at the time of image acquisition, such as the air temperature and relative humidity.

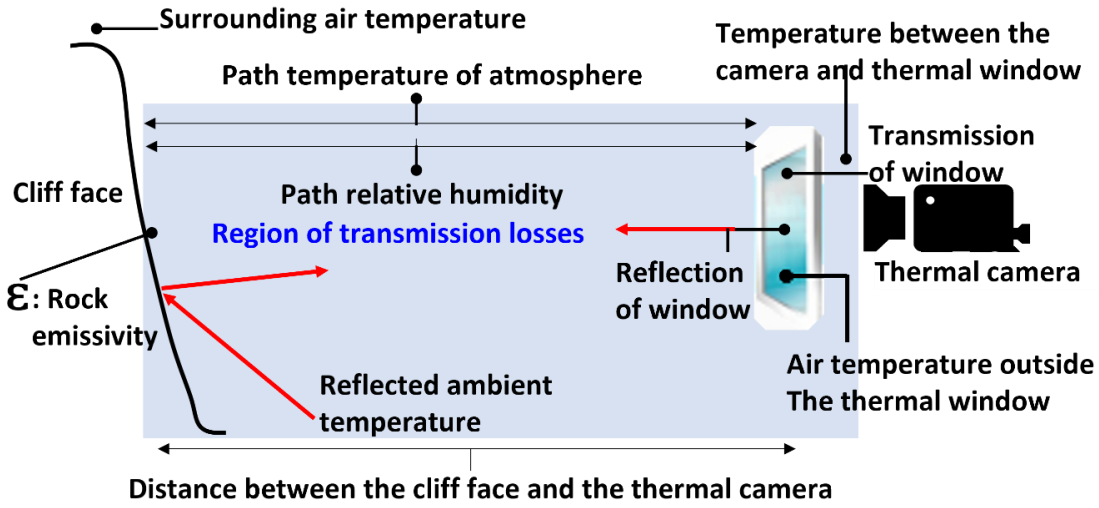

Figure 4. 8: *Conceptual model of the thermographic calibration protocol used in this IRT survey. Oval arrows show the parameters that were acquired to correct each thermal image. The atmospheric region generating transmission losses in the infrared radiation captured by the thermal camera is highlighted using a blue box. The red arrows indicate corrections for the thermal window reflection and the reflected ambient temperature.*

The importance of measuring the relative humidity and temperature during IRT field surveys is widely recognized, however, many IRT studies make measurements only at the thermal camera location and use this to correct atmospheric attenuations (Ball and Pinkerton, 2006). In the view of the potential bias that this introduces, it has been recommended that the minimum number of measurements needed are two: one at the thermal camera location and other close to the object being measured (Ball & Pinkerton, 2006). Following this approach, relative humidity and temperature were collected using two data loggers and thermocouples; one was installed on a rockface at the top of the cliff and the other alongside the thermal camera on the exterior of the lighthouse (Figure 4.9). This monitored the air temperature and relative humidity at the cliff face, the air tempetature and humidity outside the thermal window, and hence the average air temperature and humidity that characterized the atmospheric path between the thermal camera and the thermal window, enabling a calculation of the transmission losses at the site.

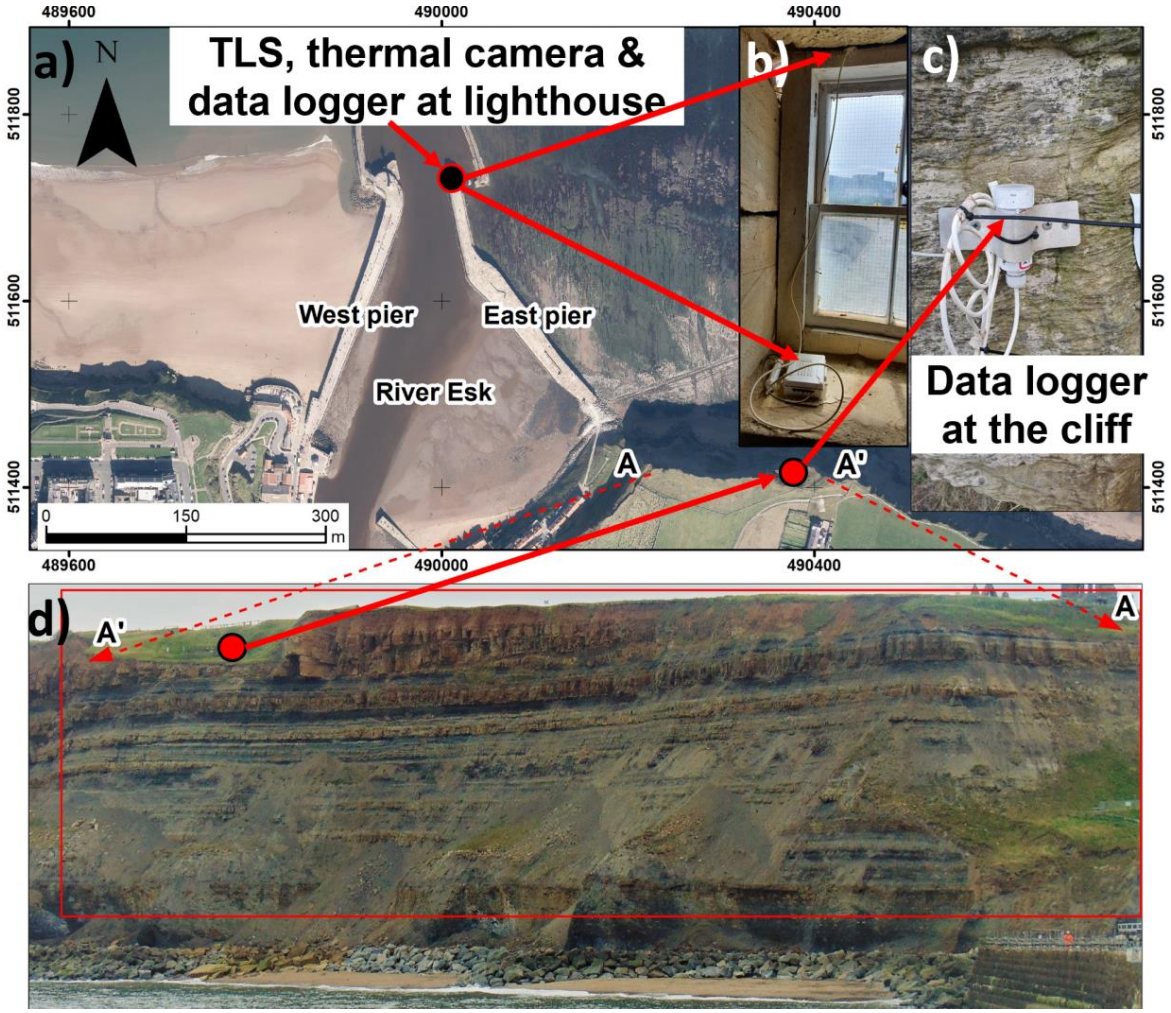

Figure 4. 9: *Field deployment of the data loggers collecting air temperatures and relative humidity for thermal imagery correction. a) Map showing the location of the data logger installed at the lighthouse (black dot) and the data logger located at the top of the cliff face (red dot). b) Installation of the data logger located at the lighthouse. c) Data logger installed in the quarry at the top of the cliff face. d) Frontal view of the cliff face, indicating the position of the data logger installed at the top of cliff (red dot), which is shown in detail in Figure c). In each figure, the red arrows indicate the position of the data loggers. The accuracy of the data loggers was ± 0.21°C and ± 2.5% of relative humidity.*

For each thermal image, a radiometric correction of temperarues was undertaken using calibration schemes provided by the thermal camera manufacturer using IRBIS 3.1 Professional (InfraTec GmbH Ltd). Using the calibration curve of the camera, the recalculation of the radiation intensity $M(T_0)$ of the object with temperature T_0, considering the emissivity of the object and radiation from the reflected ambient temperature on the object's surface, follows the general equation given by InfraTec GmbH (2021):

$$M_{BB}(T_0) = \frac{M(T_0) - M_{BB}(T_U)}{\varepsilon} + M_{BB}(T_U) \qquad \text{[Eq. 4.1]}$$

Where $M_{BB}(T_0)$ is the corrected radiation intensity value (referring to a black body with identical temperature to the object's temperature), ε is the emissivity of the object, and $M_{BB}(T_U)$ is the black body temperature equivalent to the reflected ambient temperature. Using this approach (Eq. 4.1), per-pixel emissivity corrections can be undertaken using three approaches, as follows: First, by applying one common user defined emissivity value for all pixels of the thermal image (i.e., a global correction of the thermal scene): Second, by applying a set of similar emissivity values for all pixels within geometrically defined local areas (i.e., local spatial corrections of the scene); Third, by applying individual emissivity values for each single image pixel (pixel-by-pixel emissivity correction, although this can be the most time consuming computational approach) (InfraTec GmbH, 2021). In this research, a global correction of the emissivity of each thermal scene was adopted as way to allow and speed up the automated correction of a total of 4,277 thermal images, as explained below in this section. As a result, the temperatures reported in this study were only corrected for the rock face outcrop of the thermal scene.

A further radiometric correction was applied, which corrects the impact on the radiation intensity due to wave propagation through the atmosphere. This was described by the transmissivity, τ_P, and black body temperature equivalent to the radiation path T_P, which follows the general equation given by InfraTec GmbH (2021):

$$M_{BB}(T_0) = \frac{M(T_0) - M_{BB}(T_P)}{\tau_P} + M_{BB}(T_P) \qquad \text{[Eq. 4.2]}$$

In this study, a single (i.e., global) value of transmissivity, τ_P, was obtained for each thermal scene, by considering the path temperature and path relative humidity at the specific time of the thermal scene acquisition (and so, considering the specific atmospheric conditions across the radiation path, T_P, that were present at the time of thermal imagery collection), as well as the mean distance between the cliff and the location of the thermal camera (see Figure 4.8 and Table 4.4). Moreover, the attenuation caused by the thermal window, which represents a solid body with limited thickness located within the radiation path, was also considered. The transmissivity of the window (in the spectral range of the thermal camera) can deviate more or less from an ideal value of 1 (100%). As such, after estimating the atmospheric transmission loss between cliff face and outside face of the thermal window, the transmission of the window itself was considered as τ_P in equation 4.2. This correction was undertaken using the combined correction scheme "*object with transmission distance and thermal window*", implemented in IRBIS 3.1 Professional. The combined equation for correction used in this scheme follows the general equation given by InfraTec GmbH (2021):

$$M_{BB}(T_0) = \frac{\frac{M(T_0) - M_{BB}(T_P)}{\tau_P} + M_{BB}(T_p) - M_{BB}(T_U)}{\varepsilon} + M_{BB}(T_U) \quad \text{[Eq. 4.3]}$$

Table 4.4 shows the calibration parameters in the correction scheme *"object with transmission distance and thermal window*". Due to the large number images to be corrected (4,277 scenes), a workflow for automatization was developed using Desktop Automation (Macro Recorder 2.0, Bartels Media Ltd). As showed in Table 4.4, in order to facilitate the process of automation, the correction of the dataset was performed based on the distinction of two types of parameter: first, constant parameters, as these were globally applied for each thermal image (e.g., emissivity, mean distance, thermal window transmission); and second, variable parameters that changed through time and so, specific for each thermal scene at the time of data collection (e.g., path air temperature, path relative humidity). Each parameter was associated with the corresponding thermal imagery based upon the date and time of data collection, as shown in Table 4.4. Despite that a global value of emissivity and mean distance between the cliff and the thermal camera were assumed in this study, the impact of using constant parameters integrated over 7.5 and 14μm spectral range is discussed at the end of this section (Section 4.2.5).

Table 4. 4*: Calibration parameters used during IRT monitoring.*

Thermal imagery date and time			Thermal imagery correction parameters		
ID	**Date**	**Time**	**Parameter type**	**Parameter name**	**Value**
1	yyyy-mm-dd	hh:mm:ss	Constant	Emissivity (ε)	0.97
			Constant	Mean distance (m)	430
			Constant	Thermal window transmission (%)	0.83
			Constant	Thermal window reflection (%)	0.06
			Variable	Cliff surrounding air temperature (°C)	Variable
			Variable	Path air temperature (°C)	Variable
			Variable	Path relative humidity (%)	Variable
			Variable	Temperature outside T. Window (°C)	Variable
			Variable	Temperature Camera-Window (°C)	Variable

As mentioned above, a key parameter needed to calibrate the thermal data is the selection of the emissivity of the object. Commonly, the determination of the emissivity (ε) is estimated using laboratory-based analysis of rock samples (e.g., Ball and Pinkerton, 2006; Frodella et al., 2017), field-based measurements using reference temperatures across reflective surfaces when the site is accessible (e.g., Guerin et al., 2019), or as in most remote-sensing applications from spectral libraries in the literature (e.g., Salisbury and D' Aria, 1992; 1994; Kotthaus et al., 2014; FLIR Systems Inc., 2018) with examples including Pappalardo et al., (2016), Pappalardo and

Mineo (2017), Frodella et al., (2017), Loiotine et al., (2022). In this study, the near-vertical cliff profile and frequent rockfall activity restricted the ability to measure emissivity in the field or extract rock samples from the cliff profile. Consequently, the spectral libraries provided by Salisbury and D'Aria (1992, 1994) were used as these include typical reflectance and emissivity coefficients at the mid-range of the spectral window for rock types typical of those outcropping at East Cliff (bedded sandstones, siltstones, and shales). Given the limited variability in emissivity for these rock types, an mean emissivity coefficient of 0.97 was adopted (Table 4.5).

Following Spampinato et al., (2011), even when an appropriate coefficient has been used, errors can occur as emissivity can vary based on surface roughness and viewing angle (Becker et al., 1986; Ball and Pinkerton, 2006), or due to increasing path distance, with reported variability in emissivity of up to ~ 3% for distances between 100 to 400 m (James et al., 2006). To assess if variations in emissivity have a significant impact on the measured surface temperature of the cliff face, a sensitivity analysis was conducted. A total of 24 thermal images were selected, representing a complete typical summer day. For each hourly image, the calibrated temperatures was assessed by changing the mean emissivity from 0.90 to 0.99, a range spanning all relevant coefficients for sandstones, from Kern, (1928), Kotthaus et al., (2014), FLIR Systems Inc., (2018), while every other calibration parameter shown in Table 4.4 remained constant at the hour of data acquisition (Figure 4.10).

Figure 4.10a demonstrates that by varying the emissivity between 0.90 to 0.99, no significant impacts on the average surface temperatures of the cliff face were obtained. Indeed, for most of the time the average temperatures remained near constant, and only minor gradual variations of temperatures were detected with sequentially changing values of emissivity between 16:00 and 20:00 h. The maximum variation of the temperatures was ~ 1°C but this occurred exclusively between the minimum and maximum value of emissivity of 0.90 and 0.99 at 17:00 h. Figure 4.10b demonstrates that the temperature difference between sequentially increasing values of emissivity were minimal during most of the diurnal cycle, ranging from ~ ± 0.01°C to ± 0.05°C between 01:00 and 15:00, and then between 21:00 and 23:00 h. Slightly higher variations occurred between ~ -0.06 and up to -0.1°C between midday and sunset (16:00 to 20:00 h). Positive variations in temperature to varying emissivity were detected during the heating phase of the day (from 06:00 to 13:00 h), while negative variations were observed during some of the cooling hours (14:00 to 22:00 h). Although a uniform average emissivity coefficient of 0.97 was applied, meaning that only temperatures on the exposed rock face were properly corrected to absolute values, it has been demonstrated that no significant impacts within the area of interest were

introduced with most temperature differences ranging, on average, between ± 0.01°C to ± 0.05°C, and a maximum difference of only -0.1°C at 17:00

Table 4. 5: Typical average emissivity (ε) for samples of sandstones, siltstones, and shales.

Rock sample	Reflectance (%)	Emissivity (%)	Emissivity (0.000)	Spectral range (μm)
Sandstone 1	2.84	97.16	0.971	11.3 – 11.6
Sandstone 2	2.66	97.34	0.973	11.3 – 11.6
Sandstone 3	3.47	96.53	0.965	11.3 – 11.6
Sandstone 4	3.85	96.15	0.961	11.3 – 11.6
Sandstone 5	3.09	96.91	0.969	11.3 – 11.6
Sandstone 6	2.20	97.80	0.978	11.5 – 12.5
Sandstone 7	2.07	97.93	0.979	11.5 – 12.5
Sandstone 8	2.54	97.46	0.974	11.5 – 12.5
Sandstone 9	2.54	97.46	0.974	11.5 – 12.5
Sandstone 10	2.69	97.31	0.973	11.5 – 12.5
Sandstone 11	3.60	96.40	0.964	10.3 – 11.3
Sandstone 12	3.23	97.77	0.967	10.3 – 11.3
Sandstone 13	4.02	95.98	0.959	10.3 – 11.3
Sandstone 14	4.02	95.98	0.959	10.3 – 11.3
Sandstone 15	4.21	95.79	0.957	10.3 – 11.3
Siltstone 1	3.70	96.30	0.963	11.3 – 11.6
Siltstone 2	2.85	97.15	0.971	11.3 – 11.6
Siltstone 3	2.96	97.04	0.970	11.5 – 12.5
Siltstone 4	2.22	97.78	0.977	11.5 – 12.5
Siltstone 5	3.69	96.31	0.963	10.3 – 11.3
Siltstone 6	3.25	96.75	0.967	10.3 – 11.3
Shale 1	2.55	97.45	0.974	11.3 – 11.6
Shale 2	2.74	97.26	0.972	11.3 – 11.6
Shale 3	3.30	96.70	0.967	11.3 – 11.6
Shale 4	2.85	97.15	0.971	11.3 – 11.6
Shale 5	2.77	97.23	0.972	11.3 – 11.6
Shale 6	3.45	96.55	0.965	11.3 – 11.6
Shale 7	1.86	98.14	0.981	11.5 – 12.5
Shale 8	2.50	97.50	0.975	11.5 – 12.5
Shale 9	2.86	97.14	0.971	11.5 – 12.5
Shale 10	2.31	97.69	0.976	11.5 – 12.5
Shale 11	2.15	97.85	0.978	11.5 – 12.5
Shale 12	2.68	97.32	0.973	11.5 – 12.5
Average	2.96	97.07	**0.970**	10.3 – 12.5
Standard dev.	0.60	0.62	**0.006**	10.3 – 12.5

Note: Table modified from Table 1 in Salisbury & D'Aria (1992; 1994, p. 89 and p. 347, respectively).

.

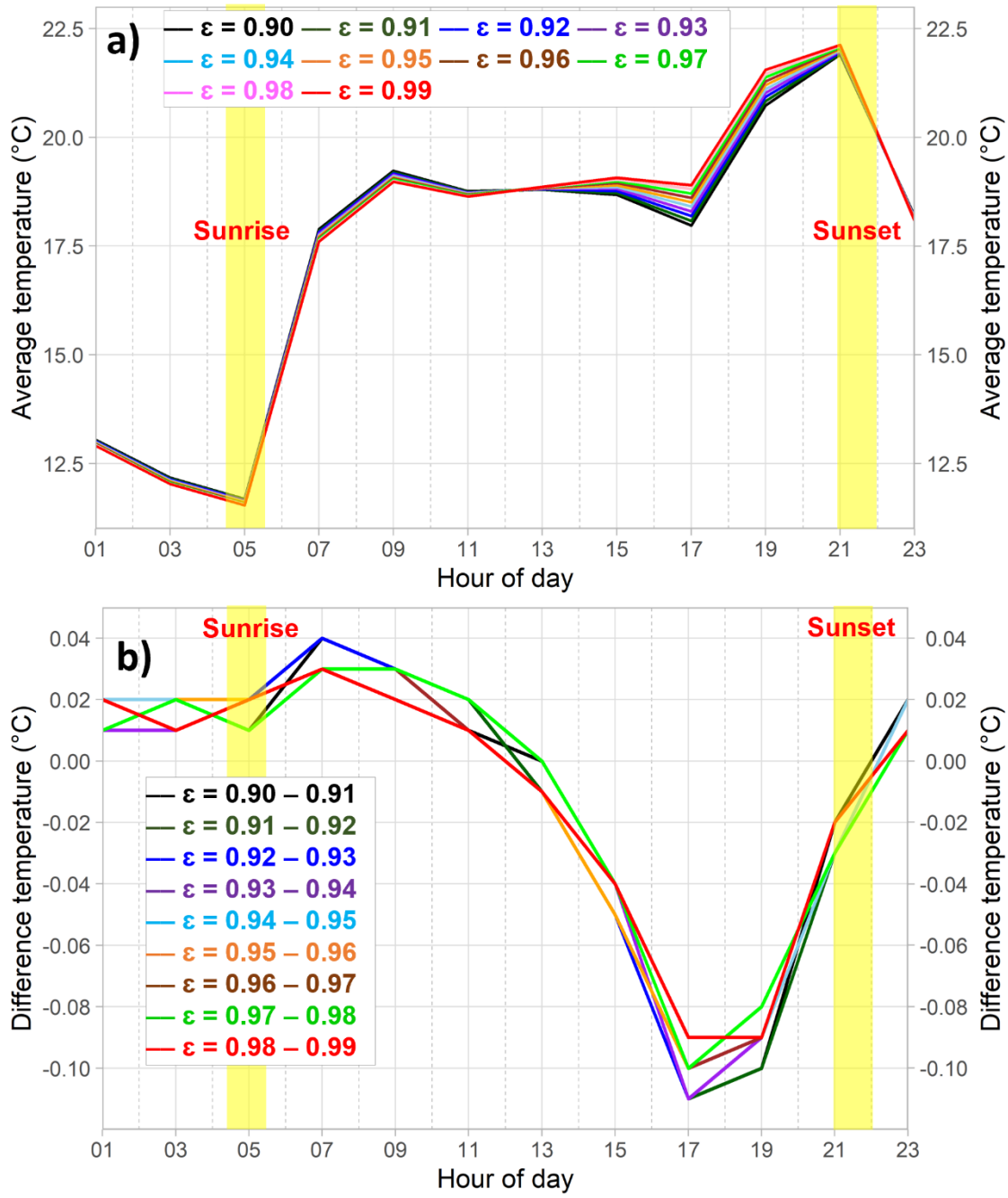

Figure 4. 10: *Sensitivity analysis of the cliff temperatures to changes in the parameter of emissivity for a complete diurnal cycle of summer (ε = 0.90 – 0.99).* ***a)*** *Changes in the average temperature to variations in the emissivity.* ***b)*** *Difference temperature between sequential values of emissivity. For each figure, all the temperature values were calculated within the General Window of assessment of the cliff face (GW1), which is shown in Figure 5.1 (see Chapter 5, Section 5.2). Imagery date: 16th June 2021. Sunrise and sunset time: 04:48 and 21:27 h, respectively. The approximate time of the sunrise and sunset is highlighted using yellow vertical bars.*

The final correction addressed the distance from the camera to the cliff and thermal window, under the "*object with transmission distance and thermal window*" (Eq. 4.3). The

transmission of the thermal window was supplied by the window manufacturer (Knight Optical Ltd.), giving a transmission coefficient of 83% (or 0.83, see Table 4.4) as the average transmission over the spectral range of 7.5 and 14 µm. Maximum transmission was 92% between 10 and 11 µm (Figure 4.11). Following manufacturer advice, a window reflection coefficient equal to 6% (or 0.06, see Table 4.4) was selected as the maximum feasible reflection of the window. The final parameter needed for calibration was the mean distance between the cliff face and the lens of the thermal camera. This parameter was estimated from ortho-rectified aerial imagery (source: Channel Coastal Observatory, UK), which provided an average cliff to sensor distance of ~ 430 m.

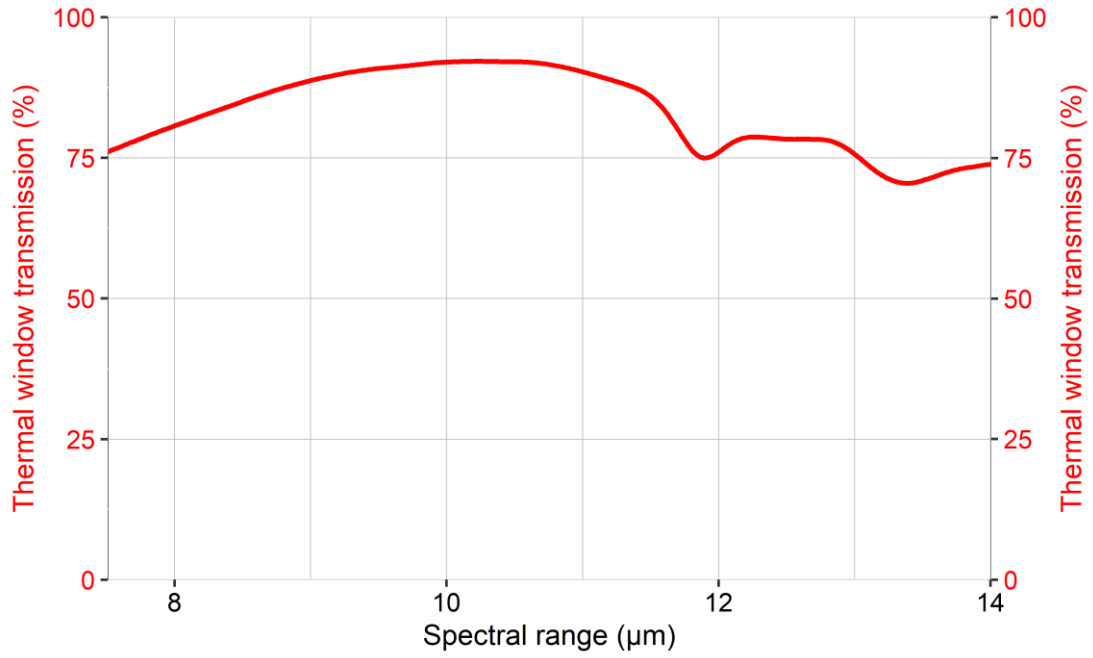

Figure 4. 11: *Transmission of the used thermal window over the spectral range of 7.5 – 14 µm. Data courtesy of the thermal window manufacturer, Metrology division (Knight Optical Ltd).*

Figure 4.12 shows the values of the differences in temperature between corrected and non-corrected thermal data using a day (24 thermal images) in summer and a day in winter. As such, the curves presented in this figure represent the temperature subtraction of the corrected imagery with the corresponding non-corrected thermal scene across the general window of assessment of cliff temperatures (GW, see Section 5.2, Chapter 5). During summer, changes in temperatures due to calibration resulted in a rise in apparent temperature which fluctuated between ~ 0.5 and 2°C, in addition to decreases of temperature up to ~ –3.2°C between 13:00 and 17:00 h. Smaller increases in temperature were detected through the night, of around ~ 0.5°C. During winter, temperature reduction was more frequent through the diurnal cycle, with temperatures changes after calibration of ~ -0.2 to -3.2°C. However, similar patterns in fluctuation

mirrored those in the summer, with the higher changes around 2 h after sunrise, reaching at 09:00 h followed by a decrease of temperatures to a minimum at 13:00 h. Again, lower changes in temperature were observed throughout the fluctuating between ~ -1.0 and -2.0°C.

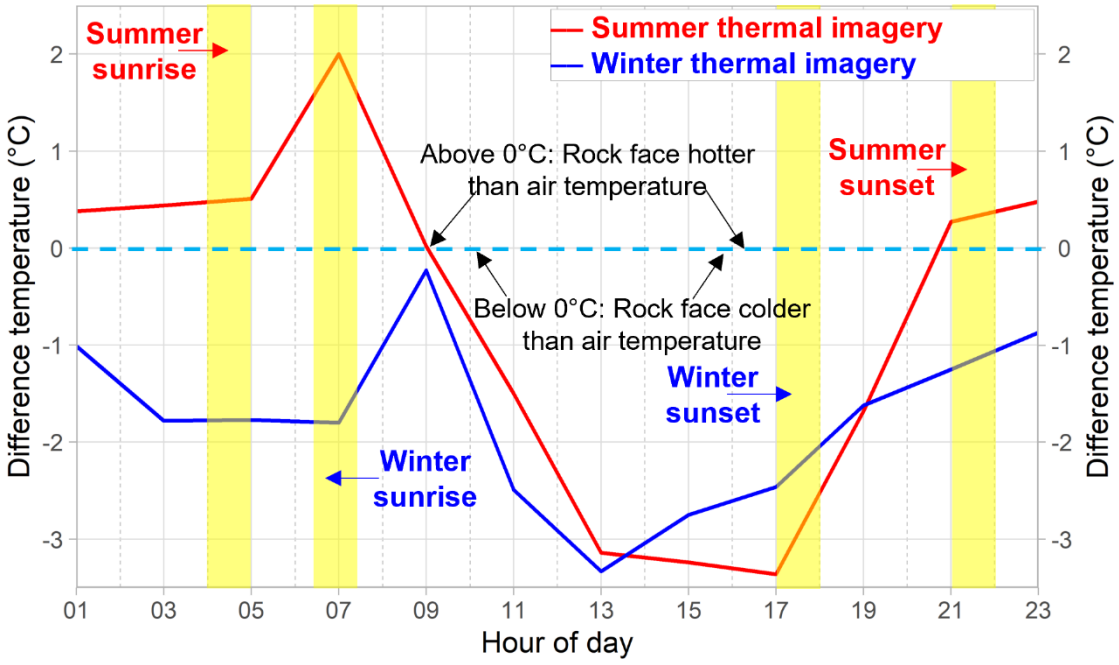

Figure 4. 12: *Values of the differences in temperature between corrected and non-corrected thermal imagery for a complete diurnal cycle of summer and winter. Summer imagery date: 16th June 2021 (24 thermal images). Summer sunrise and sunset: 04:26 and 21:40 h, respectively. Winter imagery date: 27th February 2021 (24 thermal images). Winter sunrise and sunset: 06:56 and 17:35 h, respectively. The approximate boundaries of the sunrise and sunset times is highlighted using yellow vertical bars. The horizontal dashed line across 0°C (light blue), highlights the times in which the surface temperature of the rock face was hotter or colder than the environmental temperature.*

Overall, Figure 4.12 demonstrates that temperature correction has a variable effect through both the year and through the day, characterised by three key features: (1) a temperature gain during summer (~ 0.5°C), especially 2 h after sunrise (07:00 h); (2) a temperature reduction in summer but more distinct in winter where the reduction of temperature fluctuated between ~ -0.2 and -3.2 °C; and (3) consistent calibration effects through the day with pronounced changes after sunrise and sunset of both of summer and winter. These calibrations can be explained at times when the cliff temperature is lower or higher than the ambient temperature. For example, if the cliff temperature is higher than the ambient temperature, the correction scheme increases the measured temperature, but the opposite effect occurs if the cliff surface temperature is lower than the air temperature (InfraTec GmbH, 2018). As such, the calibration responds to diurnal phases in which the cliff face was hotter (summer) or colder (winter) than the surrounding atmosphere.

The differential seasonal divergence in temperature of cliff and the air is explored in Chapter 5 (Section 5.2). Overall, the results of the calibration confine the expected net decrease in temperatures due to attenuation, especially related to distance, the often high relative humidity, and also transmission losses associated with the thermal window.

It is also important to note here that, while the emissivity and distance are not constant across the radiation path when monitoring natural settings of variable composition and complex geometry such as here (this is because, while the emissivity can have spatial variations across the different materials that form the cliff, the concave shape of the East Cliff in addition to local slope variations produce different path lengths for all pixels), it is considered that the assumed value of emissivity across the centre of the wavelength range at 11μm (ε = 0.97) is representative of the sandstones and siltstones that predominates in the studied rock face, as minimal variations in cliff temperatures were observed from the sensitivity analysis of emissivity variations, even if an emissivity value between 0.90 and 0.95 would have been chosen as demonstrated in Figure 4.10 (a range including all relevant emissivity coefficients for sandstones, from Kern, 1928; Kotthaus et al., 2014; FLIR Systems Inc.2018). In addition, due the relatively short distance between the cliff and the camera (mean distance of 430 m) and the predominance of a relatively low angle between the instrument and the cliff (less than 20°), it is assumed here that local variations in the distance had a minimal impact on the reported temperatures in this setting. As such, the application of a global correction for emissivity and distance was necessary to permit the automated data processing of the large dataset (4,277 thermal scenes) by reducing the time for data processing, but capable to detect temperature differences between the bedded sandstones (BS) and interbedded sandstones and siltstones (IBBS) that form the area of research and so, able to account for geological variation, as demonstrated below in Section 4.3 and in Chapter 5. For practical reasons, similar approaches, which involve the using of a single mean value of emissivity for a global correction of the hillslope being imaged has been applied in rock slope temperature monitoring studies, as well as the using of a single mean distance value between the slope and thermal camera (e.g., Frodella et al., 2017; Guerin et al., 2019; Loiotine et al., 2022). Therefore, based on the aim and objectives of this thesis (see Chapter 1, Section 1.2), it is important to highlight that the thermal imagery and temperature results reported in this study are only calibrated for the rock face, excluding any other surfaces captured by the thermal scenes, such as the topsoil and the debris or patches of vegetation forming the talus.

In the next section of this chapter, an initial analysis of the surface temperature is undertaken, as a verification of the quality of the data collected and the degree to which this dataset reflects the nature of the cliff surface under inspection. This forms the basis for the detailed thermal time-series analysis which follows in Chapter 5.

4.3 Summary of rock-slope surface temperatures

This section begins with a general overview of the detected patterns, where five summary thermal maps representing the average, maximum, minimum, standard deviation, and differential surface temperatures detect in 2021 are analysed. From this an assessment of the degree to which the thermal camera system adequately captures the thermal characteristics of the cliff is presented.

To consider the fidelity with which the thermal monitoring system describes the cliff face temperatures and emergent thermal features in space and through time, general statistics of the dataset, and a summary of key surface temperature characteristics detected between 1st January and 31st December 2021 is presented. 4,277 thermal images were stacked to calculate the average (mean) pixel temperatures through 2021, to derive a summary thermal map (Figure 4.13a). The same stack was used to extract absolute maximum and minimum pixel temperatures (Figures 4.13b and Figure 4.13c, respectively), as well as the pixel standard deviation temperature over the same period (Figure 4.13d). In this section, analysis of each summary thermal map and the corresponding histogram of temperature distribution are used to explore the spatial distribution of temperatures upon the cliff face (Figure 4.14).

Figure 4.13a illustrates the thermal map of the mean temperatures detected during 2021. The average surface temperature was 8.7°C, the maximum and minimum average temperatures were 10.7 and 6.5°C, respectively, giving a 4.2°C range in average temperature across the ROI (Figure 4.14a). Although average values, a marked pattern of thermal variability between beds is clear, with bedded sandstones (BS) ~ 1°C hotter than the interbedded siltstones and sandstones (IBSS), demonstrating a clear bedding / lithological control on surface temperature. Indeed, bedding control on the distribution of temperature is notable in the central and west of the ROI mirroring the exposure bedding. Secondly, a clear variability indicative of aspect control on temperature was detected, with a zone of hotter temperatures extending vertically through multiple beds, as shown for example in the eastern side of the thermal map. Outside the ROI, no notable differences between the average temperatures of the solid bedrock or talus deposit were identified. To exemplify this, within the ROI (black line in Figure 4.13a) which, distinguishes between the free/fall face unit of the cliff (ROI) and the debris forming the talus, it was noticed that the average temperatures remained around ~ 7.5 to 8°C. Also, no temperature gradient from the base to the top of the cliff was identified, so average cooler temperatures associated with slash or wetting due to the proximity to the sea were not observed. Conversely, a clustering of zones of hotter temperatures were identified around the cliff base (dashed ellipses in Figure 4.13a), which appeared indicative of aspect and exposure to direct sunlight along the cliff base.

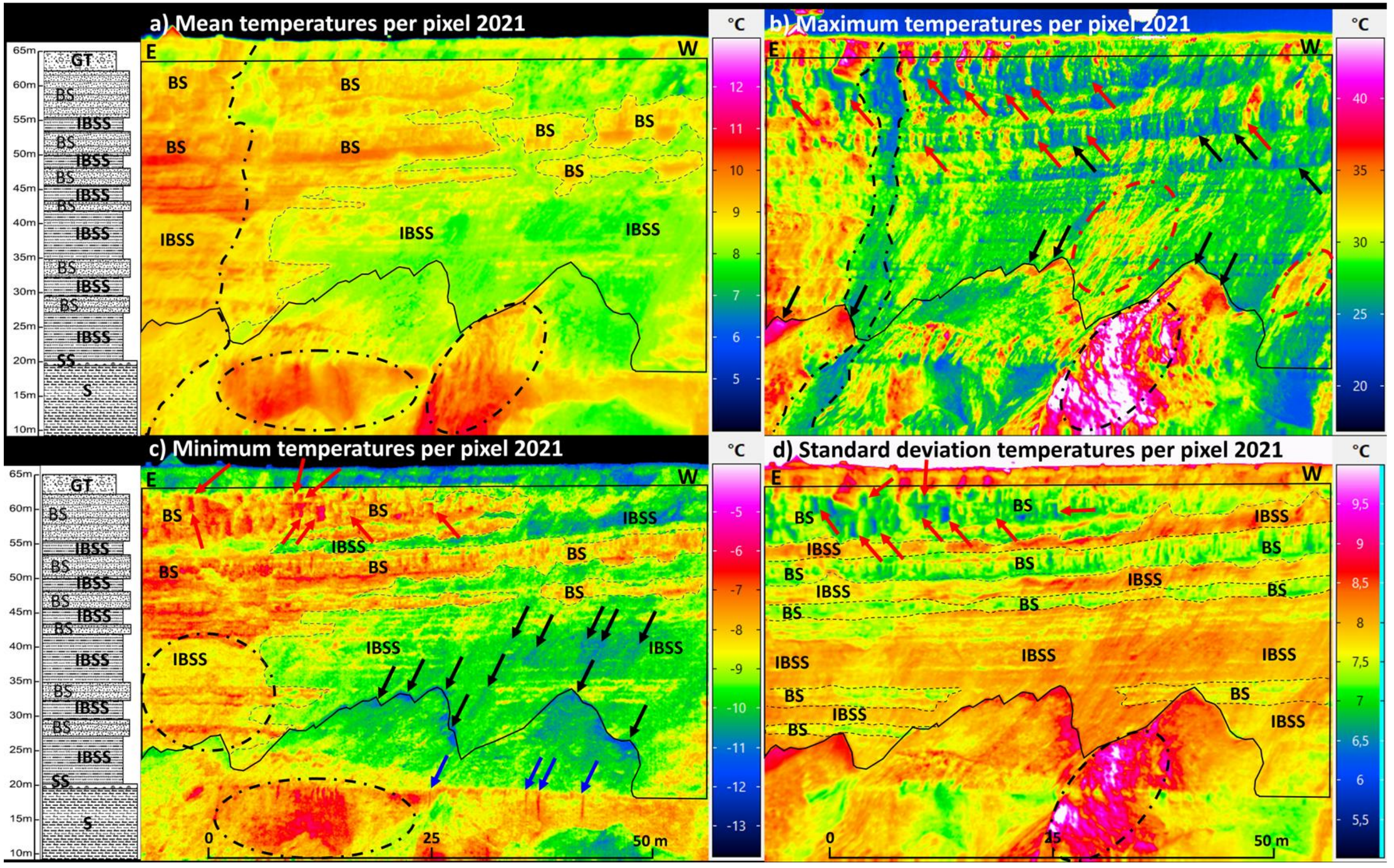
a) Mean temperatures per pixel 2021
b) Maximum temperatures per pixel 2021
c) Minimum temperatures per pixel 2021
d) Standard deviation temperatures per pixel 2021
E
W
°C
GT
BS
IBSS
SS
S
65m
60m
55m
50m
45m
40m
35m
30m
25m
20m
15m
10m
12
11
10
9
8
7
6
5
40
35
30
25
20
-5
-6
-7
-8
-9
-10
-11
-12
-13
9,5
9
8,5
8
7,5
7
6,5
6
5,5
0
25
50 m

Figure 4. 13: *Overleaf. Summary of surface temperatures detected between 1st January and 31st December 2021.* ***a)*** *Map of mean temperatures 2021.* ***b)*** *Map of maximum temperatures 2021.* ***c)*** *Map of minimum temperatures 2021.* ***d)*** *Map of standard deviation temperatures 2021. To the left, the stratigraphic log of the Early to Middle Jurassic sequence at East Cliff of Whitby is presented, where GT: Glacial till; BS: Bedded sandstones; IBSS: Interbedded sandstones and siltstones / carbonaceous muds; SS: Siderite sandstones; S: Shales (Figure modified from Figure 3 in Rosser et al., 2005, p. 365). Black boundary lines show the Region of Research (ROI) for this study. Near horizontal dashed lines show bedding controls on temperatures. Black dot-dashed ellipses / dot-dashed vertical lines show large-scale aspect controls (≥ ~ 10 m). Red dot-dashed ellipses show hottest temperatures over relatively uniform or rectilinear slope sections. Red arrows show small-scale aspect controls (≥ ~ 1.0 m). Black pointing-up arrows indicate shadowing effect generated by hanging rock-blocks of BS. Black pointing-down arrows show concave slope zones and/or the contact between the free face and the talus slope units where hottest or coolest thermal contrast were detected. In each image, the Eastern and Western directions are shown using the letters E and W.*

The thermal maps of the maximum temperatures (Figure 4.13b), and the corresponding histogram indicates that the average maximum temperature was 28.5°C, but perhaps remarkably the absolute maximum recorded surface temperature within the ROI was 40.2°C (Figure 4.14b). The pattern of maximum temperatures shows similar spatial distribution to the average temperatures (Figure 4.13a), through for instance the distinctive large-scale aspect control with the hottest temperatures clustered on the east side of the ROI, extending vertically across multiple beds, and adjacent to an extended area of the coolest again reflecting large-scale (≥ 10 m) aspect-control on surface temperatures.

Three additional thermal characteristics are apparent in the maximum temperature data: (1) Small-scale (≥ 1 m) aspect control on temperature, as perpendicular or rectangular proximal zones, such as those seen along the top of the ROI coincident with angular sandstone blocks with very different orientation faces. The nature of the temperature change in these areas is seen to respond to the angular nature of these blocks (indicated as red arrows around the top of the cliff in Figure 4.13b). (2) The lowest maximum temperatures followed the sub-horizontal bedding of the cliff sandstones (BS), and in particular the basal limit of these exposures, demonstrating not only bedding control but also local shadowing effects produced by overhanging blocks (highlighted by upwards-pointing black arrows in Figure 4.13b). (3) Throughout relatively planar or rectilinear cliff surface which dominate the central and west sections of the ROI (IBSS), narrow vertical clustering of highest maximum temperatures were detected (indicated as red dot-dashed ellipses). Outside the ROI, this thermal pattern also extends into the top of the debris forming the talus, below the contact with the free face of the cliff, which spatially correspond with surficial deposits (such as colluvium), transported from the top of the cliff, covering some areas of the IBSS and talus, as demonstrated below in Figure 4.17.

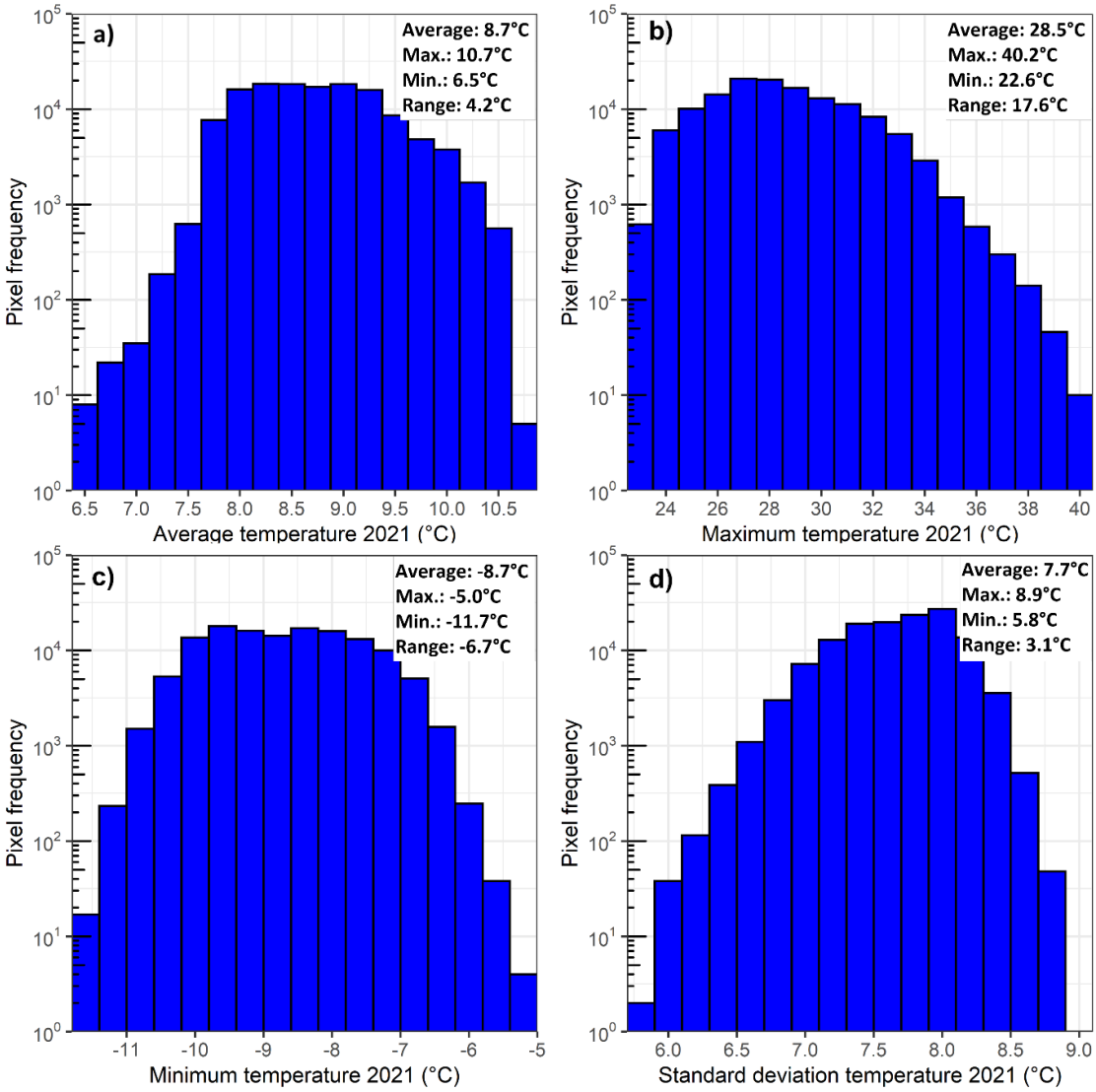

Figure 4. 14: *Histograms of surface temperatures detected between 1nd January and 31st December 2021. a) Histogram of average (mean) temperatures 2021. b) Histogram of maximum temperatures 2021. c) Histogram of minimum temperatures 2021. b) Histogram of standard deviation temperatures 2021. Histograms were extracted within the Region of Research (ROI) of this study.*

The minimum temperatures map for 2021 and corresponding histogram shows that the average minimum temperature was -8.7°C, but significantly, the absolute minimum temperature was -11.7°C. Such low temperatures potentially hold implications for the development of freezing conditions if these conditions persist over multiple hours or days (Figure 4.14c). The thermal map of minimum temperatures shows patterns seen in the averages temperature data (Figure 4.13a). The highest minimum temperatures (~ -6 to -8°C) were preferentially clustered across the sub-horizontal structure of bedded sandstones (BS), while the lowest minimum temperatures (~ -9 to -11°C) were throughout the interbedded sandstones and siltstones (IBSS). Aspect also clearly controls large scale variations notably towards the east side of the ROI (indicated as black dot-

dashed ellipses), in addition to small-scale variations association with exposure of individual jointing and fracture surfaces particularly at the top of the ROI (see red arrows in Figure 4.13c).

The minimum temperature data provides further detail on the nature of the surface thermal characteristics, notably: (1) The lowest minimum temperatures were clustered both across the relatively planar or rectilinear cliff areas IBSS (central-west zone of the ROI), or clustered across the top of the talus debris where a sharp thermal gradient from ~ -10 to -12°C was detected (downwards arrows in Figure 4.13c). (2) Outside the ROI, the highest minimum temperatures clustered into vertical bands with values ≤ -7°C at the base of the cliff coincident with a thick bed of shales (indicated as blue arrows).

Figure 4.13d shows the standard deviation in temperature for each pixel to assess any variability in the distribution of temperatures experienced across the cliff. The histogram of the standard deviation shows an average standard deviation value of 7.7°C, and the maximum and minimum of 8.9 and 5.8°C, respectively, reflecting a relatively high degree of temperature variability through the year across the whole cliff face (Figure 4.13d). The interbedded sandstones and siltstones (IBSS) showed greatest variability in temperature (s.d. values of 8.0 - 8.5°C), whereas sandstones alone were more consistent (BS, s.d. 6.5 - 7.5°C), suggesting a greater differentiation in temperature characteristics between contiguous sub-horizontal beds. Interestingly, standard deviation in temperatures was less sensitive to large-scale aspect controls the signal of which was almost absent relative to the average and maximum temperature maps (Figures 4.13a and 4.13b). In addition, overhanging blocks of sandstone (BS), located towards the upper-east side of the ROI showed the lowest standard deviation (~ 6°C), but again, small-scale aspect controls were apparent (indicated as red arrows in Figure 4.13d). Conversely, outside the ROI, the debris at the top of the talus deposit, as well as aspect-control along the base of the cliff (black dot-dashed ellipses) showed the highest standard deviation in temperature (~ 9 - 10°C).

Finally, a map of the temperature range per pixel (the subtraction of the minimum per-pixel temperature from the maximum across 2021) shows the magnitude and distribution of the amplitude of temperature changes experienced (Figure 4.15). The map and corresponding histogram (Figure 4.16) shows that the average difference in temperature across all pixels was 37.2°C, but remarkably the maximum difference was 50.0°C, demonstrating surprisingly high fluctuations in temperature, particularly given the temperate coastal location of the study site. Notably, fluctuations of this scale are not observed in meteorological records of air temperature

at this location, and so using atmospheric temperature as a proxy for rock surface temperature significantly truncates the distribution of observed surface temperatures.

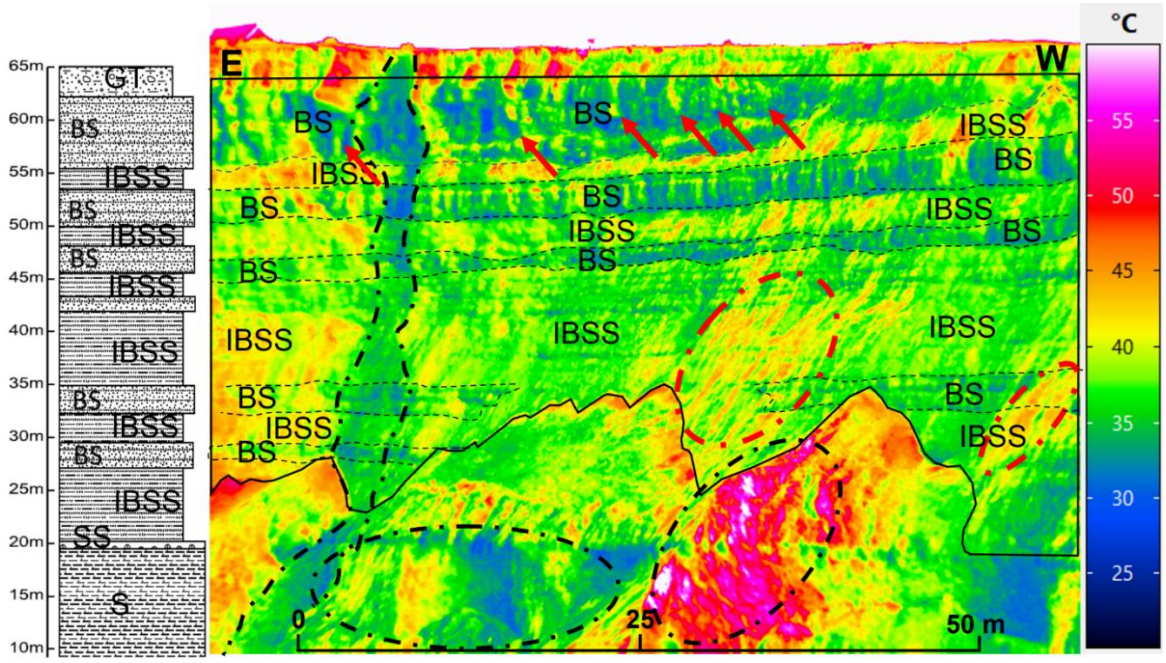

Figure 4. 15: *Temperature difference map 2021 (Temperature range per pixel). The stratigraphic log of the Early to Middle Jurassic sequence at East Cliff of Whitby is presented, where GT: Glacial till; BS: Bedded sandstones; IBSS: Interbedded sandstones and siltstones/carbonaceous muds; SS: Siderite sandstones; S: Shales (Figure modified from Figure 3 in Rosser et al., 2005, p. 365). Black boundary continuous line shows the Region of Research (ROI). Near horizontal dashed lines indicates bedding controls on temperatures. Black dashed ellipses / dashed vertical lines show large-scale aspect controls. Red dashed ellipses show hottest temperature differences over rectilinear slope zones. Red arrows show small-scale aspect controls. The Eastern and Western directions are shown using the letters E and W.*

The map of temperature range per pixel also provides further insight on the nature of the surface thermal characteristics: (1) The greatest temperature differences were detected across the major slope surfaces, exhibiting both large-scale (> ~ 10 m) or small-scale (< 1 m) aspect control. For example, large-scale aspect control particularly on the east-side of the ROI showed temperature differences ranging between ~ 40 and 45°C. (2) Lower temperature differences (~ 25 - 35°C) were identified preferentially within the bedded sandstones (BS), and were particularly coincident with surfaces located below overhanging angular blocks of sandstone, towards the upper side of the cliff. This suggests the occurrence of small-scale aspect/shadow controls inducing lower temperature differences; (3) Overall, the greatest and lowest temperature differences clustered systematically in areas where large-scale and small-scale aspect controls were prevalent and coincident, suggesting that aspect exerts more control over extreme

temperature values than the other metrics considered above. Conversely, in this study site, bedding / lithological control influences temperature differences to a notable but lesser degree.

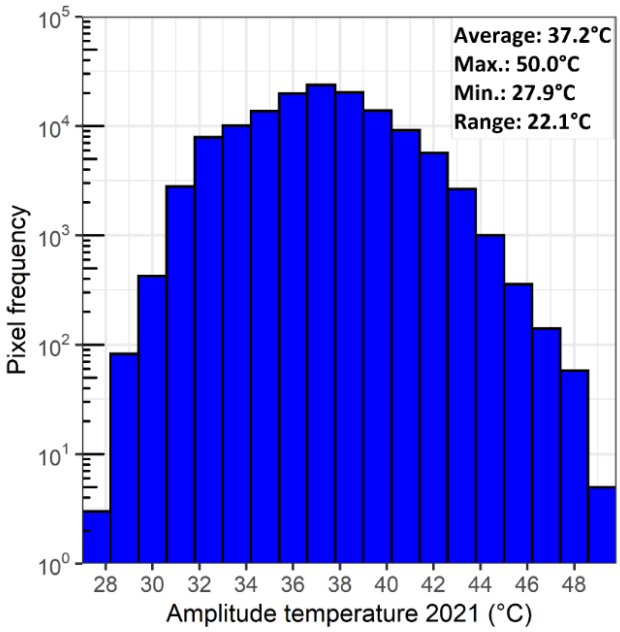

Figure 4. 16: *Histogram of the temperature difference map calculated between the maximum and minimum temperatures detected in 2021 (Figure 4.15). Histograms were extracted for the Region of Research (ROI) of this study*

To allow an evaluation of the links between the thermal characteristics identified and general rock-mass properties, Figure 4.17 shows a high-resolution colour photograph of the cliff face, coupled with the stratigraphic log showing the main lithological beds. The approximate boundaries between the principal sub-horizontal discontinuities also help here to define the relative thickness of each bed and help to identify of two key features. First, there appears to be an association between the surface temperature and the exposure colour whereby lighter beds, such as bedded sandstones (BS), showed the highest average temperatures since, regularly 1°C warmer than adjacent interbedded sandstones and siltstones (IBSS) (Figure 4.13a). Similarly, the highest minimum temperatures (~ -6 to -8°C) were also preferentially within BS (Figure 4.13c) alongside a lower standard deviation in temperature (~ 6.5 to 7.5°C) (Figure 4.13d). Although lighter-coloured beds exhibited higher average temperatures, these beds were associated with the lower overall temperature differences (~ 25 - 35°C) (Figure 4.15). Conversely, darker beds, such as the interbedded sandstones and siltstones (IBBS), showed an opposite pattern with the lowest average temperatures (7.5 – 8.5°C), the lowest minimums (~ -9 to -11°C), a higher standard deviations (~ 8 .0- 8.5°C) and correspondingly, in areas where large-scale aspect controls were absent, greater temperature differences (~ 35 - 40°C).

Secondly, associations between the cliff surface temperatures, the cliff face topography, and rock-mass structure have been identified. Higher average temperatures and higher minimum temperatures were detected across medium-grained bedded sandstones (BS), which corresponded with protuberant surfaces, widely-spaced discontinuities (vertically and horizontally) and vertical heterogeneity of fractures associated with horizontal bedding. These combined control the size of the overhanging blocks and from a thermal perspective generate large local scale variation in orientation with respect to the general aspect of the cliff face (small-scale aspect controls). Towards the top of the cliff face, temperature variations due to small-scale aspect control correspond to protuberant rock surfaces (e.g., Figures 4.13b, c, d, and Figure 4.15). These areas also correspond to local reductions in temperature due to shadowing. Conversely, lower average temperatures and the lowest minimum temperatures were identified over fine-grained faces of interbedded sandstones and siltstones (IBSS), coincident with indented surfaces, small-scale sub-horizontal discontinuities, and the absence of evident vertical fractures (cm <), which combined generate a lower degree of surface roughness as compared to BS, and so, producing a lower degree of variation in cliff surface temperature.

Figure 4.17 demonstrates that the narrow vertically-oriented clustering of the highest and lowest minimum temperatures (see: Figures 4.13b, c), are spatially coincident with light-coloured colluvium draped over the relatively rectilinear cliff surface exposure of IBSS, or are found within the colluvium located at the top of the talus. Within the ROI, this material represents features that were detected either as warm or cold thermal anomalies relative to the lower temperatures characteristics of the darker IBSS exposures. This anomaly suggests that uncompacted colluvium is highly sensitive to temperature variations conditions, possibly due to a high moisture content, as seen in the average temperature maps previously discussed. The deposition of colluvium is to some extent controlled by the general topography of the cliff face (i.e., rectilinear towards concave slope planes), which may also control the flow of water or moisture from the cliff face, again influence the thermal properties at this location (the thermal anomalies affected by colluvium were highlighted as red dot-dashed ellipses in Figures 4.13b, black arrows in Figure 4.13c, and red dashed ellipses in Figures 4.15 and 4.17).

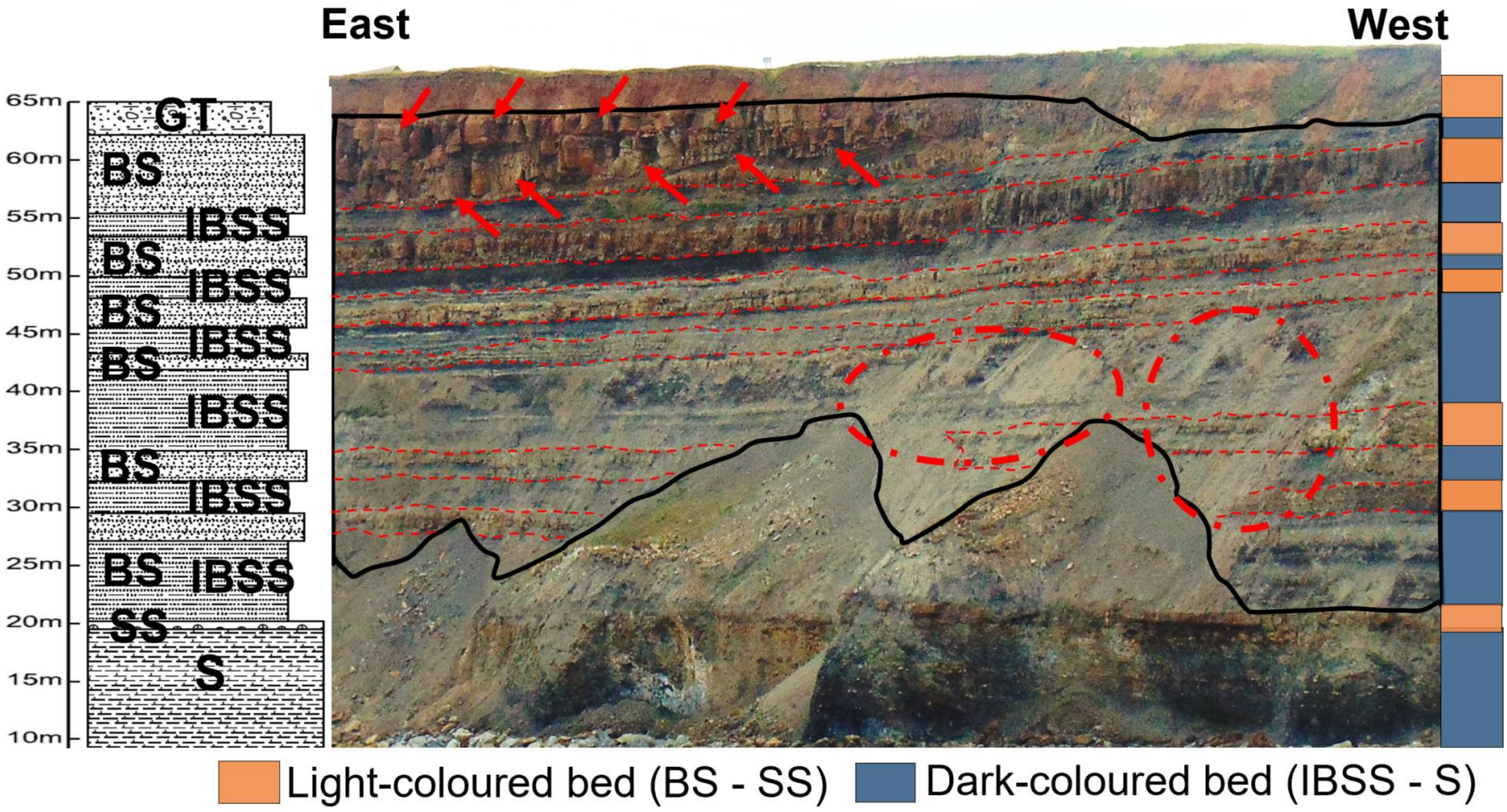

Figure 4. 17*: High-resolution photo of the cliff face illustrating the distributions of the main beds by colour. To the left, the stratigraphic log of the Early to Middle Jurassic sequence at East Cliff of Whitby is presented, where GT: Glacial till; BS: Bedded sandstones; IBSS: Interbedded sandstones and siltstones / carbonaceous muds; SS: Siderite sandstones; S: Shales (Figure modified from Figure 3 in Rosser et al., 2005, p. 365). To the right, the approximate thickness of the beds by colour. Black boundary continuous line shows the Region of Research (ROI) for this study. Near horizontal (red) dashed lines indicate the approximate boundaries between beds. Red arrows points hanging-rock blocks of BS where small-scale aspect controls were detected. This zone correlated with widely-spaced sub-horizontal discontinuities, vertical fractures, and differing orientations (aspect) regarding the general aspect of the cliff face (20° N). Dot-dashed red ellipses show the location of colluvial deposits, inducing thermal anomalies over the characteristic temperatures of the IBSS. At the top, the approximate east and west directions of the sun path.*

4.4 Summary

In summary, a high-resolution high-frequency rock surface temperature monitoring system has been established to run in parallel to the constant 3D laser scanning at East Cliff Whitby. The resulting data has been processing using a filtering and then calibration protocol, and the pre-processed data has then been analysed to assess the apparent sensitivity to small and large spatial and temporal variations in cliff surface temperature. Using five summary thermal maps that were composed from a total of 4,277 corrected thermal images, we have characterized emergent thermal patterns and demonstrated that the nature of the surface thermal activity detected during the whole monitored period. The primary observations from this initial appraisal of this dataset shows that:

- Bedding/lithology controls variability of surface temperatures that adhere to the shape, colour, and rock-mass structure of each bed (e.g., sandstone were 1°C hotter, on average, than the interbedded sandstones).

- Aspect control generates a preferential clustering of both the highest and lowest temperatures on the cliff, resulting in a pattern that extends vertically across multiple beds. This control therefore overrides the influence of rock-type (large-scale aspect controls, > ~ 10 m). Aspect control is also seen at a more local scale, where small (> ~ 1 m) but high gradients in temperature reflect the surface that results from bedding, discontinuities and fracturing of the surface. For example, highly angular exposures of sandstone show significant difference of temperature associated with different dominant joint sets.

- Rock-mass properties and topographic controls influence the rock-mass surface temperature, including the composition, colour, discontinuity spacing and orientation (horizontal and vertically), and the resulting presence of indentations (concavities) or protuberances (convexities).

- Surficial deposits, such as colluvium, generate thermal anomalies with higher temperatures than the underlying bedrock (e.g., 1°C), and their distribution appears potential related to the retention of moisture.

- Some sections of the rockface were subject to extreme temperature ranges during the year, ranging from ~ +40.2°C for a pixel showing maximum temperature to -11.7°C for a pixel displaying minimum temperature but these were not spatially coincident (and 50°C for the maximum range for the individual pixel that displayed the highest differences between the minimum and maximum temperature in 2021) reflecting the combined superimposition of the controls identified above. Such a scale of temperature variability is not currently reflected in the literature on rock face fracturing or collapse in similar environments to the study site, and so the implications of such a variability represents a significant gap in current understanding which will be explored in the following chapters.

Chapter 5: The characteristics of cliff surface temperature change through time

5.1 Introduction

This chapter presents the analysis of this IRT dataset to investigate the variability of surface cliff temperatures through 2021 (Thesis Objective 4 -O4). As such, a characterization of the cliff surface temperature based upon time-series of hourly IRT imagery through 2021 is presented (Section 5.2). A series of summary spatial samples and statistical derivatives from the IRT imagery are used to examine seasonal and then diurnal variability (Section 5.3). IRT maps of the mean temperatures and rates of change are finally considered with respect to a stereographic projections of the cliff surface to examine the nature of aspect controls on the cliff surface temperature (Section 5.4). The surface temperatures reported below have an accuracy of $\pm$2.0°C (see section 4.2.1 for further details, Chapter 4), and the terms *warm* and *cold* are used in a relative sense.

5.2 Temperature changes through the year

Monitoring studies of rock-slope temperature changes using infrared cameras (IRT) have been usually limited to relatively short monitoring periods (e.g., < 1 day), rarely capture a complete spectrum of the diurnal thermal cycle (e.g., are commonly restricted to daylight), infrequent epoch based monitoring (e.g., one image per month), or are limited to an assessment of a small surface area e.g., < 10 m^2) (e.g., Wu et al., 2005; Pappalardo et al., 2016; Pappalardo & Mineo, 2017; Fiorucci et al., 2018). Importantly, one consequence is that the frequency, duration and timing of IRT data capture is often at odds with the time scales of variability of environmental triggering conditions. Therefore, to gain insight into rockfall triggering, I seek to collate and analyse a high-frequency (1 hour) long-term (1 year) dataset on cliff surface temperatures using time-series IRT imagery.

Data from IRT surveys of rock-slopes commonly report results using either discrete mapping windows from which summary statistics are reported; horizontal or vertical profiles that follow either specific lithologies analogous to scanlines, or gradients, such as up cliff; or discrete points or pixels of interest (e.g., Teza et al., 2012; Frodella et al., 2017; Guerin et al., 2019;

Loiotine et al., 2022). As such, within the wider region of interest (ROI) captured by the sensors deployed in this study, a sampling strategy based upon four extracts from the IRT data was developed (Figure 5.1):

- First, a general rectangular window (*GW*) that covered the majority of the imaged cliff area (~ 1,410 m^2 out of a total of 1,730 m^2), which spanned all lithological beds, as well as key discrete point/pixels of interest such as the point of maximum and minimum temperatures in 2021 (+40.0 and –11.7°C, respectively, see Figure 5.1). *GW* also encapsulated the locations of the maximum and minimum hour-by-hour temperatures difference (Chapter 4, Section 4.3).

- Second, two 50 m^2 mapping windows that covered each of the main outcropping beds were delineated: *W1-BS* captures the bedded sandstones, while *W2-IBSS* the interbedded sandstones and siltstones.

- Third, complementarily to the bed-specific mapping windows, two horizontal profiles of 34 m were positioned across each bed: *PR1-BS* across the bedded sandstones, and *PR2-IBSS* the interbedded sandstones and siltstones.

- Fourth, to track temperatures across discrete point/pixels of interest a series of monitoring points were identified. *P1Max, P2Min and P3Mean* represent the position of the maximum, minimum and mean temperatures 2021. *P4Maxdiff* and *P5Mindiff* represent the maximum and minimum temperature differences, as extracted from the temperature difference map (Chapter 4, Section 4.3).

The sampling strategy was used to examine the temporal evolution of temperatures, as described in Sections 5.2 and 5.3 of this chapter.

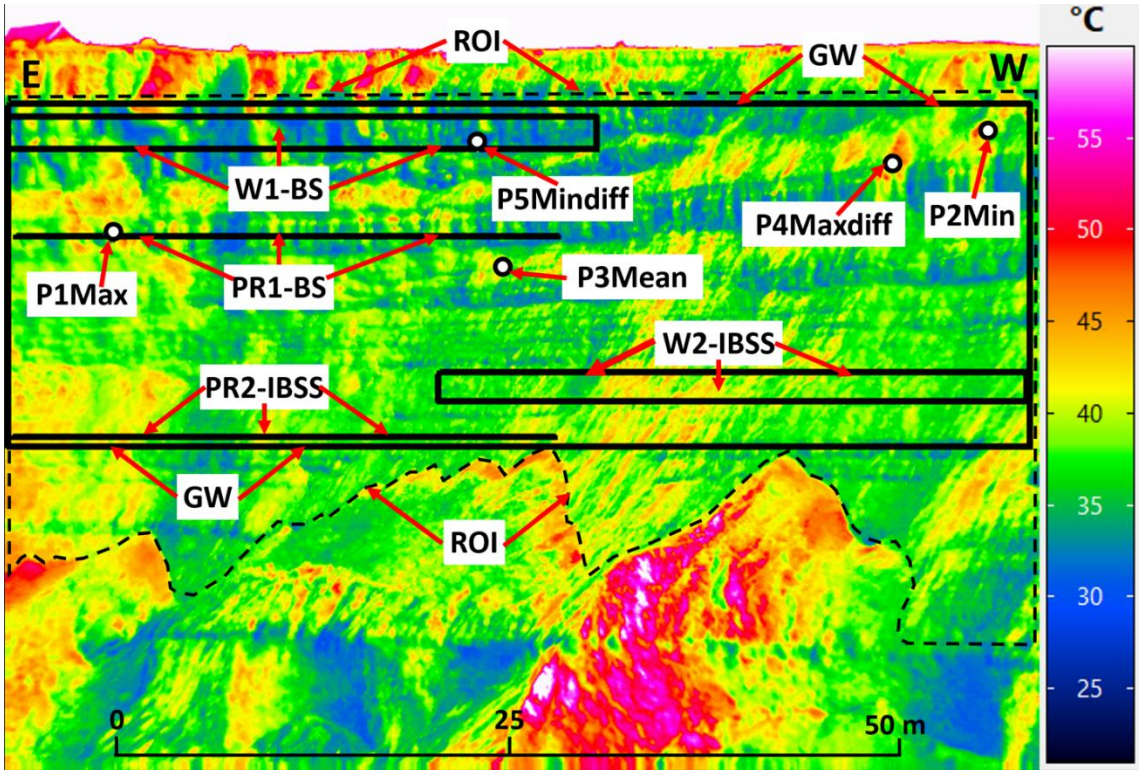

Figure 5. 1: *Sampling zones of temperature measurements across the Region of Research (ROI). The ROI is showed using dashed lines. Inside the ROI, the General Window of assessment (GW) is showed as a black bounding box (~ 1410 m2). W1-BS shows the mapping window 1 across Bedded Sandstones (BS). PR1-BS is a horizontal profile of ~ 34 m length across BS. W2-IBSS indicates the mapping window 2 across Interbedded Bedded Sandstones and Siltstones (IBSS). PR2-IBSS is a horizontal profile of ~ 34 m length across IBSS. P1Max, P2Min. and P3Mean, represent the location of the individual pixels showing the maximum, minimum and mean temperatures detected in 2021, which were extracted from the surface maps of maximum, minimum and mean temperatures, respectively (Figure 4.13 in Section 4.3). P4Maxdiff and P5Mindiff represent the position of the pixels of maximum and minimum difference temperature extracted from the differential surface temperature map (Figure 4.15 in Section 4.3). The central location of these points is highlighted using white and black dots. Red arrows indicate each area, profile, or pixel of measurement. The thermal scene presented here is the temperature difference map 2021 (Figure 4.15, see Section 4.3, Chapter 4) and thus, explaining the high annual temperature range across the cliff face.*

Figure 5.2a shows the variability in temperatures through 2021 for the mean, maximum and minimum temperature observed within *GW*. Overall, a high degree of variability in surface temperature was observed, with values ranging between a low of -11.7°C in winter, to a maximum of 40.2°C in summer, yielding an intra-annual range of 51.9°C. Through the year, daily temperature oscillations had a lower magnitude in winter, but increased gradually into and out of summer. For example, the seasonal temperature range was 27.3°C in winter, but notably higher in spring as the range was 49.9°C (i.e., the highest of the year, reflecting high surface temperature variability and the transitional character of this season), 36.4°C in summer, and 31.8°C in autumn,

again, reflecting the transitional behaviour of the later season (see Table 5.2). As such, the average temperature in winter was 0.1°C, while in summer was 17.0°C. Day-to-day extreme temperatures were highest in spring and summer with fluctuations ranging from 40 to 10°C (Δ = 30°C), but in winter ranged from 5 to -5°C were identified (Δ = 10°C), indicative of a lower range in surface temperatures in winter (Figure 5.2a). Therefore, the range in temperatures upon the cliff surface varied significantly during the year and so the exposition to thermal actions (Figure 5.2a).

Remarkably, Figure 5.2a shows that minimum and mean surface temperatures in winter, spring and autumn commonly dropped below 0°C. To exemplify this, 1,162 out of a total of 4,277 hourly thermal images (~ 27% of the dataset) showed pixels with minimum temperatures <0°C. Uninterrupted periods with sustained minimum temperatures <0°C were observed to last between 2 and 18 days (e.g., 2nd to 18th January, 186 h). After a data gap of 3 days in January, uninterrupted minimum daily temperatures <0°C were observed between 21st January and 1st February (12 days). Also, minimum temperatures <0°C were observed to occur intermittently between 2nd January (winter) until 18th May (mid-spring), and then again from 23rd November (late-autumn) until 29th December (winter). Minimum temperatures approaching ~ -5 or even -10°C were frequently detected in spring and autumn, holding key similarities with the magnitude of the minimum temperatures detected in winter. As a result, the dataset also demonstrates that the cliff face is susceptible to both short term and sustained periods of low temperatures for almost six months of the year.

Conversely, Figure 5.2a also illustrates that relatively warm surface temperatures were observed between mid-spring and throughout most of the summer (mean temperatures ≥ 20°C, maximum temperatures ≥ 25°C), with peaks in both seasons of similar magnitude (maximum temperatures ~ 40°C); the period experiencing the highest extreme warm temperatures was therefore not just confined to summer. Surface temperatures of ≥ 30°C were often observed in late-spring and in the lead up to mid-summer. Mean temperatures increased through spring and summer, rising from ~ 9°C to 17°C. Multiple uninterrupted days with a mean surface temperature >10°C occurred between 5th June and 27th September (approximately four months), and included 1,515 hourly thermal images (~ 35.4% of the dataset). This period represents the proportion of the year in which mean temperatures ≥ 20°C, or maximum temperatures ≥ 25°C, were detected. Notably, 261 hourly thermal images (~ 6% of the dataset) had mean temperatures ≥ 20°C, which occurred between late-spring and mid-summer, while 428 images (~ 10% of the dataset) had maximum temperatures ≥ 25°C , occurred preferentially between mid-spring and late-summer.

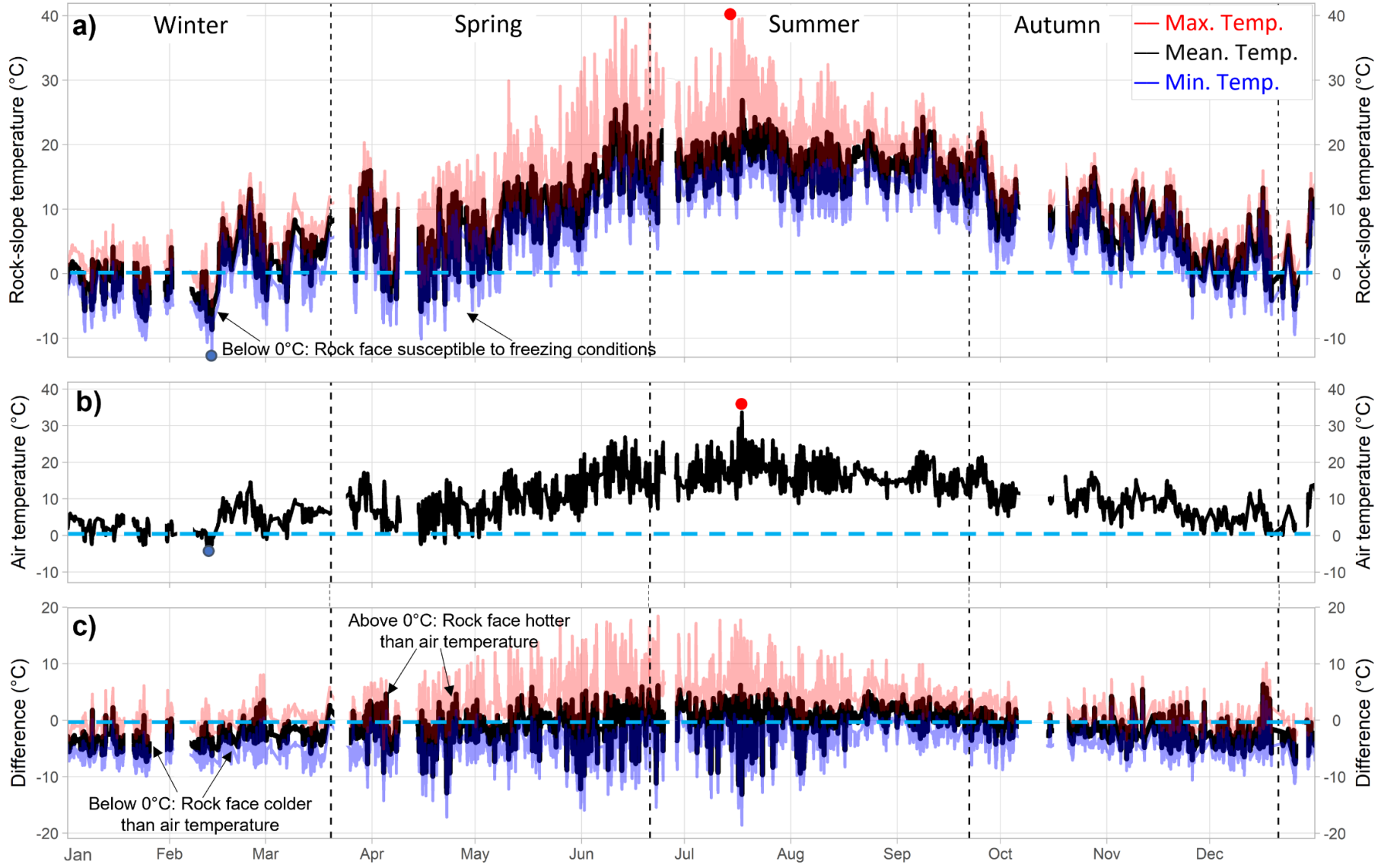
a)
Winter
Spring
Summer
Autumn
Max. Temp.
Mean. Temp.
Min. Temp.
Rock-slope temperature (°C)
Below 0°C: Rock face susceptible to freezing conditions
b)
Air temperature (°C)
c)
Difference (°C)
Above 0°C: Rock face hotter than air temperature
Below 0°C: Rock face colder than air temperature
Jan
Feb
Mar
Apr
May
Jun
Jul
Aug
Sep
Oct
Nov
Dec

Figure 5. 2: *Overleaf. Temperature changes through the year at 1 h of thermal data resolution. a) Rock-slope surface temperatures detected within the General Window of assessment (GW) of the Region of Research. b) Air temperatures collected at the top of the cliff face. c) Difference between the air temperatures and the maximum (Red), mean (Black) and minimum (Blue) slope temperatures, respectively. Approximate boundaries between astronomical seasons are show using vertical dashed lines. Blank zones of the time-series indicate principal gaps created during data collection or filtering. The dates showing the maximum and minimum environmental and surface temperatures of the year are highlighted using red and blue dots, respectively. In Figures a) and b) the horizontal dashed blue line indicates the temperature threshold of 0°C to highlight susceptibility of frost conditions over the cliff face. In Figure c) the horizontal blue lines highlight the dates in which the surface temperature of the rock face was hotter or colder than the air temperature.*

The range in temperatures upon the surface varied significantly during the year (Figure 5.2a). Oscillations in temperature within a single day between cold (<0°C) and warm surface conditions (e.g., ≥ 10°) were common, particularly from winter up to mid-spring, and then from late-autumn. During winter, the daily temperature range, was on average between -3.0 and 3.0°C (Δ = 6.0°C), whereas by April temperatures fluctuated between ~ -8.8°C and 17.0°C were observed (Δ = 25.8°C), but these were interspersed with days with lower ranges in temperature between ~ -6.0°C and 10.0°C, or ~ -1.0°C and 15.0°C (Δ = 16.0°C). A similar pattern albeit with lower mean within day temperature ranges, was also observed in autumn with temperatures between ~ -6 and 13°C (Δ = 18.0°C), or between -6 and 6°C (Δ = 12.0°C) towards late autumn. Therefore, the coincidence in a single diurnal cycle of very cold (e.g., -5.0°C) and very warm (e.g., 10°C) conditions may hold implications for temperature gradients, heat transfer, and the development of freeze-thaw activity, which may contribute to thermomechanical mechanisms facilitating fracturing and slope failure.

Table 5.1 shows a summary of the cliff surface temperatures associated with freeze-thaw activity 2021. Following Schmidlin et al., (1987), a day was considered a freeze-thaw day if the daily minimum surface cliff temperature was ≤ -2.2°C and the maximum temperature was above zero. Then, the number of these days were calculated over each season. Notably, the majority of the freeze-thaw days was detected in winter, as a total of 49 days (70% of the days with availability of filtered and calibrated thermal imagery) experienced freeze-thaw cycles. In this season, the cliff face was exposed to total of seven days of uninterrupted freeze-thaw cycles (12th – 18th January), and the maximum surface range for freeze-thaw fluctuated between ~ -6.9 and 12.2°C the 28th of February (Δ = 19.1°C). Interestingly, while spring showed a lower number of days subject to freeze-thaw cycles (a total of 29 days, equating 35% of the days with calibrated thermal imagery), this season had the largest number of days with uninterrupted freeze-thaw cycles (10 continuous days, between 14th and 23rd April), an also the highest surface range for freeze-thaw, as these fluctuated between ~ -8.8 and 17.0°C the 22nd of April (Δ = 25.8°C). Overall,

these data not only demonstrate that winter had more times in which freeze-thaw cycling occurred, but also that spring showed the more extreme ranges of temperatures associated with freeze-thaw, which may be critical for rock fracturing. This is further discussed in Chapter 6.

Following Schmidlin et al., (1987) but in this case, by considering the total number of freeze-thaw days with respect to the measurement accuracy of the thermal camera (±2.0°C, see Section 4.2.1, Chapter 4) so that in this instance, a day was considered a freeze-thaw day if the daily minimum surface cliff temperature was lower than -4.4°C and at the same time the maximum cliff temperature was above +2.0°C (i.e., not considering any measurement within ±2°C above or below the threshold of 0°C), an expected reduction in the total number of freeze-thaw days was observed, as now a total of 35 days (previously 50) experienced freeze-thaw cycles in winter (i.e.,49% of the days with availability of calibrated thermal imagery), but the days with uninterrupted freeze-thaw activity remains the same (7 days). A similar pattern was observed in spring, as the total number of freeze-thaw days was 18 days (previously 29 days) (Table 5.1). Therefore, even by considering more extreme thermal scenarios (-4.4 to + 2.0°C), the rock face was exposed to notable thermal variability that is typically associated with freeze-thaw temperatures and so, rock cracking.

Table 5. 1: *Summary of cliff surface freeze-thaw activity 2021.*

Season	Total number of freeze-thaw days*	Total number of days with IRT data	Percentage of freeze-thaw days (%)	Total days with uninterrupted freeze-thaw	Maximum range of freeze-thaw (°C)	Total number of freeze-thaw days over the error of ± 2°C**
Winter	50	71	70	7	19.1	35 (49%)
Spring	29	83	35	10	25.8	18 (22%)
Summer	0	90	0	0	0	0
Autumn	15	73	21	6	15.3	10 (14%)
Annual	94	317	30	10	25.8	63 (20%)

Note: * is total number of freeze-thaw days that do not consider the accuracy of the thermal camera. ** is the total number of freeze-thaw days that consider the accuracy of the camera, where the percentage of freeze-thaw days with respect to the total number of days with IRT data is now showed in brackets.

Figure 5.2b shows the change in air temperatures proximal to the cliff face collected in parallel to the IRT imagery. Whilst the overall pattern of the air temperatures was similar to the mean surface temperature, on an hour-by-hour basis, the magnitude of air temperature changes showed significant differences throughout the year. For example, the maximum air temperature in 2021 was ~ 34°C on 17th July at 17:00, whilst at this time the maximum surface temperature was ~ 39°C (Δ = +5°C). The maximum surface temperature of the year was ~ 42°C on 14th July

at 20.00 h, when the air temperature was 25.6°C (Δ = -16.4°C). Similar differences were observed for the coldest temperatures. The lowest air temperature was ~ -3.1°C on 12th February at 05:00 but the lowest surface temperature was ~ -12°C, recorded one day later (13th February at 08:00 h), when the air temperature was ~ -2.4°C (Δ = -9.6°C). This demonstrates that the surface temperature of the cliff face can differ considerably from that of the surrounding air, implying that the latter is a poor proxy for the former.

Furthermore, Figure 5.2c plots the difference between air and the maximum, mean, and minimum cliff surface temperatures. From this dataset, three distinctive patterns were observed:

First, differential temperatures between the cliff surface and the air < 0°C were common through the winter and most of autumn, which suggests that the rock face was on average ~ -3.4°C cooler than the air. Differences of up to -10°C were also observed.

Second, an apparent inversion of this temperature difference behaviour was detected in spring and summer. During these periods differential temperatures > 0°C were observed, where on average, the cliff was ~ 5.5°C warmer than the air. On the hottest days differential temperature of up to ~ 18°C were observed.

Third, the hotter the season, the higher the temperature differences between the cliff surface and the air. For example, in winter the range in differential temperature fluctuated between ~ -10 and 8°C. During spring and summer, this increased to temperature differentials between ~ -18 and 18°C.

As a result, the dataset shown in Figure 5.2c shows that the IRT data from the cliff face shows different patterns of temperature variability as compared to air temperatures alone, and so is potential more appropriate for assessing the nature of temperature changes upon the cliff face itself.

To consider both the magnitude and spatial distribution of cliff surface temperatures at the time of the warmest surface conditions, Figure 5.3a shows the IRT scene at the time of maximum surface temperature in 2021 (14th July at 14:00h). Within the ROI, the maximum temperature was ~ 40.2°C upon an outcrop of the bedded sandstones (BS). Also, the mean and minimum temperatures were ~ 21.5°C and 13°C respectively, yielding an hour-by-hour temperature range (from maximum to minimum) of 27.2°C. Interestingly, marked large-scale aspect controls were detected that partition the cliff into clear zones of more consistent temperatures. These zones had length scale of ~ 10 m. Zones of warmer and colder temperatures mapped vertical sections crossing multiple lithological beds. Whilst the warmest surface

temperatures were vertically aligned from the bottom to the top of the cliff face, notably on the eastern side of the ROI. The coolest temperature zone was also located towards the mid-west side of the ROI. At the base of the cliff, just outside the GW, temperatures ranging between 40°C and 50°C were detected within a bed of shales, again showing large-length-scale aspect control. These images show that large-scale aspect controls hold an important influence on the magnitude and spatial distribution of maximum temperatures during summer. I further explore these patterns behaviour in the Section 5.4.

Figure 5.3b shows the IRT scene including the minimum temperature of 2021 on (13th February at 08:00 h). Within the ROI, the minimum temperature was ~ -11.7°C recorded on the interbedded sandstones and siltstones (IBSS). At this time, the mean and maximum temperatures was -8.7°C and -5.0°C, respectively showing a -6.7°C temperature range. This range was considerably smaller than that observed during the maximum conditions (Δ = 27.2°C). Importantly, this image show a marked bedding control, with surface temperatures tracing the sub-horizontal structures of either BS or IBSS, whereby BS surfaces had warmer temperatures than IBSS. In conditions opposite to those in summer, this indicates that bedding control had a significant influence on the magnitude and spatial distribution of temperatures during winter. Again, this behaviour is further examined in the Section 5.4. Table 5.2, below, shows a seasonal summary of the mean, maximum, minimum, and seasonal ranges in surface temperatures detected in 2021.

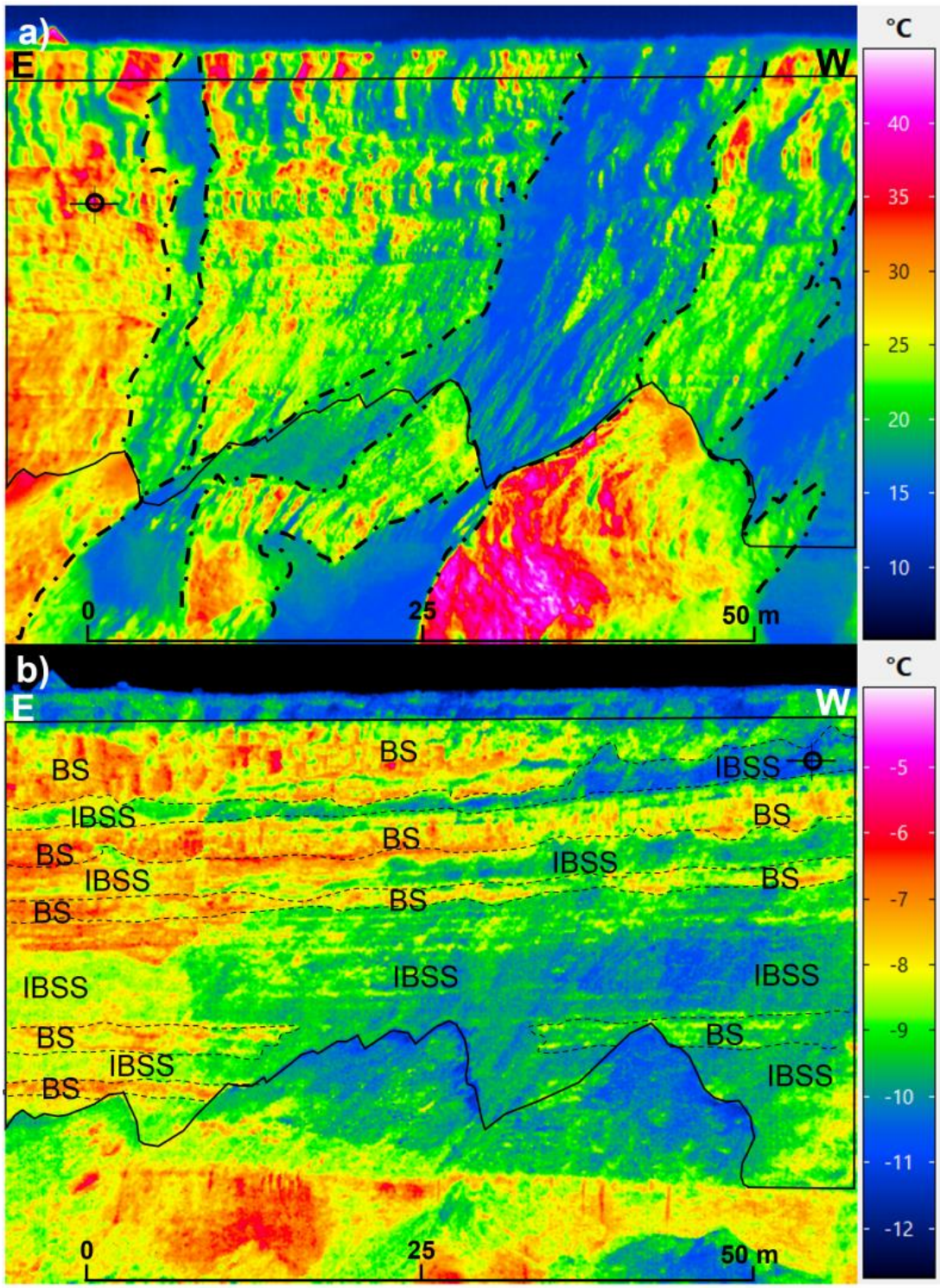

Figure 5. 3: *Thermal images of the maximum and minimum surface temperatures detected in 2021.* ***a)*** *The maximum temperature was detected the 14th of July at 14:00 h, where the pixel showing the highest value of the year is highlighted using a cross mark and circle. Aspect controls on temperatures are highlighted using vertical dashed lines.* ***b)*** *The minimum temperature was detected the 13rd of February at 08:00 h, where the pixel showing the lowest value of the year is highlighted using a cross mark and circle. Near-horizontal dashed lines show bedding controls on temperatures. In each image, the Eastern and Western directions are shown using the letters E and W, respectively.*

Table 5. 2: Summary of the annual and seasonal rock-slope surface temperatures detected in 2021.

Year and season	Mean temp. (°C)	Maximum temp. (°C)	Minimum temp. (°C)	Seasonal range (°C)	Hours below 0°C (%)
Winter	0.1	15.6	-11.7	27.3	15.8
Spring	9.0	39.8	-10.1	49.9	6.9
Summer	17.0	40.2	3.8	36.4	0
Autumn	6.3	24,9	-6.9	31.8	4.5
Annual	8.7	40.2	-11.7	51.9	27.2

Note: Values were calculated based on a total of 4,277 thermal images. Column of hours bellow below 0°C indicates the percentage of the total number of hourly scenes where pixels falling below 0°C were detected. Values were calculated within the General Window of assessment (GW) showed in Figure 5.1.

Figure 5.4 illustrates the variability of the mean surface temperature across the sampled horizontal scanlines and mapping windows for both bedded sandstones (BS) and interbedded sandstones (IBSS). This shows that both beds experienced increases in surface temperature from winter to summer, but superimposed were three distinctive behaviours:

First, in winter and autumn BS was on average, 2°C warmer than IBSS, with differences of up to ~ 4°C also observed.

Second, a seasonal inversion of this lithological control on temperature occurred, whereby IBSS was on average 1°C to 2°C warmer than BS in the summer as compared to the winter. The greatest differences of up to ~ 8.7°C were also identified, especially during mid-summer when the hottest surface temperatures of the year were recorded.

Third, for both beds the warmer the season, the higher the temperature range across the beds. To exemplify, for IBSS, the mean surface temperature range was ~ 2.9°C in winter, whilst in summer this was ~ 4.2°C (Δ = 1.3°C).

An example of the seasonal inversion of temperatures between lithological beds is shown in Figure 5.5. At around midday in winter, the surface temperature of the BS fluctuated between ~ 4.5°C and 5.5°C, whereas IBSS fluctuated between ~ 2.5°C and 3.5°C. Conversely, around midday in summer and in the absence of large-scale aspect controls, the temperature of the BS oscillated between ~ 21°C and 23°C, whereas IBSS oscillated between ~ 25°C and 27°C. This demonstrated that BS were relatively cooler than IBSS (e.g., thermal image collected the 21st of July at 12:00 h). A consequence of this seasonal inversion of temperatures dependent on rock type may be a reversal of any surface temperature gradient during the year, which may have implications for the magnitude and direction of any resultant surface stresses driven by temperature changes.

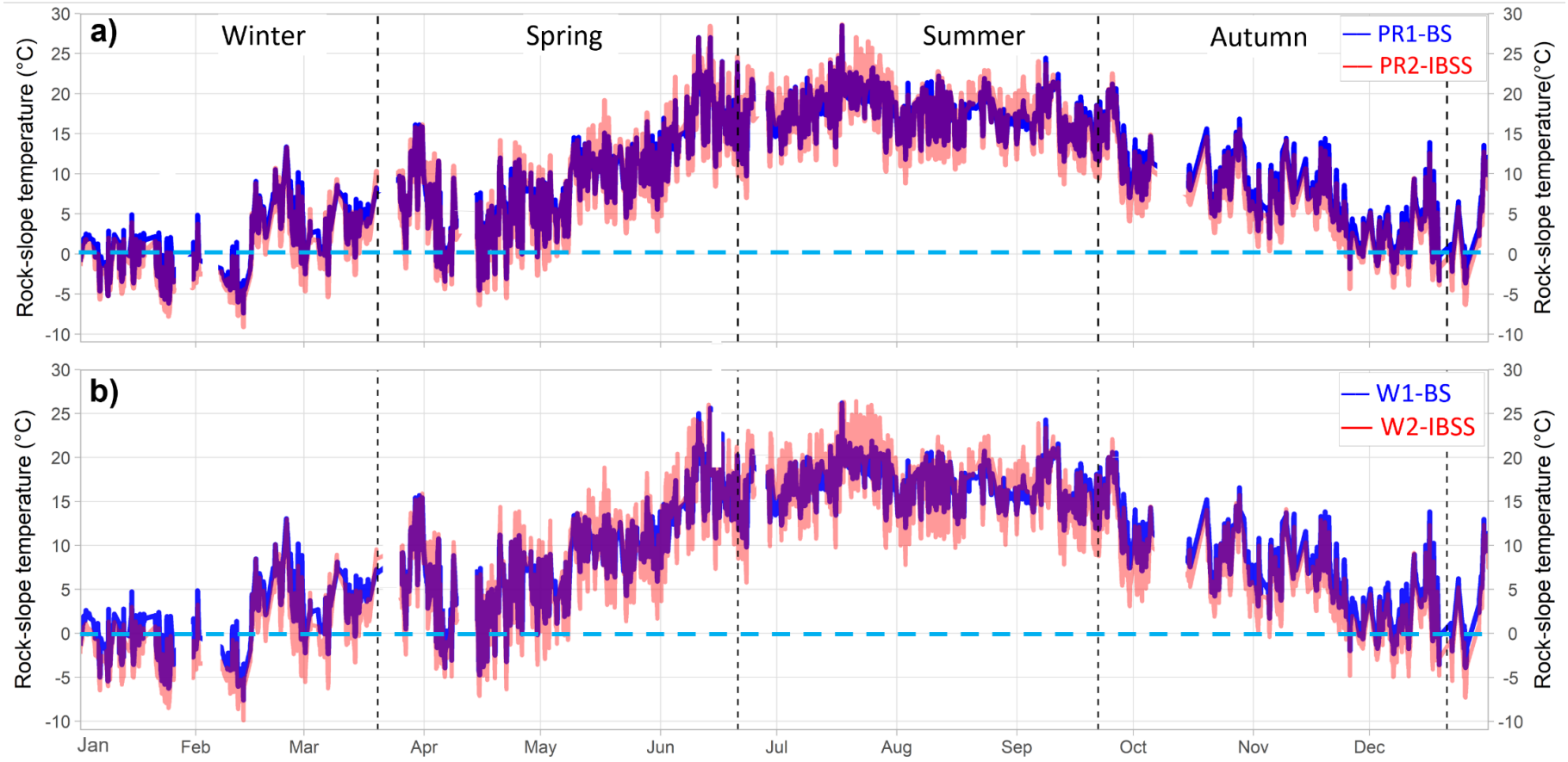

Figure 5. 4*:Temperature changes through the year by beddings. a) Evolution of the mean surface temperature across horizontal scanlines (PR1-BS and PR2-IBSS in Figure 5.1). b) Evolution of the mean surface temperature within mapping windows (W1-BS and W2-IBSS in Figure 5.1). BS: Bedded sandstones; IBSS: Interbedded sandstones and siltstones / carbonaceous muds. Boundaries between astronomical seasons (based on the equinoxes and solstices) are show using vertical dashed lines. Blank zones of the time-series indicate principal gaps created during data collection. Horizontal dashed blue lines indicate the thermal threshold of 0 °C to highlight susceptibility of frost conditions over the cliff face.*

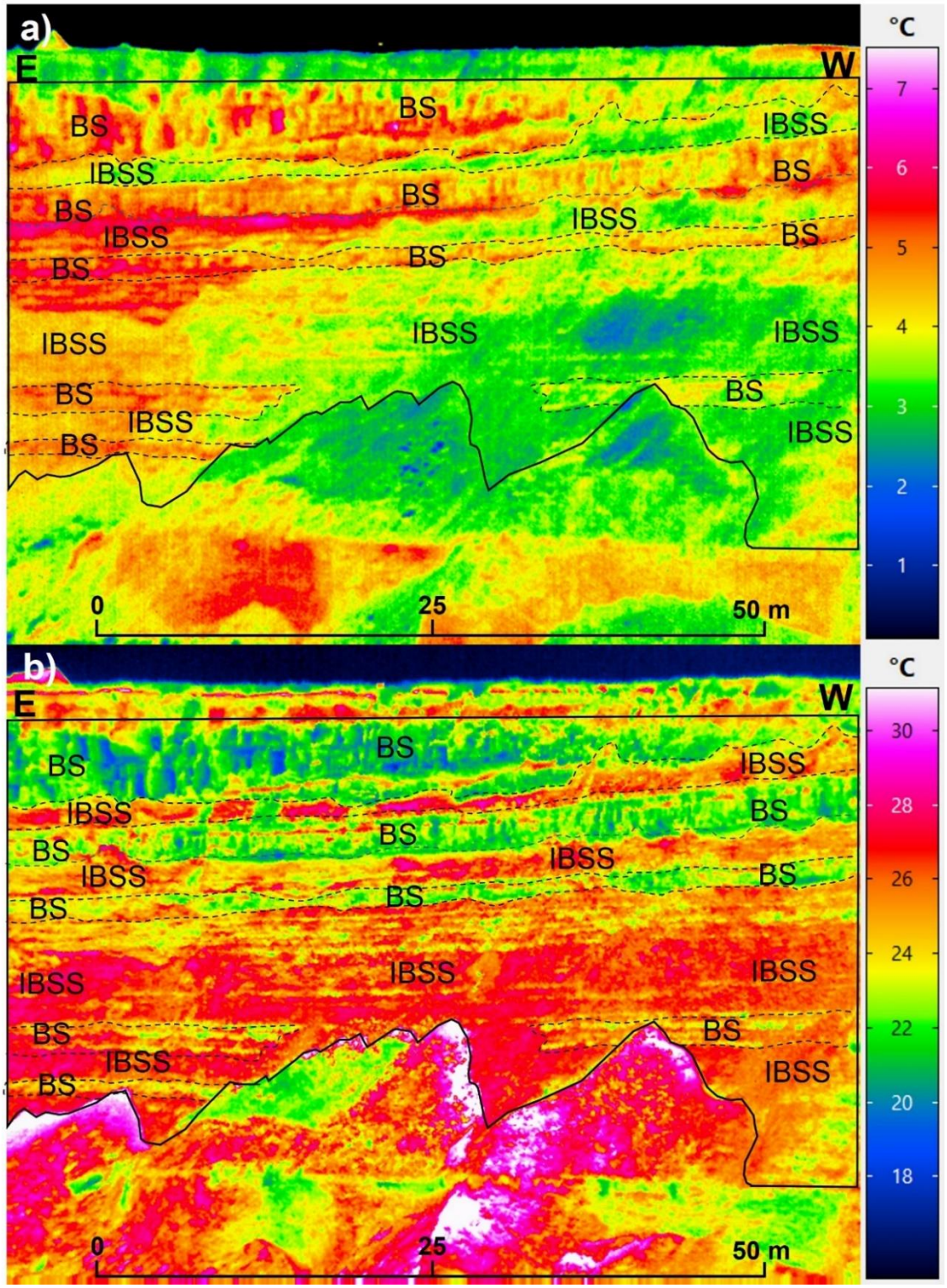

Figure 5. 5: *Example of the seasonal inversion of temperatures between beds.* ***a)*** *Bedded sandstones (BS) showing higher mean temperatures than Interbedded sandstones and siltstones (IBSS) during winter. Scene detected the 15th of January at 12:00 h.* ***b)*** *IBSS showing higher mean temperatures than BS during summer. Scene detected the 21st of July at 12:00 h. Near-horizontal dashed lines indicate bedding controls on temperatures. The region of research is highlighted using continuous black lines. The Eastern and Western directions are shown using the letters E and W, respectively.*

The temperature changes of individual pixels are shown in Figure 5.6. These include the time-history of temperatures at the locations of the maximum and minimum differential temperatures in 2021 (*P4Maxdiff* = 50°C; *P5Mindiff* = 27.9°C, see spatial locations in Figure 5.1). The surface temperatures at these locations illustrates three patterns (Figure 5.6a):

First, the temperature at *P4Maxdiff* was highest in summer, reaching ~ 40°C, with temperatures ≥ 30°C commonly observed between late spring and mid-summer. A similar pattern was detected at *P5Mindiff* with the highest temperature of ~ 23°C, and temperatures ≥ 15°C observed again between late spring until late summer. These observation reaffirm that the difference in temperature ranges which were increased during the warmest seasons.

Second, the temperatures at *P5Mindiff* was less variable in summer as compared to winter. For example, at *P5Mindiff* temperatures fluctuated between 12°C and 23°C in summer (Δ = 11°C), but between -5°C and 12°C (Δ = 17°C) in winter, suggesting that this zone was particularly susceptible to high levels of temperature change during winter.

Third, in both winter and autumn, the temperatures at *P4Maxdiff* fell <0°C more frequently and with lower minimums than temperatures recorded at *P5Mindiff.* For instance, while a total of 728 hourly IRT images < 0°C at *P4Maxdiff* (reaching a minimum of ~ -10°C, but with a seasonal mean of ~ -3°C), a total of 285 hourly scenes showed temperatures <0°C at *P5Mindiff* (reaching a minimum of ~ -5°C, but with a seasonal mean of ~ -1.7°C). This suggests that the rock surface which experiences the maximum temperature differential (*P4Maxdiff*), was overall, more exposed to extreme changes in temperature (both, continuously warm in summer, and continuously cold in winter), and so making this part of the cliff surface one of the most likely to experience thermomechanical effects, with all other variables being equal. Overall, locations such as *P4Maxdiff* capture the potential scale of temperature changes experienced throughout the year upon the cliff (Figure 5.6a).

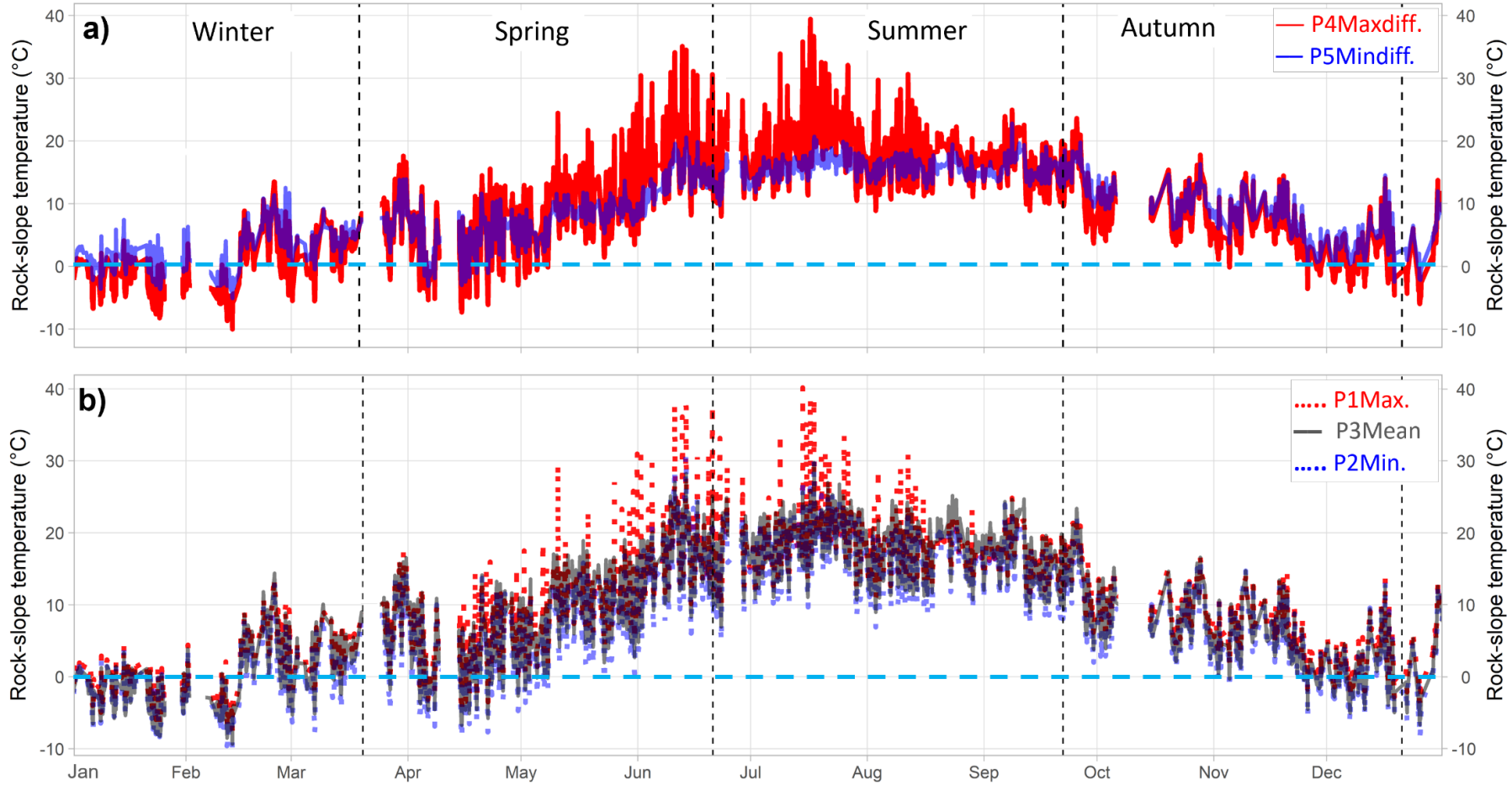

Figure 5. 6: *Temperature changes across the year by key individual pixels. a) Pixels representing the area of the slope with maximum and minimum difference temperature extracted from the differential surface temperature maps 2021 (P4Maxdiff. and P5Mindiff., see Figure 5.1). b) Pixels representing the area of the cliff with the maximum, minimum and mean temperature 2021 (P1max., P2Min., and P3Mean, see Figure 5.1). Boundaries between astronomical seasons are show using vertical dashed lines. Blank zones indicate principal gaps of data. Horizontal dashed lines show the thermal threshold of 0°C to highlight frost conditions over the cliff.*

Temperature changes at the position of the maximum (~ 40.2°C), annual mean (~ 8.7°C), and minimum (~ -11.7°C) detected temperatures is displayed in Figure 5.6b, with these positions shown in Figure 5.1. Overall, Figure 5.6b shows the same temperature patterns as the general time-series (e.g., Figure 5.2a), which can be summarized as follows:

First, a high variability through time of the surface temperature, with significant day-to-day and diurnal variations in temperature, overprinting a marked increase of temperature from winter to summer, followed by a reduction through autumn and back to winter.

Second, the point-based monitoring showed markedly cooler conditions not only in winter and autumn but also through until mid-spring. These cooler conditions were characterized by persistent low temperatures < 0°C, often with multiple weeks of uninterrupted cold conditions (~ -5°C to -10°C).

Third, marked warmer conditions occurred uninterruptedly from mid-spring until the end of the summer, where mean temperatures remained ≥ 20°C, with two similar seasonal maximum of 39.8°C and 40.2°C in spring and summer, respectively. This resulted in a continuously warm cliff face during this period.

Fourth, the frequent occurrence of large ranges in temperature during winter, up to mid-spring and autumn, where temperatures would cycle between < 0°C and warmer conditions $\geq$ 10°C were coincident in time at multiple points in the cliff face.

To further explore the nature and timing of temperature changes through the year, and in particular the speed at which temperatures change over 1 h, the hourly rate of change in temperatures was calculated for the maximum, mean, and minimum temperatures detected within the general window (*GW*). In this study, if $N+1$ thermal images of the cliff are collected at the times t_0, t_1, $t_2 \ldots$, t_N, (here, at 1 h interval of data collection, such as 00:00, 01:00, 02:00 h), and let $T_{ij}(t_o)$ and $T_{ij}(t_l)$ be the temperature at the corresponding times t_o and t_l related to the pixel ij (ith row and jth column), the pixel-by-pixel rate of change of temperatures is given by:

$$\Delta T_{ij,t} = \frac{T_{ij}(t_1) - T_{ij}(t_0)}{t_{1,ij} - t_{0,ij}} = \frac{\Delta T_{ij}}{\Delta t_{ij}} \qquad \text{[Eq. 5.1]}$$

As the IRT monitoring program was designed to collect thermal data in parallel to the laser scanner at 1 h intervals, whereby 1 h was a constant time difference for any value of Δt_{ij}, the results from Eq. 5.1 are reported in units of °C/h. As a result, this formula was computed only for

sequential hourly thermal images, and was not implemented over data gaps, yielding a total of 3,708 thermal images of the rate of change in temperature during the monitored period.

Figure 5.7a shows the pattern of the rates of change in temperatures through the year, where values > 0°C/h indicate warming phases, while rates of change <0°C/h show cooling. The mean rates of change of temperature was relatively similar during 2021, fluctuating between ~ -5.3 and 6.5°C/h (Δ = 11.8°C/h), with a mean of -0.02°C/h for 2021. However, at finer scales variability was again detected, irrespective of the season, with some days experiencing a more gradual and/or stable (e.g., from ca -1.0 to 1.0°C/h) or more sudden (e.g., between ~ -3 and 5°C/h) rates of temperature change. The difference between the maximum and minimum rates of change demonstrates that the warmer the season, the rockface experiences higher the rates of temperature change. To exemplify this, while in winter the rates of temperature change fluctuated between ~ –6.8 and 8.6°C/h (Δ = 15.4°C/h), these differences were further enhanced during spring with fluctuations between ~ -13.8 to 19.8°C/h (Δ = 33.6°C/h). A consequence is that some areas of the cliff face were frequently exposed to very high rates of change in temperatures either on the same day or from one day to the next (e.g., from ~ -10.0 up to 10.0°C/h), notably during spring and summer. A summary of the rate of change in temperatures by season is provided in the Table 5.3.

The variability in the rate of change in air temperatures proximal to the cliff face is shown in Figure 5.7b. Overall, the air rate of change fluctuated, on average between ~ -1.0 and 1.0°C/h during winter, and from ~ -3.0 to 3.0°C/h in summer. This pattern shows some correspondence with the rate of change of cliff surface temperatures whereby the warmer the season, the higher the rate of air temperature change. Nevertheless, at times, both the timing and/or magnitude of the rate of air temperature change deviated from that of the cliff surface temperature rate of change. For example, while the maximum surface temperature rate of change was ~ 19.8°C/h (1st June between the 18:00 and 19:00 h), the air temperature rate of change was ~ 2°C/h. Conversely, while the maximum air temperature rate of change was ~ 7.7°C/h detected the 16th June between 18:00 and 19:0, 15 days after the maximum surface rate of change of 2021, the maximum rate of surface temperature change was ~ 8.1°C/h. As a result, key differences were again observed between the timing and magnitude of the rates of change in air and cliff surface temperature.

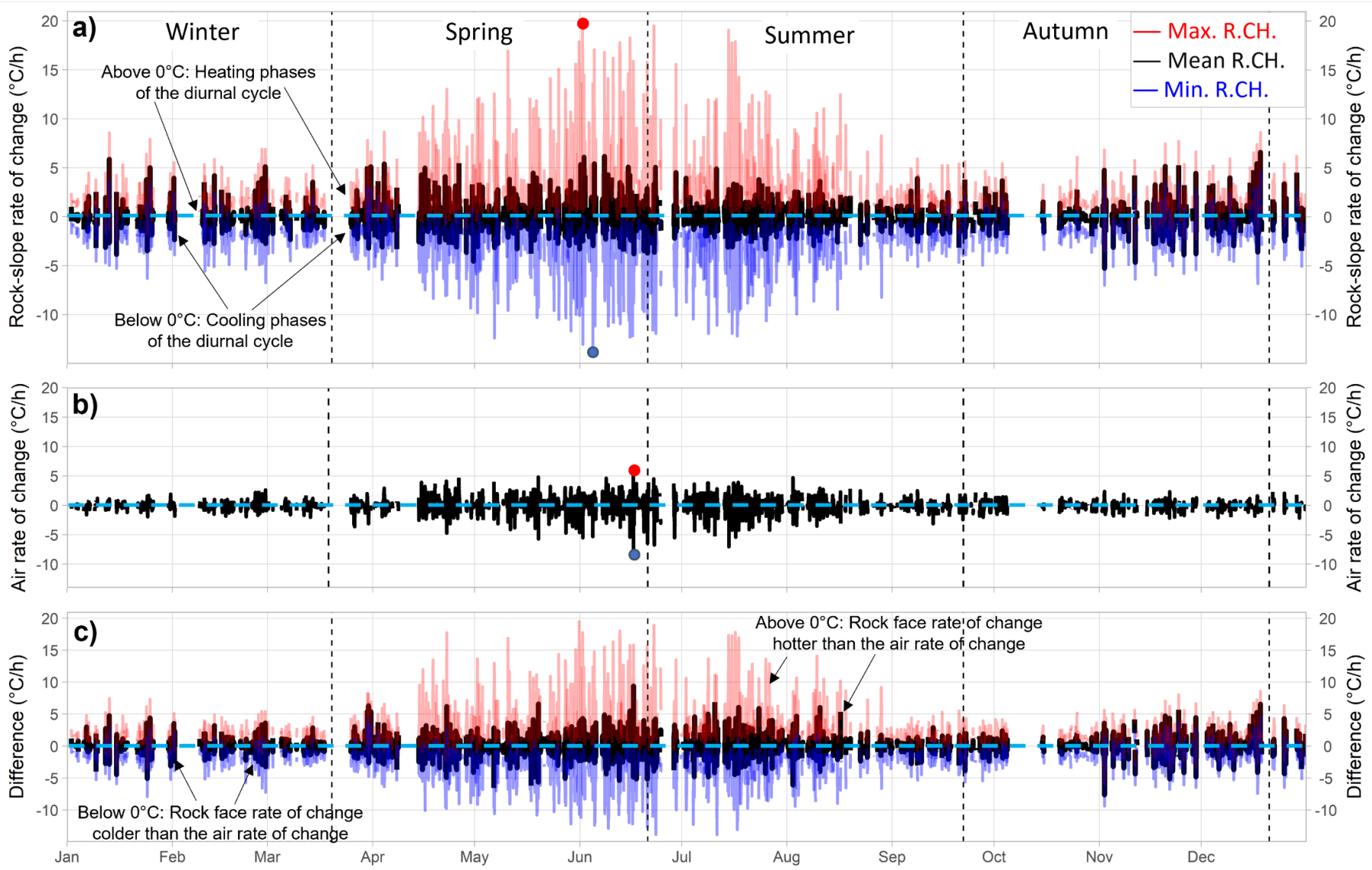
a)
Winter
Spring
Summer
Autumn
Max. R.CH.
Mean R.CH.
Min. R.CH.
Above 0°C: Heating phases of the diurnal cycle
Below 0°C: Cooling phases of the diurnal cycle
Rock-slope rate of change (°C/h)
b)
Air rate of change (°C/h)
c)
Above 0°C: Rock face rate of change hotter than the air rate of change
Below 0°C: Rock face rate of change colder than the air rate of change
Difference (°C/h)
20
15
10
5
0
-5
-10
Jan
Feb
Mar
Apr
May
Jun
Jul
Aug
Sep
Oct
Nov
Dec

Figure 5. 7: *Overleaf. Evolution of the rates of change of temperatures through the year, calculated from a total of 3,708 sequential hourly scenes. a) Rock face rate of change (R.CH) of temperatures detected within the General Window of assessment (GW) of the Region of Research. b) Air average rate of change of temperature registered at the top of the cliff face. c) Difference between the air rate of change and the maximum (Red), mean (Black) and minimum (Blue) rock face rate of change of temperatures, respectively. Boundaries between astronomical seasons (based on the equinoxes and solstices) are show using vertical dashed lines. Blank zones of the time-series indicate principal gaps created during data collection. The dates showing the maximum and minimum environmental and surface rates of change of the year are highlighted using red and blue dots, respectively. In Figure c) the horizontal blue lines highlight the dates in which the temperature rate of change of the rock face was hotter or colder than the rate of change of the environmental temperature.*

The magnitude of the difference in the rate of air temperature change, and the maximum, mean, and minimum cliff surface rate of temperature change is shown in Figure 5.7c. In winter and autumn, differences between these rates of change fluctuated between ~ -5.0 and 5.0°C (Δ = 10°C/h), with the highest occurring during spring and summer (~ -12 and 19°C/h (Δ = 31°C/h)). Consequently, the direct monitoring of rates of change in cliff surface temperature from the IRT monitoring show a clear difference to those from the air temperature monitoring alone, and so, again, is potential more suitable for examining the nature of temperature changes upon the cliff face itself.

To compare the spatial patterns of the mean rates of change in surface temperatures, Figure 5.8 shows the IRT pixel-by-pixel composite images of the mean rate of change in temperature by season. These maps were computed by stacking IRT rate of change imagery, to derive a pixel-based mean. The underlying imagery included a total of 767, 1212, 974 and 755 images (pixel values) for winter, spring, summer, and autumn, respectively. The seasonal differences in the number of available images resulted from data gaps generated by inclement weather conditions (for or rain) during the data acquisition (see Chapter 4, Section 4.2.4). Three distinctive temperature change patterns were observed across the seasons (Figure 5.8):

First, in winter, very homogenous spatial rates of change were detected across the surface of the cliff face, without apparent bedding controls on temperatures. Overall, mean values were <0 °C/h (see Table 5.3), which indicates the predominance of a long-term trend of cooling during this season, from the start to the end of the winter (Figure 5.8a).

Second, a marked pattern of mean spatial variability was detected in spring and summer, with evident bedding controls in both seasons, and aspect controls particularly in summer. It was also observed that many areas of the cliff were subject to a predominance of heating phases, as mean values of rates of change were > 0°C/h, particularly across bedded sandstones (BS).

Conversely, interbedded sandstones and siltstones (IBSS) showed a long-term predominance of cooling phases, as mean values were <0 °C/h. Therefore, these maps suggest a long-term temperature change dominated by heating across BS, but cooling thorough IBSS, specially from mid-spring to summer (Figures 5.8a,b).

Third, autumn shows a transitional spatial pattern back to winter as less mean spatial differentiation was detected, with limited apparent bedding controls and mean rates <0 °C/h, which suggest the predominance of a long-term trend of cooling from the beginning of autumn to winter (Figure 5.8d).

Therefore, two consequences can be highlighted as a result of the comparison of the thermal maps of the mean rates of change by seasons: First, for all seasons, the mean rates of change of temperatures were characterized by a relatively stable range of change (0.0 ± 0.08°C/h), which suggest that in a day-to-day basis, overall, the increases in temperature equalized the decreases in temperature, indicative of a radiation balance between the gaining and losing of heat per hour through the seasons. However, spatially variability was detected in the warmer seasons due to the effect of the cliff aspect/bedding, as it is well known that the slope factor (or cloud cover) affects the amount of solar radiation absorbed in many hillslope systems. Second, the limited differences in the mean rates of change of temperature are reflecting a general long term temperature change across the seasons, but not specific thermal conditions occurring in each season (e.g., mean warming or cooling conditions per diurnal thermal cycle or through specific intervals of hours). As such, specific thermal conditions are further investigated by assessing hourly changes in temperatures (Section 5.3), and aspect controls on surface cliff temperatures (Section 5.4).

Table 5. 3: *Summary of the average rate of change of temperatures by season.*

Season	Mean change (°C/h)	Maximum change (°C/h)	Minimum change (°C/h)	Seasonal range (°C/h)	Standard deviation (°C/h)
Winter	-0.08	8.6	-6.8	15.4	0.9
Spring	0.01	19.8	-13.8	33.6	1.4
Summer	-0.01	19.5	-12.2	31.7	1.1
Autumn	-0.04	8.6	-6.7	15.3	1.1
Annual	-0.02	19.8	-13.8	33.6	1.2

Note: Values were calculated based on a total number of 3,708 sequential hourly thermal images, where a total of 767 were available for winter, 1212 for spring, 974 for summer, and 755 for autumn. Values were calculated within the General Window of assessment (GW) showed in Figure 5.1.

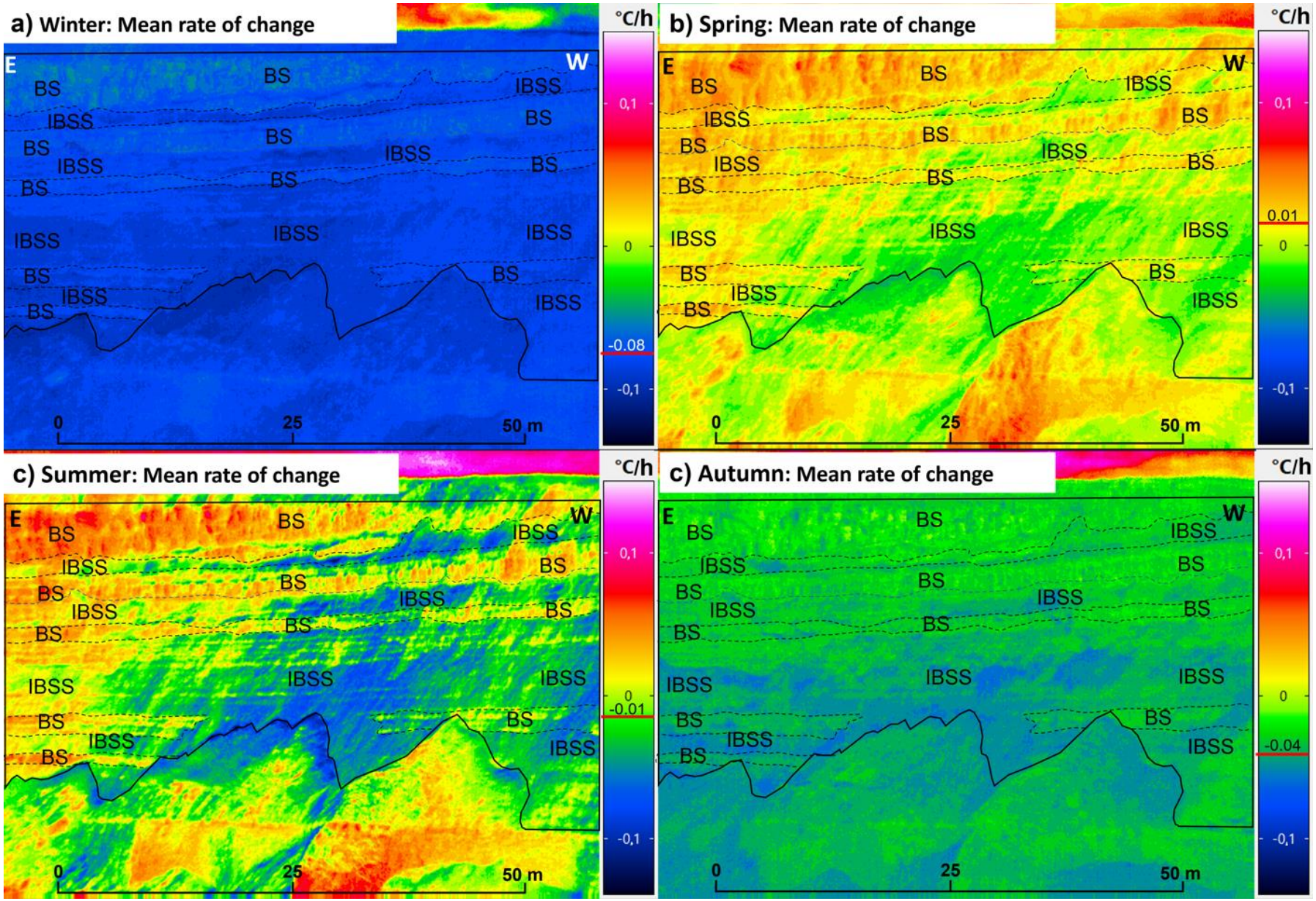
a) Winter: Mean rate of change
b) Spring: Mean rate of change
c) Summer: Mean rate of change
c) Autumn: Mean rate of change
°C/h
E
W
BS
IBSS
0
25
50 m
0,1
0
-0.08
-0,1
0.01
-0.01
-0.04

Figure 5. 8*: Overleaf. Thermal maps of the mean rates of change temperatures by seasons (Pixel by Pixel). a) Mean rate of change in Winter. b) Mean rate of change in Spring. c) Mean rate of change in Summer. b) Mean rate of change in Autumn. Black boundary lines show the Region of Research (ROI) for this study. Each thermal scene is overlapped with the principal beds outcropping in the ROI, where BS: Bedded sandstones; IBSS: Interbedded sandstones and siltstones / carbonaceous muds. Near horizontal dashed lines show bedding controls on temperatures. In each image, the Eastern and Western directions are shown using the letters E and W, respectively. Red horizontal line in each colour scale show the mean rate of change value per season, which is also quoted above the red line.*

Figure 5.9 shows the evolution of the rates of change of temperatures through the year by the beds. It can be seen that the average rates of temperature change were similar between the bedded sandstones (BS) and interbedded siltstones and sandstones (IBSS). However, during spring and summer, IBSS experienced higher fluctuations compared to BS, as the mean rate of change of IBSS ranged from ~ -5.0 to 7.0°C/h, while in BS this was ~ -2.0 to 2.0°C/h. This suggests that during warmer seasons, BS were exposed to relatively stables rates of change in temperatures compared to IBSS. Nevertheless, the highest maximum and lowest minimum rates of change occurred within the BS, particularly towards late spring and early summer (~ -14 and 17°C/h). Variations from a minimum of ~ -11 and up to 14°C/h were observed on the IBSS. Conversely, similar rates of changes across both beds were observed during both winter and autumn.

Overall, in this section the timing and nature of the changes in the cliff surface temperature through the year have been examined, revealing eight principal findings:

- A high variability of surface temperatures through time, characterized by significant day-to-day and within day fluctuations. Temperatures increase from winter to summer. An annual range of cliff surface temperature of ~ 59.2°C, between the minimum and maximum of ~ -11.7°C (winter) and 40.2°C (summer).

- The occurrence of sharp fall of cliff surface temperature were observed not only in winter and autumn, but also through until mid-spring, encapsulating a period of about six months. These falls in temperature were often associated with periods of persistent low temperatures < 0°C which lasted up to one month. Some areas of the cliff face were subject to very cold temperatures (~ -5°C or -10°C), clearly highlighting the potential for some degree of periodic freezing, albeit over localized areas of the cliff face.

- Notably warm conditions that persisted from mid-spring until the end of the summer with mean temperatures ≥ 20°C and coincident with high seasonal maxima of 40°C in both

spring and summer. This led to the rock face experiencing continuously high temperatures during around four continuous months.

- The occurrence of frequent and marked within day cliff surface temperature differences during winter, through up mid-spring, and then from autumn back to winter. These periods were characterized by very cold (e.g., -5.0°C) and relatively warm hot (e.g., 10°C) conditions either within the same day or on successive days. This demonstrates that in addition to experiencing cold, the cliff face may also have the potential to experience freeze thaw cycling.

- A seasonal inversion of the temperature gradient between different lithologies was observed. IBSS on was average ~ 1°C or 2°C warmer than BS in the summer as compared to winter. This may induce a reversal of the direction of the temperature gradient on the cliff surface through the year.

- The warmer the season, the higher the range in cliff surface temperatures. As a result, during spring and summer, the rock face was frequently exposed to very high rates of change in temperatures, either on the same day or on a day-to-day basis (e.g., from ~ -10.0 up to 10.0°C/h). Importantly over time and as a result of cumulative and/or cyclic fluctuations, these changes may facilitate thermomechanical processes upon some areas of the cliff face.

- The IRT maps of the mean rates of change of temperatures by seasons demonstrate that during spring and summer the rates of temperature change are relatively heterogeneous, and were influenced by both bedding and aspect.

- The IRT maps also showed a high degree on homogeneity in rates of surface temperature change in winter and autumn, suggesting overall heating and cooling was more uniform with a lesser degree of control due to aspect or bedding.

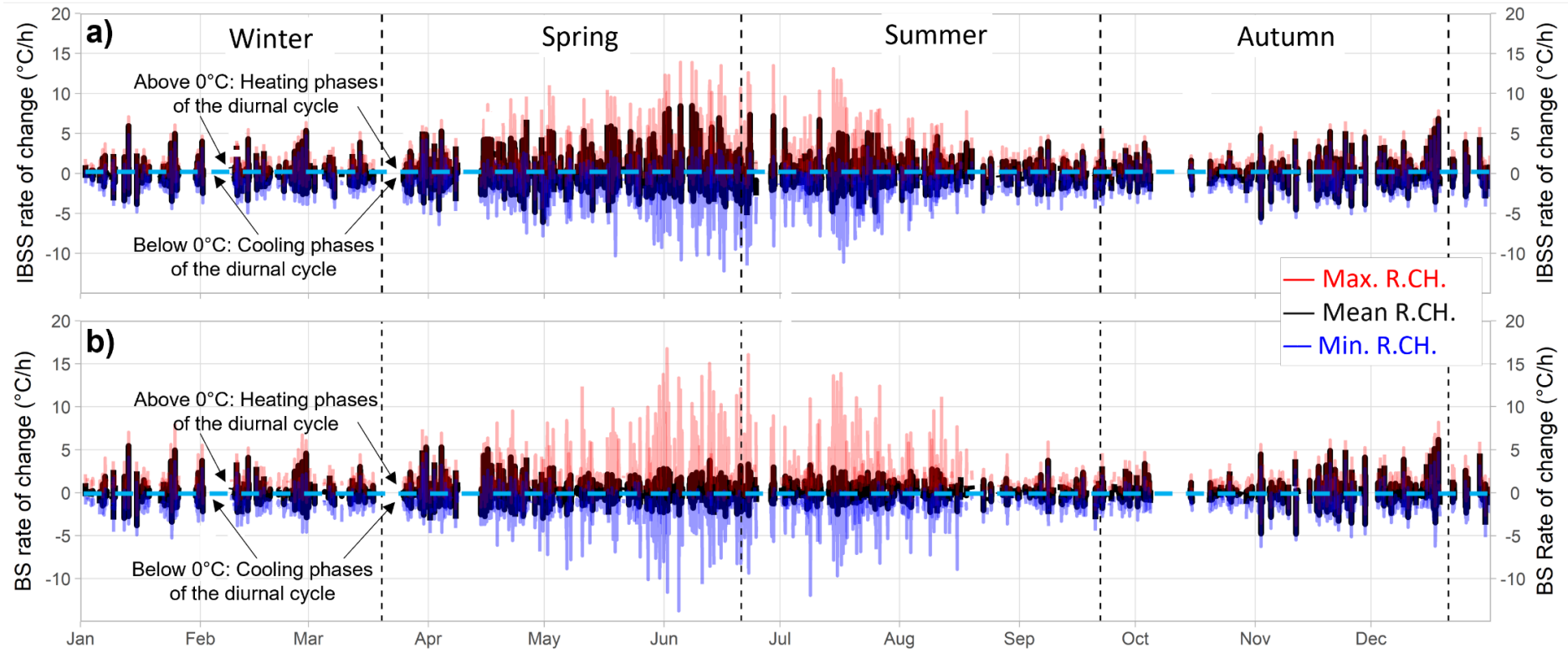

Figure 5. 9: *Evolution of the rates of change of temperatures by bedding. a) Rates of change (R.CH) of temperature across the mapping window of Interbedded Siltstone and Sandstones (W2-IBSS in Figure 5.1). b) Rates of change (R.CH) of temperature across the mapping window of Bedded Sandstones (W1-BS in Figure 5.1). Boundaries between astronomical seasons (based on the equinoxes and solstices) are show using vertical dashed lines. Blank zones of the time-series indicate principal gaps created during data collection. Horizontal dashed blue lines highlight the boundaries between positive (heating) and negative (cooling) rates of changes above and below 0 °C, respectively.*

5.3 Hourly changes of surface temperatures

In this section of results, a finer temporal resolution characterization of the IRT dataset is presented, using hourly changes in cliff surface temperature. In particular, I focus the analysis on the timing and magnitude of absolute temperature fluctuations throughout the annual and seasonal mean diurnal cycles. This is followed by an hour by hour assessment of the rate of change of temperature to consider how quickly or slowly the rock face heated or was cooled. In this study, due to the variability of temperature by hour, a heating phase is defined as uninterrupted increases in mean surface temperature for >2 h, and the equivalent for cooling periods.

Figure 5.10 shows a summary of the temperature changes for the complete mean diurnal thermal cycle throughout the monitoring period (between 1st of January and 31st of December 2021). This figure includes the mean temperature, as well as the mean hourly maximum and minimum temperatures within GW. The average diurnal cycle was characterized, as expected, by one heating and cooling phase. The heating phase began around the start of mean sunrise time, after which a more rapid increase in temperature following at around at 05:00. This rapid rate of change only reduced after 11:00. During this warming phase increases in the mean temperature ranged from ~ 5.0°C to almost 12.0°C (Δ = 7.0°C), while for the case of the mean maximum temperatures this phase ranged from ~ 8.0°C to 16.5°C (Δ = 8.5°C), and from ~ 2.0°C and 9.0°C for the mean minimum temperatures (Δ = 7.0°C). Thus, these values represent the total increase in temperature over the warming phase. The similarities in the trajectory of the mean, maximum, and minimum, indicate that over the year and on average, the increases in all three measures of temperature were similar and that there was not a marked divergence in either maximums and/or minimums. After 11:00 h, temperatures were relatively stable with a mean around 12.5°C through until 13:00 h. This period was when the peak maximum and minimum temperatures were achieved at ~ 16°C and 9°C, respectively.

Cooling began at 13:00 h, and was characterized by a steady decrease in both the mean and minimum temperatures, through sunset period up until 02:00 h which was the time of the minima. This steady cooling over this period was characterized by reductions in the mean temperatures from ~ 12.5°C to 5.0°C (Δ=7.5°C), and a reduction in mean minimum temperatures from ~ 9°C to 2°C (Δ = 7.0°C). Thus, these values represent the total decrease in temperature over the cooling phase. Interestingly, while mean and minimum temperature decreases were similar, the mean maximum surface temperatures was notably different which remained high between 13:00 and 18:00 h at around 15.5°C. This indicates that parts of the cliff with the maximum temperatures remained warm for a longer duration. After 19:00 h, a sharp reduction of the mean

maximum temperature was detected, falling from ~ 15.5°C to 8.5°C by 02:00 h (Δ = 7.5°C) over an interval of 7 h (Figure 5.10).

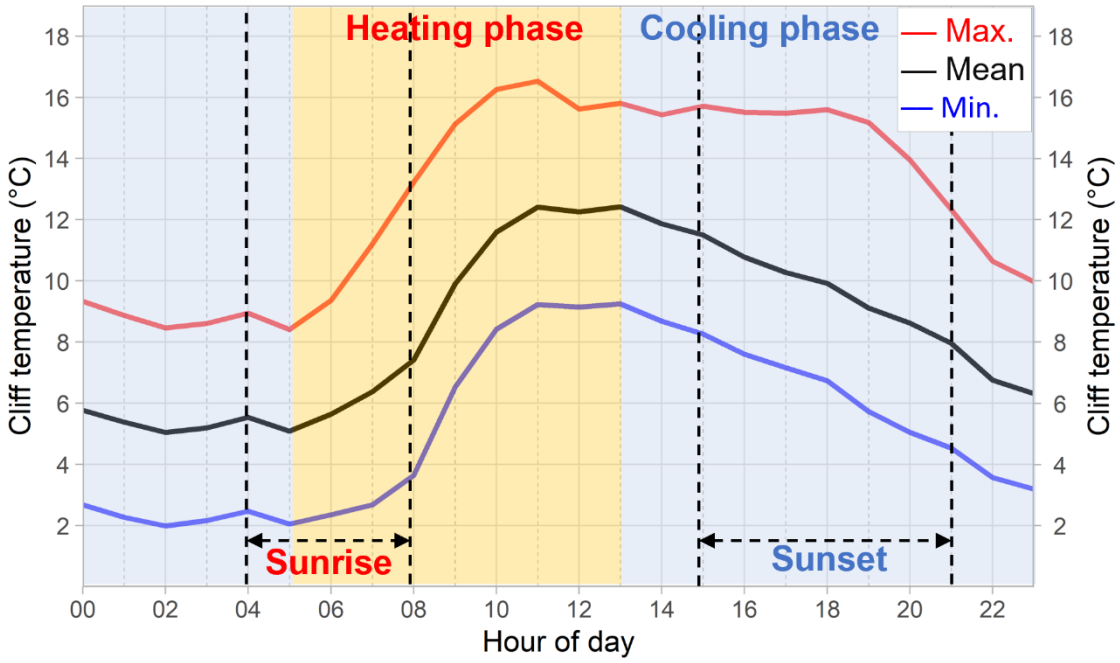

Figure 5. 10: *Summary of the cliff surface temperature changes through the day detected between 1st January and 31st December 2021. Dashed vertical lines indicate the annual boundaries of the sunrise and sunset cycles. The red and blue curves show the mean of the maximum and minimum temperatures detected by each hour of the day. The black curve shows the mean temperatures. Light yellow and blue regions highlight the daily heating and cooling phases, respectively.*

To provide further insight into the timing and nature of the surface heating and cooling Figure 5.11 illustrates the complete diurnal cycle by season. The winter cycle shows, as expected, the lowest surface temperatures compared to the other seasons, ranged from a mean minimum and maximum of ~ -5.0 and 6.5°C (Δ = 11.5°C), which was the smallest range in diurnal temperatures. The heating phase in winter started 1 h after the winter sunrise, at 07:00 h, however, more rapid increases in cliff surface temperatures were only detected after the end of the sunrise at 08:00 h. This most probably reflects the weaker winter sunlight and the resultant apparent lag in cliff surface warming. The morning heating was characterized by increases in the mean temperatures from ~ -2.0°C, reaching in 3.5°C by 11:00 h (Δ = 5.5°C). After 11:00, a relative stabilization of the cliff surface temperatures was achieved at ~ 4°C by 13:00 when the cooling phase commenced. Significant reductions of temperatures were only detected from around sunset (from 16:00 to 17:00 h), after which the mean surface temperatures dropped from ~ 2°C to near 0°C (Δ = 2°C). After sunset, a marked stabilization of the mean temperature was again detected

at ~ -1.0°C, which was maintained between 20:00 and 06:00, when the winter sunrise began (Figure 5.11a).

Three key observation can be summarised from the analysis of the diurnal thermal cycle during winter:

First, the surface of the cliff face was continuously exposed to temperatures < 0°C during a significant proportion of the day, including mean temperatures between 19:00 and 07:00 h, but notably, between 15:00 and 10:00 h for the minimum observed temperatures. This indicates that there were parts of the cliff that were persistently subject to average and minimum temperatures <0°C for 45% and 70% (respectively) of the day.

Second, between 17:00 and 07:00 h (~ 63% of the day), the mean minimum temperatures showed a marked stability around ~ -3°C and -4°C, which then warmed to 1.0°C towards the end of the heating phase (11:00 to 13:00 h). This suggests that the parts of the cliff that were uninterruptedly exposed to the minimum temperatures were potentially subject to some degree of either freezing, or freeze-thaw cycling. This might include those areas that experienced a combination of near-permanent shadow and the lowest minimum temperatures of (e.g., < -5.0°C, see Figure 5.2a).

Third, the overall pattern of the change in the maximum, mean and minimum surface temperatures were almost identical. This suggests relatively homogeneous temperature changes across the cliff as surfaces showed similar timings and magnitude of temperature change. Longer or shorter periods of surface heating or cooling were not apparent in the seasonally averaged diurnal data (Figure 5.11a).

The diurnal temperature cycle for summer showed, as expected, the highest surface temperatures ranging from a mean minimum and mean maximum of ~ 10°C and 26°C (Δ = 16°C), respectively (Figure 5.11c). The heating phase of summer started similar to winter at 1 h after the summer sunrise at 05:00 h. However, a key difference with was that sharp increases in temperature occurred quickly after sunrise. Heating was characterized by increases in the mean temperature from ~ 13°C at 05:00 to ~ 17.5°C by 08:00 h (Δ = 7.5°C). However, while the mean and minimum temperatures tracked each other, a distinctive rapid increase in maximum temperature was observed from 16.5°C to 25.5°C (Δ = 9°C) for the same period. After 08:00, a more gradual increase in temperatures was observed reaching ~ 19°C by 13:00 h, at which point heating ceases. Cooling followed, characterized by a gradual drop in temperature reaching a mean

of ~ 18°C by 17:00 h. Between 17:00 and 19:00 h, a perhaps unusual and distinctive increase in the mean temperatures was observed, perhaps coincidence with a second phase of direct insolation at this time of day during this season. This period of increasing temperatures was more evident when examining the consistent increase in mean maximum temperatures which reached ~ 23°C by 14:00 h, and later peaked at 26°C by 19:00 h (Δ = 3°C), coincident with the beginning of the summer sunset. The most rapid decline of summer surface temperatures occurred during the sunset (19:00 – 22:00 h), after which a more gradual cooling of temperatures was observed until 04:00 h.

Overall, two key consequences can be summarised from the analysis of the diurnal cliff surface temperature pattern from summer:

First, the sharp increases in temperature that occurred around the start of sunrise, which coincident with rapid increases in the mean maximum temperature (between 16.5°C and 25.5°C, yielding an increase in temperature of Δ = 9°C), demonstrates that the surface of the cliff was quickly heated as soon as the sunlight struck the cliff face.

Second, the two warming phases identified that include at times quick and uninterrupted increases in the maximum temperatures (05:00 – 08:00 h, and then again, 14:00 – 19:00 h), shows that some areas of the cliff face experienced two phases of diurnal heating: during sunrise; and, during the afternoon prior to sunset. I further examine this in Section 5.4 where I consider aspect control on surface heating.

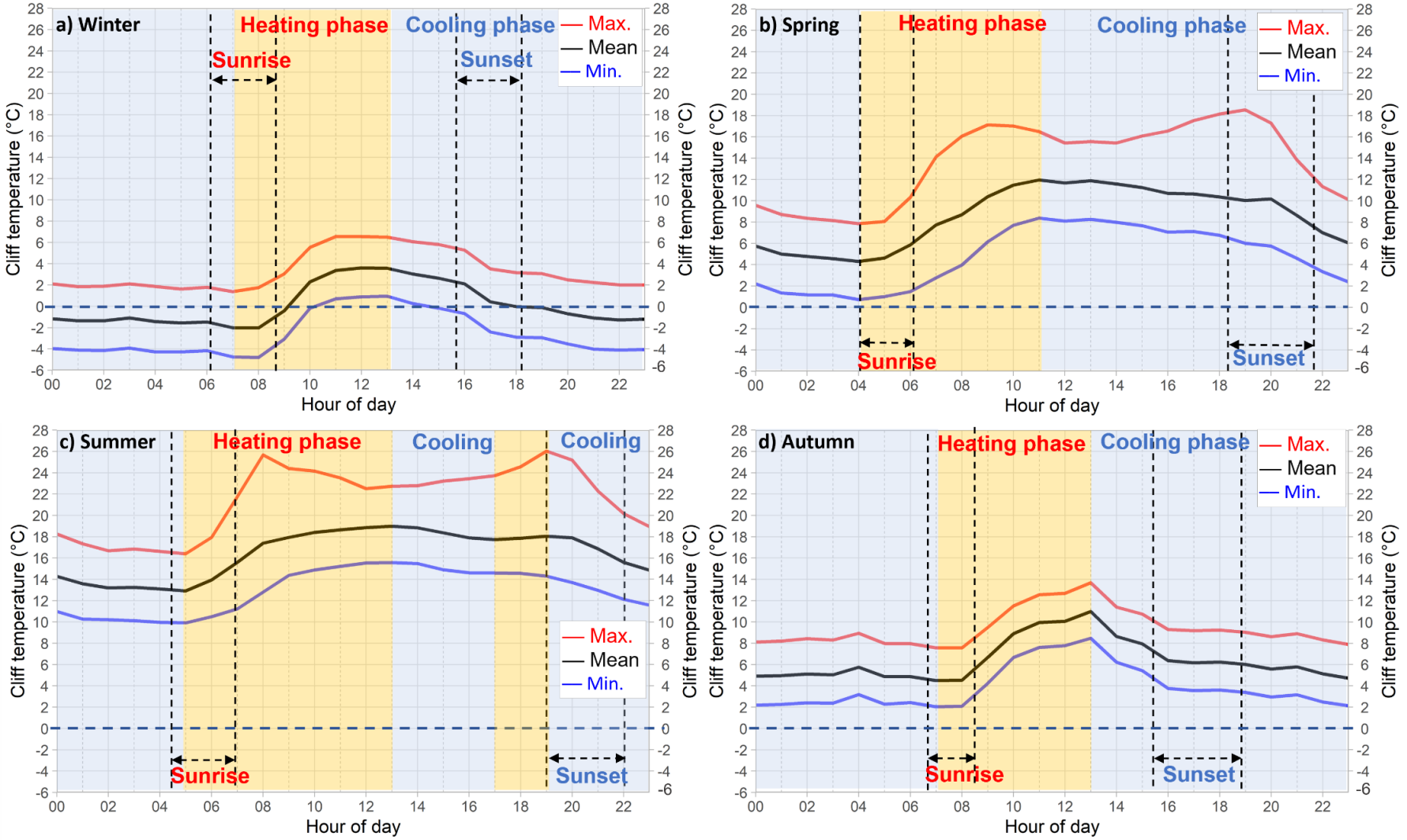
a) Winter
Heating phase
Cooling phase
Sunrise
Sunset
Max.
Mean
Min.
Cliff temperature (°C)
Hour of day
b) Spring
Heating phase
Cooling phase
Sunrise
Sunset
Max.
Mean
Min.
Cliff temperature (°C)
Hour of day
c) Summer
Heating phase
Cooling
Cooling
Sunrise
Sunset
Max.
Mean
Min.
Cliff temperature (°C)
Hour of day
d) Autumn
Heating phase
Cooling phase
Sunrise
Sunset
Max.
Mean
Min.
Cliff temperature (°C)
Hour of day

Figure 5. 11: *Overleaf. Seasonal behaviour of the mean surface temperatures through the day detected between 1st January and 31st December 2021. Dashed vertical lines indicate the annual boundaries of the sunrise and sunset cycles. The red and blue curves show the mean maximum and minimum temperatures detected by each hour of the day. The black curve shows the mean temperatures. Light yellow and blue regions highlight the duration of the daily heating and cooling phases, respectively. Horizontal dashed blue lines indicate the thermal threshold of 0 °C to highlight the freezing conditions through the day.*

Figure 5.11b shows the diurnal cliff surface temperature changes during spring. During this season, the maximum, mean, and minimum temperatures mirrored those in the summer cycle. The magnitude and range of the temperatures differed slightly, which may be explained by the marginally lower spring temperatures. The mean minimum and maximum temperatures fluctuated between ~ 1.0°C and 18.°5 (Δ = 17.5°C), demonstrating a period of transition between winter and summer conditions. Furthermore, while the mean surface temperatures increase between 17:00 and 19:00 h, as was observed in summer, the mean maximum temperatures showed again two periods of heating (04:00 h – 09:00 h; 14:00 – 19:00). Conversely, the mean minimum temperature was 1.0°C by 04:00 h at the end of the cooling phase, demonstrating that extreme minimum temperatures approaching -5.0°C or -10°C in spring were, in average, less common or sustained as compared to winter (See Table 5.2, Section 5.2). However, while uninterrupted temperatures below 0°C were less common than in winter, a 35% of the days of spring showed thermal conditions associated with freeze-thaw activity, and up to 10 days of continuous freeze-thaw cycles were observed in this season (see Table 5.1, Section 5.2), which can be critical for rock fracturing.

The diurnal cycle for autumn was comparable to that of winter with a similar pattern of change in the maximum, mean, and minimum surface temperatures, yielding heating and cooling phases of same duration to winter (Figure 5.11d). Three differences were however detected:

First, the magnitude and range of the surface temperature differences were overall higher in autumn. The mean minimum and maximum temperatures fluctuated between 2°C and 14°C (Δ = 12°C), respectively.

Second, the heating phase during autumn was characterized by sharply increasing temperatures from the end of sunrise (08:00 h) until 13:00 h, where average temperatures increased from ~ 4.5°C to 11°C (Δ = 6.5°C). This was followed by relatively sharp reductions in temperature immediately after. This behaviour generated a notably peak of temperatures at 13:00 h, not seen in the other seasons which saw more gradual temperature changes at this time.

Third, small increases in temperature for all three metrics occurred both 04:00 and 21:00 h within the cooling phase, and represented another peculiarity of cliff surface temperatures in autumn.

To provide further understanding into how quickly or slowly the rock face temperatures changed Figure 5.12 shows the mean, maximum and minimum hourly rates of change in surface temperatures within *GW* (Calculated using the Eq. 5.1, Section 5.2). In Figure 5.12, positive rates of change indicate heating, while negative values are indicative of cooling.

The diurnal surface temperature cycle in winter showed that the most rapid increases occurred during sunrise (07:00 – 09:00), reaching a maximum shortly after (09:00-10:00 h). In this period, the rate of change of the mean surface temperature showed increases from ~ -0.1°C/h to 1.8°C/h. The rate of change of the mean maximum surface temperatures varied between ~ 1.8°C/h to 4°C/h. After the maximum rate of change was reached, a rapid reduction of temperatures was observed. For instance, the mean rate of temperature change dropped from near 2°C/h (09:00 – 10:00 h) to 0.1°C/h (10:00 -11:00 h), producing a notable inflection in the rate of change. After 10:00 -11:00 h, slower rates of change were observed, followed by relatively stable conditions from halfway through sunset (16:00 – 17:00 h) until sunrise the following day.

Two observations can be made on the diurnal patterns of rates of surface temperature change in winter:

First, the rapid rates of increasing and decreasing temperature change detected around the end of sunrise and 1 hour after this (09:00-10:00 h), suggests that as the rock face experiences rapid heating on an hourly timescale during this period, this may lead to expansion and contraction.

Second, high positive or negative rates of temperature change were not observed around midday or sunset, and the majority of the day was characterized by relatively low rates of change. This suggests that during winter, temperature controls on thermomechanical behaviour may be concentrated in sunrise and/or after the sunrise, as the highest positive rates of change occurred around 07:00-10:00 h (Figure 5.12a).

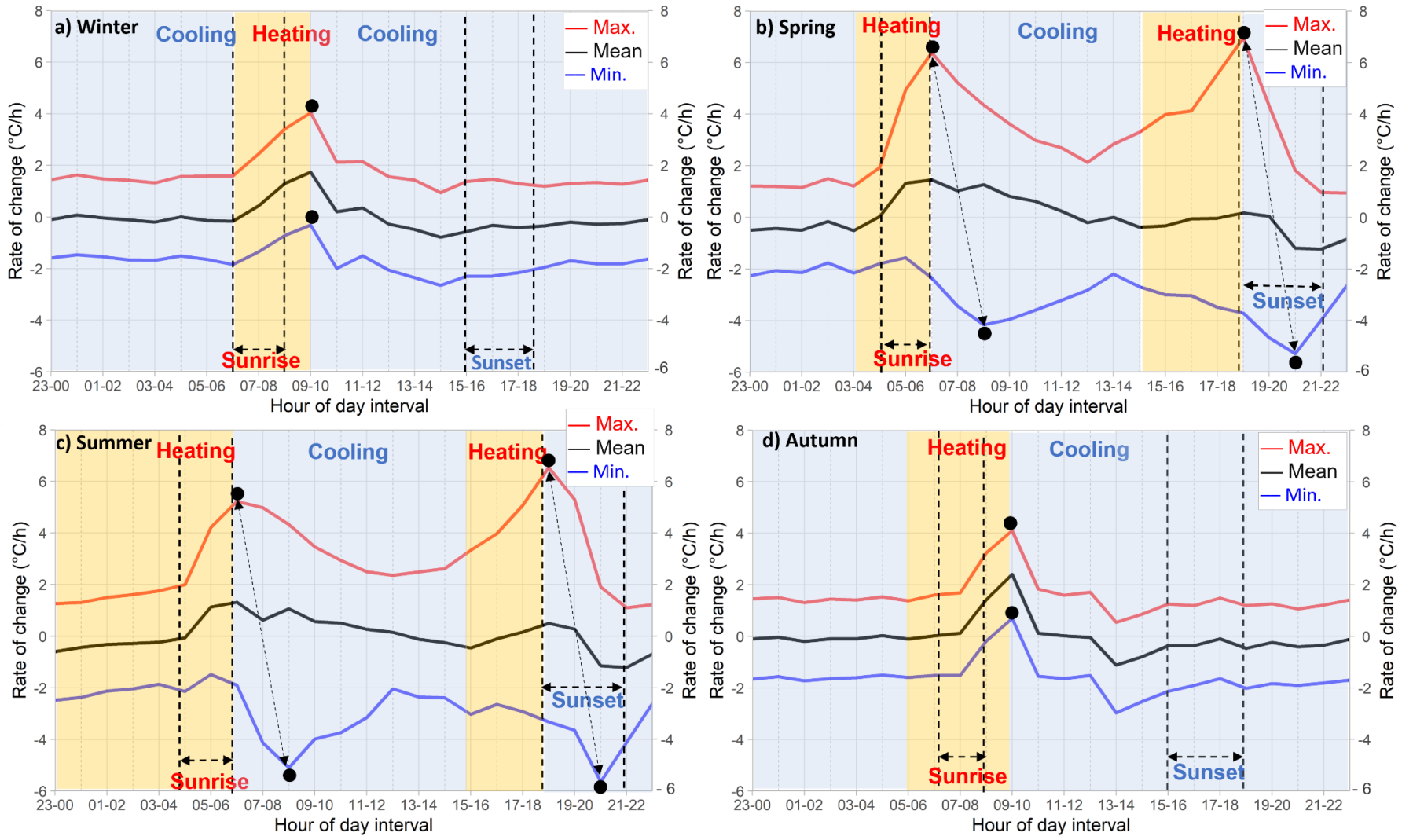
a) Winter
Cooling
Heating
Cooling
Max.
Mean
Min.
Sunrise
Sunset
b) Spring
Heating
Cooling
Heating
Max.
Mean
Min.
Sunrise
Sunset
c) Summer
Heating
Cooling
Heating
Max.
Mean
Min.
Sunrise
Sunset
d) Autumn
Heating
Cooling
Max.
Mean
Min.
Sunrise
Sunset
Rate of change (°C/h)
Hour of day interval
23-00 01-02 03-04 05-06 07-08 09-10 11-12 13-14 15-16 17-18 19-20 21-22

Figure 5. 12*: Overleaf. Seasonal behaviour of the average rate of change of surface temperatures by interval of hour. Dashed vertical lines indicate the annual boundaries of the sunrise and sunset cycles. The red and blue curves show the average rate of change of the maximum and minimum temperatures detected by each hour of the day. Light yellow and blue regions highlight the daily heating and cooling phases, respectively. Black points show the maximum rates of change (positive or negative) as well as the main inflections in the rates of change. Vertical dashed arrows are used to indicate the symmetrical lag of time (2 hours) between the main inflections in the rate of change of the maximum and minimum temperatures.*

Figure 5.12c shows the rate of change in temperatures during summer. More rapid increases in the temperature were detected during sunrise (05:00 – 07:00 h), reaching a maximum coincident at the end of this period. In this period, the rate of change of the mean surface temperature increased from ~ 0°C/h to 1.5°C/h, which was comparable to that seen during winter. However, the increase was higher for the mean maximum temperatures, from 2°C/h to 5.0°C/h. A marked inflection in the rates of temperature change was detected between 06:00 and 07:00 h coincident with the end of the sunrise, which experience a noticeable drop, particularly in the mean and minimum rate of change of temperature representing a fast rate of cooling. Between the morning and afternoon, diversions between the maximum, mean, and minimum rates of surface temperature change were observed. For example, while the rate of change of the mean temperatures gradually dropped from ~ 1.5°C/h (at 07:00 – 08:00 h) to -0.5°C/h during the afternoon (at 15:00 – 16:00 h), the rate of change of the mean maximum temperatures showed a more rapid reduction but over a shorter period. This lead to the inflection in temperature increase around midday (12:00 – 13:00 h).

Importantly, a second heating phase was detected when the rate of temperature change gradually increased from ~ -0.5°C/h (at 15:00 – 16:00 h) to 0.5°C/h at the beginning of sunset (18:00 – 19:00 h). However, this heating phase was more evident in the mean maximum temperatures, where the rate increased sharply ~ 2.5°C/h (14:00 – 15:00 h) to 6.5°C/h at the start of sunset. This period notably represents the fastest rate of temperature change in the monitored period for any season. A clear inflection in the rates of maximum temperature change occurred between 18:00 and 19:00 h, when a rapid reduction was observed dropping from ~ 6.5°C/h to 1.0°C/h by the of the sunset (21:00 – 22:00 h), punctuating the second cooling phase of the summer day (Figure 5.12c).

The rate of mean minimum temperature change showed a key difference to the maximum and mean surface temperatures. For example, a sharp increase in the magnitude of the rate of temperature change was detected from ~ -2.0°C/h (06:00 – 07:00 h) to a negative maximum of -5.0°C/h (08:00 – 09:00), which indicates that some areas of the cliff were exposed to rapid cooling

immediately after sunrise. This may be associated with the development of surface condensation around this time in the morning, discussed further below. Consistently, a rapid increase in the rate of change of the mean minimum temperatures were also observed halfway through sunset (19:00 – 21:00 h), were the rate of temperature change from ~ -3.8°C/h to -5.8°C/h. This defines a key inflection in temperature change around sunset, as the rate of temperature change increased towards midnight (Figure 5.12c).

As a result, three key observations can be made on the rates of temperature change during summer:

First, the surfaces of the cliff face that experienced the maximum rates of temperatures change showed two diurnal phases of rapid changes (fast heating), which were immediately followed by a rapid reduction in the rates of changes. These generated inflections in the rates of temperature change at the end of sunrise (06:00 – 07:00 h) and at the start of sunset (18:00 - 19:00). This distinctive behaviour suggests that cliff surfaces subject to either higher temperature change per hour (e.g., 2.0°C/h to 6.5°C/h), or rapid inflections in the rates of temperature change, may be subject to rapid expansion or contraction twice a day, facilitating thermomechanical cycling and stresses.

Second, the surfaces of the cliff on which minimum summer temperatures occurred also exhibited two diurnal period of negative temperature change of high magnitude (fast cooling, approaching ~ -5.0 to -6.5°C/h), which were followed by negative rates of temperature change of lower magnitude (slow cooling , approaching to -2°C/h), generating marked inflections in the rate of surface temperature change in the morning (08:00 – 09:00 h), and then again at the end of sunset (20:00 – 21:00 h). This behaviour indicates that surfaces of the cliff face that were exposed to either the higher negative temperature changes per hour (e.g., cooling, towards -6.0°C/h), or sudden inflections in the rates of change (from heating to cooling or *vice versa*), may also be subject to rapid expansion and contraction twice per day.

Third, based on the above observations, the cliff was exposed to a total of four periods of time during which pronounced inflections in the rates of change were observed. There was an apparent lag of around two hours between the inflection seen for the maximum and the minimum temperatures. I further explore this in Section 5.4, where aspect controls over the spatial distribution of temperatures are considered.

The rates of change across the diurnal thermal cycle of spring and autumn showed similar features when compared to the rates of change in summer and winter, respectively. This which may again be explained by the transitional nature of the spring and autumn periods (Figures 5.12b and 5.12d, respectively). However, two additional behaviours can be seen:

First, in both winter and autumn, relatively uniform rates of temperature change were observed both in terms of magnitude and timing, which suggests that the whole cliff face was experiencing a similar temperature regime.

Second, in both spring and summer, a similar deviation between the curves for the rate of change of the maximum and minimum surface temperatures was observed. This suggests that the cliff was not only exposed to a more complex behaviour than during the colder seasons, but also that in specific periods of time (between 04:00 and 09:00 h; and 14:00 and 21:00 h), a positive feedback was apparent whereby the warmest parts of the cliff face were rapidly warming, and with two hours of lag, the coldest surfaces were rapidly cooling.

To consider probable causes that drive the positive feedback identified above, in which the coldest surfaces were getting rapidly coldest during spring and summer, Figure 5.13 shows the modelled dew point temperature, which is indicative of the potential for cliff surface condensation. The dew point was estimated using the air temperature and relative humidity collected at the top of the cliff using a complete diurnal thermal cycle from summer. This dataset shows that after sunrise (between 07:00 and 08:00 h) and through the late afternoon and evening (between 15:00 and 20:00 h), the minimum surface temperatures increase to the dew point in the morning and decrease to the dew point in the afternoon. During these periods, surface condensation surface on the coolest sections of the cliff face may become moist and so may lead to a further decrease in temperature. This may explain the sharp increase in the magnitude of the negative rate of temperature change per hour between ~ -2.0°C/h (06:00 – 07:00 h) and -5.0°C/h (08:00 – 09:00) after sunrise, and then again, around halfway through sunset (19:00 – 21:00 h), were the rates changed from ~ -3.8°C/h to -5.8°C/h (see Figures 5.12b and 5.12c). The spatial distribution of the summer surface minimum temperatures are explored in the Section 5.4. The potential control of the observed high rates of change in temperature on temperature-induced rockfalls detected in 2021 are investigated and discussed in Chapter 6 (Discussions).

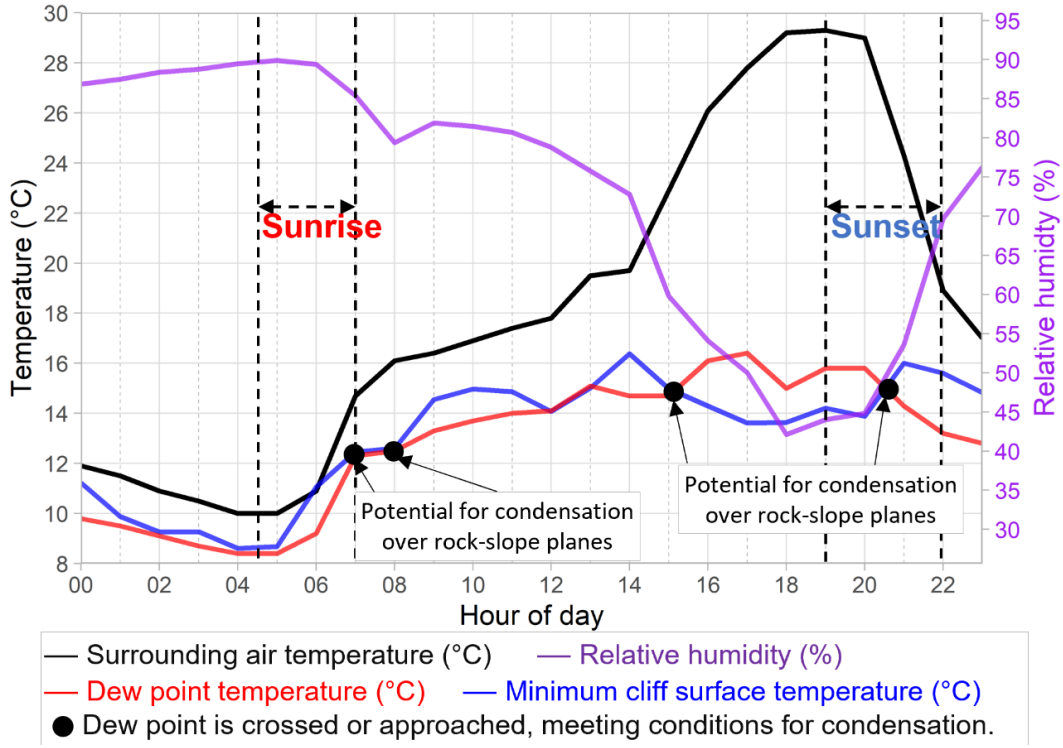

Figure 5. 13*: Diurnal intervals of time of summer, where a potential for condensation over slope planes is detected. The black dots show the threshold from which the dew point is crossed as the minimum surface temperatures of the cliff face fall below the dew point temperature or approaches this, meeting conditions for condensation to form droplets over slope planes with minimum summer temperatures. Data extracted from a typical and complete diurnal cycle of summer (16th July 2021).*

To compare how quickly or slowly the outcropping beds were heated and cooled by hour, Figure 5.14 illustrates the rates of temperature by bed for each season. This analysis was conducted in order to detect differential responses in the diurnal rates of change that characterized each bed. This analysis shows that the rate of temperature change during winter and autumn was relatively similar between beds, without notably differences in either the magnitude or timing between BS and IBSS observed. The general patter of the rate of temperature change in both beds was similar to that across the wider general window (*GW*), as discussed above using Figures 5.12a and 5.12d (for winter and autumn, respectively). However, only slight differences were observed where IBSS showed a marginally higher rate of temperature change than BS after sunrise (~ 0.3°C/h higher). This behaviour was inverted when BS showed a marginally higher rate of change than IBSS during the late afternoon and sunset (~ 0.2°C/h to 0.3°C/h higher) (Figures 5.14a, d).

Conversely, in spring and summer a more heterogeneous behaviour was observed between BS and IBSS: First, during the sunrise and into the early morning, IBSS showed notably higher rates of temperature change than BS (~ 1.0°C/h higher across the horizontal profile of

IBSS, but significantly, ~ 1.5°C/h higher across the mapping window of IBSS). Nevertheless, a notably inversion in the rates of change between both beds was observed around afternoon and throughout sunset, when BS showed higher rates of change as compared to IBSS (e.g., ~ 0.5°C/h between the mapping windows of BS and IBSS). After sunset and until the beginning of the sunrise relatively uniforms rates of change were observed in both beds (Figures 5.14b, c).

Second, a lag of time of around two hours was detected between achieving the maximum rate change in BS as compared to IBSS. For instance, while the IBSS reached a maximum of ~ 2.0°C/h by the end of the sunrise (06:00 – 07:00 h), BS reached a maximum of ~ 1.2°C/h later into the morning (08:00 – 09:00 h). Interestingly, a lag of time was again detected around the sunset: IBSS reached a maximum of ~ 0.8°C/h at the beginning of the sunset (18:00 – 19:00 h), while the BS reached a maximum of ~ 0.6 °C/h between 19:00 and 20:00 h (Figures 5.14b, c). This may reflect the effect of different exposures to the insolation angles reaching each bed, or properties of the two rock types, and their respective ability to absorb and/or reflect insolation.

Four key observations can be made from the description of the diurnal rates of change by bedding (Figure 5.14):

First, a differential response in both the magnitude and timing was detected between the rates of changes that characterized each bed. The rate of temperature change differed around sunrise and sunset for each bed. As such, this may induce a reversal of the direction of the temperature gradient and any resultant stresses.

Second, since relatively uniform rates of change were detected in both beds during the night-time, this suggests that the sunrise and sunset may hold significant controls on the timing and magnitude of any differential responses between bed to thermal controls.

Third, differential responses between beds were enhanced during the warmer seasons, as compared to the notably uniform rates of temperature change observed in the winter and autumn. This suggests the potential for some degree of seasonal control over differential rates of temperature change that characterised each bedding layer.

Fourth, the diurnal thermal inversion between the rates of temperature change of BS and IBSS was consistent with the seasonal thermal inversion of temperatures that was detected using time-series of the temperature changes through the year by beds (see Figure 5.4, Section 5.2). This is because in Figure 5.4, the IBSS were, on average, warmer than BS, particularly in the summer.

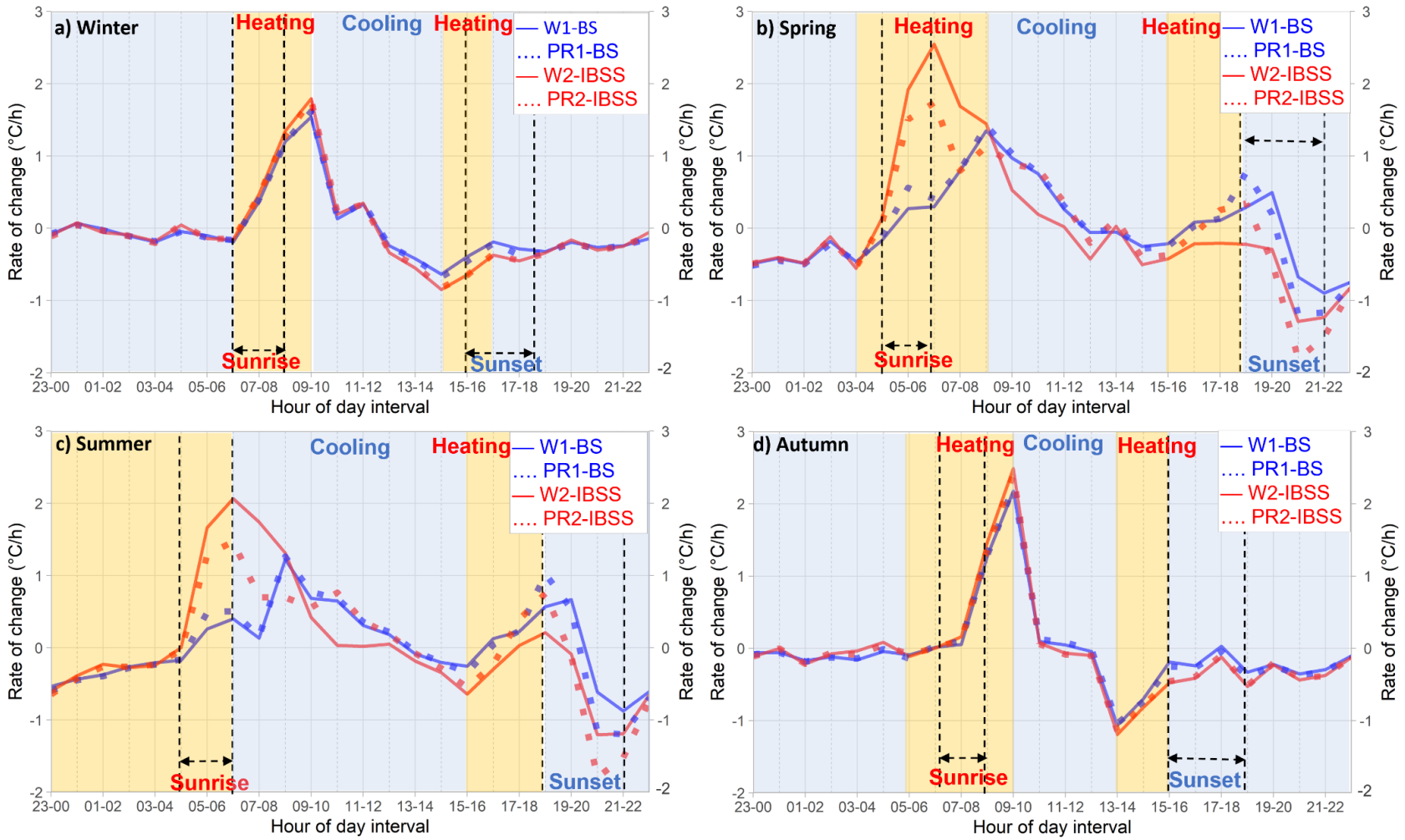
a) Winter
b) Spring
c) Summer
d) Autumn
Heating
Cooling
Heating
Sunrise
Sunset
— W1-BS
.... PR1-BS
— W2-IBSS
.... PR2-IBSS
Rate of change (°C/h)
Hour of day interval
23-00
01-02
03-04
05-06
07-08
09-10
11-12
13-14
15-16
17-18
19-20
21-22

Figure 5. 14: *Overleaf. Seasonal behaviour of the mean rate of change of surface temperatures by beds. W1-BS and PR1-BS represent the mean rates across the mapping window and horizontal profile across Bedded Sandstones, respectively. W2-IBSS and PR2-IBSS represent the mean rates across the mapping window and horizontal profile across Interbedded Sandstones and Siltstones, respectively. Dashed vertical lines indicate the annual boundaries of the sunrise and sunset cycles. Light yellow and blue regions highlight the daily heating and cooling phases, respectively.*

In this section of the IRT results, I have examined the timing and nature of the change in surface temperature across the complete diurnal thermal cycle, by season. As such, ten principal observations can be made:

- The hourly analysis of the diurnal cycle of surface temperatures for winter demonstrated that the cliff face was uninterruptedly exposed to mean and minimum temperatures <0°C during for ~ 45% and 70% of the day. During ~ 63% of the day, the average minimum temperatures remained stable around -3°C and -4°C, followed by warming of minimum temperatures approaching to ~ 1.0°C between 11:00 and 13:00 h. This suggests that the parts of the cliff at which minimum temperatures occurred are possibly subject to some degree of either freezing, or may experience freeze-thaw. These areas appear to be those subject to a combination of permanent shadow and some of the locations of the lowest minimum temperatures observed in 2021 (e.g., -5.0°C to -10°C).

- During the diurnal surface temperature cycle of both winter and autumn, the maximum, mean and minimum surface temperatures are similar showing no notable deviations through the day. This indicates that during the colder seasons, the cliff face was exposed to a relatively homogenous surface temperatures, which in the case of winter, was characterized by a marked predominance of temperatures <0°C.

- The hourly analysis of the diurnal surface temperature cycle in summer showed that sharp raises in the mean surface temperatures were coincident with the start of the sunrise and lasted until early morning generating increases in surface temperature of ~ 4.5°C. In the same period, the mean maximum temperatures increase most significantly, up to ~ 9.0°C. This suggests that the surface of the cliff can be rapidly warmed as soon as the sunrays strike at sunrise. This behaviour was not observed in the colder seasons, most probably due to the weaker sunlight as a result of the lower solar incidence angle. Temperatures in winter also showed a delayed response to increase until after sunrise and were characterised by a more gradual increasing trend.

- Two marked phases of rapid and continuous increases in the maximum surface temperature (05:00 – 08:00 h, and then again, 14:00 – 19:00 h) were observed during spring and summer. This suggests that the cliff face was exposed to two heating phases per day: the first between the sunrise and midday, and then the second around late afternoon prior to sunset, with both exhibiting similar peaks in temperatures. This behaviour was not observed during the cooler seasons, when the cliff experienced only one morning heating phase.

- The diurnal rates of change in surface temperature during winter demonstrated that rapid changes (heating) occurred between sunrise through the early morning (from ~ -0.1°C/h to 1.8°C/h). After 09:00 –10:00 h, fast negative rates of change (cooling) were detected generating a significant inflection in the rates of temperature change. This not only suggests that the rock face can experience rapid heating and then cooling hour by hour, but also that this kind of rapid transition in heating/cooling could promote themormechanical processes dependent on rates of temperature change.

- The daily rates of temperature change in spring and summer showed two phases of rapid temperature change per hour (heating), immediately followed by rapid reductions in the rate of change (cooling), again generating two inflections at the end of sunrise and at the start of the sunset. Interestingly, two marked inflections in the rate of temperature change were also detected in the surface minimum temperatures. This suggests that during the warmer seasons, the cliff face was exposed to a total of four principal inflection in the rate of temperature change per day, which over time may thermomechanical loading and stress. As in spring and summer, four inflections were detected per day, while in winter and autumn only one inflection was observed, which may lead to such processes and their consequences such as rockfall being more effective in warmer seasons, although with a potential time delay for the heating to affect the rock mass at depth and so, to cause thermal stress and cracking.

- The diurnal rate of surface temperature change in spring and summer also showed a more complex behaviour as compared to both winter and autumn. This was characterised by a notable deviations in the pattern of rates of maximum and minimum temperature change.

- Apparently systematic lags of two hours were observed between the inflections observed in the rate of change for the maximum and minimum temperatures during both sunrise and sunset. This not only demonstrates that the sunrise and sunset are key controls over the timing and magnitude of changes in the rates of surface temperature change in the

warmer seasons, but also that there was a relationship between the processes that control each inflection. I further explore this by analysing large-scale aspects effects in Section 5.4.

- During spring and summer, a differing surface temperature response was observed between the rates of change that characterized the bedded sandstones (BS) and interbedded sandstones and siltstones (IBSS), primarily as differences in the speed of the temperature changes around sunrise and sunset. For example, while rate of change of IBSS was around 2°C/h by the end of the sunrise, the rate of change of BS was ~ 1.5°C/h lower. This behaviour was inverted around the sunset, when IBSS showed lower rates of change than BS (in average, ~ 0.5°C/h lower). As a result, during the day, this may result in an inversion in the direction of the temperature gradient across portions of the cliff face, and especially at the boundaries between outcropping beds.

- Differential rates of surface temperature change between beds were enhanced during the warmer seasons, compared to similar and uniform rates of change in winter and autumn. This reaffirms that the surface temperatures of the cliff were more homogenous during the autumn and winter, but is also a seasonal control over the magnitude and timing of the differential rates of change that characterized the diurnal thermal cycle of each bed.

5.4 Aspect effects on surface temperatures

In this section, thermal imagery is combined with surface topography data to consider aspect and inclination controls on the surface temperature variability. This is used to examine large-scale aspect controls over the magnitude and spatial distribution of surface temperatures of the cliff face. This section begins with an analysis of the stereographic projection (stereonets) of the locations for the observations of mean, maximum, minimum, and differential temperatures detected throughout the monitoring period. This is followed by the analysis of a stereographic projection, and equivalent IRT maps, of the mean rates of change of surface temperature for key intervals within the diurnal cycle for each season: sunrise, midday, sunset, and midnight. These analyses were conducted to provide an understanding of the spatial distribution of the hourly rates of change in temperatures examined above (see Section 5.3).

In this study, the aspect and inclination of the local cliff surface on a pixel by pixel basis (i.e., the compass direction of the cliff from the North, which is measured clockwise from 0° or due North to 360°, again due North) was interpreted from the analysis of the dip direction (the azimuth of the steepest descent plane), which is the direction of the horizontal trace of the line of dip, measured clockwise from the North (Hoek and Bray, 1981). Like the aspect, dip direction ranges from 0° (due North) to 360° (again due North). The dip and dip directions were calculated using the *Cloud Compare* plug-in *'Facets'* (Dewez et al., 2016), which extracts dip and dip direction of individual exposed planar discontinuity surfaces, analogous to outcropping discontinuities. The application of *Facets* was undertaken using the *Fast-Matching* algorithm, which performed a segmentation of a 3D point cloud of the cliff face into sub-cells (an octree structure), and then computed elementary planar surfaces, from which individual surface were aggregated into 3D polygons according to a coplanarity criterion (Dewez et al., 2016). Here, the *Facets* was applied to the first point cloud collected in 2021 (master annual scan), which was oriented to North. Following the procedure adopted by Benjamin (2018), where *Facets* was used for similar purposes upon similar cliff structures across the North Yorkshire coast, a trial-and-error approach was used to select the optimum parameters for the coplanarity criterion, which were refined until a satisfactory surface discretisation of exposed planar discontinuity surfaces was achieved.

The principal parameters used to define the coplanarity criterion were as follows: minimum number of points per facet (10); maximum edge length (0.10 m), and a distance or roughness criterion (0.10 m), which was used to define the planarity of each facet. Here, the last parameter requires that > 99% of the points that make up a facet are within 0.10 m of the modelled facet plane. As demonstrated by Benjamin (2018), the overall result was most sensitive to

variations in the minimum number of points per facet, however, for the purposes of this research, no significant differences were obtained by varying the minimum number of points from 10 to 5, and so the highest number was used to speed the computation. The resultant polygons contained the dip and dip direction for all individual planar surfaces upon the cliff face, which were then exported to a standard GIS environment (Figure 5.15).

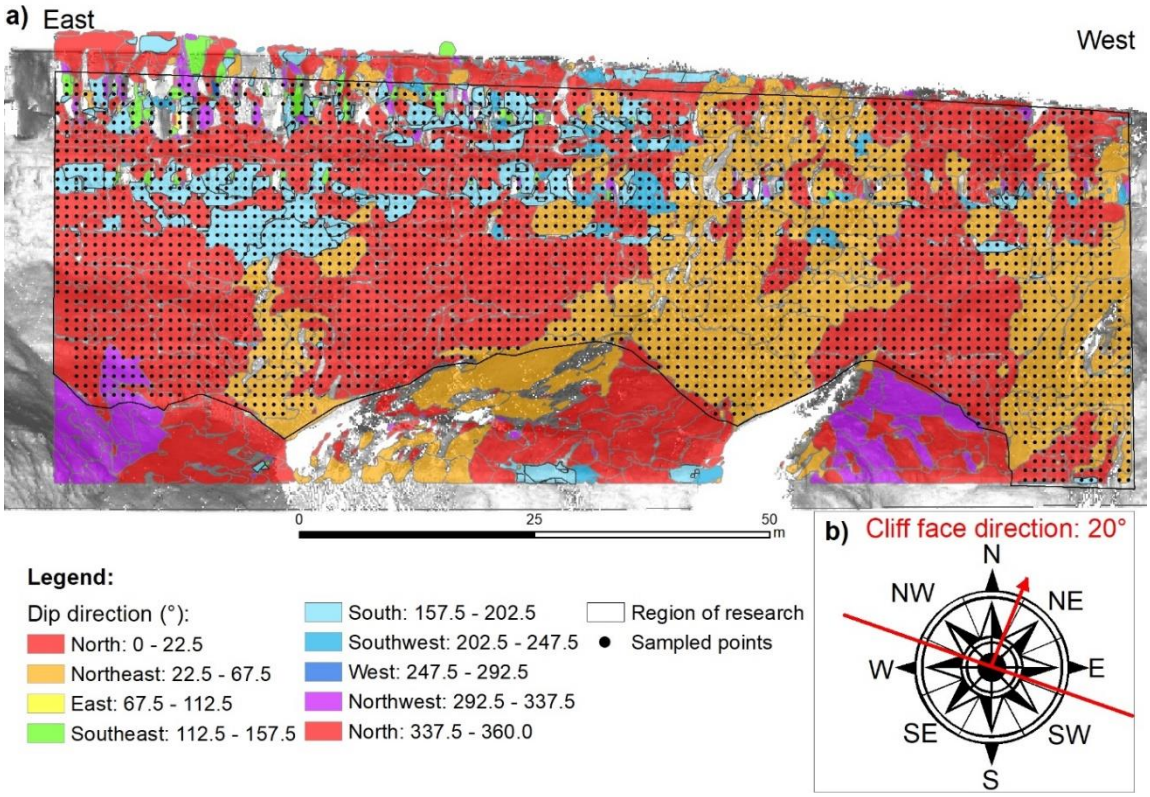

Figure 5. 15: *Calculation of the dip and dip direction of discontinuities using the Facets plug-in. a) Frontal view of the cliff face showing the distribution of the dip direction of individual planes outcropping within the Region of Research (ROI) zone that overlaps with the field of view of the thermal camera. The boundaries of the ROI are highlighted using black boundary line. b) Zenith view of the general dip direction of the cliff face (Red trace and perpendicular arrow) respect the N-S and the sunrise (E) to the sunset (W) direction.*

Using the layer of individual polygons representing individual discontinuity planes, a *Fishnet* technique was used to create a layer of sampling points from which to extract dip and dip direction across the cliff (ROI) at 1 m spacing. A 1 m regular grid for sampling was selected to sample, as much as possible, data that properly represents the spatial variability of the dip, dip direction and temperature of contiguous yet different planes upon the cliff. As a result of this strategy, over 3,300 points were obtained (Figure 5.15). The extracted dip, dip direction and temperature data was imported into the software *DIPS* (*Rocscience Ltda.)* for the generation of stereographic projections, in which the sampled surface temperatures were represented as poles,

whose spatial distribution over the stereonet were defined by the dip and dip direction. As a result, this procedure permitted the analysis of the cliff temperature as a function of dip and dip direction.

Figure 5.15 illustrates that the cliff face has a predominant northerly orientation (20°N). As such, north and northeast facing planes are the predominant in this dataset (~ 83% of the total area of the ROI). South facing planes represent exposed surfaces in which the steepest descent plane was predominantly dipping into the cliff face so that its azimuthal direction was not pointing frontally (~ 9% of the total area of the ROI), such as around the bottom of overhanging rock-blocks or indented surfaces. However, the dip direction of these planes can also be interpreted as north facing surfaces as these outcrop following the general northerly direction of the cliff face. Towards the top of the ROI, very rough surfaces are detected showing heterogeneous dip directions representing hanging rock-blocks and angular bridges in the sandstones facing north, northwest or south. It is important to note here that the cliff planes facing the N and NE, are orthogonal to the direction of incident sunrays during sunrise. Conversely, cliff planes facing NW tend to face the towards the direction of sunset.

Figure 5.16 shows the stereonets of the mean temperatures from 2021, and the maximum and minimum temperatures recorded in each pixel, in addition to the difference between the maximum and minimum values. The temperature values shown were extracted from the summary thermal maps 2021 (see Chapter 4, Section 4.3, Figures 4.13 and 4.15). The stereonets were examined to provide an overview of any aspect-dependent patterns that characterize surface temperatures. In order to enable easier examination, the underlying dataset has been grouped by ranges. The corresponding great circle of each range of temperatures is plotted, which shows the mean dip and dip direction for that the temperature range. In addition, the great circle representing the dip and dip direction of the cliff face was plotted (67°/020°) to facilitate comparison with the great circles of the temperature ranges.

Figure 5.16a shows that during 2021, mean temperatures clustered upon surfaces facing the N and NE, as this is the general azimuthal orientation of the cliff face. Mean temperatures distributed across the SW, S, and SE quadrants of the stereonets were also common, representing cliff planes dipping into the cliff face. Lower mean temperatures ($\leq$ 8.2°C) were clustered almost exclusively over cliff planes facing N and NE, and preferentially over lower dipping planes (between 56° and 59°), which corresponds to the interbedded sandstones and siltstones (IBSS, see Figure 4.13a, in Section 4.3, Chapter 4). This again implies a combined aspect and rock-type control on the distribution of the lower cliff surface temperatures, even at a fine (1 m) grid resolution. Conversely, the higher mean temperatures ($\geq$ 9.4°C) were preferentially clustered over

cliff planes facing the N, NW, S and SW, but also across planes with higher dip angles (between 76° and 79°), corresponding with the bedded sandstones (BS, see Figure 4.13a, in Section, Chapter 4). The mid-range temperatures (8.2°C – 9.4°C), showed no apparent clustering over specific cliff angles or facing directions.

The stereonet of maximum temperatures (Figure 5.16b) illustrates a heterogeneous spatial distribution, especially for the mid- and lower maximum temperatures (≤ 32.5°C), which were clustered on surface facing N, NE, NW, SE. S, and SW. However, mid-range maximum temperatures (25.0°C – 32.5°C) showed a preferential clustering upon cliff surface with lower dip angles (66° - 68°), again corresponding to the general structure of the cliff face. Interestingly, the range of the highest temperatures (≥ 35°C) occurred preferentially on N-NW facing planes and upon the least steep cliff surfaces (dip = 63°), suggesting some level of aspect control. Conversely, the range of the lowest maximum temperatures (≤ 25°C) occurred upon steeper slope surface (dip = 74°) preferentially facing N-NE, corresponding to rock-blocks in the bedded sandstones located towards the top of the cliff where shadow seems to be dominant during most of the day (see Figure 4.13b, Section 4.3, Chapter 4).

The stereonet of the minimum detected temperatures 2021(Figure 5.16c) shows that the lowest range of temperatures (≤ -10°C) were clustered upon cliff surface facing N and NE but at more shallow slope planes (dip = 56° to 59°). This corresponds with areas dominated by IBSS (see Figure 4.13c, Chapter 4). This distribution also holds similarities with the lowest range of mean temperatures in 2021 (Figure 5.16a). Conversely, the range of the highest minimum temperatures (≥ -8.0°C) occurred across all azimuthal directions but over steeper cliff surfaces, which often correspond to BS (dips ≅ 75° to 80°). This holds similarities with the locations of the highest mean temperatures in 2021. The mid-range of the minimum temperatures (between -10°C and -8.0°C) were clustered upon cliff surfaces distributed across all azimuthal directions, although these were preferentially clustered between less steep planes, and followed the general dip and dip direction of the cliff face (dip = 62 to 68°).

Figure 5.16d shows the stereonet of the temperature differences during 2021. The range of the maximum difference in temperatures, that fluctuated between 40°C and 50°C, were preferentially oriented towards NW, N and NE facing surfaces that were less steep (dip = 57° to 63°). Also, heterogeneous azimuthal orientations were detected for temperature differences that ranged between 30°C and 40°C, as these were distributed across all quadrants of the stereonet and followed the general dip and dip direction of the cliff face (dip = 66° to 72°). The range of lowest temperature differences (25°C to 30°C) was preferentially oriented towards N and NE but upon

steeper dipping surfaces (dip = 85°), and so tended to be spatially located towards the top of the cliff across hanging rock-blocks of BS (see Figure 4.15, in Section 4.3, Chapter 4). Overall, a higher degree of spatial variability across surfaces of a wider range of dip and dip directions characterizes the differential temperatures.

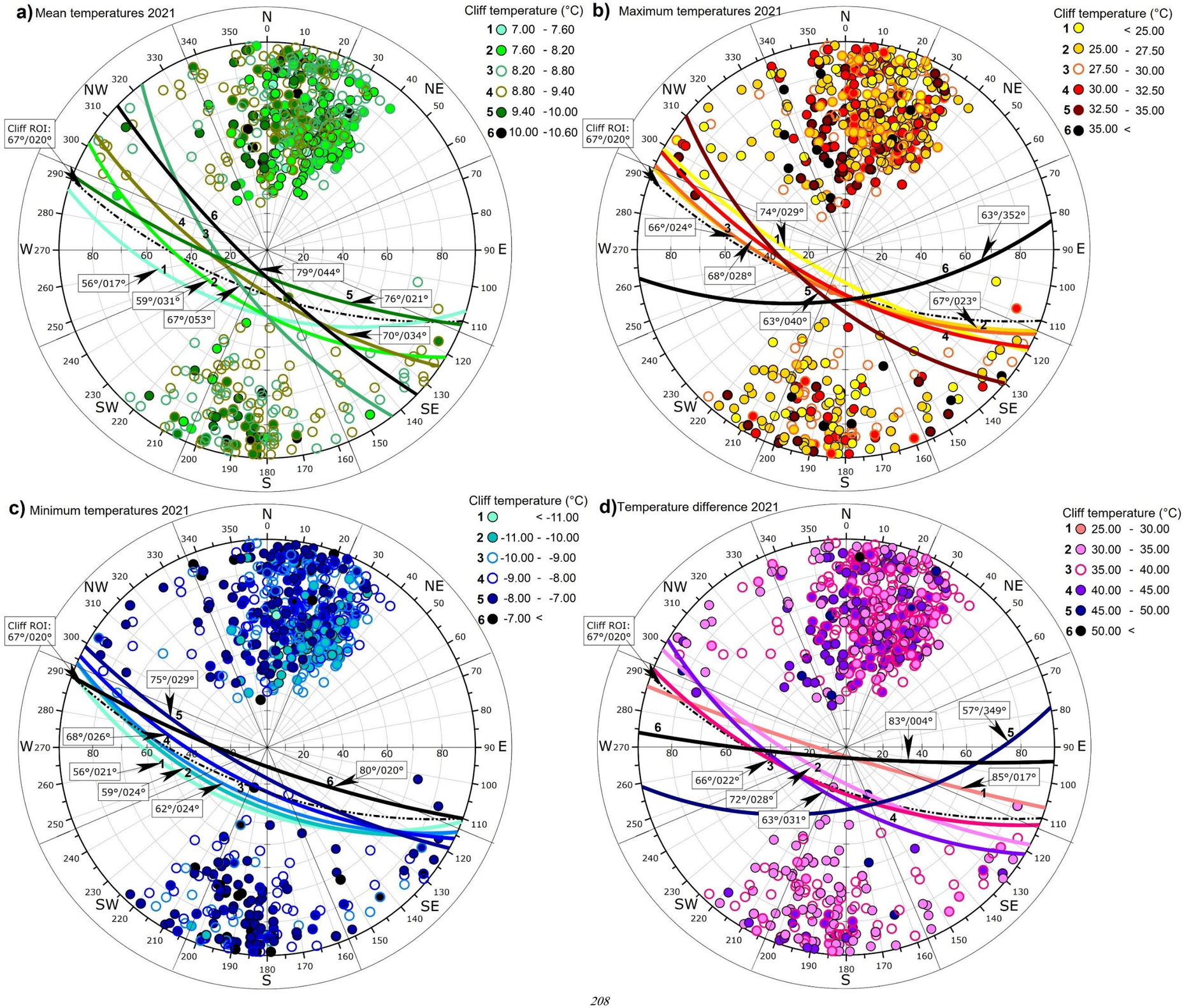
a) Mean temperatures 2021
Cliff temperature (°C)
1 7.00 - 7.60
2 7.60 - 8.20
3 8.20 - 8.80
4 8.80 - 9.40
5 9.40 -10.00
6 10.00 -10.60
Cliff ROI: 67°/020°
56°/017°
59°/031°
67°/053°
79°/044°
76°/021°
70°/034°
b) Maximum temperatures 2021
Cliff temperature (°C)
1 < 25.00
2 25.00 - 27.50
3 27.50 - 30.00
4 30.00 - 32.50
5 32.50 - 35.00
6 35.00 <
Cliff ROI: 67°/020°
66°/024°
74°/029°
68°/028°
63°/040°
63°/352°
67°/023°
c) Minimum temperatures 2021
Cliff temperature (°C)
1 < -11.00
2 -11.00 - -10.00
3 -10.00 - -9.00
4 -9.00 - -8.00
5 -8.00 - -7.00
6 -7.00 <
Cliff ROI: 67°/020°
56°/021°
59°/024°
68°/026°
62°/024°
75°/029°
80°/020°
d) Temperature difference 2021
Cliff temperature (°C)
1 25.00 - 30.00
2 30.00 - 35.00
3 35.00 - 40.00
4 40.00 - 45.00
5 45.00 - 50.00
6 50.00 <
Cliff ROI: 67°/020°
66°/022°
72°/028°
63°/031°
83°/004°
57°/349°
85°/017°
N
NE
E
SE
S
SW
W
NW

Figure 5. 16: *Overleaf. Distribution of the cliff temperatures by dip and dip direction for key summary variables of surface temperatures. a) Stereonet of the mean temperatures 2021 (see Figure 4.13a, Section 4.3, Chapter 4). b) Stereonet of maximum temperatures detected in 2021 (see Figure 4.13b, Chapter 4). c) Stereonet of minimum temperatures detected in 2021 (see Figure 4,13c, Chapter 4). d) Stereonet of the differential surface temperature calculated as the subtraction between the maximum and minimum temperatures detected in 2021 (see Figure 4.15, Chapter 4). Each stereonet was plotted using the upper hemisphere, equal angle projection and over 3,300 samples of pole vectors extracted across the region of research (ROI) at 1 m spacing (see Figure 5.15). Values around the perimeter of the stereonets represent the dip direction, while the vertical and horizontal values starting from the centre show the dip of the sampled slope planes (from 0 to 90°). Each category of cliff temperature (1 – 6) has a corresponding great circle representing the mean dip and dip direction estimated for each category, which were calculated for the sampled points belonging to the north hemisphere of the stereonets. The dip and dip direction of the great circles is showed within white boxes and using standard nomenclature (dip/dip direction), while arrows and numbers (1 – 6) were used to point each corresponding great circle. The great circle representing the mean dip and dip direction of the cliff face is shown using a point-dashed arc.*

Overall, three patterns were detected from the stereonets of 2021 summary temperatures (Figure 5.16):

First, mean lower surface temperatures were detected over N and NE facing planes with lower dip angles, which correspond to outcrops of IBSS.

Second, higher mean and minimum temperatures were distributed across all azimuthal directions but notably cluster across the steeper sections of the cliff face, corresponding to outcrops of BS.

Third, maximum and differential temperatures show a notably spatial variability, were no distinctive clustering upon cliff planes facing in particular directions, or over particular dips angles, were detected. This suggests a more complex distribution of the surface temperature dependent on fine scale (1 m) cliff morphology.

Below, the stereographic projections and equivalent thermal maps of the mean rates of change of summer cliff surface temperatures detected during the sunrise, midday, sunset, and midnight are analysed together using the Figures 5.17 and 5.18, respectively. This linked analysis was done because whilst the stereonets can be used to represent temperature as a function of dip and azimuthal direction of particular cliff planes, the thermal maps show the equivalent spatial distribution. In particular, Figure 5.17a shows the stereonet of the mean rate of surface temperature change during sunrise between 04:00 and 07:00 h. This stereonet was built using a

total of 89 individual thermal images from which a thermal scene of mean rates of change per pixel was computed to feed into this stereonet (Figure 5.18a).

Four key observations can be made from analysing Figure 5.17a and the corresponding thermal map (Figure 5.18a):

First, higher positive rates of change (≥ 1.0°C/h) were clustered almost exclusively upon N and NE facing planes, coincident with surface exposed to the first sunrays that strike the cliff face at sunrise. Also, higher rates of change occurred over less steeply dipping cliff surface most commonly within outcrops of IBSS, dipping between 60° and 67°, mirroring the general dip of the cliff face.

Second, negative rates of temperature change (≥ 0°C/h), indicative of cooling, were preferentially clustered towards N and NW facing planes, which corresponded the cliff surface not directly heated by sunrise sunrays. For example, negative rates of change were preferentially upon the steepest cliff planes (dip ≅ 74°) of hanging rock-blocks within BS facing NW (see upper left zone of Figure 5.17a).

Third, positive (~NE) and negative (~NW) rates of temperature change with higher magnitude tended to display a vertical extent upon the cliff face, which tended to cross multiple beds again demonstrating the large-scale aspect control as a result of the cliff morphology (≥ 10 m) on rates of temperature change.

Fourth, the lower positive rates of temperature change (between 0.0°C/h to 1.0°C/h), show no preferential clustering across specific surface orientations, which is explained by the fact that, in the absence of large-scale aspect controls, lower positive rates of change (0.0°C/h to 0.5°C/h) occurred within sub-horizontal structures of BS across the IRT image, and so face all azimuthal directions. Overall, the poles representing positive rates of temperature change were notably predominant during the sunrise.

The stereonets of the mean rates of change across the summer midday are presented in Figure 5.17b. This stereonet was built based on a total of 99 images representing rates captured between 11:00 and 13:00 h, from which a thermal map of mean rates per pixel was derived (Figure 5.18b). Four key patterns were identified from these figures:

First, the highest positive rates of temperature change (≥ 0.4°C/h) were clustered across NW facing planes with lower dip angles (average dip ≅ 58°), showing an opposite orientation compared to the highest rates during sunrise which faced NE.

Second, the lowest negative rates of temperature change (≥ -0.2°C/h) were exclusively located across cliff surfaces facing N and NE, but again on surface with lower dip angles within the IBSS (55° to 58°). Again, this illustrates a difference compared to the locations of the negative rates of temperature change at sunrise which faced N-NW. Hence, a diurnal spatial shift of the dip direction of those surfaces experiences the lowest and highest rates of change was detected.

Third, again, for the mid-range rates of temperature change (0.0°C/h to 0.4°C/h), which were the predominant at this time of day, showed no preferential clustering of temperatures regardless of the type of bedding (see Figure 5.18b).

Fourth, a sequential ordering of the great circles, representing the mean dip and dip directions per range of temperature, can be observed. For example, these sequentially ranged from negative rates of change (≥ -0.4°C/h) for which the dip was the lowest (55°), to 64° for mid-range rates of change (0.0 to 0.2°C/h), to 70° for the higher positive rates of temperature change (0.2°C/h to 0.4°C/h). This indicates that during the summer midday, a systematic increase in the rates of change by surface slope angle occurs, confirming a relationship between the surface temperature change and the surface dip angle. Overall, poles representing positive rates of temperature change were dominant around midday, although these were of lower magnitude when compared to those detected during sunrise.

The stereonets of the mean rates of change during the summer sunset period is shown in Figure 5.17c. This stereonet was built from a total of 113 images representing the rates detected between 19:00 and 22:00 h (Figure 5.18c). It is important to note that the rates of temperature change during sunset occurred after the second heating phase of the diurnal cycle in summer. This represented a rapid reduction of the surface temperature up until the start of the sunset (see Figure 5.12c, in Section 5.3.). Four patterns were identified from these figures:

First, a predominance of negative rates of temperature change was observed (cooling), where no preferential clustering by dip or dip direction was observed. As such, poles representing temperatures occur across most directions shown on the stereonet.

Second, a predominance of negative rates of temperature change with the highest magnitude (< -1.5°C/h) that clustered over low dip angle cliff surface were observed (average dip ≅ 60°).

Third, positive rates of temperature change (≥ 0°C/h) were the least common at this time, but where they did occur, they were across N and NE facing planes, over hanging rock-blocks of

BS at the top of the cliff, which may be indicative of the cliff face in this area retaining heat through the night.

Fourth, and as observed at midday, a sequence of great circles representing specific ranges of temperature, was detected. For instance, while the lowest dip angle surfaces showed the lowest rates of change (≥ -1.5°C/h), intermediate rates were clustered over more intermediately dipping surfaces (e.g., 65°), while higher rates of change occurred across the steepest cliff surfaces (e.g., between 73° and 79°). As such, a relationship was again detected between the dip angle of the cliff face and the observed rates of temperature change. These patterns can be explained by inspecting the corresponding thermal map (Figure 5.18c). Although both large- and small-scale aspect effects were observed, these areas exhibited a generally vertical extent, encompassing across different sections of the cliff including NW, N, and NE facing planes. At the same time, negative rates of temperature change with the highest magnitude occurred over all slope surfaces with a lower dip angle. This effect is further examined by inspecting the spatial migration of temperature by aspects per hour (see Figure 5.22, below in this Section).

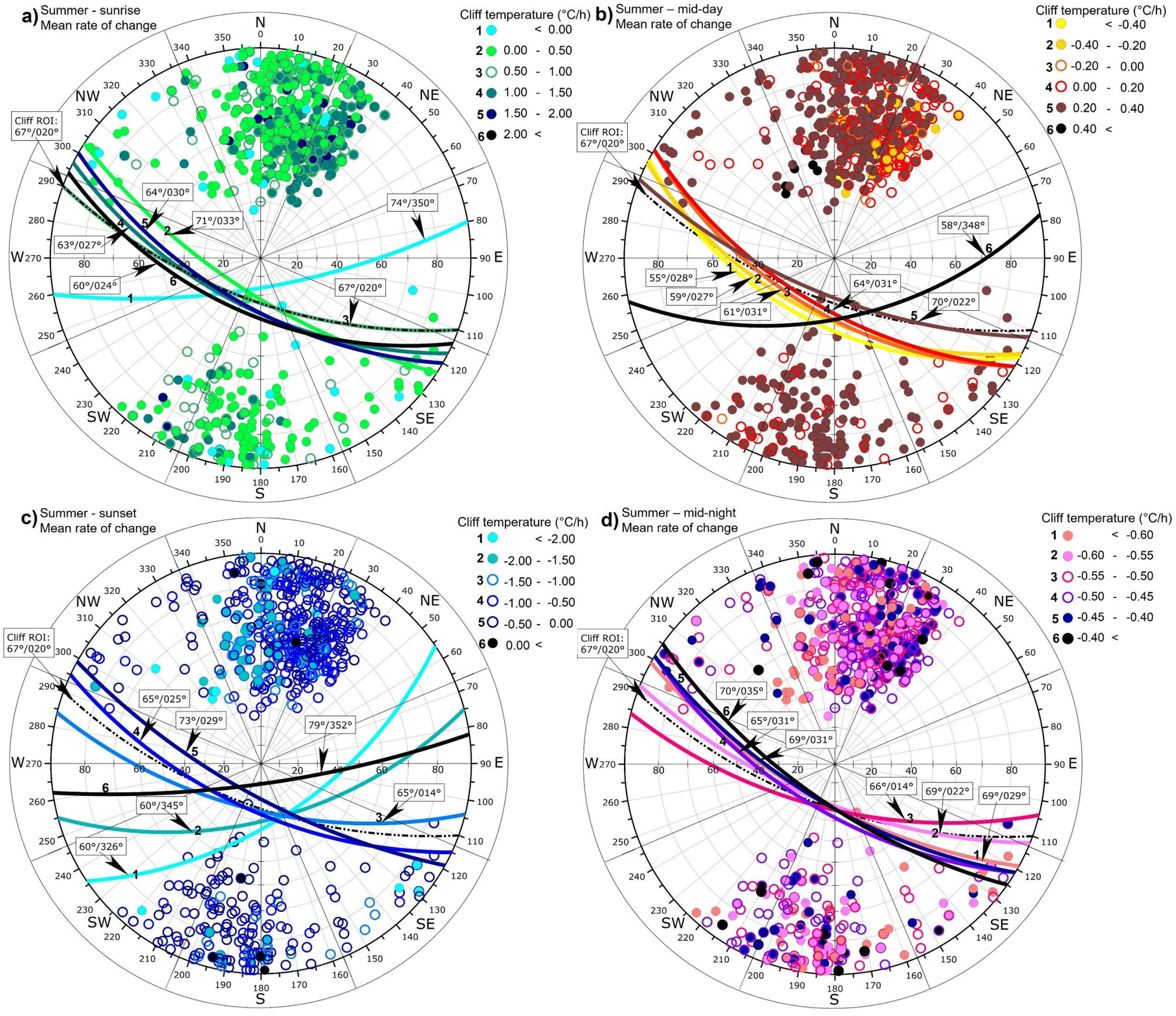
a) Summer - sunrise
Mean rate of change
Cliff temperature (°C/h)
1 < 0.00
2 0.00 - 0.50
3 0.50 - 1.00
4 1.00 - 1.50
5 1.50 - 2.00
6 2.00 <
Cliff ROI: 67°/020°
63°/027°
64°/030°
71°/033°
74°/350°
60°/024°
67°/020°
b) Summer – mid-day
Mean rate of change
Cliff temperature (°C/h)
1 < -0.40
2 -0.40 - -0.20
3 -0.20 - 0.00
4 0.00 - 0.20
5 0.20 - 0.40
6 0.40 <
Cliff ROI: 67°/020°
55°/028°
59°/027°
61°/031°
64°/031°
70°/022°
58°/348°
c) Summer - sunset
Mean rate of change
Cliff temperature (°C/h)
1 < -2.00
2 -2.00 - -1.50
3 -1.50 - -1.00
4 -1.00 - -0.50
5 -0.50 - 0.00
6 0.00 <
Cliff ROI: 67°/020°
65°/025°
73°/029°
79°/352°
60°/345°
60°/326°
65°/014°
d) Summer – mid-night
Mean rate of change
Cliff temperature (°C/h)
1 < -0.60
2 -0.60 - -0.55
3 -0.55 - -0.50
4 -0.50 - -0.45
5 -0.45 - -0.40
6 -0.40 <
Cliff ROI: 67°/020°
70°/035°
65°/031°
69°/031°
66°/014°
69°/022°
69°/029°
N
NE
E
SE
S
SW
W
NW

Figure 5. 17: *Overleaf. Daily distribution of temperature changes by dip and dip direction in summer. a) Stereonet of the mean rate of change in sunrise. b) Stereonet of the mean rate of change in mid-day. c) Stereonet of the mean rate of change in sunset. d) Stereonet of the mean rate of change in mid-night. Each stereonet was plotted using the upper hemisphere, equal angle projection and over 3,300 samples of pole vectors extracted across the region of research (ROI) (see Figure 5.15). Values around the perimeter of the stereonets represent the dip direction, while the vertical and horizontal values starting from the centre show the dip of the sampled slope planes (from 0 to 90°). Each category of cliff temperature (1 – 6) has a corresponding great circle representing the average dip and dip direction estimated for each category, which were calculated for the sampled points belonging to the north hemisphere of the stereonets. The dip and dip direction of the great circles is showed within white boxes and using standard nomenclature (dip/dip direction as 00°/000°), while arrows and numbers (1 – 6) were used to point each corresponding great circle. The great circle representing the mean dip and dip direction of the cliff face ROI is shown using a point-dashed arc.*

Figure 5.17d shows the stereonets of the means rates of temperature change during midnight in summer. This stereonet was built from 61 images captured between 23:00 and 01:00 h (Figure 5.18d). Two important behaviours were detected:

First, negative rates of temperature change were dominant during the night, but no specific clustering was identified with poles dispersed over all cliff azimuth directions.

Second, the great circles of the mean rates of temperature change were closely aligned, indeed overlapping between dips of 65° to 70°. As such, this reaffirmed that there were no preferential locations of temperature change. By inspecting the thermal map (Figure 5.18d), it can be seen that the rates of temperature change were not only negative, but notably homogenous across the cliff face. This demonstrates that insolation during sunrise and sunset had a significant role not only in driving aspect dependent heating, but also in defining the directivity and magnitude of surface temperatures. I further explore this behaviour by inspecting the spatial pattern of temperature by aspect per hour.

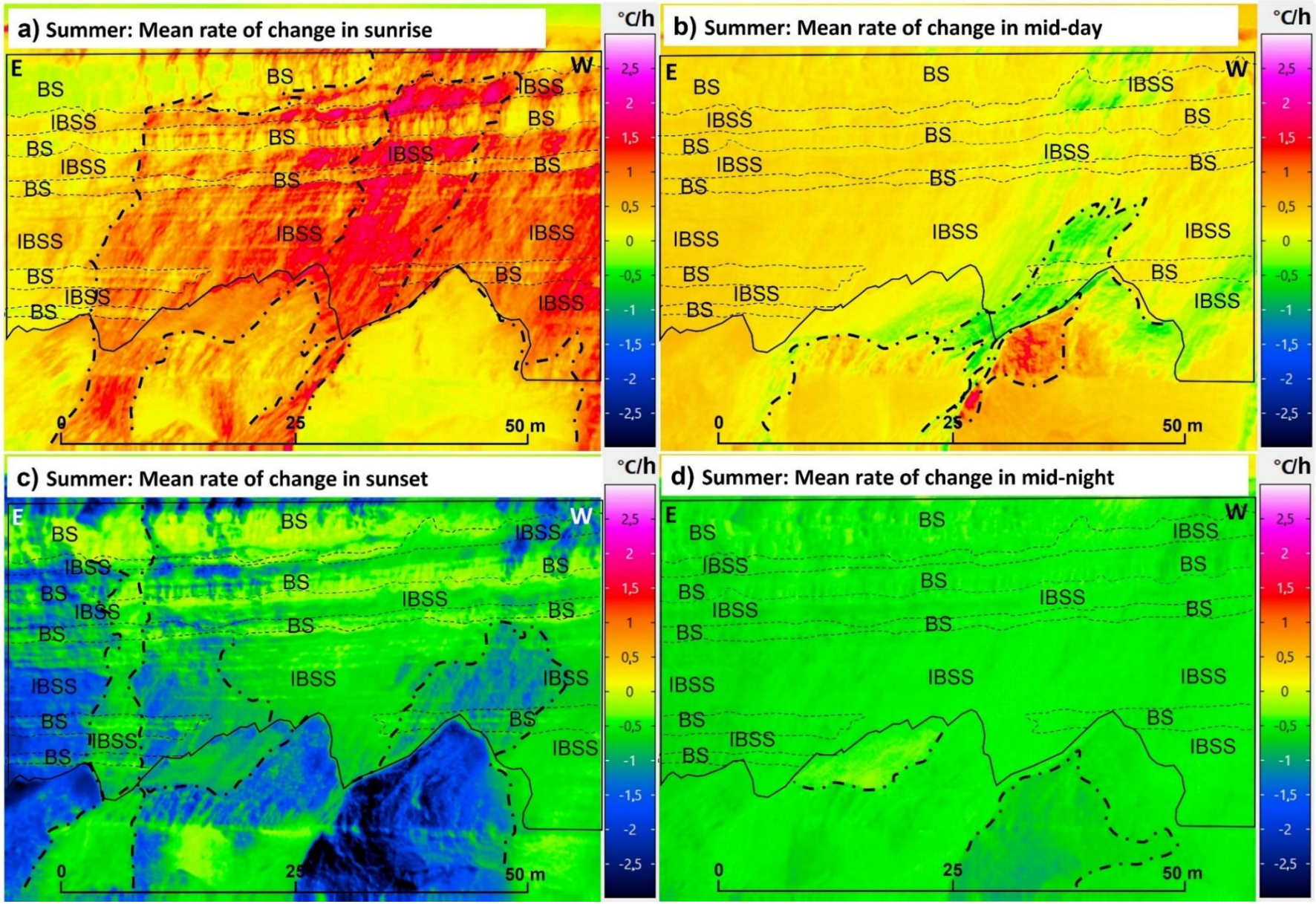
a) Summer: Mean rate of change in sunrise
b) Summer: Mean rate of change in mid-day
c) Summer: Mean rate of change in sunset
d) Summer: Mean rate of change in mid-night
°C/h
2,5
2
1,5
1
0,5
0
-0,5
-1
-1,5
-2
-2,5
E
W
BS
IBSS
0
25
50 m

***Figure 5. 18**: Overleaf. Thermal scenes of the mean rate of change detected in summer for key diurnal times. a) Mean rate of change during sunrise. b) Mean rate of change in mid-day. c) Mean rate of change in sunset. b) Mean rate of change in mid-night. Black boundary lines show the Region of Research (ROI) for this study. Each thermal scene is overlapped with the principal beds outcropping in the ROI, where BS: Bedded sandstones; IBSS: Interbedded sandstones and siltstones / carbonaceous muds. Near horizontal dashed lines show bedding controls on temperatures. Thick vertical dashed lines were used to map and show aspect controls on the rates of change. In each image, the Eastern and Western directions are shown using the letters E and W, respectively.*

Overall, four key observations can be made over the summer period (Figures 5.17 and 5.18):

(1) Positive and negative rates of temperature change of a higher magnitude were detected, during the sunrise and sunset, respectively, and in both cases showed marked large-scale (≥ 10 m) and small-scale aspect control (≥ 1 m).

(2) The lowest, more spatially homogeneous rates of temperature change were detected during both midday and midnight, where no preferential clustering by aspect or orientation were detected.

(3) A key consequence of (1) and (2) is that positive and negative rates of temperature change were closely dependent on the spatial distribution of insolation impacting upon the cliff face. For example, during sunrise, negative rates (cooling) were spatially coincident with areas that remained in shadow (e.g., upper rock-blocks of BS facing the NW, while at the same time the sunrays were striking those planes facing the NE). As a result, sunrise and sunset in summer had a significant role on the timing, magnitude, and spatial distribution of the rates of temperature change across the cliff face, where aspect controls were notably enhanced.

(4) A spatial combination of large-scale (topographic) and bedding controls (surface character, micro-topographic) was observed. For example, during sunrise and across some surfaces at sunset, lower positive rates of temperature change occurred across outcrops of BS where large-aspect effects were absent. When this occurred, no preferential clustering of rates of change occurred over cliff surfaces with particular dip directions.

Below, the stereographic projections and equivalent thermal maps of the winter mean rates of temperature change during sunrise, midday, sunset, and midnight are analysed using the Figures 5.19 and 5.20, respectively. In particular, Figure 5.19a illustrates the stereonets of the mean rates of change during the sunrise in winter. This stereonet was generated using 83 thermal

images from between 06:00 and 09:00 h (Figure 5.20a). Two spatial patterns characterized the rates of change in winter sunrise:

First, higher rates of change (0.45°C/h to 0.50°C/h) were almost exclusively detected upon N and NE facing surfaces, and on those with less steep dip angles (average dip ≅ 65°) upon IBSS. As such, this displayed a similar aspect, dip and bed distribution as compared to the higher rates of temperature change during summer sunrise.

Second, rates of temperature change <0.45°C/h did not present any clustering over particularly slope orientations, but they tended to coincide with steeper dipping surfaces (average dip ≅ 72° to 75°), which are areas typically within outcrops of BS. Poles representing positive rates of temperature change were common around winter sunrise, and these were notably more similar in magnitude and spatial distribution, especially when compared to winter midday, winter sunset, and summer sunrise.

Figure 5.19b shows the stereographic projection of the mean rates of change during midday in winter. This stereonet was built from 55 thermal images captured between 11:00 and 13:00 h (Figure 5.20b). Three patterns characterized the rates of temperature change during midday:

First, no preferential clustering in the rates of temperature change occurred over cliff surfaces of specific orientation. This suggests that there was a relatively homogeneous surface heating at this time of the day.

Second, a marked systematic change in the position of the great circles representing each range of temperature change per hour was observed. To exemplify this, the lowest rates of change occurred over the lower dip angles (59°), while at the same time, intermediate rates of change were clustered around intermediate dip angles (e.g., 65°), and the highest positive rates of change over the steepest cliff surfaces (mean dip = 78° to 79°). This again suggests a relationship between dip angle and the mean rates of temperature change at midday, which was also observed at summer.

Third, only small-scale aspect controls were observed at this time of the day, exclusively across hanging rock-blocks of BS. These areas were characterized by negative rates of temperature change, with positive rates in the periods both before and after. Overall, lower rates of temperature change were observed around midday when compared to sunrise.

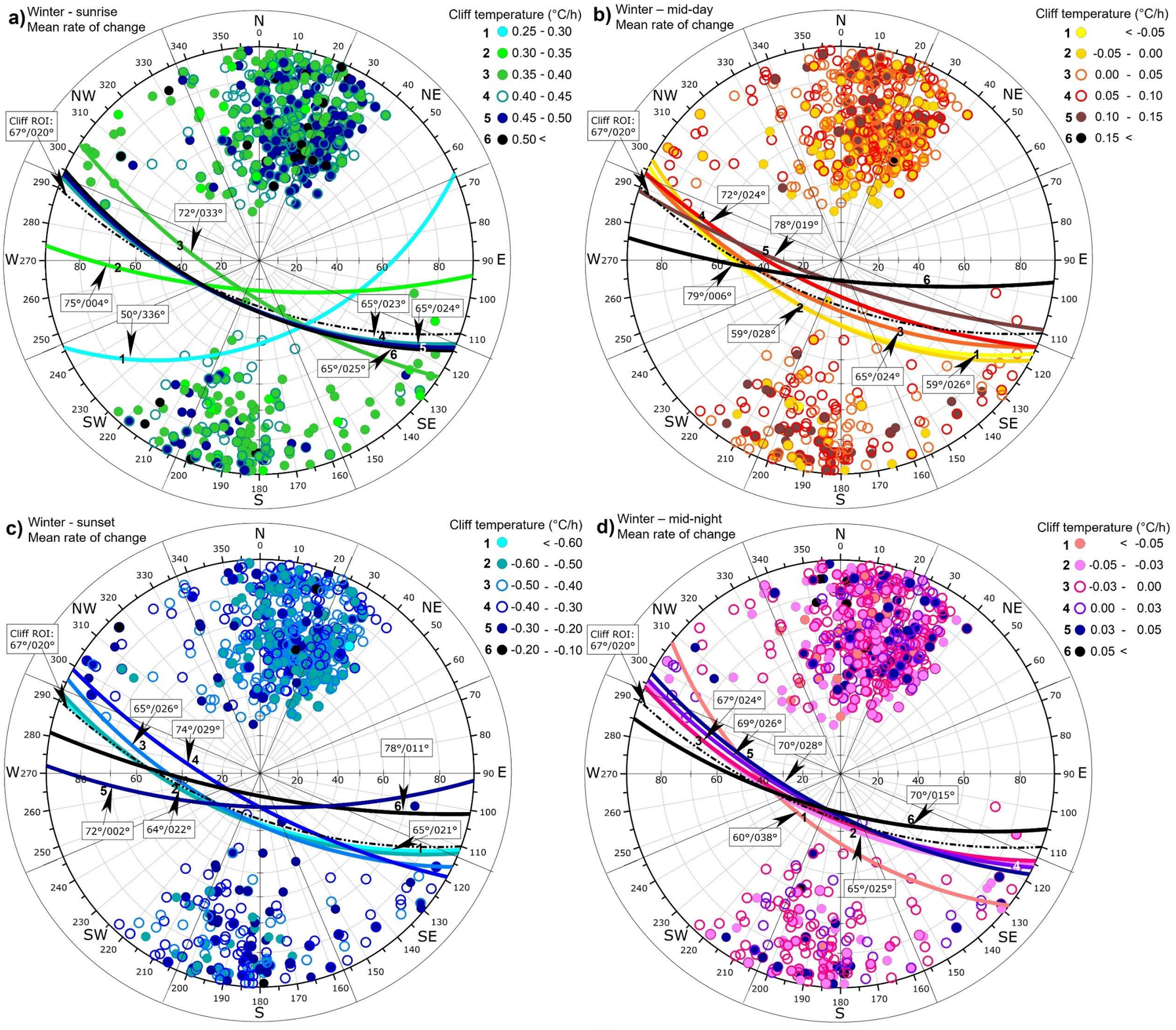
a) Winter - sunrise
Mean rate of change
Cliff temperature (°C/h)
1 0.25 - 0.30
2 0.30 - 0.35
3 0.35 - 0.40
4 0.40 - 0.45
5 0.45 - 0.50
6 0.50 <
Cliff ROI: 67°/020°
72°/033°
75°/004°
50°/336°
65°/023°
65°/024°
65°/025°
b) Winter – mid-day
Mean rate of change
Cliff temperature (°C/h)
1 < -0.05
2 -0.05 - 0.00
3 0.00 - 0.05
4 0.05 - 0.10
5 0.10 - 0.15
6 0.15 <
Cliff ROI: 67°/020°
72°/024°
78°/019°
79°/006°
59°/028°
65°/024°
59°/026°
c) Winter - sunset
Mean rate of change
Cliff temperature (°C/h)
1 < -0.60
2 -0.60 - -0.50
3 -0.50 - -0.40
4 -0.40 - -0.30
5 -0.30 - -0.20
6 -0.20 - -0.10
Cliff ROI: 67°/020°
65°/026°
74°/029°
78°/011°
72°/002°
64°/022°
65°/021°
d) Winter – mid-night
Mean rate of change
Cliff temperature (°C/h)
1 < -0.05
2 -0.05 - -0.03
3 -0.03 - 0.00
4 0.00 - 0.03
5 0.03 - 0.05
6 0.05 <
Cliff ROI: 67°/020°
67°/024°
69°/026°
70°/028°
70°/015°
60°/038°
65°/025°
N
NE
E
SE
S
SW
W
NW

Figure 5. 19: *Overleaf. Diurnal distribution of the temperature changes by dip and dip direction in winter.* ***a)*** *Stereonet of the mean rate of change in sunrise.* ***b)*** *Stereonet of the mean rate of change in mid-day.* ***c)*** *Stereonet of the mean rate of change in sunset.* ***d)*** *Stereonet of the mean rate of change in mid-night. Each stereonet was plotted using the upper hemisphere, equal angle projection and over 3,300 samples of pole vectors extracted across the region of research (ROI) at 1 m spacing (see Figure 5.15). Values around the perimeter of the stereonets represent the dip direction, while the vertical and horizontal values starting from the centre show the dip of the sampled slope planes (from 0 to 90°). Each category of cliff temperature (1 – 6) has a corresponding great circle representing the mean dip and dip direction estimated for each category, which were calculated for the sampled points belonging to the north hemisphere of the stereonets. The dip and dip direction of the great circles is showed within white boxes and using standard nomenclature (dip/dip direction as 00°/000°), while arrows and numbers (1 – 6) were used to point each corresponding great circle. The great circle representing the mean dip and dip direction of the cliff face ROI is shown using a point-dashed arc.*

The stereographic projection of the mean rates of temperature change during the winter sunset is shown in Figure 5.19c. This stereonet was built from 108 thermal images form between 15:00 and 18:00 h (Figure 5.20c). Three spatial patterns characterized the temperatures during sunset:

First, the negative rates of temperature change of relatively higher magnitude, indicative of cooling surface conditions (≥ -0.5°C/h) were preferentially clustered across N and NE oriented surfaces, and across over lower dip cliff angles (average dip = 64° to 65°), which were spatially coincident with the IBSS.

Second, negative rates of temperature change of a lower magnitude (e.g., -0.2°C/h to -0.4°C/h) were preferentially clustered on steeper cliff surfaces (average dip = 72° to 74°), but did not show a preferential aspect as they were coincident with the sub-horizontal structures of the BS.

Third, similar to midday, only small-scale aspect controls were observed at this time. These were across the hanging rock-blocks of BS, where sharp temperature contrasts were observed across the top of the cliff face. Overall, the winter rates of temperature change, indicative of the coolest conditions were detected around sunset.

The stereonet of the mean rates of change around midnight in winter is shown in Figure 5.19d. This stereonet was derived from 67 thermal images captured between 23:00 and 01:00 h (Figure 5.20d). Similar to summer midnight, no preferential clustering of rates of temperature change were detected relative to dip direction. Also, the great circles of the mean rates of temperature change almost overlapped and fluctuated between 60° and 67°, commonly faced N

and NE, and hence mirrored the general dip and dip direction of the wider cliff face. This demonstrates that the rates of temperature change were almost homogeneous across the cliff face, and hence negligible aspect and bedding control was apparent around winter midnight.

Overall, three key observation can be made from the spatial analysis of the rates of temperature change during winter (Figures 5.19 and 5.20):

(1) Lower and spatially homogeneous rates of temperature change were common, especially as compared the more heterogenous patterns in summer. This was made evident by the absence of large-scale aspect control, even during the sunrise and sunset period in winter. This suggests that while sunrise and sunset had an overall control over the temperatures, driving the diurnal heating and cooling phases (see Section 5.3), direct insolation during sunrise and sunset did not have a direct impact on the timing, magnitude, and spatial distribution reflecting an aspect control in cliff surface temperature signature, most probably due to the relatively weak sunlight at this time of year.

(2) a consequence of (1) is that the surface of the cliff face was, overall, more homogeneously heated such that the highest rates of temperature change only occurred during and after sunrise, while for the remainder of the day the cliff face experienced relatively slow and homogenous temperature changes, as demonstrated during the analysis of the Figure 5.12a (see Section 5.3).

(3) This also indicates that the apparent temperatures observed in winter were mostly a response of both heating due to air temperature and sunlight, and the inherent rock-mass response to heating and cooling, where the latter were a function of properties such as the colour of the beds, the thermal conductivity, specific heat capacity, and the ability of the discontinuities to influence air circulation.

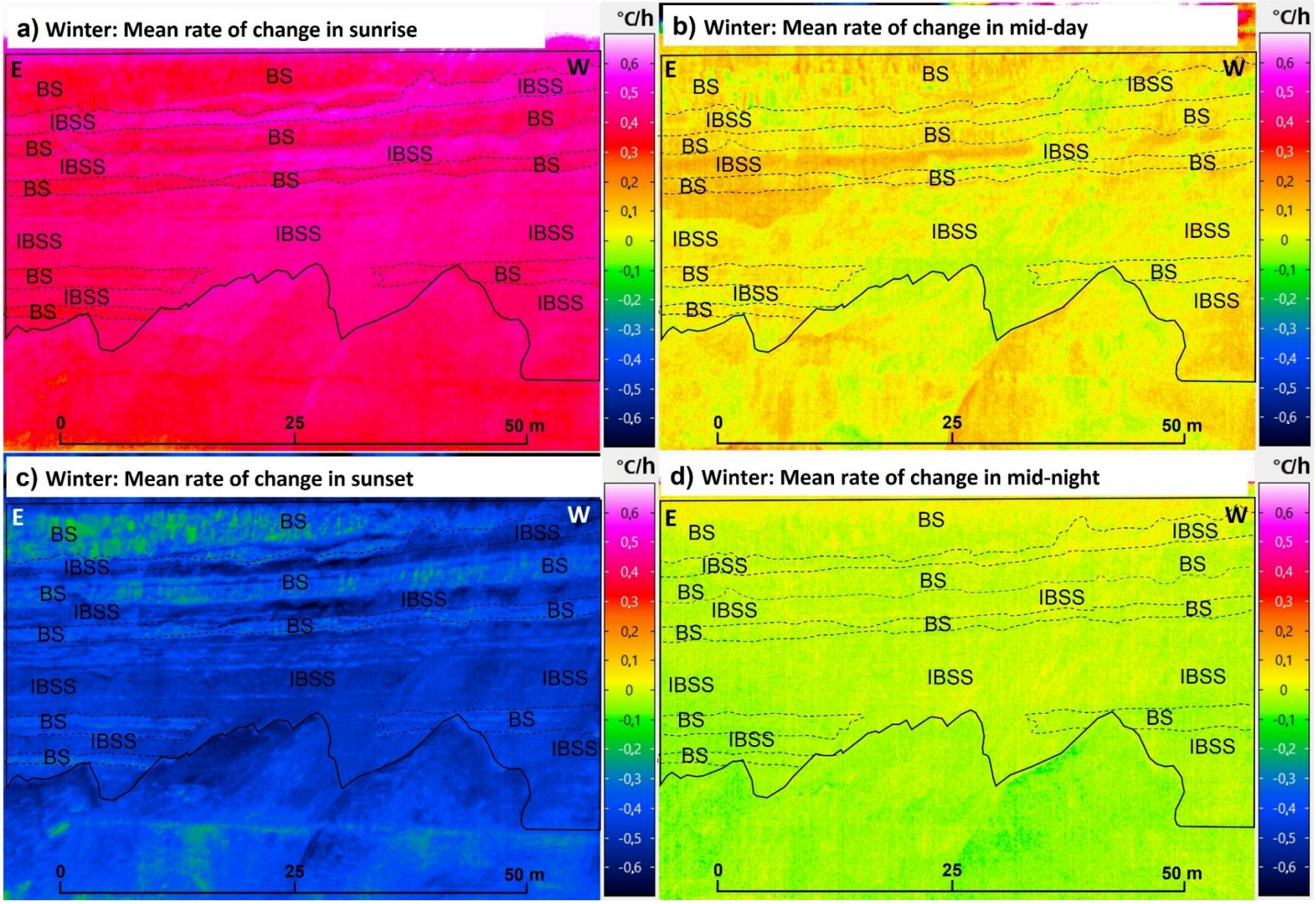
a) Winter: Mean rate of change in sunrise
b) Winter: Mean rate of change in mid-day
c) Winter: Mean rate of change in sunset
d) Winter: Mean rate of change in mid-night
°C/h
0,6
0,5
0,4
0,3
0,2
0,1
0
-0,1
-0,2
-0,3
-0,4
-0,5
-0,6
E
W
BS
IBSS
0
25
50 m

Figure 5. 20 *:Overleaf. Thermal scenes of the mean rate of change detected in winter for key diurnal times. a) Mean rate of change during sunrise. b) Mean rate of change in mid-day. c) Mean rate of change in sunset. b) Mean rate of change in mid-night. Black boundary lines show the Region of Research (ROI) for this study. Each thermal scene is overlapped with the principal beds outcropping in the ROI, where BS: Bedded sandstones; IBSS: Interbedded sandstones and siltstones / carbonaceous muds. Near horizontal dashed lines show bedding controls on temperatures. In each image, the Eastern and Western directions are shown using the letters E and W, respectively.*

To explore the above observations further, Figure 5.21 illustrates the spatial distribution of cliff surface temperatures at 1 hour intervals over the period in which the maximum rate of change per season were detected, as previously presented in Figure 5.12 (Section 5.3). This dataset shows that the maximum rates of temperature change in winter and autumn occurred 1 h after the sunrise and within the same interval (09:00 – 10:00 h), where and each experienced approximately the same magnitude of temperature change (between ~ 5°C/h and 6°C/h). This indicates that, even in the coolest seasons, the cliff surfaces experienced relatively rapid warming 1 h after sunrise. However, the aspect influences at this times appears to be negligible, as the maximum rates of change were spatially homogenous across the cliff face, with limited differentiations between beds identified (Figures 5.21a,d).

The maximum rates of temperature change in spring and summer occurred at the end of sunrise and again within the same interval of time (06:00 – 07:00 h), a period characterised by a notably heterogeneous spatial distribution coincident with some very high rates temperature change. These periods occurred within the first diurnal heating phase and fluctuated between ~ 1°C/h and 14°C/h, demonstrating that some surfaces of the cliff were exposed to extremely fast temperatures changes over even a single hour. Notably, large-scale aspect dependent distributions of surface rates of change in temperature influenced both the magnitude and spatial clustering of both the lowest and highest maximum rates of change. For example, the highest rates of temperature change (~ 8°C/h to 14°C/h) were located over cliff surfaces facing the N and NE, which corresponded to the incidence angle of sunlight at sunrise from the east. This is shown on the thermal maps as red-coloured areas located within the central west of the image. Conversely, the lowest rates of temperature change (c.a., 1°C/h to 4°C/h), were found upon cliff surfaces facing the N and NW, corresponding areas in shadow during sunrise (Figures 5.21b, c).

It is important to note that these aspect controls were clearly identified by their distinction vertical footprint, crossing multiple beds often extending from the base to the top of the cliff (see Figures 5.21b, c). In addition, it also important to note that upon the areas of the cliff facing NE, outcrops of IBSS exhibited higher rates of temperature change than the BS, demonstrating how the surface temperatures were also influenced by the outcropping rock-type.

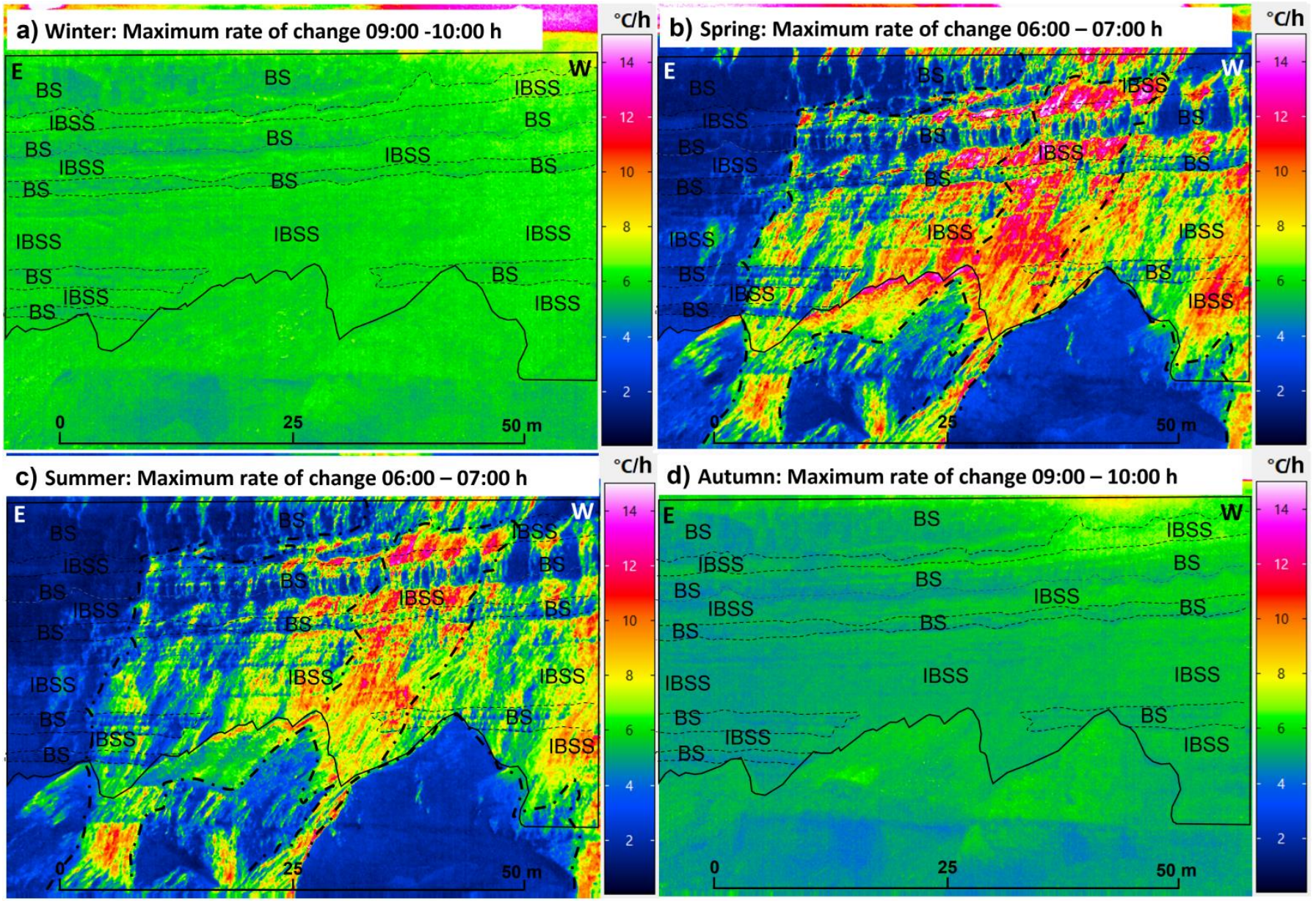
a) Winter: Maximum rate of change 09:00 -10:00 h
b) Spring: Maximum rate of change 06:00 – 07:00 h
c) Summer: Maximum rate of change 06:00 – 07:00 h
d) Autumn: Maximum rate of change 09:00 – 10:00 h
°C/h
14
12
10
8
6
4
2
E
W
BS
IBSS
0
25
50 m

Figure 5. 21: *Overleaf. Seasonal thermal scenes of the intervals of hour with the maximum rate of change detected in each pixel. a) Maximum rate of change in Winter. b) Maximum rate of change in Spring. c) Maximum rate of change in Summer. b) Maximum rate of change in Autumn. Black boundary lines show the Region of Research (ROI) for this study. Each thermal scene is overlapped with the principal beds outcropping in the ROI, where BS: Bedded sandstones; IBSS: Interbedded sandstones and siltstones / carbonaceous muds. Near horizontal dashed lines show bedding controls on temperatures. Thick vertical dashed lines were used to map and show aspect controls on the rates of change of temperatures. In each image, the Eastern and Western directions are shown using the letters E and W, respectively.*

Overall, two observations can be made from this spatial analysis of maximum rates (Figure 5.21):

First, two contrasting spatial patterns characterized the distribution of the rates of temperature change in the cooler and warming seasons. These pattern reaffirmed the observation of aspect control on the cliff temperature signature during sunrise and sunset in summer, whereas this influence was effectively negligible in winter.

Second, this dataset also demonstrates how the cliff surface temperature and their spatial distribution were a function of a complex combination of aspect and surface lithology. I further discuss these results in the context of the potential for the development of thermomechanical processes, progressive microfracture development, and the potential for temperature-induced rockfalls below (see Chapter 6, Discussion).

The almost negligible aspect control, and the dominance of a spatially homogeneous signature of rates of temperature change were apparent in winter and autumn, contrasted with a pronounced aspect control during sunrise and sunset in spring and summer with subtle shifts in the dip and dip direction of the locations of the lowest and highest rates of temperature change were observed. I now focus on the assessment of spatial shifts in the temperature signature during the warmer seasons. Consequently, Figure 5.22 shows a sequence of 25 thermal images representing hourly rates of change in temperatures during a complete, and typical, diurnal cycle between late spring and summer (during absence of cloud cover or fog). This figure is also annotated with the direction of the incident sunrays at the times when these directly strike the cliff face (arrows).

This 1 day dataset demonstrates that the temperature cycle in the warmer seasons was characterized by spatially homogeneous and relatively steady rates of change of temperature between mid-night and prior to sunset (00:00 – 05:00 h), with rates of change fluctuating between

~ -0.3°C/h and 0.3°C/h. This period had little differentiation between pixels, generating very homogeneous thermal maps (thermal scenes (*a*) to (*f*)). As soon as the first sunlight struck the cliff face (05:00 – 06:00 h), raising from the east impacting the central-west zones of the cliff, rapid rates of temperature change were observed across cliff planes facing N and NE. During the sunrise (especially between 05:00 and 07:00 h) very fast rates of change occurred ranging from ~ 4°C/h and 10°C/h, but also showed a marked variability, with cliff surfaces facing NW (towards the sunset) remained under shadow. At this time, the rates of temperature change were around 1°C/h (see scenes (*g*) to (*h*)), but within the hanging rock-blocks of BS at the top of the cliff as well as across the shales at the cliff base there were lower temperature changes per hour. Overall, this helps to explain how the first diurnal heating phase in spring and summer was generated, and why it includes both fast and high rates of temperature change (see Figure 5.12, Section 5.3).

After sunrise (07:00 onwards), a gradual reduction in the rates of temperature change was observed, but interestingly, as soon as direct insolation reduced (2 hours later), these surfaces quickly cooled with high negative rates of temperature fluctuating between ~ -1°C/h and -7°C/h. This behaviour was particularly evident between 08:00 and 12:00 h (see scenes (*j*) to (*m*)), with the lowest negative rates of temperature change between 08:00 and 09:00 h (scene (*j*)), preferentially clustered over lower dip angle cliff surfaces of IBSS, as also demonstrated using the stereographic projections. It also important to note here that 1 h before the occurrence of the lowest rates of temperature change (i.e., 07:00 – 08:00 h, scene (*h*)), was the time when the dew point temperature was reached, and so surface moisture may have formed further contributing to the cooling of the cliff surface (see Figure 5.13, Section5.3). As a result, the combined effect of rapid cooling when with the cessation of direct insolation and the potential for dew formation can potentially explain why in the Section 5.3, the diurnal curve of the mean minimum rates of change showed fast negative rates of change exactly 2 hours after the end of the sunrise period (see Figure 5.12, Section 5.3).

Figure 5.22 also shows that around midday and into the afternoon (12:00 – 17:00), both low and spatially homogeneous rates of temperature change were again detected, coincident in time when sunrays were not directly striking the cliff face. As such, this time of the day was characterized, by very low steady rates of temperature change around 0.5°C/h until 14:00 h (see scene (*o*)), and then negative rates of change around -0.5°C/h until 17:00 (see scene (*r*)). As a result, the fact that the cliff face was shadow can help to explain why in Section 5.3, the diurnal curves of rates of change showed a notable cooling occurring from midday and into the afternoon (see: Figure 5.12, Section 5.3).

Significantly, Figure 5.22 illustrates how the cliff surfaces that preferentially faced NW, pointing towards sunset, showed marked high rates of temperature change coincident with the incident of sunlight upon the cliff face from the west. This tended to influence the central-east zone of the cliff, directly heating the N and NW facing cliff surfaces. This phase occurred between 17:00 20:00 h, and was characterized by a lateral shift in the location rapid rates of temperature change that fluctuated between ~ 3°C/h and 11°C/h. Again, a high degree of spatial variability was detected, with NW facing surface being directly struck by sunrays, and the NE facing surfaces remained under shadow inducing lower rates of change (~ 1°C/h). Again, this generated a vertical footprint as a function of the large scale aspect crossing multiple lithological beds. As a result, direct insolation struck the cliff twice during the day, but opposing directions. This helps to explain why in Section 5.3, the diurnal curves of rates of temperature change showed a markedly rapid second heating phase, which was indeed the most pronounced in the thermal cycle (See Figure 5.12, Section 5.3).

During sunset (20:00 – 22:00), rapid reductions in the rate of temperature change were observed, and similar to the post-sunrise dynamic, as soon as the sunrays left the cliff face, these surfaces quickly cooled, with negative rates of temperature change of very high magnitude (see lateral spatial displacements of the rates from the scenes (*s*) to (*w*)) between -1°C/h to -7°C/h. There was also a high degree of spatial variability dependent on the local dip direction of the cliff surface, and the highest negative rates of change clustered towards less steeply dipping surfaces of outcrops in IBSS. Again, it is important to note here that from the afternoon until mid-sunset (16:00 – 20:00 h), the dew point temperature was reached, hence meeting the conditions to generate surface moisture on the cliff face, which could contribute to further promote cooling (see Figure 5.13, Section 5.3). As a consequence, again, the combined effect of rapid cooling as result of the progressive loss of direct insolation alongside with the susceptibility to generate moisture, can help to explain why in Section 5.3, the diurnal rates of temperature change exhibited a second cooling phase, where the minimum rate of change occurred with a 2 hour lag after the peak of the second diurnal heating phase (see Figure 5.12, Section 5.3).

Finally, Figure 5.22 also illustrates how after sunset, when insolation has ceased, shadowed conditions dominate, such that low and steady rates of change are observed. This, again, produced a spatially homogenous pattern of temperatures in the thermal maps from midnight through until the following sunrise (see thermal scenes (*x*) to (*f*), thus completing the cycle of diurnal temperature variations.

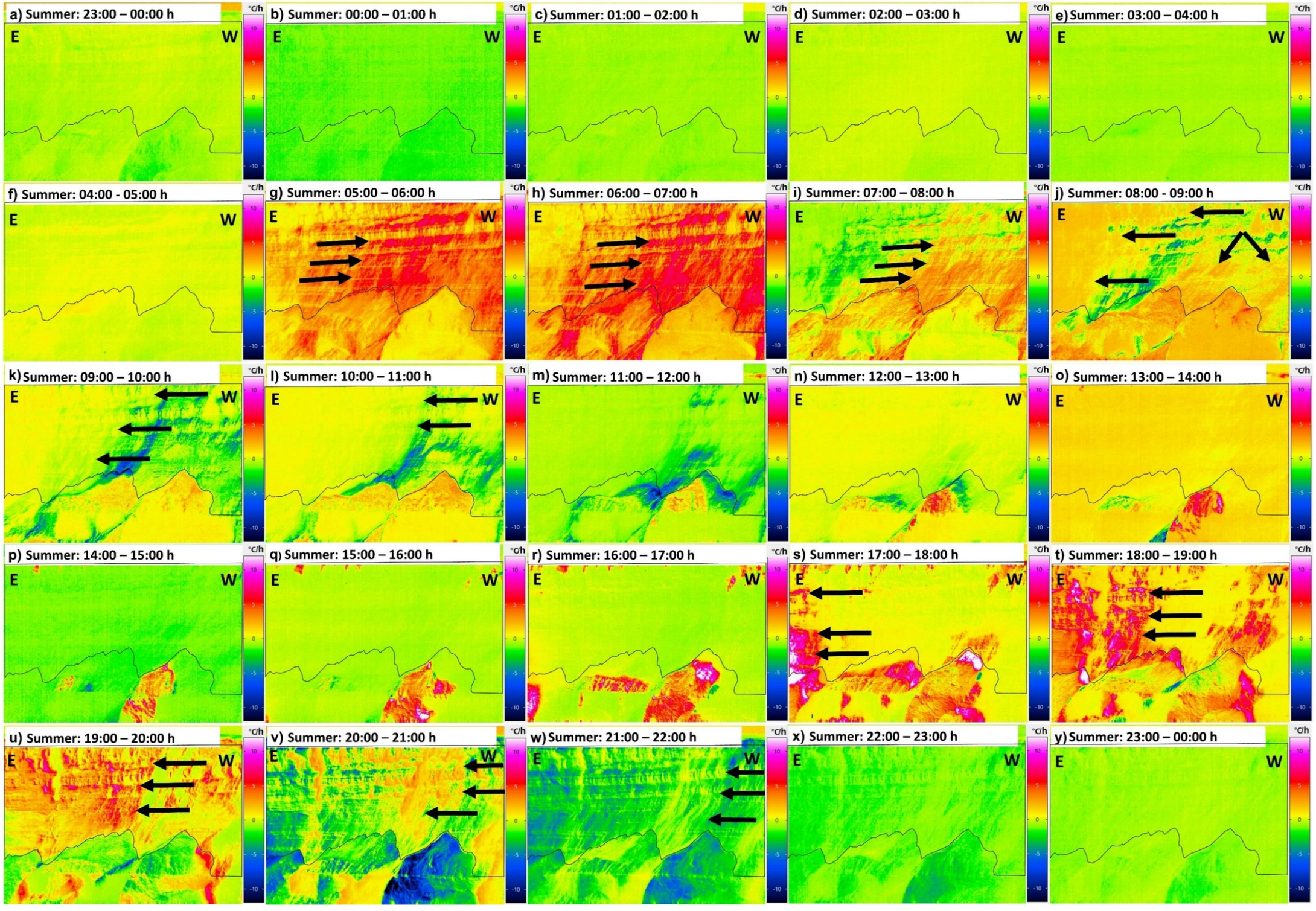
a) Summer: 23:00 – 00:00 h
b) Summer: 00:00 – 01:00 h
c) Summer: 01:00 – 02:00 h
d) Summer: 02:00 – 03:00 h
e) Summer: 03:00 – 04:00 h
f) Summer: 04:00 - 05:00 h
g) Summer: 05:00 – 06:00 h
h) Summer: 06:00 – 07:00 h
i) Summer: 07:00 – 08:00 h
j) Summer: 08:00 - 09:00 h
k) Summer: 09:00 – 10:00 h
l) Summer: 10:00 – 11:00 h
m) Summer: 11:00 – 12:00 h
n) Summer: 12:00 – 13:00 h
o) Summer: 13:00 – 14:00 h
p) Summer: 14:00 – 15:00 h
q) Summer: 15:00 – 16:00 h
r) Summer: 16:00 – 17:00 h
s) Summer: 17:00 – 18:00 h
t) Summer: 18:00 – 19:00 h
u) Summer: 19:00 – 20:00 h
v) Summer: 20:00 – 21:00 h
w) Summer: 21:00 – 22:00 h
x) Summer: 22:00 – 23:00 h
y) Summer: 23:00 – 00:00 h
E
W
°C/h
10
5
0
-5
-10

Figure 5. 22*: Overleaf. Example of aspect controls on surface temperatures during a complete diurnal cycle in summer. Figures a) to y) show the rate of change of temperatures per interval of time (°C/h), from 23:00 - 00:00 h of the 16th July to 23:00 - 00:00 h of the 17th July, 2021. Black arrows point the direction of the heating, irradiated by solar light from the East to the West during sunrise, and then from West to the East towards mid-day and again during the sunset. In each thermal scene, the Eastern and Western directions are shown using the letters E and W, respectively. The region of research is shown using a black boundary line. These scenes represent a typical variability of the solar path and subsequent heating during spring and summer.*

Figure 5.23 shows a 3D conceptual model to summarize the main findings of this section of results, based on the timing of the observed temperature changes (1 – 4), as described below:

- (1) During the late spring and summer, the first diurnal heating phase, occurring at sunrise for around 1 hour, was controlled by both the magnitude and direction of incident sunlight from the east, predominantly heating N and NE facing surfaces. As incident sunlight progressively shift from east to west during the day, rapid surface cooling was generated over those surfaces that were no longer directly illuminated, inducing a lateral spatial shift of areas subject to both positive and negative rates of change. A key consequence is that, over a relatively shot interval (05:00 – 09:00), the N and NE facing surfaces upon the cliff can be exposed to either positive or negative rates of change of extremely high magnitude (~ -7°C/h to 10°C/h), but also are exposed to surface moisture where the dew point temperature is crossed. These processes may facilitate the development of thermomechanical processes, such as the expansion and contraction of discontinuities, or progressive microfracture development.

- (2) During midday, insolation is concentration at the top of the cliff, which resulted in a generalized shadowing, producing a steady homogeneous surface heating. Indeed, only some surfaces upon the cliff toe talus receive direct heating due to their position below the main cliff face.

- (3) The second diurnal heating phase occurs in the late afternoon, but are controlled by the magnitude and direction of the incident sunlight from the west, thus predominantly heating N and NW facing planes. Again, as the incident sunlight gradually shift from east to west, fast surface cooling was produced across those surfaces that were no longer illuminated, producing a second shift of temperatures across the cliff face. Again, an important consequence is that within a short interval (17:00 – 22:00), the cliff face can be

exposed to both lateral shifts of both positive and negative rates of change of a very high magnitude (~ -7°C/h to 11°C/h), but also exposure to surface moisture given the proximity to the dew point temperature.

- (4) From midnight to the following sunrise, shadow is produced again as incident sunlight was completely absent, producing a second cooling phase characterized by a steady, homogeneous style of surface heating.

- Figure 5.24 shows a 3D conceptual model of the cliff face plotting the diurnal variations in the distribution of heating in mid-autumn and winter. In this model it can be seen that the cliff face experiences near-permanent shadow as a function of the low incident sun angle close to the horizon. This can explain, first, why large-scale aspect controls were almost negligible during these cooler seasons resulting in both low rates of temperature change and a near-homogenous temperature signature across the cliff. Second, this also explains why the cliff face at this time of year only experienced one heating and cooling phase per day, when higher rates of temperature change occurred around sunrise on N and NE facing surfaces, as demonstrated in stereographic projections of the data.

- As Figure 5.25 shows, a key the day-to-day temperature changes during cooler displayed a pattern that mapped onto the sub-horizontal structures of the bedding planes, a feature that was further enhanced during sunrise and sunset. This can help explain why no preferential clustering in locations of specific of rates of temperature change were observed during winter. Importantly, during these cooler seasons the surface temperatures are more closely controlled by the ambient air temperature rather than by direct insolation and the differential response of different lithologies.

- In summary, this section of results have provided insight into how the sun path and insolation relative to the cliff aspect controls the nature of the timing, magnitude, and spatial distribution of surface heating and cooling during spring and summer, and shows that aspect effects become almost negligible through winter and autumn.

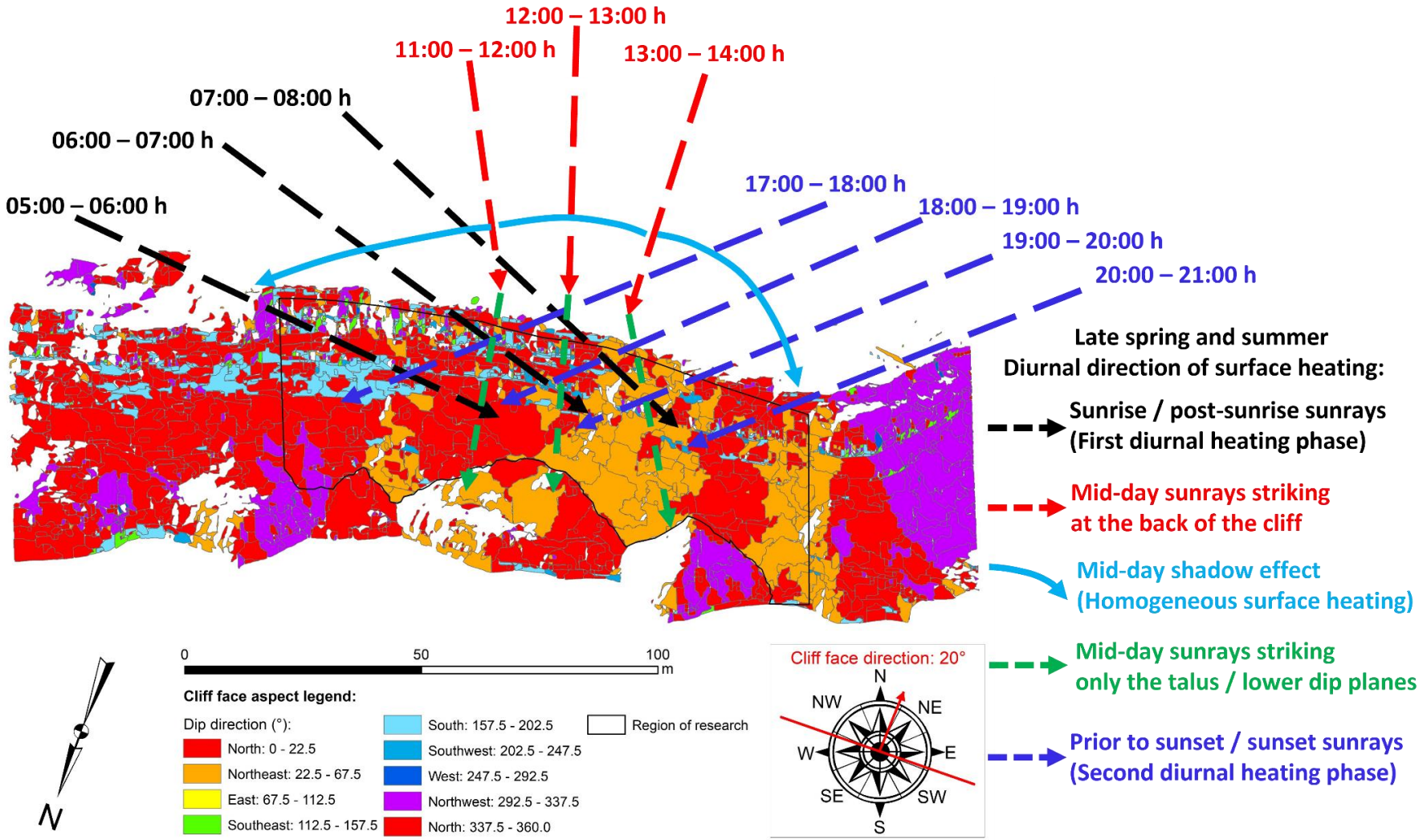

Figure 5. 23: *Conceptual model illustrating the cliff aspect and the diurnal direction of heating representative of the late spring and summer. Arrows indicate the approximate direction of the incident sunrays, directly heating the rock face at different times. Cooling occurs as the incident sunrays leave the rock face.*

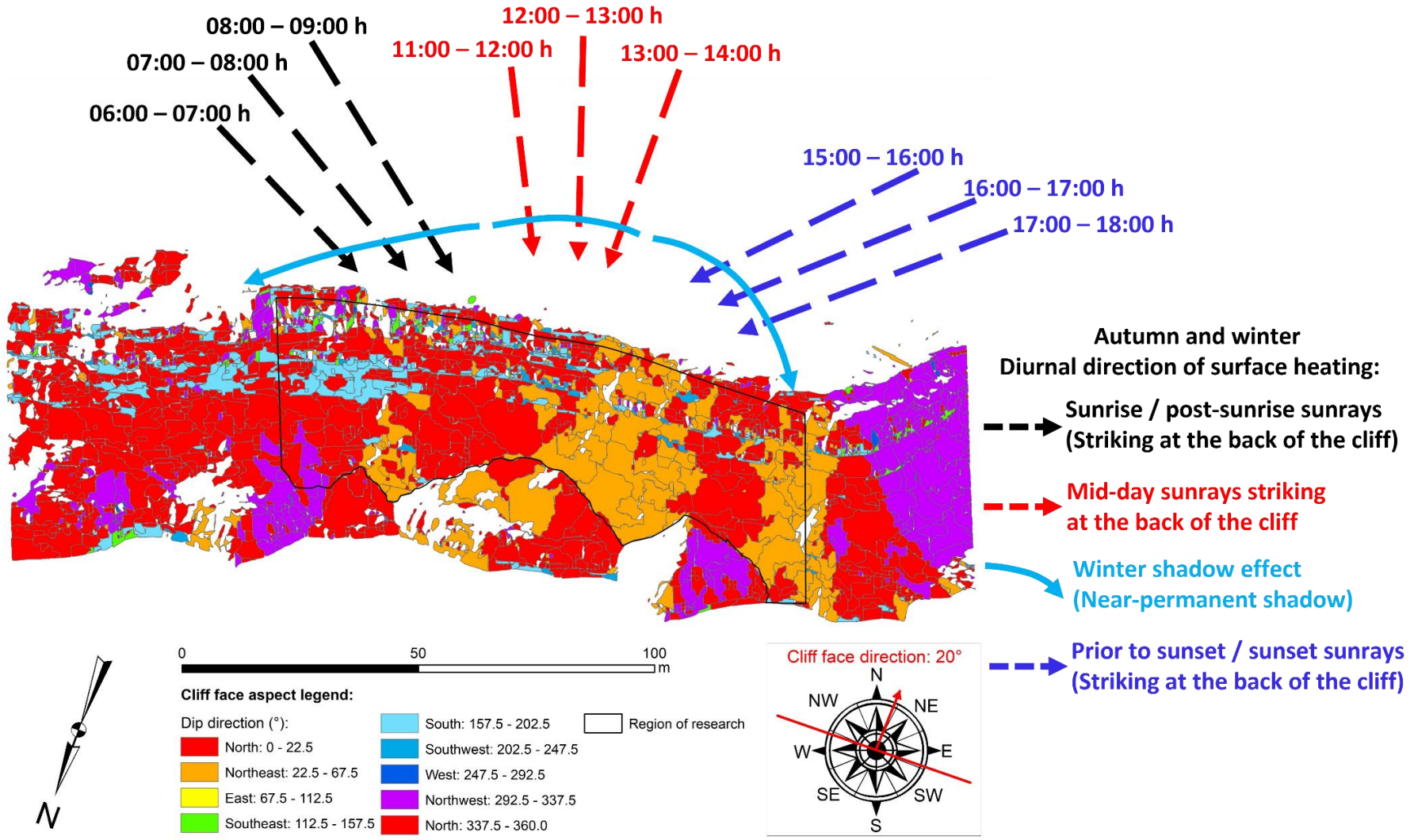

***Figure 5. 24**: Conceptual model illustrating the cliff aspect and the diurnal direction of heating representative of mid-autumn and winter. Arrows indicate the approximate direction of the incident sunrays, permanently striking at the back of the cliff face, and so generating a near-permanent shadow condition.*

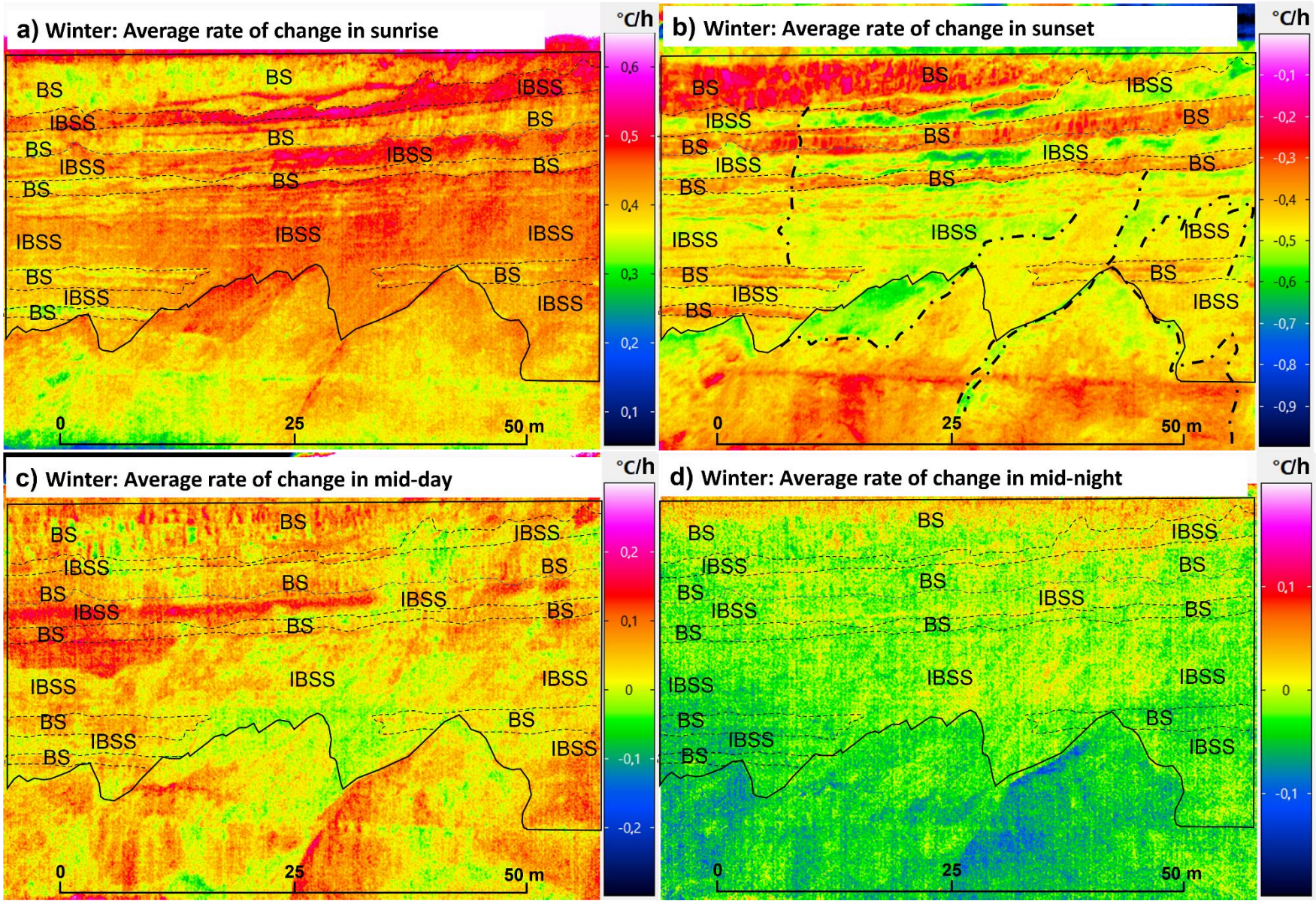
a) Winter: Average rate of change in sunrise
°C/h
0,6
0,5
0,4
0,3
0,2
0,1
BS
IBSS
0
25
50 m
b) Winter: Average rate of change in sunset
°C/h
-0,1
-0,2
-0,3
-0,4
-0,5
-0,6
-0,7
-0,8
-0,9
c) Winter: Average rate of change in mid-day
°C/h
0,2
0,1
0
-0,1
-0,2
d) Winter: Average rate of change in mid-night
°C/h
0,1
0
-0,1

Figure 5. 25*: Overleaf. Thermal images of the mean rate of change detected in winter, demonstrating the predominance of surrounding air temperatures and/or bedding controls on surface temperatures. a) Mean rate of change during sunrise. b) Mean rate of change in mid-day. c) Mean rate of change in sunset. b) Mean rate of change in mid-night. Black boundary lines show the Region of Research (ROI) for this study. Each thermal scene is overlapped with the principal beds outcropping in the ROI, where BS: Bedded sandstones; IBSS: Interbedded sandstones and siltstones / carbonaceous muds. Near horizontal dashed lines show bedding controls on temperatures. (Note that this figure is the same as Figure 5.20, however, the colour scales have been modified to enhance the differences in temperatures within each thermal image).*

5.5 Summary

Using a uniquely long-term and high-resolution dataset of IRT imagery collected at 1 h intervals through 2021, the timing and nature of the surface heating and cooling at East Cliff of Whitby have been examined in this chapter. Over 8,000 IRT images were collected between 1st January and 31st December, totalling 12 months of continuous thermographic monitoring. A novel calibration protocol was implemented to filter and correct the imagery, resulting in over 4,270 scenes for analysis. The main reason for data loss was inclement weather. The resulting dataset was used to detect the emergent behaviour of surface temperature variations. The principal observations are summarized as follows:

1) The analysis of cliff surface temperature changes through the year demonstrated a high degree of temporal variability. This variability was characterized by day-to-day and within day fluctuations of surface temperatures, but also overall warming from winter to summer and cooling from summer to autumn. This resulted in a large annual range of observed surface temperatures of ~ 51.9°C, between the minimum and maximum at ~ -11.7°C (winter) and 40.2°C (summer) respectively. As such, this high frequency data for the first time records the magnitude of surface temperatures experience during the year for a temperature mid-latitude coastal rock cliff. I note specifically that the observed temperature range is significantly higher than the ambient air temperature range.

2) Notably, the analysis of the surface temperatures also illustrates rapid decreases in temperature, not only during winter and autumn but notably through mid-spring, which in total encompass almost six months of the year. These drops in surface temperature were commonly contemporaneous with periods of persistent low temperatures < 0°C, including periods of up to on months, such as in January. These periods also witnessed cliff surface locations subject to very cold temperatures, such as ~ -5°C or -10°C.

3) Associated with (2) but at a finer-temporal resolution, the hourly analysis of winter surface temperature variations demonstrated that the cliff face was, on average, uninterruptedly exposed to both mean and minimum temperatures <0°C for ~ 45% and 70% of the day, respectively. For ~ 63% of the day, the mean minimum temperatures were stable around -3°C and -4°C, after which the cliff surface warmed to around ~ 1.0°C between 11:00 and 13:00 h. This indicates that the surfaces of the cliff which recorded the minimum temperatures were probably subject to some degree of either freezing, or freeze-thaw, particularly those exposed to a combination of permanent shadow and the lowest minimum surface temperatures (e.g., -5.0°C to -10°C).

4) Associated with (3), frequent marked temperature contrasts were observed from winter until mid-spring and the again into autumn. These were characterized by cold (e.g., -5.0°C) and warm (e.g., 10°C) surface temperatures occurring either within a single day, or between successive days, implying the potential for exposure to freeze, or freeze thaw behaviour. Indeed, in winter, a 69% of the days showed temperatures typically associated with freeze-thaw cycling, while in spring this percentage was still significant (35%). These percentages are, perhaps surprising given the mid-latitude coastal rock cliff.

5) The analysis also identified markedly warm surface conditions, that ran uninterrupted from mid-spring until the end of the summer, totalling a period of four months. These months were characterized by average surface temperatures ≥ 20°C, with seasonal peaks of around 40°C in both spring and summer. This observations may hold implications particularly under a warming climate where heat waves and hotter surface temperatures may be more frequent and intense.

6) Associated with (5), it was observed that the warmer the season, the higher the temperature range and the greater the rates of surface temperature change. For example, during spring and summer, the rock face was frequently exposed to very high rates of temperature change (both positive and negative) either the same day or on successive days (e.g., from ~ -10.0°C/h up to 10.0°C/h). These periods are likely to be when any thermomechanical processes, if present, are most effective.

7) Hourly changes in surface temperatures showing clear differences in the warming and cooling of the cliff in the hotter versus cooler seasons. To exemplify this, two marked phases of rapid and continuing increases in the maximum temperatures (sunrise - 05:00 – 08:00 h, and then again in the lead up to sunset - 14:00 – 19:00 h) were detected during both spring and summer. This was not observed during winter and autumn, as the cliff was exposed only to one heating phase between sunrise and midday. When modelling thermomechanical processes on rock-slopes, this observation holds important implications when considering the number and magnitude of thermal loading cycles that may influence fracturing processes. These observations also highlight that the identification of these cycles cannot easily be made with arrays of individual thermocouples, or non-continuous IRT monitoring campaigns.

8) The analysis of the diurnal rates of change of in surface temperature in winter demonstrated that rapid changes in temperature (heating) occurred from sunrise until early morning (on average from ~ -0.1°C/h to 1.8°C/h), however after 09:00 –10:00 h,

fast negative rates of change were detected (cooling), generating a significant inflection in the cliff surface heating. This not only indicated that the rock face can experience rapid heating and cooling within a single hour, but also this condition could promote further themormechanical processes.

9) The analysis of the rates of surface temperature change considering the maximum temperatures in spring and summer showed two diurnal phases of rapid change (heating and cooling), producing an inflections at the end of sunrise and at the start of sunset. A similar pattern was seen for the minimum surface temperatures. Notably the maximum and minimum inflections were not coincident in time during the day. This demonstrates that during the warmer seasons, some surfaces upon the cliff face could be exposed to a total of four inflection in the rate of surface temperature change each day. This suggests that if the development of thermomechanical processes relates to a reversal in the rate of heating (or cooling), then these processes are likely to be more prevalent during the warmer seasons.

10) Differential surface temperatures were detected across difference rock type outcrops. A seasonal inversion of the temperatures between lithologies was also detected. As such, it has been noted that the interbedded siltstones and sandstones (IBSS) was on average ~ 1°C or 2°C warmer than the bedded sandstones (BS) in summer as compared to the winter. This indicates that there could be an inversion in the direction of the surface temperature gradient through the year.

11) This differentiation between beds (10) was also observed at finer temporal scales. During the warmer seasons, the rates of change in temperature in both beds differed for sunrise and sunset. For instance, while rate of change of IBSS was around 2°C/h by the end of sunrise, the rate of change of BS was ~ 1.5°C/h lower. This was inverted around sunset, as IBSS showed lower rates of change than BS (in average, ~ 0.5°C/h lower). Since these differences were not observed during the colder seasons, when both beds behaved similarly, this indicates that the rock-mass surface temperature was, overall, more complex during spring and summer. This again may hold implications for modelling thermal processes affecting rock-slopes.

12) The conceptual models in Figures 5.23 and 5.24 (see Section 5.4) were used to explain how cliff surface aspect effects developed during a day in the seasons. It was observed that aspect controls developed via four broadly four-hour-long periods:
    - Sunrays that struck the cliff face from the east at sunrise, heated N and NE facing planes, leading to the first of the heating phases. This drove

lateral shifts across the cliff face from east to west, generating high rates of increasing surface temperature change on those surfaces that were directly illuminated. When illumination ceased a reduction of temperatures followed after 2 hours

- The midday sun struck from over the top of the cliff face, generating homogeneous surface heating and so almost negligible aspect controls.
- Later in the day incident sunlight from the west, towards the sunset heated N and NW facing surfaces, producing the second diurnal heating phase. This again witnessed very high rates of surface temperature change that progressively shifted from east to west, followed by rapid cooling when illumination stopped.
- The total absence of sunlight produced by nocturnal shadowing generated a phase of cooling, which was characterized by a notable homogenous surface heating, and hence, no aspect controls.

13) An important implication of (12) is that aspect relative to the incidence angle of the sunbeams controls the nature of the timing, magnitude, and spatial distribution of surface heating and cooling during spring and summer. This influence was almost negligible in winter, which was characterised by lower rates of surface temperature change and notably homogenous surface temperatures that were mainly locally influenced by the sub-horizontal structures of the outcropping beds. Consequently, in this chapter, it has also been demonstrated that the cliff surface temperatures are controlled by this complex interaction of large- and small-scale aspect and lithology.

This chapter has demonstrated that hourly-resolution fixed-monitoring using Infrared Thermography of rock-slopes provides a robust tool to investigate the variability of surface cliff temperatures through 2021 (Thesis Objective 4 – 04). As such, this research has not only complemented and upscaled previous IRT work on rock-slopes, but also, to my knowledge, provides the longest hourly resolution analysis of rock surface temperatures to date. In the next chapter (Chapter 6), the results obtained in this chapters are related to a contemporaneous 4D rockfall inventory collected during 2021 (Thesis Objective 5). The results are then discussed in the context of the wider aim of this thesis.

Chapter 6 – Exploring controls on rockfall

6.1 Introduction

In this thesis, high-resolution, long-term laser scanning and IRT monitoring has been conducted to investigate the nature rockfall activity and their correspondence with cliff surface temperature variability (*Chapters 3, 4,* and *5*). This was undertaken as one of the first attempts to consider temperature controls on rockfall activity as compared to other triggering conditions. To detect hourly rockfall activity, the work presented in *Chapter 2* developed a new methodology to obtain a 4D rockfall inventory. In *Chapter 3*, this inventory was used to investigate the magnitude and frequency of hourly rockfall activity, and how the erosive work done by rockfall accumulates into a longer-term erosional signature between 2017 and 2019. In *Chapter 4*, a method for the collection, filtering and correction of continuous IRT imagery was presented, yielding over 4,270 hourly thermal scenes from 2021. An analysis of the time-series of cliff surface temperatures was presented in *Chapter 5* that revealed hourly changes in temperatures and the controls upon this, including direct insolation, cliff surface topography and lithology.

In this chapter, a new dataset from 2021 is introduced that combines contemporaneous hourly 3D rockfall monitoring (*Section 6.2*) with the IRT data described in *Chapters 4* and *5* (cliff temperatures). Specifically, I use these data to explore: (1) evidence of temperature control on rockfall activity (*Section 6.3*); (2) the cliff surface temperature at the time of rockfall (*Section 6.4*); and (3) the relative erosive role of inclement weather and temperature on the pattern of rockfall through the year (*Section 6.5*), which are summarised in *Section 6.6.* As such, this chapter forms the discussion that brings together the ideas generated in my thesis.

I begin by summarising the characteristics of the new 2021 rockfall inventory, which was derived and analysed using the methods described in *Chapters 2* and *3*.

6.2 Inventory description for rockfalls 2021

Monitoring of the rockfall during 2021 was designed to be contemporaneous with the IRT imagery collection at East Cliff, Whitby. To accomplish this, both the laser scanning (described in *Chapter 2*, Section 2.2) and the IRT camera (described in *Chapter 4*, Section 4.2) were used to monitor the cliff face at 1h frequency between 1st January and 31st December 2021, totalling 12 months. While the characteristics of the IRT dataset for this period were described in *Chapter 4*, here I describe the 4D rockfall inventory 2021 which was derived using an application of the workflow described in *Chapter 2* executed using *Python.*

Figure 6.1 shows a summary of the data retention pipeline in processing the rockfall inventory for 2021. A total of 7,307 hourly point clouds were collected (out of a total of 8,760 possible scans acquired under ideal conditions, implying a scenario without interruptions during data collection. As such, 1,450 scans, equating ~16.5% of an ideal dataset, were not collected due to software and/or instrument failures). The partial scan filter (see *Chapter 2*, Section 2.3.1) identified 1,080 scans equating ~ 14.9% as unsuitable for processing. As during 2017, in 2021 no high-density scans were identified (see *Chapter 2*, Section 2.3.2). Similarly, as data processing was conducted across all scan intervals (1h and >1h intervals), no data loss was produced as a result of greater than 1h intervals, enabling the quantification of cliff erosion during inclement conditions when scan intervals were commonly longer due to data loss, as explained below. During the application of the *Main script II* (see *Chapter 2*, Sections 2,4 and 2.6), a further 778 M3C2 scan pairs were excluded due to high global RMS registration errors (RMSE $\geq$ 0.037 m), approximating 10.6% of the original dataset (Figure 6.1).

A remaining total of 5,433 M3C2 scan pairs were used to build the 2021 rockfall inventory, equating to 74.5% of the captured scans. This is a comparable number of total scan pairs used to build the rockfall inventories in 2017 and 2019 (see Table 3.1 in *Chapter 3*, *Section 3.2*). Table 6.1 summarizes the registration errors of the dataset for the 2021 inventory.

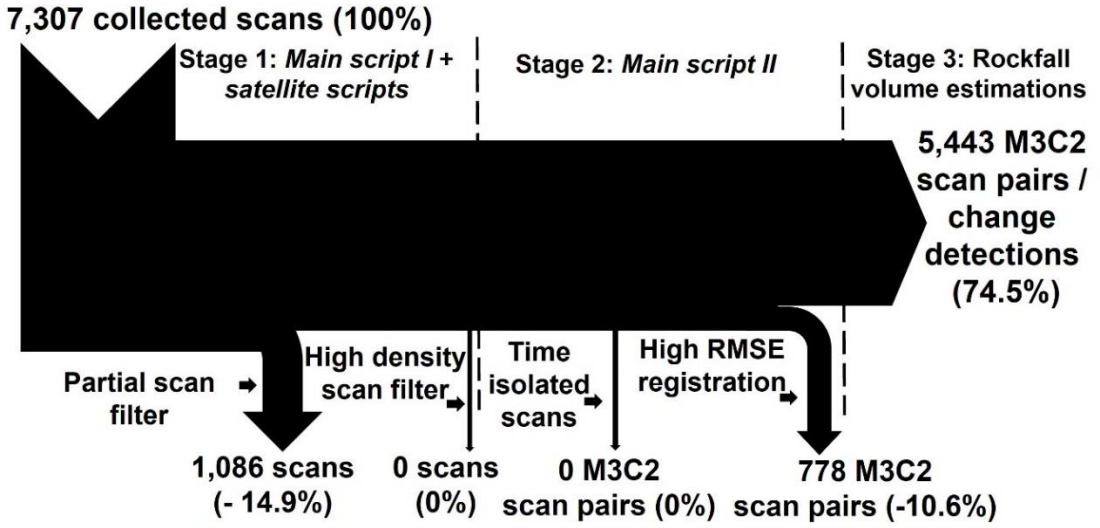

Figure 6. 1: **Data retention pipe for the 2021 rockfall inventory. Overall, a total of two stages of data retention occurred during the application of the computational routine, where a total of 5,433 scan pairs were used build the 2021 rockfall inventory.**

***Table 6. 1**: Root Mean Square Error (RMSE) of the general and fine registrations 2021.*

Master scan (Date & time)	Registration stage	Average RMSE (m)	S. Deviation RMSE (m)	Minimum RMSE (m)	Maximum RMSE (m)
2021-Jan-01 00:00 h	General registration	0.25	0.05	0.02	0.5
	Fine registration	0.03	0.01	0.02	0.5

Note: M3C2 scan pairs showing high values of fine registration (≥ 0.037 m) were discounted of the rockfall inventory 2021 (see Figure 6.1).

To assess the relative role of inclement weather conditions on rockfall, the 4D inventory for 2021 includes change detections across data gaps that exceed 1 hour. These gaps were generated by the occurrence of inclement weather, notably heavy rainfall which occludes the cliff surface from the scanner. The typical result was partial-scans with either incomplete spatial coverage of the surface, lower point densities or variable point densities, or alternatively, high-density scans. These also tended to introduce a lower-quality results in the alignment of successive point clouds (e.g., RMSE of registration ≥ 0.04 m). As a result, the 2021 rockfall database includes both:

(1) rockfalls with a timing precision of 1 hour, which were needed to link with hourly temperatures from IRT monitoring (Chapters 4 and 5); and,

(2) rockfalls with a timing precision of >1 hour, which therefore aggregate rockfall activity over multiple hours. Figure 6.2 shows a conceptual model of the two types of change detections.

Overall, this enabled a comparison of rockfall that can be attributable to both inclement weather and temperature, albeit with a variable degree of timing precision, as described in *Section 6.5.*

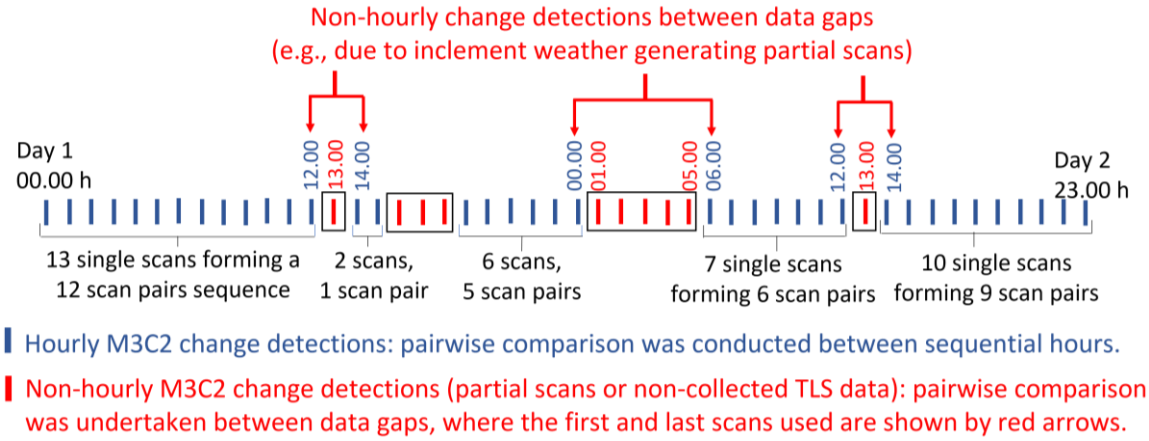

Figure 6. 2: *Conceptual model of the change detections that were used to build the rockfall inventory 2021. This inventory was build based on both hourly and non-hourly M3C2 change detections.*

Over 4,100 rockfalls were detected in 2021. Of these, a total of 2,210 (54% of the total number) were identified using hourly change detection and 1,895 (46% of the total number) from periods greater than 1 hour (referred to as '>hourly' from here on). The largest single rockfall (75 ± 19 m^3) occurred in summer during a period without rainfall (14th September sunrise (06:00 and 07:00)). The second largest rockfall (46 ± 12 m^3) occurred in winter within the period 4th and 7th February when continuous rainfall of 418 mm was observed. These two largest events represented 29.8% of the total 406 ± 159 m^3 of rockfall volume in 2021. As in *Chapter 3,* the role of large-magnitude and low-frequency failure events in driving overall erosion is clear (Table 6.2).

Table 6. 2: *Summary of the rockfall activity and cliff erosion for the East Cliff of Whitby, monitored between 1st January and 31st December 2021.*

Rockfalls detected during the parallel monitoring program with the IRT dataset 2021			
Erosive metric	**Hourly rockfalls / %**	**>hourly rockfalls / %**	**Total (100%)**
Detected number of rockfalls	2210 / 54%	1895 / 46%	4105 / 100%
Minimum rockall volume (m^3)	0.002	0.002	-
Average rockfall volume (m^3)	0.075	0.12	-
Median rockfall volume (m^3)	0.002	0.009	-
Largest rockfall (m^3)	75 ± 19	46 ± 12	121 ± 31
Total eroded volume (m^3)	165 ± 78 / 41%	241 ± 81 / 59%	406 ± 159 / 100%
Cliff face annual retreat (m)	0.030	0.044	0.074

Note: monitored cliff face area was 5,459 m^2. Rockfalls collected from periods greater than 1 hour are referred to as '>hourly' rockfalls from here on.

A larger degree of variability can be seen comparing the total eroded volume from hourly and >hourly change detections: hourly rockfalls totalled ~ 41% (165 ± 78 m^3) of the eroded volume, while >hourly rockfalls supplied almost 60% (241 ± 81 m^3). These volumes equate to annual retreat of the cliff of 0.030 and 0.044 m, respectively, totalling 0.074 m over the full year. By comparing the average and median rockfall volumes, it was observed that >hourly rockfalls generally showed higher volumes, suggesting that, overall larger rockfall volumes occurred during data gaps and hence were likely associated with inclement weather (Table 6.2). It is not possible to disaggregate rockfall during these data gaps as a result of superimposition or coalescence on the rockface (see Williams et al., 2018), so each event recorded here is considered to be a single unique rockfall. A possible effect of this assumption is that there is a degree of uncertainty if one single rockfall measured during data gaps (potentially coincident and triggered by rainfall), is a large single rockfall that includes lateral rockfalls or if this is the reflect of a set of precursory events that spatially clustered within similar areas of the cliff. As such, this represents an inherent limitation of this approach. However, it is important to note here that 10 out of 13 erosional episodes detected between data gaps (>hourly rockfalls) were coincided with moderate to heavy rainfall, where the daily rainfall was between 4.7 mm to 390 mm (see Section 6.5.1). Therefore, despite this limitation, the dataset is considered useful to assess the relative role of inclement weather conditions on rockfall versus temperature controlled rockfalls (Research Question 4, RQ4, see Chapter 1, Section 1.2).

Prior to this study, the largest near-continuous monitoring at East Cliff of Whitby was conducted by Williams et al., (2018), where the rockfall activity was monitored for the 10 months between March and December 2015. By the end of the monitoring campaign in 2015, the total estimated volume, including change detection estimated across gaps in the time-series, was 110.87 ± 52 m^3, also at 1h frequency, yielding an annualised cliff face retreat of 0.013 m. As such, the total erosion measured in 2015 was ~ 296 m^3, and somewhat lower than that observed in 2021, and also reflected in a lower annualised retreat rate (0.013 m in 2015 *v* 0.074 m in 2021). However, these differences may be attributable to a number of reasons, including: (1) the fact that in 2015, ten months were monitored, with no data collected between mid-July and towards the end of August (~1 month), and over ~15 days in September. These gaps created a difference the time monitored of around 3.5 months, including both January and February when large magnitude rockfalls appear most common. This issue also restricts the ability to annualise the retreat from this previous monitoring campaign; (2) different minimum Levels of Detection (LoD) were applied between the two studies, (0.03 m in 2015, and 0.10 m in this study). The LoD results in differences in the minimum rockfall volume detectable, the delineation of rockfall footprints, and hence the volume and erosion rates; and (3) the area of monitoring differs, whereby in 2015 this

included the cliff base and the topsoil whereas for 2021 data was analysed only for the hard rock cliff face. Combined, this constrains the ability to directly compare the monitoring campaigns of 2015 and 2021. It is however the case that the more complete 2021 dataset should be more comparable to other retreat rate datasets from this coastline and beyond.

Using monthly laser scanner surveys conducted between 2003 and 2010 across the North Yorkshire cliffs, annual retreat rates fluctuated at some locations between 0.052 and 0.079 m per year (Lim et al., 2005; Lim et al., 2010; and Rosser et al., 2013). As these surveys were conducted using regular monthly intervals, inclement weather-related rockfall would be captured in these inventories. More recently, using annual airborne LiDAR surveys conducted between 2014 and 2017 across a far greater length of coastline, an average rate of erosion of 0.06 m per year was estimated (Benjamin 2018). As a consequence, this research demonstrates the inherent inter-annual variability of cliff retreat via rockfall along this coastline reflecting both the annual variability and the occurrence of less frequent extreme triggering conditions and consequent rockfall (Brain et al., 2014; Benjamin, 2018). A comparison with global cliff recession rates (*GlobR2c2*) shows that the 0.074 m of retreat observed in here 2021 (and more generally across the North Yorkshire cliffs, as described above) is in the category of medium strength rocky cliffs (median rate: 0.1 m per year), between the 17% and 50% quantiles of the distribution, which fluctuates between 0.05 and 0.1 m per year (Prémaillon et al., 2018).

Overall, the 4D rockfall inventory acquired in 2021 represents a suitable dataset for comparison with the IRT dataset, as a total of 2,210 hourly rockfalls were captured during concurrent monitoring of the temperature conditions of the cliff face. The size of this database is also suitable to assess the relative erosional contribution of temperature effects on rockfalls, as a further 1,895 rockfalls were captured during data gaps generated by inclement weather (i.e., rainfall), permitting an attempt to estimate and compare of rockfalls potentially triggered by storminess versus temperature effects during dry environmental conditions and in absence of other triggers such as wave action (see Section 6.5).

6.3 Diurnal variability in seasonal rockfall occurrence

6.3.1 Thermal signatures on rockfall activity

As described, previous research has provided tentative evidence of an apparently subtle air temperature control on rockfall occurrence on the cliffs at the study site (see Williams, 2017), which mirrors largely anecdotal evidence from elsewhere, including laboratory tests (e.g., Ghobadi and Babazadeh, 2015; Villagra et al., 2018; Bakun-Mazor et al., 2020), field experiments (see Warren et al., 2013; Eppes et al., 2016), and observations (see Collins and Stock, 2016; Collins et al., 2018). To investigate this further, and for the first time, here I examine daily aggregated patterns of hourly rockfall (e.g., total number of rockfall per hour) with the corresponding cliff surface temperatures (e.g., absolute temperatures, and rates of change per hour). The data were compiled over the year, and by season and by hour, to derive mean rates of rockfall using sufficient rockfall numbers to support statistically significant relationships with temperature to be assessed. Importantly, given the gaps in both the laser scan and the IRT data, I first identify the data available for direct hour-by-hour comparison (Table 6.3).

Table 6. 3: *Temporal coincidence between the TLS and IRT hourly data in 2021.*

TLS and IRT data	Type of case	TLS change detection (hourly)	Thermal imagery (Hourly)	Number of temporal coincidences	Percentage (%)
Temporal coincidence between datasets	*I (both)*	Data	Data	2.773	31.7
	II (only TLS)	Data	No data	2,163	24.7
	II (only IRT)	No data	Data	1,216	13.9
	IV (none)	No data	No data	2,608	29.7
Total hours of year				8,760	100

Note: In the "type case I", TLS change detections include hourly change estimates in which rockfalls were detected, but also hours with absence of rockfalls. The later were needed to compare the thermal conditions when rockfalls occur versus the conditions observed during absence of rockfall activity (see Section 6.4).

Overall, Table 6.3 shows that for ~ 31.7% of the year the TLS based change detection and the IRT data are available. This data loss arises because of: (1) interruptions in data acquisition due to software or system failure affecting one of the two equipment's; (2) the differential effect data quality-control steps across the two datasets. For example, while light fog or slight precipitation generated low-quality thermal imagery, the laser was able to scan the cliff face; and (3) the effect of large laser scanner data gaps, when there were few thermal images. The laser was in general less affected by ambient conditions as compared to the IRT camera. Table

6.3 shows four scenarios, including the temporal coincidence of both datasets, and the absence of one or both. This demonstrated the inherent challenge associated with constant, fixed-location, long-term and high-frequency remote sensing of rock slopes. The data presented in this chapter considers scenarios where *I (both)*, *II (only TLS data),* and *III (only IRT data)* are available.

The IRT data presented in this chapter includes the mean, minimum and maximum surface temperatures calculated across the General Window (*GW*) of assessment, compromising ~ 1,410 m^2 of cliff surface (see Figure 5.1, *Chapter 5*). Importantly, in order to investigate temperature effects, only rockfall measured with 1-hour timing precision that were not coincident with rainfall were included in this section and Section 6.4. The rockfall frequencies described occurred when either of two criteria were met: (1) a total absence of rainfall within the IRT imagery; or (2) when IRT data was absent, an absence of rainfall recorded by the Whitby weather station. The application of these criteria avoided any coincidental patterns in rockfall as a result of systematic timing of raining through the day. This analysis considers a total of 1,649 rockfall detected during dry conditions, equating to ~ 40.2% of the total number observed in 2021 (see Table 6.2, *Section 6.2*). The data again is aggregated by season, for the reasons explained in *Chapter 5*.

Figure 6.3 shows the diurnal rockfall frequencies and the mean, mean of minimum and mean of maximum surface temperatures detected per hour of the day for each season. Rockfall frequencies are split by volume, from small to medium to large. This dataset illustrates that:

- In winter, notable increases in the rockfall frequency occur at midnight (23:00 and 00:00 h), sunrise (09:00 h), 1 hour after sunrise (10:00 h), noon (12:00 and 13:00 h), and sunset (16:00 and 17:00). At these times, rockfalls were two or three times more frequent than during the remainder of the day. In particular, rockfall frequency at midnight (~ 5.5 - 6.5%, where a uniformly random hourly rockfall frequency through the day would see between ~ 1 and 4% per hour), occurred when the cliff was subject to extremely low surface temperatures (~ -1.5°C and -4.0°C for the mean and minimum mean temperatures respectively at this time). At the end of the winter sunrise (09:00 h), the increase in rockall activity was notable (increasing from 4% to 10% frequency over this period), coincident with rapid increases in the surface temperature from ~ -2.0° to 2°C (Δ = 4°C). This demonstrates that rockfall frequency increases in response to changing temperature, but also that there may be an association with temperatures crossing the freezing point at 0°C. Rockfall frequency increased again during the period of maximum surface heating at noon (~ 6%) when the cliff was subject to mean and maximum temperatures of ~ 4°C and 6°C, respectively. A final rockfall increase from ~ 5% to 7% (Δ = 2%) was observed

during cooling at sunset when the mean surface temperature dropped from ~ 2°C to 0°C (Δ = -2°C) (Figure 6.3a). Conversely, and as seen throughout all seasons, the night-time periods, when absolute temperatures and the change in temperatures remained low, experienced lower than would be expected under conditions of uniformly random rockfall frequencies (<3%).

- Increases in rockfall frequency in spring occurred 1 hour after the sunrise (07:00 h), noon (13:00 h) and sunset (18:00, 19:00, 21:00 h), which all saw 2 or 3 times more rockfall as compared to the remainder of the day (5% - 8%). Like winter, the rockfall activity during spring appears to reflect the temperature increases at these times of day, albeit with an apparent 1-hour lag. It is important to note here that this 1-hour lag after sunrise was a directly function of large-scale aspect controls which slightly delay direct incident solar radiation onto the cliff between 07:00 and 08:00 h (see *Section 5.4*, *Chapter 5,* Figure 5.23). This dataset illustrates how cliff topography and aspect fundamentally controls the exposure to solar radiation at sunrise and hence, the likely generation of temperature-controlled rockfalls. The period at the end of daily heating around noon experiences a second increase in rockall frequency (8%), corresponding with both the maximum mean and minimum mean temperatures (~ 12°C and 8°C, respectively). This is the time of day with both the most intense solar insolation, but also that which experiences a very rapid cessation of insolation when the near-vertical cliff face becomes shadowed as the sun passes instantaneously over the cliff top. A third increase in the rockfall frequency occurred during and after sunset at around 19:00 h, when the maximum mean temperature surface peaked (18°C), again a function of large-scale aspect control (*Section 5.4*, *Chapter 5,* Figure 5.23). A final increase in the rockfall activity was observed at the end of sunset during a period of overall cooling (21:00 and 22:00 h). At this time, whilst mean surface temperatures dropped from ~ 10°C to 7°C (Δ = -3°C), the rockfall frequency increased from below a uniformly random hourly frequency (~ 3%) to near 6% (Δ = 3%) (Figure 6.3b).

- In summer, increases in rockfall activity correspond with the timing of the end of sunrise (07:00 h), noon (13:00 h), and the end of sunset (22:00 h), when rockfall frequencies were, overall, two or three times higher than during other hours of the day. However, the most notable increases in rockfall frequency were those following sunrise, which sharply rose from ~ 2% to ~ 19.5% (Δ = 17.5%), at a time when changes in the mean and maximum mean cliff surface temperatures increased from ~ 14°C to 16°C (Δ = 2°C), and 18°C to 22°C (Δ = 4°C), respectively. It is also interesting to note that the largest single

rockfall also occurred during this period (75 ± 19 m³), which was also coincident with multiple smaller adjacent rockfalls. Interestingly, this cluster of rockfalls occurred at the time when the incident solar radiation was driving the highest daily change in surface temperature at sunrise, but also when coastal fog was present (known locally as '*Haar*'). In the absence of commonly reported triggers, such as rainfall or waves, this observation suggests that the trigger for this event was a combination of high rates of temperature change, and the associated thermomechanical processes, and possibly surface moisture associated with coastal fog, as discussed further below. Similar to winter and spring, a second increase in rockfall frequency again occurred around noon (~ 6% frequency) when the surface of the cliff experienced the end of the heating period as the sun passed overhead (peak mean temperature ~ 19°C). A third increase in the rockfall frequency occurred by the end of summer sunset (22:00 h), again when the cliff face was cooling, when rockfall frequencies increased from ~ 2% to 8% (Figure 6.3c). As with those seasons which experienced overall systematic surface warming from sunrise until noon (summer, autumn, spring), there are tentative suggestions of a proportional increase in rockfall frequencies during this period also. It appears that this general temperature control is then superimposed by peaks at key times around sunrise, noon and sunset. Similar patterns in the changes to rockfall frequency during autumn were again associated with the periods around sunrise, noon, and sunset (Figure 6.3d).

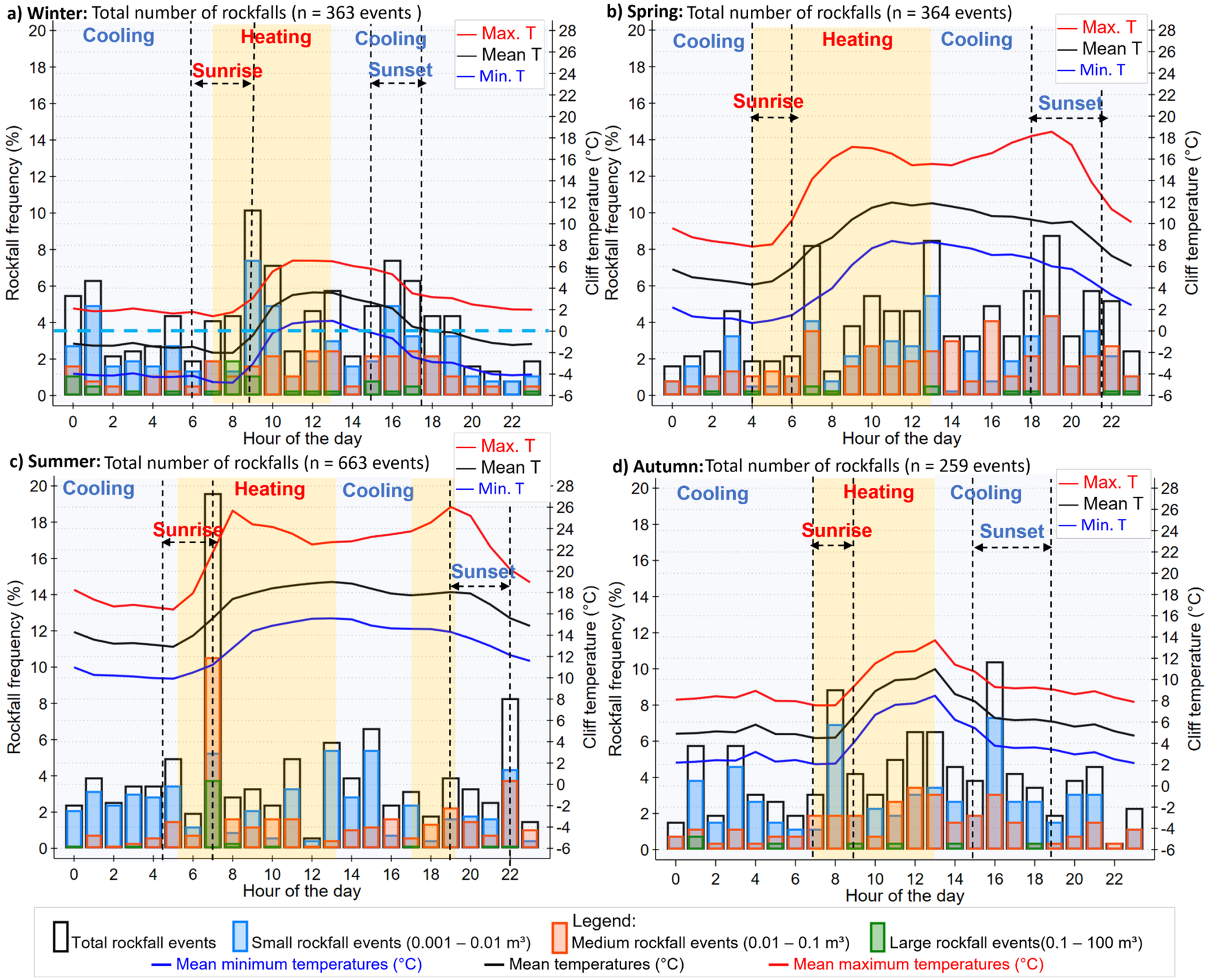
a) Winter: Total number of rockfalls (n = 363 events)
b) Spring: Total number of rockfalls (n = 364 events)
c) Summer: Total number of rockfalls (n = 663 events)
d) Autumn: Total number of rockfalls (n = 259 events)
Cooling
Heating
Cooling
Sunrise
Sunset
Max. T
Mean T
Min. T
Rockfall frequency (%)
Cliff temperature (°C)
Hour of the day
Legend:
Total rockfall events
Small rockfall events (0.001 – 0.01 m³)
Medium rockfall events (0.01 – 0.1 m³)
Large rockfall events(0.1 – 100 m³)
Mean minimum temperatures (°C)
Mean temperatures (°C)
Mean maximum temperatures (°C)

Figure 6. 3*: Overleaf. Diurnal variability of rockfall activity 2021 (Overlapped with the absolute cliff temperatures).* ***a)*** *Rockfall frequency and temperatures detected in winter, where the thermal threshold of 0°C is highlighted using a horizontal dashed blue line.* ***b)*** *Rockfall frequency and temperatures detected in spring.* ***c)*** *Rockfall frequency and temperatures in summer.* ***d)*** *Rockfall frequency and temperatures detected in autumn. Hourly rockfalls that were coincident in time with rainfall occurring between the thermal camera and the cliff face were discounted of the analysis, yielding a total of 1,649 rockfall events used in this figure. Vertical dashed lines indicate the approximate sunrise and sunset times for the latitude and longitude of Whitby. Light yellow and blue regions highlight the duration of the daily heating and cooling phases.*

To further explore if changes in rockfall frequency coincide with faster or slower changes in surface temperature, Figure 6.4 shows for each season the diurnal rockfall frequencies and the mean, mean of minimum, and mean of maximum rates of change. How quickly or slowly the temperatures change can provide an indication of the thermal stresses driving rock expansion and contraction. This demonstrates that:

- In winter, significant increases in rockfall correspond with the highest positive rates of surface temperature change at sunrise (heating). The maximum rockfall frequency during surface heating between 08:00 – 09:00h (10%) and between 09:00 and 10:00 h (7%), occurred when the cliff face was subject to the peak daily rates of heating (mean and mean maximum rates of change of 1°C/h and 3.5°C/, and ~ 1.8°C/h and 4°C/h, respectively). Between 10:00 – 11:00 h, a notable drop in rockfall frequency occurred (~ 2%). Interestingly, temperature increases at the beginning of sunset were coincident with increased rockfall frequencies between 15:00-17:00 h (7.5% to 6.5%). This implies that rockfalls during sunset showed a greater sensitivity whereby even smaller rates of temperature change were effective. At midnight and noon, the rates of change were steady and low, but frequencies were two times higher than other periods of the day. This indicates that the absolute temperatures in winter hold a key role in controlling rockfall activity in the absence of abrupt rates of change driven by direct insolation at sunrise, noon and sunset (see Figure 6.3a).

- In spring the highest increases in rockfall frequencies were coincident with the maximum positives rates of surface temperature change at the end of sunrise (06:00 – 07:00 h), and with the beginning of sunset (18:00 – 19:00 h). To exemplify this, by the end of the sunrise the maximum rates of temperature change were 6.5°C/h and the rockfall frequency was 8%, while by the beginning of the sunset, the rate of changes was 7°C/h and the rockfall frequency was 8.5%.

Again, rapid drops in the rate of change of temperature after sunrise coincided with reductions in the rockfall frequency between 07:00 - 08:00 h (1.5%). Similar drops in rockfall frequency were observed also after rapid reductions in the maximum rates of temperature change around sunset. The highest rockfall frequency (8%) around noon (12:00 – 13:00 h) was coincident with large minimum negative rates of temperature change (-3°C/h) and maximum rates of temperature change (2°C/h). This suggests that the rockfall frequencies detected around noon may have been controlled by either the maximum absolute temperatures of the day (see Figure 6.3b) or the change in temperature associated with the rapid transition of the cliff face to shadow due to the sun position and incidence angle (Figure 6.4b).

- In summer the maximum rockfall frequency was coincident with high rates of temperature change at the end of sunrise (06:00 – 07:00 h). Here, the rockfall frequency was > 19%, while the mean and mean maximum rates of temperature change were >1°C/h and 5°C/h, respectively. Around noon (12:00 – 13:00 h), and similar to spring, increases in the rockfall activity (~ 6% frequency) occurred when the cliff experienced increases in the minimum (negative) rates of change (reaching -2°C/h) and the warmest absolute mean temperatures (see Figure 6.3c). At sunset, the highest rockfall frequency (8%) did not occur when the cliff was subject to mean maximum rates of temperature change (18:00 – 19:00 h) but instead when the cliff experienced overall reductions in the mean and mean maximum rates of change alongside increases in the mean minimum (negative) rates. This again suggests the role that overall cooling may have in driving rockfall activity around the summer sunset (Figure 6.3c).

- In autumn, increases in rockfall frequency occurred during sunrise, making this the only season when rockfalls were not observed to coincide with rapid rates of surface temperature change. This may also be a reflection of an increasing dominance of non-thermal drivers on rockfall such as seasonal rainfall or storms, potentially stripping the cliff face of material available to fail, as will be explored further below. However, the peak rockfall frequency (>10%) occurred when the cliff face was subject to slight increases in the rates of surface temperature change at the beginning of sunset, as was detected in winter. This suggests again that, in the coldest seasons, only minor increases in the rate of temperature change per hour may be of sufficient magnitude to drive thermal stresses triggering rockfalls at sunset (Figure 6.4d).

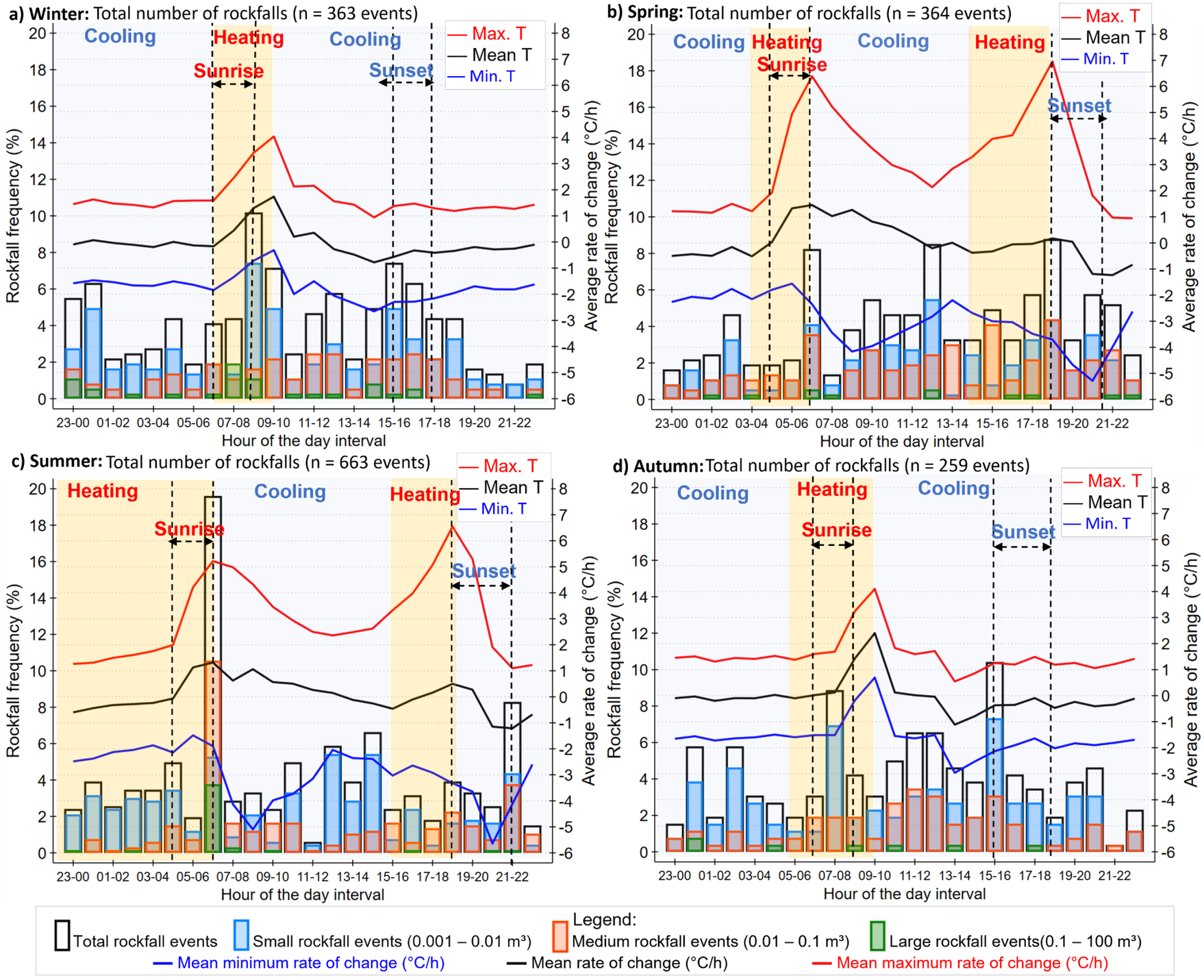
a) Winter: Total number of rockfalls (n = 363 events)
b) Spring: Total number of rockfalls (n = 364 events)
c) Summer: Total number of rockfalls (n = 663 events)
d) Autumn: Total number of rockfalls (n = 259 events)
Cooling
Heating
Sunrise
Sunset
Max. T
Mean T
Min. T
Rockfall frequency (%)
Average rate of change (°C/h)
Hour of the day interval
23-00 01-02 03-04 05-06 07-08 09-10 11-12 13-14 15-16 17-18 19-20 21-22
Legend:
Total rockfall events
Small rockfall events (0.001 – 0.01 m³)
Medium rockfall events (0.01 – 0.1 m³)
Large rockfall events(0.1 – 100 m³)
Mean minimum rate of change (°C/h)
Mean rate of change (°C/h)
Mean maximum rate of change (°C/h)

Figure 6. 4*: Overleaf. Diurnal variability of rockfall activity 2021 (Overlapped with the rates of change of temperature).* ***a)*** *Rockfall frequency and IRT rates of change detected in winter.* ***b)*** *Rockfall frequency and IRT rates of change detected in spring.* ***c)*** *Rockfall frequency and IRT rates of change detected in summer.* ***d)*** *Rockfall frequency and IRT rates of change detected in autumn. Hourly rockfalls that were coincident in time with rainfall occurring between the thermal camera and the cliff face were discounted of the analysis, yielding a total of 1,649 rockfall events used in this figure. Vertical dashed lines indicate the approximate sunrise and sunset times for the latitude and longitude of Whitby. Light yellow and blue regions highlight the duration of the daily heating and cooling phases, respectively.*

Overall, the data presented in Figures 6.3 and 6.4 illustrates several important observations, including (1) that during dry conditions and in the absence of episodic triggers (e.g., storms and rainfall), rockfall activity shows a clear departure from being random in time; and, (2) that the rockfall activity, and so, wider rock-slope erosion, shows during these periods a clear control of both ambient and surface temperature, which promote a marked diurnal pattern of erosion, eventually representing thermal signatures on rockfall activity over the diurnal cycle.

To further explore temperature controls on the rockfall activity, Figure 6.5 shows a matrix of correlation coefficients and best-fit ellipses for all the independent variables characterizing rockfall frequency and temperatures by season. For analytic consistency, the data was aggregated by hour of the day as shown in Figures 6.3 and 6.4. Here, Pearson cross-correlations were conducted at 95% confidence interval level between four rockfall variables (Total rockfall events, small, medium, and large size events) and six thermal variables (mean cliff temperature, mean maximum temperatures, mean minimum temperatures, as well as mean, mean maximum and mean minimum rates of change of temperatures per hour).

It is important to note here that the correlations were conducted between the number of rockfall events (i.e., rockfall frequency) rather than rockfall volumes to the surface temperature conditions. This was done as the aim here is to identify the influence of cliff temperatures on the rockfall occurrence, rather than the influence on the rockfall volumes or flux. At East Cliff, the later seems to only show significant correlations with environmental variables when the rockfall data is aggregated over longer periods of time, such as weeks and months (see Williams, 2017), which are timescales that were not addressed here (see *Chapter 5*, *Sections 5.2 and 5.3*). However, as the rockfall frequency was assessed by volume (small, medium, and large volume rockfalls, see caption of Figure 6.5), temperature influences on the size of rockfalls were considered.

In winter, statistically significant positive correlations (significant relationships, $p \leq 0.05$) were observed between the total number of rockfalls and the mean and maximum rates of change

of temperature (R^2 = 0.46 and 0.54, respectively), as well as between small size rockfall events and the mean, maximum and minimum rates of change (R^2 = 0.42 to 0.55). Hence, while these relationships do not indicate causation, these results attest to the importance and likely sensitivity of the rockfall occurrence, particularly small failures, to the rate of temperature change during winter, notably at sunrise (Figure 6.4). Furthermore, in this season, only medium size rockfalls significantly correlate with the absolute mean, maximum and minimum surface temperatures (R^2 = 0.53) (Figure 6.5a).

In spring, several statistically significant positive correlations at the 95% confidence interval level are apparent. For example, the total number of rockfall events correlated well with the absolute cliff temperatures (mean, maximum and minimum, R^2 = 0.45 to 0.50), as well as with the maximum rates of change of temperature (R^2 = 0.42). Medium size rockfalls correlated with the same thermal variables (R^2 = 0.41 to 0.46), while small size rockfalls, significantly correlated with the maximum cliff temperatures (R^2 = 0.41). Overall, these results highlight, again, that there was a likely sensitivity of the rockfall activity to temperature, but particularly with the maximum absolute temperatures that occur around noon and the maximum rates of change of temperature (Figure 6.5b). Similar to winter, large rockfalls do not significantly correlate with any thermal variable, which may be explained because of that the rockfall frequency of large events were relatively uniformly randomly distributed through the day in both seasons (see Figures 6.3 and 6.4).

In summer, no statistically significant relationships at the 95% confidence interval level are present (Figure 6.5c). While the rockfall frequencies in summer were two or three times higher at the end of sunrise, noon and by the end of sunset (notably higher at sunrise), a more variable hourly rate of rockfall frequencies was seen (see Figures 6.3 and 6.4). During 11 months of monitoring, Eppes et al., (2016) observed a similar pattern with a lack of relationships between the microcracking and environmental conditions. This was explained as related to fluctuating ambient stress levels needed to trigger cracking in any rock, and that the inherent variance of this processes may explain the absence of correlation between cracking rates and extreme environmental factors, which mirror well the insignificant relationships ($p \geq 0.05$) between summer cliff temperatures and rockfalls.

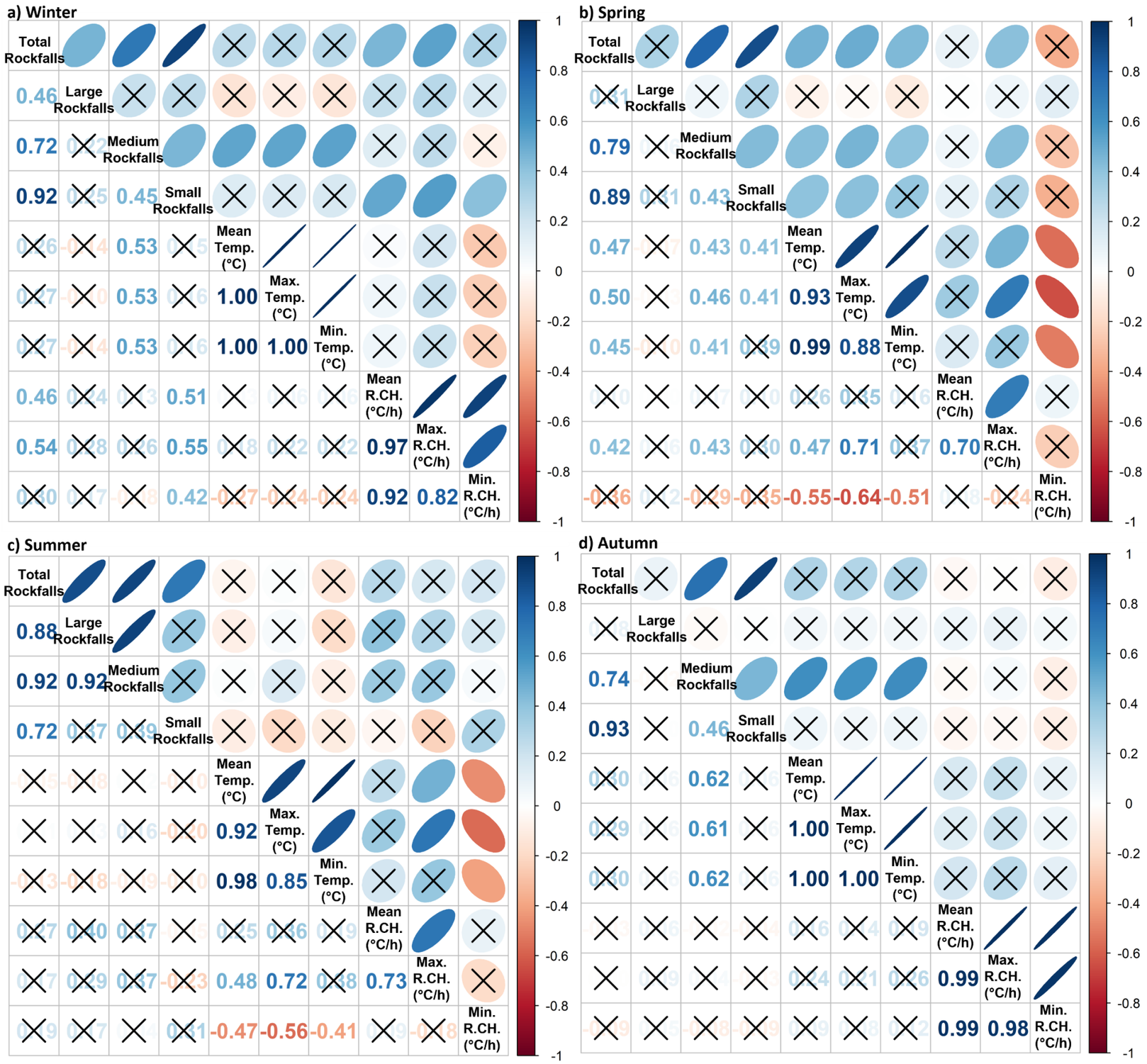
a) Winter
Total Rockfalls
Large Rockfalls
Medium Rockfalls
Small Rockfalls
Mean Temp. (°C)
Max. Temp. (°C)
Min. Temp. (°C)
Mean R.CH. (°C/h)
Max. R.CH. (°C/h)
Min. R.CH. (°C/h)
0.46
0.72
0.92
0.45
0.53
0.53
1.00
1.00
0.51
0.55
0.97
0.82
0.42
-0.27
-0.24
-0.24
0.92
b) Spring
Total Rockfalls
Large Rockfalls
Medium Rockfalls
Small Rockfalls
Mean Temp. (°C)
Max. Temp. (°C)
Min. Temp. (°C)
Mean R.CH. (°C/h)
Max. R.CH. (°C/h)
Min. R.CH. (°C/h)
0.79
0.89
0.43
0.47
0.43
0.41
0.50
0.46
0.41
0.93
0.45
0.41
0.99
0.88
0.42
0.43
0.47
0.71
0.70
-0.55
-0.64
-0.51
c) Summer
Total Rockfalls
Large Rockfalls
Medium Rockfalls
Small Rockfalls
Mean Temp. (°C)
Max. Temp. (°C)
Min. Temp. (°C)
Mean R.CH. (°C/h)
Max. R.CH. (°C/h)
Min. R.CH. (°C/h)
0.88
0.92
0.92
0.72
0.92
0.98
0.85
0.48
0.72
0.73
-0.47
-0.56
-0.41
d) Autumn
Total Rockfalls
Large Rockfalls
Medium Rockfalls
Small Rockfalls
Mean Temp. (°C)
Max. Temp. (°C)
Min. Temp. (°C)
Mean R.CH. (°C/h)
Max. R.CH. (°C/h)
Min. R.CH. (°C/h)
0.74
0.93
0.46
0.62
0.61
1.00
1.00
0.99
0.98
1
0.8
0.6
0.4
0.2
0
-0.2
-0.4
-0.6
-0.8
-1

Figure 6. 5: *Overleaf. Matrix of correlation coefficients and best-fit ellipses for all independent variables characterizing the rockfall frequency and IRT temperatures detected during the daily thermal cycle of each season. Rockfall variables are represented, respectively, by the frequency per hour of the "Total rockfalls", "Large rockfalls "(0.1 - 100 m³), "Medium rockfalls" (0.01 – 0.1m³) and "Small rockfalls" (0.001 – 0.01m³). IRT temperature variables (per hour) are represented, respectively, by the "Mean temperatures" (Mean. Temp. °C), "Maximum average temperatures" (Max. Temp. °C), "Minimum average temperatures" (Min. Temp. °C), "Average rate of change of temperatures" (Mean. R.CH. °C/h), "Maximum average rate of change of temperatures (Max. R.CH. °C/h), and the "Minimum average rate of change of temperatures" (Min. R.CH. °C/h). a) Matrix of correlation of winter. b) Matrix of correlation of spring. c) Matrix of correlation of summer. d) Matrix of correlation of autumn. The matrix of correlation was computed using the Pearson correlation in R. The colour bars show the Pearson correlation coefficient (PCC) which describes both the strength of the relationship and if it is positive or negative (1 to -1). The sign of the relationships is also expressed by the sign of the PCC values in the bottom-left side of the matrix and the orientation of the ovals in the upper-right side, where narrower ovals represent the stronger relationships. Insignificant relationships ($p \geq 0.05$) are indicated with cross marks over the corresponding ovals and associated coefficients (upper and lower sides of the matrix, respectively).*

In winter, spring and autumn, medium size rockfall significantly correlate with minimum cliff temperatures (R^2 = 0.41 to 0.62) (Figures 6.5). This finding reflects observations made elsewhere such as rockfall monitored along 40 km of the Auverge railway in France (Delonca et al., 1014). In that research, a total of 142 rockfall events were manually inventoried between 2001 and 2012, where it was suggested that environmental temperatures lower than 0°C triggered rockfalls. The highest correlations were observed between the minimum temperatures recorded two days before failure. Similarly, during the monitoring campaign of the East Cliff of Whitby conduced in 2015, it was observed that the cross correlation between air temperature and rockfall activity was significant between 2 hours and 1 hour before failure, with key negative correlations that suggested that cooling temperatures were probably associated with the occurrence of rockfall activity (Williams, 2017). Following a similar trend, by coupling temperature data and micro-seismic monitoring as a proxy for rock damage in a rock-wall located in Acuto (Italy), significant correlations were observed the occurrence of micro-seismic events and minimum temperatures (D' Angio et al., 2021).

6.3.2 Thermomechanical and cracking effects on rockfalls

Temperature fluctuations able to cause both thermal expansion and contraction of the rock and produce thermal stresses and strain (Gunzburger et al., 2005), leading to deformation across discontinuities, have been reported around sunrise, noon, or sunset (e.g., Gunzburger et al., 2005; Vlcko et al., 2009; Gischig et al., 2011a,b; Bakun-Mazor et al., 2013; Collins and Stock, 2016; Greif et al., 2017; Collins et al., 2018; Guerin et al., 2020). Such processes may induce microfracturing but also irreversible dislocation of discontinuities across critically stressed discontinuities if the stress and strength conditions permit (e.g., Gischig et al., 2011a; Marmoni et al., 2020; Fiorucci et al., 2020), resulting in general mechanical deterioration or weakening of the rock and predisposition to failure (Marmoni et al., 2020). Also, it is commonly assumed that the thermal stresses are proportional to the change in temperature, which produces proportional displacements or strains related to contraction and dilation (Rafferty, 2022; Bagdassarov, 2022). Such changes are controlled by both diurnal temperature changes but also by the rock's Poisson's ratio and differences in coefficients of thermal expansion of the rock's primary constituent minerals (Eppes and Keanini, 2017). For example, quartz-rich sedimentary rocks, such as sandstones, have relatively high values of thermal expansion because of the response of quartz to temperature (Rafferty, 2012; Eppes and Keanini, 2017). Therefore, the sandstone outcropping at East Cliff meet the criteria for the development of thermal stresses because of the existence of (but not restricted to) two key conditions: (1) high rates of change of temperature per hour (either positive or negative), especially rapid changes at sunrise and sunset (see Figure 6.4, Section 6.3.1); and (2) relatively high reported thermal expansion coefficients for this rock type (see Table 6.4). It is hypothesized that these conditions provide a suitable setting in which rapid rock contraction and expansion can occur, driving reversible thermo-elastic deformation and potentially irreversible cracking and failure depending on the stress and strength conditions.

Table 6. 4: *Typical coefficients of thermal expansion of rocks.*

Rock type	Average linear expansion coefficient $(10^{-6})°C^{-1}$
Sandstones	10 ± 2
Slates	9 ± 1
Granites and rhyolites	8 ± 3
Andesites and diorites	7 ± 2
Marbles	7 ± 2
Basalts, gabbros, and diabases	5.4 ± 1

Note: Temperature interval: 20 - 100°C. Source: Modified from Table 6-10 in Skinner (1966, p. 94).

Using integrated TLS and IRT remote detection of exfoliation sheet deformation on granitic outcrops, Guerin et al., (2020) noted that the most deformed portion of the sheet corresponded with the surfaces where both the temperature variability were the highest (-9.3°C between 20:00 and 06:00 h, and +26.7°C between 06:00 and 12:00 h) and the fracture aperture was the largest (-5.33 mm for peak contraction between 08:20 – 09:00 h, and + 5.86 mm for peak expansion between 14:21 - 15:00 h). The largest deformations were observed across the edge of the exfoliation sheets. As a result, these authors suggested that these surfaces could act as rockfalls source zones. Although the shape of granitic exfoliation sheets differs from this site (which may affect the efficiency of the temperature induced deformation of the joints, due to for example, the effect of air circulation inside fractures and differing levels coefficients of thermal expansion, as shown in Table 6.4), it is hypothesized here that based on the observations made by Guerin et al., (2020), the detected increases in the rockfall frequencies at sunrise and noon may be spatially linked with the distribution of the highest rates of change of temperature (or maximum temperatures at noon), which could induce the largest and fastest expansion of some discontinuities (i.e., moving outward or away the cliff face due to warming). This may particularly affect the edge of overhanging beds and rock bridges, creating zones more susceptible for failure. Maximum closure of discontinuities at the end of sunset associated with rapid cooling can generate inward deformation or closure of discontinuities, which may also be a factor that promotes rockfall.

Importantly, the study conducted by Guerin et al., (2020) also noted that the maximum contraction and expansion of the exfoliation sheet occurred with a delay of ~ 01:20 h from the time where the surface sheet temperature was at the minimum (~ 07:00 – 08:00 h) and with a delay of 02:40 h when the temperature was at a maximum (~ 11:40 – 12:20 h). This thermomechanical delay could explain delayed peaks in the rockall frequencies sometimes observed at noon of winter, spring and summer, as maximum noon frequencies (~ 6 to 8%) occurred at 13:00 h (i.e., with 1 hour delay with respect to the peak of the mean cliff surface temperatures at 12:00 h, see Figures 6.3a,b and c). Moreover, this delay is also sometimes observed when examining the rates of change of cliff temperatures, as peak rockfall frequencies of winter, spring and summer (~ 8 to 19%) occurred towards the end of the sunrise when maximum rates were reached, but also towards the end of the sunset of spring and summer, with around 2 hours of delay after the maximum rates of 18:00 – 19:00 h, as increases in the rockfalls frequencies (~ 6 to 8%) occurred around 21:00-22:00 h during cooling (see Figures 6.4a, b and c). It is hypothesized here that this thermomechanical (and subsequent rockfall) delay could be principally generated by large-scale aspect controls affecting the cliff illumination at sunrise and

sunset (See Figures 5.22 and 5.23, *Chapter 5*), which may have a likely effect in the surface heat balance, promoting a lag in the absorption and/or release of the heat towards the rock.

Thermomechanical forces acting deeper within the slope may also drive deformation leading to slope failure from 2D models, as it has been noted that for planar sliding in summer, the shear stress across a discontinuity daylighting at the cliff face can increase as the rock warms and expands (as the dip of the discontinuity can increase and so, the angle to produce potential sliding), producing a drop in the normal stress, and favouring failure after cumulative thermo-elastic loading or via incremental stress redistribution of critically stressed discontinuities (i.e., along those potential failure surfaces in which the shear stress reaches the strength limit) that concentrates at slip fronts. The opposite behaviour was observed in winter, inhibiting failure as the rock contracts and the shear stress decreases. For toppling, reductions in the normal stress under very cold temperatures are possible as the rock contracts, but also the effect of bending of blocks which generates tensile stresses towards the outer edge, which was suggested for natural settings promoting failure (Gisching et al, 2011a).

Figure 6.6 shows a conceptual model depicting the two principal set of discontinuities daylighting at East Cliff (set 1 = sub-horizontal; set 2 = sub-vertical, forming near orthogonal intersections between these, and so slabs and cubic shaped rock blocks and sharp breaks in the topography of the cliff face). While toppling failure seems to not be kinematically feasible, it is hypothesised that increases in shear stress can occur from sunrise to noon and may promote strains affecting rock blocks bounded by set 1 and 2 (outward the cliff face), and so exerting forces in all directions to adjacent rocks. At sunset, assuming that the rock cools and contracts, the shear strength can be reduced along critically stressed discontinuities by the contraction of the adjacent slabs (Figure 6.6).

Figure 6.6 also shows the likely effect of critically stressed nodal surfaces, especially along those located close to or that daylight at the cliff face. Here, nodes are zones characterized by near orthogonal intersections between the set 1 and 2, in which the cumulative concentration of strain and rock fatigue can occur. It is assumed that these zones can operate as zones of initiation of failure. This behaviour has been proven to be feasible at near-orthogonal intersections of discontinuities affected by thermo-elastic loading, as increasing plasticity and failure along the joint nodes is feasible. This may also be due to progressive failure around already failed nodes located even in the deepest section of the rock face (Marmoni et al., 2020). These authors also noted that when considerable temperature drops occur, nodal intersections of air filled joints show diffusive plasticity towards the most external joints, affected by the highest temperature ranges, facilitating failure.

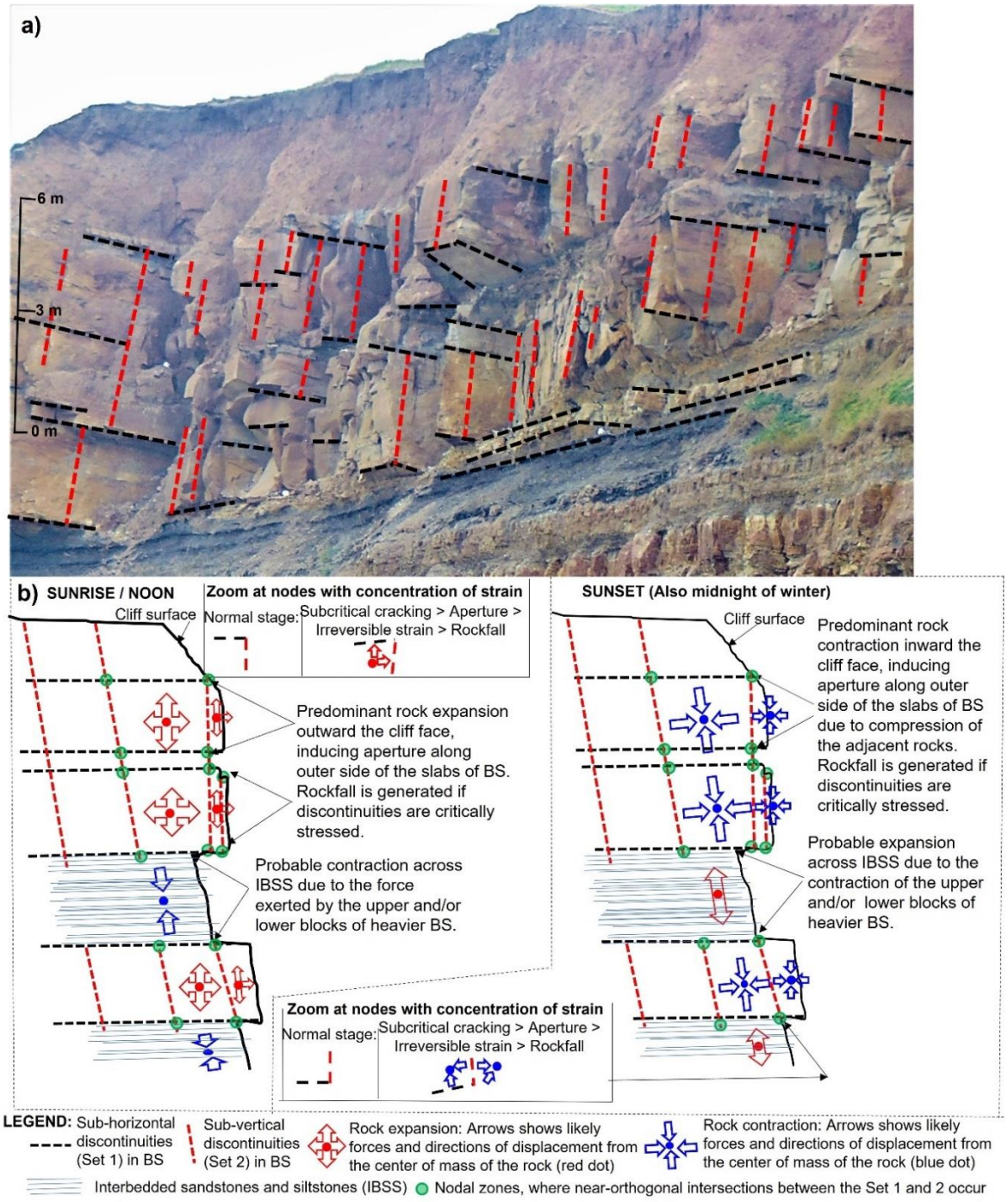

Figure 6. 6: *Conceptual model of likely thermomechanical effects operating at the East Cliff. a) The principal sets of discontinuities are mapped over a high-resolution photograph captured from the cliff base (only some of the master sets of discontinuities are mapped). b) Non-scaled conceptual model. BS: Bedded Sandstones. IBSS: Interbedded sandstones and siltstones.*

Overall, due to the discontinuity configuration of the East Cliff, the characteristic rapid rates of change in temperature experienced in sunrise and sunset, high cliff surface temperatures

that can be reached at the warmer months at noon (≥ 40°C), and the relatively high thermal expansion coefficients for sandstones (see Table 6.4), it is hypothesized here that some of the thermomechanical behaviours such us those described by Gisching et al.,(2011a), Guerin et al., (2020), and Marmoni et al., (2020) may operate in this setting, causing rockfalls along discontinuities dipping deeper (producing large temperature-controlled rockfalls ≥ 1.0 m^3) or daylighting at the cliff face, the later condition producing small but temperature-induced rockfalls (0.001 – 0.01 m^3). This is a clear area of future research.

Large-scale slope aspect controls shift sequentially during the day, heating the cliff from two opposite directions generating two daily phases of heating during the warmer months: first striking from the east around sunrise, and then striking from the west at sunset. This may have a key role in controlling the spatial distribution and efficiency of the magnitude of the absolute and rates of change of temperatures (See *Chapter 5*, *Section 5.3*, Figures 5.22 and 5.23), and hence the efficacy of thermomechanical and cracking effects. Similarly, it has been observed that the azimuth of meridional cracks across clasts composed by granite, gneiss, limestone, sandstones, and basalts aligned N-S in deserts of California, New Mexico and Arizona (McFadden et al., 2005). These cracks were produced by thermal tensile stresses due to strong radial temperature gradients as a function of insolation angle (McFadden et al., 2005). Very similar results were obtained by Eppes et al., (2010) across the surface of clast of the deserts of Mojave (USA), Strzelecki (Australia), and Gobi, Mongolia. Similarly, on Mars, cracks were found to show preferred orientations following the geometry of directional heating by the sun, driving fatigue-related cracking in preferred directions (Eppes et al. 2015). More recently, by studying anisotropy and weathering effects on rocks forming historical buildings in Spain, it was noted that the erosion rates were more efficient on the surface of those rock-wall more exposed to the solar radiation and so, enhancing the weathering and subsequent erosion (Martinez et al., 2020). Therefore, it is likely that here we see a temporal manifestation of this, whereby rockfall frequencies at sunrise, noon and sunset may have been facilitated by the large-scale aspect control on insolation described in *Chapter 5.* However, rock walls with complex topography are known to influence heat propagation and thermal stresses sufficient to induce discontinuity expansion and contraction (Marmoni et al., 2020). The same authors suggest that these effects may be more complex on different slopes due to the large number of variables and controlling factors, which may be reflected in the complexity of the patterns in the data described here.

6.3.3 Secondary processes affecting surface temperatures and rockfalls

In addition, the apparent correlation between absolute temperature, temperature change and rockfall occurrence implies either a thermal control on rockfall occurrence, or that secondary processes that respond either directly, indirectly to, or contemporaneously with, temperature may also be important in the instantaneous triggering of rockfall. Here I discuss some of these processes. For example, for rockfall detected at midnight in winter, possible explanations may be related to general cold conditions that may promote frost action. In the coastal chalk cliffs of the UK, rockfalls induced by freeze-thaw effects have been proposed to explain the cliff retreat of the Seven Sisters, along with wave abrasion (Bird, 2004). Pore water freezes between 0°C and -5°C, and that when this happens, volumetric expansion can cause frost weathering (McGreevy and Whalley, 1982; Matsuoka 1991). The coldest temperatures detected across the cliff face during the night-time in winter were within this range (mean surface temperatures sustained below 0°C, and minimum mean temperatures reaching -4°C, see Figure 6.3a, with extreme negative temperatures reaching -5°C and -10°C, as demonstrated in *Chapter 5*). It has also been reported that in fully saturated sandstones, freezing can induce pressures up to two orders of magnitude greater than the rock tensile strength (Hallet et al., 1996), and so volumetric expansion can induce mechanical weathering by hydrofracture, nucleating microcracks (Hallet, 2006).

Conversely, increasing evidence indicates that ice segregation, rather than volumetric expansion, may be important in weathering porous rocks (Hallet et al., 1996; Murton et al., 2006). Ice segregation takes place when water migrates through rock as a result of temperature-gradient driven suction, moving water towards freezing zones in rock. If this occurs, ice lenses may form, increasing the tensile stress across the boundaries between the unfrozen and frozen zones. Ice segregation has been simulated in laboratory conditions using samples of sandstones and limestones, and it has been reported that this process may be common in geomorphic settings subject to low temperature gradients and where temperatures below 0°C can persist for significant periods of time (Hallet et al., 1996; Murton et al., 2006). Whilst my data does not describe the presence or absence of ice directly, it does provide evidence of the presence of a temperature regime sufficient to promote the generation of ice if sufficient moisture is in or on the cliff, but this is something that could be considered in future work.

At East Cliff, surface temperatures <0°C were sustained during most of January (see *Chapter 5*, Figure 5.2a), meeting the conditions for frost action in localized part of the cliff face, especially at the boundaries of areas subject to near-constant shadow. Nevertheless, it has been acknowledged that a critical threshold level of saturation for each type of rock is required to develop frost conditions, and only when moisture exceeds this level will the rock be subject to

frost weathering. Rock types such as quartzites tend to be more resistant, while porous and bedded sedimentary rocks, such as shales, sandstones and chalks, tend to be less resistant to this process (Prick, 1997; Prick, 2004). At Whitby, bedded, open fractured sandstones, siltstones, and shales dominate. Combined with morning coastal fog, or rain, the provision of moisture and/or water to develop frost conditions and then volumetric expansion that occurs directly through mineral wetting, or through the water-to-ice transition may be significant. However, although it is likely that the increase in rockfall frequency observed between 00:00 and 01:00 h may be a response to a set of processes as a product of general cold conditions (where cliff temperatures were mostly between 0 and -5°C, see Figure 5.2a, *Chapter 5*), more research is indeed needed to confirm if the surface moisture availability actually exceeds the necessary moisture needed to facilitate rock damage.

Rockfall detected at winter sunrise are likely reflecting a transition from frozen to thawed conditions. It is well established that temperatures must fluctuate from above to below 0°C and vice versa (Prick, 2004), which was commonly observed in the surface temperatures at end of the sunrise (09:00 h). Nevertheless, what conditions lead to the most effective freeze-thaw cycling has been debated: some suggest minimum negative temperatures for absorbed water to freeze, or minimum durations negative and/or positive temperatures through consecutive cycles (Prick, 2004). For instance, Lewkowicz (2001), defines one cycle as complete when the hourly rock temperature goes from >1°C to <1°C and, then back again to >1°C. Matsuoka (1991), defines one cycle when temperatures drop to <-2°C, but are followed by temperature >+2°C. Moreover, based on Schmidlin et al., (1987), a day is considered a freeze-thaw day if the daily minimum ground temperature is $\leq$ -2.2°C and the maximum temperature of the day is above zero. This dataset demonstrates that mean surface cliff temperatures fluctuated between -2°C and +2°C between 08:00 and 10:00 h (i.e., from mid-sunrise to one hour after the sunrise). Hence, the development conditions to develop freeze-thaw cycles are met based on the previous suggested made above. As demonstrated in Chapter 5 (Section 5.2), a total of 49 days of winter (69% of the days with availability of filtered and calibrated thermal imagery) experienced freeze-thaw cycles following the criteria of Schmidlin et al., (1987), allowing comparability of results.

Evidence of marked diurnal patterns in wind speed across the coastline and offshore of the English Channel have been demonstrated by Lapworth (2011). These differences are created by convective heat fluxes across overlying air flows due to advective changes, so, under certain conditions, the combination of diurnal changes across the land alongside with advective changes across the sea surface can generate systematic diurnal variations in wind speed. Throughout the coast, this process results in maximum wind speeds at noon, but with increasing speeds from ~

08:00 to 17:00 h for most the examined sites, which is most apparent in summer (Lapworth, 2011). Although no wind speed data was recorded at the East Cliff during this study, it is hypothesized here that this process may alter the diurnal patterns of wind speeds nearby the cliff, affecting the air and surface temperatures.

While it has been acknowledged that the mechanical influence of wind speeds in triggering rockfalls is currently poorly constrained (Pai et al., 2019), there are some tentative indications of wind speed controls on small sized rockfalls after earthquakes (Pai et al., 2019). Using laboratory simulations, these authors show that maximum wind speeds detected around afternoon (7 – 20 m/s, but including topographic effects inducing extreme wind speeds of 40 m/s), can affect unstable and highly fractured rock bocks (0.05 - 0.1 m of mean length), inducing sliding and toppling. These authors show that disturbed bed rock after earthquakes can be the principal source of material for wind-induced rockfalls as a result of dynamic microcrack propagation, suggesting that the highest wind speed around afternoon can produce failures as a secondary triggering process. Therefore, although for the East Cliff of Whitby, and more widely across the North Yorkshire cliffs, weak and insignificant correlations have been reported between maximum wind speeds and rockfalls (e.g., R^2 = 0.01 – 0.25, see Williams, 2017; Rosser et al., 2007), it cannot be ruled out that the observed diurnal thermal control on rockfall occurrence can, under certain climatic-oceanic-land interactions as demonstrated by Lapworth (2011), be directly or indirectly assisted by diurnal high wind speeds.

It has been noted that the freezing temperatures can be lowered in presence of clay or salt by delaying the beginning or completeness of freezing (McGreevy, 1982; Prick, 2004), whereby in a coastal setting the freezing point due to salt may be <0°C. Nevertheless, it has also been shown that rocks can be weathered more quickly when they are exposed to freezing temperatures after immersion in salt solution (see Williams and Robinson, 1991). Hence, the need to study the weathering control of combined salts has been recently noted (Williams and Robinson, 2001). At East Cliff, salt may spray during the combination of high tides and storm waves, which in turn may contribute to constrain or enhance, the effectiveness of either frost weathering at night or freeze-thaw at sunrise. This is identifying, perhaps, a secondary role of salt in changing the freeze response of the cliff face, rather than the conventional view of salt driving crystal growth (e.g., Steiger, 2005a, 2005b; Genkinger and Putnis. 2007; Ruiz-Agudo et al., 2012), and subsequent rock deterioration (Oguchi and Yu, 2021). However, it is likely that secondary effects due the presence of salt, such us the reduction of freezing temperatures or the acceleration of freezing effects, if in operation, will not be uniform across the cliff face, and may be more significant across the base of the cliff as spray does not reach across the full ~ 70 m height of the cliff (Discounted of the analysis, see *Chapter 1*).

Whilst it is acknowledged that salt weathering can cause substantial deterioration of natural rocks in a wide range of environments (Evans, 1970; Mottershead, 1989; Cardell et al., 2013; Goudie and Viles, 2011; Oguchi and Yu, 2021), an important factor controlling the efficiency of salt weathering is the presence of moisture and its movement (Oguchi and Yu, 2021). This is because moisture can either be a source of salt or transport and deposit salt inside cracks and pores (Oguchi and Yu, 2021). At East Cliff, high surface temperatures can occur in the warmer seasons (see Figure 6.3) and very high rates of change of temperature that induce quick surface heating (see Figure 6.4). These behaviours could have a control on salt weathering of the cliff through a process that generates upward or outward movement of moisture, which is known as 'evaporite pumping'. This process is the result of high surface temperatures, such as the observed at the study site at noon, which induce a rise of ground moisture by the capillary forces, leading to progressive, slow impregnation of salt crystals (Al-Hurban, 2006; Lugli, 2009; Oguchi and Yu, 2021). Nevertheless, it is important to note here that for East Cliff, no gradients in rockfalls maps directly onto the likely salt spray distribution (Agar, 1960; Rosser et al., 2005; Miller, 2007; Williams, 2017), nor have typical features associated with salt weathering have been identified (such as alveoles and honeycombs, tafoni, or typical microscopic patterns associated with salt weathering, see for example Oguchi and Yu, 2021). Therefore, in spite of the coastal context, this suggests that it is unlikely that salt weathering effects constitute a direct important control over the rockfall occurrence and erosion across the study site.

In terms of moisture, principal sources of moisture across slope surfaces are precipitation, fog, dew and groundwater (Ogushi and Yu, 2021), with fog and dew being an important source of moisture across coastal settings (Rundel et al., 1991). Currently, it is acknowledged that the presence of moisture, and particularly, changes in the moisture content can substantially decrease the strength of some rocks and induce weathering (Ojo and Brook, 1990; Matsukura and Takahashi, 2000; Saas, 2005; Owen et al., 2011; Wong et al., 2016), and that its distribution within the porous rock defines the zones where rock weakening occurs (Snethlage and Wendler 1997; Ogushi and Yu, 2021). It has been shown that this zones relate with the areas of maximum content of moisture (Snethlage and Wendler 1997). Moreover, it has been shown that the combination of moisture and temperature can induce subcritical cracking as both can generate chemical reactions across weak molecular bonds, increasing the speed of cracking growth (Eppes and Keanini., 2017). The abundant availability of moisture (mean relative humidity through the year of ~ 73 to 88%, see Section 1.4.1, *Chapter 1*), particularly supplied by dew and/or coastal fog that affects the cliff surface at sunrise and sunset (dew point reached between 07:00-08:00 h, and again between 15:00 and 21:00 h in the warmer seasons, see Figure 5.13, *Chapter 5*), produce an ideal setting to enhance subcritical cracking growth accompanied by the observed high rates

of change of temperatures. As the largest instantaneous summer rockfall of 75 ± 19 m^3 was observed during sunrise and when moisture provided by fog was present (without rainfall recorded 31 hours before the event and absence of waves reaching the cliff toe), it is hypothesized that the higher rates of change of temperature and moisture are key mechanisms leading rockfall activity at sunrise and sunset. While moisture controls were not the scope of this thesis, this is certainly a critical area for research.

In summary, in this section it has been demonstrate that, regardless of the season, the rockfall activity consistently responds to surface temperature, and so to a degree mirrors the daily cliff surface thermal cycle. Therefore, the results presented adhere to widely reported thermomechanical research on the expansion and contraction of discontinuities responding to temperature fluctuations controlled by seasonal and daily thermal cycles (e.g., Gunzburger et al., 2005; Vlcko et al., 2009; Bakun-Mazor et al., 2013; Collins and Stock, 2016; Greif et al., 2017; Collins et al., 2018; Guerin et al., 2020), and the potential impact of these mechanisms when the stress state across discontinuities is near to their strength limit, may facilitate irreversible deformation and failure (Gischig et al., 2011a; Marmoni et al., 2020; Fiorucci et al., 2020).

6.4 Are cliff temperature conditions at the time of rockfall different?

In this section, I investigate if the surface thermal conditions at the time of rockfall are clearly different to those during times with no rockfall. This is undertaken to assess if: (1) there are statistically significant differences in the thermal conditions of the rock face when there are versus when there are not rockfalls, and if so, (2) is it the absolute cliff temperature, or the rate of change of temperature, that drives rockfalls? As such, this analysis provides insights into the thermal conditions needed to drive rockfalls. It is important to note here that the dataset presented in this section exclusively involves hourly change detections and hourly thermal imagery/data, including a total of 2,773 monitored hours, which represents ~ 31.7% of the dataset obtained during concurrent TLS and IRT monitoring (see Table 6.3, Section 6.3).

This section begins with an analysis of statistically significant differences in the absolute temperatures at a seasonal scale of observations. This is followed by a more detailed assessment at the diurnal scale of observations. This analysis was then repeated for the rates of change in temperatures. The complete tables with the results of the tests undertaken are provided in the *Appendices* of this thesis (*Appendix A*). Consequently, here are only presented the results of those tests that showed statistically significant differences ($p < 0.05$) or those which were close to be significant at $p = 0.05$.

6.4.1 Absolute surface temperatures

To choose the appropriate tests needed to determine if there are statistically significant differences between the rockfall and non-rockfall periods, a Shapiro-Wilk test was conducted first to examine if the temperature dataset displays a normal distribution. The outcomes of this test were used to choose if a parametric (e.g., *Student's T-tests*) or non-parametric (e.g., *Mann-Whitney test*) test is more appropriate to compare the two groups. The Shapiro-Wilk test (Table 6.5) showed that the absolute temperatures of the cliff were not normally distributed, with 95% confidence interval ($p = 0.00001$). Thus, the non-parametric *Mann-Whitney* test was used which does not make assumptions on the underlying distribution of the dataset, and compares the medians between the two periods.

Table 6. 5: *Results of statistical tests to determine if the temperature datasets follow or not a normal distribution. Bold italicised p-values ($p < 0.05$) indicate that the dataset does not follow a normal distribution with a 95% Confidence Interval level.*

Temperature parameter 2021 (°C)	Shapiro-Wilk test statistic	p-value
Mean temperature	0.959	***0.00001***
Minimum temperature	0.949	***0.00001***
Maximum temperature	0.981	***0.00001***

At the seasonal level of analysis, only the winter cliff temperatures showed statistically significant differences when rockfalls occurred, with only 3 of 12 tests returning relatively robust differences (Table 6.6). The corresponding box and whiskers plots (Figure 6.7) illustrate three general observations:

(1) By comparing the median between the two groups of temperature conditions (Figure 6.7), it can be seen that in winter, the mean, maximum and minimum temperatures of the cliff were, overall, statistically significantly colder when rockfalls occurred and so, warmer temperatures were observed during the absence of rockfalls. For example, the median of the mean surface temperatures was below 0°C (-0.5C°) when rockfalls occurred, while it was above 0°C (1°C) during absence of rockfalls. Similarly, the median of the minimum temperatures was -3°C when rockfall took place, while this values was -2°C in absence of failure. Thus, these data demonstrates that freezing temperatures, as discussed in *Section 6.3*, play a key role on controlling winter rockfall;

(2) In spring and summer, the mean, minimum and maximum cliff temperatures were slightly higher when rockfalls occurred, suggesting that overall, the rockfalls were driven by warmer

temperatures during the warmer seasons. However, using all the seasonal temperatures, these differences were not statistically significant;

(3) In autumn, the cliff temperatures were overall warmer when rockfalls occurred, and the range of the temperatures was much wider when compared with those characterizing the thermal conditions during absence of failures. However, again, using all the seasonal temperatures, these differences were not significantly different. This also illustrates the inherent transitional thermal character of this season when controlling rockfall activity.

Table 6. 6*: Results of non-parametric statistical tests to determine significant difference in the surface temperatures of the cliff face when there are and there are not rockfalls by season. Bold italicised p-values are significantly different (p < 0.05). Bold underlined p-values are close to being significant at p = 0.05.*

Season	Temperature parameter (°C)	Mann-Whitney test statistic	p-value	95% Confidence Interval	Difference in medians
Winter	**Mean temperature**	54653	**0.052**	-0.007 to 1.32	0.684
	Minimum temperature	54680	**0.051**	-1.82 to 1.18	0.589
	Maximum temperature	54958	***0.038***	0.03 to 1.19	0.619
Spring	Mean temperature	86684	0.710	-1.17 to 0.76	-0.175
	Minimum temperature	88109	0.992	-0.90 to 0.93	0.000
	Maximum temperature	85767	0.537	-1.56 to 0.79	-0.380
Summer	Mean temperature	137379	0.195	-0.65 to 0.15	-0.258
	Minimum temperature	134639	0.070	-0.71 to 0.02	-0.329
	Maximum temperature	137338	0.193	-0.99 to 0.21	-0.400
Autumn	Mean temperature	33948	0.195	-0.40 to 1.84	0.775
	Minimum temperature	33629	0.269	-0.48 to 1.77	0.629
	Maximum temperature	34377	0.121	-0.24 to 1.88	0.800

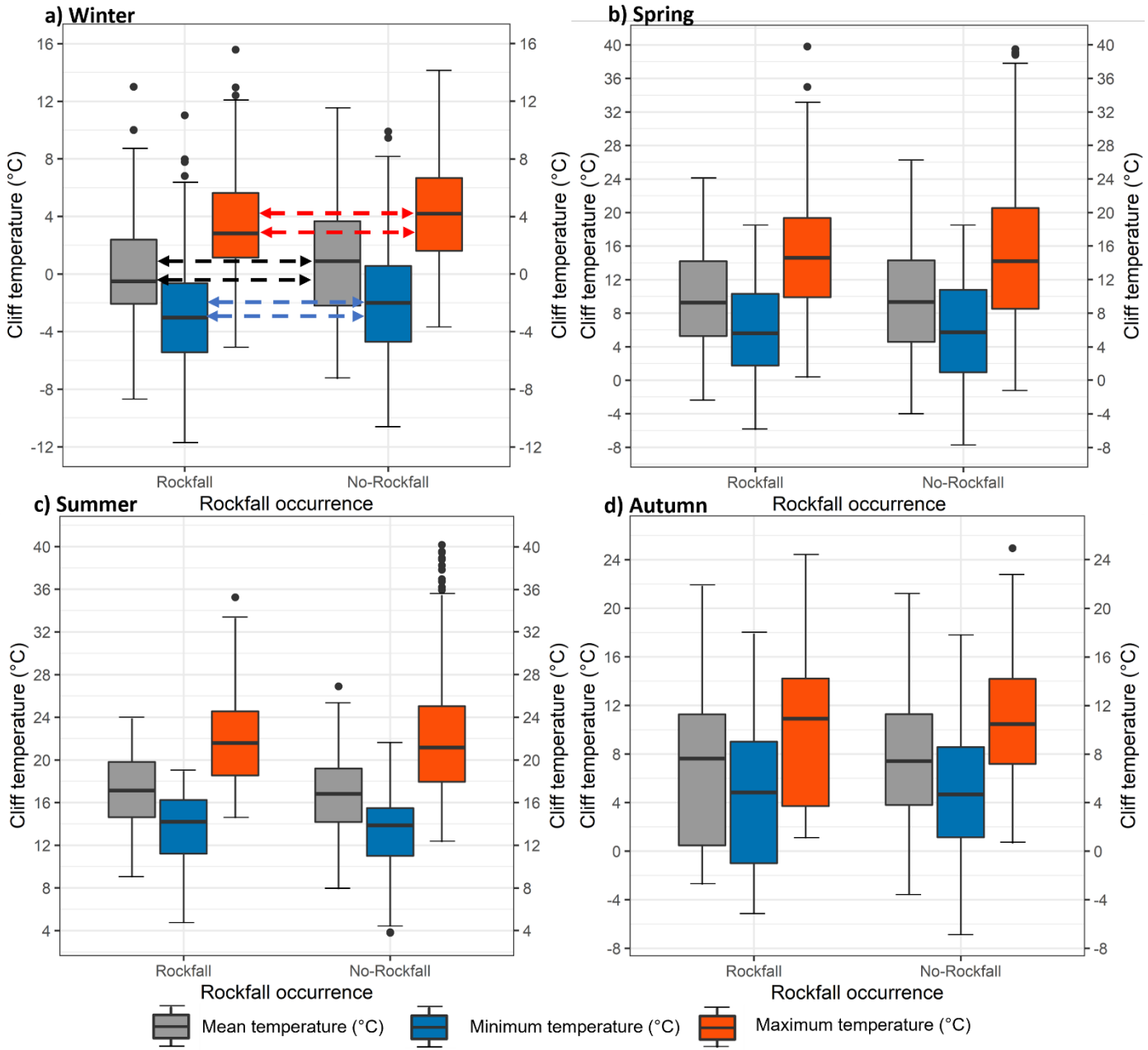
a) Winter
b) Spring
c) Summer
d) Autumn
Cliff temperature (°C)
Rockfall
No-Rockfall
Rockfall occurrence
Mean temperature (°C)
Minimum temperature (°C)
Maximum temperature (°C)

Figure 6. 7*: Overleaf. Comparison of the variations in the surface temperatures of the cliff face when there are and there are not rockfalls at seasonal scale. Box and whiskers demonstrate the range of thermal conditions, where whiskers cover the full range of data and boxes show 25th, 50th and 75th percentiles. Black circles show outliers. Horizontal dashed lines with arrows at both ends highlight boxes with statistically significant differences (or close to being significant) in the thermal conditions when there are and there are not rockfalls according to the Mann-Whitney non-parametric statistical tests (see Table 6.6). Black, blue, and red horizontal dashed lines are used for the box representing the mean, minimum and maximum temperatures, respectively. Note that y-axis values do not match between seasons as the aim is to assess if there are significant differences in the thermal conditions when there are and there are not rockfalls within each season.*

A more detailed depiction of the thermal characteristics of the cliff when there were and were not rockfalls was achieved when diurnal data was considered, when 15 of 48 tests (see Table 1 in *Appendices*) showed statistically significant differences. For example, while at a seasonal scale there was no statistically significant differences in spring, summer and autumn, diurnal data illustrates that for all these seasons there were significant differences in the absolute temperatures when rockfalls occurred (Table 6.7 and Figure 6.8). Overall, this dataset illustrates four important observations:

(1) In winter, statistically significant differences in the mean, maximum and minimum cliff temperatures occurred only around midnight. The corresponding box and whisker plot (Fig. 6.8a) shows that the median and the 25th percentile of the mean temperatures is almost -2°C and -3.5°C (respectively) when rockfalls occur, equating to 2°C colder if compared with the same statistics that characterize the mean temperatures when no rockfall occur. The median and interquartile range of the minimum and maximum temperatures demonstrates that the cliff had a colder and more consistent temperature when rockfalls occurred. Therefore, the coldest temperatures that affected the cliff during the winter nights had a key role driving rockfalls, particularly between -2°C and -5.5°C.

(2) There was a common feature at sunset in spring, summer, and autumn, when the cliff face was statistically significantly colder when rockfalls occurred, and the range in temperatures was more restricted than during no rockfall periods (Figure 6.8b, d, f). For example, at the summer sunset, the median and 25th percentile of the mean temperatures were 16°C and 14°C when rockfalls occurred, while when no rockfalls took place, the same values where 17°C and 15°C, respectively (Δ = 1°C colder when rockfalls occurred). However, these differences were higher when comparing the median interquartile of the spring and autumn temperatures, when again the cliff face was subject to colder temperatures at the time of rockfalls (Δ = 2°C colder in spring

sunset, and Δ = 3.5°C colder in autumn sunset). This helps to explain why significant increases in rockfall frequencies (> 5%) in spring, summer and autumn correspond well with major reductions in cliff temperatures at the end of sunset, as the cliff surface cools and discontinuities contract (Figure 6.3, in *Section 6.3*).

(3) In summer, statistically significant differences in the maximum cliff temperature were detected at midnight, as the cliff face was subject to warmer temperatures when rockfalls occurred, and again when the temperature was more consistent (Figure 6.8c). For instance, the median temperature was near 22°C when rockfalls occurred, but 18.5°C with no rockfall (Δ = 3.5°C hotter to drive failure). When comparing the 25th percentiles, this difference was about 2.5°C. This shows that there is a thermal control on the rockfalls of midnight that varies by season in its effectiveness. This is because at winter midnight the rock face was significantly colder when rockfalls occurred, while at midnight in summer, the cliff face was warmer at the time of failure.

(4) Only the autumn sunrise showed a statistically significant difference in the absolute cliff temperatures when rockfall occurred (Figure 6.8e). Interestingly, similar to the sunset, the cliff face was experiencing significant colder temperatures when rockfalls occurred at autumn sunrise. For example, the median of the mean temperatures was -0.1°C when rockfalls did occur, but 7.5°C when no rockfall occurred (Δ = 7.6°C colder to drive rockfalls).

It is important to note here that despite that some of the above reported temperature differences are within the instrumental error of the thermal camera (± 2°C, see Chapter 4, Section 4.2.1), these dataset can be considered useful as the results show a general trend and constant patterns in which for example, at sunset of spring, summer and autumn, the cliff face was experiencing statistically significant colder temperatures when rockfalls occurs (i.e., rather than being random), which is also demonstrated later when examining the rates of change of temperature that characterizes these seasons, as the data shows again a level of consistency between the rates of changes that characterizes the sunrise and sunset when rockfalls occur (see Section 6.4.2). It is also important to note that for this coastal setting and based upon these dataset, extreme thermal differences were not necessary to trigger rockfalls of small size, so that the data suggest that the inherent thermal nature of the differences are withing the instrumental error used in this research, or even within 50% error if a thermal camera of higher accuracy (± 1°C) would be used.

Table 6. 7: *Summary of the non-parametric statistical tests to determine significant difference in the surface temperatures of the cliff face when there are and there are not rockfalls during key daily thermal phases of each season. Bold italicised p-values are significantly different (p < 0.05). Bold underlined p-values are close to being significant at p = 0.05. The complete table, which provides non-significant statistical differences, is provided in the Annexes (Table 1).*

Season	Thermal phase	Temperature parameter (°C)	Mann-Whitney test statistic	p-value	95% Confidence Interval	Difference in medians
Winter	Midnight	**Mean T.**	686	***0.0005***	1.22 to 3.32	2.62
		Minimum T.	636	***0.0060***	0.52 to 2.23	1.35
		Maximum T	702	***0.0002***	0.56 to 3.36	2.58
Spring	Sunset	**Mean T.**	1612	***0.0398***	0.11 to 4.85	2.44
		Minimum T.	1596	**0.0511**	-4.07 to 4.34	2.16
		Maximum T	1622	***0.0338***	0.32 to 7.77	3.67
Summer	Midnight	**Maximum T**	374	***0.0012***	-4.33 to -1.22	-2.29
	Sunset	**Mean T.**	4866	***0.0115***	0.25 to 1.96	1.16
		Minimum T.	4778	***0.0289***	0.05 to 1.89	0.93
Autumn	Sunrise	**Mean T.**	867	***0.0127***	0.36 to 7.68	4.59
		Minimum T.	851	***0.0211***	0.49 to 7.48	4.42
		Maximum T	887	***0.0066***	0.80 to 7.84	4.11
	Sunset	**Mean T.**	1283	***0.0217***	0.50 to 5.24	2.18
		Minimum T.	1285	***0.0210***	0.41 to 4.96	2.44
		Maximum T	1256	***0.0378***	0.28 to 5.10	1.96

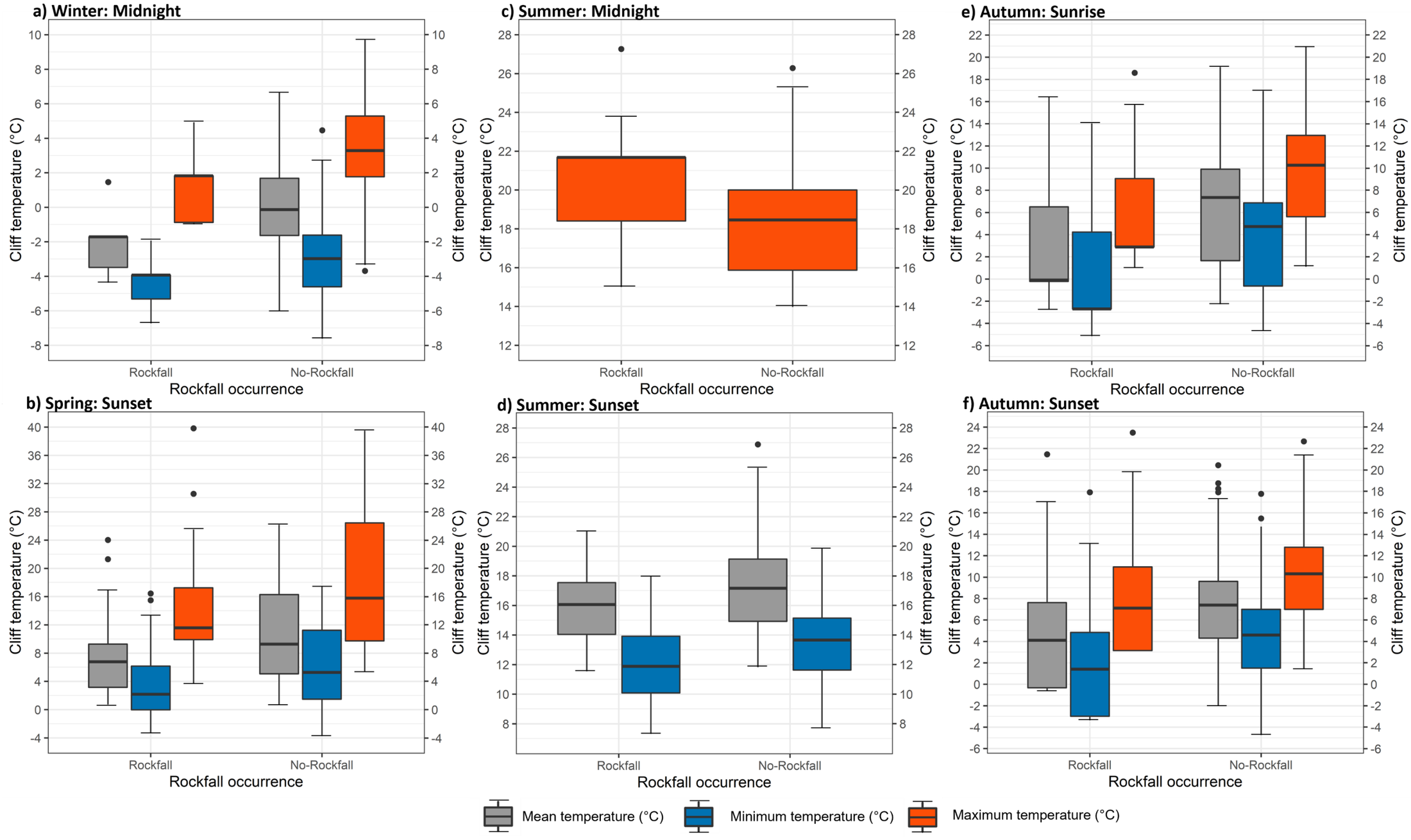

Figure 6. 8*: Box plots and whiskers of statistically significant differences (or close to being significant) in the surface temperatures of the cliff when there are and there are not rockfalls during key daily thermal phases of each season. Significant differences were determined using the Mann-Whitney non-parametric statistical tests (see Table 6.7). Box and whiskers demonstrate the range of thermal conditions, where whiskers cover the full range of data and boxes show 25th, 50^{h} and 75th percentiles. Black circles show outliers. Note that y-axis values do not match between individual figures as the aim is to show statistically significant differences in the thermal conditions when there are and there are not rockfalls within each daily thermal phase of each season, but not to stablish comparisons between seasons. Note that the figures corresponding to the same season are presented by column.*

6.4.2 Rates of change of surface temperatures

The temperature changes on the cliff face when there were and were not rockfalls is now considered. For analytical consistency, this was conducted first, at a seasonal level of observation, and then at a diurnal scale of observation, by extracting only those rates corresponding with the midnight, sunrise, noon, and sunset. A Shapiro-Wilk test was conducted first to confirm if the temperature dataset follows a normal distribution. As explained above, this step permitted to choose the appropriate statistical test to compare the two groups of temperature of interest. The results of the Shapiro-Wilk tests (Table 6.8) confirm, again, that the rates of change of temperatures were not normally distributed with 95% confidence interval ($p = 0.00001$). Thus, the non-parametric Mann-Whitney test was appropriate for this section of analysis.

Table 6. 8: *Results of statistical tests to determine if the rates of change of temperature data follow or not a normal distribution. Bold italicised p-values ($p < 0.05$) indicate that the dataset does not follow a normal distribution with a 95% Confidence Interval level.*

Temperature parameter 2021 (°C/h)	Shapiro-Wilk test statistic	p-value
Mean rate of change	0.931	***0.00001***
Minimum rate of change	0.850	***0.00001***
Maximum rate of change	0.741	***0.00001***

The analysis of the rates of change using all the seasonal data show that statistically significant differences when rockfalls occurred were observed in almost all seasons (in 5 out of 12 tests, see Table 6.9), suggesting key differences as compared to absolute cliff temperatures, whereby rates of change in temperature may be more important. Overall, this analysis shows two general observations:

First, in winter, the mean and maximum rates of change in temperature were statistically significantly different when failure took place. The comparison between the interquartile ranges indicates that the rates of change needed for rockfalls were, overall, slightly higher than the rates observed during periods with an absence of rockfalls (about 0.5°C/h higher by comparing the median and 75th percentile of the maximum rates of change). This demonstrates that, overall, faster rates of change were needed to induce thermal stresses controlling rockfalls in the coldest season (Figure 6.9a).

Second, in summer, only the minimum rates of change, indicative of the role of negative temperature changes per hour (i.e., cooling), showed statistically significant differences. The

mean of the box plots shows that the cliff face was subject to slightly lower rates of change when rockfalls occurred, however, when comparing the 25th percentile the cliff was, overall, subject to negative rates of change of a higher magnitude at the time of rockfall occurrence (-4.5°C/h versus -3.5°C/h during absence of rockfalls). A similar behaviour was detected in autumn, as the mean and minimum rates of change were statistically significantly different, but again, the cliff face was experiencing slightly lower rates when compared with the mean, but negative rates of change with a higher magnitude at the 25th percentile (Figures 6.9c and d). An important consequence is that it is not always the highest positive rates of change, indicating rapid surface heating, that were associated with the occurrence of rockfall activity. Importantly rapid surface cooling was also important in facilitating rockfalls. This is further explored next using the key daily thermal phases of observations.

Table 6. 9: *Results of non-parametric statistical tests to determine significant difference in the rates of change of temperatures when there are and there are not rockfalls by seasons. Bold italicised p-values are significantly different (p < 0.05). Bold underlined p-values are close to being significant at p = 0.05.*

Season	Temperature parameter (°C/h)	Mann-Whitney test statistic	p-value	95% Confidence Interval	Difference in medians
Winter	**Mean rate of change**	33520	***0.001***	-0.31 to -0.07	-0.189
	Minimum rate of change	43319	0.070	-0.01 to 0.31	0.150
	Maximum rate of change	27297	***0.000***	-0.62 to -0.34	-0.480
Spring	Mean rate of change	78227	0.361	-0.09 to 0.26	0.083
	Minimum rate of change	79273	0.219	-0.10 to 0.43	0.169
	Maximum rate of change	74983	0.947	-0.27 to 0.27	-0.009
Summer	Mean rate of change	106869	0.074	-0.01 to 0.25	0.115
	Minimum rate of change	107519	**0.051**	-1.30 to 0.41	0.199
	Maximum rate of change	102632	0.467	-0.12 to 0.27	0.070
Autumn	**Mean rate of change**	23429	**0.056**	-0.005 to 0.34	0.161
	Minimum rate of change	24162	***0.012***	-0.05 to 0.43	0.239
	Maximum rate of change	22961	0.125	-0.04 to 0.32	0.139

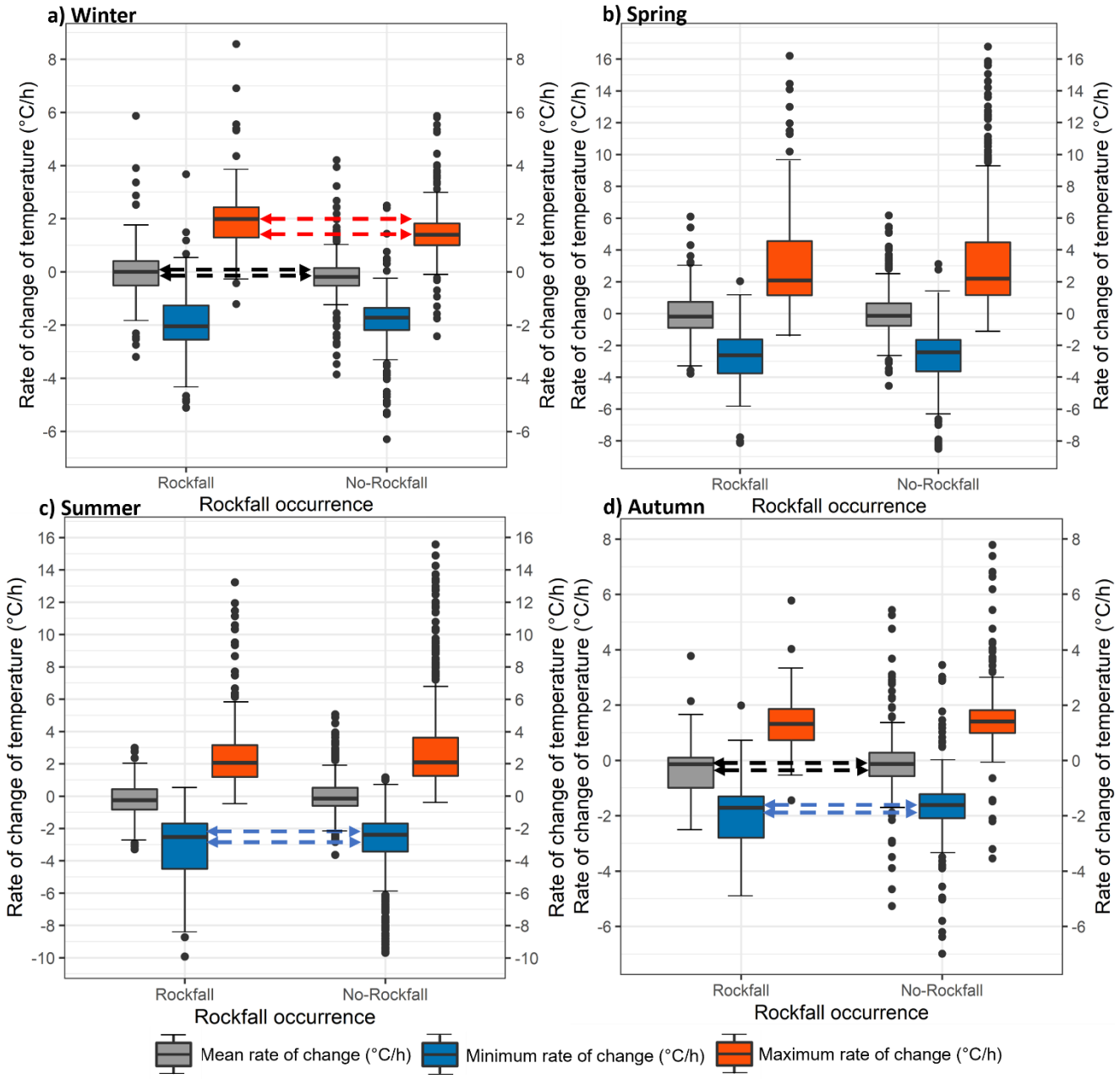
a) Winter
b) Spring
c) Summer
d) Autumn
Rate of change of temperature (°C/h)
Rockfall
No-Rockfall
Rockfall occurrence
Mean rate of change (°C/h)
Minimum rate of change (°C/h)
Maximum rate of change (°C/h)

Figure 6. 9*: Overleaf. Comparison of the variations in the rates of change of temperature of the cliff face when there are and there are not rockfalls at seasonal scales. Box and whiskers demonstrate the range of thermal conditions, where whiskers cover the full range of data and boxes show 25th, 50th and 75th percentiles. Black circles show outliers. Horizontal dashed lines with arrows at both ends highlight boxes with statistically significant differences (or close to being significant) in the thermal conditions when there are and there are not rockfalls according to the Mann-Whitney non-parametric statistical tests (see Table 6.9). Black, blue, and red horizontal dashed lines are used for the box representing the mean, minimum and maximum temperatures, respectively. Note that y-axis values do not match between seasons as the aim is to assess if there are significant differences in the thermal conditions when there are and there are not rockfalls within each season, but not to stablish comparisons between seasons.*

The analysis of the rates of change in temperature at four key points during the day in each season illustrates that there were many significant differences between when there were and were not rockfalls (20 of 48 tests, see Table 2 in *Appendices*) (Table 6.10 and Figure 6.10). Overall, this dataset illustrates six important observations:

(1) statistically significant differences were identified at most sunrise phases, with the only exemption being summer. Indeed, during winter and spring, the cliff face was subject to statistically significant higher positive rates of temperature change when rockfalls occurred, demonstrating that rapid hourly heating is important trigger. For instance, by comparing with the winter sunrise, the median of the mean and maximum rates was 0.4°C/h higher when rockfalls took place, and the interquartile ranges indicate that these rockfalls occurred under a notably more narrow range of surface temperatures. Furthermore, by comparing the interquartile ranges for the spring sunrise, the rock face was exposed to higher positive rates of change when rockfalls occurred (e.g., the median of the mean rates was 0.7°C/h higher at the time of failure), and similarly these rockfall occurred under highly variable temperature conditions, critically reaching 12°C/h (75th percentile) (Figures 6.10b,d).

(2) Three additional consequences can be identified: (i) that very high positive rates of temperature change implies the likely role of rapid discontinuity expansion and microcrack growth in rock detachment, especially considering the high thermal expansion coefficients that normally characterize sandstones, as discussed in *Section 6.3* (see Table 6.4)*;* (2) the lack of statistically significant differences in the absolute temperatures during sunrise (see Table 6.7, Section 6.4.1) indicates that the rate of temperature change per hour at sunrise has a role in driving rockfalls, over and above solely high absolute temperatures; and (3) only during the summer sunrise was there a lack of statistically significant difference in the rate of change in temperature when rockfalls occurred, despite the highest rockfall activity rates (~ 20%) occurred at this time

(see Figure 6.4 in *Section 6.4).* As such, this observation suggests that in summer the variability of rates of change in temperature were not sufficient to identify a difference when rockfall occurred. This implies the likely combined role of higher rates of change in temperature, and potentially other factors such as moisture in driving rockfalls during morning hours. I note again that largest rockfall event observed in 2021 (volume = 75 ± 19 m^3), occurred at this time when coastal fog and hence moisture was also present.

(3) During the sunset of winter, spring, and summer, the cliff face was exposed to either statistically significant higher rates of negative temperature change (cooling) when rockfalls occurred, or experienced a statistically significantly lower magnitude of positive rates of temperature change. The implications are twofold: (1) In winter, the mean and 25th percentile temperature was ~ -2.7°C/h and -3.3°C/h (respectively) when rockfalls occurred, while -1.9°C/h and -2.6°C/h during periods with an absence of rockfall. Similar patterns (below 0°C/h) were detected during the sunsets in the warmer seasons. This illustrates that negatives rates of temperature change of a higher magnitude, indicative of faster cooling per hour, were critical in controlling rockfalls at sunset. Conversely (2), during spring sunset, the mean of the maximum rates of temperature change was ~ 1.9°C/h when rockfalls occurred, but ~ 3.9°C/h with period of no rockfall. As such, the cliff was experiencing relatively lower positive rates of change (~ 2°C/h) when rockfalls occurred. This illustrates that whilst at sunset cooling was the dominant force driving rockfalls, when the cliff was exposed to changes greater than 0°C/h, larger positive rates of temperature change were not always needed to drive rockfalls. This suggests that across sunset rockfalls were more sensitive to lower magnitude positive rates of temperature change to drive failure.

(4) Statistically significant differences were observed between the rates of change during the midnight of winter. Overall, the cliff face was exposed to higher magnitude rates of temperature change when rockfalls occurred (Figure 6.10a). For example, the median of the mean rates of change was near 0.5°C/h when rockfalls took place, but ~ -0.1°C/h during the absence of failures (0.6C/h difference). This result supports the earlier observation that in the coldest hours around midnight, higher rates of change in temperature per hour were needed to drive rockfalls.

(5) Statistically significant differences were observed between the rates of change of at noon in warmer seasons (Figure 6.10e, g). However, while at midday in spring the cliff was exposed to negative rates of temperature change of a lower magnitude when rockfalls occurred, slightly higher positive rates were prevalent when rockfalls occurred in summer. In both cases, the interquartile ranges indicate that the cliff face was exposed to a lower range of temperature when rockfalls occurred, which may be associated to the fact that at these times, the cliff face was

in shadow, while the cliff face temperature was relatively homogenous and subject to the highest temperatures of the day, so the changes in temperature per hour where of a low magnitude (see Figures 6.3 and 6.4 in Section 6.3).

(6) In autumn, statistically significant differences in the mean, minimum and maximum rates of change were observed only at sunrise and sunset. At sunrise, the cliff face was exposed to lower rates of temperature change when rockfalls occurred, but there was a higher variability in the range of temperature. Conversely, at sunset, the rates of change were higher and less variable across the cliff when rockfalls occurred (Figure 6.10i, j). As such, these two patterns differ to those that characterize rockfall occurrence during sunrise and sunset in winter, spring, and summer, as here an inversion in the thermal conditions favouring rockfall is observed (e.g., higher rates in the sunrise of winter and spring when rockfalls took place, but notably lower rates in the sunrise of autumn, and lower rates in the sunset of winter and spring when rockfalls occurred, but higher in the sunset of autumn). While this behaviour may be associated with the inherent transitional character of the temperatures of autumn - from summer to winter - this also supports the previous observation of a seasonal variability in the thermal response at key times during the day. This was also observed when comparing rockfalls that occurred at midnight in winter compared to summer (see Figures 6.7a, c). As a result, it cannot be assumed that the same response will be observed at the same time of day throughout the year.

In summary, this section has provided new insights into the influence of the rates of change in temperature on rockfall activity by both season, and at key times of day. The dataset has provided robust evidence that indicates that the thermal conditions across the surface of the cliff at times differed when rockfall occurred as compared to when they did not. Therefore, the analysis of the dataset provides two main findings: First, in most of the cases, particularly, at sunrise in most seasons, higher positive rates of surface temperature change (fast heating) were coincident with rockfall. This implies that at these times relatively higher rates of temperature change were needed to induce proportional thermal stresses to drive rockfalls; Second, and conversely to the dynamic observed at sunrise, at sunset in most of the seasons, rockfalls occurred under higher magnitude negative rates of change (fast cooling), which were significantly different in absence of rockfall.

***Table 6. 10**: Summary of the non-parametric statistical tests to determine significant difference in the rates of change (RCH) of temperatures of the cliff face when there are and there are not rockfalls during key daily thermal phases of each season. Bold italicised p-values are significantly different ($p < 0.05$). Bold underlined p-values are close to being significant at $p = 0.05$. The complete table, which provides non-significant statistical differences, is provided in the Annexes (Table 2).*

Season	Thermal phase	Temperature parameter (°C/h)	Mann-Whitney test statistic	p-value	95% Confidence Interval	Diff. in medians
Winter	Midnight	**Mean RCH**	70	***0.0001***	-0.77 to -0.39	-0.59
		Minimum RCH	87	***0.0001***	-0.95 to -0.54	-0.76
		Maximum RCH	108	***0.0001***	-0.76 to -0.44	-0.56
	Sunrise	**Mean RCH**	1205	***0.0387***	-0.58 to -0.04	-0.28
		Maximum RCH	1128	***0.0119***	-1.05 to -0.14	-0.66
	Sunset	**Minimum RCH**	3244	***0.0008***	0.21 to 0.84	0.48
Spring	Sunrise	**Mean RCH**	498	***0.0256***	-1.65 to -0.08	-0.73
		Maximum RCH	519	***0.0416***	-5.02 to -0.04	-1.03
	Noon	**Minimum RCH**	597	***0.0067***	-1.80 to -0.22	-0.97
	Sunset	**Mean RCH**	1475	***0.0352***	0.03 to 1.06	0.58
		Maximum RCH	1456	***0.0487***	9.07 to 0.01	1.18
Summer	Noon	**Mean RCH**	992	**0.0587**	-0.54 to 0.07	-0.25
	Sunset	**Mean RCH**	4253	***0.0005***	0.31 to 1.08	0.68
		Maximum RCH	4305	***0.0002***	0.46 to 1.49	0.94
Autumn	Sunrise	**Mean RCH**	659	***0.0005***	0.97 to 1.86	1.51
		Minimum RCH	658	***0.0006***	0.67 to 2.02	1.47
		Maximum RCH	676	***0.0002***	0.98 to 1.85	1.50
	Sunset	**Mean RCH**	372	***0.0002***	-0.85 to -0.25	-0.57
		Minimum RCH	402	***0.0006***	-0.81 to 0.17	-0.51
		Maximum RCH	373	***0.0002***	-0.89 to -0.28	-0.55

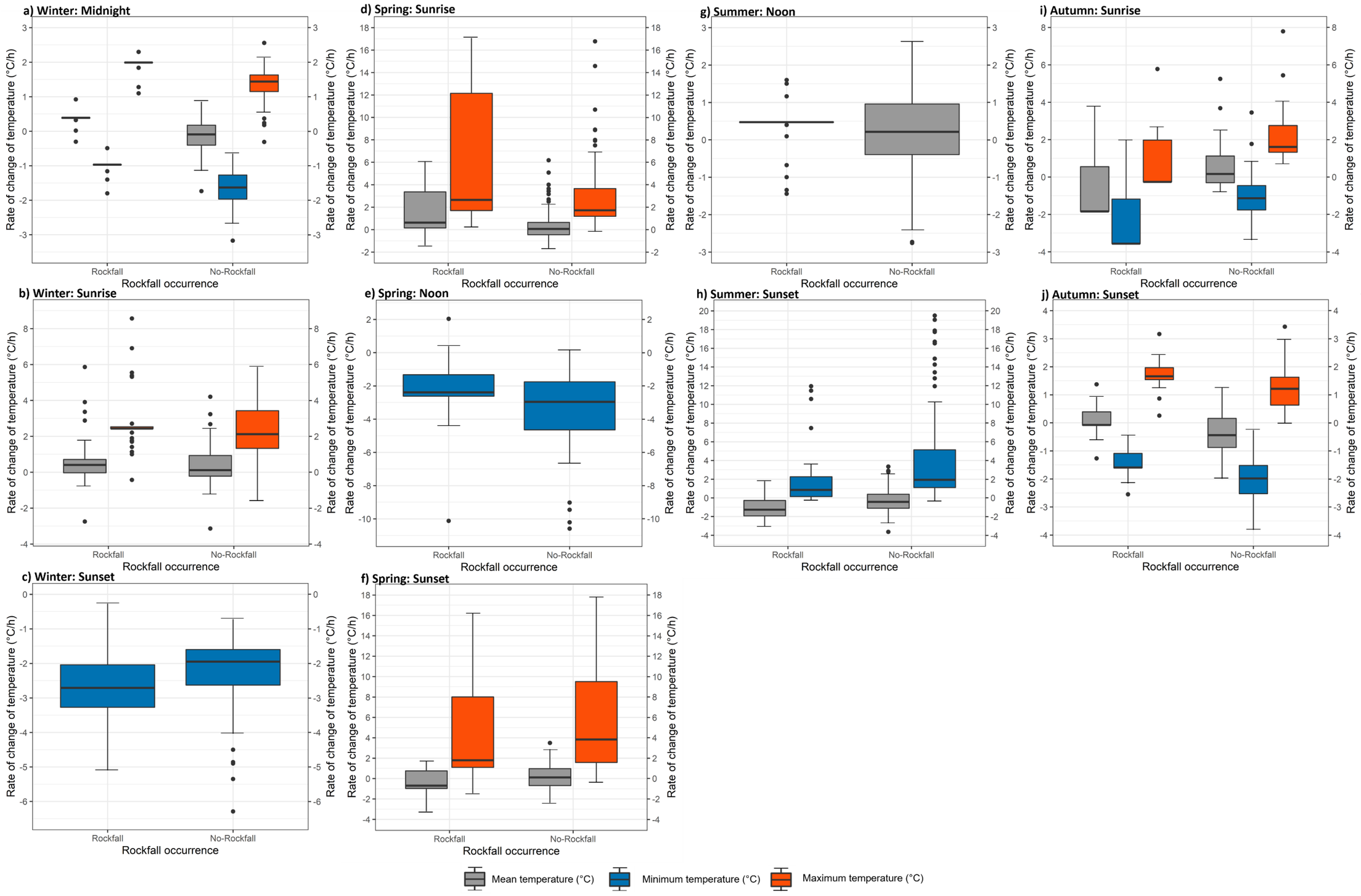
a) Winter: Midnight
b) Winter: Sunrise
c) Winter: Sunset
d) Spring: Sunrise
e) Spring: Noon
f) Spring: Sunset
g) Summer: Noon
h) Summer: Sunset
i) Autumn: Sunrise
j) Autumn: Sunset
Rate of change of temperature (°C/h)
Rockfall
No-Rockfall
Rockfall occurrence
Mean temperature (°C)
Minimum temperature (°C)
Maximum temperature (°C)

Figure 6. 10: *Overleaf. Box plots and whiskers of statistically significant differences (or close to being significant) in the rates of change of temperatures of the cliff when there are and there are not rockfalls during key daily thermal phases of each season. Significant differences were determined using the Mann-Whitney non-parametric statistical tests (see Table 6.10). Box and whiskers demonstrate the range of thermal conditions, where whiskers cover the full range of data and boxes show 25th, 50th and 75th percentiles. Black circles show outliers. Note that y-axis values do not match between individual figures as the aim is to show statistically significant differences in the thermal conditions when there are and there are not rockfalls within each daily thermal phase of each season, but not to stablish comparisons between seasons. Also, note that the figures corresponding to the same season are presented by column.*

6.5 The relative role of inclement-weather and temperature induced rockfall activity

6.5.1 Time-series analysis of rockfall activity and erosion

While doubts have been previous raised about the effectiveness of thermal stresses in driving rockfall (Yatsu, 1998; Goudie, 1989; Cooke et al., 1993; Smith, 1994), considerable field-monitoring evidence exploring microcrack growth and discontinuity flexure in response to temperature is available (e.g., Gunzburger et al., 2005; Eppes et al., 2010; Gischig et al., 2011a,b; Collins and Stock, 2016; Eppes and Keanini., 2017; Marmoni et al., 2020; among others). While this thesis has provided robust evidence of the existence of temperature control on seasonal rockfall activity (see *Sections 6.3* and *6.4*), to date the degree to which temperature controls on rockfalls as compared to other processes remains poorly understood. Importantly, it remains necessary to consider cliff rockfall conditions: (1) dominated by dry environmental conditions, when temperature induced rockfall activity take place; and those (2) dominated by inclement-weather, when rockfalls are driven by storms.

By taking advantage of the one year dataset generated here, in this section I consider the relative erosive role of temperature-induced rockfall versus those associated with inclement-weather. I examine the cumulative erosional signature of inclement-weather and temperature controlled erosion to obtain an estimation of total erosion supplied when the cliff is subject to these two contrasting process regimes. Importantly, these results hold potential implications under a changing climate where both temperatures are expected to increase, but also the frequency and magnitude of storms may change. The implications for rockfall and cliff erosion are considered within the context of three possible climate change scenarios.

Figure 6.11 shows the time-series of the 4D rockfall activity in 2021, showing data binned to 1-day intervals. This figure highlights the principal erosive episodes with high rockfall losses, referred to here as erosional episodes 1 to 13, as defined in *Chapter 3* as periods of abrupt volume loss. Rockfall volumes that occurred during gaps in the data (i.e., non-hourly change detections, see *Section 6.2*, Figure 6.2) are indicated by the letter "*g*" (indicating change detections measured across "gaps"). In this figure, blue vertical bars highlight erosional episodes that were coincident with rainfall, or that occurred within one day after precipitation, whereby the assumption is some form of causation. Large rockfalls ($\geq$ 1.0 m^3) that occurred during dry conditions with an absence of precipitation are highlighted using yellow vertical bars.

Ten out of 13 erosional episodes coincided with moderate to heavy rainfall, where the daily rainfall was between 4.7 mm to 390 mm. This implies that inclement-weather controlled the majority of the larger rockfalls in 2021, including episodes, 1, 2, 3, 4, 5, 6, 8, 10, 11, and 13. The volume of these erosional episodes varied between 2.6 $\pm$ 1.9 m^3 (Episode 13, detected in December) to 102 $\pm$ 34 m^3 (Episode 5, detected in February). Only three erosional episodes occurred during apparently dry conditions, of which the Episode 7 (detected in February, totalling 18 $\pm$ 7 m^3) and Episode 12 (detected in December, totalling 4.0 $\pm$ 1.3 m^3) were measured across only small gaps in the data (up to 18 hours, during which no rainfall was recorded). Episode 9 was identified using hourly change detection at the end of the summer (14th of September, between 06:00 and 07:00 h), and was an episode dominated by a large single rockfall (main event = 75 $\pm$ 19 m^3, totalling 88.4 $\pm$ 25 m^3 with coincident proximal detachments). As noted in Section 6.3.2, this event occurred at sunrise, and was coincident with local coastal fog and had a notable absence of precipitation in the 31 hours beforehand. This event was however coincident with relatively high magnitude rates of change in temperature in the morning (mean, highest positive and negative rates of temperature change of -0.01°C/h, 0.76°C/h, -1.35°C/h, respectively). There is potential that this event may reflect some accumulation of longer-term damage to the rock mass (see: Rosser et al., 2007), whereby final failure was facilitated by a relatively small magnitude combined action of the temperature change and moisture, likely facilitating subcritical cracking (Eppes and Keanini, 2017).

Figure 6.11 also illustrates that a total of 5 periods of iterative erosion were detected through 2021(Periods *I* to *V*), dominated by small (0.001 – 0.01 m^3) and some medium rockfalls (0.01 – 0.1 m^3). These periods were interspersed by a larger episode which tended to be clustered in the first half of February. At least qualitatively the largest erosional episodes appear to be following by the longer periods of quiescence in rockfall activity (e.g., Period *III*, covering total of six and a half months).

This time-serie can also be used to highlight the fact that temperature-controlled rockfall activity (*Section 6.3*, Figures 6.3 and 6.4, that induced notably increments in the rockfall frequencies (>5%) across the midnight of winter, and sunrise, noon, and sunset of the four seasons), dominates erosion during the periods of iterative mass wasting, demonstrating that temperature-induced rockfalls had a role in contributing to the background erosion to the cliff, such as for example between the periods *I* to *V*. Even small changes to the cliff surface temperature associated with climate change, may therefore increase the rate of iterative background weather, and change the timing and duration of periods of time during which these processes dominate. This is further discussed in Section 6.5.2.

In order to quantify and assess the relative role of rockfalls associated with inclement-weather and temperature in driving overall mass wasting from the cliff in the context of future changes (Table 6.11), the identification of rockfall volumes was based on two basic sets of observations from my earlier analysis:

1. That the thermally induced rockfall activity was likely to be dominant during the midnight of winter, and sunrise, noon, and sunset phases of each season during dry environmental conditions, when no other evident trigger appears dominant. This is because increased rates of rockfall were coincident with either extremely cold cliff temperatures at winter midnight, or very high rates of temperature change (either positive or negative) during sunrise and sunset, or the warmer temperatures around noon, as demonstrated in *Sections 6.3* and *6.4*.

2. Rockfalls induced by inclement weather were those coincident with hourly and/or precedent precipitation, and therefore final failure was likely facilitated by either swelling of minerals or incremental increases in pore water pressure, and the associated reductions in frictional strength and shifts in stresses in the cliff.

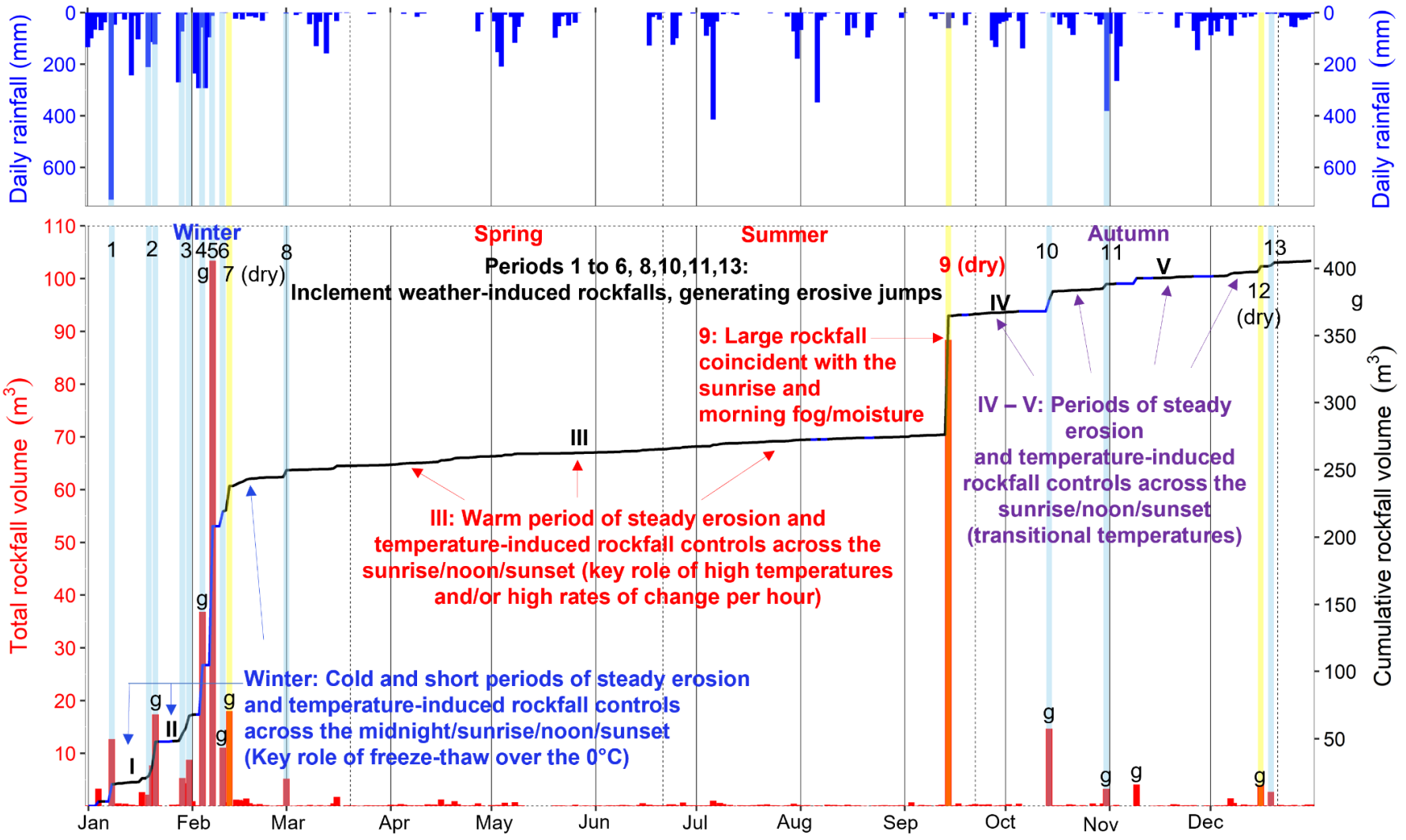
Daily rainfall (mm)
Daily rainfall (mm)
Total rockfall volume (m3)
Cumulative rockfall volume (m3)
Winter
Spring
Summer
Autumn
Periods 1 to 6, 8,10,11,13:
Inclement weather-induced rockfalls, generating erosive jumps
9: Large rockfall coincident with the sunrise and morning fog/moisture
III: Warm period of steady erosion and temperature-induced rockfall controls across the sunrise/noon/sunset (key role of high temperatures and/or high rates of change per hour)
IV – V: Periods of steady erosion and temperature-induced rockfall controls across the sunrise/noon/sunset (transitional temperatures)
Winter: Cold and short periods of steady erosion and temperature-induced rockfall controls across the midnight/sunrise/noon/sunset (Key role of freeze-thaw over the 0°C)
7 (dry)
9 (dry)
12 (dry)
Jan
Feb
Mar
Apr
May
Jun
Jul
Aug
Sep
Oct
Nov
Dec

Figure 6. 11: *Long-term erosive contribution of inclement-weather and temperature-induced rockfall activity detected between 1st January and December 31st, 2021. From the top to the bottom, single large rockfall events (≥ 1.0m³) that corresponded with hourly rainfall or up to two days of precedent rainfall are shown as vertical blue bars and numbered according to occurrence of the rockfall event from 1 to 17. Blue bars show the role of inclement weather inducing large rockfall events. From the top to the bottom, yellow vertical bars indicate the occurrence of large rockfall events (≥ 1.0m³) that were detected during dry environmental conditions (i.e., no hourly rainfall was recorded during/before failure and/or clear hourly thermal scenes were detected, which were indicative of the local absence of rainfall affecting the cliff face). Periods of steady or gradual erosion are shown using Roman letters from I to V. "g" letters indicate total rockfall volumes that were estimated across periods of gap of laser scanner data (i.e., non-hourly sequential change detections). Note that "g" letters are placed at the top or next to the corresponding columns representing the total rockfall volume estimated across gaps. For an easier representation of the patterns, hourly rockall volumes were binned by day (24 h). The boundaries between the astronomical seasons are indicated using dashed vertical lines.*

Table 6.11 shows that rockfall activity driven by inclement weather produced around 60% of the total number of rockfalls and supplied ~ 68% of the total eroded volume (~ 277 ± 81 m$^{3)}$. This is not surprising given the recognition of rainfall as a key preparatory and/or triggering factor (e.g., Gunzburger et al., 2005; Rosser et al., 2007; Guzzetti et al., 2007; 2008; Pradham et al., 2022; among others), despite this process for rockfall at least rarely being directly observed at the slope scale. Temperature-induced rockfalls were estimated to contribute with approximately ~ 17% of the total number of rockfalls and notably supplied ~ 27% of the total eroded volume (~ 109 ± 37 m^3) in 2021. Significantly, the total volume loss during periods of steady erosion was ~ 48.2 m^3, of which ~ 20.6 m^3 was estimated to be temperature-controlled (~ 42.7%), suggesting that an important proportion of iterative mass wasting during apparently stable conditions was supplied by thermally-induced rockfalls of a small and medium size. This demonstrates that temperature alongside precipitation and surface moisture that occurs around sunrise and sunset may provide a significant control on driving rockfall and coastal cliff erosion.

Previous research at this site has shown a negligible control on marine conditions on the behaviour and occurrence of rockfalls from the cliff face (e.g., Rosser et al., 2007; Williams, 2017). It was estimated here that 'other' controls (non-thermal and non-inclement weather) were associated with the timing of ~ 23% of the total number of rockfalls, but only contributed ~ 5% of the total volume measured in 2021. So, whilst by number they may be more frequent that temperature controlled rockfalls, their erosion contribution is significantly less (Table 6.11).

Table 6. 11: Relative role of inclement-weather and temperature-induced rockfall activity in 2021.

	Environmental controls and relative contribution to the erosion			
Erosive metric	**Inclement weather/ (%)**	**Temperature-controlled / (%)**	**Other controls / (%)**	**Total 2021 (100%)**
Detected number of rockfalls	2,456 (60%)	725 (17%)	924 (23%)	4,105 (100%)
Minimum rockall volume (m^3)	0.002	0.002	0.002	-
Average rockfall volume (m^3)	0.12	0.15	0.02	-
Median rockfall volume (m^3)	0.008	0.007	0.006	-
Largest single rockfall (m^3)	46 ± 12	75 ± 19	0.76 ± 0.2	122 ± 31
Rockfall density	0.09	0.02	0.008	0.12
Total eroded volume (m^3)	277 ± 81 (68%)	109 ± 37 (27%)	20 ± 17 (5%)	406 ± 159 (100%)
Cliff face annual retreat (m)	0.05	0.02	0.004	0.074

Note: monitored cliff face area = ~ 5,459 m^2. The quantification of temperature-induced rockfalls were estimated from those events that occurred within the sunrise/noon/sunset phases, in which the higher daily temperatures (associated with the higher rates of change) and significant increments in the seasonal rockfall frequency (≥ 5%) were both coincident in time (see Figure 6.4, Section 6.3).

Given the cliff setting, other controls not investigated here may also be associated with rockfall occurrence (see Table 6.12), such as the combined effect of storminess and microseismic ground displacements affecting the rock mass (Adams et al., 2002; 2005; Rosser et al., 2007; Brain et al., 2014). Indeed, the fact that environmental controls do not operate in isolation, and are rather a part of a range of complex interacting processes contributing to subcritical crack growth and rock weakening, has also been suggested (Brain et al., 2014). As a consequence, it is important to note here that the results shown in Table 6.11 provide an assessment of the role of thermal effects, both directly but also with temperature as a proxy for other erosive processes. Future research should ideally try to unpick this wider spectrum of processes to assess their relative efficacy (some processes are briefly proposed in Table 12, although it is not the scope of this section to discuss each of these), but what is clear from this research is the sensitivity of the cliff face to even small magnitude variations in temperature, and the therefore wider sensitivity of the cliff rockfall to forcing. The value of near-constant monitoring has been shown in this investigation, and it is only with this temporal resolution of data that the distinction between preparatory and triggering factors can be identified (Brain et al., 2014).

Table 6. 12: Summary of other likely processes generating rockfalls at the study site.

Process	Likely influence on rockfalls	Example from literature
Wace action	Wave inundation and impact at the cliff base	Rosser et al. (2007); Lim et al., (2011); Norman et al., (2013).
Microseismicity	Microseismic ground displacements via cyclic loading and rock damage	Brain et al. (2014); Vann Jones et al., (2015); Benjamin (2017).
Salt-weathering	Cristal growth pressures and rock damage	Johannsen et al., (1982); Lawrence et al., (2013).
Wind	Diurnal peak wind force and angles of attack	Pai et al., (2019).
Wetting and drying	Cyclic hydration and dehydration can induce rock expansion and contraction and fracturing	Diop et al., (2008); Bierman and Montgomery (2014); Yang et al., (2019).
Seepage	Ground water flow inducing pore water pressures and shear strength reduction	Hoek and Bray (1981); Frayssines and Hantz (2006); Contino et al., (2017)
Clay swelling in joint rock	Strongly hydrating cations that force crystal layers apart (if swelling clays present within BS or IBSS)	Hoek and Bray (1981); Bleam (2012); D'Amato et al., (2016).
Moisture	Changes in moisture content can cause accelerated weathering and reductions in shear strength	Hoek and Bray (1981); Ojo and Brook., (1990); Messenzehl et al., (2017).

BS: Bedded Sandstones. IBSS: Interbedded Sandstones and Siltstones / Carbonaceous muds. Note: Some processes may be closely related between them (e.g., moisture inducing clay swelling affecting the rock matrix of IBSS; or wave action inducing microseismic loading).

To date this study remains the only long-term hourly-resolution rockfall and IRT dataset that enables the estimation of volumetric loss. The results in general adhere to observations previously reported that have concluded that while wind-driven precipitation associated with inclement-weather is the most aggressive erosive process, rapid surface temperature changes associated with solar insolation is a significant agent albeit dependent on cliff face aspect, as also observed on the sedimentary rock surfaces of historical monuments in semiarid Spain (Martinez et al., 2022). Indeed, this research has demonstrated that the aspect of the cliff favoured the generation of cyclical daily temperature, and likely associated temperature changes, inducing the highest rates of change at sunrise and then again at sunset (as demonstrated in *Chapter 5,* See *Section 5.3*).

The results presented in this section demonstrate that rockfall are controlled by two processes: (1) inclement weather conditions that generated the significant erosive events; and (2) temperature-controlled iterative rockfall occurrence, which supplied ~ 42.7% (~ 20.6 m^3 out of a total of ~ 48.2 m^3) of the total volume loss. Overall, the combined action of these two regimes contributes to a metastable equilibrium style of erosion (Shum, 1977; Bloom, 1997) at East Cliff of Whitby.

6.5.2 Implications for coastal cliff rockfall under a changing climate

Given this, it is important to discuss the degree to which temperature-control may produce rockfalls in the context of a changing climate. All areas of the UK are projected to experience an increased in the probability of warmer, wetter winters, in addition to hotter drier summers, in addition to an overall increase in the frequency and magnitude of extreme events (UKCP18, 2021). According to the seasonal average warming scenario, between the 10% and 90% probability levels by 2070, under the worst case high emissions scenario, global temperatures are expected to increase in the UK in a range between 1.3°C to 5.1°C in summer, and 0.6 °C to 3.8 °C in winter (UKCP18, 2021).

Using the *UKCP Climate Projections User Interface*, key projections for Whitby were extracted using the RCP 2.6 and RCP 8.5 scenarios by 2070. These are scenarios in which the greenhouse gas emissions are strongly reduced, or continue to grow unmitigated, respectively. The projection of anomalous values that represent differences in environmental mean temperatures, average precipitation, and sea level relative to the baseline dataset between 1981 and 2000 are summarized in Table 6.13.

Table 6. 13: *UKCP18 climate projections for the area of Whitby (25 km grid).*

Scenario	Climate variable	10th Percentile	50th Percentile	90th Percentile
RCP 2.6	Winter mean air temperature anomaly (°C)	*-1 to 0*	0 to 1	*2 to 3*
RCP 2.6	Summer mean air temperature anomaly (°C)	*0 to 1*	1 to 2	*2 to 3*
RCP 2.6	Winter mean precipitation rate anomaly (%)	*-30 to -20*	0 to +10	*+40 to +50*
RCP 2.6	Summer mean precipitation rate anomaly (%)	*-60 to -50*	-20 to -10	*+30 to +40*
RCP 2.6	Mean sea level anomaly (m)	*0.20*	0.28	*0.39*
RCP 8.5	Winter mean air temperature anomaly (°C)	*0 to 1*	2 to 3	*4 to 5*
RCP 8.5	Summer mean air temperature anomaly (°C)	*1 to 2*	3 to 4	*5 to 6*
RCP 8.5	Winter mean precipitation rate anomaly (%)	*-30 to -20*	0 to +10	*+50 to +60*
RCP 8.5	Summer mean precipitation rate anomaly (%)	*-60 to -50*	-30 to -20	*+20 to +30*
RCP 8.5	Mean sea level anomaly (m)	*0.31*	0.42	*0.56*

Note: For mean precipitation rate anomalies (%), negative values indicate less precipitation and positive values indicate more precipitation with respect to the 1981-2000 baseline. Mean air temperature anomalies are estimated at 1.5m of elevation. Source: UKCP18 – Met Office © Crown Copyright 2021.

Given the projections shown in Table 6.13, in order to consider these scenarios, Figure 6.12 displays a conceptual model that considers qualitatively how the monitored dataset observed from 2021 may change under three possible scenarios. Key changes are associated with the magnitude and frequency of large events, and the rates of background iterative rockfall driven by thermal activity, as described below:

(1) *Scenario I*, in which climate change induces increases in the cliff surface temperature (Figure 6.12a);

(2) *Scenario II*, in which climate change induces an increase in the magnitude and frequency of inclement weather and sea level rise (Figure 6.12b); and

(3) *Scenario III*, in which climate change is characterized by the combined occurrence of both temperature increases, and an increasing magnitude and frequency of storms and sea level rise (Figure 6.12c).

Under the *Scenario I* (Figure 6.12a), an increase in the rate of temperature-controlled rockfall activity would be expected, which is manifest by rockfall at noon towards sunset. Cumulatively, this may increase the overall rockfall yield from the cliff face through the year, and potentially reduce the distinction between quiescent periods, and those periods of significant rockfall events. At present 42.7% of the total volume loss was within these periods, and so the erosional contribution during these times would be expected to be higher. Under the scenario RCP 2.6 (see Table 6.13), mean air temperatures in summer for the coastal areas including Whitby are expected to rise between 0-1°C or 2-3°C (10^{th} and 90^{th} percentiles, respectively), while under the scenario RCP 8.5, between 1-2°C or 5-6°C (10^{th} and 90^{th} percentiles, respectively). It is important to note that the projected increases in air temperature, based upon the findings presented above, will likely to be of higher magnitude across the surface of the cliff in summer (*Chapter 5*). For example, the cliff surface was ~ 5.5°C warmer than the recorded air temperature (see Figure 5.2c, *Section 5.2, Chapter 5*). The maximum cliff temperature detected in 2021 was 40.2°C (See Table 5.2 in *Section 5.1, Chapter 5*), meaning that, assuming a proportional increase in the surface temperature, this value could rise to 46.2°C under scenario RCP 8.5. Importantly, this scenario also includes the likely effect of synoptic climate conditions promoting the generation of heatwaves through the mid-summer, which is the period when the cliff surface temperatures are hotter, as demonstrated in *Chapter 5*.

Three probable consequences can be expected based on this dataset: (1) A decreasing magnitude and frequency of the rockfall during winter midnight due to a reduced potential for frost weathering; (2) A decreasing frequency of rockfalls occurring across the sunrise and sunset,

as this research demonstrates that for this setting, the rate of change of temperature is critical in driving temperature controlled rockfalls for small size events, so that higher temperatures in the atmosphere may produce an overall attenuation of the magnitude of the rates of change of temperature across the cliff surface; and (3) Increased magnitude and frequency of temperature-controlled rockfalls at noon towards sunset (and larger rockfall size events) due to heatwaves.

Under the *Scenario II* (Figure 6.12b), a substantial increase in the magnitude and frequency of heavy storms may be expected in winter, but also during summer. This is because future increases in the intensity of heavy precipitation are predicted (UKCP18, 2021). In particular, on the North Yorkshire coast more precipitation is expected in winter (ranging from +50% to +60% at the 90th percentile under the scenario RCP 8.5; see Table 6.13) but also in summer (fluctuating between +20% to +30% at the 90th percentile at RCP 8.5. see Table 6.13). Although sea level or state conditions were not addressed in this thesis, it is considered here that future sea level change impacts cannot be ruled out, and so may become more significant as a control on erosion rates based on the UKCP18 projections, despite that under current conditions, this is not appearing to be a significant control over the rockfall occurrence at the East Cliff (see Section 4.1, Chapter 1).

Two main consequences can be expected based on *scenario II*: (1) Increasing the magnitude and frequency of inclement weather controlled rockfall, promoting larger magnitudes erosive jumps, but also higher volume loss during periods of steady erosion due to the likely increment of rockfall activity of small and medium size; and (2) A decrease in the thermally induced rockfall activity across the cliff face, due to more aggressive wet weather conditions.

Under the *Scenario III* (Figure 6.12c), it is expected the occurrence of a combination of the above mechanisms, will increase the overall magnitude and frequency of erosive events due to inclement weather conditions or temperature extremes promoting large rockfalls. This also may be accompanied of a higher rate of iterative erosion associated with thermally induced rockfalls of small and medium size.

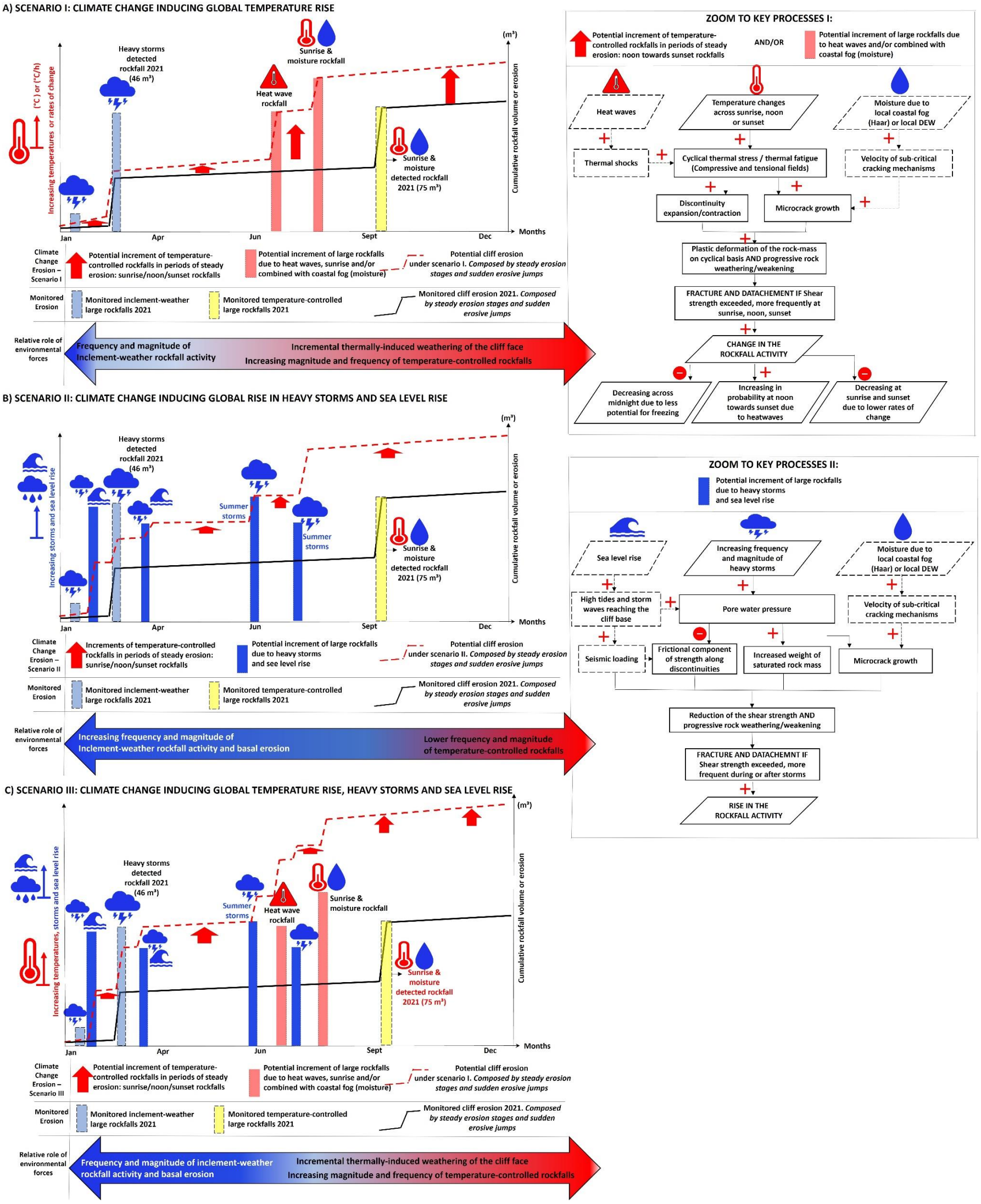

Figure 6. 12: *Relative role of inclement-weather and temperature-induced rockfalls under three likely climate change scenarios. Three different hypothetical scenarios are presented based on the erosional behaviour of the monitored rockfall activity during 2017, 2018, 2019 (Chapter 3) and 2021 (Chapter 6). A) Scenario I: The relative role of environmental forces is dominated by the global rise in temperatures, increasing the magnitude and frequency of temperature-controlled rockfall activity. B) Scenario II: The relative role of environmental forces is dominated by global rise in the frequency and magnitude of heavy storms and sea level rise, increasing occurrence of inclement weather rockfall activity. C) Scenario III: The relative role of environmental forces is dominated by the increasing occurrence of both temperature-controlled and inclement-weather rockfall activity. Vertical blue and red bars show the increasing magnitude and frequency of large rockfalls controlled by inclement-weather and temperatures, respectively. The height of the bars, indicative of the magnitude of the events, is only conceptual, hence, these do not represent modelled or predicted rockfall magnitudes. To the right of the figure, a zoom to the key geo-processes occurring during the climate change is presented. Positive and negative signs indicate positive and negative relationships between processes, respectively.*

6.6 Summary

The research undertaken in this thesis has developed novel workflows that have enabled the quantification of rockfall volumes from large dataset of time-series laser scans (> 27,400 point clouds processed), in parallel to high-resolution thermal imagery (> 8,000 thermal scenes). These workflows were developed in order to: (1) Assess the long-term erosional signatures of hourly rockfall activity and associated magnitude-frequency distributions (*Chapter 3*); (2) Explore the timing and nature of surface cliff temperatures (*Chapters 4* and *5*); and (3) Investigate if there are temperature controls on rockfall activity and cliff erosion. In particular, the analysis presented in this chapter has attempted to link in time the 4D rockfall inventory and cliff surface temperatures between 1st of January and 31st of December 2021, totalling 12-months of continuous concurrent data.

The dataset presented in *Section 6.3* demonstrates that the rockfall occurrence are indeed at certain time temperature-controlled, as rockfall frequencies are observed to be two or three times higher at specific times: midnight, sunrise, noon, and sunset. Consistent increases in the rockfall activity occurred through all seasons of the year, and seasonal shifts in sunrise and sunset cliff surface temperatures showed a clear correspondence with significant increases in the rockfall activity particularly during dry conditions. Several statistically significant relationships have been identified, including between the absolute temperature, rates of change in temperature, and rockfall occurrence, particularly during winter and spring seasons. Importantly, the results strongly mirror similar temporal patterns observed from field monitoring and laboratory testing made in the fields of subcritical cracking growth and thermomechanical monitoring and modelling of discontinuities.

The results discussed in *Section 6.4* provide evidence for statistically significant differences in the cliff surface temperature when rockfalls occurred, when compared to periods with no rockfalls. During sunrise in most seasons, the cliff face was exposed to statistically significant higher positive rates of change in temperatures when rockfalls occurred, which suggests that relatively rapid surface heating is a key control driving rockfalls. Conversely, during sunset in most seasons, the cliff face was subject to statistically significant higher negative rates of temperature change when rockfalls occurred, which indicates that faster surface cooling also had an important control in driving rockfalls. Statistically significant differences in the rates of temperature change were also observed during winter, and around midday in both spring and summer. Overall, the data presented demonstrates that significant differences between rockfall and non-rockfall periods were more common when considering the rates of change in temperature

as opposed to the absolute temperatures. This suggests that the rate of heating or cooling was a significant control on the rockfall occurrence in addition to the absolute temperature.

The dataset presented in *Section 6.5* focused on the assessment of the relative erosional role of rockfall activity induced by inclement weather conditions as compared to temperature-controlled rockfalls. The analysis demonstrated that inclement weather was the dominant controlling factor on rockfall yield whereby these conditions produced ~ 68% of the total eroded volume in 2021. This observation perhaps directly and unequivocally quantifies the assertion that moderate and heavy rainfall is key in directly triggering (cliff) rockfall. Temperature-controlled rockfall activity supplied almost one third of the total erosion detected in 2021 (~ 27%). Notably, this erosive contribution was higher during periods of relative quiescence, with temperature-induced rockfalls supplying up to 42.7% of the total volume loss during these periods. As a result, these analyses demonstrate that temperature-controlled rockfall activity has an important erosive role, especially during periods of iterative surface change, which is observed here for the first time.

Chapter 7 – Conclusions

The aim of this research was to use high-frequency laser scanning and infrared thermography monitoring to improve understanding of temperature controls on rockfall activity and cliff erosion at the East Cliff, Whitby, UK. A series of research questions and objectives were outlined in *Chapter 1*. The development of a new method enabled the automated quantification of rockfall volumes from laser-scanner data collected between 2017 – 2019, and 2021, comprising a total of four years of rockfall monitoring (> 27,400 point clouds processed). As such, this method has enabled the acquisition of the largest multi-annual, hourly 4D rockfall inventory produced to date.

The key rockfall monitoring and processing method involved the development of a computational routine that takes point cloud data as ASCII files of *XYZ* positions which is then automatically processed in *Cloud Compare* in three principal stages of automation. A set of quality-control geomatic filters were developed and applied to point clouds. Subsequently, new workflows for point-cloud registration, change detection (M3C2; Lague et al., 2013) and volume estimation were developed, as the focus of the new approach was on optimizing the speed of data processing and providing flexibility for future geoscience applications (*Chapter 2*).

The resulting rockfall inventory contains >8,300 rockfalls captured in the period 2017 – 2019 with 1-hour timing precision, and > 4,100 rockfalls captured in 2021; the latter is complemented by contemporaneous cliff surface-temperature. The results obtained provided unique insight into the multi-annual erosional signature of rockfall activity, cliff erosion and associated magnitude-frequency relationships (*Chapter 3*), as well as into the timing and nature of cliff surface temperatures from >4,270 corrected hourly thermal images (*Chapters 4 and 5*). The contemporaneous rockfall and cliff surface temperature data from 2021 were analysed in *Chapter 6*. These data considerably improves our ability to understand temperature controls on rockfall activity and to assess the relative significance of thermally-induced rockfall occurrence and cliff erosion. Section 7.1 summarise these findings in relation to the research questions outlined in *Chapter 1*.

7.1 Summary of key findings

RQ1. How do rockfall magnitude, frequency and timing vary over hourly, diurnal, and seasonal timescales?

Objectives *1* and *2* have been completed to answer this research question. This included (O1) developing a method for processing large time series (10^4) of sequential laser scanner data to continuously monitor rockfalls; and (O2) produce a multi-annual 4D rockfall inventory, to quantify the timing, magnitude, and frequency of rockfalls captured in all conditions. The resulting inventory of rockfall activity and cliff erosion has been used to show that:

- The long-term erosion is characterised by infrequent large rockfalls ($\geq$1.0 m^3) and small scale iterative mass wasting. This research is the first time that the cumulative effects of small (0.001-0.01 m^3), medium (0.01-0.1 m^3), and large (0.1-100 m^3) volume rockfalls contribute to a multi-annual erosion on a near vertical rock slope.

- The rate of material loss is highly variable. For example, the two largest erosion events captured in 2017 – 2019 had a total volume loss of ~23 ± 5 m^3, and low magnitude-frequency power-law scaling exponents indicative of a higher proportional contribution from large rockfall (β = -1.31 and -1.68). Conversely, periods of iterative erosion were characterised by lower and near-constant rates of volume loss (2.5 to 4.6 mm y^{-1}) that resulted in high magnitude-frequency power-law scaling exponents that reflect a greater erosional contribution from small rockfalls (β = -1.96 to -3.35). Overall, these results demonstrate that the cliff face experiences a high degree of erosional variability over both long (seasons) and short (hours) time scales.

- The observed rockfall volume (magnitude)-frequency relationships revealed a marked 'roll-up' and 'heavy-tail' during both high-magnitude erosional episodes (EPs) and periods of iterative or gradual erosion (GEs). This reflects the high frequency monitoring over a multi-annual period, which reduces the likelihood of underrepresentation of certain sizes and frequencies of rockfalls due to the effect of spatial superimposition and coalescence.

- Two key implications are highlighted from the detection of a 'roll-up' and 'heavy-tail' distribution of rockfalls: 1) the roll-up of rockfalls is interpreted to two processes

superimposed: both rockfall which characterise the majority of the curve, and small-scale spalling of very frequency fragments (~75% of the total number of rockfalls between 2017-2019) that do not adhere to the wider negative power law; 2) the heavy-tail for larger rockfalls represents that the largest events which although less common (~0.2% of the total number of rockfalls between 2017-2019), contributed significantly to the overall volume lost.

- Although medium-size rockfalls contributed to a significant proportion of the total observed erosion (~35.1% of total volume loss), the most significant volumetric contribution to erosion (~50.8%) resulted from large, low frequency rockfalls. This is a key finding in the context of landslide literature that considers magnitude-frequency relationships where it has been assumed that a dominant portion of erosive work results from relatively frequent events of moderate magnitude, and that it cannot be assumed that larger size, less common events are the most significant (Wolman and Miller, 1959). However, this study has demonstrated that, at East Cliff, 17 large rockfalls captured between 2017 and 2019 contributed around half of the total volume loss, while medium-magnitude rockfalls supplied around one third of the total volume loss.

- Large magnitude rockfalls driving significant erosion occurred not only in winter, but also in spring and summer, particularly associated with summer storms and/or during dry conditions. The implications of this are twofold: first, distinct seasonal controls on large rockfall events are not clear, supporting the observations made by Rosser et al., (2007); Second, this pattern of behaviour is important to consider in the context of climate change as, for the UK in particular, extreme climate events will be more frequent in both winter and summer, which may lead to increasing rates of cliff erosion.

- At hourly resolution, rockfall frequencies showed a clear correspondence with the time of sunrise, noon and sunset during all seasons. The rockfall dataset captured in 2021 during dry environmental conditions shows that rockfall frequencies were two or three times higher at or shortly after sunrise, noon and sunset than throughout the remainder of the day. At these times, the increases in rockfall frequency were similar in percentage terms, and consistent in timing during all seasons, which indicates that diurnal rockfall activity is not random. As such, the coincidence in time with the sunrise, noon and sunset suggests the existence of a temporal link between rockfall occurrence and rock-surface temperatures, leading to a marked diurnal pattern of rockfalls, which represents thermal signatures on rockfall activity.

RQ2. How do surface cliff temperatures vary over hourly, diurnal, and seasonal timescales?

Objectives *3* and *4* have been completed to answer this research question. These include (O3): developing an approach to continuously monitor cliff surface temperatures using Infrared Thermography (IRT) through 2021; and (O4) investigate the variability of surface cliff temperatures at 1 hour resolution. The findings demonstrate that:

- In winter, structure, lithology and surface character control the surface temperatures across the cliff. For example, the bedded sandstones were 1°C warmer, on average, than the interbedded sandstones and siltstones. This is particularly evident when solar insolation does not directly strike the cliff surface, as during winter. Overall, this suggests that during colder months, the spatial variability in the cliff temperatures is controlled by the thermal properties of the cliff rock face in absorbing and releasing heat.

- From mid-spring to late summer, cliff surface aspect controls the spatial variability of temperatures, producing a preferential clusters of both the highest and lowest temperature areas on the cliff. These clusters transcend across multiple strata and overrides the influence of rock-type (large-scale aspect controls, > ~10 m). Aspect control is also seen at a more local scale, where small (> ~1 m) but marked gradients in temperature trace bedding, discontinuity and fracturing dependent microtopography on the surface. Aspect controls are more pronounced at times with no cloud and direct solar insolation.

- Some sections of the rockface were subject to extreme temperature ranges during the year, ranging from ~-11.7°C to +40.2°C (annual range = 51.9°C), reflecting the combined superimposition of the controls on surface temperature identified above. Such a scale of temperature variability, notably at a temperate mid-latitude coastal location, is not currently reflected in the literature on rock fracturing. This variability represents an important gap in current understanding around the range and magnitude of surface temperatures that can be experienced.

- Despite the mid-latitude coastal rock setting, the cliff face is susceptible to freezing conditions or freeze-thaw behaviour for extended periods of time. Freezing temperatures were observed in January at particular with sustained surface temperatures < 0°C evident, and extreme surface temperatures reaching ~-5°C or even -10°C. From winter until mid-spring, cliff surface locations were exposed to cold (e.g., -5.0°C) and warm (e.g., 10°C) surface temperatures within a single day, or between successive days, implying the potential for exposure to freeze thaw behaviour. In winter, 69% of all days monitored

showed temperatures typically associated with freeze-thaw cycling, while in spring this percentage was still significant (35%). The number of days with uninterrupted freeze-thaw cycles was 7 to 10 days in winter and spring, respectively, which holds critical implications for the potential for temperature driven rock fracturing.

- Conversely, the cliff face has been observed to experience markedly warm surface conditions, which will be more intense and frequent under a warming climate and the influence of heat waves. Sustained average surface temperatures ≥ 20°C were detected from mid-spring until the end of the summer, totalling a period of four months. In this period, two seasonal peaks of cliff-surface maxima (40°C) were recorded, which may be enhanced by future increased air temperature projections for the UK.

- The data suggests that the warmer the season, the higher the temperature range and the greater the rates of surface temperature change per hour. For instance, in spring and summer, the rock face was frequently exposed to very high rates of temperature change (both positive and negative), either on the same day or on successive days (e.g., from ~-10.0°C/h up to 10.0°C/h). These periods are likely to be when thermomechanical cracking, if present, is most effective.

- The cliff surface experienced the highest rates of change of temperature during sunrise and sunset. In winter and autumn, the highest positive rate of temperature (mean and maximum rates of ~1.8°C/h and ~4.0°C/h, respectively) occurred 1 hour after the sunrise (09:00 – 10:00 h), compared to rates of ±0.2°C/h throughout the remainder of the day. In spring and summer, the highest positive rates of temperature change occurred by the end of sunrise (06:00-07:00 h) and at the beginning of sunset (18:00-19:00 h). At both times the mean and maximum rates were ~1.6°C/h and up to ~6.5°C/h, respectively, while a high variability in the rates was observed across the remaining hours of the day of spring and summer.

- Diurnal rates of change of temperature in winter and summer differ. This is characterized by only one phase of rapid positive and a negative temperature change in winter, and two diurnal phases of rapid change in summer. For example, in spring and summer, the first of these occurs at sunrise between 04:00 – 07:00 h (mean rate from ~0°C/h to 1.8°C/h, indicative of rapid cliff surface heating), which is immediately followed by rapid negative drops in the rate of temperature change during the early morning (between 07:00 – 09:00 h). This generates the first daily inflection in the rates in the warmer seasons between 06:00 – 07:00 h, coincident with the end of the sunrise when the cliff is exposed to very

high maximum rates of temperature change (~5.0 to 6.0°C/h). The second phase of rapid temperature change occurs before and after sunset, as rapid positive changes commence between 15:00 – 16:00 h through 18:00 – 19:00 h. This is followed by very fast negative rates of temperature change between 18:00 – 19: 00 and 21:00 – 22:00, representing very fast surface cooling throughout the period around sunset.

- Cyclic exposure to these rates of temperature change may hold critical implications for rock fracturing and rockfall, given the magnitude and sequencing of rapid surface heating and cooling. Maximum cooling occurred consistently with a 2-hour lag after the maximum rates of heating around sunrise and sunset. These observations highlight that the detection of these thermal dynamics cannot easily be characterised using point measurement thermocouples, or non-continuous or long-term IRT monitoring.

- The magnitude, timing and divergent rates of temperature change in winter and summer is controlled by direct solar insolation onto the cliff face, which varies both across cliff (10^1 – 10^2 m) and locally (10^{-2} – 10^0 m) across micro topography as a function of surface dip angle and aspect. In spring and summer, aspect controls are manifest as three four-hour-long periods:

    - Solar insolation driving heating that strikes the cliff face from the east at sunrise, heating northerly and north easterly facing planes (04:00 – 07:00 h). This drives across cliff shifts from east to west of areas of increasing temperature under direct illuminated. When illumination ceased, temperatures reduced for 2 hours, generating rapid cooling between 07:00 – 09:00 h.
    - At midday the sun become obscured by the cliff edge, and as the cliff moves behind the cliff edge, a rapid cessation in direct insolation occurs, the response to which is a homogeneous surface temperature distribution with almost negligible aspect control. The period that follows also sees the highest mean surface temperatures, accompanied by low rates of temperature change.
    - Later in the day incident sunlight from the west, illuminates N and NW facing surfaces, producing a second daily heating phase between 15:00 – 19:00 h. This period again experiences very high rates of surface temperature change that progressively shift from east to west, followed by rapid cooling when direct illumination ceases between 19:00 and 22:00 h.
    - The above influence was however almost negligible in winter as the cliff face is under near-constant shadow, promoting notably low and homogenous surface

temperatures, and lower rates of surface temperature change. In winter, absolute temperatures and rates of change were mainly influenced by lithology with the sub-horizontal structures of the beds showing the greatest control on surface temperature. This research has for the first time therefore defined the temporal cycle of controls on cliff surface temperature, which alternates between air, insolation, aspect and lithologically controlled.

RQ3. To what extent does cliff surface temperature variability trigger rockfall?

Objective 5 involved the combination of the 4D rockfall inventory and contemporaneous IRT data captured in 2021 to quantify controls on rockfall occurrence, which showed that:

- Increases in hourly rockfall frequency correspond with the diurnal patterns in hourly surface temperature and their associated rates of change. This was pronounced at midnight in winter, and at sunrise, noon, and sunset in all other seasons. This apparent correlation was particularly apparent at the times with maximum rates of temperature change at sunrise and sunset.

- Hourly rockfall frequencies during non-rainfall conditions correlate significantly with cliff surface temperatures, particularly in winter and spring. Statistically significant positive relationships were observed between absolute surface temperatures, rates of change in temperatures and rockfall occurrence, including the number of observed rockfalls, and the total number of small size rockfalls. As such, while it is well established that correlations do not indicate causation, these results attest to the critical importance of surface thermal conditions on rockfall.

- There are statistically significant differences in the surface thermal conditions when rockfalls occur as compared to periods with no rockfall. During the sunrise in most seasons, the cliff face experiences statistically higher positive rates of temperature change when rockfalls occur. This implies that faster surface heating has a key control in driving rockfalls. Conversely, at sunset in most seasons, the cliff face experiences large negative rates of temperature change when rockfalls occur, suggesting that rapid surface cooling also holds an important control in driving rockfall.

- In this setting, the rates of change in cliff surface temperature appear to hold a greater control than absolute temperatures over rockfall occurrence. Out of the total 16 key daily

thermal phases through winter to autumn, where each season has four phases: midnight, sunrise, noon, sunset, statistically significant differences in the rates of temperature change are present in a total of 10 (63%), while for absolute temperatures this is observed in only 6 (37%). This suggests that how quickly or slowly the cliff face temperature changes is critical, especially around sunrise and sunset.

- In summary, during non-rainfall conditions rockfall occurrence was not random, and showed a clear and consistent correspondence with the pattern of cliff-temperature variability, providing evidence of temperature controls on rockfall occurrence at certain times of the diurnal cycle.

RQ4. What is the relative erosive contribution of rockfall activity resulting from (a) inclement weather conditions versus (b) temperature effects?

This research question draws upon the results of objective 5 (O5), which aimed to obtain insight into the relative significance of temperature-induced rockfall activity versus other controls. The results demonstrate that:

- Inclement weather conditions constitute the dominant environmental force controlling the total production of rockfalls, producing ~68% of the total eroded volume in 2021 and ~60% of the total number of detected rockfalls.

- Relative to inclement weather, surface temperature variability had a secondary role in controlling rockfall. It was possible to identify that temperature controlled ~27% of the rockfall volume and ~17% of rockfall number in 2021. Notably, the largest rockfall event captured (75 ± 19 m^3) occurred in a summer sunrise and was coincident with local coastal fog. This suggest that, together with the faster rates of change of temperature at sunrise, surface moisture/dew may have an important role in leading the cliff to final failure.

- Temperature-controlled rockfall activity had an important erosive role, contributing up to ~42.7% of the total eroded volume within periods of iterative erosion in 2021. To date, such observations have not been previously reported, and so this analysis contributes to improving the understanding of temperature control on rockfall occurrence. An important consequence of this observation is that when considered as a function of the duration of different controls during the year, temperature control dominates behaviour for the vast majority of the time in the year. As a result, and whilst periods of inclement weather result

in the largest hazards, rockfall hazard and therefore risk through the majority of the year is primarily a function of temperature.

7.2 Directions for future research

In this thesis, high-resolution, long-term laser scanning and infrared thermography were used to investigate temperature control on rockfall occurrence. The completion of the research objectives has provided a flexible methodology for efficient automated data processing. It has also yielded a unique multi-annual and hourly resolution 4D rockfall inventory and a complete one-year contemporaneous monitoring of rockfalls and thermal data of the cliff surface. Therefore, many of these computational routines along with the unique rockfall and thermal datasets generated, serve as a basis for future rockfall research. These include, but are not limited to:

- Modelling cliff erosion response to climate change scenarios. The near-constant monitoring developed here, provides a truly unique opportunity to generate a long-term multi-annual 4D rockfall inventory. The system has been running since 2015, and so now includes eight years of data (e.g., 2015 – 2023), from which it would be possible to extract a very rich time series dataset that potentially captures a higher level of variability enabling different controlling conditions to be considered. Exploring realistic future scenarios based upon a growing time-series archive dataset could be used to consider positive and negative geomorphic feedbacks that are not visible in shorter length datasets.

- Investigating the links between thermally-induced rock damage accumulation, cliff surface temperature and rockfall occurrence. The IRT data presented in this thesis can be used to support laboratory-based rock simulations of microcracking, allowing exploration of rock-mass response based upon field-observed rates of changes in temperature.

- Examining the links between the thermomechanical behaviour of the cliff face and rockfall occurrence. The IRT and rockfall data generated in this thesis can be used to model heat propagation and thermomechanical response of the cliff surface as a function of lithology and joint-set configuration. The thermal patterns observed, such us the freeze-thaw oscillations in winter, could be used to parameterise simulations of shallow cyclical thermal stresses on rock faces. Importantly, this may allow the identification of thresholds associated with rock detachment.

- Exploring the extent to which temperature-induced rockfalls occur in other geomorphic and climatic settings. This thesis has attempted to make a step-change in understanding of thermal controls on seasonal rockfall activity. However, more research is needed to understand the extent to which temperature-induced rockfall activity is a 'global' process and how this varies. It is important to investigate the boundary conditions, morphoclimatic, lithological and structural settings that enable or inhibit temperature-control on rockfall occurrence. This will require the challenges associated with installing monitoring systems in other settings to be addressed, using low-cost remote sensing devices capable of producing comparably robust results. This also will require a careful selection of the locations to be monitored at high temporal and spatial resolution, such as extreme desert environments like the Atacama Desert (Chile) and/or tropical environments where humidity controls may be significant. Overall, this is of critical importance in the context of a warming global climate and the resultant for potential changes in the role of thermally-induced mechanisms that generate rock-slope failure. The benefits of this future research may not only be purely scientific, but will hold implications for end-users to reduce the hazard and risk that these mechanisms pose to engineering structures and society.

References

Abellán, A., Jaboyedoff, M., Oppikofer, T., & Vilaplana, J. M. (2009). Detection of millimetric deformation using a terrestrial laser scanner: experiment and application to a rockfall event. Natural *Hazards and Earth System Science, 9(2)*, pp. 365-372.

Abellán, A., Calvet, J., Vilaplana, J. M., & Blanchard, J. (2010). Detection and spatial prediction of rockfalls by means of terrestrial laser scanner monitoring. *Geomorphology*, *119*(3–4), pp. 162–171.

Abellán, A., Oppikofer, T., Jaboyedoff, M., Rosser, N. J., Lim, M., & Lato, M. J. (2014). Terrestrial laser scanning of rock slope instabilities. *Earth Surface Processes and Landforms*, *39*(1), pp. 80–97.

Adams, P. N., Anderson, R. S., & Revenaugh, J. (2002). Microseismic Measurement of Wave Energy Delivery to a Rocky Coast, *Geology*, 30(10), pp. 895-898.

Adams, P. N., Storlazzi, C. D., & Anderson, R. S. (2005), Nearshore Wave-Induced Cyclical Strain of Sea Cliffs: A Possible Fatigue Mechanism, *Journal of Geophysical Research – Earth Surface*, (110), No. F2.

Agar, R. (1960). Post-glacial erosion of the North Yorkshire coast from the Tees estuary to Ravenscar. *Proceedings of the Yorkshire Geological and Polytechnic Society*, *32*(4), pp. 409–427.

Aldred, J., Eppes, M. C., Aquino, K., Deal, R., Garbini, J., Swami, S., Tuttle, A., & Xanthos, G. (2016). The influence of solar-induced thermal stresses on the mechanical weathering of rocks in humid mid-latitudes. *Earth Surface Processes and Landforms*, *41*(5), pp. 603–614.

Al-Hurban, A. (2006). Sabkha. In A. Goudie (Ed.), *Encyclopedia of Geomorphology* (Vol. 1st), London & New York: Routledge Taylor & Francis Group, 1156 p.

Anders, M. H., Laubach, S. E., & Scholz, C. H. (2014). Microfractures: A review. *Journal of Structural Geology*, *69*(PB), pp. 377–394.

Anderson, T. (2005). *Fracture Mechanics: Fundamentals and Applications* (3rd Ed.). London & New York: CRC Press, 610 p.

Arosio, D., Longoni, L., Papini, M., Boccolari, M., & Zanzi, L. (2018). Analysis of microseismic signals collected on an unstable rock face in the Italian Prealps. *Geophysical Journal International*, *213*(1), pp. 475–488.

Atkinson, B. K. (1984). Subcritical crack growth in geological materials. *Journal of Geophysical Research*, *89*(B6), pp. 4077–4114.

Babaeian, E., & Tuller, M. (2023). Proximal sensing of land surface temperature. In Goss, M., & Oliver, M. (Ed.*). Encyclopedia of Soils in the Environment* (2nd Edition). Elsevier, pp. 600-609.

Bae, K. H., & Lichti, D. D. (2008). A method for automated registration of unorganised point clouds. *ISPRS Journal of Photogrammetry and Remote Sensing*, *63*(1), pp. 36–54.

Bagdassarov, N. (2021). Thermal Properties of Rocks and Minerals. In Bagdassarov, N (Ed.). *Fundamentals of Rock Physics*. Cambridge University Press, pp. 455-504.

Bakun-Mazor, D., Hatzor, Y. H., Glaser, S. D., & Carlos Santamarina, J. (2013). Thermally vs. seismically induced block displacements in Masada rock slopes. *International Journal of Rock Mechanics and Mining Sciences*, *61*, pp. 196–211.

Ball, M., & Pinkerton, H. (2006). Factors affecting the accuracy of thermal imaging cameras in volcanology. *Journal of Geophysical Research: Solid Earth*, *111*(11), pp. 1–14.

Barlow, J., Lim, M., Rosser, N., Petley, D., Brain, M., Norman, E., & Geer, M. (2012). Modeling cliff erosion using negative power law scaling of rockfalls. *Geomorphology*, *139–140*, pp. 416–424.

Barlow, J., Gilham, J., & Ibarra, I. (2017). Kinematic analysis of sea cliff stability using UAV photogrammetry. *International Journal of Remote Sensing*, *38*(8–10), pp. 2464–2479.

Barnhart, T. B., & Crosby, B. T. (2013). Comparing Two Methods of Surface Change Detection on an Evolving Thermokarst Using High-Temporal-Frequency Terrestrial Laser Scanning, Selawik River, Alaska. *Remote Sensing*, *5*(6), pp. 2813–2837.

Barron, A. J. M., Lott, G. K., Riding, J. B., & British Geological Survey. (2012). *Stratigraphical framework for the Middle Jurassic strata of Great Britain and the adjoining continental shelf*. British Geological Survey report RR/11/006. 177 p.

Becker, F., Nerry, F., Ramanantsizehena, P., & Stoll, M. P. (1986). Mesures d' émissivité angulaire par reflexion dans I'infrarouge thermique—implications pour la télédétection. *International Journal of Remote Sensing*, *7*(12), pp. 1751–1762.

Beer, A. R., Turowski, J. M., & Kirchner, J. W. (2017). Spatial patterns of erosion in a bedrock gorge. *Journal of Geophysical Research: Earth Surface*, *122*(1), pp. 191–214.

Benjamin, J. (2018). *Regional-scale controls on rockfall occurrence*. PhD Thesis, Durham University. Available at Durham E-Theses Online: http://etheses.dur.ac.uk/12813/.

Benjamin, J., Rosser, N. J., & Brain, M. J. (2020). Emergent characteristics of rockfall inventories captured at a regional scale. *Earth Surface Processes and Landforms*, *45*(12), pp. 2773–2787.

Besl, P. J., & McKay, N. D. (1992). A Method for Registration of 3-D Shapes. *IEEE Transactions on Pattern Analysis and Machine Intelligence*, *14*(2), pp. 239–256.

Bierman, P., & Montgomery, D. (2014). *Key Concepts in Geomorphology*. New York: W.H. Freeman and Company Publishers, 555 p.

Bird, E. (2006). Cliff, Coastal. In A. Goudie (Ed.), *Encyclopedia of Geomorphology* (Vol. 1st), London & New Yor: Routledge Taylor & Francis Group, 1156 p.

Birien, T., & Gauthier, F. (2023). Assessing the relationship between weather conditions and rockfall using terrestrial laser scanning to improve risk management. *Natural Hazards and Earth System Sciences*, *23*(1), pp. 343–360.

Bleam, W. (2012). Clay Mineralogy and Clay Chemistry. In W. Bleam (Ed.), *Soil and Environmental Chemistry*. Oxford: Elsevier, Academic Press, pp. 85 – 116.

Bloom, A. (1998). *Geomorphology: A Systematic Analysis of Late Cenozoic Landforms* (3rd ed.). New Jersey: Prentice-Hall, Inc., 482 pp.

Boehler, W., Vicent, M.B. and Marbs, A. (2003). Investigating laser scanner accuracy. The *International Archives of Photogrammetry, Remote Sensing and Spatial Information Sciences*, 34(5), pp. 696-701.

Bonneau, D. A., & Hutchinson, D. J. (2019). The use of terrestrial laser scanning for the characterization of a cliff-talus system in the Thompson River Valley, British Columbia, Canada. *Geomorphology*, *327*, pp. 598–609.

Brain, M. J., Rosser, N. J., Norman, E. C., & Petley, D. N. (2014). Are microseismic ground displacements a significant geomorphic agent?. *Geomorphology*, *207*, pp. 161–173.

Brantut, N., Heap, M. J., Meredith, P. G., & Baud, P. (2013). Time-dependent cracking and brittle creep in crustal rocks: A review. *Journal of Structural Geology*, *52*(1), pp. 17–43.

Brenner, C., Dold, C., & Ripperda, N. (2008). Coarse orientation of terrestrial laser scans in urban environments. *ISPRS Journal of Photogrammetry and Remote Sensing*, *63*(1), pp. 4–18.

Brunetti, M. T., Guzzetti, F., & Rossi, M. (2009). Probability distributions of landslide volumes. *Nonlinear Processes in Geophysics*, *16*(2), pp. 179–188.

Cardell, C., Rivas, T., Mosquera, M. J., Birginie, J. M., Moropoulou, A., Brieto, B., Silva, B., & Van Grieken, R. (2003). Patterns of damage in igneous and sedimentary rocks under conditions simulating sea-salt weathering. *Earth Surface Processes and Landforms*, 28(1), pp. 1–14.

Chau, K. T., Wong, R. H. C., Liu, J., & Lee, C. F. (2003). Rockfall Hazard Analysis for Hong Kong Based on Rockfall Inventory. *Rock Mechanics and Rock Engineering*, *36*(5), pp. 383–408.

Chiodini, G., Vilardo, G., Augusti, V., Granieri, D., Caliro, S., Minopoli, C., & Terranova, C. (2007). Thermal monitoring of hydrothermal activity by permanent infrared automatic stations: Results obtained at Solfatara di Pozzuoli, Campi Flegrei (Italy). *Journal of Geophysical Research: Solid Earth*, *112*(B12), 12206.

Coe, J. A., Michael, J. A., Crovelli, R. A., & Savage, W. Z. (2000). Preliminary map showing landslide densities, mean recurrence intervals, and exceedance probabilities as determined from historic records, Seattle, Washington. United States Geological Survey Open File Report 2000-303, 25 p.

Collins, B. D., & Stock, G. M. (2016). Rockfall triggering by cyclic thermal stressing of exfoliation fractures. *Nature Geoscience*, *9*(5), pp. 395–400.

Collins, B. D., Stock, G. M., Eppes, M.-C., Lewis, S. W., Corbett, S. C., & Smith, J. B. (2018). Thermal influences on spontaneous rock dome exfoliation. *Nature Communications*, *9*(1), pp. 1–12.

Cook, K. L. (2017). An evaluation of the effectiveness of low-cost UAVs and structure from motion for geomorphic change detection. *Geomorphology*, *278*, pp. 195–208.

Cooke, R., Warren, A., & Goudie, A. (1993). *Desert geomorphology*. London: UCL Press Limited, 526 pp.

Cox, B. M., Sumbler, M. G., & Ivymay-Cook, H. C. (1999). A formational framework for the Lower Jurassic of England and Wales (offshore area). *British Geological Survey Research Report. RR/99/01*, pp. 1–25.

Crovelli, R. A. (2000). *Probability Models for Estimation of Number and Costs of Landslides.* United States Geological Survey Open File Report 00-249, 23 p.

Crozier, M. (2006). Magnitude-Frequency Concept. In A. Goudie (Ed.), *Encyclopedia of Geomorphology* (Vol. 1st), London & New Yor: Routledge Taylor & Francis Group, 1156 p.

Dalrymple, J. B., Blong, R. J., & Conacher, A. J. (1969). An hypothetical nine-unit landsurface model. *Zeitschrift Fur Geomorphologie*, *12*, pp. 60–76.

D'Amato, J., Hantz, D., Guerin, A., Jaboyedoff, M., Baillet, L., & Mariscal, A. (2016). Influence of meteorological factors on rockfall occurrence in a middle mountain limestone cliff. *Natural Hazards and Earth System Sciences*, *16*(3), pp. 719–735.

D'Angiò, D., Fantini, A., Fiorucci, M., Iannucci, R., Lenti, L., Marmoni, G. M., & Martino, S. (2021). Environmental forcings and micro-seismic monitoring in a rock wall prone to fall during the 2018 Buran winter storm. *Natural Hazards*, *106*(3), pp. 2599–2617.

de Vilder, S. J., Rosser, N. J., & Brain, M. J. (2017). Forensic analysis of rockfall scars. *Geomorphology*, *295*, pp. 202–214.

de Vilder, S. J., Brain, M. J., & Rosser, N. J. (2019). Controls on the geotechnical response of sedimentary rocks to weathering. *Earth Surface Processes and Landforms*, *44*(10), pp. 1910–1929.

Delonca, A., Gunzburger, Y., & Verdel, T. (2014). Statistical correlation between meteorological and rockfall databases. *Natural Hazards and Earth System Sciences*, *14*(8), pp. 1953–1964.

Dewez, T. J. B., Girardeau-Montaut, D., Allanic, C., & Rohmer, J. (2016). Facets: A Cloud Compare plugin to extract geological planes from unstructured 3D point clouds. *The International Archives of the Photogrammetry, Remote Sensing and Spatial Information Sciences - ISPRS Archives*, *41*, pp. 799–804.

Dietze, M., Cook, K. L., Illien, L., Rach, O., Puffpaff, S., Stodian, I., & Hovius, N. (2020). Impact of Nested Moisture Cycles on Coastal Chalk Cliff Failure Revealed by Multiseasonal Seismic and Topographic Surveys. *Journal of Geophysical Research: Earth Surface*, *125*(8), e2019JF00548.

DiFrancesco, P. M., Bonneau, D., & Hutchinson, D. J. (2020). The implications of M3C2 projection diameter on 3D semi-automated rockfall extraction from sequential terrestrial laser scanning point clouds. *Remote Sensing*, *12*(11), pp. 1-27.

Diop, S., Ogawa, Y., & Zhang, M. (2008). Effects of Cyclic Wetting and Drying on Physical and Mechanical Properties of Neogene Sandstones and Siltstones from Boso Peninsula, Japan. *Journal of the Japan Society of Engineering Geology*, 49(3), pp. 150–163.

do Amaral Vargas, E., Velloso, R. Q., Chávez, L. E., Gusmão, L., & do Amaral, C. P. (2013). On the effect of thermally induced stresses in failures of some rock slopes in Rio de Janeiro, Brazil. *Rock Mechanics and Rock Engineering*, *46*(1), pp. 123–134.

Dunn, Fletcher., & Parberry, Ian. (2002). *3D Math Primer for Graphics and Game Development*. Texas, USA: Wordware Publishing, Inc., 429 p.

Dussauge-Peisser, C., Helmstetter, A., Grasso, J. R., Hantz, D., Desvarreux, P., Jeannin, M., & Giraud, A. (2002). Probabilistic approach to rock fall hazard assessment: potential of historical data analysis. *Natural Hazards and Earth System Sciences*, *2*(1/2), pp. 15–26.

Earlie, C., Masselink, G., Russell, P., & Shail, R. (2013). Sensitivity analysis of the methodology for quantifying cliff erosion using airborne LiDAR – examples from Cornwall, UK. *Journal of*

Coastal Research: Special Issue - International Coastal Symposium Volume 1, *65*(1), pp. 470–475.

Einstein, H. H., Veneziano, D., Baechert, G. B., O'reilly, K. J. & Railly, JO. (1983). The Effect of Discontinuity Persistence on Rock Slope Stability. *International Journal of Rock Mechanics and Mining Sciences.* 20, pp. 227-236.

Eppes, M. C., McFadden, L. D., Wegmann, K. W., & Scuderi, L. A. (2010). Cracks in desert pavement rocks: Further insights into mechanical weathering by directional insolation. *Geomorphology*, *123*(1–2), pp. 97–108.

Eppes, M. C., Willis, A., Molaro, J., Abernathy, S., & Zhou, B. (2015). Cracks in Martian boulders exhibit preferred orientations that point to solar-induced thermal stress. *Nature Communications*, *6.*: 6712, 11 p.

Eppes, M. C., Magi, B., Hallet, B., Delmelle, E., Mackenzie-Helnwein, P., Warren, K., & Swami, S. (2016). Deciphering the role of solar-induced thermal stresses in rock weathering. *Bulletin of the Geological Society of America*, *128*(9–10), pp. 1315–1338.

Eppes, M. C., & Keanini, R. (2017). Mechanical weathering and rock erosion by climate-dependent subcritical cracking. *Reviews of Geophysics*, *55*, pp. 470–508.

Evans, I. (1970). Salt crystallization and rock weathering: a review. *Rev. Geomorph. Dynam.*, 19, pp. 153–177.

Fell, R., Corominas, J., Bonnard, C., Cascini, L., Leroi, E., & Savage, W. Z. (2008). Guidelines for landslide susceptibility, hazard and risk zoning for land-use planning. *Engineering Geology*, *102*(3–4), pp. 99–111.

Feng, L., Intrieri, E., Pazzi, V., Gigli, G., & Tucci, G. (2021). A framework for temporal and spatial rockfall early warning using micro-seismic monitoring. *Landslides*, *18*(3), pp. 1059–1070.

Finlayson, Brian., & Statham, I. (1980). *Hillslope analysis*. London: Butterworths-Heinneman, 230 p.

Fiorucci, M., Marmoni, G. M., Martino, S., & Mazzanti, P. (2018). Thermal response of jointed rock masses inferred from infrared thermographic surveying (Acuto test-site, italy). *Sensors (Switzerland)*, *18*(7), pp. 1-25.

Fiorucci, M., Martino, S., Bozzano, F., & Prestininzi, A. (2020). Comparison of approaches for data analysis of multi-parametric monitoring systems: Insights from the acuto test-site (central Italy). *Applied Sciences (Switzerland)*, *10*(21), pp. 1–25.

FLIR Systems Inc. (2018). *User's manual FLIR Tools/Tools+*. USA, 196 p.

Frodella, W., Gigli, G., Morelli, S., Lombardi, L., & Casagli, N. (2017). Landslide mapping and characterization through Infrared Thermography (IRT): Suggestions for a methodological approach from some case studies. *Remote Sensing*, *9*(12), pp. 1-25.

Genkinger, S., & Putnis, A. (2007). Crystallisation of sodium sulfate: Supersaturation and metastable phases. *Environmental Geology*, 52(2), pp. 295–303.

Ghobadi, M. H., & Babazadeh, R. (2015). Experimental Studies on the Effects of Cyclic Freezing–Thawing, Salt Crystallization, and Thermal Shock on the Physical and Mechanical Characteristics of Selected Sandstones. *Rock Mechanics and Rock Engineering*, 48(3), pp. 1001–1016.

Gilham, J., Barlow, J., & Moore, R. (2018). Marine control over negative power law scaling of mass wasting events in chalk sea cliffs with implications for future recession under the UKCP09 medium emission scenario. *Earth Surface Processes and Landforms*, *43*(10), pp. 2136–2146.

Gilleland, E. (2021). Package "extRemes": Extreme Value Analysis. R package documentation (R Report), 130 p.

Gilleland, E., & Katz, R. W. (2016). ExtRemes 2.0: An extreme value analysis package in R. *Journal of Statistical Software*, *72*(8).

Girardeau-Montaut, D., Roux, M., Marc, R., & Thibault, G. (2005). Change detection on point cloud data acquired with a ground laser scanner. *The International Archives of Photogrammetry, Remote Sensing and Spatial Information Sciences*, *36*(3), W19.

Gischig, V. S., Moore, J. R., Evans, K. F., Amann, F., & Loew, S. (2011a). Thermomechanical forcing of deep rock slope deformation: 1. Conceptual study of a simplified slope. *Journal of Geophysical Research: Earth Surface*, *116*(4), pp. 1–18.

Gischig, V. S., Moore, J. R., Evans, K. F., Amann, F., & Loew, S. (2011b). Thermomechanical forcing of deep rock slope deformation: 2. the Randa rock slope instability. *Journal of Geophysical Research: Earth Surface*, *116*(4), pp. 1–17.

Goldstein, M. L., Morris, S. A., & Yen, G. G. (2004). Problems with fitting to the power-law distribution. *The European Physical Journal B - Condensed Matter and Complex Systems 2004 41:2*, *41*(2), pp. 255–258.

Gómez-Heras, M., Smith, B. J., & Fort, R. (2006). Surface temperature differences between minerals in crystalline rocks: Implications for granular disaggregation of granites through thermal fatigue. *Geomorphology*, *78*(3–4), pp. 236–249.

Goudie, A. (1989). Weathering processes. In D. Thomas (Ed.), *Arid zone geomorphology*. New York: Halsted Press: A division of John Wiley & Sons, Inc., , pp 11-24.

Goudie, A. S., & Viles, H. (2010). Weathering hazards. In I. Alcántara-Ayala & A. Goudie (Eds.), Geomorphological Hazards and Disaster Prevention. Cambridge: Cambridge University Press, pp. 145–160.

Greif, V., Brcek, M., Vlcko, J., Varilova, Z., & Zvelebil, J. (2017). Thermomechanical behavior of Pravcicka Brana Rock Arch (Czech Republic). *Landslides*, *14*(4), pp. 1441–1455.

Grossi, C. M., Brimblecombe, P., Menéndez, B., Benavente, D., Harris, I., & Déqué, M. (2011). Climatology of salt transitions and implications for stone weathering. *Science of the Total Environment*, *409*(13), pp, 2577–2585.

Gruber, S., Hoelzle, M., & Haeberli, W. (2004). Permafrost thaw and destabilization of Alpine rock walls in the hot summer of 2003. *Geophysical Research Letters*, *31*(13), 4 p.

Guerin, A., Jaboyedoff, M., Collins, B. D., Derron, M. H., Stock, G. M., Matasci, B., Boesiger, M., Lefeuvre, C., & Podladchikov, Y. Y. (2019). Detection of rock bridges by infrared thermal imaging and modeling. *Scientific Reports, Nature research*, *9*(1), 9 p.

Guerin, A., Jaboyedoff, M., Collins, B. D., Stock, G. M., Derron, M. H., Abellán, A., & Matasci, B. (2021). Remote thermal detection of exfoliation sheet deformation. *Landslides*, 18(3), pp. 865–879.

Gunzburger, Y., Merrien-Soukatchoff, V., & Guglielmi, Y. (2005). Influence of daily surface temperature fluctuations on rock slope stability: Case study of the Rochers de Valabres slope (France). *International Journal of Rock Mechanics and Mining Sciences*, *42*(3), pp. 331–349.

Gunzburger, Y., & Merrien-Soukatchoff, V. (2011). Near-surface temperatures and heat balance of bare outcrops exposed to solar radiation. *Earth Surface Processes and Landforms*, *36*(12), pp. 577–1589.

Guzzetti, F., Carrara, A., Cardinali, M., & Reichenbach, P. (1999). Landslide hazard evaluation: a review of current techniques and their application in a multi-scale study, Central Italy. *Geomorphology*, 31, pp. 181-216.

Guzzetti, F., Reichenbach, P., Cardinali, M., Galli, M., & Ardizzone, F. (2005). Probabilistic landslide hazard assessment at the basin scale. *Geomorphology*, *72*(1–4), pp. 272–299.

Guzzetti, F., Peruccacci, S., Rossi, M., & Stark, C. P. (2007). Rainfall thresholds for the initiation of landslides in central and southern Europe. *Meteorology and Atmospheric Physics*, *98*(3–4), pp. 239–267.

Guzzetti, F., Peruccacci, S., Rossi, M., & Stark, C. P. (2008). The rainfall intensity-duration control of shallow landslides and debris flows: An update. *Landslides*, *5*(1), pp. 3–17.

Hallet, B., Hunter, L., & Bogen, J. (1996). Rates of erosion and sediment evacuation by glaciers: A review of field data and their implications. *Global and Planetary Change*, *12*(1–4), pp. 213–235.

Hallet, B. (2006). Why do freezing rocks break? *Science*, *314*(5802), pp. 1092–1093.

Hodge, R., Brasington, J., & Richards, K. (2009). In situ characterization of grain-scale fluvial morphology using Terrestrial Laser Scanning. *Earth Surface Processes and Landforms*, *34*(7), pp. 954–968.

Hoek, E., & Bray, J. (1981). *Rock Slope Engineering* (3rd ed.). London: Inst. Mining and Metallurgy, 368 p.

InraTec GmbH. (2017). *VarioCAM ® HD head: User Manual.* Dresden, Germany: InfraTec. *31 p.*

InfraTec GmbH. (2018). *IRBIS ® 3.1 Infrared Thermographic Software: User Manual.* Dresden, Germany: InfraTec, 130 p.

InfraTec GmbH. (2021). *Radiometric Correction in IRBIS 3.1: Calculation Basics and Formulas.* Dresden, Germany: InfraTec, 4 p.

Iverson, R. M. (2000). Landslide triggering by rain infiltration. *Water Resources Research*, *36*(7), pp. 897–1910.

Jaboyedoff, M., Oppikofer, T., Abellán, A., Derron, M. H., Loye, A., Metzger, R., & Pedrazzini, A. (2012). Use of LIDAR in landslide investigations: A review. *Natural Hazards*, 61(1), pp. 5–28.

Jaiswal, P., & van Westen, C. J. (2009). Estimating temporal probability for landslide initiation along transportation routes based on rainfall thresholds. *Geomorphology*, *112*(1–2), pp. 96–105.

James, M. R., Robson, S., Pinkerton, H., & Ball, M. (2006). Oblique photogrammetry with visible and thermal images of active lava flows. *Bulletin of Volcanology*, *69*(1), pp. 105–108.

Jenkins, K. A., & Smith, B. J. (1990). Daytime rock surface temperature variability and its implications for mechanical rock weathering: Tenerife, Canary Islands. *Catena*, *17*(4–5), pp. 449–459.

Jennings, J. E. (1970). A mathematical theory for the calculation of the stability of open cast mines. Proc. Symp. On the Theoretical Background of the Planning of Open Pit Mines, pp. 87–102.

Johannessen, C. L., Feiereisen, J. J., & Wells, A. N. (1982). Weathering of ocean cliffs by salt expansion in a mid-latitude coastal environment. *Shore Beach*, 50, pp. 26–34.

Julian, M., & Anthony, E. (1996). Aspects of landslide activity in the Mercantour Massif and the French Riviera, southeastern France. *Geomorphology*, *15*(3–4), pp. 275–289.

Keefer, D. K., Wilson, R. C., Mark, R. K., Brabb, E. E., Brown, W. M., Ellen, S. D., Harp, E. L., Wieczorek, G. F., Alger, C. S., & Zatkin, R. S. (1987). Real-Time Landslide Warning During Heavy Rainfall. *Science*, *238*(4829), pp. 921–925.

Kern, Clifford. (1928). *Evaluation of infrared emission of cloud and ground as measured by weather satellites.* Defence Documentation Center (USA), AD 617 417.

Khan, A., Chatterjee, S., & Weng, Y. (2021). Characterizing thermal fields and evaluating UHI effects. In Khan, A., Chatterjee, S., & Weng, Y. (Eds.). *Urban Heat Island Modeling for Tropical Climates*. Elsevier, pp. 37–67.

Knight Optical Ltd. (2015). *Optical Glasses (Technical Report).* United Kingdom: Knight Optical Ltd., 1 p.

Kotthaus, S., Smith, T. E. L., Wooster, M. J., & Grimmond, C. S. B. (2014). Derivation of an urban materials spectral library through emittance and reflectance spectroscopy. *ISPRS Journal of Photogrammetry and Remote Sensing*, *94*, pp. 194–212.

Kromer, R. A., Hutchinson, D. J., Lato, M. J., Gauthier, D., & Edwards, T. (2015a). Identifying rock slope failure precursors using LiDAR for transportation corridor hazard management. *Engineering Geology*, *195*, pp. 93–103.

Kromer, R. A., Abellán, A., Hutchinson, D. J., Lato, M., Edwards, T., & Jaboyedoff, M. (2015b). A 4D filtering and calibration technique for small-scale point cloud change detection with a terrestrial laser scanner. *Remote Sensing*, *7*(10), pp. 13029–13058.

Kromer, R. A., Abellán, A., Hutchinson, D. J., Lato, M., Chanut, M. A., Dubois, L., & Jaboyedoff, M. (2017a). Automated terrestrial laser scanning with near-real-time change detection - Monitoring of the Séchilienne landslide. *Earth Surface Dynamics*, *5*(2), pp. 293–310.

Kromer, R., Lato, M., Hutchinson, D. J., Gauthier, D., & Edwards, T. (2017b). Managing rockfall risk through baseline monitoring of precursors using a terrestrial laser scanner. *Canadian Geotechnical Journal*, *54*(7), pp. 953–967.

Lague, D., Brodu, N., & Leroux, J. (2013). Accurate 3D comparison of complex topography with terrestrial laser scanner: Application to the Rangitikei canyon (N-Z). *ISPRS Journal of Photogrammetry and Remote Sensing*, *82*, pp. 10–26.

Lato, M. J., Diederichs, M. S., & Hutchinson, D. J. (2010). Bias correction for view-limited lidar scanning of rock outcrops for structural characterization. *Rock Mechanics and Rock Engineering*, *43*(5), pp. 615–625.

Lawrence, J. A., Mortimore, R. N., Stone, K. J., & Busby, J. P. (2013). Sea saltwater weakening of chalk and the impact on cliff instability. *Geomorphology*, *191*, pp. 14–22.

Lewkowicz, A. G. (2001). Temperature regime of a small sandstone tor, latitude 80 °N, Ellesmere Island, Nunavut, Canada. *Permafrost and Periglacial Processes*, *12*(4), pp. 351–366.

Leyva, S., Cruz-Pérez, N., Rodríguez-Martín, J., Miklin, L., & Santamarta, J. C. (2022). Rockfall and Rainfall Correlation in the Anaga Nature Reserve in Tenerife (Canary Islands, Spain). *Rock Mechanics and Rock Engineering*, *55*(4), pp. 2173–2181.

Lichti, D. D., Gordon, S. J., & Tipdecho, T. (2005). Error Models and Propagation in Directly Georeferenced Terrestrial Laser Scanner Networks. *Journal of Surveying Engineering*, *131*(4), pp. 135–142.

Lichti, D. D., & Jamtsho, S. (2006). Angular resolution of terrestrial laser scanners. *The Photogrammetric Record*, *21*(114), pp. 141–160.

Lillesand, T., Kiefer, R., & Chipman, J. (2015). *Remote Sensing and Image Interpretation* (7th ed.). USA: Wiley, 720 p.

Lim, M., Petley, D. N., Rosser, N. J., Allison, R. J., Long, A. J., & Pybus, D. (2005). Combined digital photogrammetry and time-of-flight laser scanning for monitoring cliff evolution. *Photogrammetric Record*, *20*(110), pp. 109–129.

Lim, M., Rosser, N. J., Allison, R. J., & Petley, D. N. (2010). Erosional processes in the hard rock coastal cliffs at Staithes, North Yorkshire. *Geomorphology*, *114*(1–2), pp. 12–21.

Lockwood, J. (2017). Atmospheric processes. In J. Holden (Ed.), *An Introduction to Physical Geography and the Environment*. Harlow, UK: Pearson, 810 p.

Loiotine, L., Andriani, G. F., Derron, M. H., Parise, M., & Jaboyedoff, M. (2022). Evaluation of InfraRed Thermography Supported by UAV and Field Surveys for Rock Mass Characterization in Complex Settings. *Geosciences, 12*, 116, 19 p.

Luckman, B. H. (1976). Rockfalls and rockfall inventory data: Some observations from surprise valley, Jasper National Park, Canada. *Earth Surface Processes*, *1*(3), pp. 287–298.

Lugli, S. (2009). Evaporites. In V. Gornitz (Ed.), E*ncyclopedia of Paleoclimatology and Ancient Environments. Encyclopedia of Earth Sciences Series*. Springer, Dordrecht, pp. 4020–4411.

Malamud, B. D., Turcotte, D. L., Guzzetti, F., & Reichenbach, P. (2004). Landslide inventories and their statistical properties. *Earth Surface Processes and Landforms*, *29*(6), pp. 687–711.

Marmoni, G. M., Fiorucci, M., Grechi, G., & Martino, S. (2020). Modelling of thermo-mechanical effects in a rock quarry wall induced by near-surface temperature fluctuations. *International Journal of Rock Mechanics and Mining Sciences*, *134*, pp. 1-20.

Martel, S. J. (2006). Effect of topographic curvature on near-surface stresses and application to sheeting joints. Geophysical Research Letters, 33(1), pp. 1-5.

Martínez-Martínez, J., Abellán, A., & Berrezueta, E. (2022). Erosion directionality and seasonality study using the anisotropy matrix. Application in a semiarid Mediterranean climate (SE Spain). *Science of the Total Environment*, *804*, 14 p.

Marzorati, S., Luzi, L., & de Amicis, M. (2002). Rock falls induced by earthquakes: a statistical approach. Soil Dynamics and Earthquake Engineering, 22(7), pp. 565–577.

Matsuoka, N. (1990). The rate of bedrock weathering by frost action: Field measurements and a predictive model. *Earth Surface Processes and Landforms*, *15*(1), pp. 73–90.

Matsuoka, N. (1991). A model of the rate of frost shattering: Application to field data from Japan, Svalbard and Antarctica. *Permafrost and Periglacial Processes*, *2*(4), pp. 271–281.

Matsuoka, N., & Sakai, H. (1999). Rockfall activity from an alpine cliff during thawing periods. *Geomorphology*, *28*(3–4), pp. 309–328.

Matsuoka, N. (2008). Frost weathering and rockwall erosion in the southeastern Swiss Alps: Long-term (1994-2006) observations. *Geomorphology*, *99*(1–4), pp. 353–368.

Matsuoka, N. (2019). A multi-method monitoring of timing, magnitude and origin of rockfall activity in the Japanese Alps. *Geomorphology*, *336*, pp. 65–76.

McFadden, L. D., Eppes, M. C., Gillespie, A. R., & Hallet, B. (2005). Physical weathering in arid landscapes due to diurnal variation in the direction of solar heating. *Bulletin of the Geological Society of America*, *117*(1–2), pp. 161–173.

McGreevy, J.P. (1982). 'frost and salt' weathering: Further experimental results. *Earth Surface Processes and Landforms*, 7(5), pp. 475–488.

McGreevy, J. P., & Whalley, W. B. (1982). The Geomorphic Significance of Rock Temperature Variations in Cold Environments: A Discussion. *Arctic and Alpine Research*, *14*(2), pp. 157–162.

McGreevy, J. P. (1985). Thermal properties as controls on rock surface temperature maxima, and possible implications for rock weathering. *Earth Surface Processes and Landforms*, *10*(2), pp. 125–136.

McGreevy, J. P., Warke, P. A., & Smith, B. J. (2000). Controls on stone temperatures and the benefits of interdisciplinary exchange. *Journal of the American Institute for Conservation*, *39*(2), pp. 259–274.

Mclnnes, R. G., & Moore, R. (2011). Cliff Instability and Erosion Management in Great Britain: A Good Practice Guide. Halcrow Group Ltd, Birmingham, 87 p.

Messenzehl, K., Meyer, H., Otto, J. C., Hoffmann, T., & Dikau, R. (2017). Regional-scale controls on the spatial activity of rockfalls (Turtmann Valley, Swiss Alps) — A multivariate modeling approach. *Geomorphology*, *287*, pp. 29–45.

Miller, P. E. (2007). *A robust surface matching technique for coastal geohazard monitoring*. PhD Thesis, Newcastle University.

Mitra, N. J., Gelfand, N., Pottmann, H., & Guibas, L. (2004). Registration of point cloud data from a geometric optimization perspective. *ACM International Conference Proceeding Series*, *71*, pp. 22–31.

Molaro, J. L., & Mckay, C. P. (2010). Processes controlling rapid temperature variations on rock surfaces. *Earth Surface Processes and Landforms*, *35*(5), pp. 501–507.

Moore, R., & Mclnnes, R. G. (2020). Coastal Erosion and Climate Change: Guidance for policymakers, Planners and Stakeholders, Jacobs, 87 p.

Mottershead, D. N. (1989). Rates and patterns of bedrock denudation by coastal salt spray weathering: A seven-year record. *Earth Surface Processes and Landforms*, 14(5), pp. 383–398.

Mufundirwa, A., Fujii, Y., Kodama, N., & Kodama, J. Ichi. (2011). Analysis of natural rock slope deformations under temperature variation: A case from a cool temperate region in Japan. *Cold Regions Science and Technology*, *65*(3), pp. 488–500.

Murton, J. B., Peterson, R., & Ozouf, J. C. (2006). Bedrock fracture by ice segregation in cold regions. *Science*, *314*(5802), pp. 1127–1129.

Nissen, K. M., Rupp, S., Kreuzer, T. M., Guse, B., Damm, B., & Ulbrich, U. (2022). Quantification of meteorological conditions for rockfall triggers in Germany. *Natural Hazards and Earth System Sciences*, 22(6), pp. 2117–2130

Norman, C. (2012). *Microseismic monitoring of the controls on coastal rock cli erosion*. PhD Thesis, Durham University. Available at Durham E-Theses Online: http://etheses.dur.ac.uk/3586/

Norman, E. C., Rosser, N. J., Brain, M. J., Petley, D. N., & Lim, M. (2013). Coastal cliff-top ground motions as proxies for environmental processes. *Journal of Geophysical Research: Oceans*, *118*(12), pp. 6807–6823.

Oguchi, C. T., & Yu, S. (2021). A review of theoretical salt weathering studies for stone heritage. *Progress in Earth and Planetary Science*, 8(1), pp. 1- 23.

Ojo, O., & Brook, N. (1990). The effect of moisture on some mechanical properties of rock. *Mining Science and Technology*, 10, pp. 145–156.

Ollier, C. (1984). *Weathering* (2nd ed.). London: Longman, 270 p.

Olsen, M. J., Johnstone, E., Driscoll, N., Ashford, S. A., & Kuester, F. (2009). Terrestrial Laser Scanning of Extended Cliff Sections in Dynamic Environments: Parameter Analysis. *Journal of Surveying Engineering*, *135*(4), pp. 161–169.

Olsen, M. J., Kuester, F., Chang, B. J., & Hutchinson, T. C. (2010). Terrestrial Laser Scanning-Based Structural Damage Assessment. *Journal of Computing in Civil Engineering*, *24*(3), pp. 264–272.

Olsen, M. J., Wartman, J., McAlister, M., Mahmoudabadi, H., O'Banion, M. S., Dunham, L., & Cunningham, K. (2015). To Fill or Not to Fill: Sensitivity Analysis of the Influence of Resolution and Hole Filling on Point Cloud Surface Modeling and Individual Rockfall Event Detection. *Remote Sensing*, *7*(9), pp. 12103–12134.

Oppikofer, T., Jaboyedoff, M., & Keusen, H. R. (2008). Collapse at the eastern Eiger flank in the Swiss Alps. *Nature Geoscience 2008 1:8*, *1*(8), pp. 531–535.

Oppikofer, T., Jaboyedoff, M., Blikra, L., Derron, M. H., & Metzger, R. (2009). Characterization and monitoring of the Åknes rockslide using terrestrial laser scanning. *Natural Hazards and Earth System Science*, *9*(3), pp. 1003–1019.

Owen, J. J., Amundson, R., Dietrich, W. E., Nishiizumi, K., Sutter, B., & Chong, G. (2011). The sensitivity of hillslope bedrock erosion to precipitation. *Earth Surface Processes and Landforms*, 36(1), pp. 117–135.

Paluš, M., Novotná, D., & Zvelebil, J. (2004). Fractal rock slope dynamics anticipating a collapse. *Physical Review E* , *70*(3), pp. 0362121–0362127.

Pappalardo, G., Mineo, S., Zampelli, S. P., Cubito, A., & Calcaterra, D. (2016). InfraRed Thermography proposed for the estimation of the Cooling Rate Index in the remote survey of rock masses. *International Journal of Rock Mechanics and Mining Sciences*, *83*, pp. 182–196.

Pappalardo, G., & Mineo, S. (2017). Investigation on the mechanical attitude of basaltic rocks from Mount Etna through InfraRed Thermography and laboratory tests. *Construction and Building Materials*, *134*, pp. 228–235.

Parker, R. N., Densmore, A. L., Massey, C. I., Petley, D. N., Rosser, N. J., & Hancox, G. T. (2015). Spatial distributions of earthquake-induced landslides and hillslope preconditioning in the northwest South Island, New Zealand. *Earth Surface Dynamics*, *3*(4), pp. 501–525.

Peel, M. C., Finlayson, B. L., & Mcmahon, T. A. (2007). Updated world map of the Köppen-Geiger climate classification. *Hydrology and Earth System Sci*ence, 11(5), pp. 1633-1644.

Pei, X., Luo, J., & Huang, R. (2019). Failure mechanisms of wind-induced post-seismic rockfall hazard. *Bulletin of Engineering Geology and the Environment*, 78(8), pp. 5707–5725.

Phillips, M., Wolter, A., Lüthi, R., Amann, F., Kenner, R., & Bühler, Y. (2017). Rock slope failure in a recently deglaciated permafrost rock wall at Piz Kesch (Eastern Swiss Alps), February 2014. *Earth Surface Processes and Landforms*, *42*(3), pp. 426–438.

Powell, J. H. (2010). Jurassic sedimentation in the Cleveland Basin: a review. *Proceedings of the Yorkshire Geological Society*, *58*(1), pp. 21–72.

Pradhan, S., Toll, D. G., Rosser, N. J., & Brain, M. J. (2022). An investigation of the combined effect of rainfall and road cut on landsliding. *Engineering Geology*, *307*.

Prémaillon, M., Regard, V., Dewez, T. J. B., & Auda, Y. (2018). GlobR2C2 (Global Recession Rates of Coastal Cliffs): A global relational database to investigate coastal rocky cliff erosion rate variations. *Earth Surface Dynamics*, 6(3), pp. 651–668.

Prick, A. (1997). Critical degree of saturation as a threshold moisture level in frost weathering of limestones. *Permafrost and Periglacial Processes*, *8*(1), pp. 91–99.

Prick, A. (2006). Frost and frost weathering. In A. Goudie (Ed.), *Encyclopedia of Geomorphology* (Vol. 1st), London & New Yor: Routledge Taylor & Francis Group, 1156 p.

Rabbani, T., Dijkman, S., van den Heuvel, F., & Vosselman, G. (2007). An integrated approach for modelling and global registration of point clouds. *ISPRS Journal of Photogrammetry and Remote Sensing*, *61*(6), pp. 355–370.

Rafferty, J. (2012). *Rocks* (1st ed.). Britannica Educational Publishing, New York. 271 p.

Rawson, P. F., & Wright, J. K. (2000). The Yorkshire Coast. Geologist's Association Guide. *The Geologist's Association. Piccadilly, London: Burlington House, 34* p.

Rees, W. G. (2001). *Physical Principles of Remote Sensing* (2nd ed.). Cambridge University Press.

Riegl. (2007). *Data Sheet Riegl VZ-1000.* Available at (Accessed: 9 February 2023): http://www.riegl.com/uploads/tx_pxpriegldownloads/DataSheet_VZ-1000_2017-06-14.pdf

Rodrıguez, C. E., Bommer, J. J., & Chandler, R. J. (1999). Earthquake-induced landslides 1980–1997. *Soil dynamics and earthquake engineering*, *18*, pp. 325–346.

Rosser, N. J., Petley, D. N., Lim, M., Dunning, S. A., & Allison, R. J. (2005). Terrestrial laser scanning for monitoring the process of hard rock coastal cliff erosion. *Quarterly Journal of Engineering Geology and Hydrogeology*, *38*(4), pp. 363–375.

Rosser, N., Lim, M., Petley, D., Dunning, S., & Allison, R. (2007). Patterns of precursory rockfall prior to slope failure. *Journal of Geophysical Research: Earth Surface*, *112*(F4), 14 p.

Rosser, N. J., Brain, M. J., Petley, D. N., Lim, M., & Norman, E. C. (2013). Coastline retreat via progressive failure of rocky coastal cliffs. *Geology*, *41*(8), pp. 939–942.

Ruiz-Agudo, E., Putnis, C. V., Pel, L., & Rodriguez-Navarro, C. (2013). Template-assisted crystallization of sulfates onto calcite: Implications for the prevention of salt damage. *Crystal Growth and Design*, 13(1), pp. 40–51.

Rundel, P. W., Dillon, M. O., Palma, B., Mooney, H. A., Gulmon, S. L., & Ehleringer, J. R. (1991). The Phytogeography and Ecology of the Coastal Atacama and Peruvian Deserts. *Aliso: A Journal of Systematic and Floristic Botany*, 13, pp. 1–49.

Sala, Z., Jean Hutchinson, D., & Harrap, R. (2019). Simulation of fragmental rockfalls detected using terrestrial laser scans from rock slopes in south-central British Columbia, Canada. *Natural Hazards and Earth System Sciences*, *19*(11), pp. 2385–2404.

Salisbury, J. W., & D'Aria, D. (1992). Emissivity of Terrestrial Materials in the 8 - 14 μm Atmospheric Window. *Remote Sensing of Environment*, *42*, pp. 83–106.

Salisbury, J. W., & D'Aria, D. (1994). Emissivity of Terrestrial Materials in the 3 - 5 μm Atmospheric Window. *Remote Sensing of Environment*, *47*, pp. 345–361.

Sass, O. (2005). Rock moisture measurements: Techniques, results, and implications for weathering. *Earth Surface Processes and Landforms*, 30(3), pp. 359–374.

Sass, O., & Oberlechner, M. (2012). Is climate change causing increased rockfall frequency in Austria? *Natural Hazards and Earth System Science*, *12*(11), pp. 3209–3216

Schmidlin, T. W., Dethier, B. E., Eggleston, K. L., Schmidlin, T. W., Dethier, B. E., & Eggleston, K. L. (1987). Freeze-Thaw Days in the Northeastern United States. *Journal of Applied Meteorology*, *26*(1), pp. 142–155.

Schmidt, J. U., Etzelmüller, B., Schuler, T. V., Magnin, F., Boike, J., Langer, M., & Westermann, S. (2021). Surface temperatures and their influence on the permafrost thermal regime in high-Arctic rock walls on Svalbard. *Cryosphere*, *15*(5), pp. 2491–2509.

Schumm, S. (1977). *The fluvial system*. New York: John Wiley & Sons, 338 p. .

Schürch, P., Densmore, A. L., Rosser, N. J., Lim, M., & Mcardell, B. W. (2011). Detection of surface change in complex topography using terrestrial laser scanning: application to the Illgraben debris-flow channel. *Earth Surface Processes and Landforms*, *36*(14), pp. 1847–1859.

Shan, Jie., & Toth, C. K. (2008). *Topographic Laser Ranging and Scanning: Principles and Processing*. LLC, UK: CRC Press/Taylor & Francis Group, 590 p.

Skinner, B. (1966). Thermal expansion. In S. Clark (Ed.), *Handbook of Physical Constantes*. Geological Society of America, Boulder, CO.

Smets, B., d'Oreye, N., Kervyn, M., & Kervyn, F. (2017). Gas piston activity of the Nyiragongo lava lake: First insights from a Stereographic Time-Lapse Camera system. *Journal of African Earth Sciences*, *134*, pp. 874–887.

Smith, B. (1994). Weathering processes and forms. In A. Abrahams & A. Parsons (Eds.), *Geomorphology of desert environments*. London: Chapman and Hall, pp. 39-63.

Spampinato, L., Calvari, S., Oppenheimer, C., & Boschi, E. (2011). Volcano surveillance using infrared cameras. *Earth-Science Reviews*, *106*(1–2), pp. 63–91.

Stark, C. P., & Guzzetti, F. (2009). Landslide rupture and the probability distribution of mobilized debris volumes. *Journal of Geophysical Research: Earth Surface*, 114 (F2), 16 p.

Steiger, M. (2005a). Crystal growth in porous materials - I: The crystallization pressure of large crystals. *Journal of Crystal Growth*, 282(3–4), pp. 455–469.

Steiger, M. (2005b). Crystal growth in porous materials - II: Influence of crystal size on the crystallization pressure. *Journal of Crystal Growth*, 282(3–4), pp. 470–481.

Stoffel, M., Ballesteros Cánovas, J. A., Luckman, B. H., Casteller, A., & Villalba, R. (2019). Tree-ring correlations suggest links between moderate earthquakes and distant rockfalls in the Patagonian Cordillera. *Scientific Reports*, 9:12112, 9 p.

Stumpf, A., Malet, J. P., Allemand, P., Pierrot-Deseilligny, M., & Skupinski, G. (2015). Ground-based multi-view photogrammetry for the monitoring of landslide deformation and erosion. *Geomorphology*, *231*, pp. 130–145.

Sturzenegger, M., & Stead, D. (2009a). Quantifying discontinuity orientation and persistence on high mountain rock slopes and large landslides using terrestrial remote sensing techniques. *Natural Hazards and Earth System Sciences*, 9, pp. 267-287.

Sturzenegger, M., & Stead, D. (2009b). Close-range terrestrial digital photogrammetry and terrestrial laser scanning for discontinuity characterization on rock cuts. *Engineering Geology*, *106*(3–4), pp. 163–182.

Teza, G., Galgaro, A., Zaltron, N., & Genevois, R. (2007). Terrestrial laser scanner to detect landslide displacement fields: A new approach. *International Journal of Remote Sensing*, *28*(16), pp. 3425–3446.

Teza, G., Marcato, G., Castelli, E., & Galgaro, A. (2012). IRTROCK: A MATLAB toolbox for contactless recognition of surface and shallow weakness of a rock cliff by infrared thermography. *Computers and Geosciences*, *45*, pp. 109–118.

Trenhaile, A. S. (2011). Predicting the response of hard and soft rock coasts to changes in sea level and wave height. *Climatic Change*, *109*(3–4), pp. 599–615.

UKCP. (2022). *UK Climate Projections: Headline Findings* (Report). Available at: www.metoffice.gov.uk (Accessed: 19 February 2023).

van Veen, M., Hutchinson, D. J., Kromer, R., Lato, M., & Edwards, T. (2017). Effects of sampling interval on the frequency - magnitude relationship of rockfalls detected from terrestrial laser scanning using semi-automated methods. *Landslides*, *14*(5), pp. 1579–1592.

Vann Jones née Norman, E. C., Rosser, N. J., Brain, M. J., & Petley, D. N. (2015). Quantifying the environmental controls on erosion of a hard rock cliff. *Marine Geology*, *363*, pp. 230–242.

Veveakis, E., Vardoulakis, I., & di Toro, G. (2007). Thermoporomechanics of creeping landslides: The 1963 Vaiont slide, northern Italy. *Journal of Geophysical Research: Earth Surface*, *112*, F03026, pp. 1-21.

Villarraga, C. J., Gasc-Barbier, M., Vaunat, J., & Darrozes, J. (2018). The effect of thermal cycles on limestone mechanical degradation. *International Journal of Rock Mechanics and Mining Sciences*, 109, pp. 115–123.

Vlcko, J., Greif, V., Grof, V., Jezny, M., Petro, L., & Brcek, M. (2009). Rock displacement and thermal expansion study at historic heritage sites in Slovakia. *Environmental Geology*, *58*(8), pp. 1727–1740.

Voigtländer, A., Leith, K., & Krautblatter, M. (2018). Subcritical Crack Growth and Progressive Failure in Carrara Marble Under Wet and Dry Conditions. *Journal of Geophysical Research: Solid Earth*, *123*(5), pp. 3780–3798.

Warren, K., Eppes, M. C., Swami, S., Garbini, J., & Putkonen, J. (2013). Automated field detection of rock fracturing, microclimate, and diurnal rock temperature and strain fields. *Geoscientific Instrumentation, Methods and Data Systems*, *2*(2), pp. 275–288.

Westermann, S., Lüers, J., Langer, M., Piel, K., & Boike, J. (2009). The annual surface energy budget of a high-arctic permafrost site on Svalbard, Norway. *Cryosphere*, *3*(2), pp. 245–263.

Whadcoat, S. K. (2017). *Numerical modelling of rockfall evolution in hard rock slopes*. PhD Thesis, Durham University. Available at Durham E-Theses Online: http://etheses.dur.ac.uk/11994/

Wheaton, J. M., Brasington, J., Darby, S. E., & Sear, D. A. (2010). Accounting for uncertainty in DEMs from repeat topographic surveys: improved sediment budgets. *Earth Surface Processes and Landforms*, *35*(2), pp. 136–156.

Williams, J. G. (2017). *Insights into rockfall from constant 4D monitoring*. PhD Thesis, Durham University. Available at Durham E-Theses Online: http://etheses.dur.ac.uk/12172/

Williams, J. G., Rosser, N. J., Hardy, R. J., Brain, M. J., & Afana, A. A. (2018). Optimising 4-D surface change detection: An approach for capturing rockfall magnitude-frequency. *Earth Surface Dynamics*, *6*(1), pp. 101–119.

Williams, J. G., Rosser, N. J., Hardy, R. J., & Brain, M. J. (2019). The Importance of Monitoring Interval for Rockfall Magnitude-Frequency Estimation. *Journal of Geophysical Research: Earth Surface*, *124*(12), pp. 2841–2853.

Williams, P. (1995). Permafrost and climate change: geotechnical implications. *Philosophical Transactions of the Royal Society of London. Series A: Physical and Engineering Sciences*, *352*(1699), pp. 347–358.

Williams, R. D. (2012). DEMs of Difference. *Geomorphological Techniques.* British Society for Geomorphology *(BSG),* Chapter *2*, pp. 1–17.

Williams, R. B. G., & Robinson, D. A. (1991). Frost weathering of rocks in the presence of salts - a review. *Permafrost and Periglacial Processes*, 2, pp. 347–353.

Williams, R. B. G., & Robinson, D. A. (2001). Experimental frost weathering of sandstone by various combinations of salts. *Earth Surface Processes and Landforms*, 26(8), pp. 811–818.

Wolman, M. G., & Miller, J. P. (1960). Magnitude and Frequency of Forces in Geomorphic Processes. *The Journal of Geology*, *68*(1), pp. 54–74.

Wong, L. N. Y., Maruvanchery, V., & Liu, G. (2016). Water effects on rock strength and stiffness degradation. *Acta Geotechnica,* 11(4), pp. 713–737.

Woolf, D. K., Challenor, P. G., & Cotton, P. D. (2002). Variability and predictability of the North Atlantic wave climate. *Journal of Geophysical Research: Oceans*, *107*(C10), 14 p.

Wu, J. H., Lin, H. M., Lee, D. H., & Fang, S. C. (2005). Integrity assessment of rock mass behind the shotcreted slope using thermography. *Engineering Geology*, *80*(1–2), pp. 164–173.

Yagoda-Biran, G., Hatzor, Y. H., Amit, R., & Katz, O. (2010). Constraining regional paleo peak ground acceleration from back analysis of prehistoric landslides: Example from Sea of Galilee, Dead Sea transform. *Tectonophysics*, *490*(1–2), pp. 81–92.

Yang, C., & Medioni, G. (1992). Object modelling by registration of multiple range images. *Image and Vision Computing*, *10*(3), pp. 145–155.

Yang, X., Wang, J., Zhu, C., He, M., & Gao, Y. (2019). Effect of wetting and drying cycles on microstructure of rock based on SEM. *Environmental Earth Sciences*, 78(6), pp. 1–10.

Yatsu, E. (1988). *The nature of weathering: an introduction*. Sozosha, Tokyo, 634 pp.

Zahs, V., Hämmerle, M., Anders, K., Hecht, S., Sailer, R., Rutzinger, M., Williams, J. G., & Höfle, B. (2019). Multi-temporal 3D point cloud-based quantification and analysis of geomorphological activity at an alpine rock glacier using airborne and terrestrial LiDAR. *Permafrost and Periglacial Processes*, *30*(3), pp. 222–238.

Zheng, L., Wu, Y., Zhu, Z., Ren, K., Wei, Q., Wu, W., & Zhang, H. (2022). Investigating the Role of Earthquakes on the Stability of Dangerous Rock Masses and Rockfall Dynamics. *Frontiers in Earth Science*, 9:824889, 11 p.

Appendices

Appendix A - Non-parametric statistical tests to determine significant difference in the surface temperatures of the cliff face when there are and there are not rockfalls

Table 1. *Results of non-parametric statistical tests to determine significant difference in the surface temperatures of the cliff face when there are and there are not rockfalls during key daily thermal phases of each season. Bold italicised p-values are significantly different ($p < 0.05$). Bold underlined p-values are close to being significant at $p = 0.05$.*

Season	Thermal phase	Temperature parameter (°C)	Mann-Whitney test statistic	p-value	95% Confidence Interval	Difference in medians
Winter	Midnight	**Mean T.**	686	***0.0005***	1.22 to 3.32	2.62
		Minimum T.	636	***0.0060***	0.52 to 2.23	1.35
		Maximum T	702	***0.0002***	0.56 to 3.36	2.58
	Sunrise	Mean T.	1776	0.7463	-0.50 to 1.18	0.15
		Minimum T.	1949	0.2061	-0.18 to 1.60	0.68
		Maximum T	1874	0.3917	-0.41 to 1.11	0.47
	Noon	Mean T.	391	0.5610	-1.21 to 2.65	0.48
		Minimum T.	367	0.8693	-1.40 to 2.26	0.28
		Maximum T	385	0.6337	-1.30 to 2.51	0.40
	Sunset	Mean T.	2650	0.5621	-1.53 to 0.85	-0.35
		Minimum T.	2693	0.6774	-1.43 to 0.89	-0.22
		Maximum T	2589	0.4194	-1.71 to 0.76	-0.47
Spring	Midnight	Mean T.	406	0.2170	-1.35 to 6.90	1.98
		Minimum T.	401	0.2490	-1.52 to 6.16	2.18
		Maximum T	403	0.2390	-1.37 to 8.60	2.30
	Sunrise	Mean T.	773	0.3847	-4.87 to 2.36	-1.59
		Minimum T.	845	0.7700	-3.49 to 2.83	-0.47
		Maximum T	729	0.2218	-8.61 to 1.73	-2.88
	Noon	Mean T.	1269	0.1679	-0.59 to 4.25	1.79
		Minimum T.	1309	0.0930	-0.30 to 4.23	1.98
		Maximum T	1314	0.0859	-0.39 to 5.08	2.26
	Sunset	**Mean T.**	1612	***0.0398***	0.11 to 4.85	2.44
		Minimum T.	1596	**0.0511**	-4.07 to 4.34	2.16
		Maximum T	1622	***0.0338***	0.32 to 7.77	3.67

Table 1 - CONTINUATION. *Results of non-parametric statistical tests to determine significant difference in the surface temperatures of the cliff face when there are and there are not rockfalls during key daily thermal phases of each season. Bold italicised p-values are significantly different ($p < 0.05$). Bold underlined p-values are close to being significant at $p = 0.05$.*

Season	Thermal phase	Temperature parameter (°C)	Mann-Whitney test statistic	p-value	95% Confidence Interval	Difference in medians
Summer	Midnight	Mean T.	571	0.2222	-2.45 to 0.49	-0.69
		Minimum T.	560	0.1827	-2.63 to 0.35	-0.97
		Maximum T	374	***0.0012***	-4.33 to -1.22	-2.29
	Sunrise	Mean T.	777	0.9365	-0.95 to 1.37	0.02
		Minimum T.	768	1.0000	-1.30 to 1.18	-3.83
		Maximum T	730	0.7218	-1.42 to 1.15	-0.28
	Noon	Mean T.	1772	0.6334	-0.75 to 0.61	-0.16
		Minimum T.	1563	0.1310	-0.89 to 0.20	-0.39
		Maximum T	2154	0.1597	-0.35 to 1.72	0.74
	Sunset	**Mean T.**	4866	***0.0115***	0.25 to 1.96	1.16
		Minimum T.	4778	***0.0289***	0.05 to 1.89	0.93
		Maximum T	4663	0.0755	-0.08 to 3.28	1.47
Autumn	Midnight	Mean T.	120	0.4745	-4.56 to 2.36	-0.85
		Minimum T.	122	0.5129	-4.73 to 2.30	-0.69
		Maximum T	120	0.4745	-4.56 to 1.90	-0.74
	Sunrise	**Mean T.**	867	***0.0127***	0.36 to 7.68	4.59
		Minimum T.	851	***0.0211***	0.49 to 7.48	4.42
		Maximum T	887	***0.0066***	0.80 to 7.84	4.11
	Noon	Mean T.	369	0.9379	-3.08 to 4.06	0.40
		Minimum T.	377	0.8286	-2.52 to 4.15	0.41
		Maximum T	375	0.8557	-3.27 to 3.57	0.37
	Sunset	**Mean T.**	1283	***0.0217***	0.50 to 5.24	2.18
		Minimum T.	1285	***0.0210***	0.41 to 4.96	2.44
		Maximum T	1256	***0.0378***	0.28 to 5.10	1.96

Table 2 ANEX. *Results of non-parametric statistical tests to determine significant difference in the rates change of temperature (RCH) across the cliff face when there are and there are not rockfalls during key daily thermal phases of each season. Bold italicised p-values are significantly different (p < 0.05). Bold underlined p-values are close to being significant at p = 0.05.*

Season	Thermal phase	Temperature parameter (°C/h)	Mann-Whitney test statistic	p-value	95% Confidence Interval	Diff. in medians
Winter	Midnight	**Mean RCH**	70	***0.0001***	-0.77 to -0.39	-0.59
		Minimum RCH	87	***0.0001***	-0.95 to -0.54	-0.76
		Maximum RCH	108	***0.0001***	-0.76 to -0.44	-0.56
	Sunrise	**Mean RCH**	1205	***0.0387***	-0.58 to -0.04	-0.28
		Minimum RCH	1851	0.0897	-0.07 to 0.72	0.41
		Maximum RCH	1128	***0.0119***	-1.05 to -0.14	-0.66
	Noon	Mean RCH	250	0.7113	-0.59 to 0.86	0.10
		Minimum RCH	271	0.3835	-0.75 to 1.17	0.37
		Maximum RCH	265	0.4665	-0.46 to 0.83	0.20
	Sunset	Mean RCH	2877	0.0696	-0.01 to 0.37	0.17
		Minimum RCH	3244	***0.0008***	0.21 to 0.84	0.48
		Maximum RCH	2164	0.2475	-0.50 to 0.14	-0.18
Spring	Midnight	Mean RCH	238	0.7179	-0.36 to 0.73	0.06
		Minimum RCH	206	0.7726	-0.79 to 0.84	-0.11
		Maximum RCH	233	0.7964	-0.40 to 0.47	0.06
	Sunrise	**Mean RCH**	498	***0.0256***	-1.65 to -0.08	-0.73
		Minimum RCH	684	0.6081	-0.47 to 0.30	-0.09
		Maximum RCH	519	***0.0416***	-5.02 to -0.04	-1.03
	Noon	Mean RCH	796	0.3255	-0.68 to 0.20	-0.19
		Minimum RCH	597	***0.0067***	-1.80 to -0.22	-0.97
		Maximum RCH	1094	0.1119	-0.05 to 0.89	0.37
	Sunset	**Mean RCH**	1475	***0.0352***	0.03 to 1.06	0.58
		Minimum RCH	1034	0.3098	-1.18 to 0.41	-0.43
		Maximum RCH	1456	***0.0487***	9.07 to 0.01	1.18

Table 2 - CONTINUATION. *Results of non-parametric statistical tests to determine significant difference in the rate of change of temperatures across the cliff face when there are and there are not rockfalls during key daily thermal phases of each season. Bold italicised p-values are significantly different (p < 0.05). Bold underlined p-values are close to being significant at p = 0.05.*

Season	Thermal phase	Temperature parameter (°C/h)	Mann-Whitney test statistic	p-value	95% Confidence Interval	Diff. in medians
Summer	Midnight	Mean RCH	561	0.6763	-0.23 to 0.22	-0.04
		Minimum RCH	756	0.0770	-0.01 to 0.58	0.22
		Maximum RCH	503	0.2809	-0.35 to 0.18	-0.15
	Sunrise	Mean RCH	629	0.7354	-0.32 to 0.58	0.09
		Minimum RCH	648	0.5847	-0.19 to 0.31	0.09
		Maximum RCH	626	0.7653	-0.71 to 0.95	0.12
	Noon	**Mean RCH**	992	**0.0587**	-0.54 to 0.07	-0.25
		Minimum RCH	1174	0.4994	-0.92 to 0.32	-0.40
		Maximum RCH	1322	0.7621	-0.25 to 0.49	0.03
	Sunset	**Mean RCH**	4253	***0.0005***	0.31 to 1.08	0.68
		Minimum RCH	3331	0.7011	-0.50 to 0.77	0.09
		Maximum RCH	4305	***0.0002***	0.46 to 1.49	0.94
Autumn	Midnight	Mean RCH	178	0.1344	-0.12 to 0.92	0.48
		Minimum RCH	127	0.2561	-0.25 to 0.78	0.32
		Maximum RCH	187	0.0755	-005 to 0.69	0.29
	Sunrise	**Mean RCH**	659	***0.0005***	0.97 to 1.86	1.51
		Minimum RCH	658	***0.0006***	0.67 to 2.02	1.47
		Maximum RCH	676	***0.0002***	0.98 to 1.85	1.50
	Noon	Mean RCH	189	0.1200	-0.09 to 1.66	0.96
		Minimum RCH	190	0.1159	-0.17 to 1.75	0.89
		Maximum RCH	167	0.4220	-0.83 to 1.61	0.45
	Sunset	**Mean RCH**	372	***0.0002***	-0.85 to -0.25	-0.57
		Minimum RCH	402	***0.0006***	-0.81 to 0.17	-0.51
		Maximum RCH	373	***0.0002***	-0.89 to -0.28	-0.55